UNIVERSITÀ DEGLI STUDI DI FIRENZE
DIPARTIMENTO DI INGEGNERIA INDUSTRIALE
Doctor of Philosophy in Industrial Engineering
CURRICULUM: Energy and Innovative and Environmental Technologies

A systematic study of thermodynamic energetic and environmental aspects of harnessing geothermal power plants

Candidate
Vitantonio Colucci

Supervisors
Prof.Giampaolo Manfrida
Prof. Daniele Fiaschi

PhD Coordinator
Prof. Giovanni Ferrara

PH.D. SCHOOL CYCLE: XXXIII, 2017-2020

Università degli Studi di Firenze, Dipartimento di Ingegneria Industriale (DIEF).

Alla mia famiglia

Abstract

Over the last years, the growing energy demand worldwide and the development of stringent international, national and regional regulations on polluting emissions have favoured the development of innovative energy systems in the field of renewable energy. In this context, geothermal energy, which boasts for a hundred years of exploitation systems of heat and hot water of the Earth, has returned to interest most of the nations for the optimization and efficiency of geothermal systems for the production of electricity and heat for a large part of the world population. The Tuscany region boasts its primacy in using geothermal energy thanks to the first high enthalpy exploitation experiment in Larderello in 1904, and in 1913 the first plant for the production of electricity from 250 kW up to the current value of 810 MW was built of installed power. Geothermal energy, having a simple operation, uses steam or biphasic fluids to represent the raw material to power the turbine. According to the geothermal fluid, there are three main types of geothermal power plants:

a. dry steam, the simplest technology that extracts steam from fractures in the ground and uses it directly to drive a turbine;
b. flash, a transformation of boiling and high-pressure water into steam which is expanded in a turbine
c. binary, water or steam are run alongside a second fluid with a lower boiling point than water; production of vapour and introduction into the turbine.

The whole process defines alternative and clean geothermal energy. "Clean" because it produces low emissions compared to the combustion processes of fossil fuel plants that emit CO_2 and fine dust while alternative because through other renewable sources (wind and solar in particular) they contribute to the production of electricity at "zero km", exploiting natural and renewable resources even in the most inaccessible places in the region.

But at the same time, some disadvantages can be solved thanks to scientific research. They are the presence of unwanted species in geothermal fluids with particular attention to carbon dioxide (CO_2), hydrogen sulphide (H_2S) and methane (CH_4) and rarely the presence of heavy metals such as mercury (Hg), Cadmium (Cd) and lead (Pb).

They are present at the moment of extraction from the geothermal reservoir and, in the absence of efficient abatement methods, throughout the process up to the cooling towers and the consequent reinjection wells.

The present study analyses and compares thermodynamic models (TM) on geothermal fluids containing unwanted species and salts. The work starts with the campaign to collect experimental data in the various sectors of applied thermodynamics. Thanks to the French research centre's contribution, IFP energies nouvelles (IFPEN), the most influential binary, ternary and quaternary mixtures that influence geothermal plants' processes, have been selected. Furthermore, more than a thousand experimental data were collected and subsequently selected thanks to the databases present in IFPEN and the scientific publications from 1918 to 2020.

The experimental data, filtered, verified in their congruity, and grouped by temperature, pressure and molality of the NaCl salt were the source of comparison with the results of the TM defined for a geothermal process.

Considering the variable composition of geothermal mixtures and the IFPEN team's experience, it was discussed which TM can obtain the best results of solubility and enthalpy, applicable in a subsequent work also for the transport properties (density, viscosity, thermal conductivity, diffusion coefficient). Furthermore, the work aims to

indicate which TM is the most appropriate in process simulation. The best choice of a TM depends on the percentage of the non-condensable gas components inside the geothermal fluid and dissolved salts. The performance of the TM depends not only on the kinds of reservoirs present in the world (Chapter 2) but also on the pressure and temperature conditions. Starting from the developed TM, their performances (Chapter 4) and the corresponding analysis (Chapter 5), the suggested TM for process simulation, for fluids without salts, are Sour Peng- Robinson (SPR) and OLI AQ for geothermal mixtures containing CO_2 and H_2S as the main components, while OLI MSE for geothermal mixtures containing CH_4, CO_2 and H_2S as main components. The presence of salt affects the choice of the TM. For this reason, the best TM is represented by OLI MSE SRK. From all the tested TM studied in this work, the modified version of the Duan-Sun model provides good agreement with literature data and, therefore, can be integrated into commercial process software like Unisim Design.

In a second step, three different geothermal plants were identified and analyzed:

a. Castelnuovo (Tuscany Region, Italy): an ORC-based geothermal power generation (5 MWe) with CO_2 reinjection prototype;
b. Hellisheidi (Iceland): double flash combined heat and power plant (303.3 MWe and 133 MWt);
c. Chiusdino (Tuscany Region, Italy): a standard power plant with a nominal capacity of 20 MWe connected to a district heating network, with a planned capacity of 7 MWth.

A thermodynamic package appropriate to the species present in the geothermal fluid was chosen for each geothermal plant. For some case studies, the following were applied:

- An economic evaluation of the main constituent components of the geothermal plant;
- An environmental feasibility analysis - Life cycle Assessment (LCA), particularly for two case studies on the Icelandic Hellisheidi geothermal plant.

The models and the data obtained by simulations made it possible to identify geothermal plants' methods. As a result, the choice of a thermodynamic model and the validation of the numerical results, which was among the main objectives of this work, can be reliably used for the accurate and optimized Geothermal power plants' design (GTPPs).

Therefore, this study showed that selecting a thermodynamic model for the GTTP process simulation defines the best way to optimize energetic and environmental performance processes.

Acknowledgements

In this three-year international PhD thesis in Industrial Engineering, many people, things and events have influenced my study and research path.

First of all, I would like to express my deep gratitude to Prof. Manfrida and Prof. Fiaschi for entering Florentine university and being part of their research group. Thanks to them, I increased my passion in research thanks to their advice, their teaching and research methodologies, and the opportunity to carry out part of my "Pegasus" international PhD program at the French research centre IFPen.

In IFPen, near Paris, I was placed in the department of Thermodynamics and in the team of Dr Eng Pascal Mougin. Together with Dr P. Mougin, I met Dr Angela Di Lella and Prof. Jean-Charles de Hemptinne.

I would like to thank Dr Angela Di Lella for her kindness and her availability during the various moments of the week.

I would like to thank Prof. Jean Charles de Hemptinne for his lessons in thermodynamics applied to industrial processes and for his valuable advice for the suitable selection of thermodynamic models for those like me who have used process engineering software for simulations over the years.

I would also like to thank Dr Angelo Damone for his patience and for the time devoted to the approaches to undertake during the thermodynamic numerical elaborations.

I also thank my colleagues in the laboratory for these years spent together.

My thoughts also go to the people outside the academic world, who have been a reference point for my life. First of all, to my family, whom I constantly see in my new job and who have been close to me in all the good and bad times. My gratitude goes to them, especially when they could not support us when the covid virus was in me.

Thanks to Eng. Alessandro Frassi, his family and Prof. Gabriele Pannocchia. I thank all my friends in Pisa for the various moments spent together in which only describing everything that has been passed together would publish a new encyclopedia.

Table of Contents

Chapter 1

Introduction

Table of Contents

The international scenario has recently been characterized by a significant demand for energy consumption, associated with a series of impacts on the costs of raw materials and environmental impacts. In this context, there is a growing encouragement in using renewable energy as a solution for new plants with advanced technologies to reduce the use of fossil fuels and improve current energy systems and their impacts on the environment.

Research on energy systems to produce alternative energy to fossil fuels has become increasingly relevant in recent years. These solutions also included all geothermal energy production plants.

The generation of geothermal energy represents a green sector, widespread at a regional and national level to produce electrical and thermal energy. Better investments in these plants' optimization and energy efficiency can be the growth vector of the local population's current energy and economic demand, even at a regional level. The need for industry regulations could further promote the efficient use of geothermal resources. To do this, it will be necessary to carry out scientific research applied to the reduction of emissions, the better exploitation of geothermal fluids and the optimization of plants with the use of advanced technologies for the economic saving of the entire production process and the protection of the environment and human health.

Appropriate thermodynamic models, process management and design and development of geothermal plants for medium-low enthalpy resources are industrial programs to be developed for the potential of the various geothermal resources present on the regional and international territory, also in combination with energy systems that produce energy from biomass, solar and wind.

In this context, this work focuses, even in a complex system such as geothermal resources and its different plants, on geothermal fluids analysis. The geothermal analysis concern thanks to the choice of the appropriate thermodynamic models to be applied to the simulations and optimization of industrial processes for energy efficiency and reduction of emissions into the atmosphere and underground.

1.1 Motivation

The application of a reliable thermodynamic package in the detailed simulation of a geothermal process could improve the design in the different types of simulation tools, enhance the production of electrical and thermal energy and ensure the right investments for maintenance, for the replacement of old technologies in newer more advanced ones and decrease the pollutants emitted from a traditional geothermal system. Therefore, it is of great interest to conduct a detailed research analysis for each type of geothermal fluid involved in the process and to provide the potential optimization and technological renewal to each characteristic geothermal power plants (GTPPs).

The interest of this work concerns both the plant aspects of the process concerned and social, economic, and environmental.

1.2 Objectives and structure

1.2.1 Objectives

The research project is part of the project of the Tuscany Region for international doctoral work concerning the issues on industrial-energy and environmental engineering that may have a social and economic interest at a regional level and according to the EU guidelines of the topics of innovative interest industrial and environmental.

The research project aims to define an attractive methodology for developing a rigorous simulation

model of geothermal power plants for energy efficiency, plant engineering, and emissions control.

The main objectives of the present research can be resumed in the following:

1) Define process inputs: research and select the most influential geothermal flows present at regional and international levels involved in the production processes of electrical and thermal energy.
2) Collection of experimental data on the different geothermal mixtures selected in point (1). Compare the experimental data under the same conditions of temperature, pressure and molality, eliminating those with unacceptable numerical variation;
3) define the thermodynamic models applicable to the species present in the thermodynamic fluid. Calculation of solubility and enthalpy residue at different conditions of temperature, pressure and molality. Compare the results of the thermodynamic model with the experimental result. With excessive variations, if possible, some equations and critical coefficients that define the thermodynamic fluid are modified;
4) Choice of the thermodynamic method and validation of its results when the results of the model are similar to the experimental data under the same operating conditions;
5) Validation of the output properties through the simulation of processes of real geothermal plants;
6) Exergo-economic, environmental characterization and application of the Life Cycle Assessment (LCA) of the most consistent case studies of this work.

Figure 1.1 Objective and structure of this PhD work

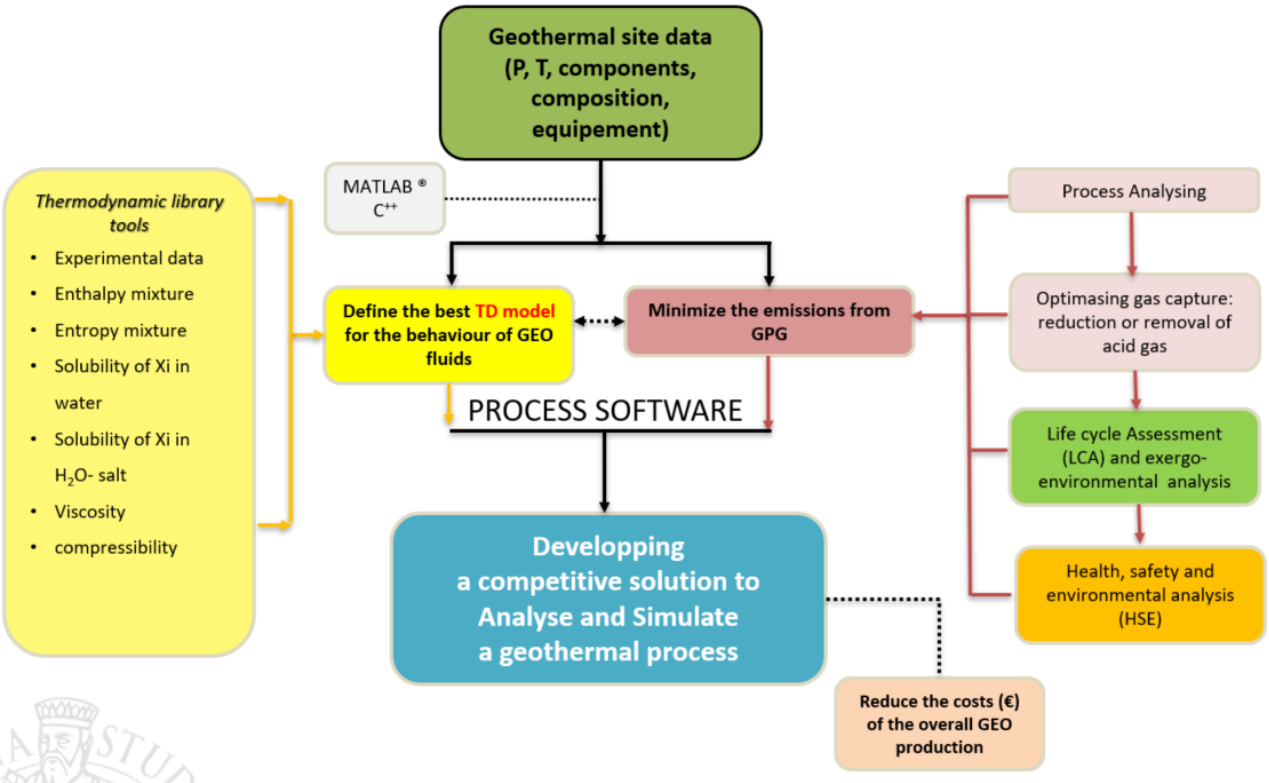

1.2.2 Structure

The thesis is comprised of five chapters, including the initial introduction chapter.

Chapter 2 is dedicated to the literature review, where the geothermal power generation is described in its differentiation and use in Italy, Europe, and some countries with strategic interest in exploiting geothermal resources. This is accompanied by the concept of sustainability for geothermal systems and comparison with other electricity production plants. Finally, the chapter highlights the typical characteristics of the geothermal fluid and the energy conversion systems for the geothermal sector.

Chapter 3 describes the thermodynamic models used in the study according to the methodology and practical guide taught by the IFPen team.

Chapter 4 is dedicated to the analysis of results. The obtained results are divided into three main sections. The first section deals with the experimental champaigns for CO_2-H_2O and CO_2-H_2O in brine, H_2S-H_2O and H_2S-H_2O in brine and CH_4-H_2O and CH_4-H_2O in brine. The second section depicts the solubilities analyses, and the last section displaying the mixing enthalpies analyses. In the end, there is an extensive table for the choice of a thermodynamic model for the temperature, pressure or salt molalities operative conditions.

Chapter 5 is dedicated to designing, economic considerations and Environmental analysis.

Conclusions

Chapter 2

Literature review

This chapter offers a brief overview of geothermal energy potential in Italy - Europe, and globally, highlighting the generation systems for producing electrical/thermal energy from the different geothermal fluids present in different areas of the Earth. Sustainability is one of the key factors in defining geothermal energy as sustainable.
The first part of the chapter briefly introduces some of the geothermal fluids' geochemistry, while the second part deals with current energy conversion systems. Finally, the chemical physics of fluids and the technologies that can be adopted allow us to analyze the present work's geothermal systems (Tuscany and Iceland).

List of Contents

List of Figures

List of Tables

Chapter 2 provides the initial and essential elements for the investigation of geothermal energy and its use to benefit the population.
The approach used is to identify the existing geothermal sources distributed globally, focusing at the same time on all the most important ones at the national and European levels. Through a global analysis of geothermal energy, it is possible to understand the possible benefits of geothermal energy from an environmental and sustainability point of view.
The heart of the chapter focuses on evaluating and interpreting geothermal fluids, their differentiation and their complexity when they contain a certain number of non-condensable gases (NCG) such as CO_2, H_2S and CH_4 and others when NaCl salt is also present. Therefore, the appropriate evaluation of geothermal fluid is the basis of a good specific thermodynamic model to be developed within different energy conversion systems. The latter analyzed here are single, double flash, organic Rankine cycle (ORC) and geothermal combined cycles
The highlighted analyzes lead to identifying the advantages and disadvantages of geothermal energy of existing geothermal plants, thus identifying the innovative contribution of this thesis in improving energy production.

2.1 Introduction

In this PhD research, the objective is to understand the importance of using geothermal energy in Italy and Europe as one of the alternatives energy sources which can supply base-load power, independent of climate and weather. The preview section shows that it is not distributed geographically, but its potential in many countries like Italy.
Therefore, the research analysis is to enhance and optimize a geothermal plant according to its location, reservoirs, the fluids in question and the best applicable technology thanks to the thermodynamic study of the geothermal fluid. Furthermore, it follows that the optimization of a geothermal plant, depending on the production capacity, can be accompanied by careful environmental and economic attention.
Today, the upgrading of large plants with a capacity of over 10 GW is of considerable importance, particularly in the countries of the European community. But, sometimes, the benefit of clean and renewable energy is confused with the destabilization of the territory that prevents larger power plants.

In geothermal power generation, most of the capital costs are incurred upfront in developing the resource. The major risks and challenges are related to the exploration, drilling and managing of the resource. So, the geothermal fluids are available in a wide range of temperatures and consist of steam, brine of various chemical properties and non-condensable gases.
In the literature, it is not easy to find an in-depth study on geothermal fluids in which the different geothermal chemical components are present at the different pressures and temperatures of the reservoirs and the entire process. One of the possible causes relates to the laboratory costs to thermodynamically analyze a geothermal fluid in its different characteristics that distinguish it in the various geographical areas.

Power conversion is the most predictable part of a geothermal project, as it consists of well-established engineering designs. Most plants use steam turbines, and about 20% [1] use the Organic Rankine Cycle (ORC). The economic exploitation of a geothermal fluid of given characteristics is achieved by choosing the power station configuration to maximize the exergy efficiency of the whole system (resource and plant) and not only the plant's thermal efficiency.

This research covers subjects dealing with the nature of geothermal energy resources, their utilization, conventional technologies, and future development. The chapters also highlight the greatest challenge in geothermal development thanks to the study of geothermal resources. As we see in the three case studies, the power conversion is the least uncertain part of a geothermal project but requires designs to ensure the economic exploitation of the resource over the designed life of the project. Optimization depends on how the power station configuration is adapted to the available resource.

The distribution of geothermal resources is uneven due to the uneven distribution of volcanoes, hot springs and manifestations of heat in specific places on the earth's surface. Thus, geothermal resources are a reflection of the underlying global, local geological and hydrological structures. The thermally richest resources tend to be concentrated in environments with abundant volcanic activity and tend to be controlled by plate tectonic processes or centres of diffusion evident as volcanic chains associated with subduction zones and hot spots. Local geological features favouring useful resources

include relatively shallow resource depths with high permeability in the rocks surrounding the resource and suitable resource fluids. For this reason, the bibliographic research and consequently the physical and chemical properties of the geothermal resource is one of the fundamental aspects of geothermal power plants. By studying the thermodynamic properties of fluids, it is possible to improve the conversion of geothermal energy. Geothermal power conversion is the technique used to convert the thermal energy content of the geothermal fluid into mechanical energy to drive a generator and produce electricity. It is the most predictable part of a geothermal project as it consists of a well-established engineering design.
Today, more geothermal power plants use steam turbines that operate on dry steam or steam produced by single or double flash or organic Rankine cycle (ORC) or geothermal combined cycles.
However, to optimize power generation beyond dry steam and flash steam plants, ORC cycles have been implemented over the past 15 years and will likely continue to grow as a standard technology driving the future development of geothermal resources.
Operational experience confirms the benefits of ORC power plants, not only for low-temperature liquid-dominated resources but also for some high-temperature resources where the brine is aggressive or the fluid contains a high percentage of non-condensable gas. Long-term environmental and resource management considerations justify the higher cost of installing these economically feasible systems.
However, to optimize power generation beyond dry steam and flash steam plants, ORC cycles have been implemented over the past 15 years and will likely continue to grow as a standard technology driving the future development of geothermal resources. Therefore, one of the case studies in this PhD research shows the Best Available Technologies (BAT) of an ORC cycle. The scientific literature confirms that the advantages of ORC power plants are not only for low-temperature resources dominated by the liquid but also for some high-temperature resources where the brine is aggressive, or the fluid contains a high percentage of gas not condensable. Long-term environmental and resource management considerations justify the higher cost of installing these economically feasible systems.

From the concept of *sustainability and renewability* of geothermal systems and the relationship between renewable and sustainable capacities, it is possible to estimate a geothermal system's commercial, sustainable, and renewable capacities. In this case, *sustainability* for a geothermal process is defined as the ability to install and economically maintain the energy capacity for the entire amortized life of a power plant and the drilling of "trick" wells as required to compensate for resource degradation. *Renewability* is defined as maintaining an installed power capacity indefinitely without undergoing any degradation of resources. Typically, the renewable energy capacity at a geothermal site is too small for commercial development of electricity capacity but may be adequate for district heating or other direct uses of geothermal energy. The latter aspect was addressed with the case study of the Hellisheidi geothermal plant.

The *cost of production* for geothermal electric generation is important. In particular, the balanced cost of power is the applicable measurement for the cost of geothermal energy. Unlike fossil fuel power plants, most of the capital costs are incurred upfront in resource development. Therefore, power cost is an objective criterion that favours geothermal solutions compared to other alternative energy sources. However, the costs are heavily tied to the resource and the need for makeup well drilling to maintain full generation capacity over the planned period of operation to provide an adequate return on investment.

Figure 2. 1. Research and investigation on Geothermal Energy in this PhD thesis

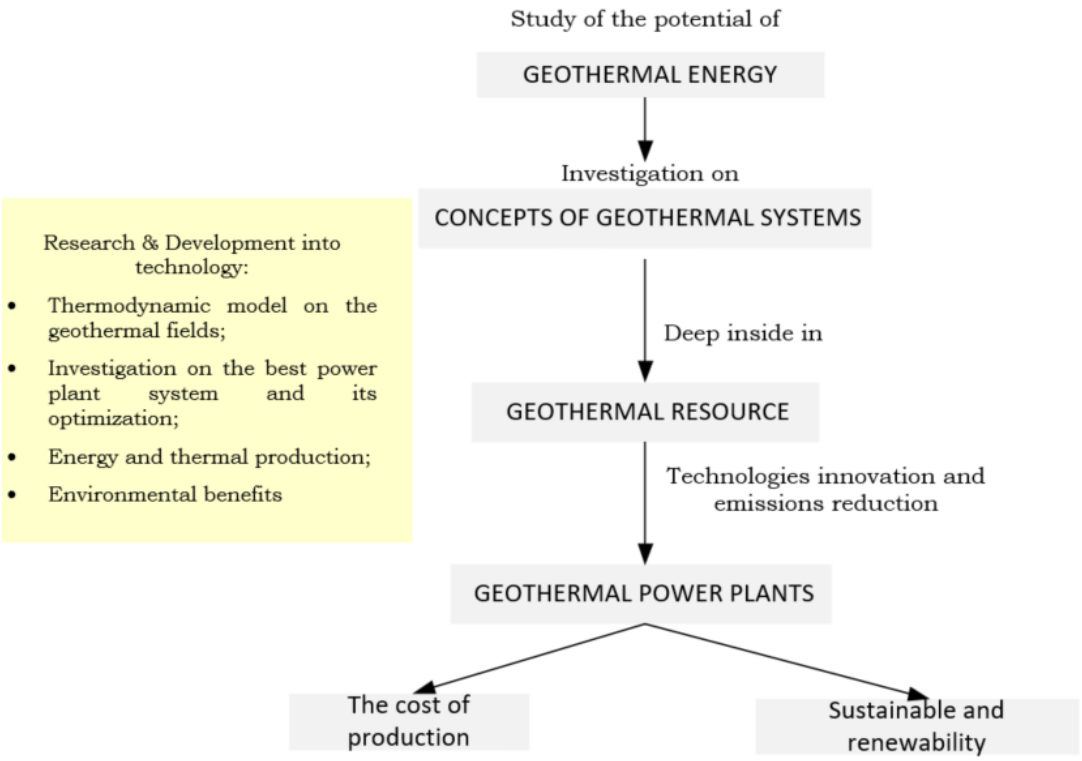

2.2 Overview of geothermal resources

The accessibility of energy is one of the most critical aspects of the development of any society. A significant portion of the energy comes from carbon, oil and natural gas to produce electricity. But, these primary fuels are limited and to a rapid depletion of resources. The energy consumption figures change over time, depending on the consumption model. Unlike the current pandemic situation, energy demand is expected; it will increase over time. From 1990 to 2050, up to 275% of 1990 demand use [2]. To better manage energy demand, it is possible to introduce renewable energy technologies to replace conventional fossil fuel technologies.

Geothermal energy is one of the most important renewable energies available, an alternative to fossil fuels. Its peculiarity is that of being the only alternative energy source capable of providing the baseload, independent of the climatic conditions compared to wind and solar energy. Although not evenly distributed geographically, geothermal energy's potential is very important, especially for actively pursuing research and development in technology such as Engineered Geothermal Systems (EGS). Geothermal power is utilized around the world. The total world geothermal power resources reached 12.7 GW in 2014, mainly from low and medium temperature sources [3]. A geothermal increase is 10% since 2010. Figure 1 illustrates the growth of geothermal technology from 1995 to 2020 [4].

Figure 2. 2. Installed capacity of geothermal power worldwide with the installed capacity for the year 2020 [4].

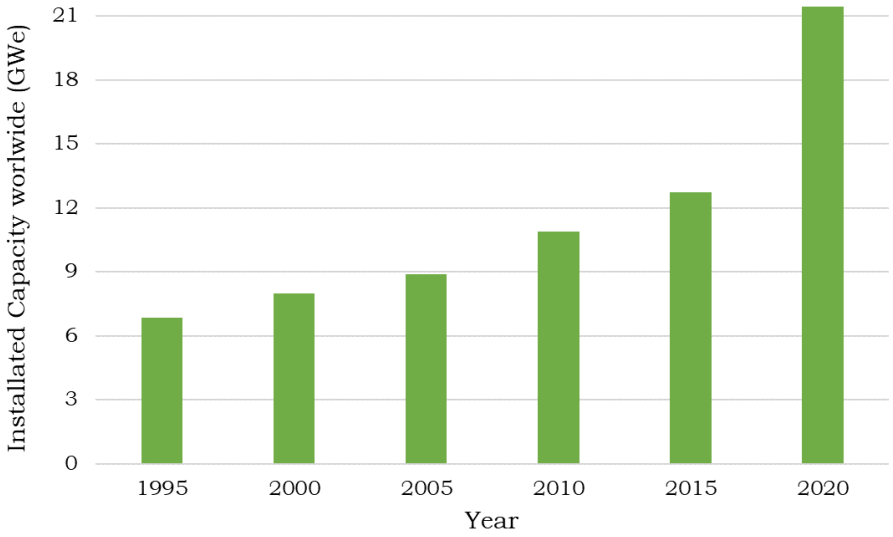

Recent studies present the linear trend of about 350 MW per year from 2020 to 2014, intending to claim 21 G.W. of power capacity by 2020 and 140 GW by 2050. With these values, geothermal would cover 8.3% of the world's energy production and meet the energy needs of 17% of the world's population, with 40 countries generating 100% of their energy from geothermal sources, such as Iceland [5]. Then, geothermal technology can eliminate over 1000 million tons of CO_2 from the atmosphere annually. Another study depicted a more conservative figure where 3% of power generation and 5% of heating load are supplied by geothermal resources in 2050 [6]. The major barrier to applying geothermal technology lies in finding the proper location and technology for extraction. Their play type often classifies geothermal resources. The geothermal play type assists in understanding a potential resource and defining exploration strategies to aid in evaluating a reservoir in terms of its potential use.

Two main types of geothermal are convection-dominated play and conduction-dominated play. The ratio of the porosity to permeability is the key aspect to recognize the type. The geothermal play seeks to define geothermal potential on the characteristics of the material instead of the temperature and enthalpy of the fluid, while the goal is to use a geothermal play type with a more accurate identification resources in the future [7]

The purpose of studies in renewable energy, respectful of the environment, of the cost-effectiveness of production/products through the use of increasingly advanced technologies is to satisfy the world's energy needs, especially due to the growing demand for energy from new countries development, usually located in Asia and South America. But, unfortunately, when it talks about renewable energy, it often thinks that this energy has zero or lower emissions than oil and natural gas.

Even in this thesis, it will be possible to highlight some positive traits of geothermal energy as, at times, plant modifications or installations of new geothermal plants are subject to criticism at the local level. Public opinion evaluation of geothermal energy indicates that people lack information on geothermal technology. The media and the European public projects (*Horizon 2020*) can educate people on geothermal power technologies.

The geothermal resources of the Earth are extremely large. The part of geothermal energy stored at a depth of 3 km is estimated to be $4.3 \cdot 10^8$ EJ[1] [8]. The small part (< 1%) corresponds to the currently available share and is extracted using existing technology that was 16424 TWh[2] in 2004 and grew up to 30364 TWh in 2030 [9]. Geothermal resources are larger compared to all fossil fuel resources, that correspond to [9]:

- Oil: 8062 EJ or 223900 TWh;
- Natural gas: 6678 EJ or 185500 TWh;

[1] 1 EJ= 10^{18}J. The EJ is usually used for the source of the geothermal energy is the Earth's internal heat.

[2] 1 TWh = 1 billion kWh. This unit of energy is used to measure the electricity production of a power station (a few TWh) or national production (around 400 TWh for French nuclear production). Source: https://www.asn.fr/Lexique/T/TWh.

- Coal: 21634 EJ or 600900 TWh.

Of this data, only a small part of the geothermal energy resources can be tapped, such as low-enthalpy wet geothermal systems[3] (WGS) such as enhanced geothermal systems[4] (EGC). They use advanced heat exchanger technologies that reduce the minimum fluid temperature required for power generation for both cases. Thanks to the advanced exploration methods, the world geothermal resources will remain available for future generations long after the oil decreasing exploitation. Continuous development of innovative drilling and power generation technologies makes this source the best future option available to meet the world's required electricity demand, reduce greenhouse gas emissions, and mitigate global climate change. Then, the enthalpy geothermal resource is the keystone for the energy development of a geothermal plant. The potential of low enthalpy geothermal resources with temperatures less than 473.15 K, which are suitable for electricity generation, is much higher than that of high-enthalpy resources (> 473.15 K) since these reservoirs are widespread and occur at shallow depths.
These reservoirs include shallow wet geothermal systems surrounding high-enthalpy systems and low-temperature conduction dominated enhanced geothermal systems. Figure 2.3 shows the high and low enthalpies worldwide.

The classification of countries with commercial geothermal power generation with installed geothermal capacity (MW) and geothermal electricity generation (GWh) and share of total national electricity production in 2014 is described below [3], [10]. The nations with the highest exploited geothermal energy are listed:
For Europe:
- Iceland (202 MW, 1483 GWh and 17.2 %);
- Italy (791 MW, 5340 GWh and 1.9%);
- Portugal, Azores (16 MW, 90 GWh and 0.1%)

For North America:
- USA (2564 MW, 17917 GWh and 0,5 %);
- Mexico (953 MW, 6284 GWh and 3.1 %)

For Africa:
- Ethiopia (7.3 MW, o GWh and 0 %);
- Kenya (129 MW, 1088 GWh and 19.2 %)

Figure 2. 3. Distribution of high- and low- enthalpy geothermal resources along plate boundaries and active volcanic zone. Source: [11]

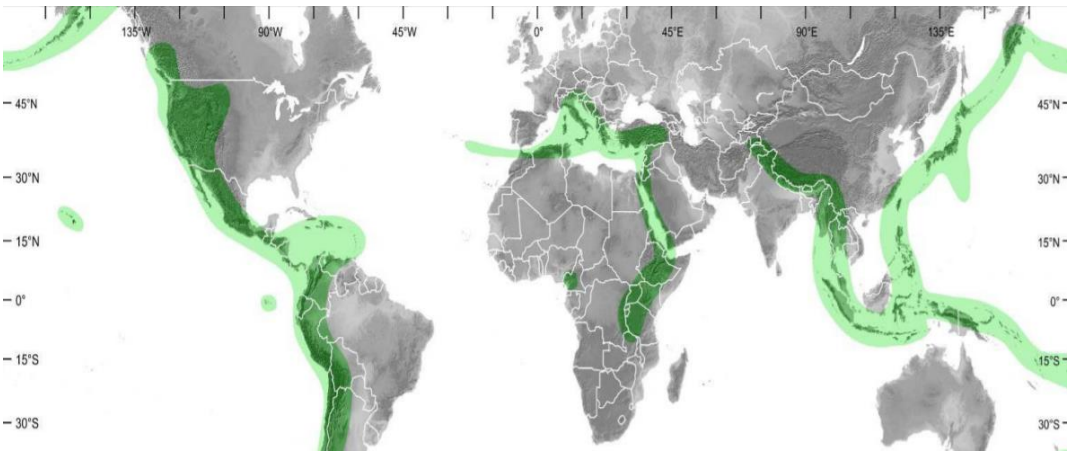

[3] There are two types of geothermal field. The first is the *wet* (or "liquid dominated") field which produces water under pressure at temperatures over 373.15 K. On reaching the surface, the pressure is reduced, and part of the water is "flashed" to steam, leaving a larger fraction as boiling water. The second is the *dry* (or "vapor dominated") field, which produces dry saturated, or superheated, steam at pressures higher than that of the atmosphere.

[4] A naturally occurring geothermal system, known as a hydrothermal system, is defined by three key elements: heat, fluid, and permeability at depth. An *Enhanced Geothermal System* (EGS) is a man-made reservoir, created where there is hot rock but insufficient or little natural permeability or fluid saturation. In an EGS, fluid is injected into the subsurface under carefully controlled conditions, which cause pre-existing fractures to re-open, creating permeability. Increased permeability allows fluid to circulate throughout the now-fractured rock and to transport heat to the surface where electricity can be generated. https://www1.eere.energy.gov/geothermal/pdfs/egs_basics.pdf

Low-enthalpy geothermal resources are yet to be exploited intensively in developed countries, particularly in Iceland and North America, for electricity generation. Simultaneously, the high-enthalpy resources in developing countries are not exploited to the extent that they could be [12].

Geothermal systems can be classified based on their association with the tectonic regime in different geological domains. Most of them are cycling systems with rainwater as the main carrier of heat from the deeper parts of the Earth to the surface. Depending on the local geological and thermals regimes, the systems could be steam-dominated or liquid-dominated. These systems should be accessible at reasonable depths with sufficient geothermal fluids to sustain long productivity.
High-temperature hydrothermal systems are restricted to plate boundaries and active volcanism areas, while low-enthalpy resources are available in various geological and tectonic settings.

In most developing countries, the geothermal potential is not well known, particularly the low-enthalpy resource's potential. This is because they are not considered economically viable for electricity generation. However, this has been true in the past. But the technological advances made in heat exchangers and drilling methods urgently call for all countries to evaluate low-enthalpy resources. Fridleifsson [2] developed a method that uses active volcanoes' distribution and their correlation to the geothermal activity to assess the high-temperature geothermal resources. The electricity generation from UARB (*Useful Accessible Resource base*, less than 3 km deep) in a specific country is correlated to the number of active volcanoes through the following equation:

$$Producible\ electricity\ from\ UARB\ (TWh/year) = 9.4 \cdot number\ of\ active\ volcanoes \quad (2.1)$$

where *9.4* is a correlation factor for the USA, Iceland, Italy, Indonesia, Japan, New Zealand and Mexico.

For this equation, the world potential is about $12 \cdot 10^3$ TWh/year. To assess the low-temperature potential, Fridleifsson[2] indicates that the world's low-enthalpy geothermal resource potential is about $60 \cdot 10^4$ EJ for the direct use that corresponds to a power generation of about $16.56 \cdot 10^8$ TWh.

According to their electricity generation suitability, Stefansson et al. [12] estimated the geothermal resources using conventional and binary fluid technology. His studies indicated that geothermal fluids with a least 273.15 K would double the energy available for electricity generation from $11.2 \cdot 10^3$ TWh/year using conventional technology to $22.4 \cdot 10^3$ TWh/year using conventional and binary technologies. Table 2.1 shows the geothermal energy potentials in the regions like Europe, North America and Africa.

Table 2. 1. Regional geothermal energy potentials

Region	Known Geothermal potential [TWh/year]	UARB	
		Electricity [TWh/year]	Direct Use [E.J.]
Europe	97	2030	105035
North America	200	1482	75555
Africa	101	1354	146936
Region	High-temperature electricity production [TWh/year]		Low- temperature; direct use [E.J./year]
	Conventional technology	Conventional and binary technology	
Europe	1830	3700	>370
North America	1330	2700	>120
Africa	11200	22400	>1400

Based on Table 2.1, it is possible to see that the potential of geothermal energy resources, especially the low-enthalpy resources, is vast.

Low and high-enthalpy geothermal resources suitable for power generation are "underutilized market opportunities." The lack of development is due to regulatory, institutional, economic and financial barriers. These barriers exist even though low enthalpy resources are available throughout the year and have considerable social, environmental and economic benefits for all the countries, particularly for Europe, the USA, China, India and Brasil.

Compared with the alternative of fossil fuels and other renewables (wind, photovoltaic and

hydropower), geothermal energy has substantial advantages in a social context. The most important point is that it is a clean source of energy for all countries. It isn't easy to define the limits and advantages of the investors and public entities in geothermal financing, which are sometimes obstacles to increasing geothermal production.

The countries could break down these barriers to exploit the potential gains of geothermal energy by increasing geothermal resources applications for electricity generation. The European policies integrate geothermal energy in their development plants, and many decisions are not made exclusively from a market point of view. Growth and optimization of geothermal energy production can be improved by preparing an extensive national energy plan to develop regions with geothermal potential and reduce the costs of using new performing technologies. By encouraging research and development in new technologies and optimizing production efficiency, it is possible to reduce pollution and, therefore, reduce, inherent for some industrialized countries, of the "carbon tax". The social advantage of "clean energy" thus become visible.

So, geothermal sources' real potential, such as renewable energy sources in general, is to satisfy an increasing percentage of the fast-growing energy demand, thanks to overcoming economic obstacles associated with geothermal projects and promoting geothermal energy and other clean energy sources.

Modern geothermal power plants have the marginal benefits of clean energy production, especially in the costs and environmental benefits; the latter is missing in the plants of a few decades ago.

So that new plants can be built or revamps developed, it is necessary to introduce incentives for private investors and public electricity institutions and their financing entities to obtain the required international loans.

Since 2020, regulations, laws and market instruments are being developed to promote renewable energies through the "bonus", despite the current low oil prices. Without incentives, investors could select projects with the highest benefits from purely market-economic value. Private investments are very important due to the high costs and risks of exploration, particularly in the high initial costs of developing a geothermal field.

It is essential to find appropriate private investors' incentives, to make private investors follow social interests. However, a review of geothermal energy production's economic properties indicates that private investors may be reluctant about developed development in developing countries. This is because, still, high capital costs make the economy of geothermal energy plants more vulnerable to uncertainties in the energy market and technology performance than alternative plants. The uncertainty about the geothermal plants' technology or performance is larger concerning conventional energy production. It is well known that this uncertainty significantly determines the choice of technology. But, the Kyoto protocol [13] may be the crucial instrument to encourage the clean development mechanism (CDM) for geothermal energy. So, the uncertainties might be reduced thanks to the management and coordination of CDM projects.

Finally, capacity building and popularization of geothermal energy could create awareness and acceptance by politicians and decision-makers. Therefore, there is a need for institutional strengthening, human resources formation and consideration of geothermal projects (CDM/ Horizon 2020) as opportunities by lowering electricity generation costs.

The applications of all these measures would improve the economic and sustainable development of the countries and regions, including the social development of the world's poorest countries.

2.3 Geothermal fluids

Geothermal fields are found worldwide in various geological settings and are increasingly being developed as an energy source. Each of the different geothermal systems types has distinct characteristics reflected in the geothermal fluids' chemistry and potential applications. However, they all have a heat source in common at a few kilometres depth, and it is this which sets water, present in the upper sections of the Earth's crust, into convection [14]. The geothermal resources are used for heating applications and to generate electricity through the production of steam. Since aqueous geochemistry is involved in the exploration, evaluation, and production phases of a geothermal plant field, understanding fluid chemistry is essential for developing a resource. The chemistry of water and geothermal gases contains important information on the hydrology of the field and the conditions in the basin.

Furthermore, the study of fluid chemistry is necessary to define and choose the thermodynamic models needed for different geothermal systems. The magma presents a few kilometres away enters some cracks in the rainwater reservoir, heating the fluid and, through convective motions, the water-rock interaction is one of the causes which determine the chemical characteristics of geothermal fluids. Figure 2.4 denotes various chemical constituents present in the magma mix with the circulating

geothermal fluids with magma's intrusion. The percolating rainwater reacts with the "host rocks" and mix with magmatic fluids, giving rise to different chemical types of geothermal fluids.

Ascending geothermal fluids mix with shallow groundwater and modify their chemical composition; the isotherms' position and lateral extension depend on the magma chamber's volume or the intrusion [15]. Thus, these chemical components provide vital data to evaluate reservoir characteristics, temperature and other crucial information during the pre-drilling exploration phases of geothermal resource development.

Figure 2. 4. Typical geothermal system. Source Chandrasekharam and Bundschuh [11]

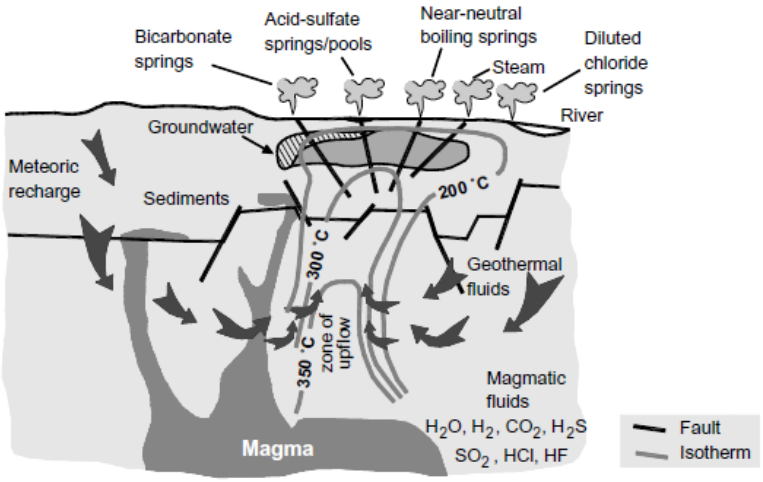

Geothermal fields are classified based on the state fluid such as liquid or vapour dominated, low or high temperature, sedimentary or volcanic-hosted.
The classifications are:

- *Reservoir equilibrium state*: It is a fundamental division between geothermal systems because it is based on the circulation of the reservoir fluid and heat transfer mechanism. The dynamic equilibrium systems are recharged by water entering the reservoir. Indeed the water is heated and discharged out the reservoir or to the surface. Heat is transferred through the system by convection and circulation of the fluid. On the other hand, the static equilibrium systems have only minor recharge to the reservoir, and heat is transferred only by conduction.

- *Fluid type*: The reservoir fluid is composed mainly of liquid water (liquid dominated) or steam (vapour dominated). An example of liquid dominated is Castelnuovo Val di Cecina. In some reservoirs, such as in Hellisheidi, Island, both steam and liquid water exist in varying proportions as two-phase zones. Liquid-dominated systems are the most common, and they contain a steam cap. Systems that discharge only steam are rare in Larderello, Chiusdino and Bagnore 3-4.

- *Reservoir temperature*: The temperature of geothermal reservoirs is an important factor in fluid chemistry and potential resource usage. Systems as a low-temperature (T< 423.15 K) or high-temperature (> 453.15 K). Generally, an intermediate temperature reservoir is 393.15-453.15 K range.

- *Host rock*: the rocks which contain the geothermal reservoir react with the geothermal fluid. The rock-fluid reactions determine the final composition of the geothermal waters and gases. An important distinction is made between volcanic and sedimentary (clastic or carbonate) rocks.

- *Heat source*: the heat source for the system is a function of the geological or tectonic setting. If the magma provides the heat flux, the system is volcanogenic, and it has high temperatures. When the heat flux is not supplied by magma, the geothermal system is generated by tectonic activity.

Other classifications are:

- Dynamic (convective) systems

High-temperature systems: the geothermal gradient is several times above the crustal average of 30 °C/km and the rock temperatures up to a hundred degrees Celsius at few kilometres depths. The geothermal fields' locations are tectonically controlled, and they are often found in areas of block faulting with reservoir depths of around 1-3 km. High-temperature systems are often volcanogenic. Hot fluids discharge chloride waters with a total dissolved solids (TDS) concentration of 3000÷5000 mg/l. Regarding Castelnuovo (Tuscany, Italy), its TDS concentration is about 25 mg/l, for Chiusdino (Tuscany, Italy) is 30-33 mg/l, while Hellisheidi (Island) has a high TDS concentration of more than 3000 mg/l. Silica sinter is often deposited around boiling or near-boiling springs. Saline or brine fields form crucial for most geothermal power plants. High-temperature systems with a non-volcanogenic or tectonic heat source are few common. They occur in tectonically active areas and not active vulcanism like Larderello and Tuscany region. In this case, Minissale [16] demonstrated that the Larderello area shows many characteristics typical of a static (conductive) system.

Low-temperature systems: Low-temperature or low-enthalpy systems can occur in various geological settings of elevated and normal heat flow. The deep circulation of fluid through faults or permeable layers, the tectonic uplift of warmer rocks from the depths, can produce low-temperature fields. This aspect defines low-temperature geothermal energy, a topic of interest for many European and Asian countries in recent years. Low-temperature systems discharge dirty water, with a TDS of approximately 100 mg/l or less, through hot springs at temperatures ranging from 303.15 to 343.15 K. Many of these springs deposit minerals have retrograde solubilities like calcite and gypsum but with very low silica values. All of this depends on rainwater formation, which may contain salts from 1 to 6 molality. Another aspect is the waters from reservoirs composed of marine clastic sediments, particularly shales, which often have high chloride, boron, and carbon dioxide concentrations.

- Static (conductive) systems

Static systems are typically found in layers deposited in deep sedimentary basins. The fluids result from the formation of water trapped within the thick sedimentary sequences. These waters reach reservoir temperatures of around 343.15- 423.15 K at a 2-4 km depth and are therefore low-temperature systems. The fluids are typically chlorinated water or very saline brines, which get trapped, such as vertical permeability is low within formations until it is released tectonically or by drilling. Some examples are present in Eastern Europe and Turkey. This section includes the geo-pressurized system, present in particular in the Gulf of Mexico and USA areas. Such systems are found at depths of 3-7 km and consist of permeable sedimentary rocks within impermeable layers with low conductivity. Under these conditions, the heat and fluids within the permeable layers can not be expelled during compaction. Therefore, they are trapped in the system. As a result, the fluid pressure approaches the lithostatic pressure, far exceeding the hydrostatic pressure. These systems also contain high quantities of methane, and therefore these fluids are also significantly studied for the recovery of the fuel itself.

2.3.1 Classification of geothermal waters

Early geothermal studies showed that magmas were the source of heat, water and solutes in geothermal systems. However, in the last twenty years, an accurate model shows that fluids are predominantly meteoric and that solutes arise from water-rock reactions [17].
Therefore, it is believed that the rock-water reaction is the main source of many of the solutes, although they can also be made by mixing formation waters, seawater, or magmatic brine. However, there is no doubt that geothermal fluids are predominantly of meteoric origin and that 5-10% of geothermal waters come from an alternative source, perhaps a magmatic brine. Also, mixing with a small amount of magmatic brine would significantly affect the chemistry of the final geothermal fluid determinations, and the isotopes cannot ignore a magmatic contribution subsequently diluted by rainwater [18]. A mass balance indicates magmatic brines rich in solutes such as Cl, SO_2 and CO_2.
The evolution of geothermal fluids can be summarized as follows. Rainwater penetrates the crust permeable zones and circulates at depths of about 5-7 km. As they descend, they are heated, react with the host rocks and rise by convection. These deep waters are the main geothermal fluid chloride, and all other types of geothermal water are derived directly or indirectly from these chlorinated waters. In-depth, the fluids typically contain 1000 - 10,000 mg/l CI at temperatures of approximately 623.15 K. The soluble elements are the first to be leached from the host rocks by the waters, followed by other elements controlled by temperature-dependent reactions. These reactions change the host rocks' primary mineralogy into a characteristic alteration of the fluid's characteristic assembly and

temperature. In particular, the chlorinated fluids that leave the tank and rise to the surface can boil to create a two-phase boiling zone (vapour + liquid). Residual chloride water can discharge to the surface in hot springs or travel sideways to emerge many kilometres from the upflow zone finally. Vapours from this boiling zone can migrate to the surface independently of the liquid phase and discharge as fumaroles. Alternatively, the vapours can dissolve in groundwater or condense in colder soil to form water heated with steam, acid sulphate or bicarbonate [19].

As a geothermal fluid rises to the surface, the pressure exerted on it by the overlying water column decreases. The pressure drops to a level that allows the dissolved gases and vapour to separate from the liquid phase. This phase separation is one of the most important processes that control the liquid and steam discharges' chemistry. Haas [20] illustrated the relationship between boiling point and depth. He shows the depth at which a reservoir fluid at a given temperature will commence boiling. From this depth, the two-phase zone can extend upwards towards the surface. The curve assumes that only hydrostatic pressure acts upon the fluid. It has been found that hydrodynamic pressures exist at depth in a geothermal system at about 10% above hydrostatic [21], [22]. This excess pressure is necessary to maintain flow through the system. Hot water buoyancy creates it relative to cold water recharge and a hydrostatic head in recharge waters from greater relief areas [14]. Increasing water salinity lowers water vapour pressure, raises the curve, and prevents boiling until shallower depths are attained [23].
However, for most geothermal systems, the fluids are dilute, and small changes in salinity will not significantly alter the boiling point-depth profile of the system. More important, however, is the gas content of the fluid. Several wt% gases in the fluid depress the isotherms in a system below the usual boiling point-depth curve. The boiling zones in high-gas systems appear at much greater depths than in low-gas systems, which follow the relationship for pure water. This boiling point depression is caused by an increase in the fluid's vapour pressure, which is created by the additional pressure of the dissolved gases. A higher gas content requires a higher confinement pressure to prevent gases from escaping from the solution. Production from a gas-rich field can rapidly depressurize the system as gases are removed from the fluid, and this pressure drop can allow cold groundwater to enter the field. The boiling leads to a reduction of the residual liquid temperature since the vapour separation involves mass and enthalpy losses. Groundwater dilution and conduction are the other two main processes that lower the fluid temperature. Diluted fluids can never reach boiling point before being discharged to the surface.

The major systems are liquid-dominated, and they commonly have a magmatic heat source at depths of 8 km. The magma is convective to keep the upper sections fused, thus providing a continuous heat source to drive the geothermal convection system. The dynamic nature of the system is shown by the cycle - meteoric water descent, geothermal fluid formation (replenished by meteoric waters descending from the recharge zone) and surface discharge of geothermal waters and vapours through springs and fumaroles. It is possible to display lateral flow structures created by the hydraulic gradient in the liquid-dominated systems. Many systems show lateral flow structures created by steep hydraulic slopes. They are formed due to the high relief, having low horizon surface permeability. Conduction cooling and mixing of groundwater are reflected in the chemistry of the sewage. Lateral flows near the surface can extend for several kilometres. This is remarkably extensive in high mountainous terrain (> -1000m), typical of andesitic volcanoes, where flows are 10-50 km in length. Pools of chloride water characterize the low-relief systems (Figure 2.5). The deep geothermal fluid can attain the surface because of the gentle topography. Two-phase or steam zones are present but are not as thick as in high-relief systems. These steam zones can increase in depth when fluid removal on the system's exploitation exceeds natural fluid recharge. Oxidation of hydrogen sulphide gas in the steam, with the condensation, produced acid sulphate waters. While the condensation of carbon dioxide, less soluble than H_2S, produces bicarbonate-rich waters found on the margins of the field.

Figure 2. 5. The conceptual structure of liquid-dominated geothermal systems

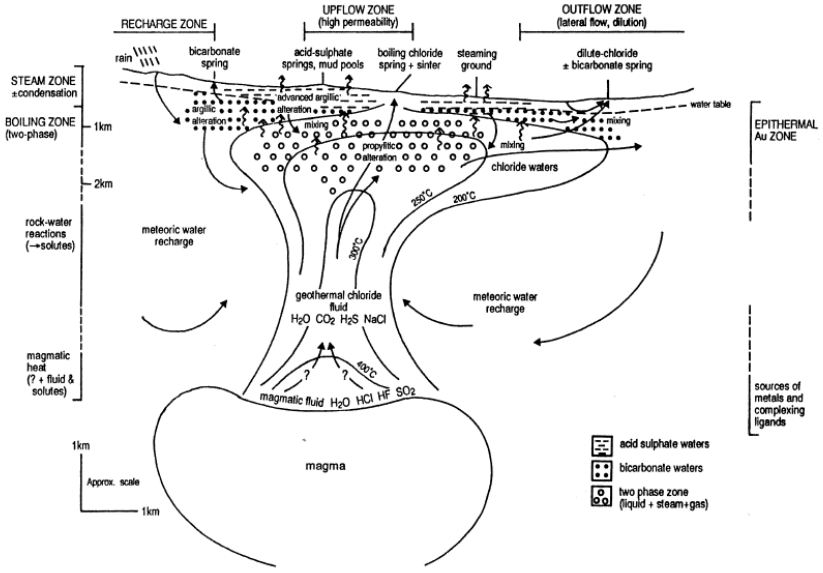

The high-relief systems are characterized in vulcanic islands, and the steep topography prevents the chloride fluid from reaching the surface (Figure 2.6). The chloride fluid can be diluted with groundwater or mix with descending sulphate waters and steam condensates. These acid waters are produced in a two-phase zone, often several hundred metres deep, where steam condenses or mixes with groundwaters.

Figure 2. 6. The conceptual structure of liquid-dominated geothermal systems in a high-relief setting.

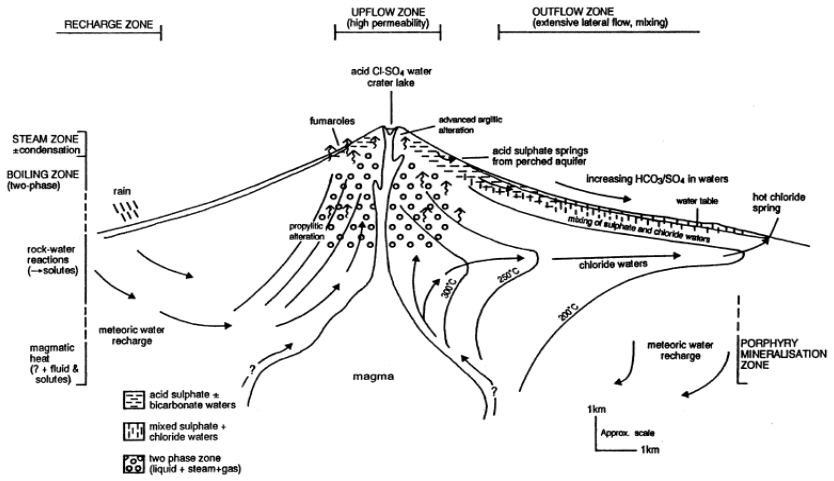

Fumaroles, steaming Earth, and hot springs of acid sulfate water are the typical discharge characteristics of these systems. The tank comprises steam (with gas), although the saline boiling water that feeds the steam into the tank probably occurs deep. Vapour-dominated reservoirs exhibit a relatively constant temperature with depths of about 509.15 K (the maximum enthalpy temperature of saturated vapour). The tank's pressure profile is controlled by vapour (static vapour) and is similarly relatively constant with depth. The system is convective with the ascending flow of steam rising from the depth and flowing laterally along the base of the roof's low permeability rocky horizon. The vapour cools as it flows eventually; it condenses and descends into the deep tank for recirculation. Since less soluble gases remain concentrated in the vapour phase more readily than more soluble gases, the vapour changes' chemistry changes with lateral flow and condensation. The oxidation of hydrogen sulfide in the vapour can produce acid condensates that dissolve the host rock, increasing the steam tank's size as the system matures. Vapour-dominated systems are much less common than liquid-dominated systems, and among these, a greater number of Tuscan geothermal systems have been well characterized (Figure 2.7).

Figure 2. 7. The conceptual structure of vapour-dominated geothermal systems.

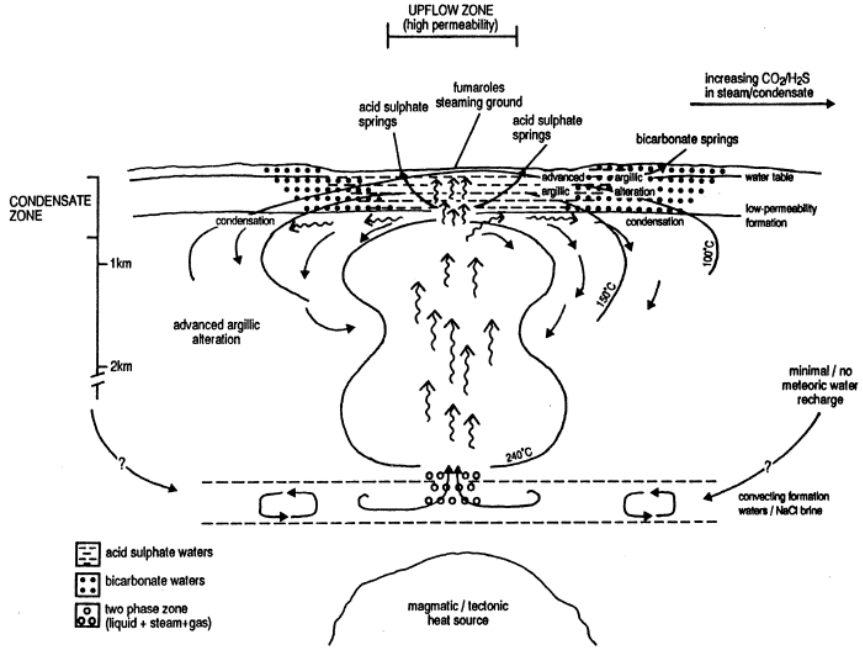

2.3.2 Processes affecting water composition

This section examines the chemical and physical processes that influence the composition of the geothermal fluid in the reservoir and ascends to the surface. The chemical processes focus on mineral-fluid reactions, both dissolution and deposition, while the dominant physical process is boiling, in addition to the importance of cooling and mixing.

For the mineral-fluid equilibria, various data analyses demonstrate that the commonly dissolved constituents in the deep chloride reservoir fluids fall into two groups based upon their solubility behaviour:

- *Soluble group species* (Cl, As, Br, B, Cs) quickly pass into solution. These tend to remain in solution, and they are unreactive species. This is true for Cl, but other species can be involved in near-surface reactions [24].
- *Common rock-forming species* (Na, SiO_2, K, Ca, Mg). Their solubilities are controlled by temperature-dependent mineral-fluid equilibria and only enter the solution after altering the host minerals.

The reactions that occur are a function of the geothermal system's temperature, pressure, salinity, and host rocks. There are two kinds of competitive reactions to be considered: salt precipitations and ion-exchange equilibria.

The solubility reactions determine how much a particular species can enter and remain in solution before precipitation occurs. The temperature is the dominant control on mineral solubility in geothermal systems, but changes in pH, pressure, or salinity can also affect it.

Silica and calcite equilibria are important because the amount of SiO_2 and Ca govern in solution.

The solubility of any silica mineral is:

$$SiO_{2\,(s)} + 2H_2O_{(l)} = H_4SiO_{4(aq)} = H_3SiO_4^-{}_{(aq)} = H_3SiO_4^-{}_{(aq)} + H^+_{(aq)} \quad (2.2)$$

and the solubility constant is given by

$$K_{SiO2} = \alpha_{H4SiO4} \quad (2.3)$$

Calcite generally is not found in some fields where the temperature exceeds 300 °C. The solubility of calcite is:

$$CaCO_{3\,(s)} + H_2O_{(l)} + CO_{2(g)} = Ca^{2+}_{(aq)} + 2HCO^-_{3(aq)} \quad (2.4)$$

Calcite solubility, therefore, increases with increasing P_{C02} [25], [26].

The Ion-exchange reactions involve the transfer of ions between two or more aluminosilicate minerals and control cations' ratios in solution, including H^+. It means a silicate mineral assemblage can buffer that solution pH.

Table 2. 2. Typical chemical composition ranges of geothermal fluids[27]

Gas component	(vol %)
CO_2	≈ 67 - 95
H_2S	≈0.08-2
H_2	≤ 0.5
CH_4	≈0.04-4.6
N_2	≈1.12-13.5
O_2	≈0.01-1.3

2.4 Energy conversion systems

This section aims to describe the details of geothermal energy conversion into electricity after the geothermal fluid examination. First, here is described the role of the arc of the life of the geothermal fluid. Then, it explains the processes needed, starting from the reservoir and ending with the geofluid disposal after being extracted to make electricity. It begins with the geothermal reservoir in which is hot water or steam. The reservoir consists of a large volume of high-temperature fractured rock that holds hot geofluid liquid, steam, or a mixture of the two within its open space.
Five specific characteristics must be present:

1. *Source of heat*;
2. The *permeable volume of rock*, the body of the reservoir that contains the fluid needed for the power plant;
3. A *supply of liquid* in the permeable formation that has to move the thermal energy from the hot rocks;
4. There is an *impermeable cap* to seal the permeable formation from the surface of the Earth. The cap doesn't permit the dissipation of the geofluid through fissures or faults. An impermeable cap may develop over a long period due to a precipitation of chemical compounds such as Silica and calcite, blocked the hot fluid inner to the reservoir;
5. A *recharge mechanism* for the reservoir is mandatory, particularly when the fluid is isolated from its surroundings as production reduces the fluid.

The Geothermal power plant system consists of four principal sections:

1. Getting the energy out of the reservoir

After the feasibility study on the reservoir, a report is published for regional and national environmental sustainability bodies to decide whether to continue or stop the project. A positive result of the analysis of the "Feasibility Report" leads to the drilling of wells. Unlike the Gas & Oil sector, geothermal energy must be used close to the source. Hot water and steam lose much of their stored energy when being transported over long distances via pipelines [28]. Drilling programs begin with creating small diameters and shallow wells to determine the formation's three-dimensional temperature trend. They are referred to as "temperature gradient holes". After this first part, we proceed with a deep and large diameter "discovery well" as the presumed production area. The drilling site of the first well represents, in many cases, the success of the potential producing customer.
An excellent well produces a constant, high-volume flow of high-temperature geofluid. The hotter the fluid, the greater the potential it has for generating energy. There are two ways to use hot fluid taken from a well. The first is the thermal one, for heating buildings, making the fire flow in a heat exchanger, considering the fluid's chemical properties. The second method is electricity production, through the conversion of thermal energy into electricity and the conversion rate is crucial. The problem is transferring heat continuously and constantly at a high enough speed to produce significant quantities of electricity. The basic difficulty lies in the mode of heat transfer: conduction versus convection. The latter happens in a geothermal well that extracts hot fluid from the formation, while the former happens in a downhole heat exchanger. The rate of energy transfer is generally slow to produce much power. A series of wells must be planned to extract large amounts of energy from the reservoir at high

energy. Planning consists of defining the depth of the wells to reach the most productive layers of the reservoir. Nowadays, it is routine to perform exercises vertically up to 2000 m depth and up to 4000 and 5000 m for very deep production areas using specialized drilling machines. The wells are rarely perforated horizontally. Wells can be drilled with a horizontal offset to depths of over 1000 m, allowing several wells to be drilled from a single pad without interfering with each other. Deviated wells are best deployed at geothermal fields marked by steeply dipping faults that act as fluid conduits. If there are several fluid-carrying, nearly vertical faults, then a sharply deviated well approaching horizontality could be a strong producer by tapping several faults at once. On the other hand, when a well with good thermal characteristics appears but with a flow rate lower than the desired one, "stimulation" is used. It is used to increase permeability. A typical geothermal capacity well is around 5-10 MW, while some can even be around 40-50 MW in the early stages of exploitation [29]. Assuming that reinjection should be used to help refill the tank and avoid environmental problems and recognize that poorer wells could be used for re-injection, 7 and 12 wells might require re-injection. Therefore, the 50 MW plant would likely require 12 to 22 wells in total to start operating. In the course of a drilling campaign to create so many wells, some could inevitably be failures. These could be suitable for monitoring wells [30].

2. Connecting the wells to the power station

A piping system gathers and delivers the geofluid from the wells, which may be scattered widely across the field, to a central point where the power station is constructed. The system includes many elements such as valves, straight pipes, elbows, bends, expansion rings, drains, separators, flash tanks, emergency ponds and vent stations. Many plants use two-phase liquid-vapour piping from each well to a separation station. This works very well when the wellheads are located higher than the power plant. However, the pipes must keep the pressure drops low to preserve the power potential of the geofluid. Some types of fluid require elaborate structures to purify the steam to be used in the turbine. Some examples contain high contaminants of dissolved solids or highly corrosive fluids due to hydrogen sulphide.
Innovative technologies cope with highly corrosive fluids such as *flash-crystallizer/reactor-clarifier* technology and *pH modification*. This solution is adopted for Salton Sea geothermal area in southern California[5]. The chemical processing and treatment facilities actually dwarf the power generating equipment but have proved to be effective and reliable, allowing over 350 MW of power production from several plants in the Salton Sea area.

Figure 2. 8. Systems for the collection of geothermal fluids.Source [31].

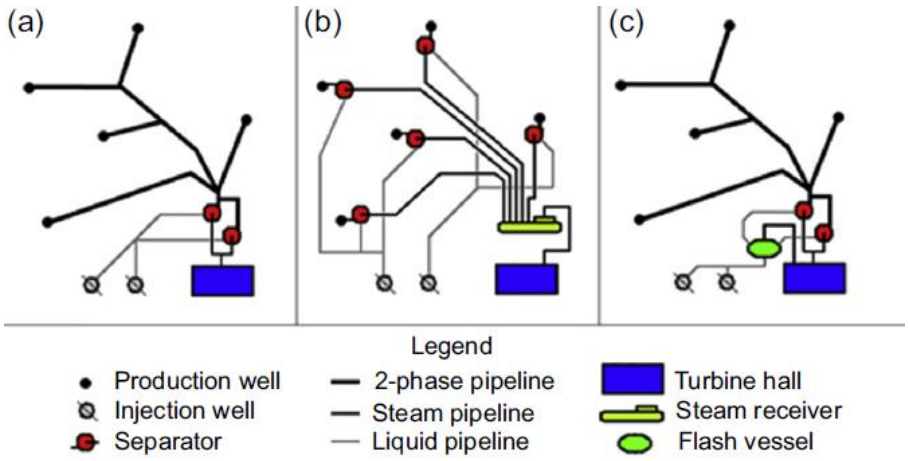

Figure 2.8 shows the piping systems. For the case (a) liquid-vapour two-phase system. Pipelines connect the wells to the power plant. The separators produce steam for the turbines and liquids for re-injection—a single flash pattern. In case (b), the separators individually produce steam in the well sent to the turbines through specific pipelines to the steam, while the liquid is sent for reinjection. Case (c) is similar to case (a) except for the liquid. The last fluid is flashed to produce low-pressure steam useful for a double pressure turbine. This is a double flash plant.

[5] https://www.energy.gov/eere/geothermal/imperial-valley-geothermal-area

3. Central power station

There are many different design options available for current energy conversion equipment; they will be listed in the last part of this paragraph. When the resource is a *dry steam system*, then the option of choice is the steam turbine. As a preventive measure, any impurities (rock dust and drops of liquid) formed in the pipes are eliminated before being introduced into the turbine. The turbine rotates and drives the generator for the production of electricity. In this last part, the geothermal plant looks like any electricity production plant[32].

The common type of geothermal resource is *liquid predominant*. For this type of geofluid, the power plant can be a flash-steam unit in which the steam, after the separation from the two-phase geofluid mixture, is deployed in a turbine (dry steam case). The new geothermal power plants use until *three stages of flash/separation* because the efficiencies increase with flash processes. Another solution is using a binary plant. Here, the hot geofluid is the heating medium to boil a secondary processing fluid, an organic substance (refrigerant or a hydrocarbon), with a low boiling point temperature. The geochemical fluid doesn't enter into the turbine, but it only gives part of its thermal energy to the heat power plant. Binary power plants are the best options for the low-temperature geofluids (< 423.15 K and pressure less than 15 bar), while flash plants are the best option for high temperatures and high pressures. Generally, binary power plants using is the best solution for reinjections of cooled fluids.
The geothermal fluid characteristics, analyzed before, determine which conversion system options is best to use. After this, engineers choose the plant's specifications respecting the environmental regulations, financial/economic aspects, cost of work, lifetime and maintenance operations.
Periodic shut-downs are planned to inspect various pieces of equipment and repair. Maintenance of the wells is vital, and replacement wells could need to be drilled. In 30 years, the electromechanical equipment needs to be monitored and maintained. The monitoring of the plant's performance and the withdrawal/reinjection wells are foundations for maximizing production. This is done through the counter systems' electronics capable of recording the data and parameters to be optimized. These systems aim to ensure long-term electricity production[33].

4. Geofluid re-injection

All countries have regulations regarding the disposal of hazardous fluids and other materials. The old power plants did not care for waste and non-condensable gas emissions. However, since waste liquids are usually supersaturated with dissolved substances such as Silica, precipitations quickly settle in the ponds, making the surface impermeable and creating bigger lagoons. With tight constraints on the disposal of fluids, it has become an almost universal practice to re-inject waste geofluids and treats gases before discharge if they can hurt human health. Given the potential difficulty in identifying reinjection wells to not interfere with well production, along with the need for full reinjection, the power that a given field can develop can be held back by a lack of enough reinjection capacity, regardless of the capacity of the production wells.

The reinjection wells can be of two categories:
- Disposal wells;
- Recharge wells.

The disposal wells are sited on the periphery of the field, downstream of the main production zone. The recharge wells are in the production zone. The aim is to replace some of the fluid being withdrawn via the production wells.

2.5 Overview of geothermal power plant systems

The heating application in geothermal resources is worthy and globally addressed. The heating technology growth is around 7% annually, and the world is employing about 200 TWh annually [34] compared to 70GW of direct usage capacity in place worldwide in 2015. 55.2% of the power was reported using geothermal heat pumps (GHPs) to transfer heat from the geofluid to the heating space, and their usage saves around 52.8 million tons of crude oil annually. It has been determined that the Earth's land surface comprises 16% of suitable aquifers, and the energy range of 125 and 1793 of EJ/year is available from aquifers for global heating use [35]. The thermal gradient is roughly 32 °C/km, meaning significant energy is found for direct use on the surface. The usage of aquifers should

ensure sustainable development [36]. The contamination of shallow aquifers should enforce the regulation level and their safeguard [36]. Between the extraction and re-injection wells, allowable temperature drops have been found in a range of distances of 5-300 m [36]

The technologies used for geothermal energy extraction depend on the state of the resource.

At high temperatures with geofluid as superheated steam, there are dry steam systems used [17]. Dry steam plants make up about 23% of the world total
geothermal capacity, with 63 plants in operation generating a total of 2863 MW as of 2014 [3]. Plants of this kind are the simplest and least expensive. The superheated steam coming from the earth at high pressure is conveyed
directly into a steam turbine, where the energy is extracted. Dry steam power plants have higher efficiencies thanks to high-temperature sources, but they have limitations because high-pressure fluids are more difficult to detect [18], creates greater corrosion problems to the turbine blades and contain larger quantities of non-gas condensable.

In addition to dry steam technology, there is another technology based on flash steam. It has become common to many geothermal plants, which have installed a capacity of approximately 42% for single flash and 19% for double flash since 2014 [3].

Flash steam cycles exploit geothermal energy resources composed of two-phase mixtures below high pressure and high temperature [37]. When these sources are brought to the surface, the geofluids are expanded within a separator, resulting in part of the geofluid's flash vaporisation. The steam is expanded through a turbine for power generation.
Most of the total fluid remains a liquid, which is further expanded again at lower pressure to recover more energy in a double flash cycle. Double flashing often results in higher efficiencies and output power under the same input conditions.
An example of a double flash plant is the Icelandic Hellisheidi plant (Table 2.6).

Table 2. 3. Geothermal fluid from well in this work. Castelnuovo has 8 %wt dissolved gasses (NCG) composed of 2% H_2S, 97.50 % of CO2 and the rest in others

Hellisheidi									
T [°C]	P [bar]	H2O [w%]	CO_2 [w%]	H_2S [w%]	CH_4 [w%]	NH_3 [w%]	Hg [w%]	N_2 [w%]	H_2 [w%]
346.8	158.8	92	7.24	0.69	$3.2 \cdot 10^{-3}$	-	-	0.030	0.034
Chiusdino									
T [°C]	P [bar]	H2O [w%]	CO_2 [w%]	H_2S [w%]	CH_4 [w%]	NH_3 [w%]	Hg [w%]	N_2 [w%]	H_2 [w%]
210.8	20.20	92.39	7.04	0.11	0.20	0.22	$1.264*10^{-5}$	0.036	$4.213*10^{-3}$
Castelnuovo									
T [°C]	P [bar]	H2O [w%]	CO_2 [w%]	H_2S [w%]	CH_4 [w%]	NH_3 [w%]	Hg [w%]	N_2 [w%]	H_2 [w%]
180	10.00	92	7.8	0.16	-	-	-	0.04	-

Consequently, the technological improvements of the geothermal plants of:

1. Flash steam geothermal energy conversion systems: single-, double- and combined-cycle plants;
2. Direct steam geothermal energy conversion systems: dry steam and superheated steam plants;
3. Binary geothermal energy conversion systems: basic binary organic Rankine cycle
4. Alternative systems for power recovery based on two-phase expansion
5. Hybrid geothermal power systems: geothermal concentrating solar power hybrid plants.

2.5.1 Flash steam geothermal energy conversion systems

These technologies are growing as they focus on increasing the amount of power extracted and improving efficiency. The flash plant is widely used in cycles that employ a steam turbine. In addition, there are binary cycles that also flash the incoming geofluid into separate steam and water phases. In this section, when a flash plant is described, it means a cycle that relies primarily on a steam turbine to generate the majority of its power.

- Single flash

The mainstay of the geothermal industry for higher-temperature resources has historically been the single-flash plant. A typical flash cycle is shown in Figure 2.9. Geofluid flows from the wells to a high-pressure (HP)separator, producing separated steam and brine. Before entering the steam turbine, the separated steam is led through a demister to remove fine carryover droplets. The single-pressure steam turbine would be similar to those used for dry steam plants. The steam turbine exhausts [6]to heat rejection equipment, consisting of the condenser, circulating water or hot well-pumps, and cooling tower. The liquid from the first separator would simply be injected back to the reservoir for the single-flash plant. The separator pressure is selected depending on the characteristics of the field, the wells' ability to deliver fluid at a selected wellhead pressure, and a natural performance tension that exists between a desire for higher-pressure steam at the inlet to the turbine and a desire for a higher mass flow rate of steam to the turbine.

Figure 2.9. Flash plant schematic, showing potential for second and third flash stages. Source: [40]

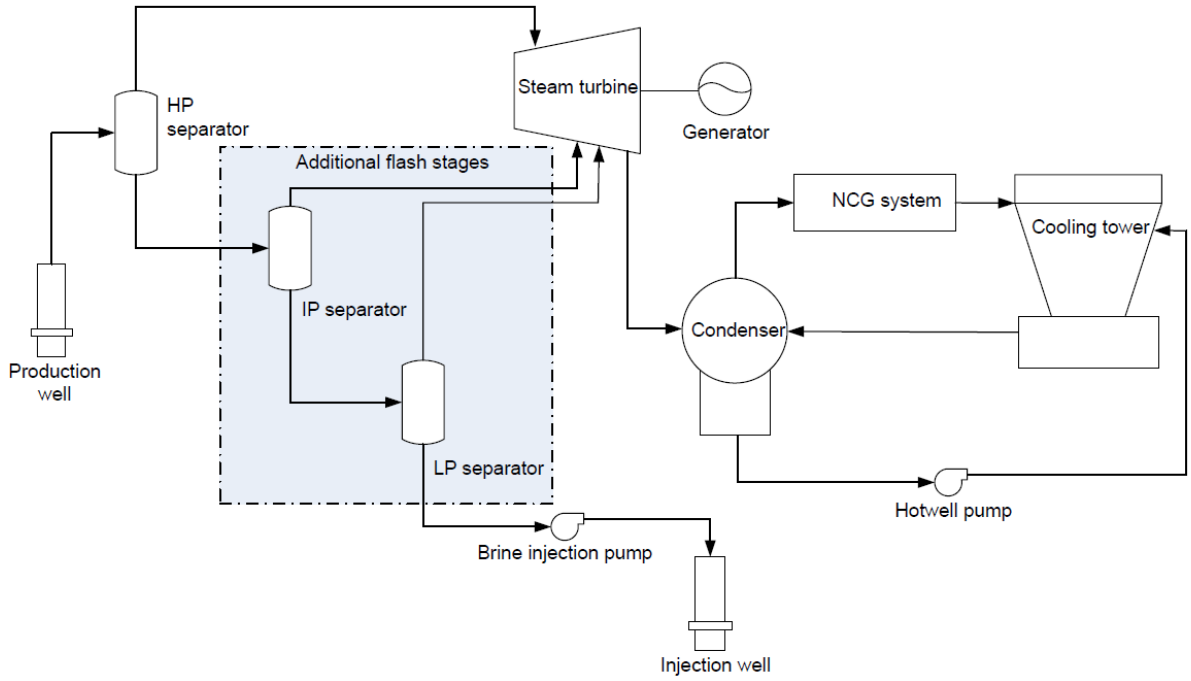

Single-flash plants generally carry out the separation in the 6-20 bar_a[7] range. So, the brine to be injected back to the reservoir is already at elevated pressure, reducing the head requirements of brine injection pumps compared with multiple-flash plants with lower separator pressures. The resultant concentration of solids in the brine due to flashing and the brine temperature dictate the propensity for precipitation of solids. Because the resultant injection temperature of the separated brine is also high for single-flash plants, this cycle can have a large margin of safety from the onset of scaling in the brine. However, one of the key strengths of the single-flash plant, its high separator pressure and brine temperature, is also a limitation; it may forego an opportunity to generate more power. Exergy analysis is a useful way to illustrate the potential for power generation from various streams. An exergetic efficiency of a single-flash plant should be around 30-35 % to generate around 50-55 MW of

[6] https://power.mhi.com/products/steamturbines/lineup/geothermal/exhaust-direction

[7] bar_a: absolute pressure (relative pressure + atmosferic pressure)

net electrical power with this resource. But, the exiting stream of brine to be injected carries with it significant exergy. If some fraction of this can be harnessed usefully, the cycle can generate more power if the total geofluid flow remains the same. Alternatively, if a fixed output is desired, increasing the power extracted per kg/s of fluid may allow the geofluid flow to be reduced, lowering the cost of wells and the gathering system. A key trade-off for flash plants is the attempt to increase resource efficiency and generally by increasing the number of flashes and cycle complexity and against the investment in drilling additional wells. The single-flash is a good solution where resources are substantial and energetic, and drilling costs are low. However, an increasing number of flashes needs to be used to reduce the geofluid extraction rate and mitigate drilling risks.

- Double and triple flash

Double- and triple plants are a logical extension of the single-flash process. There are some combinations of high-,intermediate-, and low pressure (HP, IP, LP) steam. The flash pressures and temperatures would normally be distributed between the equivalent resource temperature and the condenser temperature following the philosophy of an "equal temperature split"[41]. Modifying temperature or pressure spacings are the solutions to keep the LP steam pressure above atmospheric pressure to avoid air in-leakage or piping design complications when operating at a vacuum. In Table 2.7 is assumed resource conditions of 500 kg/s total geofluid flow (pure H_2O) and 1200 kJ/kg enthalpy, corresponding approximately to an equivalent single-phase resource temperature of 546.15 K. The HP separator pressure has been kept the same for both cases for ease of illustration, although this may not be optimum thermodynamically.

Table 2. 4. Sample comparison of single- and double-flash cycle parameters.

	Single Flash	Double Flash
HP separator pressure (bar_a)	8	8
HP steam flow (kg/s)	117	117
HP brine flow (kg/s)	383	383
LP separator pressure (bar_a)	-	2
LP steam flow (kg/s)	-	38
HP turbine output (MW)	60	60
LP turbine output (MW)	-	13.5
Net output (MW)	56.5	69.0
Exergetic efficiency (%)	35	43

Table 2.7 illustrates that the additional flash stage can theoretically add significant power as 22% more. While this increase in efficiency and potential output is highly resource and cycle-specific and often limited by the resource chemistry, a more conservative assessment would be to estimate that a double flash can add around 10-15% net output compared with a single flash, and a triple flash might add another 5- 7%, with flash pressures redistributed for each case. The incremental increase in capital cost for a greater number of flashes lies primarily in the design of the separator station(s) and the steam turbine. First, the separator station must be configured with multiple stages of separators and demisters to handle each flash stage. The turbine design then must accommodate the admission of steam at multiple pressures. While multiple-pressure turbines are long-standing common practice at fossil thermal plants are more complex in geothermal applications due to the relatively lower pressures of the steam and the resultant need for larger-diameter piping. Generally, steam at each pressure level is admitted to the turbine via two pipelines ("right hand" and "left hand"), each equipped with main stop and governor valves. A triple-pressure turbine thus may have six inlet pipelines and 12 of these large hydraulically actuated control valves, adding cost and requiring additional space. Following the turbine, a multiple-flash power cycle configuration would be similar to that for a single-flash or dry steam plant. The turbine exhausts to a condenser, which is supplied with circulating water from a cooling tower. Noncondensable gases from the condenser are removed, generally using a multistage configuration of steam ejectors, and for hybrid systems, last-stage vacuum pumps. An array of circulating and cooling water pumps drive the water flows between the condenser and cooling tower and provide cooling water to other components such as lubricating oil and generator air coolers.

The amorphous silica and silicate deposition in geothermal fluid processing systems affect the injection temperature and concentration constraints on the performance of a flash plant. For example, with the same conditions of Table 2. 7, a concentration of 563 ppm silica is estimated in the geofluid. As a

result, the silica concentration in the brine increases through each flash, and the temperature is reduced. Due to the lowering temperature, the solubility of constituents such as amorphous silica (SiO_2) is reduced; hence the increasing number of flashes brings the brine closer (or past) the point of precipitation.

Scientific research has identified the double flash cycle's potential compared to the single flash cycle (Figure 2.10), using energy and exergy analysis for a single and double flash unit (Figure 2.11). The exergy efficiency for double flash reached 43.35% compared to 32.7% for single flash [42]. The single water flash's output temperature was about 428.15 K, where the double flash was about 375.15K, indicating a higher usage. Optimizing flash cycles can produce significant improvements in power plant performance. It can be noted that the pressures of 7.63 bar and 1.06 bar can be optimal for the first and second stage separator, respectively [43].

Figure 2. 9. Single-flash system. Source: [31]

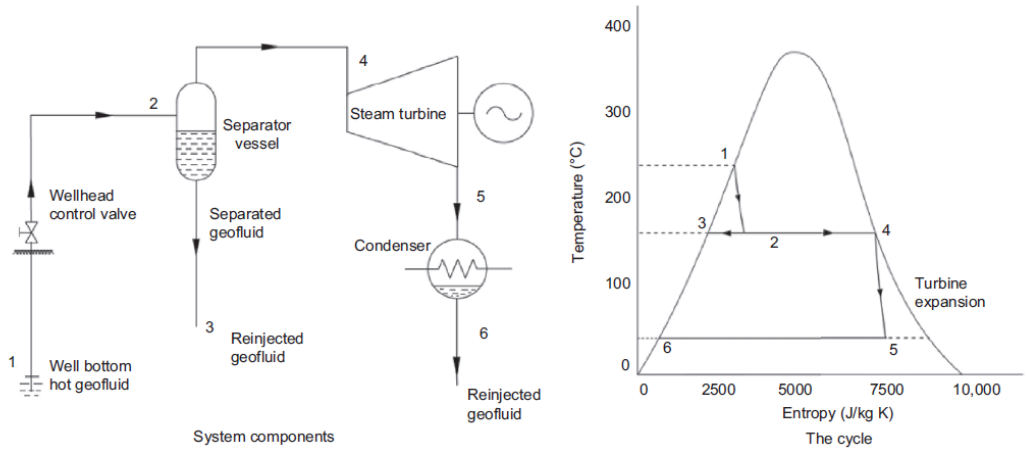

Double flash generally produces 25% more power than single flash, and energy and exergy efficiencies were much higher in double flash [4]. As will be better described in the next point, the net power and thermodynamic efficiency of a single and double flash cycle combined with the ORC and Kalina cycles by genetic algorithm (GA) [44]. These scientific studies show that double with the ORC flash cycle had the maximum exergy efficiency at 46.12%, while double flash Kalina followed with an exergy efficiency of 36.75%, and third the normal double flash with an exergic efficiency of 31.92%.

Figure 2. 10. Double-flash system. Source: [31]

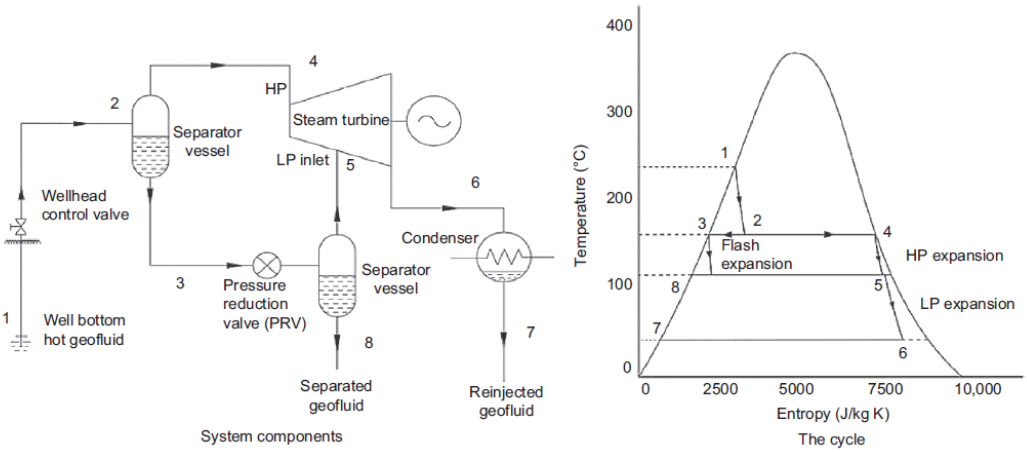

Despite the relatively high exergic efficiency of the Kalina flash cycle, an increase in turbine inlet pressure of 4 bar and 14 bar was required for the double ORC flash and the double flash, respectively. It later occurred that pairing ORC plants with double flash plants used more than the available geothermal resource. Up-to-date scientific studies describe an enhanced organic flash cycle (EOFC), which has been modelled using an internal heat exchanger to recover waste heat from the geofluid further, leaving the flash separator [45]. When the separator has been replaced with a two-phase expander, net power increased by 36.7%. Furthermore, the double flash was less expensive and mechanically less complicated than the single flash with binary from an economic perspective.

- Mixed and combined cycles

A mixed cycle uses a steam turbine plus binary technology where the two units can operate independently of one another. The simplest example would be that of a single-flash plant with a steam turbine harnessing the flashed steam and a binary plant harnessing the brine (Figure 2.12)

Figure 2. 11. Mixed-cycle schematic.

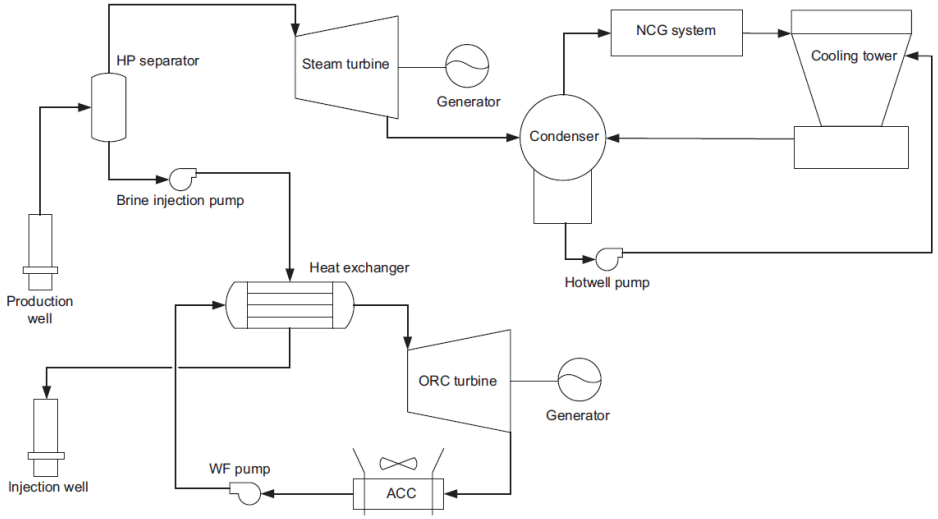

The mixed cycle is common to encounter as retrofits to an existing flash plant. The advantage of a retrofit is that the operation of the flash plant over some time before the binary addition allows the operators to characterize the chemistry of the brine injectate more precisely. As a result, a more accurate determination of the appropriate injection temperature reduces the likelihood that scaling will occur and helps optimize the potential output of the binary "bottoming" plant. While, in contrast to the mixed cycles, a combined cycle couples the two technologies directly together. Many configurations are used, like air- and water-cooled options.
A typical air-cooled combined cycle is shown in Figure 2.13. Geofluid is flashed to steam that passes through a backpressure steam turbine and exhausts to a binary vaporizer. Brine from the separator can be led to preheaters or a separate bottoming binary cycle.

Figure 2. 12. Air-cooled combined-cycle configuration.

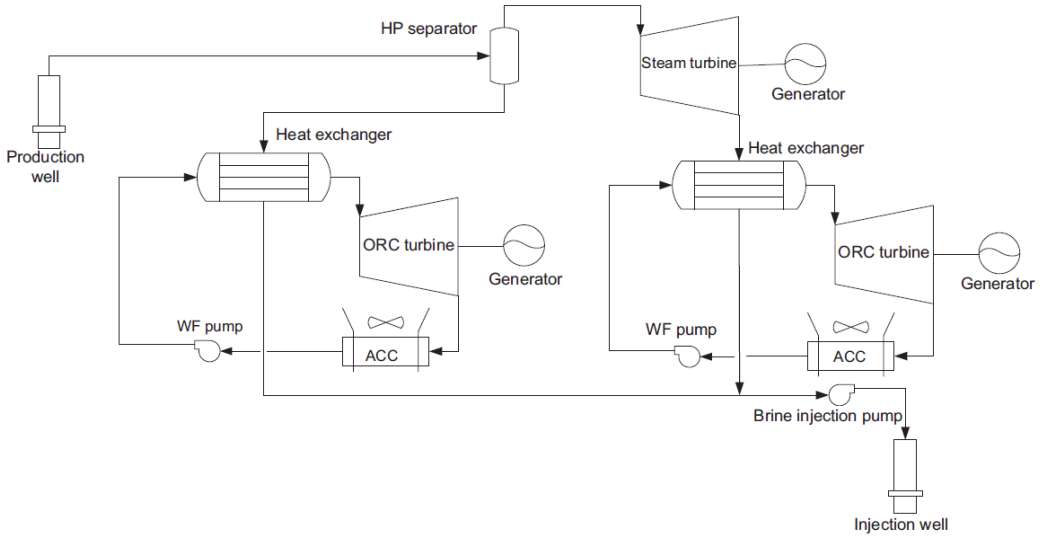

The balance of the binary cycles would be similar to standard binary plants. The combined cycle may have several advantages over all-flash or all-binary cycles. The combined cycle can use air cooling; while air cooling for a flash plant is not impossible, it has certain limitations that have resulted in it not being widely used in the geothermal industry. Air-cooled plants may also be desirable for enhanced geothermal systems (EGS) resources if there will be a limited supply of water to circulate to the reservoir as the geofluid.
The other is the water-cooled combined cycles. A water-cooled combined cycle configuration is shown in Figure 2.14. The HP steam from the first flash separator drives a backpressure steam turbine and associated binary plant. However, the brine from the separator is further flashed and used in an LP steam turbine. The combined condensate from the HP and LP cycles is sufficient to allow evaporative cooling. These cycles have been applied to high enthalpy, where the geofluid contains a high percentage of NCGs.

Figure 2. 13 Water-cooled combined cycle configuration

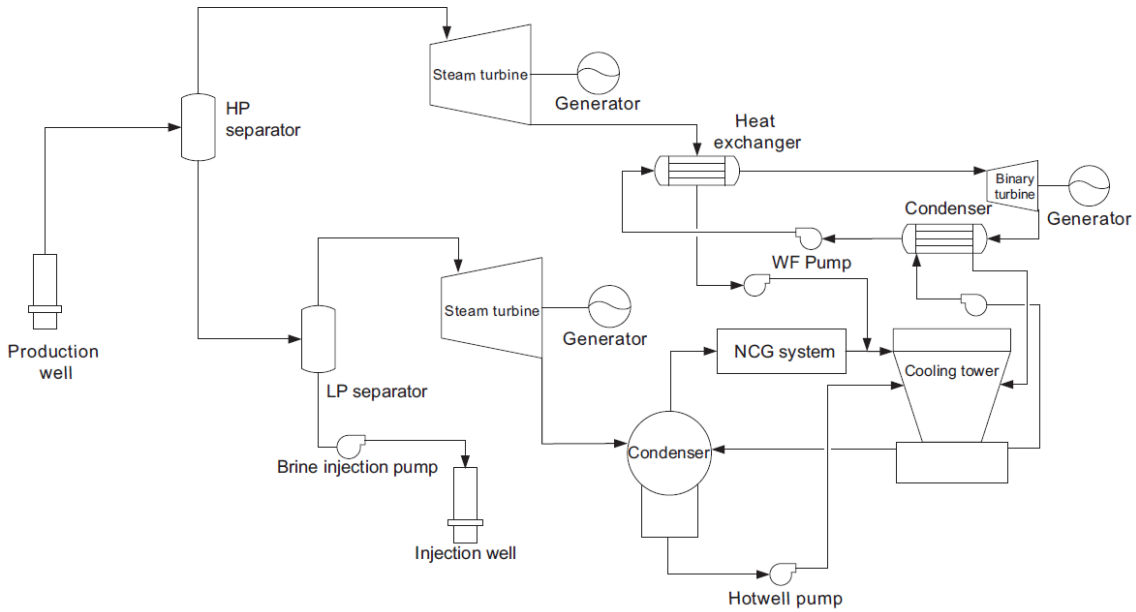

In this configuration, the HP portion of the cycle, consisting of a backpressure steam turbine with a bottoming binary, does not require such equipment,
and the LP portion requires only a modest NCG removal system for the condenser since most all the NCGs are carried into the HP steam with the first flash. The deeper flashes provide sufficient makeup water to allow the complete cycle to be water-cooled.

Evaporative cooling can offer lower capital costs and operations closer to the design point for more of the year compared with air-cooled units. However, since deviations from the design point result in reduced turbine and other component efficiencies, a water-cooled unit can usually generate some 3-5% more annual energy output than a comparable air-cooled unit of the same design point net capacity depending on the climate. Combined cycle configurations offer flexibility between steam and binary equipment economy, performance benefits, reduced sensitivity to geofluid conditions and composition, and a range of cooling options. In addition, these cycles can provide unique solutions to site-specific challenges for larger units that deserve the additional investment in cycle complexity.

Chapter 5 will deal with the plants in which the two-phase fluid is exploited and the use of cogeneration and co-production from flashed brines. Flash plants have multiple product streams of condensate, brine, and noncondensable gases. The designers have shown commendable ingenuity in leveraging aspects of these different streams for additional benefits and revenue. The goals of these geothermal installations are to integrate a variety of uses, support the sustainable development of society, connect technical and social cultures, and consider activities on a time scale of centuries. From these considerations, three essential resources can be collected by flash plants: *thermal energy*, *fluids* and solids.

District heating is a significant contribution to the cycle design. A real case study is reported in Chapter 5 concerning the Hellisheidi power plant. In the same context, a case study that illustrates the district heating, one part of the goals of the geothermal installation, is the Nesjavellir flash plant in Iceland (Figure 2.15). It shows a cycle diagram of the first phase of the project, nominally 60-MW gross output. The single pressure turbine operates at an elevated exhaust pressure of 0.2 bar_a. Makeup water from an external source is preheated as it flows through the tubes of the surface condenser while condensing the turbine exhaust steam on the shell side. The water is heated further using separated brine and then deaerated. The hot water is then sent to the district heating system for the city of Reykjavik. The turbine and condenser are designed with flexibility in the steam flow and condenser pressure/temperature to accommodate variations in annual heating demands. The steam turbine exhaust and the brine from the single-flash separator are harnessed to provide 128 MW of thermal output (hot water) at the design point via a pipeline 27 km long. During colder conditions, the geofluid flow rate increases from 326 to 373 kg/s, and the turbine exhaust pressure increases from 0.2 to 0.35 bar_a, increasing thermal power from 128 to 227 MW [46].

Figure 2. 14. Cycle diagram of the Nesjavellir plant (Island). An example of cogeneration and coproduction from flash brines.

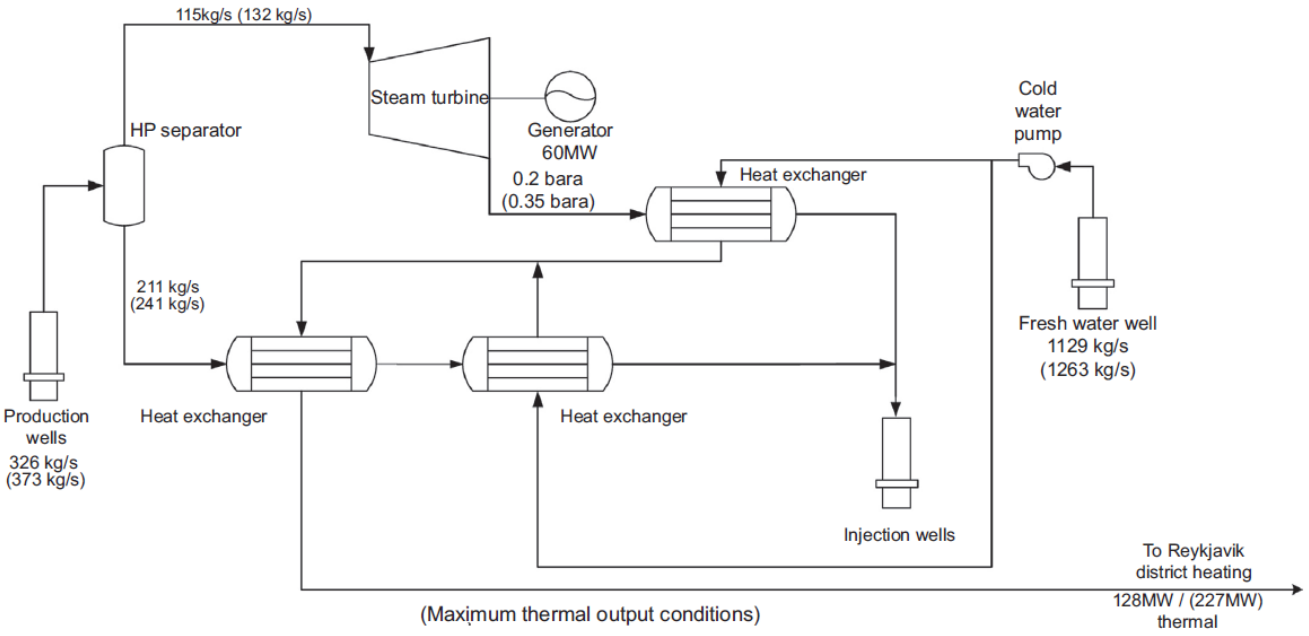

Nesjavellir was expanded to 120 MWe[8] and 290 MW_{th}[9] in 2005. In 2012, it can be seen that hot water contributed 18-25% of total revenue over the 2 years[10]. The contributions that a cogeneration plant can make are naturally highly dependent on the surroundings. A flash plant in Iceland such as Hellisheidi or Nesjavellir, relatively close to population centres, is more advantageous for contributing to district heating systems than projects in the tropics. However, an increasing number of projects throughout Europe, regardless of power plant technology,
are being configured to include a cogeneration mode. Flash plants advantageously sited to serve thermal energy users should consider this potential.
Regarding the fluids, any product stream can be considered for potential revenue, and several types of fluids can be harnessed from flash plants. Noncondensable gases in geothermal steam are extracted from the condenser and discharged to the atmosphere. These are predominantly carbon dioxide (CO_2) but may contain other constituents such as hydrogen (H_2), hydrogen sulfide (H_2S), or methane (CH_4), as shown in Table 2.2 and Table 2.6.
Dunstall and Foster [47] describe a new project in New Zealand in which it uses geothermal energy for heating of a greenhouse and uses CO_2 to enrich the atmosphere by several 100 ppm to increase growth rates. They describe strategies to balance the temperature, humidity, and CO_2 concentrations in a synchronized manner to maximize the growth rates of the plants. Noxious gases such as H_2S must be filtered out to tolerable levels. Greenhouses in Iceland also use geothermal CO_2 to enhance the greenhouse growth of various species of flowers and vegetables. Thermal energy and CO_2 may also be used to accelerate the growth of algae, which can be harvested for fuel or other useful byproducts [31]. At locations in Turkey and Iceland, geothermal CO_2 is harvested for industrial uses, such as bottling carbonated beverages. The George Oleh Renewable Methanol Plant, operated by Carbon Recycling, Inc. (CRI), captures CO_2 and H_2 from the exhaust of the Svartsengi geothermal plant in Iceland, combining those gases with hydrogen from electrolysis to synthesize methanol. The methanol is blended with gasoline and used for vehicle fuel. So, many flash plants harness the multiple potential benefits, the resource park at Svartsengi serves as a particular exemplar. Providing electrical power, district heating to nearby communities, thermal waters and spa products at the nearby Blue Lagoon, and gas for fuel synthesis, research, and development activity continues on other potential outputs. It would be hoped that many other flash plants would follow their lead to convert more "waste streams" to "value streams."

In the flash-systems plant is common to remove NCGs. Geothermal steam often contains H_2S, which is generally vented to the atmosphere. H_2S is a noxious gas that can lead to respiratory problems and environmental corrosion even at minor (several ppm) concentration levels. While many nations do not have emissions limitations on H_2S, several jurisdictions, such as Italy, California in the United States and Japan, have emissions limits that often require flash plants to install abatement systems for the vented NCGs. There is a proliferation of techniques, and more nations are considering limiting these emissions. Some of the H_2S abatement techniques used include:

a) Regenerative thermal oxidation. When the NCGs contain sufficient flammable constituents such as H_2S, H_2, or CH_4. The burner/scrubbers at the AMIS systems at Larderello 19) is an example of these processes.
b) BIOX, which uses biocides in the cooling water to convert H2S to water-soluble sulfates. This technique is used at the John Featherstone plant in the Salton Sea.
c) Liquid redox methods. This method focuses on the H_2S conversion to elemental sulfur, which is disposed of as a solid.
d) Separation/injection where H_2S is removed from the NCGs and reinjected to the reservoir. Experiments are underway at the Hellisheidi plant in Iceland for this technique.

In chapter 5, the case studies related to simulations will consider the H_2S abatement techniques of points (a) and (d).

[8] MWe: electrical power

[9] MWth: thermal power

[10] Reykjavik Energy. 2013 Annual Report; 2013

2.5.2 Dry steam and superheated steam plants

The power cycle for generating electricity from steam-dominated resources is comparatively simple: a turbine-generator, condenser, and waste heat rejection system. The simplicity of the power cycle and the unique nature of the geothermal fluids have led to refinements in the power cycle to improve both overall plant efficiency and economic performance with high reliability and availability. Both direct contact and surface condensers are used in geothermal power plants operating on vapour-dominated resources. Typical power cycles with direct contact and surface condensers are shown in Fig. 2.16 and Fig. 2.17. From a thermodynamic perspective, the direct contact condenser offers slightly better performance than a surface condenser. However, operational costs in the form of additional power requirements for the hotwell pumps and increased chemical costs for emissions control, when required, have resulted in using surface condensers in some geothermal steam power plants.
Geothermal steam typically contains a small amount of noncondensable gases that must be managed to operate the thermal power cycle efficiently. Whereas a typical thermal power plant will have a small air removal system to extract and compress air in-leakage from the condenser, geothermal steam power plants require a significantly larger system to remove the air in-leakage plus the noncondensable gases that entered the condenser with the geothermal steam.

Figure 2. 15. Geothermal steam power cycle e direct contact condenser

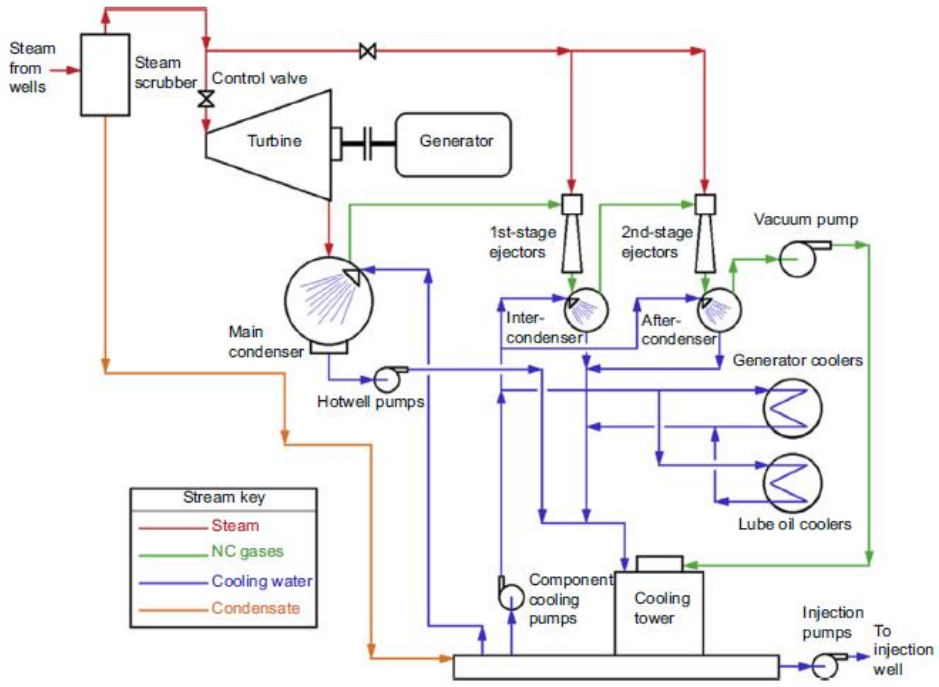

Despite the simplicity of the system, technological improvements are complicated. Dry fluid requires temperatures above 473.15 K and requires a sophisticated gas removal system consisting of one and two-stage steam ejectors, one and two-stage liquid ring vacuum pumps (LRVP), and a hybrid system ejector plus one LRVP. Single-stage LRVP increased net power by 7.6%.
Gas removal systems, such as geothermal steam power plants use steam jet ejectors or ejectors with mechanical compressors in a hybrid system to remove non-condensable gases and air from the capacitor. Steam geothermal power plants use evaporative cooling systems with mechanical systems cooling tower projects. The cooling towers e other cooling system components require specific differences of plant cooling system components to provide reliable service in geothermal applications.

Figure 2. 16. Geothermal steam power cycle- surface condenser. Source: [31].

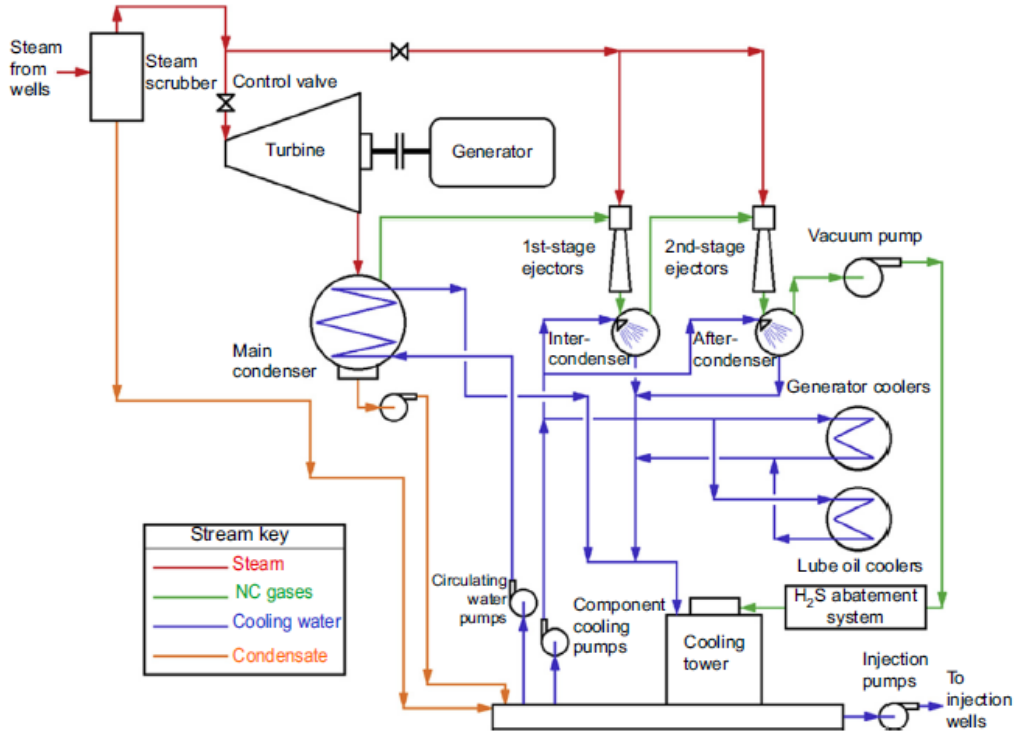

2.5.3 Binary organic Rankine cycle

The concept of an engine is based on the Rankine thermodynamic cycle, whereby the fluid is an organic compound instead of water and is originated from two main observations:

- Selection of the working fluid for the design of the thermodynamic cycle. The properties of the fluid, e.g., the vapour-liquid critical point, the saturation line, and the specific heat, directly affect how well the temperature profile of the thermal energy source and sink can be matched by the corresponding cycle heating and cooling processes.
- For low power output, the realization of an efficient, reliable, and cost-effective steam expander is challenging: the mass flow is extremely small, the expansion ratio is comparatively large, and the specific work over the expansion is also very large, thus the design of a simple axial or radial turbine is problematic and the efficiency bound to be low. However, if the working fluid is organic, an expanding vapour's much smaller enthalpy decrease allows designing an expander, be it a turbine or a positive displacement machine featuring a lower rotational speed and higher volumetric flow for given power output. For the majority of the ORC working fluids, the expansion process is completely dry, thus blade erosion issues in turbines and inherent expansion inefficiency due to condensation are avoided. Several ORC working fluids are also suitable as a lubricant for rotating machinery, thus further simplifying the system. Finally, for many such fluids, the freezing temperature is much lower than that of water, and freezing does not involve a detrimental volume increase.

The most common geothermal systems are at temperatures below 473.15 K, so the latest research and plant designs focus on improving ORC binary performance (Figure 2.18) [48]. One way to improve the loop is file selection optimal working fluid. The selection of working fluids affects the thermodynamic performance of the system and the design of all its components, such as the power plant's efficiency, cost, and safety.

Among the optimal working fluids of scientific interest are isopentane, isobutane, R245fa and R227ea, particularly suitable for combined heat and power (CHP) installation at temperatures below 450.15 K.

Figure 2. 17. ORC power plant. Source: [49]

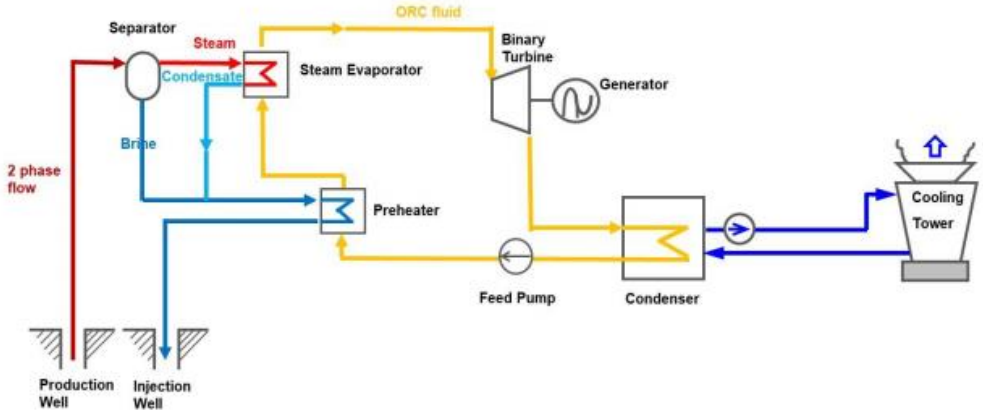

Many scientific studies have tested exergy efficiency both in parallel and in a series set. For example, it is shown that cogeneration increases the cycle's thermal efficiency by up to 20% more than just power generation [50].

2.5.4 Alternative systems for power recovery based on two-phase expansion

This section describes a binary system using organic working fluids. The screw expander used here can expand two-phase fluids with good efficiency over volume ratios of up to ~30:1 when the working fluid enters the machine in the pure liquid or very dense vapour phase. In the case of binary cycle systems, using *organic working fluids*, critical temperatures are much lower than that of water, while in most cases, the critical pressure is in the region of only 25-40 bar. A consequence of this, as explained by [51] is that organic fluid vapours have much higher pressures and, hence, are far denser than steam at normal condensing pressures and lower vapour pressures than steam at higher temperatures. This implies that volume ratios for expanding the working fluid from saturated liquid down to normal condensing temperatures can be orders of magnitude less than that of water. In addition, organic liquids are ~30-50% denser than water. This implies that there will be a greater expansion in the filling process at the inlet to the expander.
As a consequence, a single-screw expander can operate with good efficiency over a large temperature range. This can be used to good effect in the binary plant to include two-phase expansion processes in the cycle, thereby improving both the heat recovery and the overall plant efficiency. The following two systems can be considered viable with currently available machinery: a binary system for medium enthalpy sources, trilateral flash cycle, and wet organic Rankine cycle systems.

The first is a *binary system for medium enthalpy sources*. For pumped wells, producing saturated liquid brines at the wellhead with temperatures in the 453.15- 473.15 K, a closed-cycle system using neo-pentane or pentane as the working fluid with a first-stage screw expander, followed by a separator and a second-stage turbine as shown in Fig. 2.18, can produce more net power than either a subcritical or supercritical organic Rankine cycle (ORC) system. This is due to both better matching in the primary heat exchanger and less feed pump work in the case of supercritical systems since this compound system works at significantly lower pressure differences.

Figure 2. 18. *Combined screw-turbine organic fluid closed-cycle (Smith) system.*

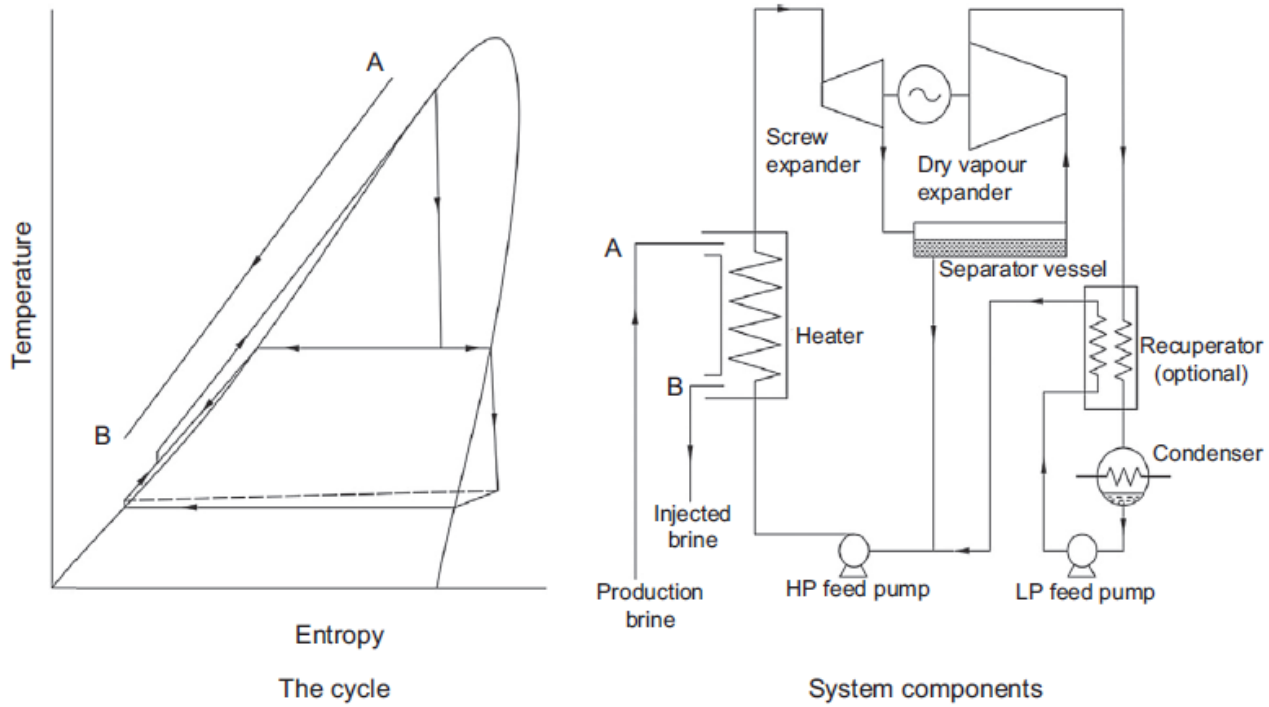

The second is a trilateral flash cycle and wet organic Rankine cycle systems. For geofluids with wellhead conditions of saturated liquid at 363.15-383.15 K, a possible alternative to an ORC system is shown in Fig. 2.19 using an organic working fluid. This has been called a trilateral flash cycle (TFC) system by Smith et al. [52], and by heating the working fluid in the liquid phase only, it is, in principle, possible to maximize the system efficiency.

Figure 2. 19. *Trilateral flash cycle system.*

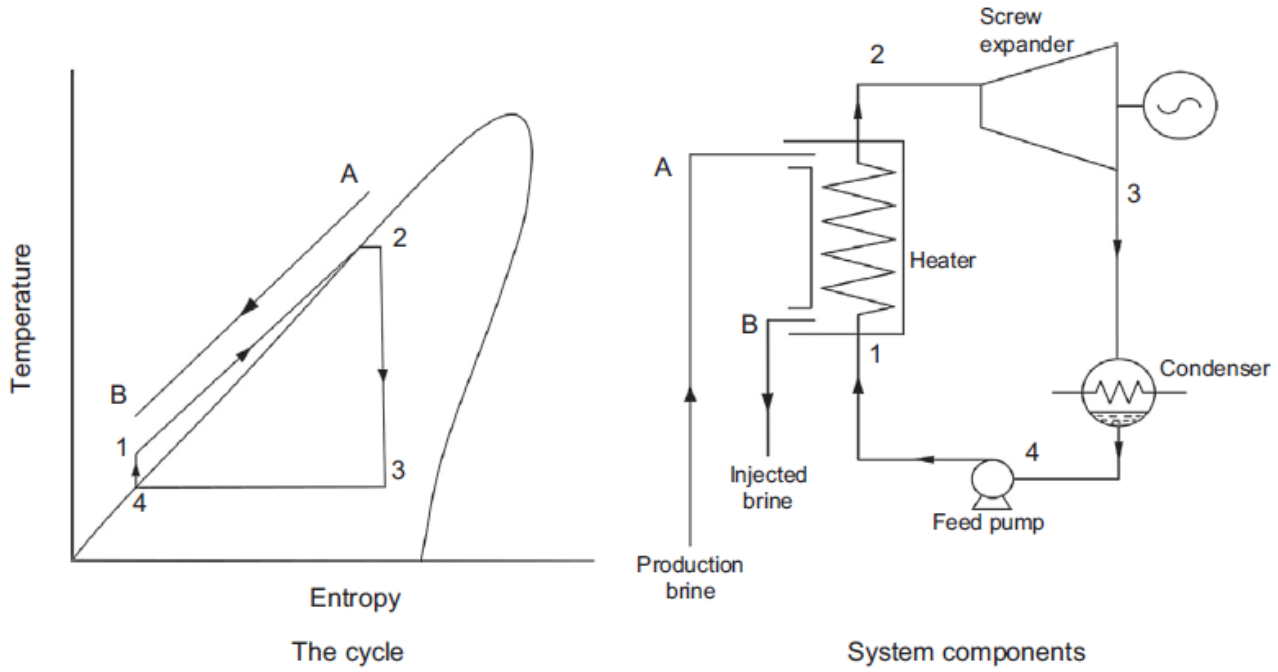

However, the TFC requires a much greater feed pump power than the conventional dry vapour ORC. This is due, mainly, to the lower energy input in heating the working fluid with no evaporation and

hence the need for a much greater working fluid mass flow rate per unit of heat received, partly because higher working fluid temperatures and pressures are attainable if there is no evaporation. More detailed studies have shown that, in practice, when using a screw expander, higher overall efficiencies may be possible if the working fluid is pressurized to lower pressure and partially evaporated with an inlet dryness fraction of the order of 5-10%, as shown in Fig. 2.20.

Figure 2. 20. *Wet organic Rankine cycle system.*

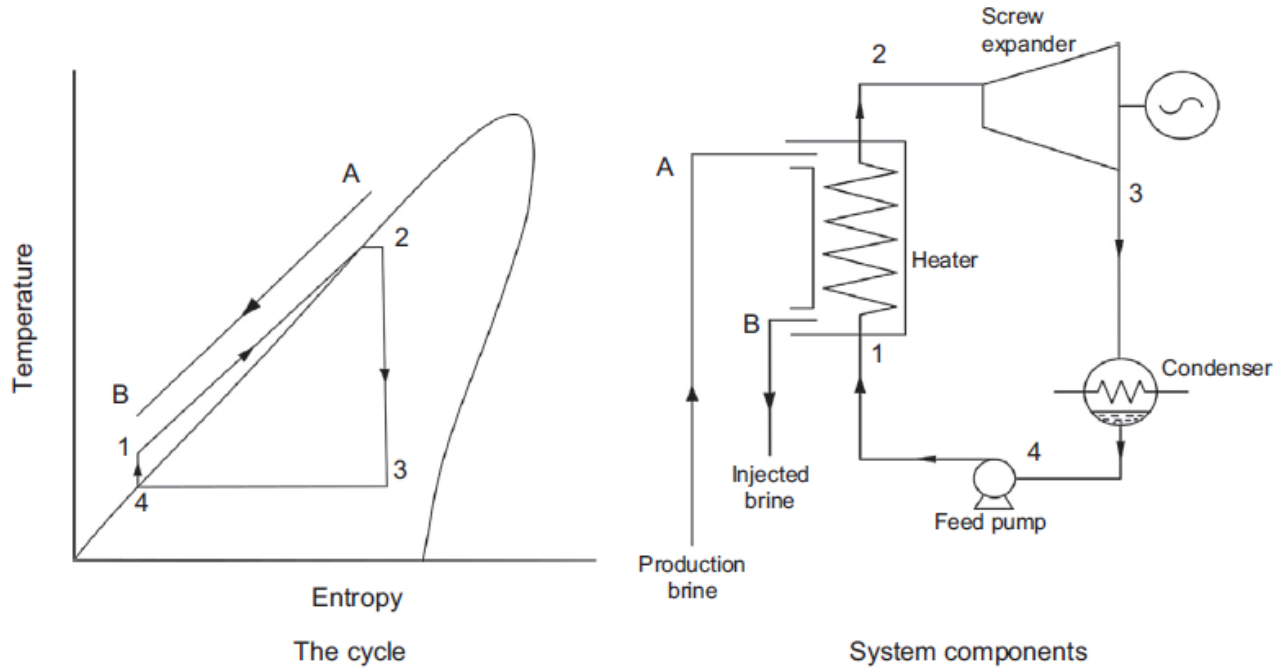

The volume ratio of the expansion process is thereby greatly reduced, permitting a single screw expander to operate with adiabatic efficiencies of the order of 75%, while the working fluid mass flow rate required is significantly reduced. Overall, this reduces the feed pump power requirement, resulting in greater net power output from the system then would be obtained from a TFC system at these lower temperatures. It has been estimated that using screw expanders of ≈ 500-mm rotor diameter, gross outputs of up to ≈ 4 MWe are possible from a single machine. This system could produce up to twice the gross output of an equivalent ORC system expanding dry vapour from a given resource in this temperature ranger. Though the feed pump power required at these temperatures is still very large, a wet ORC (WORC) system of this type would produce again in the net output of only 30-50% over an ORC system expanding dry vapour. However, it should be noted that in both the WORC and TFC systems, this large increase in power is derived from much greater heat extraction from the geofluid and its correspondingly lower injection temperature. This is associated with much larger heat exchangers than are needed for conventional ORC systems. Therefore, careful attention to costing, including that of developing the resource, is necessary to determine which system is the most suitable.

2.5.5 Hybrid geothermal power systems:geothermal-concentrating solar power hybrid plants

This section discusses integrated power plant systems that consist of some geothermal plants combined with a plant using at least one other different energy source, which means that the integrated system is capable of superior performance compared to separate individual plants. Since there are many options available to measure the performance of an integrated plant, equations are developed to provide the basis to assess the synergistic characteristics of these designs. At the basis are the thermodynamic principles and the theoretical integrated designs involving various flash steam Units. Next, many examples of hybrid plants such as geothermal and fossil energy resources are integrated to form hybrid plants of different designs or plants that combine geothermal and solar energy resources. Nuclear, hydroelectric and wind power plants do not lend themselves to hybrid designs with geothermal plants. The appropriate description is for the geothermal-concentrating solar power hybrid plants subjected to extensive research or feasibility studies.

Of the hybrid systems, a case of interest for Italy and the Mediterranean countries is selected. In the hybrid system of Figure 2.21, a parabolic solar collector can be used to superheat the working fluid in a geothermal binary system. Since binary plants suffer from a small temperature range during the feeding cycle, raising the upper temperature will increase thermal efficiency. However, the turbine can deal with saturated steam when the solar circuit is idle. Therefore, the choice of the turbine is a fundamental element during the design. The figure shows a simple storage system (ST) to allow a few hours of continuous operation in hybrid mode after sunset, but when the hot fluid in the storage tank is exhausted, the system returns to basic geothermal operation.

Figure 2. 21. Configuration of geothermal flash plant and with a parabolic collector[11]. Source: [37]

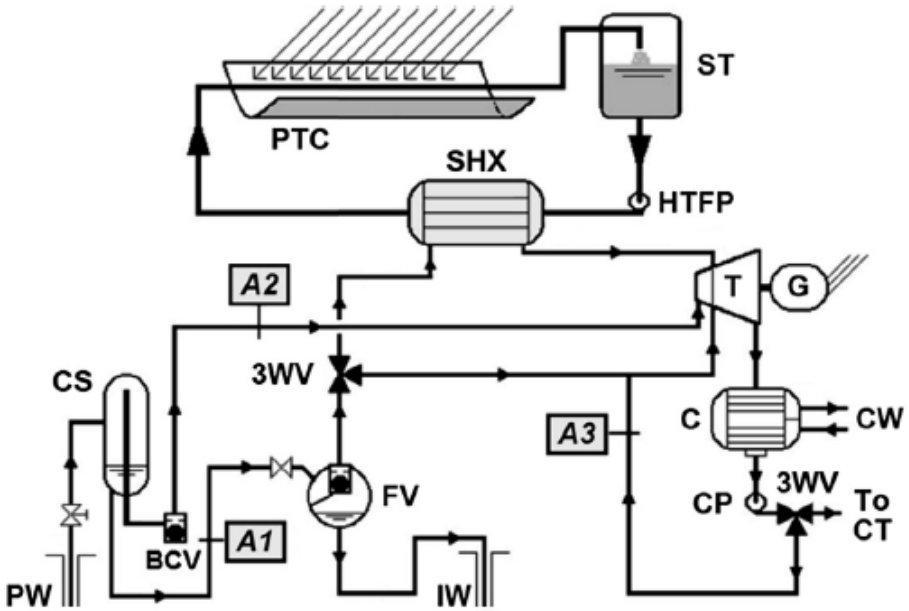

A double flash geothermal plant enhances solar energy. The solar heat exchanger (SHX) is shown overheating the low-pressure steam flashed before mixing with the steam, leaving the first stages of the steam turbine. With this setting, the first low-pressure stages can see superheated steam instead of wet steam and produce a drier and higher expansion line turbine efficiency. Three other options for locating the SHX are shown as A1, A2, and A3. In A1, the separated brine would preheat and allow the flash process to be generated more steam; in A2, it would superheat the vapour separated from the cyclone separator for turbine inlet; and finally, in A3, it would heat and evaporate a portion of the steam condensate for reuse in the low-pressure turbine section. Some examples give good results at the moment [53]. The temperature would be fairly low, about 413.15 K, but would be raised to about 428.15 K using solar collectors during the day. Parabolic collectors would be used to heat a heat transfer medium (oil), as shown in Fig. 2.22, which in turn would impart heat to the brine in a simple tube-in-tube heat exchanger formed by the brine transmission pipeline. The plant would be an air-cooled binary in which the cycle working fluid would enter the turbine as an enhanced superheated vapour when the sun is shining but as essentially a saturated vapour otherwise.

[11] Nomenclature: 3WV: Three-way valve; BCV:Ball check valve; C Condenser; CP Condensate pump; CS Cyclone separator; CT Cooling tower; CW Cooling water; F, FV Flasher, flash vessel; G Generator; HTFP Heat transfer fluid pump; IW Injection well; PW Production well; PTC Parabolic trough collector; SHX Solar heat exchanger; ST Steam turbine; storage tank; T/G Turbine/generator

Figure 2. 22. Example of means of superheating of geothermal steam travelling from the separators to the turbine

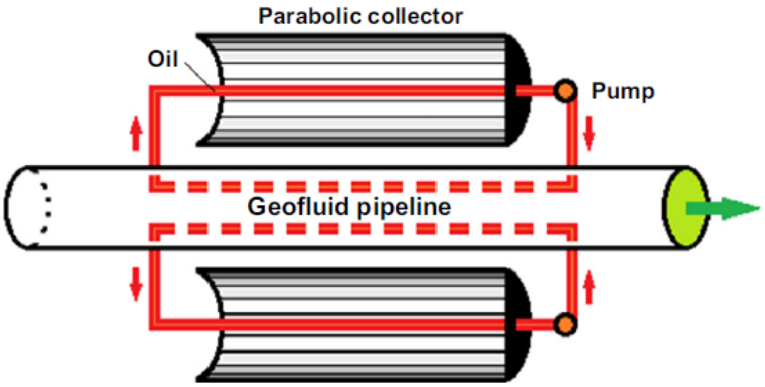

The total daytime power attributed to the solar input would compensate for the poor heat transfer in the air-cooled condensers, limiting power output due to the hot ambient conditions.

2.6 Sustainability, environment and benefits of geothermal energy

In the previous paragraph, geothermal energy was well defined as "clean" and renewable energy, which despite these positive aspects, it finds obstacles in its diffusion in many industrialized and developing countries. But at the same time, it is possible to include energy / thermal production from geothermal sources as a sustainable system.
The first definition of sustainability dates back to the Bruntland Commission in 1987 as "*Meeting the needs of the present generation without compromising the needs of future generations*". Concerning the geothermal resources and their utilization for energy purposes, sustainability means the production system's ability to sustain production levels over long periods [54]. Generally, the resources used for energy production are put into production to achieve economic objectives; in other words, rapid recovery of the investment costs of exploration and equipment, resulting in the tank running out quickly. Even today, the approach to using the resource for the sole purpose of obtaining maximum economic benefits is the most widely used worldwide.
On the contrary, the sustainable geothermal energy production guarantees the resource's longevity at a lower production level, as is the case in the European Union's environmental programs.
Geothermal resources are usually exploited by taking the Fluid and extracting its heat content. Many prominent examples of how this can be accomplished in a renewable way: Hot springs in many parts of the world have been producing staggering amounts of heat (and fluid) on the surface for centuries, showing no signs of decline. In such situations, a balance between the surface discharge and the recharge of the fluid/heat in-depth exists. Any balanced fluid/heat production in a geothermal utilization scheme, i.e. that does not produce more than natural waste, can be considered completely renewable[55]. A balance between injection and exhaust is one of the Horizon 2020 projects' main purposes, including the GeCo project (https://geco-h2020.eu/), which part of the present thesis is built.
However, the production speeds often present are limited and not cheap in many cases. The intensified production rates exceed the recharge rate and ultimately deplete the resource, particularly the Fluid, while the heat stored in the matrix remains largely in place. Many usage schemes, such as in the GeCo Horizon 2020 project of the Hellisheidi geothermal plant, Iceland, have therefore recourse to reinjection (high enthalpy steam and/or water-dominated tanks, doublets in hydrothermal aquifers), which at least replenish the fluid content and helps maintain or restore tank pressure. However, cold reinjected Fluid can lead to temperature drops in ever-larger volumes of the tank. The optimum reinjection temperature must consider the temperature of the extraction fluids so that the temperature gradient does not exceed 303.15 K.
The geothermal fluid and heat extraction subsequently creates a hydraulic/thermal system sink into the tank. This leads to pressure and temperature gradients, which generates an influx of fluid and heat to re-establish the pre-production state after extraction ends [56].

Many numerical (dynamic) simulations have been developed to determine the time scale of recovery for the main use patterns (high enthalpy reservoir for energy production, based on aquifer doublet, geothermal heat pumps) [57]. The recovery shows an asymptotic file behaviour, strong at the beginning and then slowing down, with the recovery of the original state reached theoretically only after an infinite time. However, practical replenishment (e.g. 95% recovery) could typically be achieved much earlier on a time scale of the same order as the duration of geothermal production systems [58].

Table 2. 5. Estimated recovery of a two-phase field[12] after 50 years of production [59]

Reservoir properties	Years after production shut-down		
	50	100	250
Pressure (%)	68	88	98
Temperature (%)	9	21	77
Steam volume	-	5	55

- In the case of a high enthalpy tank (used for electricity generation), the recovery, to be fully adequate, could take a few hundred years, depending on local charging conditions (Table 2.2) [60]. For a low-medium enthalpy tank, recovery can occur with a maximum of 35-50 years [61].
- On the other hand, recovery could take 100-200 years [56], [62].
- In a shallow and decentralized heat pump system, in the heating only mode, the recovery time is roughly equal to the production duration (e.g. functional recovery in 30 years after a production period of 30 years; Figure 2.3) [63],[64], [65]. Thus, recovery occurs during the annual cycle for geothermal heat pumps in heating/cooling mode [66], [60].

Figure 2. 23 Calculated temperature change within a depth of 50 m and a distance of 1 m from a borehole heat exchanger, over a production period and a recovery period of 30 years each [67]–[70] and after 30 years recovery is almost total (ΔT=0.1 °C).Source: [56].

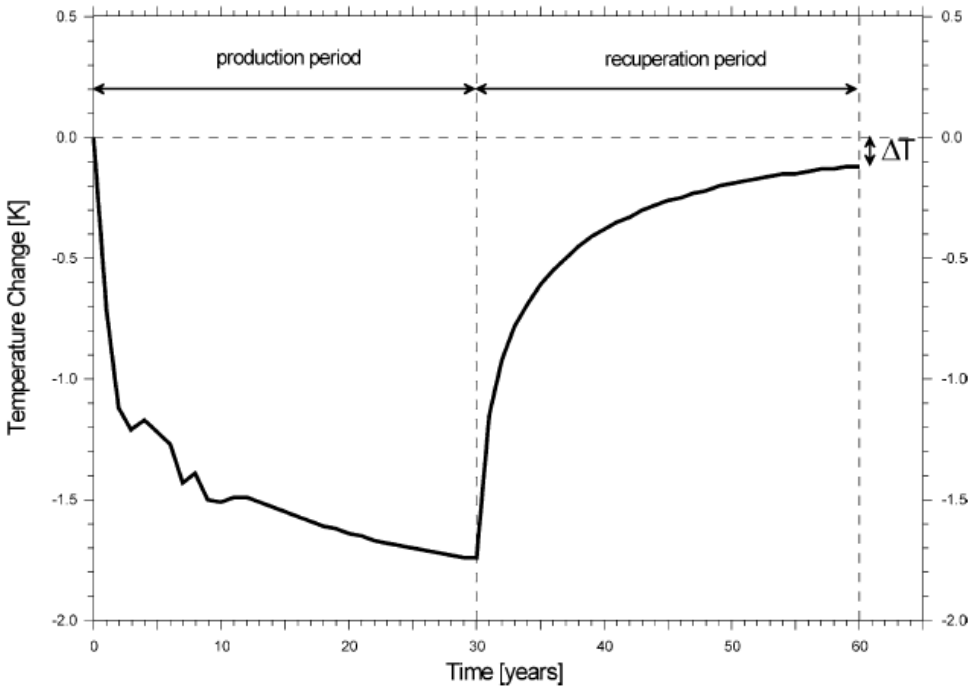

Then, another point of discussion regarding the benefits of emission reduction. Industrialized and developing countries are forced to implement the Kyoto protocol (1997) and the clean development mechanism (CDM). The general problem is the constant increase in CO_2 content in the atmosphere and the rise in the globe's surface temperature [71]. Under this situation, all countries are compelled

[12] The geothermal fluid consists, for the most part, of a two-phase mixture of water containing dissolved salts, steam and non-condensable gases.

to look for alternate CO_2-free energy sources for their competitive activities. Of course, any energy production impacts the environment, but the degree or extent depends on the technology used. Both major geothermal applications, power generation and direct use, can affect the environment [72]. These must be identified, quantified, and, if necessary, eliminated or reduced to comply with environmental regulations. But geothermal energy, combined with the best CDMs, turns out to be one of the best options to provide a safe, stable, and clean energy source.

The first geothermal application is *power generation* which is mainly affected by the properties of the geothermal fluid, and it consists of four phases:

- Exploration[73]–[75];
- Production tests [76]–[79];
- Construction- Operation – Maintenance [80]–[84];
- End of life[85]

The environmental effects may include:

- changes to the landscape, land use;
- emissions into the atmosphere, surface and subsurface waters;
- noise;
- land subsidence, seismicity;
- solid waste.

Figure 2.5 shows that geothermal power generation creates much lower greenhouse gas emissions compared to most other technologies. In any comparison, it is important to consider the file the entire production cycle, i.e. all the phases before, during and after the plant's operation. Geothermal power plants have particularly low CO_2 emissions compared to other technologies; as regards reducing CO_2, there are more attractive options for power generation over coal, oil or gas. The studies of greenhouse gas equivalent emissions for nuclear power come from Sovacool lifecycle studies [86].

Figure 2. 24 Greenhouse gas emissions measured in CO_2 equivalent[13] (g/kWh of electricity) of actual different power generation technologies. Geothermal energy production is competitive with the best clean, renewable energies [31][87], [88].

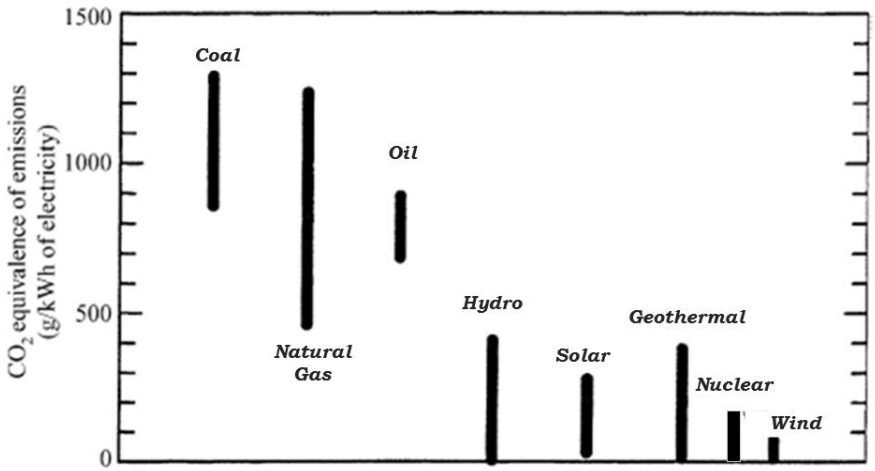

Environmental effects cannot be excluded during geothermal energy production. These could differ based on the characteristics of the site, tank and power plant. Binary type power stations (i.e. a closed system in which a working fluid drives a turbine, not steam or geothermal fluid) have by far the least impact, except for waste heat (Figure 2.25).

The second geothermal application is *direct use*. The degree to which usage affects the environment is proportional to its size. The extracted Fluid is inferior to the first case, so the effects of direct uses are correspondingly smaller.

[13] A carbon dioxide equivalent is a metric measure used to compare the emissions from various greenhouse gases (GHG) on the basis of their flobal-warning potential (GWP), by converting amounts of other gases to the equivalent amount of carbon dioxide with the same global warning potential.

Figure 2. 25. Waste heat from various power generation systems. Due to its low conversion efficiency, geothermal binary power plants release relatively large amounts of heat. Therefore, co-generation or cascaded direct use of the waste heat is recommended [89][90], [91].

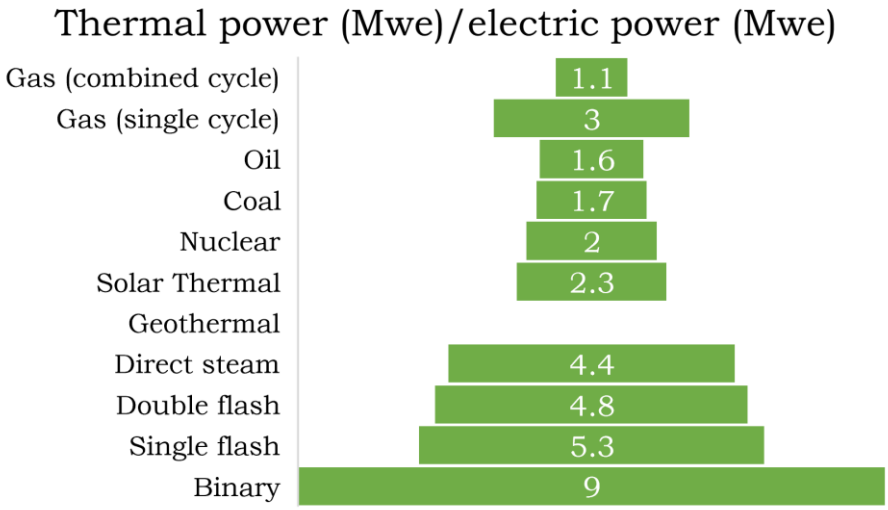

The potential use of low enthalpy geothermal energy for power production is based on various criteria:
- its importance for countries that use predominantly imported fossil fuels for electricity generation;
- improvement of electricity supply in areas without access to grid electricity;
- its values for countries that use predominantly hydroelectric, wind and solar power.

Countries that meet the first two criteria produce most of their electricity from Oil and Gas, and their principal objective is to benefit from reduced CO_2 and other greenhouse gas emissions to cut down negative economic, social and environmental impacts. Reducing the use of fossil fuels is a consequence for eliminating the uncertainties of fluctuating fossil fuel prices. But, also, it diminishes trade deficits by reducing external debts. In addition, countries meeting the criteria three, like Italy, which relies on hydroelectric power, can use geothermal energy to diversify their renewable energy reducing their reliance on hydroelectric power, which is sensitive to climate events.

One of the fundamental characteristics in choosing an energy production system over another is the potential for reducing emissions [92]. Geothermal is a clean energy source that contributes to the reduction of greenhouse emissions, but at the same time, geothermal power generation does have some associated greenhouse gas emissions, which depend on the type of plant (i.e., flash vs binary) and the geothermal Fluid. The predominant emissions are CO_2, the principal greenhouse gas in the atmosphere; methane (CH_4) and hydrogen sulphide (H_2S) are also present in the geothermal fluid. While, during a process, sulfur oxides (SO_x), nitrogen oxides (NO_x) from a geothermal plant are present but less than 2% of the emission of these gases by fossil fuel-based power plants [93]. The CO_2 equivalence of emission for geothermal is 122 g/kWh [94], particularly for an ORC cycle, but it is has a maximum value for a single flash (≈ 400 g/kWh); it depends on the location of geothermal energy production. For example, for the plants of the present work, the average emissions of the Hellisheidi plant, Iceland, are 34 g/ kWh [94] and those Italians working with a medium emission factor of 330 g / kWh [95]. As described in the preview, geothermal fluids contain H_2S, and their emissions are normally carefully regulated and monitored. In Chapter 5, numerical simulations on the Hellisheidi power plant has shown potential benefits to reinjecting these gases into reservoirs to manage/maintain research pressure. Laboratory-scale experiments [96] also show that the geochemical effects may cause a helpful enhancement of porosity and permeability near wells when these gases are injected. Injection of CO_2 and H_2S is being pursued in a team led by Reykjavik Energy in the CarbFix project [97]–[99]. That project has shown that 95% of injected CO_2 was mineralized into carbonate rock within 2 years in their pilot's subsurface in the Hellisheidi power plant. The CarbFix team has quoted this operation as costing €24.8 per ton, making it a cost-effective sequestration approach. The CarbFix team is extending their work to collaborate with Climeworks (https://www.climeworks.com/) to filter CO_2 from the air. Modern geothermal power plant designs typically re-inject liquids produced below the surface so that there is no net discharge of fluid to the surface.

The economic, social and environmental value and importance of emissions reduction underline the

benefits of geothermal energy. The expected CO_2 emissions are calculated for different world regions. The results for the 2004-2030 period are given in Table 2.3.

The source-specific and total CO_2 emissions are listed along with the average annual increases and shares of CO_2 emissions from total anthropogenic CO2 emissions from power plants. From Table 2. 6, it is possible to understand that CO_2 emissions are due to coal.

Table 2. 6. Present and future yearly CO_2 emissions from power generation in the central geothermal locations of the world with data estimated [100][101], [102].

	CO_2 emissions from power generation [10^6 t CO_2] in the year 2004			
	Coal	*Oil*	*Gas*	*Total*
North America	2017.5	339.9	327.5	4246.9
Usa	1886.0	99.7	138.0	2123.7
Canada	93.4	9.8	6.4	109.6
Europe	1002.6	80.9	102.5	1185.9
Africa	216.3	40.9	24.1	281.3
South America	24.8	74.3	27.8	126.9
Brasil	7.6	7.4	3.3	18.3
	CO_2 emissions from power generation [10^6 t CO_2] expected in 2030			
	Coal	Oil	Gas	*Total*
North America	3420.3	175.7	254.2	3850.2
Usa	3173.5	87.4	181.8	3442.7
Canada	144.9	8.2	12.9	166.0
Europe	787.2	54.7	269.0	1111.0
Africa	539.4	53.1	91.7	684.2
South America	82.9	80.1	71.2	234.2
Brasil	44.8	10.6	12.0	67.4

In 2004 the coal-fired power plants emitted $8092.6 \cdot 10^6$ tonnes of CO_2 worldwide, corresponding to 82% of CO_2 emitted by thermal power plants. In comparison, CO_2 emissions from oil and gas were 712 and 629 million tonnes (t), about 10 % of CO_2 released by fossil fuel power plants [103]–[105]. Due to the increase in fossil fuel for electricity generation, it is estimated that in the year 2030, the CO_2 emissions from fossil fuel power plants could increase by annual averages of 2.8, 0.9 and 3.3 % from coal, oil, and gas. This average increase could be present in the USA, Canada and Brasil (for the country cited in this table, but also China, India and South Corea), while for Europe, the emission is expected to decrease by -0.3 % per year on 2030 (Figure 2.26).

It is estimated that geothermal or other renewable energy resources substitute fossil fuel's CO2 emission reduction potential. It needs to consider the CO_2 emissions from the power plants (CO_{2p}) concerning the respective countries' total anthropogenic CO2 (CO_{2T}) emissions. In Table 2.7, the CO_{2p} contributed in 2004 with 29% to $CO_{2T,}$ and the share is expected to increase to 36% in the year 2030. The lowest CO_{2p}/ CO_{2T} ratios are found in the countries that use renewable energies (Canada, South America, and Europe). The highest absolute emission values are 43% for the USA and 46% and 55% for China and India [11]. From power plants in 2030, China and the USA could be responsible for 33% of the world CO_2 emission in 2030.

Figure 2. 26. Average CO_2 emission increase from 2004-2030

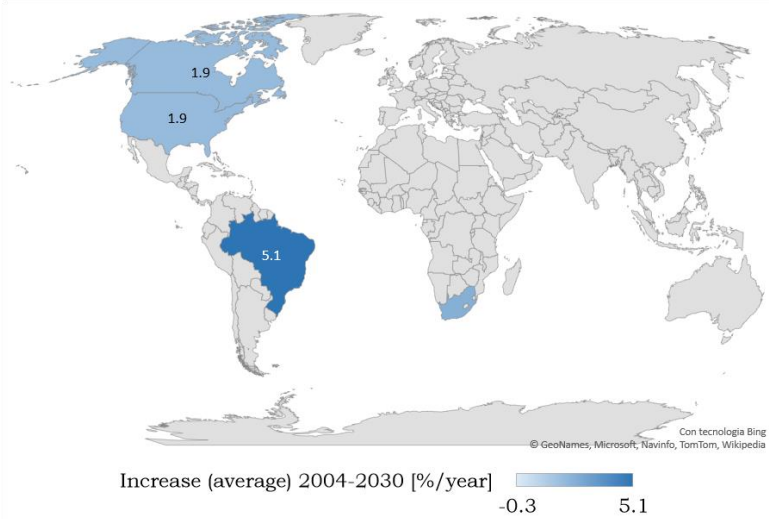

Table 2. 7. World CO_2 emissions from power generation (CO_{2p}) and comparison with total anthropogenic emission (CO_{2T}) values by region. The emission values from power generation are calculated from the different sources according to the energy mix and power generation data from EIA (2019) [106] using average emission data from Kasameyer [107] for coal, gas, and oil-fired power plants; the total CO2 emission data are from EIA (2019) [106].

	Share of world CO_{2p}		Share of CO_{2p} from CO_{2T}		Share of CO_{2p} from world CO_{2T}	
	2004 [%]	2030 [%]	2004 [%]	2030 [%]	2004 [%]	2030 [%]
North America	54.5	38.0	32.1	35.2	15.8	13.7
USA	30.1	25.0	34.1	41.0	8.7	9.0
Canada	27.2	22.3	35.9	43.3	7.9	8.0
Europe	15.2	7.2	27.1	23.7	4.4	2.6
Africa	3.6	4.4	19.5	21.8	0.9	1.2
South Africa	1.6	1.5	30.6	41.3	1.0	1.6
Brasil	0.2	0.4	5.5	11.3	0.1	0.2

A decrease in atmospheric emissions and a reduction in consumption from non-renewable sources can be tackled by an increase in developed small and medium-sized geothermal plants, especially in countries with a low presence of fossil fuels, such as Italy.
Geothermal energy can be used in rural electrification or to reduce the consumption of energy from fossil fuels by installing small (< 10 MW) low-temperature plants that could improve the region's development [108], [109]. Many small geothermal plants are an economical alternative to the costly extension of national grids in the Tuscany region [110], [111]with innovation technologies [112]–[114].

This thesis highlights some Tuscan geothermal plants in the Horizon 2020 European projects that the University of Florence, in collaboration with foreign research bodies and companies, seeks to develop new technological and cognitive skills to develop geothermal energy in the territory.

2.7 Advantages and disadvantages of the current aspects

This section describes the pros and cons of geothermal energy. Many considerations come with geothermal power. Even as a renewable energy source, it is important to weigh the pros and cons of geothermal energy to understand better how it can fit into the greater energy mix. On the pros side,

geothermal energy is a reliable source of power with a small land footprint compared to other renewable sources, and it can be harnessed at both large and small scales. On the cons side, geothermal power plants can only be built in certain locations, they are often expensive to build at first, and they can cause surface instability and earthquakes. Table 2.8 shows some key advantages and disadvantages.

Table 2. 8. Pros and cons of geothermal energy

Pros	Cons
✓ This energy source is more environmentally friendly than conventional fuel sources	× The largest single disadvantage of geothermal energy is that it is location-specific.
✓ A source of renewable energy.	× Gases are released into the atmosphere during digging
✓ The number of exploitable geothermal sources will increase with outgoing research and development in the industry.	× Geothermal energy runs the risk of triggering earthquakes.
✓ A sustainable source of energy as its always available unlike wind and solar.	× The expensive resource to tap into, with high upfront costs ranging from around € 2-7 million for a plant with a 1 MW capacity.
✓ A reliable source as it's easier to predict the power output from a geotherma plant with a high degree of accurancy.	× Energy fluid needs to be pumped back into the underground reservoirs faster than it is depleted. Management is required to maintain sustainability.
✓ No fuel is required.	
✓ An increase in exploration meaning that new technologies are being created to improve the energy process.	
✓ Pollution levels are much lower compared to fossil fuels.	

As seen before, geothermal energy is environmentally friendly than conventional fuel sources like coal and fossil fuels. In addition, the carbon footprint of a geothermal power plant is low. While there is some pollution associated with geothermal energy, this is relatively minimal compared to fossil fuels. The huge potential is estimated that geothermal power plants could provide between 0.0035 and 2 terawatts of power. Therefore, it is part of worldwide energy consumption. Effective use of geothermal for electricity generation requires water temperatures of over 423.15 K to drive turbines. Alternatively, the temperature difference between the surface and a ground source can be used. Energy generated from this resource is easy to calculate since it does not fluctuate similarly to other energy sources, such as solar and wind. It means that it is possible to predict the power output from a geothermal plant with a high degree of accuracy. There is a great deal of exploration into geothermal energy at the moment, meaning that new technologies are being created to improve the energy process. As a result, there is an increasing number of projects to improve and grow this industry area as the thesis project. With this rapid evolution, many of the current cons of geothermal energy will be mitigated.

The main advantages of geothermal energy are:

1. *Geothermal energy is a very reliable source of power*

   One of the biggest advantages of geothermal energy is that geothermal power is a very predictable and reliable energy source, especially in comparison to other renewable energy resources like wind energy and solar energy. While wind and solar are more intermittent sources that require energy storage to be used most effectively at a large scale, geothermal power plants have a generally consistent power output no matter the time of day or season. This has many positive implications, notably that geothermal power is appropriate for meeting baseload energy demand.

2. Geothermal power plants have a small land footprint

   Another advantage of geothermal power plants over other large-scale wind power, solar energy, or

hydroelectric installations is the relatively low footprint of a geothermal plant. This is because, unlike wind, solar, and hydropower, geothermal energy comes from within the Earth, and we don't need to build out collection setups over large swaths of land surface to harness it. For reference, National Geographic[14] estimates that a geothermal power plant capable of producing 1 GWh of electricity would take up approximately 1046.36 km^2 of the land surface, while a wind farm at the same energy output would need about 3457.64 km^2, and a solar farm would need about 6060 km^2. That's 88 % less space for a geothermal power plant than a solar farm; both are sized at 1 GWh.

3. There are large-scale and small-scale applications for geothermal power

   Geothermal energy isn't just for large power plants; in fact, one of the most efficient ways to use heat from the Earth is to harness it with a geothermal heat pump for a residential or commercial building. Unlike geothermal power plants, geothermal heat pumps take advantage of low-temperature geothermal reservoirs which are available just about everywhere.

The largest single disadvantage of geothermal energy is that it is location-specific. Geothermal plants need to be built in places where the energy is accessible, which means that some areas cannot exploit this resource. In this thesis, the place described where geothermal energy is readily accessible are Iceland and Tuscany region. Then geothermal energy is characterized by typically release greenhouse gases. These gases, stored under the Earth's surface, are released into the atmosphere during digging or released into the atmosphere naturally. However, these gas emissions are still far lower than those associated with fossil fuels. In order to maintain the sustainability of geothermal energy, fluid needs to be pumped back into the underground reservoirs faster than it is depleted. This means that geothermal energy needs to be properly managed to maintain its sustainability.

The main disadvantages of geothermal energy are:

1. *Geothermal power plants can only be built at specific sites*

Unfortunately, geothermal power plants can't be built anywhere. Geothermal reservoirs above ~~100°C~~ are usually necessary for most large geothermal plants, and these reservoirs are only found in specific locations, usually near tectonic plate boundaries or hot spots. This is why the vast majority of U.S. geothermal power plants are in California: the state lies close to an active fault zone that is part of the largest "ring of fire" around the Pacific Ocean. Other parts of the country have lower temperature geothermal resources readily available. However, power plants are often not feasible.

2. *Geothermal facilities have high upfront construction costs*

The cost of deploying geothermal power plants is heavily skewed towards early expenses, as there are no fuel purchasing costs once the plant is up and running. According to Lazard's LCOE analysis[15], the upfront cost to build a geothermal energy plant is between $4,000 and $6,000 per kilowatt-hour (kWh). Utility-scale solar energy maxes out at $1,250/kWh, and wind maxes out at $1,550/kWh, making geothermal electricity significantly more expensive upfront than other common renewable options. Even compared to combined-cycle gas plants, geothermal energy is four to six times as expensive initially. The high upfront development costs associated with geothermal power plants is largely a function of the difficulty and cost of drilling deep into the Earth to access geothermal reservoirs.

3. *Geothermal plants can cause earthquakes*

Constructing a geothermal power plant involves drilling deep within the Earth to release hot steam or water trapped in rock formations. This process has been known to cause instability underground, leading to earthquakes at Earth's surface. Additionally, geothermal power plants can cause slow land subsidence over time as geothermal reservoirs are depleted.
The industry needs to assess the pros and cons of geothermal energy to consider the advantages while mitigating against any potential problems.

[14] https://www.nationalgeographic.org/encyclopedia/geothermal-energy/

[15] https://www.lazard.com/media/450784/lazards-levelized-cost-of-energy-version-120-vfinal.pdf

2.8 Conclusions

Geothermal energy is an inexhaustible, stable, and economically valuable source, which is why scientific and industrial research is stemming and increasing in this sector. At the same time, some disadvantages related to the characteristics of the geothermal fluid in the reservoir and the existing geothermal plants are highlighted. The geothermal fluid is not unlimited since, over the years, the amount of geothermal fluid could decrease depending on temperature as a function of industrial production. Furthermore, the chemical components in the geothermal fluid, i.e. the presence of CO_2 and H_2S, cause corrosion to the geothermal system equipment, which leads to more periodic maintenance than other renewable energy plants. The general limitations related to the geothermal plant are associated with the voluminous structure and the new systems under development to reduce H_2S and CO_2 emissions into the air, which cause environmental and social problems. From an engineering point of view, the flash plants were configured as single-flash systems with exhausting bottom turbines by many 20-60 MW plants, particularly in the Tuscany region. However, the trends and the scientific research focus on flash plants, including combined and binary cycles applied to flash resources and axial exhaust turbines. These innovative technologies led to the building of plants with significant MW ratings and combined with hybrid and flexible NCG systems due to the introduction of H_2S abatement systems. The last improvements consist of scaling prediction and control, which led to refined plant efficiencies thanks to multiple flashes and bottom units better tuned to the geofluid chemistry. Indeed, flash plants are increasing because of proven cogeneration or coproduction of harnessing gases, brine, and potentially valuable solids.
Then, changes in chemical resources over time, and other specific factors, make flash plants well suited to custom designs that can maximize the economic output of the project. For these reasons, part of this research aims to use ORC systems. The possible difficulties encountered are associated with the combination of the descending temperature of the geothermal fluid with the rising temperature of the working fluid in a primary heat exchanger of a binary cycle plant, can be significantly reduced by including a two-step expansion process in the cycle to enable the heating of the working fluid to be carried out entirely in the liquid phase. In fact, an innovative system allows the recovery of more heat and reaches maximum temperatures of the working fluid higher in the binary cycle and an increase in power. However, the increase in power is associated with significantly larger heat exchangers, both for the recovery and disposal of more heat and the tiny average temperature difference in the primary exchanger. Accordingly, a careful evaluation of the cost is required to determine if increasing the output power brings tangible benefits related to the global price during a regular working regime. For instance, the drilling and the site costs are very high; hence they should be considered to increase the output power.
Furthermore, among the systems described in this chapter, the author has included the description of hybrid solar energy plants with geothermal concentration for professional reasons inherent to the environmental conditions of his territory. Hybrid power plants involving geothermal and other energy sources can be designed and built in a wide variety of ways. Indeed, the combination of different types of geothermal plants is routinely carried out to obtain more power by intelligently combining the two sources of energy or power systems. Therefore, this allows obtaining more significant power than what could be produced using two separate power plants. The thermodynamics and the required conditions are complex but necessary for further scientific reinforcement to achieve relevant objectives for energy production with low pollution emissions. However, the feasibility of hybrid plants is based on many site-specific factors that must be favourable to success, including co-location of energy sources, energy and electricity prices, availability of energy supplies, environmental authorizations in compliance with all regulatory requirements.

Therefore, the innovation of this Ph.D. program in this topic is to highlight the characteristics of current geothermal systems by enforcing these technological challenges through the implementation of thermodynamic models. These thermodynamic models have been chosen specifically for geothermal and plant fluids with the related environmental analyses. The thermodynamic model's research helps develop hybrid technologies that reuse different energy sources to eliminate emissions and increase sustainability and economic production.

REFERENCE LIST

[1] L. Y. Bronicki, *Introduction to geothermal power generation*. Elsevier Ltd, **2016**.

[2] I. B. Fridleifsson, 'Geothermal energy for the benefit of the people', *Renewable and Sustainable Energy Reviews*, vol. **5**, no. 3, pp. 299–312, **2001**, doi: 10.1016/S1364-0321(01)00002-8.

[3] R. Bertani, 'Geothermal power generation in the world 2010-2014 update report', **60**,*Geothermics*, **2016**, 31-43.doi: 10.1016/j.geothermics.2015.11.003.

[4] A. Anderson and B. Rezaie, 'Geothermal technology: Trends and potential role in a sustainable future', *Applied Energy*, vol. **248**, no. March, pp. 18–34, **2019**, doi: 10.1016/j.apenergy.2019.04.102.

[5] R. Bertani, 'Geothermal power generation in the world 2005-2010 update report', **41**,*Geothermics*, **2012**, 1-22.doi: 10.1016/j.geothermics.2011.10.001.

[6] R. Shortall, B. Davidsdottir, and G. Axelsson, 'Geothermal energy for sustainable development: A review of sustainability impacts and assessment frameworks', *Renewable and Sustainable Energy Reviews*, vol. **44**, pp. 391–406, **2015**, doi: 10.1016/j.rser.2014.12.020.

[7] I. S. Moeck, 'Catalog of geothermal play types based on geologic controls', *Renewable and Sustainable Energy Reviews*, vol. **37**, pp. 867–882, **2014**, doi: 10.1016/j.rser.2014.05.032.

[8] I. B. Fridleifsson, R. Bertani, E. Huenges, J. W. Lund, A. Ragnarsson, and L. Rybach, 'The possible role and contribution of geothermal energy to the', *IPCC scoping meeting on renewable energy sources*, pp. 75–118, **2009**, [Online]. Available: http://citeseerx.ist.psu.edu/viewdoc/download?doi=10.1.1.362.1202&rep=rep1&type=pdf#page=75.

[9] Titiek Ambarwat, R. Iqbal Robbie.Effect of the ethical climate on employee engagement through work satisfationas an intervening variables. Vol.**5**, 1, **2021**,International Journal of Economocs, Business and Accounting Research.

[10] R. Bertani, 'World geothermal power generation in the period 2001-2005',**34**, *Geothermics*, **2005**, 651-690. doi: 10.1016/j.geothermics.2005.09.005.

[11] D. Chandrasekharam and J. Bundschuh, 'Low-enthalpy geothermal resources for power generation', *Low-Enthalpy Geothermal Resources for Power Generation*, no.**67** January, pp. 621–622, **2010**, doi: 10.1080/00207233.2010.498602.

[12] A. C. de Jesus, *Environmental benefits and challenges associated with geothermal power generation*. Elsevier Ltd, **2016**.

[13] J. E. Oliver, 'Kyoto protocol', in *Encyclopedia of Earth Sciences Series*, **2005**, p. 443.

[14] R. W. Henley and A. J. Ellis, 'Geothermal systems ancient and modern: a geochemical review', **19**(1),*Earth Science Reviews*, **1983**, doi: 10.1016/0012-8252(83)90075-2.

[15] R. W. Henley, 'Geothermal fluids: Chemistry and exploration techniques',**52**(3) ,*Journal of Geochemical Exploration*, **1995**, 0-383.doi: 10.1016/0375-6742(95)90013-6.

[16] A. Minissale, 'The Larderello geothermal field: a review',**31**(2) ,*Earth Science Reviews*, **1991**, 0-151.doi: 10.1016/0012-8252(91)90018-B.

[17] Y. K. Kharaka and R. H. Mariner, 'Geothermal systems', in *Isotopes in the Water Cycle: Past, Present and Future of a Developing Science*, **2005**.243-270.Springer.

[18] V. G. Gude, 'Geothermal source potential for water desalination - Current status and future perspective',**57**, *Renewable and Sustainable Energy Reviews*. **2016**,1038-1065. doi: 10.1016/j.rser.2015.12.186.

[19] S. Arnórsson, 'Geothermal systems in Iceland: Structure and conceptual models-I. High-temperature areas',**24**(5-6) ,*Geothermics*, **1995**, 561-602.doi: 10.1016/0375-6505(95)00025-9.

[20] J. L. Haas, 'The effect of salinity on the maximum thermal gradient of a hydrothermal system at hydrostatic pressure',**66** (6) ,*Economic Geology*, **1971**, 940-946. doi: 10.2113/gsecongeo.66.6.940.

[21] W. F. Giggenbach, 'Geothermal gas equilibria', **44**(12),*Geochimica et Cosmochimica Acta*, **1980**, 2021-2032. doi: 10.1016/0016-7037(80)90200-8.

[22] L. Eppelbaum, I. Kutasov, and A. Pilchin, 'Thermal properties of rocks and density of fluids', in *Lecture Notes in Earth System Sciences*, **2014**.

[23] R. W. Henley, A. H. Truesdell, P. B. Barton, and J. A. Whitney, 'Chemical Geothermometers for Geothermal Exploration', vol.**1**, in *Fluid-Mineral Equilibria in Hydrothermal Systems*, **1984**. 1-284. https://doi.org/10.5382/Rev.01

[24] T. K. Flaathen and S. R. Gislason, 'The effect of volcanic eruptions on the chemistry of surface waters: The 1991 and 2000 eruptions of Mt. Hekla, Iceland', **164**(4),*Journal of Volcanology and Geothermal Research*, **2007**, 293-316.doi: 10.1016/j.jvolgeores.2007.05.014.

[25] Z. Duan and D. Li, 'Coupled phase and aqueous species equilibrium of the H_2O-CO_2-NaCl-

$CaCO_3$ system from 0 to 250 °C, 1 to 1000 bar with NaCl concentrations up to saturation of halite', **72**(20),*Geochimica et Cosmochimica Acta*, **2008**, 5128-5145.doi: 10.1016/j.gca.2008.07.025.

[26] A. Mucci, 'The solubility of calcite and aragonite in seawater at various salinities, temperatures, and one atmosphere total pressure.', **283**(7),*American Journal of Science*, **1983**,780-799 doi: 10.2475/ajs.283.7.780.

[27] V. Duchi, A. A. Minissale, S. Ortino, and L. Romani, 'Geothermal prospecting by geochemical methods on natural gas and water discharges in the vulsini mts volcanic district (central Italy)', *Geothermics*, vol. **16**, no. 2, pp. 147–157, **1987**, doi: 10.1016/0375-6505(87)90062-9.

[28] J. Nogara and S. J. Zarrouk, 'Corrosion in geothermal environment: Part 1: Fluids and their impact', *Renewable and Sustainable Energy Reviews*. **2017**, doi: 10.1016/j.rser.2017.06.098.

[29] T. A. Vu, D. Van Tuyen, T. T. Anh, D. Van Toan, and L. H. Phong*, 'Identification of geothermal reservoir from exploration data in the Bang hot spring area, Central Vietnam', Vietnam Journal of Earth sciences, **2017**, doi: 10.15625/0866-7187/39/3/10590.

[30] M. H. Dickson and M. Fanelli, *Geothermal energy: Utilization and technology*. **2003**.pag.224. London, Taylor &Francis Group.

[31] R. DiPippo, 'Geothermal power plants', in *Comprehensive Renewable Energy*, **2012**.Elsevier,

[32] D. L. Gallup, 'Production engineering in geothermal technology: A review',**38**(3) ,*Geothermics*, **2009**, 326-334.doi: 10.1016/j.geothermics.2009.03.001.

[33] G. Axelsson, 'Sustainable geothermal utilization - Case histories; definitions; research issues and modelling',**39**(4) ,*Geothermics*, **2010**, 283-291.doi: 10.1016/j.geothermics.2010.08.001.

[34] E. C. Angcoy and S. Arnórsson, 'Geochemical Modeling of Wells Discharging Excess Enthalpy By Mechanism of Phase Segregation in Mahanagdong , Leyte , Philippines', *Stanford Workshop on Geothermal Reservoir Engineering*, **2011**.

[35] K. L. Brown and G. D. McDowell, 'pH control of Silica scaling', **1983**. Proc. of 5th New Zealand Geothermal Workshop, pp. 157- 162.

[36] K. Brown, 'Thermodynamics and kinetics of silica scaling',**33**(5) ,*Proceedings International Workshop on Mineral Scaling 2011*, **2012**,475-483. doi: 10.1002/jcc.21990.

[37] R. DiPippo, *Geothermal power plants: Principles, Applications, case studies and environmental impact*. **2012**.Elsevier book.

[38] B. F. Tchanche, G. Lambrinos, A. Frangoudakis, and G. Papadakis, 'Low-grade heat conversion into power using organic Rankine cycles - A review of various applications', **15**(8),*Renewable and Sustainable Energy Reviews*. **2011**, 3963-3979.doi: 10.1016/j.rser.2011.07.024.

[39] S. Quoilin, M. Van Den Broek, S. Declaye, P. Dewallef, and V. Lemort, 'Techno-economic survey of organic rankine cycle (ORC) systems',**22** ,*Renewable and Sustainable Energy Reviews*. **2013**, 168-186.doi: 10.1016/j.rser.2013.01.028.

[40] W. Harvey and K. Wallace, *Flash steam geothermal energy conversion systems: Single-, double-, and triple-flash and combined-cycle plants*. Elsevier Ltd, **2016**.

[41] R. DiPippo, 'Geothermal power plants: Evolution and performance assessments',**53** ,*Geothermics*, **2015**, 291-307.doi: 10.1016/j.geothermics.2014.07.005.

[42] S. Jalilinasrabady, R. Itoi, P. Valdimarsson, G. Saevarsdottir, and H. Fujii, 'Flash cycle optimization of Sabalan geothermal power plant employing exergy concept', **43**,*Geothermics*, **2012**, doi: 10.1016/j.geothermics.2012.02.003.

[43] A. Aali, N. Pourmahmoud, and V. Zare, 'Exergoeconomic analysis and multi-objective optimization of a novel combined flash-binary cycle for Sabalan geothermal power plant in Iran', *Energy Conversion and Management*, **2017**, doi: 10.1016/j.enconman.2017.04.025.

[44] L. Cao, J. Wang, P. Zhao, and Y. Dai, 'Thermodynamic comparison among double-flash, flash-Kalina and flash-ORC geothermal power plants', **143**,*International Journal of Thermodynamics*, **2016**, 377-390.doi: 10.5541/ijot.5000156088.

[45] A. H. Mosaffa and A. Zareei, 'Proposal and thermoeconomic analysis of geothermal flash binary power plants utilizing different types of organic flash cycle',**72** ,*Geothermics*, **2018**, 47-63.doi: 10.1016/j.geothermics.2017.10.011.

[46] C. Ballzus, H. Frimannson, G. I. Gunnarsson, and I. Hrolfsson, 'The geothermal power plant at Nesjavellir, ICELAND', *Proceedings World Geothermal Congress 2000*, pp. 3109–3114, **2000**.

[47] M. Dunstall and B. Foster, 'GEOTHERMAL', no. **1**, pp. 21–23, **1994**.

[48] M. Kanoglu and A. Bolatturk, 'Performance and parametric investigation of a binary geothermal power plant by exergy', **33**(11),*Renewable Energy*, **2008**, 2366-2374.doi: 10.1016/j.renene.2008.01.017.

[49] J. Bonafin, C. Pietra, A. Bonzanini, and P. Bombarda, 'CO_2 emissions from geothermal power plants : evaluation of technical solutions for CO2 reinjection', *European Geothermal Congress 2019*, **2019**.

[50] F. Heberle and D. Brüggemann, 'Exergy based fluid selection for a geothermal Organic Rankine Cycle for combined heat and power generation',**30**(11-12) ,*Applied Thermal Engineering*, **2010**, 1326-1332.doi: 10.1016/j.applthermaleng.2010.02.012.
[51] D. Fiaschi, V. Colucci, G. Manfrida, and L. Talluri, 'Geothermal power plant case study for a new ORC plant including CO 2 reinjection', no. June, pp. 11–14, **2019**.
[52] Smith IK., 'Development of the trilateral flash cycle system. Part 1: fundamental considerations.', *J Power Energy Proc IMechE*, vol. **207**, pp. 179–94, **1993**.
[53] S. Handal, Y. Alvarenga, and M. Recinos, 'Geothermal steam production by solar energy', 2007.
[54] B. Shakouri and S. K. Yazdi, 'The sustainable city', **2010**, doi: 10.1109/ICEEA.2010.5596145.pp.272-276.
[55] V. Stefansson, 'The renewability of geothermal energy', *World Geothermal Congress*, **2000**.
[56] L. Rybach, 'Geothermal energy: Sustainability and the environment', *Geothermics*, vol. **32**, no. 4, pp. 463–470, **2003**, doi: 10.1016/S0375-6505(03)00057-9.
[57] F. Calise, D. Capuano, and L. Vanoli, 'Dynamic simulation and exergo-economic optimization of a hybrid solar-geothermal cogeneration plant', *Energies*, vol. **8**, no. 4, pp. 2606–2646, **2015**, doi: 10.3390/en8042606.
[58] L. Rybach, T. Megel, and W. J. Eugster, 'At what time scale are geothermal resources renewable?', *Proceedings World Geothermal Congress 2000 Kyushu-Tohoku, Japan*, **2000**.
[59] J. W. Pritchett, 'Modeling Post-Abandonment Electrical Capacity Recovery for a Two-Phase Geothermal Reservoir', *Geothermal Resources Council, Transactions*, **1998**. v. **22**, p. 521-528
[60] W. Huang, W. Cao, and F. Jiang, 'Heat extraction performance of EGS with heterogeneous reservoir: A numerical evaluation', *International Journal of Heat and Mass Transfer*, vol. **108**, pp. 645–657, **2017**, doi: 10.1016/j.ijheatmasstransfer.2016.12.037.
[61] M. Babaei and H. M. Nick, 'Performance of low-enthalpy geothermal systems: Interplay of spatially correlated heterogeneity and well-doublet spacings', *Applied Energy*, vol. **253**, no. January, p. 113569, **2019**, doi: 10.1016/j.apenergy.2019.113569.
[62] M. D. Aliyu and H. P. Chen, 'Sensitivity analysis of deep geothermal reservoir: Effect of reservoir parameters on production temperature', *Energy*, vol. **129**, pp. 101–113, **2017**, doi: 10.1016/j.energy.2017.04.091.
[63] T. Chandrasiri Ekneligoda and K. B. Min, 'Determination of optimum parameters of doublet system in a horizontally fractured geothermal reservoir', *Renewable Energy*, vol. **65**, pp. 152–160, **2014**, doi: 10.1016/j.renene.2013.08.003.
[64] M. Chen, A. F. B. Tompson, R. J. Mellors, and O. Abdalla, 'An efficient optimization of well placement and control for a geothermal prospect under geological uncertainty', *Applied Energy*, vol. **137**, pp. 352–363, **2015**, doi: 10.1016/j.apenergy.2014.10.036.
[65] Y. Chen, G. Ma, and H. Wang, 'Heat extraction mechanism in a geothermal reservoir with rough-walled fracture networks', *International Journal of Heat and Mass Transfer*, vol. **126**, pp. 1083–1093, **2018**, doi: 10.1016/j.ijheatmasstransfer.2018.05.103.
[66] P. Jiang, X. Li, R. Xu, and F. Zhang, 'Heat extraction of novel underground well pattern systems for geothermal energy exploitation', *Renewable Energy*, vol. **90**, no. 2016, pp. 83–94, **2016**, doi: 10.1016/j.renene.2015.12.062.
[67] L. Rybach and W. J. Eugster, 'Sustainability aspects of geothermal heat pump operation, with experience from Switzerland',**39**(4) ,*Geothermics*, **2010**,365-369. doi: 10.1016/j.geothermics.2010.08.002.
[68] L. Rybach and W. J. Eugster, 'Sustainability aspects of geothermal heat pumps', vol.**39** n.4 *Geothermics Journal*, **2010**.pp.365-369. 10.1016/j.geothermics.2010.08.002
[69] P. A. Østergaard and H. Lund, 'A renewable energy system in Frederikshavn using low-temperature geothermal energy for district heating',vol.**88** n.2 ,*Applied Energy*, **2011**,pp.479-487. doi: 10.1016/j.apenergy.2010.03.018.
[70] L. Rybach, 'Geothermal Sustainability', 2007.
[71] R. J. Norby and Y. Luo, 'Evaluating ecosystem responses to rising atmospheric CO_2 and global warming in a multi-factor world', *New Phytologist*, vol. **162**, no. 2, pp. 281–293, **2004**, doi: 10.1111/j.1469-8137.2004.01047.x.
[72] Y. Başoğul, 'Environmental assessment of a binary geothermal sourced power plant accompanied by exergy analysis', vol.**195**,*Energy Conversion and Management*, **2019**, pp.492-501.doi: 10.1016/j.enconman.2019.05.033.
[73] J. W. Martin and L. Croukamp, 'Exploration into the potential for a low-enthalpy geothermal power plant in Cape fold belt', vol.**89**,*Geothermics*, **2021**,pp.9 doi: 10.1016/j.geothermics.2020.101934.
[74] L. Croukamp, 'Exploration into the potential for a low-enthalpy South Africa', vol.**89** n.9 *Geothermics*, **2021**: 101934.

[75] I. Aguirre, J. Clavero, S. Simmons, A. Giavelli, C. Mayorga, and J. M. Soffia, "'Colpitas" - A new geothermal project in Chile', Geotherm. Resour. Counc. Trans. **2011**, **35**, 1141–1146.
[76] E. M. Vasini *et al.*, 'Interpretation of production tests in geothermal wells with T2Well-EWASG', *Geothermics*, **2018**, doi: 10.1016/j.geothermics.2017.06.005.
[77] G. Axelsson, G. Björnsson, and F. Montalvo, 'Quantitative Interpretation of Tracer Test Data', *World Geothermal Congress*, **2005**.
[78] G. Radilla, J. Sausse, B. Sanjuan, and M. Fourar, 'Interpreting tracer tests in the enhanced geothermal system (EGS) of Soultz-sous-Forêts using the equivalent stratified medium approach', vol.**44**,*Geothermics*, **2012**, pp.43-51.doi: 10.1016/j.geothermics.2012.07.001.
[79] H. Fisch, J. Uhde, C. Bems, P. Lang, and J. Bartels, 'Hydraulic Testing and Reservoir Characterization of the Taufkirchen Site in the Bavarian Molasse Basin, Germany', *World Geothermal Congress 2015*, **2015**.
[80] A. F. M. Parada, 'Geothermal Binary Cycle Power Plant Principles , Operation and Maintenance', n.**20**,*Geothermal Training Programme Reports Orkustofnun*, **2013**.
[81] G. Ricci and G. Viviani, 'Maintenance operations in geothermal power plants', **2**, *Geothermics*, **1970**,pp.839-847. doi: 10.1016/0375-6505(70)90085-4.
[82] H. Ghasemi, A. Tizzanini, M. Paci, and A. Mitsos, 'Optimization of binary geothermal power systems', vol.**32**, in *Computer Aided Chemical Engineering*, **2013**.pp.391-396.
[83] H. A. Yuniarto and I. Baskara, 'Development of procedure for implementing reliability centred maintenance in geothermal power plant', **2017**.
[84] R. S. Atlason and R. Unnthorsson, 'Operation and maintenance in Icelandic geothermal power plants-structure and hierarchy', **2013**, July 2013, Boston, Massachusetts, USA.doi: 10.1115/POWER2013-98207.
[85] R. Basosi, R. Bonciani, D. Frosali, G. Manfrida, M. L. Parisi, and F. Sansone, 'Life cycle analysis of a geothermal power plant: Comparison of the environmental performance with other renewable energy systems',vol.**12** n.7 ,*Sustainability (Switzerland)*, **2020**,doi: 10.3390/su12072786.
[86] B. K. Sovacool, 'Valuing the greenhouse gas emissions from nuclear power: A critical survey', *Energy Policy*, vol. **36**, no. 8, pp. 2950–2963, **2008**, doi: 10.1016/j.enpol.2008.04.017.
[87] M. A. Mongillo and C. J. Bromley, 'The international energy agency geothermal implementing agreement international cooperation for sustainable geothermal development', Bali, **2010**.
[88] T. M. Hunt, *Five Lectures on Environmental Effects of Geothermal Utilization*. 2001.
[89] G. Manente, R. Field, R. Di Pippo, J. W. Tester, M. Paci, and N. Rossi, 'Hybrid solar-geothermal power generation to increase the energy production from a binary geothermal plant', **2011**, Denver, Colorado, USA.doi: 10.1115/imece2011-63665.
[90] R. DiPippo, 'Geothermal energy Electricity generation and environmental impact', *Energy Policy*, 1991, doi: 10.1016/0301-4215(91)90050-X.
[91] R. DiPippo, *Geothermal Power Plants*. **2005**.Elsevier , Third Edition.
[92] E. G. Systems, *The Future of Geothermal Energy The Future of Geothermal Energy*. **2006**. https://www.energy.gov/eere/geothermal/geothermal-technologies
[93] UNFCCC, 'Kyoto Protocol 1997', **1997**.
[94] B. Sigfússon, M. P. Arnarson, S. Ó. Snæbjörnsdóttir, M. R. Karlsdóttir, E. S. Aradóttir, and I. Gunnarsson,vol.**146**,'Reducing emissions of carbon dioxide and hydrogen sulphide at Hellisheidi power plant in 2014-2017 and the role of CarbFix in achieving the 2040 Iceland climate goals', **2018**, pp.135-145.doi: 10.1016/j.egypro.2018.07.018.
[95] B. Goldstein *et al.*, 'Chapter 4 - Geothermal energy', *IPCC Special Report on Renewable Energy Sources and Climate Change Mitigation*, **2011**.
[96] A. G. M. Saldaña, E. Kaya, S. J. Zarrouk, V. Callos, and B. W. Mountain, 'Numerical Simulation of Mixed Brine-CO_2 / H_2S-Rock Interaction During the Reinjection of Non-condensable Gases', *41st Workshop on Geothermal Reservoir Engineering*, **2016**.
[97] J. M. Matter *et al.*, 'The CarbFix Pilot Project - Storing carbon dioxide in basalt',vol.**4**, **2011**,pp.5579-5585. doi: 10.1016/j.egypro.2011.02.546.
[98] E. S. Pind Aradóttir and E. Hjálmarsson, 'CarbFix - Public engagement and transparency', vol.**146**,**2018**, pp.115-120.doi: 10.1016/j.egypro.2018.07.015.
[99] J. Declercq, E. H. Oelkers, and and E. H. O. Declercq, Julien, 'CarbFix Report PHREEQC mineral dissolution kinetics database', *IET Power Electronics*, **2014**.
[100] Office of Energy Markets and End Use, *Annual Energy Review 2007*. **2008**.
[101] EIA, *Monthly Energy Review - April 2020*. **2020**.
[102] EIA, 'International Energy Outlook 2016-World energy demand and economc outlook - Energy Information Administration', *International Energy Outlook*. **2016**.
[103] R. Quadrelli and S. Peterson, 'The energy-climate challenge: Recent trends in CO_2 emissions

from fuel combustion',vol.**35** n.11 ,*Energy Policy*, **2007**,pp.5938-5952. doi: 10.1016/j.enpol.2007.07.001.
[104] IEA, 'CO_2 EMISSIONS FROM FUEL COMBUSTION Highlights', *Iea*, **2015**.
[105] G. Climate and E. Project, 'Global Climate & Energy Project An Assessment of Solar Energy Conversion Technologies and Research Opportunities', *Assessment*, **2006**.
[106] EIA, 'International Energy Outlook 2019 (IEO2019)', *U.S. Energy Information Administration*, **2019**.
[107] W. Cumming, *Geophysics and resource conceptual models in geothermal exploration and development*. Elsevier Ltd, **2016**.
[108] H. M. Covarrubias, R. T. Hinojosa, M. L. Díaz, and R. A. S. Velasco, 'Rural Electrification with a Binary Power Plant Maguarichic Project in Mexico', **2002**.
[109] R. A. Sánchez Velasco, 'Rural Electrification in Mexico from Low Entalphy Geothermal Resources : Maguarichic Off-Grid Power Plant , Mexican Experience', **2005**, Antalya, Turkey.
[110] G. Gianelli, A. Manzella, and M. Puxeddu, 'Crustal models of the geothermal areas of southern Tuscany (Italy)', vol.**281** n.3-4,*Tectonophysics*, **1997**, pp.221-239.doi: 10.1016/S0040-1951(97)00101-7.
[111] A. Brogi *et al.*, 'Crustal structures in the geothermal areas of southern Tuscany (Italy): Insights from the CROP 18 deep seismic reflection lines',vol.**148** ,*Journal of Volcanology and Geothermal Research*, **2005**, pp.60-80.doi: 10.1016/j.jvolgeores.2005.03.014.
[112] F. Minichilli, D. Nuvolone, E. Bustaffa, F. Cipriani, M. A. Vigotti, and F. Bianchi, 'State of health of populations residing in geothermal areas of Tuscany', *Epidemiologia e Prevenzione*, **2012**.
[113] M. Procesi, M. Buttinelli, and M. Pignone, 'Geothermal favourability mapping by advanced geospatial overlay analysis: Tuscany case study (Italy)', *Energy*, **2015**,pp.1-11 doi: 10.1016/j.energy.2015.06.077.
[114] M. Gasparrini, G. Ruggieri, and A. Brogi, 'Diagenesis versus hydrothermalism and fluid-rock interaction within the Tuscan Nappe of the Monte Amiata CO2-rich geothermal area (Italy)', vol.**13**, n.2*Geofluids*, **2013**, pp.159-179.doi: 10.1111/gfl.12025.

Chapter 3

Methodology and Models: models for the mixture properties

In this chapter, the models used for the study of thermodynamic mixtures are described. After an intense bibliographic study and according to the selected and studied implants, the following models were chosen: Soreide & Whitson, PRH, Duan & Sun, Sour-SRK, Cubic Plus Association and OLI. The codes are developed in collaboration between the French Institute of Petroleum and Renewable Energy (IFPEN) and the University of Florence (UNIFI). Some of them are C ++, others in Matlab and others are present in process software such as Unisim Design Suite and Oli Studio through particular modifications. Thanks to this immense and delicate process of selecting thermodynamic models applicable to geothermal mixtures, defining a tree of choices as possible.

Table of Contents

List of Figures

List of Tables

3.1 Introduction

The modelling of the geothermal well-reservoir system and the plant design makes it necessary to use the thermodynamic properties of the geothermal fluids. Furthermore, the increasing use of the thermodynamic packages in the computer software to predict the state of the fluid at the wellhead requires the use of the simpler and accurate functional expression for the properties of the non-condensable gases and salt solutions. This chapter illustrates which equations are intended to illustrate the basic equations used in the thermodynamic packages of process software, including the basic concepts of chemical potentials, fugacities, fugacity coefficients, solubilities and flash calculation.
Furthermore, in the second part of the chapter, the possible thermodynamic models are listed, used to simulate the geothermal flow within a geothermal plant with particular attention to solubility and mixing enthalpies (where possible).

3.2 Thermodynamics of Geothermal Fluid

Geothermal fluids, in the broadest sense, span large variations in composition and cover a wide range of temperature and pressure. Their composition may also be dynamic and change in space and time on both short and long time scales. In addition, physicochemical properties of fluids such as *density*, *viscosity*, *compressibility* and *heat capacity* determine the transfer of heat and mass by geothermal systems, whereas, in turn, the physical properties of the fluids are affected by their chemical properties. Quantitative models of the short spatial and temporal evolution of geochemical fluid processes are, therefore, very demanding concerning the accuracy and broad range of applicability of thermodynamic databases and thermodynamic models (or equations of state) that describe the various datasets as a function of temperature, pressure, and composition. Therefore, the application of thermodynamic calculations is a central part of geochemical studies of diverse processes ranging from the aqueous geochemistry on the reservoir to the energy production plant in which CO_2, H_2S and salt solutions are relevant for their utilization or removal.
Application of thermodynamics to understand geothermal fluid chemistry and transport requires essentially three parts: first, equations of state to describe the physiochemical system; second, a geochemical model involving minerals and fluid species; and, third, values for various thermodynamic parameters from which the thermodynamic and chemical model can be derived.
The two biggest current challenges for comprehensive geochemical modelling of geothermal systems are that thermodynamic data for species in fluids are often missing, particularly at high temperatures (>473.15 K) and pressures (> 50 bar). Then, none of the existing equations of state for aqueous solutes and the thermodynamics of chemical reactions has been validated over the entire range of temperatures, pressures and compositions encountered in the various reservoirs present in the geothermal areas of the world.
Furthermore, it is well known that inconsistencies within and between existing thermodynamic databases and theoretical formulations or equations of state that provide thermodynamic data such as equilibrium constants and activity or fugacity coefficients can lead to large differences e uncertainties in geochemical modelling. For this reason, also in the second part of this chapter, the choice of the models is dictated by the current applicability fluid typology in the most important uses of chemical engineering software. Therefore, an appropriate temperature-pressure range for each experimental data on fluid species can be considered accurate for typical temperatures below 573.15 K[1]. However, for high temperature and high-pressure geothermal fluids, there is a disadvantage of the methods that determine the necessary free Gibbs energies since, under these conditions, many thermodynamic properties of interest (such as enthalpy, entropy, heat capacity and volume) are derived from measurements concerning temperature and pressure rather than being directly determined. Thus, interpolation between the experimental data points is necessary to obtain these data, which requires adequate mathematics formulation by interpolation.
The most popular model and thermodynamic database used among geochemists over the past three decades has been the Helgeson-Kirkham-Flowers (HKF) equation of state [2] and the Supcrt92 database [3], and the density model [4]. However, these models do not work over a large range of temperatures, pressures, and compositions encountered by different types of geothermal fluids. For example, supercritical fluids that exsolve into high-density saline brines and low-density vapour, high-pressure fluids associated with subduction zones, high-enthalpy and low-pressure fluids like superheated vapour and volcanic gas, to name just a few. [5]. In recent years, considerable progress has been made with thermodynamic models for aqueous solutions and solutes that can be used over a wide range of temperatures, pressures and compositions and liquid-vapour phase changes based on electrostatic, macroscopic volumetric and microscopic statistical-mechanical approaches [6].

Moreover, linking aqueous solute thermodynamics to the properties of water is also expected to be the key route for accessing the supercritical region that has been known as notoriously difficult in the construction of equations of state. Over the last two or so decades, much insight into the thermodynamics of supercritical fluids has been obtained, and many rigorous relationships have been derived. Most of our basic thermodynamic parameters come from experimental work on welldefined chemical systems, which allow control of the governing parameters such as temperature, pressure, pH, ionic strength, or redox state with sufficient accuracy. A common method is to study the non-condensable gas (NCG) solubility in the water or in a salt solution and then simultaneously determine the Gibbs free energy. Other popular methods are potentiometry and conductivity measurements, as well as various spectroscopic methods, particularly to demonstrate the lack of data or inconsisten sets of thermodynamic data. Recent data acquired using various experimental tools as Unisim Design are compared with previous data and discussed.

Therefore, reasonably accurate knowledge of the thermophysical properties of geothermal fluids is necessary to predict the power of a geothermal plant. This need becomes apparent when certain variables are calculated, such as the flow quantities in the geothermal well, the steam yield upon flashing (in or out of the well) or the heat transfer rate to a secondary fluid in a binary installation. In addition, properties like the density, enthalpy, entropy, viscosity, saturation pressure, and temperature of the fluid must be known previously for any power plant design. It was common practice to use the properties of pure water for some calculations, but this may result in intolerable calculations. This section provides simple correlations in polynomials for the properties of geothermal salt solutions like solutions of chloride, sulfide and carbonate salts in water. The salts are primarily NaCl, KCl, $CaCl_2$, and to a less extent, K_2SO_4, K_2CO_3, $KHCO_3$, Na_2CO_3, $NaHCO_3$, K_2SO_4 and Na_2SO_4. Not all of the above salts are present in every fluid; NaCl is the most abundant salt. In some fluids, the salts are not present.

Considering the geothermal mixture strictly, an accurate determination of the thermophysical properties of brines would have involved the calculation of fluid properties due to the salt effect, but at the same time is complicated. So, an "equivalent NaCl content" is the amount of NaCl in the solution. This assumption is supported by the fact that the major constituent of the salts is NaCl and the effect of the other chlorides on the properties is similar to the effect of NaCl. Therefore, the brines can be modelled as NaCl solutions and their properties are identified with the corresponding properties of these solutions. Therefore, as the first approximation, in this section, the geothermal fluid has been considered a brine solution.

The necessary properties for the plant design are the density, the enthalpy, the entropy, the viscosity and the saturation pressure at a given temperature. In addition, the properties of the liquid phase (salt solutions) have been considered:

1. Density

Hass [7] presented the expression for the density of NaCl solution [kg/m^3] with an accuracy claimed of 0.5%:

$$\rho = \frac{1000+mM}{1000v_0+m\emptyset} \tag{3. 1}$$

where

$$\emptyset = c_0 + c_1 v_0 + c_2 v_0^2 + \frac{[c_3+c_4 v_0]v_c^2}{[v_c-v_0]^2} \tag{3. 2}$$

and v_0 is the specific volume of pure water given by the equation:

$$v_0 = \frac{v_c+c_5\theta^{1/3}+c_6\theta+c_7\theta^4}{1+c_8\theta^{1/3}+c_9\theta} \tag{3. 3}$$

θ (°C) is the difference of the saturation temperature of brine from the critical temperature of pure water, T is in °C, and ΔT is given from Equation 3.17:

$$\theta = 647.27 - 273.15 - T - \Delta T \tag{3. 4}$$

In Equation 3.1, m is the molality of the solution (moles of salt per kg of water), and the numerical constants c_0 =-167.219), c_1=448.55, c_2=-261.07, c_3=-13.644, c_4=13.97, c_5=-0.315154, c_6=$-1.203374\cdot10^{-3}$, c_7= $7.48908\cdot10^{-13}$, c_8= 0.1342489 and c_9=$-3.946963\cdot10^{-3}$. Also v_c is the critical volume of pure water (3.1975 dm^3/kg) and M is the molecular weight of NaCl : 58.44 kg/kmol.

2. Enthalpy

For the enthalpy of the salt solution [kJ/kg], h_l, the expression is:

$$h_l(T,m) = x_1 h_1(T) + x_2 h_2(T) + m\Delta h(T,m) \quad (3.\ 5)$$

where x_1 and x_2 are the mass fractions of water and salt in the solution (x_1=1000/(1000+58.44 m)), (x_2=58.44 m/(1000+58.44 m)); h_1(T) and h_2(T) are the enthalpies of pure water and salt at temperature T, in °C, m is the molality of the solution, and ΔH(T,m) is the enthalpy of mixing [kJ/kg] which the following expression has correlated:

$$\Delta h(T,m) = \frac{4.184}{1000+58.44m}\sum_{i=0}^{3}\sum_{j=0}^{2} a_{ij}T^i m^j \quad (3.\ 6)$$

The a_{ij} coefficients are : a_{00}=9633.6, a_{01}=-4080.0, a_{02}=286.49, a_{10}=166.58, a_{11}=68.577, a_{12}=-4.6856, a_{20}=-0.90963, a_{21}=-0.36524, a_{22}=0.249667·10^{-1}, a_{30}=0.17965·10^{-2}, a_{31}=0.71924·10^{-3} and a_{32}=-0.4900·10^{-4}.

The function for the enthalpy of pure saturated water and pure salt were computed from data of properties of the substances [8]. The correlations for these properties, in kJ/kg, are as follows:

$$h_1(T) = 0.12453 \cdot 10^{-4} \cdot T^3 - 0.45137 \cdot 10^{-2}T^2 + 4.81155T - 29.578 \quad (3.\ 7)$$

and

$$h_2(T) = [-0.83624 \cdot 10^{-3} \cdot T^3 + 0.16792 \cdot T^2 - 25.9293 \cdot T] \cdot \frac{4.184}{58.44} \quad (3.\ 8)$$

The reference level for this expression of the enthalpy of solutions is °C. The temperature T is always in °C.

3. Entropy

Hildebrandt and Scott [9] observed that the entropy of salt solutions [kJ/kmol·K]could be approximated with the entropies of regular solutions up to molalities of 5.

$$S(T,m) = n_1 s_a(T) + n_2 s_2(T) + n_2 \acute{R} ln\frac{n_1+n_2}{n_2} \quad (3.\ 9)$$

$\acute{R}$ is the universal gas constant 8.314 kJ/kmol·K. The first two terms are the entropy terms of pure water and salt, expressed in kJ/kmol·K:

$$s_1(T) = 5.382 \cdot 10^{-7}T^3 - 4.1508 \cdot 10^{-4}T^2 + 2.70882 \cdot 10^{-1} \cdot T + 3.4092 \cdot 10^{-2} \quad (3.\ 10)$$

and

$$s_2(T) = -0.5247 \cdot 10^{-2}T^2 + 4.2707 \cdot T - 1274.5 \cdot\ ln[T + 273.15] + 7150.2 \quad (3.\ 11)$$

In terms of the molality m, the specific entropy of the solution becomes:

$$s(T,m) = \frac{1}{1000+58.44\,m}\left[55.56 \cdot s_1(T) + m \cdot s_2(T) + m\acute{R} ln\frac{55.56+m}{m}\right] \quad (3.\ 12)$$

4. Viscosity

The viscosity of the salt solution becomes important in the calculation of the pressure drop in the wells. Therefore, the correlation developed by Kestin and Khalifa [10] has adopted from the determination of this property:

$$log\left[\frac{\mu(T,m)}{\mu_w(T)}\right] = A(m) + B(m) log\left[\frac{\mu_w(T)}{\mu_w(20)}\right] \quad (3.\ 13)$$

where $\mu_w(T)$ is the viscosity of pure water, and A e B are functions of molality:

$$A(m)=0.3324\cdot10^{-1}m+0.3624\cdot10^{-2}m^2-0.1879\cdot10^{-3}m^3 \quad (3.\ 14)$$

$$B(m)= -0.3961\cdot10^{-1}m+0.102\cdot10^{-1}m^2-0.702\cdot10^{-3}\cdot m^3 \quad (3.\ 15)$$

The expression gives the viscosity of pure water:

$$log\left[\frac{\mu_w(T)}{\mu_w(20)}\right] = \frac{20-T}{96+T}\cdot[1.2378 - 1.303\cdot10^{-3}[20-T]] + 3.06\cdot10^{-6}[20-T]^2 + 2.55\cdot10^{-8}[20-T]^3 \quad (3.\ 16)$$

$\mu_w(20) = 1002\mu Pas$. The function log is for logarithm base 10.

5. Elevation of the Saturation temperature

The saturation temperature of a salt solution (°C) is higher than the saturation temperature of pure water by an amount:

$$\Delta T = \frac{1.8\acute{K}\,[T+273.15]^2}{L}\cdot\frac{m}{55.56} \quad (3.\ 17)$$

where T is in °C and L is the latent heat of the solution. The constant 1.8 is derived empirically and is related to the fact that the salt s ionized in the solution. Equation 3.17 is a modification of Raoul's law. Similarly, the vapour pressure (kPa) at temperature T (saturation pressure) is lowered by an amount:

$$\Delta P = \frac{1.8\acute{K}\cdot[T+273.15]}{v_v - V_l}\cdot\frac{m}{55.56} \quad (3.\ 18)$$

where v_v and v_l are the specific volumes of steam and liquid water at temperature T in m^3/kg. The following simplified correlation gives the saturation pressure (bar) of pure water:

$$P(T)=\exp[0.21913\cdot10^{-6}T^3-0.17816\cdot10^{-3}\cdot T^2+0.653665\cdot10^{-1}-4.96087] \quad (3.\ 19)$$

The properties of the vapour phase are following described. Usually, the geothermal brine flash inside the well and some vapour are produced. All the salt present in the geothermal fluids is non-volatile; the produced vapour is free of salts. However, the vapour phase contains often non-condensable gases such as CO_2, H_2S, and CH_4. These gases, together with the flashed steam, may be considered as gas mixtures with their specific properties obeying the ideal mixing rule:

$$\emptyset = \sum_i x_i \emptyset_i \quad (3.\ 20)$$

where x_i is the mass fraction of the gas i^{th} and $\emptyset_i$ is a specific property apart from entropy. For entropy calculations, the entropy of mixing ($\sim R\,\acute{\sum} y_i ln y_i$) must be included. The properties of the gases can be calculated from the ideal gas equation of state and data of their specific heats. Since CO_2 is generally the major constituent of the gases, it is often assumed for simplicity that the vapour phase is a binary mixture of steam and CO_2. The properties of interest are enthalpy [kJ/kg], entropy [kJ/kg·K], and density [kg/m³]. The following correlations are fitted to data tables [11] at saturated conditions:

$$h_v(T) = -0.81257\cdot10^{-2}T^2 + 3.65228\cdot T + 2388.4 \quad (3.\ 21)$$

$$s_v(T) = -0.12143\cdot10^{-6}T^3 + 0.809328\cdot10^{-4}T^2 - 0.247983\cdot10^{-1}\cdot T + 9.135745 \quad (3.\ 22)$$

$$P_v(T)= 100P(T)/[-0.1296\cdot10^{-2}\,T^2+0.6325\cdot T+121.05] \quad (3.\ 23)$$

T is in °C, and P(T) is given by Equation 3.19. These simple expressions, in polynomial form, of the properties of geothermal systems were derived for the saturation properties of the brines and steam. Their knowledge is needed for the modelling of geothermal systems as wells as for energy conversion plants.

3.3 The basic equations used in the thermodynamic packages

In this section, the basic equations implemented in the thermodynamic packages for Unisim Desing process software are described to simulate the properties of geothermal fluids inside the GTPP. The following sub-sections are listed the basic concepts: chemical potentials, vapour phase fugacity, liquid phase fugacity, flash calculation, excess Gibbs energy and the activity coefficients, gas solubility in water and brine and mixing enthalpy.

3.3.1 The phase equilibrium condition

According to the thermodynamic principles, equilibrium is reached, considering the constraints on the system and at given pressure and temperature, when the Gibbs energy (G) is lowest:

$$[d(U - TS + PV)] = dG \leq 0 \tag{3. 24}$$

It can be shown that this minimum leads to the statement that the chemical potential is identical in all phases for any component i. Thus, for example, for two phases α and β, this is written as:

$$\mu_i^{\alpha} = \mu_i^{\beta} \tag{3. 25}$$

For a two-phase equilibrium, equation (3.25) provides as many relationships as components in the mixture (¥). Thus, for equilibrium with Φ phases, ¥(Φ-1) relationships can be written.
Using the definition of fugacity ($d\mu_i|_T \triangleq RTdlnf_{i|_T}$), the same rule can be written as:

$$f_i^{\alpha} = f_i^{\beta} \tag{3. 26}$$

3.3.2 The vapour phase fugacity

The vapour phase fugacity is always expressed using the residual approach:

$$f_i^V = Py_i\varphi_i^V \tag{3. 27}$$

where P is the total pressure, y_i is the vapour fraction of component i, φ_i^V is the vapour phase fugacity coefficient of component i. At the low pressure (P< 5 bar), the ideal gas approximation can be used, i.e. $\varphi_i^V = 1$.

3.3.3 The liquid phase fugacity

The fugacities in the liquid phase can be computed using either the residual or the excess approach [12]. Using the residual approach, i.e. with an equation of state, the same expressions can be written as for a vapour phase:

$$f_i^L = Px_i\varphi_i^L \tag{3. 28}$$

with x_i is the liquid fraction of component i, φ_i^L is the liquid phase fugacity coefficient of component i. Using the excess approach, the fugacity is calculated using the definition of the activity coefficient [$\gamma_i = \frac{f_i}{f_i^{id}} = \frac{f_i}{f_i^* \cdot x_i}$]:

$$f_i^L = f_i^{L*}(T,P)\gamma_i x_i \tag{3. 29}$$

The most general expression for the liquid phase fugacity is given by:

$$f_i^L = f_i^{L*}\gamma_i x_i = P_i^{\sigma}\varphi_i^{\sigma}\wp_i\gamma_i x_i \tag{3. 30}$$

where $\wp_i \approx exp\left(\frac{v_i^L(P-P_i^\sigma)}{RT}\right)$ is the Poynting correction that uses v_i^L, the liquid molar volume of component i at T and assumed to be independent of P, φ_i^σ is the fugacity coefficient of component i at saturation calculated using the vapour phase and γ_i is the activity coefficient of component i in the liquid.
When the vapour pressure of component i, P_i^σ is lower than 5 bar, the pure component liquid fugacity can be approximated as:

$$f_i^{L*} = P_i^\sigma \tag{3. 31}$$

3.3.4 Flash calculation

This section focus on the case of two-phase equilibrium vapour-liquid equilibria, also valid for liquid-liquid equilibrium calculations. The equilibrium coefficient must then be defined as the ratio of molar compositions of the two phases present. When more than two phases are present, the number of equations and unknowns increases, but the basic principles remain the same. For the sake of simplicity, the feed compositional vector is defined as (z) to distinguish it from the liquid (x) and the vapour (y) compositions, while the phase equilibrium calculation is indicated as "flash" depending on the type of the two-state variables given. The flash types are PT (pressure and temperature given for basic case and used in all calculations), Tθ or Pθ (Temperature or pressure and vapour fraction given for bubble point, dew point and partially vaporized flash), TV (temperature and volume given for closed vessel at known temperature), PH (Pressure and enthalpy given for adiabatic distillation columns and adiabatic expansions) and PS (Pressure and entropy given for ideal adiabatic compressors, pumps and turbines). Here, it is described the flash type at PT, Tθ and Pθ.
Any phase property can be calculated by knowing its composition, pressure and temperature. In addition, the vapour fraction, the ratio of mole number in the vapour phase concerning the total mole number, ($\theta=N^v/N$) must also be known to evaluate the material balance. Hence, the basic equations are identical for PT, Tθ or Pθ flash calculations:

- The iso-fugacity condition:

$$f_i^L = f_i^V \tag{3. 32}$$

which for calculating K_i, can be written as:

$$x_i K_i = y_i \tag{3. 33}$$

Note that there are two phases in equilibrium, resulting in as many equations as components in the mixture (¥). If there had been three phases, the iso-fugacity condition would have given rise to 2 ¥ equations, and so on (¥ more equations for each additional phase).

- The mass balance equations:

$$\dot{F}z_i = \dot{L}x_i + \dot{V}y_i \rightarrow z_i = (1-\theta)x_i + \theta y_i \tag{3. 34}$$

where $\dot{F}$, $\dot{L}$ and $\dot{V}$ are respectively the molar feed flow, the liquid flow and the vapour flow. If more phases had been present, there would have been more terms on the right-hand side of the equation, but the number of equations would be the same. As unknowns, we have the composition vector of the phases (liquid x and vapour y), in addition to the vapour fraction θ (in the case of a PT flash). This makes 2¥+1 unknowns in the case of a two-phase flash. An additional equation is required to solve the problem. The simple consideration finds that the sum of all molar fractions must be one. This sum can be applied to the liquid [$\sum_{i=1}^{¥} x_i = 1$], or to the vapour [$\sum_{i=1}^{¥} y_i = 1$]. It is replaced by:

$$\sum_{i=1}^{¥} x_i - \sum_{i=1}^{¥} y_i = 0 \tag{3. 35}$$

With substitution in equations (3.30) and (3.34), the resulting [13]are:

$$\begin{cases} x_i = \frac{z_i}{1+\theta(K_i-1)} \\ y_i = \frac{K_i z_i}{1+\theta(K_i-1)} \end{cases} \tag{3. 36}$$

These values of x_i and y_i can be substituted in equation 3.35, which yields:

$$\sum_{i=1}^{¥} \frac{(K_i-1)z_i}{1+\theta(K_i-1)} \quad (3.\ 37)$$

Equation 3.37 is known as the Rachford-Rice equation [13] and is used inside the software algorithms.

A Tθ flash is conceptually identical to the Pθ flash, except that the unknown is the pressure P instead of the temperature T.

3.3.5 The excess Gibbs energy and the activity coefficients

The excess properties for phase equilibrium calculations are the excess Gibbs energy, whose expression is related to the activity coefficients. The excess properties are defined as the difference between the true mixture properties and those of the ideal mixture. Using Euler's theorem [$X = \sum_{i=1}^{¥} N_i \bar{x}_i$. where $\bar{x}_i$ is the partial molar property, X is the extensive property, and N_i is the amount of substance expressed as the number of moles of component i), so:

$$G^E = G - G^{id} = \sum N_i(\bar{g}_i - g_i^*) - RT \sum N_i ln x_i \quad (3.\ 38)$$

The excess property models are based on the excess Gibbs energy, which, using the definition of the fugacity ($\mu_i^\alpha - \mu_i^\beta = RTln\frac{f_i^\alpha}{f_i^\beta}$ in which α and β are at the same temperature) can also be written as ($\bar{g}_i$ is nothing but a chemical potential):

$$G^E = G - G^i = \sum N_i\left(\bar{g}_i - \overline{g_i^{id}}\right) = RT \sum N_i ln \frac{f_i}{f_i^{id}} \quad (3.\ 39)$$

If the activity coefficient is defined as:

$$\gamma_i = \frac{f_i}{f_i^{id}} = \frac{f_i}{f_i^* x_i} \quad (3.\ 40)$$

It is easy to see that the excess Gibbs energy can be calculated from:

$$G^E = RT \sum_i N_i ln\gamma_i \quad (3.\ 41)$$

Inversely, the activity coefficients can be calculated from the excess Gibbs energy using:

$$RTln\gamma_i = \left(\frac{dG^E}{dN_i}\right)_{T,P,N_{j\neq i}} \quad (3.\ 42)$$

In general, the excess Gibbs energy is a function of temperature, pressure and mixture composition.

3.3.6 A vapour-liquid phase equilibrium: gas solubility in water and brine

As mentioned in paragraph 3.2, the geothermal fields contain essentially hot water and steam. CO_2-H_2O, H_2S-H_2O, CH_4-H_2O and the identical systems in salt presence are typical geological fluids involved in the geothermal plant design. Vapour-liquid phase equilibria of the systems are fundamental in the quantitative interpretation of *boiling*, *immiscibility*, *gas solubility* and *fluid migration*. The geothermal fluids have non-ideal mixing properties.

- Gas solubility in water

CO_2 (or H_2S or CH_4) solubility in water depends on the balance between the chemical potential of CO_2 (or H_2S or CH_4) in the liquid phase μ_i^l (i=CO_2 or i=H_2S or i=CH_4 of the binary mixtures) and that in the vapour phase μ_i^v. As described previously, the chemical potential (μ_i in J/mol), who is the fundamental property needed for the equilibrium calculations, can be written in terms of fugacity in the vapour phase and activity in the liquid phase:

$$\mu_i^V(T,P) = \mu_i^{v(0)}(T) + RT \cdot lnf_i(T,P) = \mu_i^{v(0)}(T) + RT \cdot lny_i P + RT \cdot ln\varphi_i(T,P) \quad (3.\ 43)$$

$$\mu_i^l(T,P) = \mu_i^{l(0)}(T) + RT \cdot lna_i(T,P) = \mu_i^{l(0)}(T) + RT \cdot ln\, m_i + RT \cdot ln\gamma_i(T,P) \quad (3.\ 44)$$

where $\mu_i^{l(0)}$, the standard chemical potential of i in liquid, is defined as the chemical potential in the hypothetically ideal solution of unit molality[14], and $\mu_i^{v(0)}$, the standard chemical potential in vapour, is the hypothetical ideal gas chemical potential when the pressure is set to 1 bar, y_i is the mole fraction of i in the vapour phase, and φ_i is the fugacity coefficient of i in the vapour phase.

For phase equilibrium $\mu_i^l = \mu_i^V$, the main relation is obtained:

$$ln\frac{y_i P}{m_i} = \frac{\mu_i^{l(0)}(T,P) - \mu_i^{v(0)}(T)}{RT} + ln\gamma_i(T,P) - ln\varphi_i(T,P) \quad (3.\ 45)$$

where the fugacity coefficient of i in gaseous mixtures is generally calculated from an equation of state (EOS). y_i , the mole fraction of i in the vapour phase, is calculated from:

$$y_i = 1 - y_{H2O} = \frac{P - P_{H2O}}{P} \quad (3.\ 46)$$

where the partial pressure of water in vapour (P_{H2O}) is approximated as the saturated pressure of pure water. The approximation leads to errors for $\mu_i^{l(0)}/RT$ and $ln\gamma_i{}^l$. But, these errors tend to cancel out to a large extent in the parameterization. They have a small effect on the calculated gas solubility in water because, in calculating gas solubility, only the chemical potential difference between liquid and vapour is important. In fitting to the experimental solubility data, the error in the vapour phase can be transferred to the empirical parameters of the liquid phase. And the following error in the liquid phase calculation is negligible. The saturated pressure of pure water here is from the equation of Wagner and Pruss [15].

- Gas solubility in aqueous NaCl solutions

CO_2 (or H_2S or CH_4) solubility in aqueous solutions is determined by balancing its chemical potential in the liquid and gas phases. The potential can be re-written in terms of fugacity in the vapour phase and activity in the liquid phase, similar to equations 3.43 and 3.44 as:

$$\mu_i^l(T,P,y) = \mu_i^{l(0)}(T) + RTln\alpha_i(T,P.m) = \mu_i^{l(0)}(T,P) + RTlnm_i + RTln\gamma_i(T,P,m) \quad (3.\ 47)$$

$$\mu_i^V(T,P,y) = \mu_i^{V(0)}(T) + RTlnf_i(T,P,y) = \mu_i^{V(0)}(T) + RTlny_iP + RTln\varphi_i(T,P,y) \quad (3.\ 48)$$

At equilibrium, $\mu_i^l = \mu_i^V$ and, so, it is possible to obtain:

$$ln\frac{y_i P}{m_i} = \frac{\mu_i^{l(0)}(T,P) - \mu_i^{v(0)}(T)}{RT} - ln\varphi_i(T,P,y) + ln\gamma_i(T,P,m) \quad (3.\ 49)$$

$ln\gamma_i$ is obtained from a virial expansion of excess Gibbs energy (see equation 3.41).

3.3.7 Mixing enthalpy

Aqueous phase. The geothermal enthalpy is expressed in terms of temperature and salinity under a normal state (usually, the temperature is 298.15 K and pressure is 1.013 bar). The basic equation considered the temperature from 273.15 to 573.15 K, solution saturation pressure to 1000 bar and (salt) NaCl molality (m) from 0 to 6 mol/kg water. As analyzed by Michaelides [16] and Lorenz and Müller [17], the enthalpy formula as follows

$$H_{sol} = x_1 H_{water} + x_2 H_{salt} + \Delta H_{mix} \quad (3.\ 50)$$

where H_{water} and H_{salt} are both in a saturated state, and the reference temperature for this expression of enthalpy of the aqueous solution is 0 °C. For the sake of convenience, pure saturated water and pure salt are calculated by following the polynomial proposed by Keenan, Keyes, Hill and Moore [18] and Silvester and Pitzer [19].

$$H_{water} = 0.12453 \cdot 10^{-4}T^3 - 0.45137 \cdot 10^{-2}T^2 + 4.81155 \cdot T\text{-}29.578 \quad (3.\ 51)$$

$$H_{salt} = [-0.83624 \cdot 10^{-3} T^3 + 0.16792 \cdot T^2 - 25.9293 \cdot T\,] \cdot \frac{4.184}{58.44} \quad (3.\ 52)$$

In Michaelides equations [16], $x_1 = 1000/(1000 + 58.44 \cdot m)$ and $x_2 = 58.44 \cdot m/(1000 + 58.44 \cdot m)$. While in Lorenz and Müller equations [17], $x_1 = 1$ and $x_2 = 0$. The last for temperature below 373.15 K, while Michaelides equations are used from 373.15 up to 573.15 K.
In the specific, the ΔH_{mix} is expressed as Equation 3.53 with the coefficients a_{ij} used in Michaelides correlation [16] or Equation 3.54 with the coefficients b_{ij} used in Lorenz and Müller correlation [17].

$$\Delta H_{mix} = \frac{4.184}{1000+58.44 \cdot m} \sum_{i=0}^{3} \sum_{j=0}^{2} a_{ij} T^i m^j \quad (3.\ 53)$$

$$\Delta H_{mix} = \sum_{i=0}^{2} \sum_{j=0}^{3} b_{ij} m^i T^j \quad (3.\ 54)$$

Gas dissolution in the aqueous phase. For the gas dissolution in water or brine, a general equation expression is given by Sherwood and Prausnitz [20]:

$$\frac{\partial ln H_{coeff}}{\partial (1/T)} = \frac{\Delta H_{mix}}{R} \quad (3.\ 55)$$

where H_{coeff} is the Henry's Law coefficient. Then, H_{coeff} is defined as follows:

$$H_{coeff} = K_h \gamma \quad (3.\ 56)$$

where K_h is Henry's constant for gas dissolving in pure water, and γ is the activity coefficient of various gas species.

3.4 General theory of Electrolyte model and Equation of State

In this section, the electrolytes models and a general introduction to the equation of states (EoS) are briefly described to study the behaviour of geothermal fluids. Therefore, this section is divided into two main sub-sections represented by:

1. Electrolyte models
2. Equations of State (EoS).

3.4.1 Electrolyte models

The presence of dissociated salts or, more generally, electrolyte species in a solution results in large non-idealities. An additional difficulty, in this case, is that the reference state that has been used so far (pure component at the same pressure and temperature as the mixture) cannot but used for the simple reason that electrolytes cannot exist in their pure state. Hence, the activity coefficients are defined as:

$$\gamma_i = \frac{f_i}{f_i^{ref}} \quad (3.\ 57)$$

uses as reference state, for ionic species the infinite dilution in the solvent, and the solvent (generally water) the pure component. In addition, since ions cannot exist in the absence of their counter-ion, their activity coefficients cannot be measured. The mean ionic activity coefficient is therefore defined as:

$$ln\gamma_i = ln\gamma_i^{lr} + ln\gamma_i^{sr} \quad (3.\ 58)$$

The first term (lr) refers to the "long-range" interactions, and the second term(sr) to the "short-range" interactions. For this second term, authors have proposed to use, for example, an e-NRTL model [21]. For all models, the "long-range" Coulomb interactions are described using the model proposed by Debye and Hückel [22],[23],[24]. They assume that the electrostatic interactions, can be described using point charges surrounded by an electron cloud of opposite charge. Using the Poisson and Boltzmann equations, it is then possible to calculate the excess energy and thus the activity coefficient of the charged species predictively (i.e. without adjustable parameter) as a function of the ionic

strength, $I = \frac{1}{2}\sum_i^{ions} m_i z_i^2$, where m_i is the ion molality [mol/kg], and z_i is the ionic charge:

$$ln\gamma_{\pm}^{(m)} = -|z_+ z_-|A^{DH}\sqrt{I} \quad (3.\ 59)$$

This expression provides an accurate limiting law but must be corrected for an ionic strength up to 0.1 mol/kg [25]:

$$ln\gamma_{\pm}^{(m)} = -\frac{|z_+ z_-|A^{DH}\sqrt{I}}{1+aB^{DH}\sqrt{I}} \quad (3.\ 60)$$

where a can be related to the ionic, closest approach diameter, and $B^{DH} = eN_{Av}\sqrt{\frac{8\pi d_s}{\varepsilon RT}}$. This is often called the "Pitzer-Debye-Hückel" model. The superscript (m) indicates that this activity coefficient is on a molality basis and

$$A^{DH} = \frac{\sqrt{2d_s}}{8\pi} \cdot \frac{N_{Av^2}e^3}{(\varepsilon RT)^{3/2}} \quad (3.\ 61)$$

where d_s stands for the solvent density [kg/m^3], e is the electronic charge (e = 1.60218·10^{-19} C), ε is the permittivity of the solvent (ε = $\varepsilon_0\varepsilon_r$ where ε_0 = 8.85419·10^{-12} C^2 N^{-1} m^{-2} and ε_r is the relative permittivity), R is the ideal gas constant and T the temperature in kelvin.
For concentrations up to 1 mol/kg, a linear, empirical improvement can be used [26]:

$$ln\gamma_{\pm}^{(m)} = -\frac{|z_+ z_-|A^{DH}\sqrt{I}}{1+aB^{DH}\sqrt{I}} + bI \quad (3.\ 62)$$

where b is an adjustable parameter.

3.4.2 Equations of State (EoS)

Molecules of the same kind also interact, so the theories that consider all types of interaction and the effect of density on these interactions are called equations of state (EoS). They allow the calculation of pure as well as mixture properties as a function of the density. Therefore, their application range covers all fluid phase conditions and can calculate many more properties. The very first important EoS is attributed to Van der Waals [27]. An EoS is considered as a relationship between pressure, volume and temperature. The most important properties calculated from an EoS are pressure and chemical potential. The first can be regarded as an expression of the Helmholtz energy as a function of temperature, phase volume and phase composition [A (T, V, N)]. The pressure is not an independent variable in the EoS, and it is calculated as :

$$P(T,V,N) = -\left.\frac{\partial A}{\partial V}\right|_{T,N} \quad (3.\ 63)$$

The second most important property that can be calculated from an EoS is the chemical potential:

$$\mu_i(T,V,N) = \left.\frac{\partial A}{\partial N_i}\right|_{T,V,N_{j\neq i}} \quad (3.\ 64)$$

The EoS describes the deviation of the real fluid behaviour concerning the ideal gas. These deviations are called the residual properties. For phase equilibrium calculations, the residual chemical potential $\mu_i^{res}(T,P,N)$ is also expressed as a fugacity φ_i. So,

$$\mu_i^{res}(T,P,N) = \left.\frac{\partial A}{\partial N_i}\right|_{T,V,N_{j\neq i}} - \left.\frac{\partial A^{\#}}{\partial N_i}\right|_{T,V^{\#}=\frac{RT}{P},N_{j\neq i}} = RTln\varphi_i = \int_{\infty}^{V}\left(-\left.\frac{\partial A}{\partial N_i}\right|_{T,V,N_j} + \frac{RT}{V}\right)dV - RTlnZ \quad (3.\ 65)$$

where Z is the compressibility factor.

Molecular basis for EoS. The EoS equation can be written at a sum of contributions and is referred to different molecular interactions:

$$A(T,V,N)=A^{\#}(T,V,N)+A^{rep}(T,V,N)+A^{att}(T,V,N)+A^{pol}(T,V,N)+\ldots \quad (3.\ 66)$$

The first of these terms refers to the ideal gas, while the other contributions are repulsion (rep), attraction (att) and polar (pol).

The repulsion contribution is also described by Mansoori et al.[28] for the mixture:

$$A^{rep} = RT\frac{6V}{\pi N_{Av}}\left[\left(\frac{\xi_2^3}{\xi_3^2}-\xi_0\right)ln(1-\xi_3)+\frac{3\xi_1\xi_2}{1-\xi_3}+\frac{\xi_2^3}{\xi_3(1-\xi_3)^2}\right] \quad (3.\ 67)$$

with $\xi_n = \frac{\pi}{6}\frac{N}{V}\sum_i x_i d_i^{\eta}$ and d is the hard-sphere diameter and N_{Av} is the Avogadro number needed to transform the molecular properties into molar properties.

The Van der Waals repulsive term (it corresponds to the ideal gas equation with the assumption that the available volume is reduced with the hard-sphere volume of the molecules, b):

$$A^{rep} = RT\sum_i N_i ln(V-\sum_i N_i b_i) \quad (3.\ 68)$$

Concerning the attractive term, the theories are more complex because they generally use the perturbation theory approach [29], thus the deviation for a reference fluid as a mathematical expansion, which may be truncated at the first or the second order.
When it is used the first-order thermodynamic perturbation theory, assuming a mean-field and taking attractive potential energy, the attractive pressure can be calculated as:

$$P^{att} = -\left.\frac{\partial A}{\partial V}\right|_T = \frac{8\pi}{3}\frac{\sigma_{ij}^3\varepsilon_{ij}}{(V/N_{Av})^2} \quad (3.\ 69)$$

The equation 3.69 is related to Van der Waals' attractive term: $P^{att} = -a_{ij}/v^2$, with the parameter $a_{ij} = 8\pi(N_{Av})^2\sigma_{ij}^3\varepsilon_{ij}/3$.

Another important interaction in EoS is the chemical association. The association occurs between sites. The sites are labelled below as A_i and B_j. The equilibrium constant can be written as:

$$\Delta^{A_iB_j} = \frac{[A_iB_j]}{[A_i][B_j]} \quad (3.\ 70)$$

where the square brackets designate a molar concentration of either bonds ($[A_iB_j]$) or free sites ($[A_i]$). The equilibrium constant is computed using:

$$\Delta^{A_iB_j} = D_{ij}^3 g_{ij}(v)k^{A_iB_j}\left[exp\left(\frac{\varepsilon^{A_iB_j}}{kT}\right)-1\right] \quad (3.\ 71)$$

Where D_{ij} is the hard-sphere distance between components i and j, g_{ij} is the radial distribution function at close contact between the two molecules, which is a function of the system density; $k^{A_iB_j}$ (dimensionless interaction volume) and $\varepsilon^{A_iB_j}$ (interaction energy) are adjustable parameters for the association. The two last parameters are site-site parameters.
When two different associating molecules coexist in the same mixture, both auto- and cross-association can be observed. The interaction parameters for cross-association between sites are often determined using so-called combination rules, which can be either arithmetic or geometric averages:

$$\varepsilon^{A_iB_j} = \sqrt{\varepsilon^{Ai}\varepsilon^{B_j}} \quad (3.\ 72)$$

$$k^{A_iB_j} = \sqrt{k^{A_i}k^{B_j}} \quad (3.\ 73)$$

$$\varepsilon^{A_iB_J} = \frac{\varepsilon^{A_i}+\varepsilon^{B_j}}{2} \quad (3.\ 74)$$

$$k^{A_iB_j} = \frac{k^{A_i} + k^{B_j}}{2} \tag{3. 75}$$

Elliott's rule also has sometimes been recommended:

$$\Delta^{A_iB_j} = \sqrt{\Delta^{A_i}\Delta^{B_j}} \tag{3. 76}$$

Another aspect is polarity. Some molecules may not be considered associating because the interactions between electron donor and electron acceptor sites are not strong enough. Their electronic structure, however, is such that they contain a native dipole or quadrupole (example, CO_2). The approximation equation expressed by Stell [30]:

$$A^{polar} = A_2^{polar}\left[\frac{1}{1-A_3^{polar}/A_2^{polar}}\right] \tag{3. 77}$$

where A_2^{polar} represents the second-order perturbation and A_3^{polar} the third-order perturbation.

The virial coefficients is a generalisation of the ideal gas law using development in power of $1/\nu = N/V$. They are the multiplicative factors of each term of the expansion. The expression is most often written in terms of the compressibility factor:

$$\frac{P(T,V,N)V}{NRT} = Z(T,V,N) = 1 + \frac{B(T)}{\nu} + \frac{C(T)}{\nu^2} + \ldots \tag{3. 78}$$

The coefficients are called the second virial coefficient (B), the third virial coefficient (C). In a mixture, since the second virial coefficient concerns interactions between two molecules, it is possible to show rigorously that the mixing rule for this parameter is

$$B = \sum_i \sum_j y_i y_j B_{ij} \tag{3. 79}$$

where a binary interaction parameter Bij expresses the interactions between unlike molecules i and j. Then, the fugacity coefficient of a component i in a mixture may be written as:

$$ln\varphi_i = \frac{\left(2\sum_{j=1}^{n} y_j B_{ij} - B\right)P}{RT} \tag{3. 80}$$

the chemical engineers use a virial equation of state for the liquid phase, after many more than two terms. These modified virial equations are pseudo-experimental equations proposed by Benedict, Webb and Rubin (BWR). They [31] indicate that an exponential term is also required to represent the critical point region correctly. The equation of state for CO_2 or H_2S or CH_4 has the following form:

$$Z = \frac{P_r V_r}{T_r} = 1 + 1 + \frac{a_1 + a_2/T_r^2 + a_3/T_r^3}{V_r} + \frac{a_4 + a_5/T_r^2 + a_6/T_r^3}{V_r^2} + \frac{a_7 + a_8/T_r^2 + a_9/T_r^3}{V_r^4} + \frac{a_{10} + a_{11}/T_r^2 + a_{12}/T_r^3}{V_r^5} + \frac{a_{13}}{T_r^3 V_r^2}(a_{14} + + \frac{a_{15}}{V_r^2})exp(-\frac{a_{15}}{V_r^2}) \tag{3. 81}$$

where $T_r = \frac{T}{T_c}$, $P_r = \frac{P}{P_c}$, $V_r = \frac{V}{V_c}$ are reduced temperature, reduced pressure and reduced volume, respectively. Then, P_c and T_c are the critical pressure and critical temperature, while V_c is defined as $V_c = \frac{RT_c}{P_c}$. R is the universal gas constant which is equal to 8.314467 Pa m^3 K^{-1} mol^{-1}. Critical properties of CO_2 are T_c = 304.2 K; P_c = 73.825 bar; the critical properties of H_2S are Tc =373.6 K, and P_c =90.08 bar and the critical properties of CH_4 are: Tc = 190.6 K; Pc = 46.41 bar.

The fugacity coefficient of pure CO_2 or H_2S or CH_4 can be derived from Equation 3.81:

$$ln\varphi(T,P) = Z - 1 - lnZ + \frac{a_1 + a_2/T_r^2 + a_3/T_r^3}{V_r} + \frac{a_4 + a_5/T_r^2}{2V_r^2} + \frac{a_7 + a_8/T_r^2 + a_{12}/T_r^3}{5V_r^5} + \frac{a_{13}}{2T_r^3 a_{15}} \cdot \left[a_{14} + 1 - \left(a_{14} + 1 + \frac{a_{15}}{V_r^2}\right) \cdot exp(-\frac{a_{15}}{V_r^2})\right] \tag{3. 82}$$

The most well-known predictive extension of the BWR EoS is the Lee and Kesler [32]. In addition, an extension to multi-components has been proposed by the authors using mixing rules on the corresponding state's parameters:

$$\omega_m = \sum x_i \omega_i \tag{3. 83}$$

$$Z_{cm} = 0.2905 - 0.085 \cdot \omega_m \tag{3. 84}$$

$$v_{cm} = \sum_i \sum_j x_i x_j \left(\frac{v_{ci}^{1/3} + v_{cj}^{1/3}}{2} \right)^3 \tag{3. 85}$$

The mixture critical temperature is calculated as:

$$T_{cm} = \frac{1}{v_{cm}^{\eta}} \sum_i \sum_j x_i x_j \left(\frac{v_{ci}^{1/3} + v_{cj}^{1/3}}{2} \right)^{3\eta} \sqrt{T_{ci} T_{cj}} \tag{3. 86}$$

where the empirical parameter η, initially equal to one, has been introduced by Plocker [33] to improve the mixing enthalpy predictions.

The Cubic equations of state for mixtures. The mathematical expression was published in 1873 by Van der Waals [34]:

$$P = \frac{RT}{v-b} - \frac{a}{v^2} \tag{3. 87}$$

In this equation, the first term corresponds to the repulsive part of the pressure and the second to the attractive part. The attractive part was introduced as depending on temperature by Clausius. Through the introduction of the cohesion function $[\alpha(T) = \alpha_c \alpha(T)]$ with $\alpha(T) = 1/T$. The most frequently used cubic equations are that of Redlich and Kwong, adapted by Soave (called SRK) with $\alpha(T) = \left[1 + m(1 - \sqrt{T})\right]^2$:

$$P = \frac{RT}{v-b} - \frac{\alpha_c \alpha(T)}{v(v+b)}$$

And that of Peng and Robinson (called PR):

$$P = \frac{RT}{v-b} - \frac{\alpha(T)}{v^2 + 2bv - b^2} \tag{3. 88}$$

using the same cohesion function as Soave.

At low temperature ($T < T_c$), it shows three distinct volumes at a given pressure. At high temperatures ($T > T_c$), monotonic behaviour is observed. The limiting isotherm is called the critical isotherm with an inflection point at $T = T_c$. These equations are called cubic because when solving for the volume at fixed pressure and temperature, an equation of the third order in v must be solved. All basic cubic equations can be written using a common shape as:

$$P = \frac{RT}{v-b} - \frac{\alpha(T)}{(v - r_1 b)(v - r_2 b)} = \frac{RT}{v-b} - \frac{\alpha(T)}{(v^2 + ubv + wb^2)} \tag{3. 89}$$

where r_1 and r_2 (or u and w) can take different values (Table 3.1).

Table 3. 1 The parameters to be used for the cubic EoS

Parameter	Van der Waals	Redlich-Kwong (Soave) [SRK]	Peng-Robinson [PR]
r_1	0	0	$-1-\sqrt{2}$
r_2	0	-1	$-1+\sqrt{2}$
u	0	1	2
w	0	0	-1
Ω_a	27/64	0.427480	0.457235
Ω_b	1/8	0.08664	0.077796
Z_c	3/8	1/3	0.30740

The fugacity coefficient, required for the phase equilibrium calculation, is:

$$ln\varphi_i = -ln\frac{P(v-b)}{RT} + \frac{b_i}{b}(Z-1) + \frac{a}{bRT}\left(\frac{2\sum_j a_{ij}z_j}{a} - \frac{b_i}{b}\right)U(v,b,r_1,r_2) \quad (3.90)$$

where $a_{ij} = \sqrt{a_i a_j}(1-k_{ij})$ *and* z_j is the molar fraction of component j in the phase considered. Parameters a_i and b_i describe pure component *i* while a and b are for the mixture parameters. The k_{ij} is a binary interaction parameter (BIP). Z is the compressibility factor. *U* depends on the equation chosen.

For the cubic EoS for mixture, the usual approach uses mixing rules based on the pure component parameters. It consists in:

- The covolume (b) parameter mixing rule. The mixing rule generally applied is a simple linear combination usually named after Lorentz and Berthelot:

$$b_m = \sum_i x_i b_i \quad (3.91)$$

And it also is written as:

$$b_m = \sum_i \sum_j x_i x_j b_{ij} \quad (3.92)$$

where $b_{ij} = \frac{b_i + b_j}{2}$.

- The a parameter mixing rules

The mixing rule on the a parameter can have many different shapes. Therefore, the quality of the phase equilibrium calculation greatly depends on the choice of this mixing rule. The *classic mixing rule* is:

$$a = \sum_i \sum_j x_i x_j a_{ij} \quad (3.93)$$

where

$$a_{ij} = \sqrt{a_i a_j}(1-k_{ij}) \quad (3.94)$$

Here, k_{ij} is an empirical parameter. Note that $k_{ij} = k_{ji}$. This parameter may be temperature-dependent, using:

$$K_{ij} = k_{ij}^{(0)} + k_{ij}^{(1)}T + k_{ij}^{(2)}T^2 \quad (3.95)$$

A method for calculating the Kij of the PR EoS is the following equation:

$$k_{ij}(T) = \frac{-\frac{1}{2}\left[\sum_{K=1}^{Ng}\sum_{l=1}^{Ng}(\alpha_{ik}-\alpha_{jk})(\alpha_{il}-\alpha_{jl})A_{kl}\left(\frac{298.15}{T/K}\right)^{\left(\frac{B_{kl}}{A_{kl}}-1\right)}\right] - \left[\frac{\sqrt{a_i(T)}}{b_i} - \frac{\sqrt{a_j(T)}}{b_j}\right]^2}{2\frac{\sqrt{a_i(T)a_j(T)}}{b_i b_j}} \quad (3.96)$$

α_{ik} is the fraction of group k in molecule i; $A_{kl} = A_{lk}$ and $B_{kl} = B_{lk}$ are interaction parameters between groups. This method has proven useful for VLE calculation, particularly with all mixtures containing CO_2, H_2S and N_2.

Then, another mixing rules fundamental for the geothermal thermodynamic model is the G^E based mixing rules. Huron and Vidal [47] observed that EoS could be used to calculate the Gibbs excess energy as a function of pressure if all pure components have a liquid phase root:

$$g^E(P,T,N) = RT\left(\sum x_i ln\left(\frac{\varphi_i(P,T,N)}{\varphi_i^*(P,T)}\right)\right) \quad (3.97)$$

Generally, the excess Gibbs energy models give good results for non-ideal mixtures, so Huron and Vidal propose calculating the mixture a parameter of the cubic equation of state using this equation and assuming a linear mixing rule for *b* parameter. The main representative of the G^E-type mixing rules for the method Huron-Vidal is:

$$\frac{a_m}{b_m RT} = \sum_i x_i \frac{a_i}{b_i RT} - \frac{g^E}{q_0 RT} \quad (3.\ 98)$$

The parameter q0 is a constant that depends on the EoS. The Huron and Vidal mixing rules assume the linear mixing rule on the covolume (bm). Thus, the second virial coefficient with the Huron-Vidal expression is:

$$B_m = \sum\sum x_i x_j B_{ij} = b_m - \frac{a_m}{RT} \quad (3.\ 99)$$

The rule assumes the linear mixing rule on the covolume (b_m), so that:

$$b_m = \frac{\sum_i \sum_j x_i x_j \frac{\left(b_i - \frac{a_i}{RT}\right) + \left(b_j - \frac{a_j}{RT}\right)}{2}\left(1 - l_{ij}\right)}{1 - \left(\sum_i x_i \frac{a_i}{b_i RT} - \frac{g^E}{q_0 RT}\right)} \quad (3.\ 100)$$

with another binary interaction parameter l_{ij}.
The excess Gibbs energy g^E is also proposed as:

$$g^E = RT \sum_i x_i \sum_j \frac{b_j x_j exp(-\alpha_{ji}\tau_{ji})}{b_k x_k exp(-\alpha_{ki}\tau_{ki})} \tau_{ji} \quad (3.\ 101)$$

Many thermodynamics applied the g^E type mixing rule to the Peng-Robinson EoS, reviewing several number inconsistencies, thus improving asymmetric mixtures forecasts. The covolumes bi is introduced in the equation. τ_{ji} is defined as:

$$\tau_{ji} = \frac{q_0}{RT}\left(\frac{a_i}{b_i} - \frac{2\sqrt{a_i a_j}}{b_i + b_j} \cdot \left(1 - k_{ij}\right)\right) \quad (3.\ 102)$$

3.5 List of Thermodynamic models

In this second part of Chapter 3, the thermodynamic models used to evaluate the properties of the geothermal fluid and to perform the simulation of a GTPP have been introduced. This section describes the main equations employed in the thermodynamic codes that represent the basis of the evaluation and comparison with the experimental data that will be carried out in Chapter 4. In addition, the pros and cons of the models are identified based on the type of geothermal fluid (including non-condensable gas in water and saline solution) under specific conditions of temperature and pressure range. Subsequently, starting from evaluating the performance of these models comparing them with the experimental data, the designer can choose the most appropriate ones to simulate/optimize a binary system (real case). This outcome of this choice is represented in Chapter 5, where a single model has been chosen as the most appropriate to the case study after analyzing the results in Chapter 4.
The thermodynamic models used in this work of thesis are the following: Soreide & Whitson (SW), Peng-Robinson with Huron and Vidal mixing rules (PRH), Duan-Sun (DS), Cubic Plus Association (CPA), Sour-Peng-Robinson (SPR), OLI Aqueous (AQ), OLI Mixed Solvent Electrolyte (MSE) and OLI Mixed Solvent Electrolyte-Soave Redlich-Kwong (MSE-SRK).

3.5.1 Soreide & Whitson

The first thermodynamic model used in these studies is the cubic EoS (see Section 3.4.2) proposed by Søreide and Whitson [36], called SW, which is a revised form of the Peng-Robinson EoS (PR-EoS) [37]. The IFPEN team of J.C. De Hemptinnne and P. Mougin has developed many studies on acid gas solubility in water in salts' presence and not [38], [39].

The Soreide-Whitson model is widely used in the oil and gas field, especially for systems in the presence of water or brine, but it is possible to use in the geothermal reservoir. The model is implemented in software simulators like Simulis Thermodynamics by Prosim, while for this work, it was used an IFPEN code in C^{++}. To describe the phase equilibria of gas-water and gas-brine systems, Soreide and Whitson (SW) proposed two modifications to the PR-EoS.
The state equation expression (PR EoS) remains the same, while the alpha function (introduced in section 3.4.2) and the mixing rules were modified through the following procedure[40].

From Equation 3.88, The PR EoS [37] is also expressed as:

$$P(T,v) = \frac{RT}{v-b} - \frac{a(T)}{v(v+b)+b(v-b)} \quad (3.\ 103)$$

where P is the pressure, T the temperature, R the ideal gas constant, v the molar volume. The energy parameter a and the molar co-volume b for pure compound ith are given by:

$$a_i(T) = 0.457235529 \frac{R^2 T_{c,i}^2}{P_{c,i}} \cdot \alpha(T) \quad (3.\ 104)$$

$$b_i = 0.0777960739 \frac{RT_{c,i}}{P_{c,i}} \quad (3.\ 105)$$

where $P_{c,i}$ and $T_{c,i}$ are respectively the critical pressure and the critical temperature of compound ith. The modifications applied by Soreide and Whitson (SW) are as follows:

- The first modification concerns the alpha function $\alpha(T)$:

The generalized alpha function proposed by Soave [41]has been selected:

$$a_g(T) = \left[1 + 0.37464 + 1.54226\omega_i - 0.26992\omega_i^2\left(1 - \sqrt{\frac{T}{T_{c,i}}}\right)\right]^2 \quad (3.\ 106)$$

where ω_i is the acentric factor. To improve the vapour pressure of water+brine, a specific alpha function for α_w depending on the reduced temperature and NaCl molality m_s was proposed and is given by:

$$\alpha_w(T) = \left[1 + 0.4530\left[1 - \frac{T}{T_{c,w}}(1 - 0.0103 m_s^{1.1})\right] + 0.0034\left(\left(\frac{T}{T_{c,w}}\right)^{-3} - 1\right)\right]^2 \quad (3.\ 107)$$

The alpha function a in equation 3.104 is equal to a_g for gases and to α_w for water or brine.

- The second modification concerns the mixing rules:

The classical mixing rules have been used with two different binary interaction parameters (k_{ij}). The first one is for the aqueous phase and the second one is for the gas phase (liquid-vapour equilibrium) or the other liquid phase (liquid-liquid equilibrium):

$$a_m^{AQ}(T) = \sum_{i=1}^{nc}\sum_{i=1}^{nc} x_i x_j \sqrt{a_i(T)a_j(T)}\ \left(1 - k_{ij}^{AQ}\right) \quad (3.\ 108)$$

$$a_m^{NA}(T) = \sum_{i=1}^{nc}\sum_{i=1}^{nc} y_i y_j \sqrt{a_i(T)a_j(T)}\left(1 - k_{ij}^{NA}\right) \quad (3.\ 109)$$

a_m^{NA} is the attractive parameter of the gas-rich phase(example acid gas), a_m^{AQ} is the attractive parameter of the water-rich phase (aqueous phase).

The second modification concerns the use of two different binary interaction coefficients (k_{ij}), one for the aqueous phase k_{ij}^{AQ} and the other for the non-aqueous (gas-rich) phase k_{ij}^{NA}. For the binary mixture water- acid gas, $k_{ij}^{AQ}$is calculated as $k_{ij}^{AQ} = a(1 + \alpha_0 m_s) + bT_{ri}(1 + \alpha_1 m_s) + cT_{ri}^2(1 + \ +\alpha_2 m_s)$.

Table 3. 2. Parameters of Equation 3.109

a	$1.1120 - 1.7369\omega_i^{-0.1}$
b	$1.1001 + 0.8360\omega_i$
c	$-0.15742 - 1.0988\omega_i$
α_0	$4.7863 \cdot 10^{-13}\omega_i^4$
α_1	$1.4380 \cdot 10^{-2}$
α_2	$2.1547 \cdot 10^{-3}$

These two parameters are respectively adjusted on gas solubility data and water content data of gas

water- NaCl systems. The k_{ij}^{NA} is generally constant or slightly dependant on temperature; however, the k_{ij}^{AQ} depends on temperature and molality.

Furthermore, using two different k_{ij} makes the pattern inconsistent; this limitation is evident above all near the region of the system's critical points [42] and does not represent a problem for the reservoir simulation. Using the model in dynamic simulations of the process can create some inconsistency as the salinity in SW is considered static. Precisely in the dynamic simulations of re-injection of acid components in a geothermal reservoir, Petitfrere et al. [43] implemented the SW model considering a dynamic salinity in its process software. From the results, Chebab et al. [40]state that changing the salinity equation does not have a profound effect as long as the model correctly predicts solubilities. Yan et al.[44] show that the SW model underestimates the solubility of carbon dioxide for high molalities of salt, proposing a modification of the correlation on k_{ij}^{AQ} .This is because the experimental data with the salt were few. The phase equilibria (liquid and vapour phase) was measured by Hou et al.[45]. The adjusted binary interaction parameters for CO_2 are:

$$k_{CO2,w}^{NA} = 0.68208385571 \cdot 10^{-3} T - 2.066623464504 \cdot 10^{-2} \quad (3.\ 110)$$

$$k_{CO2,w}^{AQ} = \left(\frac{T}{T_{c,CO2}}\right)\left[a + b\left(\frac{T}{T_{c,CO2}}\right) + c\left(\frac{T}{T_{c,CO2}}\right)m_s\right] + m_s^2\left[d + e\left(\frac{T}{T_{c,CO2}}\right)\right] + f \quad (3.\ 111)$$

where T is in K, Tc is the critical temperature of CO_2 of 304.13 K, m_s is the salt salinity. Coefficients of Equation 3. 112 are listed in Table 3. 3.

Table 3. 4. Coefficients of the $k_{CO2,w}^{AQ}$ correlation by Hou et al. [45].

a	0.4357516
b	-0.0576691
c	0.0082646
d	0.0012954
e	-0.0016699
f	-0.4786610

3.5.2 PRH

The thermodynamic model is a Peng and Robinson EoS with Huron and Vidal mixing rules [46]. Huron and Vidal [47] observed that equations of state could be used to calculate the Gibbs excess energy as a function of pressure if all pure components have a liquid phase root (Equation 3.97). The G^E-type mixing rules equation of Huron -Vidal model [47] is Equation 3.98. The Huron and Vidal mixing rules assume the linear mixing rule on the covolume (bm). The second virial coefficient with the Huron-Vidal expression in Equation 3.99. The excess Gibbs energy g^E is Equation 3.101
For a quaternary system composed of H_2O, H_2S, CH_4 and CO_2, 50/40/5/5 molar per cent, when an NCG has a high molar per cent, the details are shown in the following reference[1]. However, for the geothermal mixtures analyzed in chapter 5, the same molar composition (mol/mol) presented in the example is not present, but there is always an excess of water. Therefore, the presented geothermal mixtures using the PRH thermodynamic model can be approximated as binary mixtures. In addition, the implemented PRH code cannot model the presence of salts in geothermal mixtures.

3.5.3 Duan & Sun

The thermodynamic study is concentrated on the most common species in geological fluids such as water with CO_2, H_2S, CH_4 and NaCl. Accurate prediction of these elements solubilities over a wide range of temperature, pressure, and ionic strength (T, P, m) is important to create predicted thermodynamic models. Thanks to many experimental studies on the solubilities in pure water and aqueous NaCl solutions, Duan and Sun [48]created models for each element. Based on the Peng-Robinson (PR) EoS, Henry's law and predict phase equilibrium of gas and water/brine mixtures, the model covers a large T-P-m range described by Li and Ngheim [49]. The approach uses the chemical

[1] http://books.ifpenergiesnouvelles.fr/ebooks/thermodynamics.

potential of CO_2 in the vapour phase using the equation of state [50], and the chemical potential of the species in the liquid is described by the Pitzer interaction model [24]. The model results evaluate the experimental data. For this system, the resulting model can predict one of the NCG solubility in pure water from 273 to 533 K and from 1-2000 bar, and in salt solutions up to high temperature, pressure and ionic strength (273-533 K, 0-2000 bar, 0-4 m) with accuracy close to experiments, i.e. less of 7% in CO_2 solubility. The same model can be extrapolated for other aqueous electrolyte solution systems such as aqueous $CaCl_2$, $MgCl_2$ and $(NH_4)_2SO_4$ solutions and seawater. The ith solubility component in aqueous solutions is determined from the balance between its chemical potential in the liquid phase μ_i^l and that in the gas phase μ_i^V. The potential can be written in terms of fugacity in the vapour phase and activity in the liquid phase as Equations 3.47 and 3.48. At equilibrium, $\mu_i^l = \mu_i^V$ and hence, it is possible to obtain Equation 3.49. ith is CO_2 or H_2S or CH_4.

The standard chemical potential of the species in the liquid phase, $\mu_i^{l(0)}$is the chemical potential in the hypothetically ideal solution of unit molality [14]. The vapour phase standard chemical potential, $\mu_i^{v(0)}$, is the hypothetically ideal gas chemical potential when the pressure is equal to 1 bar. In the parameterization, $\mu_i^{v(0)}$, as a reference number, can be set to any number because only the difference between $\mu_i^{l(0)}$ and $\mu_i^{v(0)}$is important. According to the equation of state of Duan et al [50].

It is possible to assume that the mixtures' water vapour pressure is the same as pure water saturation pressure. As Equation 3.46, P_{H2O} is the pure water pressure from steam tables [51]. A virial expansion of excess Gibbs energy is used to obtain $ln\gamma_i$,

$$ln\gamma_i = \sum_c 2\lambda_{i-c} m_c + \sum_a 2\lambda_{i-a} m_a + \sum_c \sum_a \zeta_{i-a-c} m_c m_a \qquad (3.\ 113)$$

where λ and ζ are second-order and third-order interaction parameters, respectively, c and mean cations and anions. Equation 3.113 is substituted in Equation 3.49; it is possible to obtain:

$$ln\frac{y_i P}{m_i} = \frac{\mu_i^{l(0)}}{RT} - ln\varphi_i + \sum_c 2\lambda_{i-c} m_c + \sum_a 2\,\lambda_{i-a} m_a + \sum_c \sum_a \zeta_{i-c-a} m_c m_a \qquad (3.\ 114)$$

In the above equation, λ's, ζ's and the dimensionless standard chemical potential $\mu_i^{l(0)}/RT$ are dependent upon temperature and total pressure. Following Ptizer et al.[24], the following equation for the parameters are:

$$Par(T,P) = c_1 + c_2 T + c_3/T + c_4 T^2 + c_5/(630-T) + c_6 P + c_7 P lnT + c_8 P/T + c_9 P/(630-T) + c_{10} P^2/(630-T)^2 + c_{11} T lnP \qquad (3.\ 115)$$

The term "*Par*" indicates a general formulation of the parameters $\mu_i^{l(0)}/RT$, λ_{i-a}, and ζ_{i-c-a} depending on the temperature and pressure conditions.

Table 3. 5 Interaction parameters for CO_2 (Equation 3.115)

T-P coefficient	$\mu_i^{l(0)}/RT$	λ_{i-a}	ζ_{i-c-a}
c_1	28.94477	-0.41137	0.00034
c_2	-0.03546	0.00061	-0.00002
c_3	-4770.67077	97.53477	-
c_4	0.00001	-	-
c_5	33.81261	-	-
c_6	0.00904	-	-
c_7	-0.00115	-	-
c_8	-0.30741	-0.02376	0.00212
c_9	-0.09073	0.01707	-0.00525
c_{10}	0.00093	-	-
c_{11}	-	0.00001	-

Table 3. 6 Interaction parameters for H_2S (Equation 3.115)

T-P coefficient	$\mu_i^{l(0)}/RT$	λ_{i-a}	ζ_{i-c-a}
c_1	42.56496	0.0850050	-0.01083259
c_2	-0.08626	0.0000353	-
c_3	-6084.37750	-1.5882605	-
c_4	0.00007	-	-
c_5	-102.76849	-	-
c_6	0.00084	0.0000119	-
c_7	-1.05908	-	-
c_8	0.00357	-	-

Table 3. 7 Interaction parameters for CH_4 (Equation 3.115)

T-P coefficient	$\mu_i^{l(0)}/RT$	λ_{i-a}	ζ_{i-c-a}
c_1	43.0210345	0.0992231	-0.0062394
c_2	-0.0683277	0.0000258	-
c_3	-5687.1873000	-	-
c_4	0.0000357	-	-
c_5	-57.9133791	-	-
c_6	0.0061162	-	-
c_7	-0.0007855	-	-
c_8	-0.0942541	0.0183451	-
c_9	0.0192132	-	-
c_{10}	-0.0000092	-0.0000081	-

The basis for the previous equations is equations 3.81 and 3.116. Their parameters are in Table 3.8.

Table 3. 8. Parameters for the equation. 3.81

	CO_2	H_2S	CH_4
a_1	0.0899288	0.0523861	0.0877554
a_2	-0.4947831	-0.2746391	-0.7525995
a_3	0.0477922	-0.0967602	0.3754199
a_4	0.0103809	0.0136181	0.0107291
a_5	-0.0282517	-0.0886818	0.0054963
a_6	0.0949888	0.0411769	-0.0184773
a_7	0.0005206	0.0003635	0.0003190
a_8	-0.0002935	0.0022719	0.0002111
a_9	-0.0017727	-0.0007696	0.0000202
a_{10}	-0.0000251	-0.0000219	-0.0000166
a_{11}	0.0000893	-0.0001171	0.0001196
a_{12}	0.0000789	0.0000408	-0.0001081
a_{13}	-0.0166727	0.0575823	0.0448262
a_{14}	1.3980000	1.0000000	0.7539700
a_{15}	0.0296000	0.0600000	0.0771670

The formula to calculate the fugacity coefficient $ln\varphi_i$ is:

$$ln\varphi(T,P) = Z - 1 - lnZ + \frac{a_1+a_2/T_r^2+a_3/T_r^3}{V_r} + \frac{a_4+a_5/T_r^2}{2V_r^2} + \frac{a_7+a_8/T_r^2+a_{12}/T_r^3}{5V_r^5} + \frac{a_{13}}{2T_r^3 a_{15}} \cdot \left[a_{14} + 1 - \left(a_{14} + 1 + \frac{a_{15}}{V_r^2}\right) \cdot exp(-\frac{a_{15}}{V_r^2})\right] \quad (3.\ 116)$$

The empirical model to calculate pure water pressure is:

$$P = (P_c T/T_c) \cdot [1 + c_1(-t)^{1.9} + c_2 t + c_3 \cdot t^2 + c_4 t^3 + c_5 \cdot t^4] \quad (3.\ 117)$$

where is the temperature in K, t=(T-T_c)/T_c. Parameters of Equation 3.117 are in Table 3.9.

Table 3. 9. Parameters for Equation 3.117

c_1	-38.640844
c_2	5.8948420
c_3	59.876516
c_4	26.654627
c_5	10.637097

In conclusion, for the calculation of solubility, the steps are:

1. Estimation of the compressibility (Z) starting from the coefficients listed in Table 3.8;
2. The compressibility allows calculating the fugacity coefficient, as shown in equation 3.116;
3. Estimation of the chemical potential $(\mu_i^{l(0)}/RT)$ and the interaction parameters λ_{i-a}, ζ_{i-c-a} starting from the coefficients listed in Table 3.5, 3.6, and 3.7;
4. Estimation of the vapour composition of the ith components using the equation 3.46;
5. Calculation of the solubility (in terms of molality) applying the equation 3.114.

For the mixing enthalpy, the DS model is modified as the following equations. Starting from Equation 3.56 and for gas species, CO_2, H_2S and CH_4, K_h follow the form proposed by Mao, Zhang, Li and Liu [52]:

$$lnK_{hi} = a_1 + a_2 T + \frac{a_3}{T} + a_4 T^2 + \frac{a_5 P}{T^2} + a_6 P + a_7 PT + \frac{a_8 P}{T} + a_9 PT^2 + a_{10} P^2 T + a_{11} P^3 \quad (3.\ 118)$$

where a_1-a_{11} are constants listed in Table 3.10.
Activity coefficients follow Pitzer [24] and Pitzer, Peiper and Busey [53] equations.

$$ln\gamma_i = \sum_c 2m_c\lambda_{i-c} + \sum_a 2m_a\lambda_{i-a} + \sum_c \sum_a m_a m_c \zeta_{i-a-c} \quad (3.\ 119)$$

where m_c is cation molality, m_a is anion molality, λ_{i-c}, λ_{i-a} and ζ_{i-a-c} are parameters of functions of temperature and pressure. It refers to Li, Wei and Li [54] approach λ_{i-c} – is supposed to be 0 (with NaCl). The parameters calculations are listed in Table 3.11.

Table 3. 10 Parameters for Henry's constants of CO_2, H_2S and CH_4. a_i is taken from Mao, Zhang, Li and Liu [52].

	CO_2	H_2S	CH_4
a_1	23	-825.352	-16.3979
a_2	-0.03654057	1.466009	326
a_3	-1836.6895	208000	9470
a_4	$2.03 \cdot 10^{-5}$	-0.00097	$-2.66 \cdot 10^{-05}$
a_5	-390723.84	$-2 \cdot 10^{07}$	-1435285
a_6	-0.05826933	0.823685	-0.01323
a_7	0.000151	-0.00222	$3.13 \cdot 10^{-05}$
a_8	7.81	-101.113	2.26048
a_9	$-1.30 \cdot 10^{-07}$	$1.96 \cdot 10^{-06}$	$-2.91 \cdot 10^{-08}$
a_{10}	$1.11 \cdot 10^{-09}$	$3.78 \cdot 10^{-08}$	$3.44 \cdot 10^{-09}$
a_{11}	$-1.31 \cdot 10^{-10}$	$2.92 \cdot 10^{-09}$	$-6.12 \cdot 10^{-10}$

Table 3. 11. Pitzer parameters for activity coefficients [55]

Parameters	Equation
$\lambda_{CO_2-Na^+}$	$-0.31312239+0.5532647\times 10^{-3}\mathrm{T}+7.5844401/\mathrm{T}\text{-}0.18950519\times 10^{-3}\mathrm{P}+7.1628762\times 10^{-5}\mathrm{PT}\text{-}1.458572\times 10^{-8}\mathrm{P}T^2$
$\lambda_{CH_4-Na^+}$	$-0.718015779+1.014419\times 10^{-3}T+166.24239122/T+8.138894\times 10^{-5}P+2.302452724\times 10^{-11}P^2T-2.34735335\times 10^{7}\mathrm{PT}$
$\lambda_{H_2S-Na^+}$	$1.3392459-0.0020334494T-2.03201235\times 10^{2}/T-7.700316\times 10^{3}P$ $-4.36067312\times 10^{-8}P^2T+2.500095\times 10^{-5}PT$
$\lambda_{N_2-Na^+}$	$-2.4434074+0.36351795\times 10^{-2}T+0.44747364\times 10^{3}/T-0.13711527\times 10^{-4}P$ $+0.7103721\times 10^{-5}P^2/T$
$\zeta_{CO_2-Na^+-Cl^-}$	$0.340968\times 10^{-2}-0.276711\times 10^{-4}T-0.83847525\times 10^{-7}PT+0.34225403\times 10^{-10}P^2T$
$\zeta_{CH_4-Na^+-Cl^-}$	$-1.65439125285\times 10^{-3}$
$\zeta_{H_2S-Na^+-Cl^-}$	$2.54763081450856\times 10^{-3}$
$\zeta_{N_2-Na^+-Cl^-}$	$-0.58071053\times 10^{-2}$

3.5.4 Sour-PR

The Sour PR model (SPR) is a combination between the Peng-Robinson equation (PR) and Wilson's API Sour Model [56]. This thermodynamic model[2] is applied to any process containing acid gases or hydrocarbons, and water. The K-values for the aqueous phase is calculated using Wilson's API-Sour method [56]. The aqueous model employs a modification of Van Krevelen's original model [57], with many of the critical limitations removed. The K-value of water is calculated using an empirical equation, which is a function of temperature only. Using the PR equation of state to correct vapour phase non-idealities extends the range over 293.15 K- 413.15 K. The method performs well when the H_2O partial pressure is below 6.90 bar. The sour water equilibrium model obtains the various chemical and physical equilibria of CO_2 and H_2S in Sour water systems. This method is used in the software when most components are CO_2, H_2S and NH_3 in water.
While Van Krevelen et al. [57] assumed that H_2S and CO_2 only exist in aqueous solutions as ionized species, Wilson [56] considered the chemical equilibrium between ionic species of H_2S or CO_2 and undissociated H_2S or CO_2 in the liquid. Simultaneously, the model doesn't consider the equilibrium dissolved CO_2 and the carbonic acid (H_2CO_3) because other acids or basic components don't affect the equilibrium. Then, the partial pressure of the two compounds in the vapour phase is calculated with Henry's constants, where Henry's constants are dependent on the solution's composition. Two analytics properties give the vapour-liquid calculation:

- Effect of the temperature and composition on Henry's law constants so that CO_2 and H_2S concentrations in the liquid phase can calculate the partial pressures in the vapour phase;
- The temperature and composition affect chemical equilibrium constants so that the liquid's CO_2 and H_2S concentrations can be calculated.

Regarding the Sour PR parameters elaborated in the process simulator (Unisim Design R480, licensed by University of Firenze), the considerations set are:

- Enthalpy: property package PR EoS;
- Density: EoS Density;
- Viscosity Index parameters in the software follow this equation:

$$A \cdot log10(log10(\nu + C)) + B \qquad (3.\ 120)$$

where A is a constant at a fixed temperature, ν is the kinematic viscosity of a component in cSt, C is an adjustable parameter and B is a constant [58]:

- Thermal Conductivity: API 12A3.2-1 Method;
- Phase identification: the thermodynamic method uses the Venkatarathnam-Oellrich approach[59] to determine the fluid phase from the partial derivatives of pressure, volume and temperature without reference to saturated properties. It is used for liquid-liquid or vapour-liquid-liquid equilibria calculations.

The Sour model package (SPR) is integrated into Unisim Design R480. The first step is the component's attachment, and then the thermodynamic engine is ready to perform flash and physical property calculations of the defined system. First, the vapour pressure of water is calculated by the Steam Table of Irvine and Liley [60] through the following equation:

$$lnp_w^* = 6.9078 + \left(\sum_{i=0}^{9} a_i T^i + \frac{a_{10}}{T - a_{11}}\right) \qquad (3.\ 121)$$

where p_w^* is the vapour pressure of water, T is the temperature and a_i is the coefficient with the values listed in Table 3. 12.

[2] API publication 955 titled "A New Correlation of NH_3, CO_2, and H_2S Volatility Data from Aqueous Sour Water Systems."

Table 3. 12 Coefficients for the vapour equation of water in SPR model

i	a_i	i	a_i
0	10.4592	6	$9.0367 \cdot 10^{-16}$
1	$-4.0490 \cdot 10^{-3}$	7	$-1.9969 \cdot 10^{-18}$
2	$-4.1752 \cdot 10^{-5}$	8	$7.7929 \cdot 10^{-22}$
3	$3.6851 \cdot 10^{-7}$	9	$1.9148 \cdot 10^{-25}$
4	$-1.0152 \cdot 10^{-9}$	10	$-3.9681 \cdot 10^{+3}$
5	$8.6531 \cdot 10^{-13}$	11	39.574

In the liquid-liquid or the vapour-liquid-liquid equilibrium, the algorithm considers the heaviest phase as the aqueous phase only when mole fraction of water, x_w^l is more robust than 0.5. To ensure the model continuous at x_w^l=0.5, a transition range is created where 0.4 <x_w^l< 0.6. If x_w^l < 0.4, the fugacities of all components are calculated by EOS, and if $x_w^l > 0.6$, the API model is used. In this transition range, the fugacities of all the components are revised by the following equation:

$$f = f_{EoS} + (f_{API} - f_{EoS}) \cdot (x_w^l - 0.4)/(0.6 - 0.4) \quad (3.\ 122)$$

In this equation, f is the fugacity of a compound, while f_{EoS} and f_{API} are the compound's fugacities calculated by the state and the API model equation, respectively.
The binary interaction parameters (BIP) in UniSim Design for the EOS part are shown in Table 3.13. The BIPs between H_20-$C0_2$ and H_20-H_2S are the same as those used by Oellrich et al.[61]. The other constants, such as Henry constants and chemical equilibrium constants of all components, are taken from Wilson's report job [22]. Some of these parameters are user-tunable, but our geothermal fluid values are used [61].

Table 3. 13. Interaction parameter used in Unisim Design for the PR Eos part

H_2O-CO_2	$-0.5572 + 0.001879 \cdot T - 1.274 \cdot 10^{-6}T^2$
H_2O-H_2S	$-0.3897 + 0.001565 \cdot T - 1.142 \cdot 10^{-6}T^2$
CO_2-H_2S	0.1

Compared with many experimental data, the Sour PR model's prediction fits the trend of experimental data very well, especially in the dilute region [62]. Ying Wu et al. [62] suggest that the Sour PR property package models dilute sour gas solutions more accurately than high concentration solutions.

3.5.5 Cubic Plus Association (CPA)

Kontogeorgis et al. [63] proposed the Cubic Plus Association (CPA) using the association term from SAFT [64]. It is an additional contribution to the classic cubic equation of state. The equation is written as :

$$A^{res} = A^{SRK} + A^{ass} \quad (3.\ 123)$$

The CPA EoS can be expressed for mixtures in terms of pressure P:

$$P = \frac{RT}{V_m - b} - \frac{\alpha(T)}{V_m(V_m + b)} - \frac{1}{2}\frac{RT}{V_m} \cdot \left(1 + \rho \frac{\delta lng}{\delta \rho}\right) \sum_i x_i \sum_{A_i} (1 - X_{Ai}) \quad (3.\ 124)$$

The key element of the association term is X_{Ai} which represents the fraction of A-sites on molecule i^{th} that do not form bonds with other active sites, while x_i is the mole fraction of component i^{th}. The form of the association term (X_{Ai}) is related to the association strength $\Delta^{A_iB_j}$ between two sites belonging to two different molecules, where the association strength $\Delta^{A_iB_j}$ in CPA is expressed like:

$$\Delta^{A_iB_j} = g(\rho) \cdot \left[exp\left(\frac{\varepsilon^{A_jB_i}}{RT}\right) - 1\right] b_{ij} \beta^{A_iB_j} \quad (3.\ 125)$$

where $g(\rho) = \frac{1}{1 - 1.9\eta}$ is the radial distribution function and $\eta = 1/4b\rho$, $b_{ij} = \frac{b_i + b_j}{2}$. The b_i is the temperature-indipendent covolume parameter of the component i^{th}. The energy parameter of the EoS

is given by a Soave-type temperature dependency:

$$\alpha(T) = a_0\left[1 + c_1(1 - \sqrt{T_r})\right]^2 \quad (3.\ 126)$$

where T_r is the reduced temperature.Finally, the c_1 is a CPA parameter in the energy term (see Equation 3.126). In Equation 3.125, the $\varepsilon^{A_jB_i}$ and $\beta^{A_iB_j}$ are called association energy and the association volume, respectively. The two parameters are only used for associating components, and the three additional parameters of the SRK term (a_0, b, c_1) are the five pure compound parameters of the model. They are obtained by fitting vapour pressure and liquid density data. When the CPA EoS is used for mixtures, the conventional mixing rules are employed for the energy and covolume parameters in the physical term. The interaction parameters K_{ij} is the only adjustable binary parameter of CPA:

$$\alpha = \sum_i \sum_j x_i x_j \alpha_{ij} \quad (3.\ 127)$$

where $\alpha_{ij} = \sqrt{\alpha_i \alpha_j}(1 - k_{ij})$

and

$$b = \sum_i x_i b_i \quad (3.\ 128)$$

For extending the CPA EoS to of two associating compounds, combining rules for the associating energy ($\varepsilon^{A_jB_i}$) and the association volume ($\beta^{A_iB_j}$) are required.
The expression of the cross-association energy and cross-association volume parameters are:

$$\varepsilon^{A_jB_i} = \varepsilon_{cross} = \frac{\varepsilon^{A_iB_i} + \varepsilon^{A_jB_j}}{2} \text{ and } \beta^{A_iB_j} = \beta_{cross} = \sqrt{\beta^{A_iB_i}\beta^{A_jB_j}} \quad (3.\ 129)$$

Therefore, the expression of the cross-association strength ($\Delta^{A_iB_j}$) is:

$$\Delta^{A_iB_j} = \sqrt{\Delta^{A_iB_i}\Delta^{A_jB_j}} \quad (3.\ 130)$$

The CPA EoS is considered the best approach for systems containing CH_4 and water and H_2S-water and H_2S-CH_4-water.
In literature, Courtial et al. [65] have adopted the Cubic Plus Association (CPA) and, in particular the electrolyte version eCPA, for the system containing CH_4, CO_2, H_2O and also NaCl (up to 5 molal) at pressures up to 2000 bar and temperatures up to 773 K for salt-free systems and 573 K for salt-containing systems. This model can represent the phase behaviour, including the salting-out effect and critical point, and the phase densities in a reservoir's range of temperatures and pressures. The parameters used fr CPA EoS model are defined in Table 3.14.
The model used in this thesis is implemented in Unisim Design but the version with salt is not implemented, since it is not included in the package. Therefore, the CPA's model parameters (Table 3.14) without including salt were used to simulate geothermal streams containing CO_2 and CH_4 (defined light gases).

Table 3. 14. Pure component parameters used for CPA EoS model.

	T_c (K)	a_0 (Pa m^6/mol)	b (m^3/mol)	m (-)	Number of associating site	ε/R (K)	β (m3/mol)
H_2O [66]	647.35	0.12274	0.000015	0.67359	4 C	2003.2	0.06920
CO_2 [67]	304.19	0.35079	0.000027	0.76020	1	1412.6	0.01313
CH_4 [68]	190.55	0.23204	0.000029	0.44718	0	-	-
H_2S [69]	373.50	0.34797	0.000028	0.6061	1	-	-

In Table 3.14, Tsivintzelis et al.[69] proposed the parameters for H_2S. It is applicable up to 363.36 K. Using Unisim Design code for the enveloping geothermal mixture, without salts, The three binary interaction parameters A_{ij}, B_{ij} and C_{ij} are shown on the *Binary Coefficients* tab, and the general formula is:

$$K_{ij} = 1 - A_{ij} - B_{ij}T - C_{ij}T^2 \quad (3.\ 131)$$

While the binary interaction parameters for Courtal et al. [31] are as a parabolic trend, and the general equation is:

$$K_{ij} = {K_{ij}}^0 + {K_{ij}}^1 T + {K_{ij}}^2 T^2 \quad (3.\ 132)$$

T is the temperature in K. The parameters ${K_{ij}}^0$, ${K_{ij}}^1$ and ${K_{ij}}^2$ are in Table 3.15.

Table 3. 15. Binary interaction parameters for the CPA model in Unisim Design code

System	Temperature [K]	${K_{ij}}^0$	${K_{ij}}^1$	${K_{ij}}^2$
CO_2+H_2O [65]	323-537	$-9.12960 \cdot 10^{-1}$	$5.40410 \cdot 10^{-3}$	$-6.49667 \cdot 10^{-6}$
CH_4+H_2O [65]	283-663	-2.18100	0.01111	$-1.27902 \cdot 10^{-5}$
CO_2+H_2O [70]	298.15-477.6	-0.15508	0.000877	0

In Tsivintzelis et al. [67], K_{ij} for H_2S-H_2O is presented for various approach and the mixing rules selected in the software follows the equation 3.129. Most of the binary interaction parameters applied for water and gases were obtained from the literature [71] [72] [73][74][75]. The binary interactions can be inserted within the Unisim Design software through the parameters from the literature data so that the CPA model can give the best results. In the following Table 3.17, Table 3.18 and Table 3.19, more of these parameters are used to calculate solubility and enthalpy mixing of geothermal fluid systems.

Table 3. 16. Binary interaction parameters for the CPA model in Unisim Design R480 for temperature range.

Binary System	Temperature [K]	Aij	Bij	Cij
CO_2+H_2O	323-537	1.091296	-0.005404	$6.49667 \cdot 10^{-6}$
CH_4+H_2O	283-663	3.181	-0.01111	$1.27902 \cdot 10^{-5}$
H_2S+H_2O [67]	310.9-444.3	1.0098	0	0
H_2S+H_2O [76]	298.15- 500	0.083	0	0

Table 3. 3.17. Binary interaction parameters for geothermal gas in CPA EoS In Unisim Design R480

k_{ij}	CH_4	CO_2	H_2S
CH_4	-	0.093	0.081
CO_2	0.093	-	0.099
H_2S	0.081	0.099	-

In the Unisim Design R480, the option to use in *Binary Coeffs* is inserting Aij, Bij, Cij and the mixing rules.

Table 3. 18. Binary interaction parameters between water and geothermal compound (T in K): Source: [63], [76].

kij	H_2O
CH_4	−0.210+0.00185T
CO_2	−0.070+ 0.00072T
H_2S	0.17- 0.00010T

The CPA EoS, in the absence of salts, is applied to binary and multicomponent systems containing H_2S with other compounds, both non-polar (CO_2) and polar (H_2O). Judging from its physical properties and various theoretical literature studies, the CPA model has the best results when H_2S concentration is in the majority concerning CO_2 and CH_4. In addition, the CPA model results in very good correlations for the phase behaviour (vapour- and liquid-liquid equilibria) of H_2S-water.

3.5.6 OLI

In this section, it is possible to analyze three thermodynamic models in OLI Package regarding streams with the presence of salts. This package is integrated into Unisim Design software and cannot be modified. The main thermodynamic models implemented in OLI are the following:

1. The OLI AQ (Aqueous) model;
2. The OLI MSE (Mixed Solvent Electrolyte) model;
3. The OLI MSE-SRK (Mixed Solvent Electrolyte-Soave Redlich-Kwong) model.

3.5.6.1 Aqueous Thermodynamic Model (AQ)

This first model is based on the partial molal Gibbs energy of the i-th species and related to the molality (m_i) through the following equation:

$$\overline{G_i} = \overline{G_i^0} + RTln \cdot m_i\gamma_i \tag{3. 133}$$

where $\overline{G_i^0}$ is the standard-state partial Gibbs energy and γ_i is the activity coefficient. The system's thermodynamic properties can be calculated if the standard-state Gibbs energies are available for all species as functions of temperature and pressure, and the activity coefficients are known as functions of the composition and temperature. The application of the model for 6000 species has the temperature limits [223 K- 572.15 K], pressure up to 1500 bar and 30 molal ionic strength.
The accuracy of the model for temperature and pressure ranges is based on heat capacity and volume knowledge. The starting point is to use the Helgeson-Kirkham-Flowers-Tanger (HKFT) equation of state [77]. This equation accurately represents the standard-state thermodynamic functions for aqueous, ionic or neutral species as functions of both temperature and pressure. Through modifications, the HKFT equation of state can do this by reproducing the properties of the standard state up to 1273 K and 5000 bar. The HKFT equation is based on the solvation theory and shows the standard-state thermodynamic functions as sums of structural and solvation contributions, the latter being dependent on the properties of the solvent as water. The standard partial molal volume ($\overline{V^0}$) and heat capacity ($\overline{C_p^0}$) are given by:

$$\overline{V^0} = a_1 + \frac{a_2}{\psi+P} + \left(a_3 + \frac{a_4}{\psi+P}\right)\cdot\left(\frac{1}{T-\Theta}\right) - \omega Q + \left(\frac{1}{\varepsilon} - 1\right)\left(\frac{\delta w}{\delta P}\right) \tag{3. 134}$$

$$\overline{C_p^0} = c_1 + \frac{c_2}{(T-\Theta)^2} - \left(\frac{2T}{(T-\Theta)^3}\right)\left(a_3(P-P_r) + a_4 ln\frac{\psi+P}{\psi+P_r}\right) + \omega TX + 2TY\left(\frac{\delta w}{\delta T}\right)_P \tag{3. 135}$$

where a_1, a_2, a_3, a_4, c_1, and c_2 represent species-dependent non-solvation parameters, T_r is the reference temperature of 298.15 K, P_r is the reference pressure of 1 bar, ψ and Θ refer to solvent parameters equal to 2600 bars and 228 K, respectively. The variables Q, X and Y, are functions of the pressure and temperature derivatives of the dielectric constant of water, the charge of the ionic species in water, and the ion's electrostatic radius in water.
As shown by the two previous equations, the HKF equation expresses heat capacity and volume as functions of the properties of pure water and seven empirical parameters. The latter are tabulated for many ions, complex and neutral, both inorganic and organic molecules. The remaining thermodynamic properties are obtained from thermodynamic integration using the Gibbs energy values, enthalpy and entropy at the reference temperature and pressure. The activity coefficient model used for representing the non-ideality of solutions is an extended form of an expression developed by Bromley [78]. The Bromley equation combines the Debye-Hückel [79] term for long-range electrostatic interactions with a semi-empirical expression for short-range interactions between cations and anions. In a multi-component system, the activity coefficient of an ion i is given by the following equation:

$$log\gamma_i = \frac{-Az_i^2 I^{1/2}}{1+I^{1/2}} + \sum_j^{n^\circ}\left[\frac{|z_i|+|z_j|}{2}\right]^2\left[\frac{(0.06+0.6B_{ij})|z_iz_j|}{\left(1+\frac{1.5}{|z_iz_j|}I\right)^2} + B_{ij} + C_{ij}I + D_{ij}I^2\right]m_j \tag{3. 136}$$

where A is the Debye-Hückel coefficient which depends on temperature and solvent properties, z_i is the number of charges on the i^{th} ion, I is the ionic strength, n° is the number of ions with charges opposite to that the i^{th}, and B_{ij}, C_{ij}, and D_{ij} are empirical temperature-dependent cation-anion

interaction parameters. Bromley's original formulation contains only one interaction parameter, Bij, sufficient for systems with moderate ionic strength. For robust systems, the two additional coefficients Cij and Dij, usually become necessary. The Bromley model's three-parameter form can reproduce activity coefficients in solutions with ionic strength up to 30 mol/kg. The temperature dependence of the Bij, Cij and Dij parameters is usually expressed using a simple quadratic function. The Bromley model is restricted to interactions between cations. For ion-molecule and molecule-molecule interactions, the model of Pitzer is used. The Redlich-Kwong-Soave equation of state is used to calculate the fugacities of components in the gas phase. In the absence of sufficient experimental data, reasonable predictions can be made using a method due to Meissner, making it possible to extrapolate the activity coefficients to higher ionic strengths based on only a single experimental or predicted data point.

3.5.6.2 Mixed-Solvent Electrolyte (MSE)

The electrolyte thermodynamic model is referred to Wang et al. [80], [81], [25]. The chemical potential of species i[th] in a liquid phase is calculated as:

$$\mu_i^L = \mu_i^{L,0,x}(T,P) + RTlnx_i\gamma_i^{x,*}(T,P,x) \tag{3. 137}$$

The mole fraction-based standard-state chemical potential is related to the well-known molality-based standard-state chemical potential by [80]:

$$\mu_i^{L,0,x}(T,P) = \mu_i^{L,0,m}(T,P) + RTln\frac{1000}{M_{H2O}} \tag{3. 138}$$

with M_{H2O} as the molecular weight of water. $\mu_i^{L,0,x}(T,P)$ is calculated as a function of temperature and pressure from the Helgeson–Kirkham–Flowers (HKF) equation of state. For water, the standard-state chemical potential is defined as that of pure water and is calculated from the Haar–Gallagher–Kell equation of state. The activity coefficients are obtained from an expression for the excess Gibbs energy, which is expressed as a sum of three contributions:

$$\frac{G^{ex}}{RT} = \frac{G_{LR}^{ex}}{RT} + \frac{G_{II}^{ex}}{RT} + \frac{G_{SR}^{ex}}{RT} \tag{3. 139}$$

where G_{LR}^{ex} is the contribution of long-range electrostatic interactions, G_{II}^{ex} accounts for specific ionic (ion-ion and ion-molecule) interactions, and G_{SR}^{ex} is a short-range contribution resulting from intermolecular interactions. The long-range interaction contribution derived from the Pitzer–Debye–Hückel formula [82] and it is expressed in terms of mole fractions and symmetrically normalized:

$$\frac{G_{LR}^{ex}}{RT} = -(\sum_i n_i)\frac{4A_x I_x}{\rho} ln\left(\frac{1+\rho I_x^{1/2}}{\sum_i x_i\left[1+\rho\left(I_{x,i}^0\right)^{1/2}\right]}\right) \tag{3. 140}$$

where the sum is over all species, I_x is the mole fraction-based ionic strength (see Section 3.4.1), $I_{x,i}^0$ is defined as the ionic strength in the limiting case when x_i=1, $\rho = 14.0$ assigned a universal dimensionless value, and A_x is given by:

$$A_x = \frac{1}{3}(2\pi N_A d_s)^{1/2}\left(\frac{e^2}{4\pi\varepsilon_0\varepsilon_s k_B T}\right)^{3/2} \tag{3. 141}$$

where d_s and ε_s are the molar density and dielectric constant of the solvent, respectively. The specific ion-interaction contribution is calculated from an ionic strength-dependent, symmetrical second virial coefficient-type expression [80]:

$$\frac{G_{II}^{ex}}{RT} = -(\sum_i n_i)\sum_i\sum_j x_i x_j B_{ij}(I_x) \tag{3. 142}$$

where $B_{ij}(I_x) = B_{ji}(I_x)$, $B_{ii} = B_{jj} = 0$, and the ionic strength dependence of Bij is given by

$$B_{ij}(I_x) = b_{ji} + c_{ij}e^{(-\sqrt{I_x+a_1})} \tag{3. 143}$$

where b_{ij} and c_{ij} are binary interaction parameters, and a_1 is set equal to 0.01. The parameters b_{ij} and c_{ij} are calculated as functions of temperature as:

$$b_{ji} = b_{0,ij} + b_{1,ij}T + b_{2.ij}/T + b_{3,ij}T^2 + b_{4,ij}lnT \quad (3.\ 144)$$

$$c_{ji} = c_{0,ij} + c_{1,ij}T + c_{2.ij}/T + cT^2 + c_{4,ij}lnT \quad (3.\ 145)$$

The coefficients $b_{k,ij}$ (k=0, …, 4) and $c_{k,ij}$ (k=0,…, 4) are obtained from the regression of experimental data (Table 3.19 and Table 3.20).

Table 3. 19. Binary parameters used in the MSE virial interaction term about the equation 3.143.Referred to MSE Thermodynamic Model in OLI software-White Paper[3]

Species i	Species j	$b_{0,ij}$	$b_{1,ij}$	$b_{2,ij}$	$b_{3,ij}$	$b_{4,ij}$
Na^+	Cl^-	15610.63	7.964204	−357992.9	−0.003643102	−2892.662
K^+	Cl^-	15087.68	7.236058	−354195.6	−0.003141513	−2771.596
Mg^{2+}	Cl^-	−46.0902	0.036682	−12896	$8.29385\cdot10^{-6}$	0
Ca^{2+}	Cl^-	−95.9932	0.470226	−17370.9	$-5.67551\cdot10^{-4}$	0
Na^+	K^+	−93.0411	−0.234488	37002.7	$5.62879\cdot10^{-4}$	0
Na^+	Mg^{2+}	−28.8624	0.0351923	8744.27	0	0
Na^+	Ca^{2+}	11.2685	−0.0263793	2905.5	0	0
K^+	Mg^{2+}	−28.2506	0.0311345	16139	0	0
K^+	Ca^{2+}	−43.804	0.0468862	23092.5	0	0
$CO_{2(aq)}$	H_2O	−10.2134	0.0102376	783.548	0	0
$CO_{2(aq)}$	Na^+	−10.9006	0	0	0	0
$CO_{2(aq)}$	K^+	−8.51244	0	0	0	0
$CO_{2(aq)}$	Mg^{2+}	−21.1002	0	0	0	0
$CO_{2(aq)}$	Ca^{2+}	−20.4164	0	0	0	0

Table 3. 20. Binary parameters used in the MSE virial interaction term about the equation 3.144. Referred to MSE Thermodynamic Model in OLI software-White Paper[4]

Species i	Species j	$c_{0,ij}$	$c_{1,ij}$	$c_{2,ij}$	$c_{3,ij}$	$c_{4,ij}$
Na^+	Cl^-	−30086.35	−15.00973	699,848.70	0.006820989	5552.343
K^+	Cl^-	−26853.29	−12.85712	635045.60	0.005649944	4927.578
Mg^{2+}	Cl^-	110.429	−0.240247	11645.20	0.000319761	0
Ca^{2+}	Cl^-	−0.694366	−0.421581	43725.90	0.000791106	0
Na^+	K^+	−64.633	0.881525	−29428.5	−0.00128594	0
Na^+	Mg^{2+}	0	0	−6373.88	0	0
Na^+	Ca^{2+}	0	0	−6685.21	0	0
K^+	Mg^{2+}	0	0	−13262.6	0	0
K^+	Ca^{2+}	0	0	−18687.4	0	0
$CO_{2(aq)}$	H_2O	0	0	0	0	0
$CO_{2(aq)}$	Na^+	0	0	0	0	0
$CO_{2(aq)}$	K^+	0	0	0	0	0
$CO_{2(aq)}$	Mg^{2+}	0	0	0	0	0
$CO_{2(aq)}$	Ca^{2+}	0	0	0	0	0

The short-range interaction contribution is calculated from the UNIQUAC equation [83]:

[3] Copyright 2018 Oli systems, Inc., some data authorized for PhD pubblication

[4] Copyright 2018 Oli systems, Inc., some data authorized for PhD pubblication

$$\frac{G_{SR}^{ex}}{RT} = (\sum_i n_i)\left[\sum_i x_i \ln\frac{\varphi_i}{x_i} + \frac{Z}{2}\sum_i q_i x_i \ln\frac{\theta_i}{\varphi_i}\right] - (\sum_i n_i)\left[\sum_i q_i x_i \ln\left(\sum_j \theta_j \tau_{ij}\right)\right] \quad (3.\ 146)$$

with:

$$\theta_i = \frac{q_i x_i}{\sum_j q_j x_j} \quad (3.\ 147)$$

$$\varphi_i = \frac{r_i x_i}{\sum_j r_j x_j} \quad (3.\ 148)$$

$$\tau_{ij} = exp\left(-\frac{a_{ij}}{RT}\right) \quad (3.\ 149)$$

where q_i and r_i are the surface and size parameters, respectively, for the species i^{th}, Z is a fixed coordination number (Z=10), and a_{ij} is the binary interaction parameter between species i^{th} and j ($a_{ij} \neq a_{ji}$). The short-range interaction parameters are calculated as functions of temperature and pressure by

$$a_{ij} = a_{ij}^{(0)} + a_{ij}^{(1)}T + a_{ij}^{(2)}T^2 + (a_{ij}^{(P0)} + a_{ij}^{(P1)}T + a_{ij}^{(P2)}T^2)P \quad (3.\ 150)$$

where $a_{ij} \neq a_{ji}$. As shown for the ionic interaction parameters, all coefficients of Equation 3.149 are usually not needed for most species pairs. The short-range parameters in the previous equation are introduced only for interactions involving neutral molecules. The activity coefficients are calculated from Equation 3.138 by differentiation with respect to the number of moles, and they are symmetrically normalized. So they are equal to 1 for the pure component. Then, they need to be converted to unsymmetrical normalization so that they are based on the infinite-dilution reference state in water and can be used in Equation 3.137:

$$ln\gamma_i^{x,*} = ln\gamma_i^x - \lim_{xi\to 0} ln\gamma_i^x \quad (3.\ 151)$$

where $\lim_{xi\to 0} ln\gamma_i^x$ is the value of the symmetrically-normalized activity coefficient at infinite dilution in water, which is calculated by substituting x_i=0 and x_w=1 into the activity coefficient equations. The chemical potential of species i in the gas phase is given by

$$\mu_i^G = \mu_i^{G,0}(T) + RTln\frac{Py_i\varphi_i(T,P)}{P^0} \quad (3.\ 152)$$

where $\mu_i^{G,0}(T)$ is the chemical potential of pure component i in the ideal gas state, yi is the mole fraction in the gas phase, $\varphi_i(T,P)$ is the fugacity coefficient, P is the total pressure, and P^0=1 atm. The $\mu_i^{G,0}(T)$ term is calculated from the ideal-gas Gibbs energy of formation, entropy and heat capacity according to standard thermodynamics. For water, this term is obtained from the Haar–Gallagher–Kell equation of state [51]. The fugacity coefficient is calculated from the Soave–Redlich–Kwong (SRK) EoS (Equation 3.88) [14], where the parameters a and b are calculated using the classical quadratic mixing rules (Equation 3.91 and 3.93). The pure-component parameters a_i and b_i are calculated using the critical properties T_c and P_c and a temperature-dependent function α(T), which is regressed to match pure-component vapour pressures:

$$a_i = 0.42747\frac{R^2T_{ci}^2}{P_{ci}}\alpha_i \quad (3.\ 153)$$

$$b_i = 0.08664\frac{RT_{ci}}{P_{ci}} \quad (3.\ 154)$$

The binary parameter kij in Equation 3.93 is expressed as a function of temperature as:

$$k_{ij} = k_{ij}^{(0)} + k_{ij}^{(1)}/T \quad (3.\ 155)$$

Table 3. 21. Binary parameters used in the short-range interaction term and in the mixing rule for the SRK EoS regarding the mixture CO_2-H_2O.

Species i	Species j	$a_{ij}^{(0)}$	$a_{ij}^{(1)}$	$a_{ij}^{(P0)}$	$a_{ij}^{(P1)}$	$k_{ij}^{(0)}$	$k_{ij}^{(1)}$
$CO_{2(aq)}$	H_2O	−3387.02	−0.570569	−0.008550	−0.000666	0.195736	47.0126
H_2O	$CO_{2(aq)}$	6809.06	−28.489900	−0.852074	0.002504	-	-

The expressions for the chemical potentials of species in the liquid and gas phases are further used for the simultaneous calculation of phase (vapour-liquid and liquid-liquid) equilibria and chemical (or speciation) equilibria between solution species. The calculations were performed using a phase and chemical equilibrium algorithm implemented in the OLI software for Unisim Design R480. The model parameters are available in the OLI software version 10.

3.5.6.3 Mixed-Solvent Electrolyte & Soave-Redlich-Kwong (MSE-SRK)

The MSE-SRK model has been developed by the OLI system for simulating mixtures containing H_2S, CO_2, CH_4, H_2O, and various salts in geothermal production. The MSE-SRK model is based on MSE -Mixed-Solvent Electrolyte package. The MSE-SRK package provides a treatment of the nonelectrolyte-rich second liquid phase for liquid-liquid equilibria. Such as the MSE, also the MSE-SRK framework combines an equation of state for standard-state properties of individual species, an excess Gibbs energy model to account for solution non-ideality in the aqueous electrolyte phase, and the Soave-Redlich-Kwong equation of state (SRK-EOS) to calculate the properties of the gas phase. The MSE-SRK assumes the second liquid phase to be non-ionic and reproduces its properties using the state's SRK equation. Therefore, the MSE-SRK framework reproduces the critical behaviour of non-electrolyte systems more efficiently.
The phase equilibrium condition in the MSE-SRK model is defined by the equality of chemical potentials in coexisting phases. The chemical potentials are used to calculate speciation equilibria and predict the solubility of scale-forming minerals and corrosion wares. In the MSE-SRK model, the electrolyte-containing aqueous/liquid phase is accounted by combining the Helgeson-Kirkham-Flowers (HKF) equation of state for standard-state properties with the MSE activity coefficient model for solution non-ideality. As a result, the chemical potential of a species i in an electrolyte phase is evaluated as:

$$\mu_i^L = \mu_i^{L,0,x}(T,P) + RTlnx_i\gamma_i^{x,*}(T,P,x) \quad (3.\ 156)$$

with:

- $\mu_i^{L,0,x}(T,P)$ is the standard-state chemical potential from the HKF thesis [84];
- x_i is the mole fraction;
- $x_i\gamma_i^{x,*}(T,P,x)$ is the activity coefficient from the MSE thesis of Wang et al. [80], for long-range electrostatic, specific ionic and short-range intermolecular interactions.

The second liquid phase is assumed to be non-ionic and is modelled using the Soave-Redlich-Kwong equation of state (SRK-EoS)[41].
The chemical potential in the non-ionic liquid phase is then calculated as:

$$\mu_i^G = \mu_i^{G,0}(T) + RTln\frac{Py_i\varphi_i(T,P,y)}{P^0} \quad (3.\ 157)$$

where $\mu_i^{G,0}(T)$ is the chemical potential of pure component i in the ideal gas state, y_i is the mole fraction, $\varphi_i(T,P,y)$ is the fugacity coefficient from the SRK-EoS, P is the total pressure, and P^0 is the atmospheric pressure.
For the gas phase, the properties are obtained from the SRK equation according to the previous equation. The acid gases, more corrosive, are controlled by their solubility in the aqueous phase. The solubility is a result of vapour-liquid (VLE) equilibria or liquid-liquid equilibria (LLE), the latter being particularly relevant at high pressures. The vapour-liquid (VLE) and liquid-liquid (LLE) equilibrium conditions are defined by the equality of the chemical potentials in the coexisting phases, as the following equations:

$$\mu_i^L = \mu_i^G \ for\ VLE \quad (3.\ 158)$$

$$\mu_i^{L1} = \mu_i^{L2} \ for\ LLE \quad (3.\ 159)$$

The distinction between VLE and LLE is unambiguous when the components are below the critical region. However, when supercritical components are present, a smooth transition occurs between a VLE-like region at lower pressures and an LLE-like region at higher pressures. In the LLE-like region, an aqueous phase is in equilibrium with a dense phase dominated by CO_2, CH_4, H_2S. Thus, the MSE-SRK has the characteristics for studying the salts/environmental interactions and the geothermal streams.

Figure 3. 1. Structure of the MSE-SRK model used for the simulating geothermal streams with salts (Source: [85])

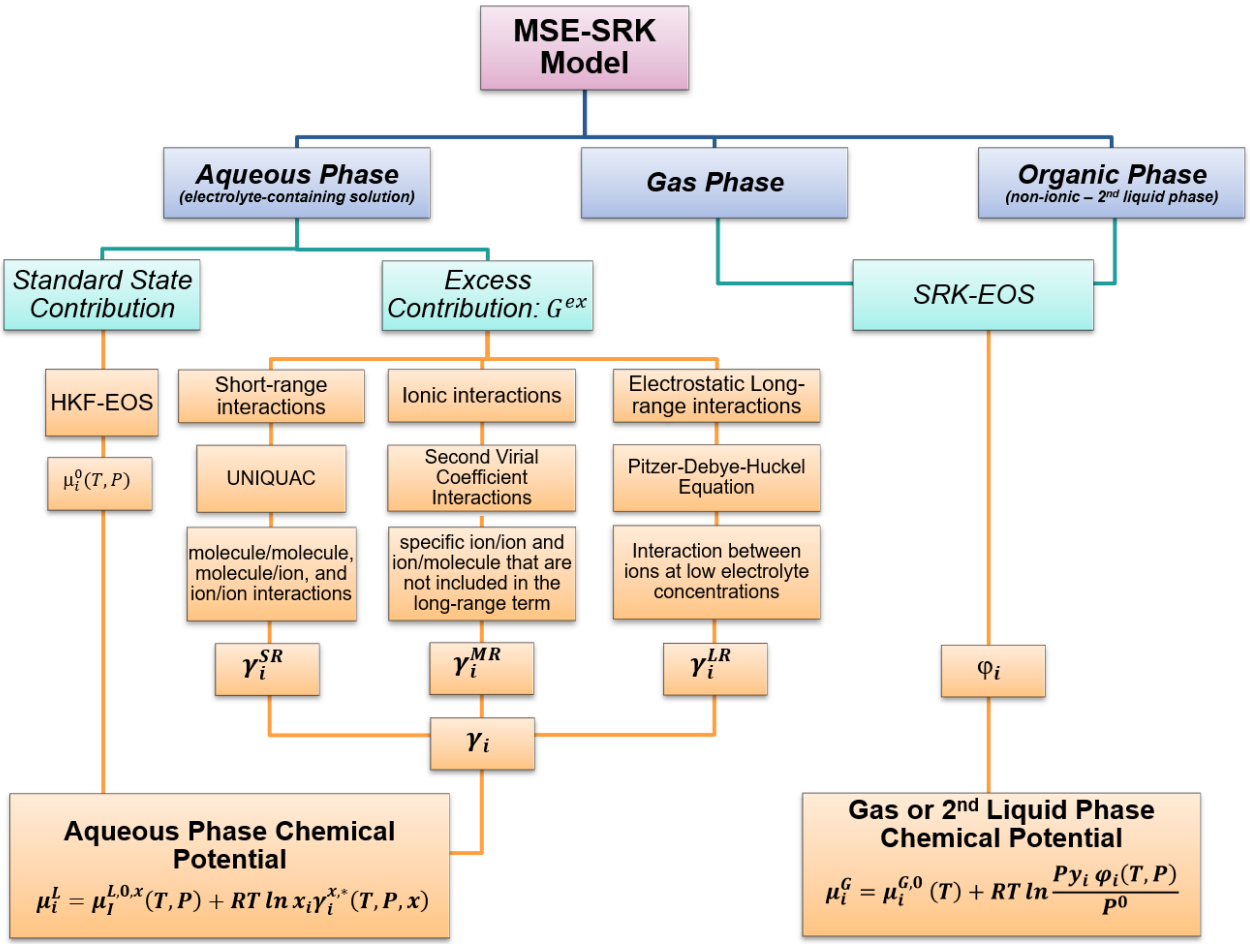

In this work with the mixtures that include lightweight components such as CO_2, H_2S, CH_4 and H_2O, the MSE-SRK model can predict a transition between a VLE and an LLE region as pressure increases. The vapour and second liquid phases can be considered supercritical fluids when they are dominated by components such as CH_4 and CO_2. In the next figures, the MSE-SRK model predictions with representative experimental data for different compositions of the $CO_2/CH_4/H_2O$ ternary system. Figure 3.5 shows the solubilities of CH_4 and CO_2 in the water at 344.15 K and pressures range of 1-1038 bar. It is noted that the solubilities of CO_2 are higher concerning those of CH_4. Then, the two compounds are above the critical temperatures and, hence no discontinuities are evident in the experimental data. The solid lines represent the experimental data referred to [86], [87]. Figure 3.6 reproduces the water solubility properties in a mixture of CH_4 and CO_2 at various temperature ranges. Here, when the temperature increases, the solubility of water in the CH_4/CO_2 phase increases.

The MSE-SRK model can predict the behaviour of fluid mixtures from subcritical to supercritical regions. Figure 3.7 shows the H_2O solubility in a mixture containing 5% CH_4 and 95% CO_2 from 288.75 K to 323.15 K and at pressure up to 200 bar. Below the CO_2 critical temperature (Tc), it is possible to observe the transition from VLE to LLE. Under the conditions of 50 bar and 288.15 K, the mixture is in the vapour phase. As pressure increases, it changes from vapour to liquid, which can be seen in the change in the slope of the curve. At T> Tc, the mixture passes into the supercritical region. Therefore, the thermodynamic model reproduces the almost critical VLE behaviour in the CO_2 / CH_4 mixture because SRK EoS replicates the liquid and vapour phases.

The MSE-SRK thermodynamic model is adapted for mixtures containing supercritical components like CO_2, H_2S, CH_4 and salts in the range of temperatures from 273.15 K- 573.15 K, pressures up to 3000 bar and salt concentrations from zero up to solid saturation. It correctly reproduced the transition from VLE to LLE, particularly for the CO_2 and CH_4 systems. This thermodynamic package is integrated into the process software Unisim Design R480.

OLI Engine in Unisim Design is the OLI System electrolytes model in Honeywell, which contains both AQ and MSE and MSE-SRK in the Unisim Design. When there are water or electrolyte streams in a process, such as geothermal streams, using OLI to simulate these units allows predictive electrolyte simulations within a more traditional flowsheet environment. The OLI database is version 10 for this work and calculates thermodynamic and transport properties specific to the electrolyte system. The three electrolytic models were used for the study of geothermal mixtures in the presence of NaCl salt.

3.6 Choice of model and conclusion

The chemical process engineer requires a simple model that predicts all types of fluid behaviour. Indeed, this work aims to find a specific thermodynamic model depending on the specific geothermal fluid. Therefore, in this chapter, a certain number of thermodynamic packages have been selected to describe the physical properties of geothermal fluids containing CO_2, H_2S, and CH_4, including salts. The previously mentioned thermodynamic models will be tested in chapter 4 and compared with experimental data taken from the literature. In contrast, one of these models will be selected based on the performance and deviation from experimental data and based on the composition of the geothermal fluid. Finally, the best-selected model will be further used for the simulation of the GTPP, which will be described in chapter 5.
Unfortunately, the advanced thermodynamic studies and the different models adopted in this thesis make us understand that the approach is not simple. Furthermore, for the same application, it is impossible to have a single answer when the parameters (and the process conditions) change in the different sections of the GTPP. Density, enthalpy, entropy, viscosity, saturation pressure, and temperature of the fluid must be known previously for any power plant design, but for this work, the best-selected models will be based on the solubility calculation and mixing enthalpy. Therefore, the results of an adequate model must be compared with the experimental data. This is the theoretical and practical aspect of J.C. de Hemptinne et al. [9], which suggest guidelines to respond to the designer's request. The guidelines are:

1. *Define the property of interest*

Two types of properties can be identified:

- *Single-phase properties* (either liquid only or vapour only). The model to be used depends on the temperature, pressure of the phase;
- *Phase equilibrium properties*. The model becomes more complicated and more inaccurate as the properties are difficult to calculate accurately.

Simulation software, such as Unisim Design, has thermodynamic packages that can be functional according to the components used and the stream's conditions. Moreover, as conditions change during the process sections, the software combines different models according to the properties under analysis and reaches the calculation convergence. This last procedure is performed automatically, based on the working conditions. Therefore, the designer must either have a solid foundation in thermodynamics or confront the experts during the project. However, without comparing the simulations and their results with the experimental data, the customer often accepts this situation in the absence of time.

2. *Identify the composition of the fluid*

The composition of the fluid undoubtedly influences the choice of the model. For example, for a common geothermal fluid, the main components are water, carbon dioxide, hydrogen sulphide, methane, nitrogen, hydrogen (in traces) and many salts such as sodium chloride par excellence which mainly affects the thermodynamic properties of the fluid. Therefore, in Chapter 4 and Chapter 5, the thermodynamic behaviour of the fluid and the simulation of the components of a geothermal plant are deeply highlighted, respectively.

3. *Identify the pressure and temperature conditions of the process*

Here the approach is in the choice of fluid phase models with activity coefficient and equation of state. The Table taken by de Hemptinne and Behar [13] is inserted to highlight the difference between the homogeneous approach of the equation of state EoS (they describe the conditions of the vapour, liquid and supercritical phase) compared to the heterogeneous approach of the activity coefficients.

3.6.1 Decision tree

According to the models defined previously in Figure 3.2, a decision tree for the liquid-vapour phase equilibrium for geothermal mixtures was inserted. This diagram, simplified concerning Figure 4.59 by J.C. de Hemptinne et al. [9], can guide the designer in choosing the appropriate thermodynamic model.For more advanced studies, such as the presence of heavy metals for some geothermal sites, a full analysis of the key components is required to provide the most accurate method. Many of these thermodynamic models are implemented in the Unisim Design R480 process software. For the presence of high and low pressures and temperatures, see the final Table in Chapter 4.

Figure 3. 2. Decision tree for vapour-liquid equilibrium calculation for geothermal fluids

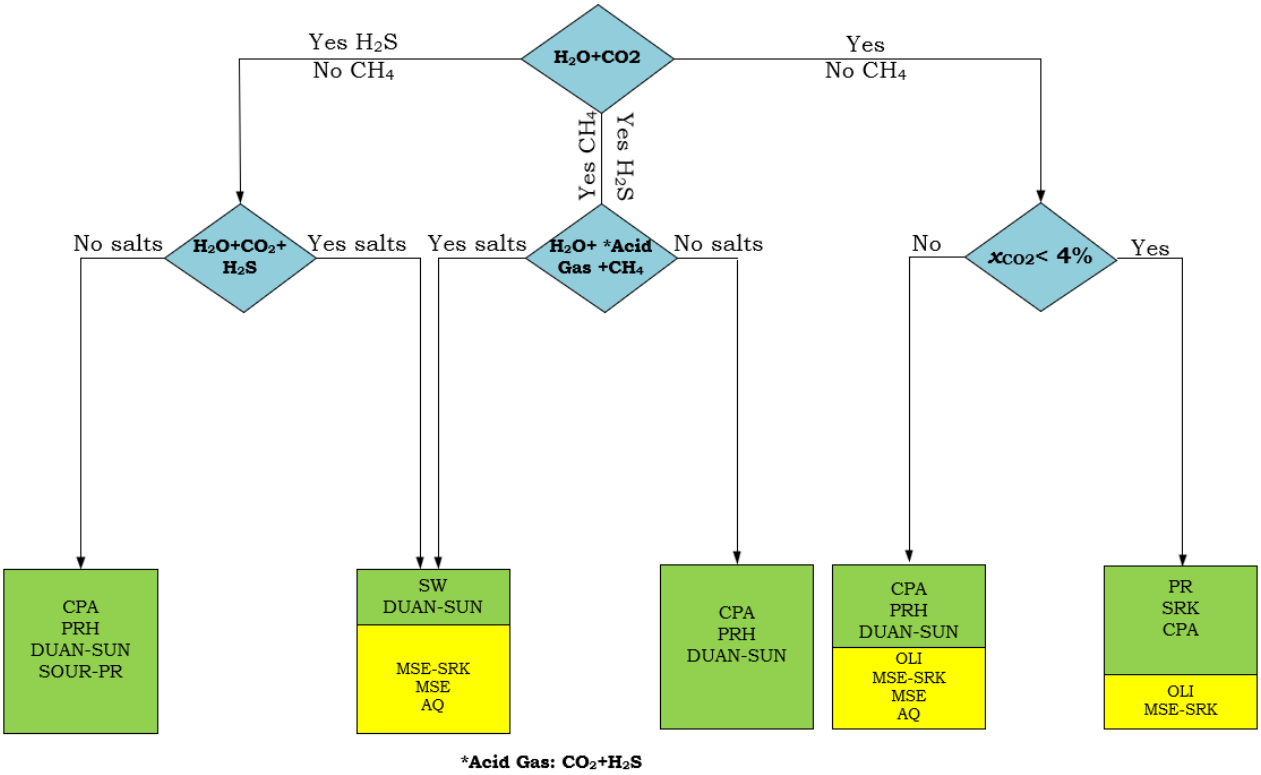

Figure 3.2 describes the possible patterns of using a thermodynamic model based on what is described in the previous paragraphs of chapter 3 to calculate fugacity, enthalpy and density. This decision free has been obtained, starting from the data available for geothermal mixtures present in the literature. The blue rhombus represents the possible cases of geothermal mixtures present in the geothermal plants. Starting from the most common mixture (water with CO_2), going to the right from the diagram, in the absence of H_2S and CH_4, the mass composition of the carbon dioxide must be taken into account. If xCO_2 (CO_2 molar composition) is less than 4%, the models to consider are the PR, SRK and CPA or OLI MSE-SRK. Instead, for xCO_2 greater than 4%, the best models of the mixture are the CPA, PRH, DS, and OLI thermodynamic packages. Therefore, these preliminary assumptions are defined when there is an absence of salts in the mixture. The interpretation of the left part of the figure is complicated when H_2S, CH_4, and salts are present. Therefore, in this case, the best models are the CPA, PRH, DS, and SPR, depending on the thermodynamic packages described above in the absence of salts and methane. While in the presence of salt, the best models are SW, DS and the OLI thermodynamic packages. On the other hand, for mixtures containing CO_2, H_2S and CH_4 in water, the thermodynamic models can be reduced to three, namely CPA, PRH and DS.

REFERENCE LIST

[1] P. R. Holland TJB, 'An improved and extended internally consistent thermodynamic dataset for phases of petrological interest, involving a new equation of state for solids.', *Metamorph Geol*, vol. **29**, pp. 333–383, **2011**.

[2] F. G. Helgeson HC, Kirkham DH, 'Theoretical prediction of the thermodynamic behavior of aqueous-electrolytes at high-pressures and temperatures: 4. calculation of activity-coefficients, osmotic coefficients, and apparent molal and standard and relative partial molal properties to 600 °C', *American Journal of Science*, no. **281**, pp. 1249–1516, **1981**.

[3] H. H. Johnson JW, Oelkers EH, 'SUPCRT92 - A software package for calculating the standard molal thermodynamic properties of minerals, gases, aqueous species, and reactions from 1 bar to 5000 bar and 0 °C to 1000 °C.', *Comp Geosci*, vol. **18**, pp. 899–947, **1992**.

[4] M. R. Anderson GM, Castet S, Schott J, 'The density model for estimation of thermodynamic parameters of reactions at high temperatures and pressures.', *Geochim Cosmochim Acta*, vol. **55**, pp. 1769–1779, **1991**.

[5] B. R. Audétat A, Pettke T, Heinrich CA, 'The composition of magmatic-hydrothermal fluids in barren and mineralized intrusions.', *Econ Geol*, vol. **103**, pp. 877–908, **2008**.

[6] H. A. Palmer DA, Fernandéz-Prini R, *Aqueous Systems at Elevated Temperatures and Pressures: Physical Chemistry in Water, Steam and Hydrothermal Solutions.* **2004**.pagg.766.Elsevier.

[7] J. Haas, J.L., 'Equation for the density of vapour saturated NaCl-H2O solutions from 75°C to 325°C', *American Journal of Science*, no. **269**, pp. 490–494, **1970**.

[8] K. S. Silvester, L.F. and Pitzer, *Thermodynamics of geothermal brines.Part.I.* **1976**.pp.62.

[9] R. L. Hildebrand, J.H. and Scott, *Regular solutions*. Englewood Cliffs, NJ, **1962**.

[10] H. E. Kestin, J. and Khalifa,vol.**71**, 'Tables of the dynamic and kinematic viscosity of acqueous NaCl solutions', **1981**.

[11] F. G. Keenan, F.G., Keyes, *Steam Tables*, Wiley. **1969**.

[12] J. M. O'Connell, J. P. and Haile, *Thermodynamics: Fundamentals for Applications*, 1st Ed. **2005**.

[13] J. D. Rachford, H. H. and Rice, 'Procedure for Use of Electrical Digital Computers in Calculating Flash Vapourisation Hydrocarbon Equilibrium', *Journal of Petroleum Technology*, vol. **1**, no. 4, pp. 19–20, **1952**.

[14] K. G. Denbigh, *The Principles of Chemical Equilibrium.* **1981**.pp.262.

[15] A. P. W. Wagner, 'International equation for the saturation properties of ordinary water substance. Revised according to the international temperature scale of 1990', *Journal of Physical and Chemical Reference Data*, vol. **22**, pp. 783–787, **1993**.

[16] E.Michaelides, *Thermodynamic properties of geothermal fluids.* **1981**. Journal Volume: **5**; Conference: Geothermal Resources Council annual meeting, Houston, TX, USA,

[17] M. S.Lorenz, W, 'Modelling of halite formation in natural gas storage aquifers', **2003**.

[18] P. G. H. Joseph H. Keenan, Frederick G. Keyes, *Steam tables : thermodynamic properties of water including vapor, liquid and solid phases*, Wiley-Inte. New York, **1978**.

[19] K. S. Silvester, Leonard F., Pitzer, *Thermodynamics of Geothermal Brines I. Thermodynamic Properties of Vapor-Saturated NaCl (aq) Solutions from 0-300 °C*, University of California. **1976**.

[20] J. M. P. A.E.Sherwood, 'The heat of solution of gases at high pressure', *AIChE Journal*, vol. **8**, no. 4, pp. 519–521, **1962**.

[21] L. B. Chen, C. C. and Evans, 'A Local Composition Model for the Excess Gibbs Energy of Aqueous Electrolyte Systems', *AIChE Journal*, vol. **32**, no. 3, pp. 444–454, **1986**.

[22] E. Debye, P. and Hückel, 'Zur Theorie der Elektrolyte I: Gefrierpunktserniedrigung und verwandte Erscheinungen', *Phys.Z.*, vol. **24**, no. 9, pp. 185–207, **1923**.

[23] E. Debye, P. and Hückel, 'Zur Theorie der Elektrolyte II: das Grensgesetz für die elektrische Leitfähigkeit', *Phys.Z.*, vol. **24**, no. 15, pp. 305–325, **1923**.

[24] K. S. Pitzer, 'Thermodynamics of electrolytes. I. Theoretical basis and general equations', **77** n.2,*Journal of Physical Chemistry*, **1973**, pp.268-277.doi: 10.1021/j100621a026.

[25] K. S. Pitzer, 'Electrolytes. From Dilute Solutions to Fused Salts', *Journal of the American Chemical Society*, 1980, doi: 10.1021/ja00529a006.

[26] N. C. Zemaitis, J. F., Clark, D. M., Rafal, M. and Scrivner, *Handbook of Aqueous Electrolyte Thermodynamics.* **1986**.Wyley, 878 pages.

[27] J. D. van der Waals, *Over de Continuiteit van den Gas en Vloeistoftestand (On the Continuity of the Gas and Liquid State)*, Hoogeschoo. **1873**.

[28] T. W. J. Mansoori, G. A., Carnahan, N. F., Starling, K. E. and Leland, 'Equilibrium Thermodynamic Properties of the Mixture of Hard Spheres', *Journal of Chemical Physics*, vol. **54**, no. 4, pp. 1523–1525, **1971**.

[29] K. E. Muller, E. A. and Gubbins, 'Molecular-Based Equations of State for Associating Fluids: A

Review of SAFT and Related Approaches"', *Industrial & Engineering Chemistry Research*, vol. **40**, pp. 2193–2211, **2001**.

[30] H. Stell, G., Rasaiah, J. C. and Narang, 'Thermodynamic Perturbation Theory for Simple Polar Fluids', *Molecular Physics*, vol. **27**, no. 5, pp. 1391–1414, **1974**.

[31] L. C. Benedict, M., Webb, G. B. and Rubin, 'An Empirical Equation for Thermodynamic Properties of Light Hydrocarbons and Their Mixtures: I. Methane, Ethane, Propane, and n-Butane', *Journal of Chemical Physics*, vol. **8**, no. 4, pp. 334–345, **1940**.

[32] M. G. Lee, B.I. and Kesler, 'A Generalized Thermodynamic Correlation Based on Three-Parameter Corresponding States', *AIChE Journal*, vol. **21**, no. 3, p. 510, **1975**.

[33] U. Plocker, 'Calculation of High Pressure Vapor-Liquid Equilibria from a Corresponding States Correlation with Emphasis on Asymmetric Mixtures', *Industrial & Engineering Chemistry Process Design & Development*, vol. **17**, no. 3, **1978**.

[34] J. D. van der Waals, 'The Equation of State for Gases and Liquids', **1873**.

[35] H. Stell, G., Rasaiah, J. C. and Narang, 'hermodynamic Perturbation Theory for Simple Polar Fluids', *Molecular Physics*, vol. **27**, no. 5, pp. 1391–1414, **1974**.

[36] I. Søreide and C. H. Whitson, 'Peng-Robinson predictions for hydrocarbons, CO2, N2, and H2 S with pure water and NaCI brine',vol.**77**,*Fluid Phase Equilibria*, **1992**, pp.217-240.doi: 10.1016/0378-3812(92)85105-H.

[37] D. Y. Peng and D. B. Robinson, 'A New Two-Constant Equation of State', *Industrial and Engineering Chemistry Fundamentals*, **1976**, doi: 10.1021/i160057a011.

[38] J. C. de Hemptinne and P. Ungerer, 'Accuracy of the volumetric predictions of some important equations of state for hydrocarbons, including a modified version of the Lee-Kesler method',**15**, *Fluid Phase Equilibria*, **1995**, pp.59-64.doi: 10.1016/0378-3812(95)93809-O.

[39] J. C. De Hemptinne and E. Behar, 'Propriétés thermodynamiques de systèmes contenant des gaz acides. Étude bibliographique', vol.**55** n.6,*Oil & Gas Science and Technology*, **2000**, doi: 10.2516/ogst:2000047.

[40] S. Chabab *et al.*, 'Thermodynamic study of the CO_2 – H_2O – NaCl system: Measurements of CO2 solubility and modeling of phase equilibria using Soreide and Whitson, electrolyte CPA and SIT models',vol.**91**, *International Journal of Greenhouse Gas Control*, **2019**,. doi: 10.1016/j.ijggc.2019.102825.

[41] G. Soave, 'Equilibrium constants from a modified Redlich-Kwong equation of state', vol.**27**, *Chemical Engineering Science*, **1972**, pp.1197-1203. doi: 10.1016/0009-2509(72)80096-4.

[42] K. Tödheide and E. U. Franck, 'Das zweiphasengebiet und die kritische kurve im system kohlendioxid-wasser bis zu drucken von 3500 bar', vol.**37**,*Zeitschrift fur Physikalische Chemie*, **1963**, pp.387-401. doi: 10.1524/zpch.1963.37.5_6.387.

[43] M. Petitfrere, L. Patacchini, and R. De Loubens, 'Three-phase EoS-based reservoir simulation with salinity dependent phase-equilibrium calculations', **2016**, doi: 10.3997/2214-4609.201601744.

[44] W. Yan, S. Huang, and E. H. Stenby, 'Measurement and modeling of CO_2 solubility in NaCl brine and CO_2-saturated NaCl brine density',vol.**5** ,*International Journal of Greenhouse Gas Control*, **2011**,pp.1460-1477. doi: 10.1016/j.ijggc.2011.08.004.

[45] S. X. Hou, G. C. Maitland, and J. P. M. Trusler, 'Phase equilibria of (CO2 + H2O + NaCl) and (CO_2 + H_2O + KCl): Measurements and modeling',**78** ,*Journal of Supercritical Fluids*, **2013**, pp.78-88.doi: 10.1016/j.supflu.2013.03.022.

[46] J.-C. de Hemptinne, J.-M. Ledanois, P. Mougin, and A. Barreau, *Select Thermodynamic Models for Process Simulation - A Practical Guide using a Three Steps Methodology*. Edition TECHNIP,**2012**.

[47] M. J. Huron and J. Vidal, 'New mixing rules in simple equations of state for representing vapour-liquid equilibria of strongly non-ideal mixtures',vol.**3** n.4 ,*Fluid Phase Equilibria*, **1979**, pp.255-271.doi: 10.1016/0378-3812(79)80001-1.

[48] Z. Duan and R. Sun, 'An improved model calculating CO_2 solubility in pure water and aqueous NaCl solutions from 273 to 533 K and from 0 to 2000 bar',vol.**103**, *Chemical Geology*, **2003**, pp.257-271.doi: 10.1016/S0009-2541(02)00263-2.

[49] L. . Li, Y., Ngheim, 'Phase equilibria of oil, gas and water/brine mixtures from a cubic equation of state and Henry's law.', *Canadian Journal of Chemical Engineering*, vol. **64**, pp. 486–496, **1986**.

[50] Z. Duan, N. Møller, and J. H. Weare, 'An equation of state for the CH_4-CO_2-H_2O system: I. Pure systems from 0 to 1000°C and 0 to 8000 bar',vol.**56** n.7, *Geochimica et Cosmochimica Acta*, **1992**, pp.2605-2617.doi: 10.1016/0016-7037(92)90347-L.

[51] G. . Haar, L., Gallagher, J.S., Kell, *NBS/NRC Steam Tables: Thermodynamic and Transport Properties and Computer Programs for Vapor and Liquid States of Water in SI Units*, Hemisphere. Washington, DC., **1984**.

[52] N. L. Shide Mao, Dehui Zhang, Yongquan Li, 'An improved model for calculating CO2 solubility in aqueous NaCl solutions and the application to CO2–H2O–NaCl fluid inclusions', *Chemical Geology*, vol. **347**, pp. 43–58, **2013**.

[53] K. S. Pitzer, J. C. Peiper, and R. H. Busey, 'Thermodynamic Properties of Aqueous Sodium Chloride Solutions',vol.**13**,*Journal of Physical and Chemical Reference Data*, **1984**, doi: 10.1063/1.555709.

[54] X. L. Jun Li, Lingli Wei, 'Modeling of CO_2-CH_4-H_2S-brine based on cubic EOS and fugacity-activity approach and their comparisons', *Energy Procedure*, vol. **64**, pp. 3598–3607, **2014**.

[55] J. Li, L.L. Wei, X.C. Li, 'Modeling of CO_2-CH_4-H_2S-brine based on cubic EOS and fugacity-activity approach and their comparisons', *Energy Procedure*, vol. **63**, pp. 3598–3607, **2014**.

[56] G. M. Wilson, 'A New Correlation for NH3, CO_2, H_2S Volatility Data from Aqueous Sour Water Systems', *EPA Report EPA-600/2-80-067*. **1980**.

[57] 'Recueil des Travaux Chimiques des Pays-Bas', vol.**55** n.12,*Recueil des Travaux Chimiques des Pays-Bas*, **1936**, pp.1143-1144.doi: 10.1002/recl.19360551217.

[58] C. H. Twu, 'Internally Consistent Correlation for Predicting Liquid Viscosities of Petroleum Fractions', *Industrial and Engineering Chemistry Process Design and Development*, **1985**, doi: 10.1021/i200031a064.

[59] G. V. Pasad and G. Venkatarathnam, 'A method for avoiding trivial roots in isothermal flash calculations using cubic equations of state', vol.**38** n.9, *Industrial and Engineering Chemistry Research*, **1999**,pp.3530-3534. doi: 10.1021/ie980661t.

[60] *Steam and Gas Tables with Computer Equations*. **1984**.

[61] L. Oellrich, U. Ploecker, J. M. Prausnitz, and H. Knapp, 'EQUATION-OF-STATE METHODS FOR COMPUTING PHASE EQUILIBRIA AND ENTHALPIES.',vol.**21**, *International chemical engineering*, **1981**.

[62] Y. A. Wu, J. J. Carroll, and Z. Du, *Carbon Dioxide Sequestration and Related Technologies*. 2011.

[63] G. M. Kontogeorgis, E. C. Voutsas, I. V. Yakoumis, and D. P. Tassios, 'An equation of state for associating fluids',vol.**35** n.11, *Industrial and Engineering Chemistry Research*, **1996**, pp.4310-4318.doi: 10.1021/ie9600203.

[64] W. G. Chapman, K. E. Gubbins, G. Jackson, and M. Radosz, 'New reference equation of state for associating liquids',vol.**29** n.8, *Industrial and Engineering Chemistry Research*, **1990**, pp.1709-1721.doi: 10.1021/ie00104a021.

[65] X. Courtial, N. Ferrando, J. C. de Hemptinne, and P. Mougin, 'Electrolyte CPA equation of state for very high temperature and pressure reservoir and basin applications',vol.**142** ,*Geochimica et Cosmochimica Acta*, **2014**,pp.1-14. doi: 10.1016/j.gca.2014.07.028.

[66] G. M. Kontogeorgis, G. K. Folas, N. Muro-Suñé, F. Roca Leon, and M. L. Michelsen, 'Solvation phenomena in association theories with applications to oil & gas and chemical industries', **63** n.3,*Oil and Gas Science and Technology*, **2008**, pp.305-319.doi: 10.2516/ogst:2008025.

[67] I. Tsivintzelis, G. M. Kontogeorgis, M. L. Michelsen, and E. H. Stenby, 'Modeling phase equilibria for acid gas mixtures using the CPA equation of state. Part II: Binary mixtures with CO_2', *Fluid Phase Equilibria*, **2011**, doi: 10.1016/j.fluid.2011.02.006.

[68] I. Tsivintzelis, S. Ali, and G. M. Kontogeorgis, 'Modeling phase equilibria for acid gas mixtures using the CPA equation of state. Part IV. Applications to mixtures of CO2 with alkanes', vol.**306** n.1,*Fluid Phase Equilibria*, **2015**, pp.38-56.doi: 10.1016/j.fluid.2015.03.034.

[69] I. Tsivintzelis, G. M. Kontogeorgis, M. L. Michelsen, and E. H. Stenby, 'Modeling phase equilibria for acid gas mixtures using the CPA equation of state. I. Mixtures with H2S', vol.**56** n.11, *AIChE Journal*, **2010**,pp.2965-2982. doi: 10.1002/aic.12207.

[70] L. Sun, G. M. Kontogeorgis, N. Von Solms, and X. Liang, 'Modeling of Gas Solubility Using the Electrolyte Cubic plus Association Equation of State', *Industrial and Engineering Chemistry Research*, **2019**, pp.1-59.doi: 10.1021/acs.iecr.9b03335.

[71] A. M. Palma, A. J. Queimada, and J. A. P. Coutinho, 'Improved Prediction of Water Properties and Phase Equilibria with a Modified Cubic Plus Association Equation of State', *Industrial and Engineering Chemistry Research*, **2017**, pp.1-69.doi: 10.1021/acs.iecr.7b03522.

[72] A. M. Palma, M. B. Oliveira, A. J. Queimada, and J. A. P. Coutinho, 'Re-evaluating the CPA EoS for improving critical points and derivative properties description', vol.**436**,*Fluid Phase Equilibria*, **2017**,pp.85-97. doi: 10.1016/j.fluid.2017.01.002.

[73] G. M. Kontogeorgis, I. V. Yakoumis, H. Meijer, E. Hendriks, and T. Moorwood, 'Multicomponent phase equilibrium calculations for water-methanol-alkane mixtures', **158**-160, *Fluid Phase Equilibria*, **1999**, pp.201-209.doi: 10.1016/s0378-3812(99)00060-6.

[74] P. M. Mathias and T. W. Copeman, 'Extension of the Peng-Robinson equation of state to complex mixtures: Evaluation of the various forms of the local composition concept', *Fluid Phase Equilibria*, **1983**, doi: 10.1016/0378-3812(83)80084-3.

[75] A. M. Palma, A. J. Queimada, and J. A. P. Coutinho, 'Modeling of Hydrate Dissociation Curves

with a Modified Cubic-Plus-Association Equation of State',vol.**13**, *Industrial and Engineering Chemistry Research*, **2019**, pp.91-108.doi: 10.1021/acs.iecr.9b02432.

[76] G. M. Kontogeorgis and G. K. Folas, *Thermodynamic Models for Industrial Applications: From Classical and Advanced Mixing Rules to Association Theories*. **2009**.Wiley, 728 pages.

[77] H. C. Helgeson, D. H. Kirkham, and G. C. Flowers, 'Theoretical prediction of the thermodynamic behavior of aqueous electrolytes at high pressures and temperatures: IV. Calculation of activity coefficients, osmotic coefficients, and apparent molal and standard and relative partial molal properties to 600oC', vol.**281** n.10,*American Journal of Science*, **1981**,pp.1249-1516. doi: 10.2475/ajs.281.10.1249.

[78] L. A. Bromley, 'Thermodynamic properties of strong electrolytes in aqueous solutions',vol.**19** n.2 ,*AIChE Journal*, **1973**, pp.313-320.doi: 10.1002/aic.690190216.

[79] E. Hückel and P. Debye, 'The theory of electrolytes. I. Lowering of freezing point and related phenomena', *Physikalische Zeitschrift*, **1923**.

[80] P. Wang, A. Anderko, and R. D. Young, 'A speciation-based model for mixed-solvent electrolyte systems',vol.**203**(1-2) ,*Fluid Phase Equilibria*, **2002**, pp.141-176.doi: 10.1016/S0378-3812(02)00178-4.

[81] P. Wang, R. D. Springer, A. Anderko, and R. D. Young, 'Modeling phase equilibria and speciation in mixed-solvent electrolyte systems',Fluid Phase Equilibria **222**-223, **2004**,pp.11-17. doi: 10.1016/j.fluid.2004.06.008.

[82] K. S. Pitzer and G. Mayorga, 'Thermodynamics of electrolytes. II. Activity and osmotic coefficients for strong electrolytes with one or both ions univalent',vol.**77** n.19, *Journal of Physical Chemistry*, **1973**,pp.2300-2308. doi: 10.1021/j100638a009.

[83] D. S. Abrams and J. M. Prausnitz, 'Statistical thermodynamics of liquid mixtures: A new expression for the excess Gibbs energy of partly or completely miscible systems', *AIChE Journal*, **1975**, doi: 10.1002/aic.690210115.

[84] E. L. Shock and H. C. Helgeson, 'Calculation of the thermodynamic and transport properties of aqueous species at high pressures and temperatures: Correlation algorithms for ionic species and equation of state predictions to 5 kb and 1000°C', vol.**21** n.1, *Geochimica et Cosmochimica Acta*, **1988**, pp.116-128.doi: 10.1016/0016-7037(88)90181-0.

[85] R. Privat and J.-N. Jaubert, 'Thermodynamic Models for the Prediction of Petroleum-Fluid Phase Behaviour', vol.**5**, in *Crude Oil Emulsions- Composition Stability and Characterization*, **2012**,pp.71-106.

[86] A. Dhima, J. C. De Hemptinne, and J. Jose, 'Solubility of hydrocarbons and CO_2 mixtures in water under high pressure',vol.**38**, *Industrial and Engineering Chemistry Research*, **1999**, pp.3144-3161. doi: 10.1021/ie980768g.

[87] W. A. Fouad, M. Yarrison, K. Y. Song, K. R. Cox, and W. G. Chapman, 'High pressure measurements and molecular modeling of the water content of acid gas containing mixtures', vol.**61** n.9,*AIChE Journal*, **2015**,3038-3052. doi: 10.1002/aic.14885.

Chapter 4

Analysis of Results: from phases to models selection

The thermodynamics study of the CO_2-H_2O, H_2S-H_2O, CH_4-H_2O, H_2O-CO_2-H_2S, H_2O-CO_2-NaCl, and H_2O-CO_2-H_2S-NaCl systems is of great importance both as environmental context both as Carbone Capture and Storage (CCS) or in an economic context for geothermal plants thanks to the CO_2 and H_2S injections or for industrial use. In this work, the performances of the different thermodynamic models that underlie the process simulators are verified through a collection of experimental data and a selection of them through the waste for our areas of interest. Experimental measurement of CO_2, H_2S and CH_4 in aqueous sodium chloride solution was performed at molalities between 0.01 and 6 m, at temperatures between 273.15 and 523.15 K and pressured up to 200 bar. SW, PRH, DS, CPA, Sour-PR, and OLI models (AQ, MSE, MSE-SRK) are considered and compared for the modelling part. All model results are in agreement with geochemical data. The model data are in good agreement with the literature data and model predictions.

Table of Contents

List of Figures

List of Tables

It is impossible to choose a model correctly if the phase behaviour of the system is unknown. Therefore, this fourth chapter aims to provide a phenomenological understanding of the various phases that may exist in mixtures of geothermal interest and the behaviour of the properties as a function of temperature and pressure. It is proposed to present the models' results described in the previous one, comparing them with the experimental data and those between models. Obviously, the reader will not be able to expect a detailed examination of the results of thermodynamic models, mostly many of them coming from the most sophisticated software in chemical engineering, but a possible analysis in dealing with chemical components (or pollutants in that case) that are not desirable during the geothermal plant design. The interested reader will be invited to consult other documents for further study.

Many scenarios in the geothermal power plants propose to reduce the amount of carbon dioxide (CO_2), H_2S and other non-condensable gases, emissions to the atmosphere, carbon capture and storage (CCS) or reinjections into geological reservoirs. All of these options are research and attractive industrial options to solve these problems.

This chapter describes the steps to analyze the problem and the results achieved relating to:

4.1 *Pseudo-experimental correlations*: this section describes the collection of experimental data, selection and comparison between authors under the same operating conditions in particular for the mixtures: CO_2-H_2O, CO_2-H_2O-NaCl, H_2S-H_2O, H_2S-H_2O-NaCl, CH_4-H2O, CH_4-H_2O -NaCl and CO_2-H_2S-H2O, CH_4-CO_2-H_2O and CO_2-H_2S-H_2O;
4.2 *Quality analysis of the investigated models on fluid phase equilibria*: This part analyses the calculation of the solubilities of the CO_2-H_2O, CO_2-H_2O-NaCl, H_2S-H_2O, H_2S-H_2O-NaCl, CH_4-H_2O, CH_4-H_2O-NaCl mixtures with the thermodynamic models selected in Chapter 3. Then, the calculation of the relative deviations between the results of the models and experimental data;
4.3 *Enthalpic data analysis*: Calculation of the residual enthalpies (or mixing) of the CO_2-H_2O, CO_2-H_2O-NaCl, H_2S-H_2O, H_2S-H_2O-NaCl, CH_4-H_2O, CH_4-H_2O-NaCl mixtures with some thermodynamic models, with greater attention to the computational thermodynamic properties present in OLI systems.
4.4 *Conclusion and model recommendation*: From the results of solubility and enthalpy of mixing, it is possible to identify a thermodynamic model for the geothermal mixture in the desired temperature, pressure and molality conditions, which can be selected in a process software such as, for example, Unisim Design R480 or Aspen Hysys.

In this chapter, sections 4.2 and 4.3 have been distinguished because it was appropriate to make a first screening of the results of a thermodynamic model as a function of solubility.

4.1 Pseudo-experimental correlations

Geothermal fluids, in the broadest sense, span large variations in composition and cover wide ranges of temperature and pressure. However, their composition may also be dynamic and change in space and time on short and long time scales. In addition, the physical properties of the fluids are affected by the chemical properties. Therefore, the principal objective in collecting data was to gather physiochemical properties of geothermal fluids such as solubilities, density, viscosity, compressibility and heat capacity to understand and examine the transfer of heat and mass by geothermal systems. Unlike petrochemical fluids, geothermal fluids are the least examined. Therefore, laboratory experiments are essentially concentrated on the solubility of binary mixtures, few on enthalpy and rarely on density, viscosity and compressibility as often the geothermal fluid has been assimilated to physical properties -chemicals of water.

The campaign for the definition and collection of experimental data is illustrated in Figure 4.1. The experimental data are fundamental to verify the congruence of the results of the chosen thermodynamic models.

Figure 4. 1. Step defining and collecting experimental data

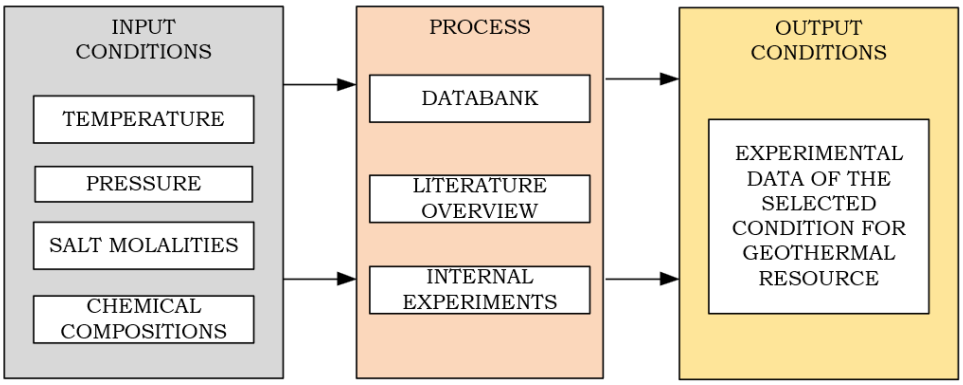

The investigation and collection of experimental data essentially focus on the main components present in many geothermal fluids in Europe, such as CO_2, H_2S, CH_4 in water and their interaction with salts. Carbon dioxide emissions, one of the main greenhouse gas (in terms of quantity) produced by human activities and with the use of fossil fuels, are continually increasing. One possible solution of great interest to industrial actors in the gas sector is capturing, transporting, and storing carbon dioxide in deep geological formations (salt caverns). In an economic context, the reversible storage of carbon dioxide, hydrogen sulphide and methane is also a perfect solution to meet the high demand for this gas in many applications. The thermodynamic study of these three main components of the geothermal fluid is the main objective for the scientific development of the geothermal plants involved in two European projects, GECO and GEOENVI. As part of the GECO project, the Hellisheiði power plant and Castelnuovo (from 2020 Qualtra) considered much non-condensable gas (NCGs). Hellisheiði power plant has 8 % max NCG (CO_2: 76.0368 kg/s, H_2S: 7.2492 kg/s, CH_4 : 0.0336 kg/s). While the Castelnuovo pilot power plants are constituted by an NCG reinjection arrangement in which the following quantities are present (CO_2: 3194.3 kg/h and H_2S: 76,72 kg/h) if considered a geothermal feed of 18 kg/s. This pilot plant is projected to have a 5 MWe power output limit. The Castelnuovo reservoir is considerably large, so that the preliminary reservoir simulations have shown that it can effectively retain the reinjected gas flow rate, which should be confined into the permeable rock porosity, helping to maintain the original reservoir pressure.
The resource is expected to be saturated vapour at a pressure within the 60-80 bar range, 280 °C temperature at about 3500 m depth. At the wellhead, the expected resource conditions are 10,3 bars pressure and 180 °C temperature. The NCG mass content is estimated at 8 %, of which about 7.8 % is CO_2 and 0.2% H_2S. The excellent layout consists of 2 production and one reinjection wells. Therefore the storage of CO_2 and H_2S in caverns is necessary. Geological storage facilities are less costly [1]. The storage facility's design and optimization require very accurate models under the thermodynamic conditions of the storage. The presence of brine in salt caverns and deep aquifers completely changes the storage gas's thermodynamic behaviour due to electrolytes such as NaCl [2] dissolved in the residual water or deep aquifer, so studying these systems becomes very complicated. Na+ and Cl- are the main species found in the salts of most geological formations. Therefore, the sodium chloride solution is considered a brine representative [3]–[5]. Therefore the thermodynamic model for the binary mixture CO_2- H_2O, H_2S-H_2O, CH_4-H_2O, ternary mixtures CO_2-H_2O-NaCl, CO_2-H_2O-H_2S and quaternary mixture CO_2-H_2O- H_2S-NaCl are of great geothermic industrial interest.

The data elaborated in this work are experimental measurements of the solubility of CO_2 in water, CO_2 in an aqueous solution of sodium chloride, CH_4 and H_2S solubilities in water, CH_4 and H_2S in an aqueous solution of sodium chloride.

4.1.1 CO_2-H_2O and CO_2-H_2O in brine

Regarding the CO_2-H_2O- salt mixtures, recently, many studies such as Yan et al. [1], Hou et al.[2]; Zhao et al. [3]; Gilbert et al.[4]; Guo et al.[5] ; Messabeb et al. [6]; Chabab et al. [7]) have been conducted to feel the lack of data for these mixtures.

The interaction of CO_2 and its properties in water and contact with rocks for different temperature and pressure conditions is the starting point for making a GTPP more efficient. When supercritical CO_2 is injected into a saline formation, it may be stored in various ways. One of the methods used is to trap CO_2 in the pores by capillary forces. Over time, some CO_2 dissolves in the forming waters (pores), a solubility trapping process; solubility entrapment can also become significant during the injection phase, accounting for approximately 20% of the CO_2 distribution [8]. Eventually, some portions of CO_2 dissolved in the formation waters can react with minerals or cations dissolved in the formation to form carbonate and other minerals via a mechanism called a mineral trap. Thus, over time, the storage mechanism evolves from one dominated by structural traps with significant solubility entrapment from injection at ~ 101 years [9], [10], [11]. Eventually, mineral entrapment (~ 102-105 years) becomes more significant [12] and although solubility, entrapment can remain dominant indefinitely [13], [9]. Here, the section summarizes available experimental PVTX (Pressure-Volume Temperature- Composition) data for the H_2O-CO_2 system and the data selected to develop a generic equation as a function of Temperature and Pressure. Each of the various storage mechanisms involves changing the system's volume and pressure (CO_2+ formation water+minerals within the saline formation). The volume and concomitant pressure changes associated with CO_2 injection and the system's subsequent evolution thus affect the storage capacity (Figure 4.2).

Figure 4. 2. A conceptual model is comparing the relative formation volume required to store CO_2 as a separate supercritical phase (centre) and as a dissolved in the formation brine (right). Source [14].

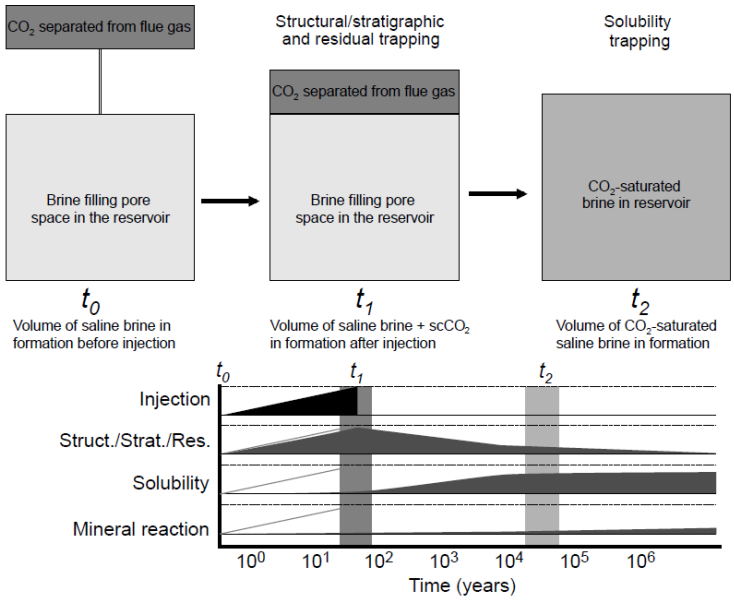

The CO_2-H_2O system is a significant experimental database developed over the years related to the PVTX properties of fluids in the H_2O-CO_2 system at conditions relevant to storage in geologic formations. Considering only water, there are several hundred experimental studies on PVT properties of the single component H_2O system. In recent years, the available experimental data have been strictly evaluated, inserted in thermodynamic models and used in work environments, including studying geothermal processes. The EOS, indicated in the literature as IAPWS-95, was adopted by the International Association for the Properties of Water and Steam (IAPSWS) and is valid from the ice melt line at 1273 K and up to 1000 bar. IAPWS-95 is generally considered to reproduce the physical and more faithfully thermodynamic properties of H_2O over a wide range of PT conditions relevant to geology environments, including the CCS environment. It is used in most formulations to predict the PVTX properties of aqueous fluids. While the CO_2 solubility in pure water has been investigated over a wide range of temperatures and pressure, indeed, this mixture is well described, and so abundant literature data exit. In the last twenty years, essential papers such as Diamond and Akinfiev (2003), Spycher (2003), Chapoy (2004) and Ji (2007). Other papers, such as Mao (2013) and Springer (2012), contained an extensive summary of the literature's experimental data. Studies with experimental data in the temperature and pressure ranges of interest are listed in Table 4.1, which enumerates each study's pressure and temperature ranges. For the mixture

CO_2-H_2O, few experimental data on gas systems have been conducted, excluding some authors (Chapoy (2005), Burgess et Germann(1969), Gillespie et Wilson (1980), Yu (1980), Caroll (1989), Selleck (1997). However, experimental results for the solubility of carbon dioxide in water are plentiful in the literature (Table 4.1). Likewise, solubility measurement in NaCl aqueous solution is also widely available in the literature (Table 4.2).

Table 4. 1. Experimental data for the CO_2-H_2O system used in this work

Temperature [K]	Pressure [bar]	M (mol/kg)	Np [-]	Reference
293.15-303.15	5-30	0		Kritschewsky et al. [15]
273.15-373.15	10-90	0		Y. Zel'vinskii
323-373	2.5-71	0	25	Wiebe and Gaddy [16]
285-313	2.5-50.7	0	26	Wiebe and Gaddy [17]
283-303	1-20	0		Bartholome and Friz
473-523	98-480	0	70	S. Malinin
323-533	200-2000	0	80	Todheide and Franck[18]
383-533	100-1500	0	30	Takenouchi and Kennedy [19]
303-353	10-39	0		Matous et al. [20]
323-473	1-54	0		Zawisza et Malesinska [21]
323-373	100-800	0		Shagiakjmetov and Tarzimanov [22]
288-366	7-203	0	8	Gillespie and Wilson
283-343	10-160	0		P.M. Oleinik [23]
323.20	Up to 200	0		Nakayama et al. [24]
244.82-298.15	6.9-137.9	0		Song and Kobayashi [25]
323-348	101-152	0	4	D'souza et al. [26]
343-421	Up to 200	0		Sako et al. [27]
288.15-313.15	60-250	0	41	King et al. [28]
313.15-383.15	10-344.8	0		Jackson et al. [29]
278- 293	64-295	0		Teng et al. [30]
274-278	8.9-20.9	0		Malegaonkar et al. [31]
344.00	100-1000	0		Dhima et al. [32]
298.00	21-77	0		Yama et al. [33]
294.00	100-600	0		Rosenbauer et al. [34]
277-283	20-42	0		Servio et al. [35]
274-288	1-22	0		G.K Andeson [36]
298.00	75-300	0		Teng and Yamasaki [37]
274-351	2-90	0		Chapoy et al. [38]
278-318	5-80	0	22	Valtz et al. [39]
298.15-448.15	Up to 180	0	21	Hou et al. [40]
283-363	Up to 130	0		Carvalho et al. [41]
288.15-433.15	100-1200	0	63	Guo et al. [42]
304.19	176-583	0	10	Gu [43]
323.15	68.2-176.8	0	14	Briones et al. [44]
323.15	21-159.9	0	7	Liu et al. [45]
323.15-353.15	40.5-141.1	0	58	Bamberger et al. [46]
373.15	72.1-272.6	0	5	Tong et al. [47]
393.15	68.9-703.2	0	10	Prutton and Savage [48]
393.15-473.15	39.1-102.1	0	18	Nighswander et al. [49]
323.15	101-301	0	3	Dohrn et al. [50]
373.15	3.2-23.1	0	7	Müller et al.[51]

Collecting experimental data has led to a selection of all the data collected since some inconsistencies were highlighted by comparing the data of the same mixture under the same operating conditions. In this thesis, the authors and the related experimental data discarded are not reported, above all for space reasons. The selection was made for all the mixtures in a very standardized way: the experimental data in the same conditions of temperature, pressure and molality of the salt must not have a deviation of more than 1.5% within themself. All data were represented in a 3D model (T, P, x) (Figure 4.3) and in a 2D model (T, P) (Figure 4.4) to highlight at which points the experimental data are few or non-existent. This method will immediately identify if the thermodynamic models' results are sufficient to define and optimize a geothermal plant process.

Figure 4. 3. Summary of the PT range covered by experimental PTx data for the system H_2O- CO_2 at zero molality of salinity. The figure shows the solubilities of the CO_2 in liquid and vapour zones in the range temperature [0- 350 °C] and pressure [1-350 bar] referred in Table 4.1. The symbols are "+" for the liquid state and "▼" for the vapour state.

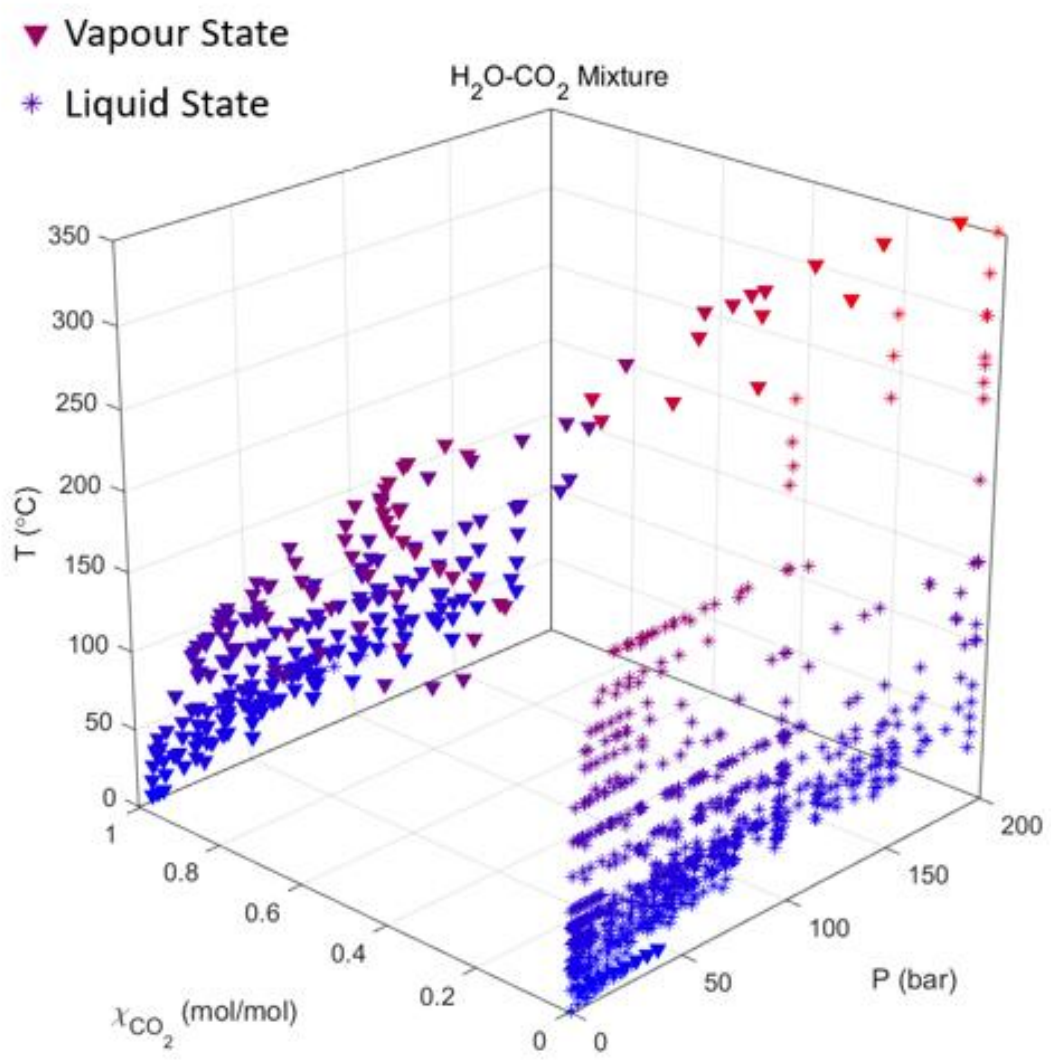

Figure 4. 4. Experimental points (n. 1397) were collected and referred to Table 4.1, and areas, where experimental data are scarce were identified with a rectangular in the figure.

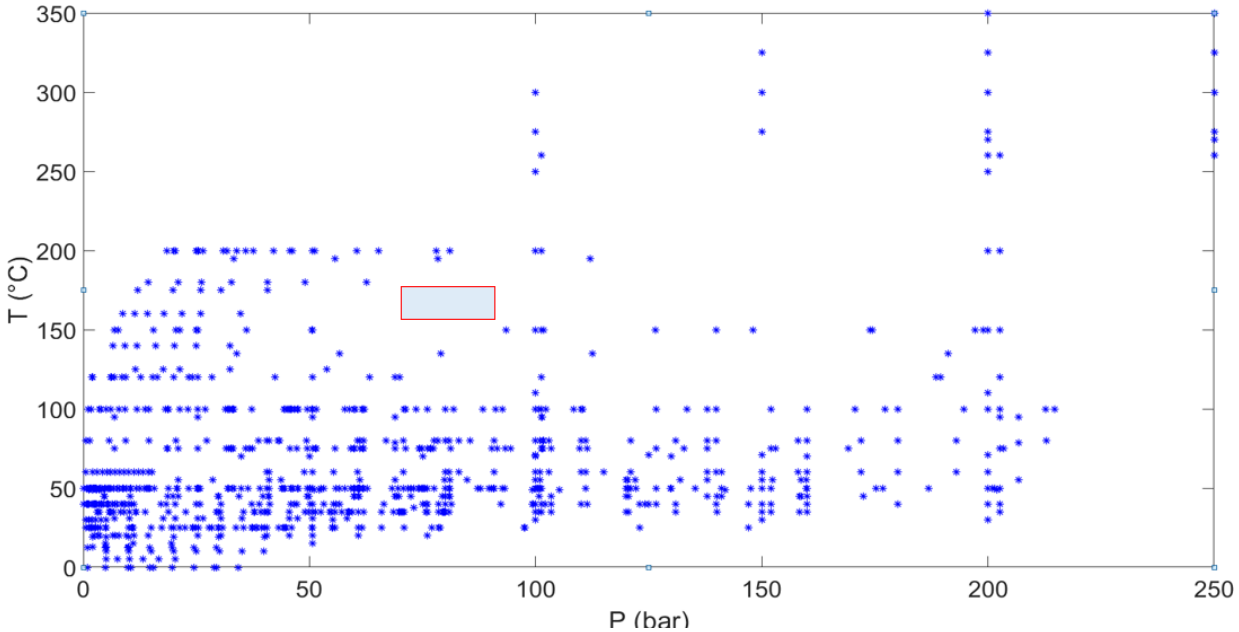

By comparison with the CO_2–H_2O system, solubility data for the CO_2–NaCl–H_2O system are scarce, especially at high salt molality (6 mol/kg), high pressure (200 bar), and high temperature (423.15 K). Koschel et al. [52] determined the solubility of CO_2 in NaCl solution by a calorimetric technique through the measurement of mixture enthalpy.
Guo et al. [5] used a Raman spectroscopy method to obtain CO_2 solubility data in NaCl solution. The calibration step involves the knowledge of the molar volume of carbon dioxide and the brine density.

In this work section, few authors took care of the CO_2-H_2O-NaCl system and not all experimental data covering a large T-P- m range. The experimental measurements are reviewed in Table 4.2. Most of the major data sets are consistently selected because of their deviations of 1.5% within themself. The experimental data that predict CO_2 solubility in aqueous NaCl solutions up to high temperature, pressure and ionic strength (273-533 K, 0-1500 bar and 0-6 m) have an accuracy < 2% in CO_2 solubility.
The most extensive studies of CO_2 solubility in aqueous NaCl solutions are those of Takenouchi and Kennedy [19], Gehrig [53], Drummond (1981) and Rumpf et al. [54]. Takenouchi and Kennedy's data set covers a large temperature– pressure–ionic strength (T–P–m) range (423–723 K, 100–1400 bar and 0–4.28 m). Gehrig extended CO_2 solubility data in 1.09 m NaCl solution up to 2800 bar, but the data amount is at higher pressure. For the lower pressure (< 400 bar), the measurements of Drummond (1981) are few. Ellis and Golding [55], Malinin and Savelyeva [56] and Malinin and Kurorskaya [57] also published some CO_2 solubility data in aqueous NaCl solutions. However, there are some disagreements among these data. For example, a few data points of Drummond (1981) measured during the pressure increasing process are inconsistent with those measured in the pressure decreasing process [58]. The deviation between them is 8–15%. The data of Takenouchi and Kennedy (1965) at 100 bar diverge sharply from that of Drummond (1981) and Rumpf et al. (1994). This study has no reliable criterion for determining which data are accurate, but it could eliminate the experimental data with high deviations within experimental data. It is possible to note that experimental measurements of CO_2 solubility in NaCl solutions at high pressure (>400 bar) and low temperature (< 423 K) range and in the high ionic strength (>4.3 m) range are absent (Table 4.2). It was highlighted that CO_2 solubility data in other salts than NaCl aqueous solutions at middle and elevated pressures are limited.

Table 4. 2. Experimental CO_2 solubility in NaCl solution (up to 6 mol/kg) at temperatures from 273 to 533 K and pressures from 1 to 1500 bar. "N" is the number of data.

T [°C]	P [bar]	NaCl [mol/kg]	N [-]	Reference [-]
20-80	10- 143	0.25-2	32	Carvalho et all. (2015)
41- 270	1-200	1 – 4	116	Duan &Sun (2003)
172-236	44-69	0.5 – 2	15	Ellis and Golding (1963)
50-100	57-192	2.5- 4	20	Hou et al. (2013)
50-150	28-181	2.5- 4	36	Hou,S.X. et all. (2013)
40-80	39- 101	2.5-4	15	Kiepe et al. (2002)
50-100	50.4-192	0-3	20	Koschel et al. (2006)
60-80	40-213	0.01-0.172	31	Mohammadian et al. (2015)
80-200	40-100	0.172	34	Nighswander et all. (1989)
40-160	4.6-92	0.7-9.7	138	Rumpf,B. Et all. (1994)
50-100	54-200	1-3	20	Salaheddine C., et all. (2019)
45	34.50-138	0.85-3.5	19	Sayegh,S.G et Najman,J. (1984)
150-350	100-200	1-3.65	14	Takenouchi and Kennedy (1965)
50-100	50-300	1-5	20	Yan et al. (2011)
50-100	48-150	1-6	9	Zhao et al. (2015)
50-400	30-266	0-6	15	Drummond (1981)
0–25	1	0–3	7	Harned and Davis (1943)
25–150	48	0–6	16	Malinin and Kurovskaya (1975)
25–75	48	0–4	16	Malinin and Savalyeva (1972)
0–40	1	0.1–4	18	Markham and Kobe (1941)
40–160	2–96	0–6	7	Nicolaisen (1994)
25	1	0–3	11	Onda et al. (1970)
135–527	30–2800	1–4.3	29	Gehrig (1980)
15-35	1	0.4-5.1	10	Yasunishi and Yoshida (1979)

Figure 4. 5. The experimental data points for salt molalities from 0 to 5 m in the CO_2-H_2O-NaCl systems. The left figure shows the experimental data in the pressure and temperature space without brine, while the right figure shows the experimental data in the pressure and temperature space with brine.

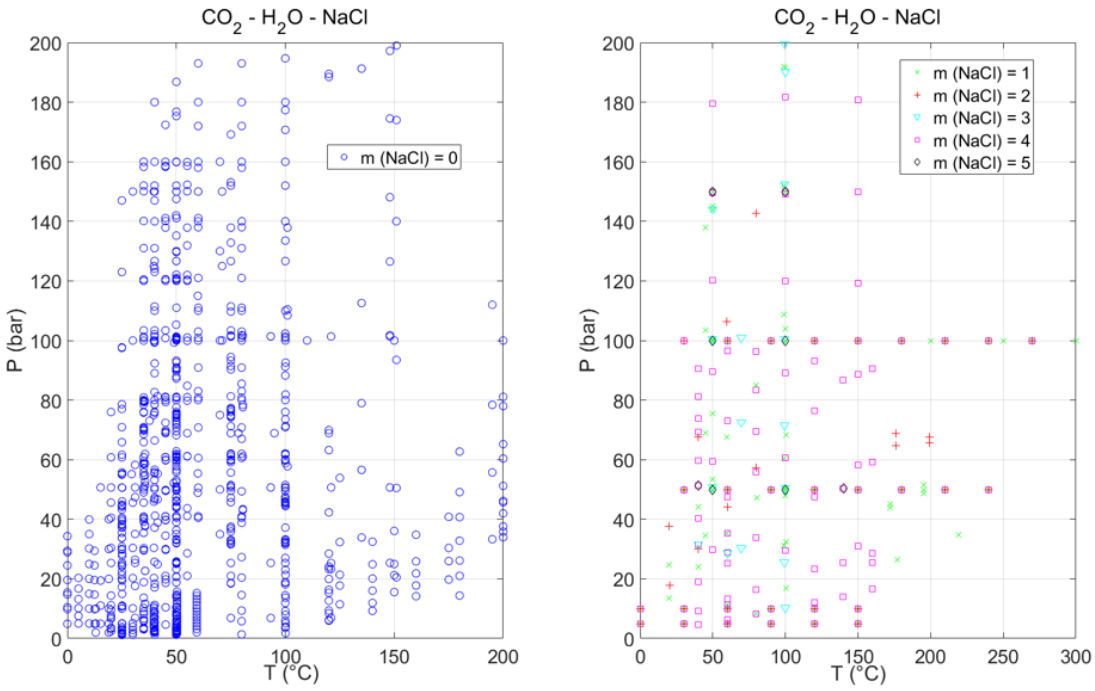

4.1.2 H_2S-H_2O and H_2S-H_2O in brine

Hydrogen sulphide (H_2S) is a common constituent of geothermal systems. Its concentrations usually are about 2-6 % wt; an accurate prediction of H_2S solubility in H_2O- NaCl is needed. Several experimental investigations (Table 4.3) on the above system have been carried out last decades (Drummond, 1981). Barrett (1988)[59], [60] uses various values to correlate previous experimental data. Barta and Bradley (1985) [61]introduced in their expression molecule-molecule interaction parameters. Other works such as Rumpf (1993)[62] and Duan (1992)[63] introduced binary and interaction parameters to interpret the experimental data carried out in previous years. The experimental and calculated data of Hervè (1997) [64] are obtained by regression of Drummond data without any molecule-molecule contribution.
This approximation seems to be reasonable as the molality of dissolved hydrogen sulphide remains small. Hervè (1997) [64] obtained a vapour phase fugacity calculated using the Peng- Robinson cubic equation of state as modified by Carroll (1989) [65], who introduced minor modifications to improve water-hydrogen sulphide vapour-liquid, liquid-liquid and liquid-liquid-vapour equilibrium prediction. Hervè's equation is valid for temperatures between 315.15 and 513.15 K. Xia et al. [66]reported H_2S solubility in aqueous NaCl solution from 313 to 393 K, from 10 to 100 bar, and from 4 to 6 m.

Table 4. 3. Review of literature data presenting H_2S solubility in NaCl-bearing aqueous solutions. "N" is the number of data (including mixtures without salts).

T (°C)	P(bar)	Solution	N[a]	Reference
10-95	*1*	NaCl (0-5 m)	516	Barrett et al. (1988)
41- 277	6-74	NaCl (0.2 – 6.04)	101	Hervè et al. (1997)
0-2.5	11-14	NaCl (0.2 – 6.04)	44	Suleimenov and Krupp (1994)
30-380	1	NaCl (0- 6 m)	49	Drummond (1981)
25	1	NaCl (0-3 m)	40	Gamsjager and Kaplan (1969)
40-120	10-100	NaCl(4-6 m)	71	Xia et al
202-262	16-60	NaCl (1m)	13	Kozintseva
50-120	17-310	NaCl (0-3 m)	23	Koschel et al. (2006)

Barrett (1988) [60] fitted the experimental data with second-order polynomial curves plus statistical data in the range temperature 283.15- 368.15 K, atmospheric pressure and 0-5 m NaCl solutions [m H_2S/kg H_2O]. As a result, the calculated standards error in Table 4.3 are equivalent at 1% of the mean solubility values at 298.15 K and increase until 15% at 368.15 K.
Information concerning H_2S solubility in pure water is less abundant than CO_2, and most of the available studies are listed in the review by Koschel (2006)[67] and Chapoy (2005)[68]. In addition, experimental data on high temperature for the mixture H_2S- H_2O have been published by Zenin (2011)[69]. Despite the apparent importance of H_2O–H_2S fluids to various geochemical processes, our knowledge of their PVTx properties refers to minimal pressure, volume, temperature, and composition of liquid and vapour phases.
Although experimental measurements of the properties of H_2O–H_2S gas mixtures have been made for temperatures above 473.15 K, with one exception, the data are restricted to low partial pressures of H_2S Kozintseva (1964) [59]; Suleimenov and Krupp,1994. Gillespie and Wilson studied the H_2O–H_2S system at high pressure and high concentration of hydrogen sulphide, which presented limited pressure–temperature-composition data for three isotherms 477.15 K, 533.15 K and 588.15 K. While existing equations of state are unable to predict the properties of H_2O–H_2S gas mixtures at elevated temperature in either the vapour-only field or along with the vapour–liquid phase boundary.
An interrupted locus of critical points characterizes the system H_2S- H_2O Van Konynenburg and Scott [70]. Two critical curves describe the critical locus. One of these curves starts at the critical point of pure H_2O and, with progressive addition of H_2S to the system, moves to sharply higher pressure and lower temperature. The other critical curve starts at the critical point of pure H_2S and, with the addition of H_2O, moves to higher pressure and temperature, and a critical endpoint corresponds to the termination of the three-phase (liquid-liquid–vapour) boundary. Other characteristic features of this system are the existence of a liquid-liquid immiscibility gap and the formation of H_2O–H_2S gas hydrates at low temperatures (Zezin [69]). The H_2O-H_2S system's properties at temperatures below 423.15 K are discussed in detail in Selleck [71] and, particularly

in Carroll [65]. At higher temperatures, intermediate mixtures consist of a denser aqueous liquid and a less dense, H_2S-dominated vapour. However, the conditions over which the two-phase state is stable have not been constrained. According to Alekhin and Sretenskeya, the H_2O–H_2S system's behaviour is similar to that of the systems, water–carbon dioxide, water– methane or mixtures of water with heavier hydrocarbons.

Numerous experimental studies have investigated the solubility of H_2S in water and phase relations at the conditions of vapour–liquid equilibrium in the system H_2O–H_2S but, with rare exception, only at low temperature and low partial pressure of H_2S (Winkler, 1906; Wright and Maass,1932; Selleck et al., 1952; Pohl, 1961; Kozintseva 1964; Clarke and Glew, 1971; Lee and Mather, 1977; Drummond, 1981; Gillespie and Wilson, 1982; Barret,1988; Carroll and Mather, 1989; Suleimenov and Krupp, 1994; Chapoy, 2005). These experimental data have led to several models for the calculation of the properties of fluids and conditions of vapour–liquid equilibrium in the system H_2O–H_2S (Carroll and Mather, 1989; Chapoy, 2005; Dubessy, 2005; Duan et al., 2007; Perfetti et al., 2008; dos Ramos and McCabe, 2010).

The properties of two-phase fluid mixtures containing a supercritical component such as hydrogen sulphide are usually modelled using an asymmetrical approach. The vapour is described with an equation of state (EOS) that accounts for non-ideality with fugacity coefficients, and the liquid phase is described using activity coefficients. Henry's law constant is employed to calculate the fugacity of the volatile, non-aqueous components in the liquid. Some researchers have also used state equations to model the properties of the liquid Chapoy, 2005 and Duan, 2007). In this section, the results of experimental measurements designed to investigate the PTx properties of H_2O–H_2S fluid mixtures in both the liquid phase, along with the vapour–liquid boundary and the vapour phase at range temperature 283.15 – 603.15 K and pressure range 1- 200 bar (Table 4.4).

Table 4. 4. Review of literature data presenting H_2S solubility in pure water

T (°C)	P(bar)	Solution	N	Reference
10-95	1	Pure water	516	Barrett et al. (1988)
10-180	2-67	Pure water	325	Lee et Mather (1977)
25-65	5-40	Pure water	46	Chapoy et al. (2005)
30-171	17-23	Pure water	39	Burgess et Germann (1969)
38-171	7-207	Pure water	98	Selleck et al. (1952)
38-104	5-17	Pure water	39	Yu et al. (1980)
50-200	41- 203	Pure water	4	Vukotic (1961)
40-105	28-92	Pure water	10	Caroll et al. (1989)
100-316	55- 297	Pure water	14	Gillespie et al. (1982)
38-204	3-103	Pure water	12	Gillespie et Wilson (1980)
50-120	17-303	Pure water	6	Koshel et al. (2007)
229-330	28-129	Pure water	12	Kozintseva (1965)

Through the experimental data present in Table 4.4, it is possible to build a 3D plot (see Figure 4.6) and understand how temperature and pressure conditions, the experimental data are absent.

Figure 4. 6. Summary of the PT range covered by experimental PTx data for the system H_2O- H_2S at zero molality of salinity referred to Table 4.4. In the left figure, the experimental data show the solubilities of the H_2S in liquid and vapour zones in the range temperature [283.15- 623.15 K] and pressure [1-250 bar]. The right figure shows the areas in which are data present or missing. The symbols are "o" for the liquid state and "*" for the vapour state.

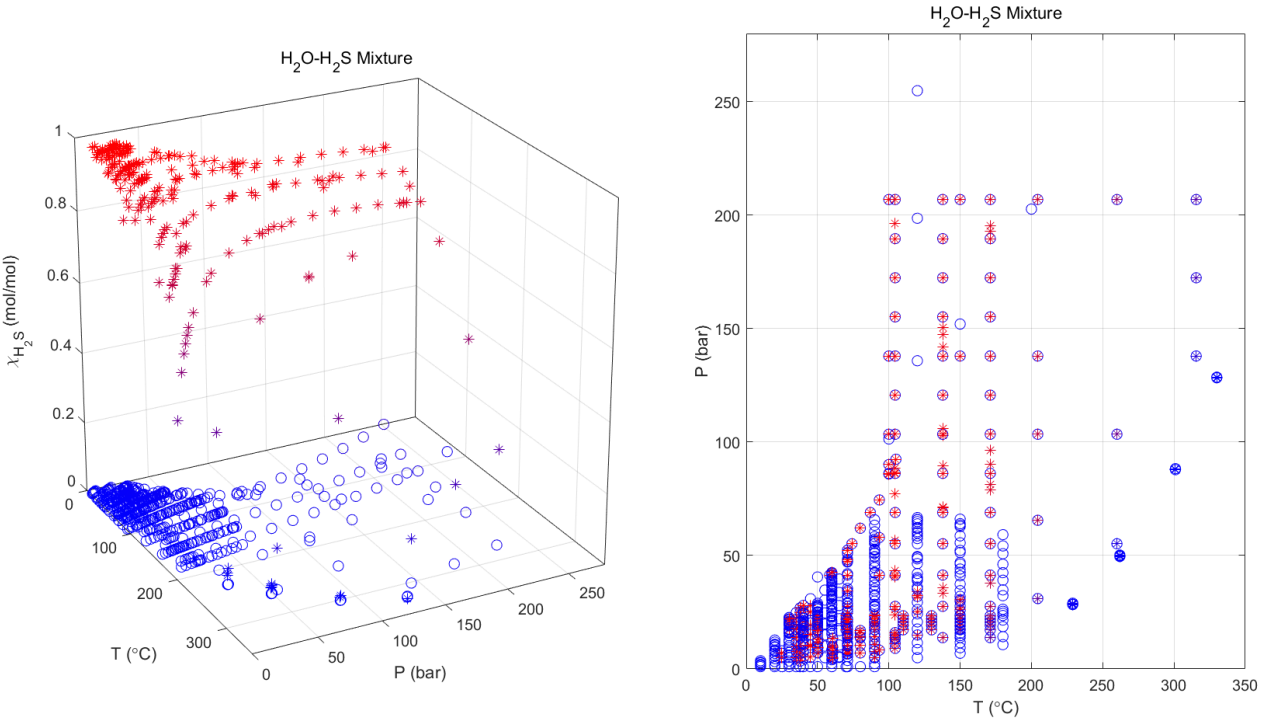

It is possible to highlight the difference in data between an H_2S-H_2O mixture and a saline mixture with different molalities (Figure 4.7). The latter has much less data than the former.

Figure 4. 7. Difference between the experimental data numbers for the H_2S-H_2O mixture and H_2S-H_2O-NaCl mixture

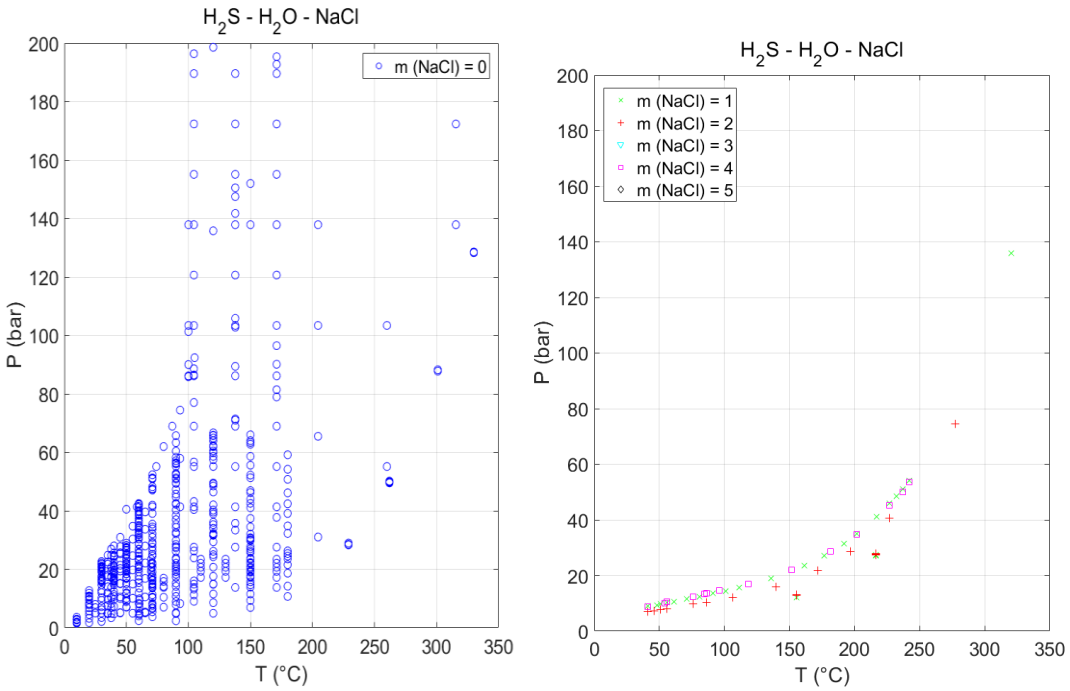

4.1.3 CH_4-Water and CH_4-H_2O in brine

CH_4 is one of the most important gases in nature, and it has been found in gas hydrate, natural gases, coalbed gas and fluid inclusions. Therefore, accurate prediction of CH_4 solubility in pure water, NaCl solutions, and other aqueous geothermal salt solutions cannot be performed due to a scares amount of experimental data. Nevertheless, this component is important in geochemical applications and to study geothermal fluid for power plants. There are many experimental studies of the solubility of CH_4 in pure water and aqueous NaCl solutions. However, there are limited pressure data and limits to comparing experimental data with the thermodynamic model's results. For example, Duan et al.'s [61] performed studies on analyzing fluid inclusions, methane hydrates and calculating methane's phase status in a geothermal and pressured reservoir. Over the last decades, different experimental data and theoretical models reported the CH_4 solubility calculations in water and NaCl aqueous solutions.
At low-temperature regions such as T < 100 °C, then, the solubility of methane in water is very low, and it decreases with increasing the carbon number of hydrocarbon. In the Geothermal industry, the hydrocarbon solubility in water depends strictly on the temperature; indeed, the hydrocarbon could be sufficiently miscible with water [72] at a temperature up to 300 °C and a pressure of 100 bar. Therefore, a significant amount of methane and other hydrocarbons can be dissolved in the aqueous phase at high temperatures and pressure.
The CH_4-H2O system belongs to the type III phase diagram [70]. This phase diagram shows two critical curves: the first curve typically originating at the critical point of the vast majority of volatile substance is very short and terminates in an upper critical endpoint at low temperature (the termination of the three-phase line); the second critical curve starts at the critical point of the less volatile substance (H_2O). Thus, the second critical curve begins as a gas-liquid critical curve but changes its character to so-called “gas-gas” immiscibility on its way to higher pressures. So, accurate experimental data and modelling on the CH_4-H_2O system in the state of high pressure “gas-gas” immiscibility region are rare; PPR78 EoS performed a recent model for this phase behaviour at high pressures. This report focuses on the P-T range of 0-350 °C and 1-200 bar pressure. There are more experimental data in the range 1-15 bar and 0-200 bar for the CH_4-H_2O and CO_2-CH_4-H_2O systems because they are relevant for the natural gas industry (upstream & downstream) and geothermal processes.
As for the CH_4-H_2O system, significant amounts of mass transfer may occur between the H_2O and CH_4-rich phases at high pressure and temperature. Therefore, geologic formations are capable of storing vast amounts of dissolved methane. Ganjdanesh et al. [73] proposed a new concept to recover methane/geothermal energy from high temperature (~ 150°C) aquifer formations using CO_2-saturated brine. This strategy is attractive while treating methane production while storing CO_2 in the aquifer could help offset the cost of CO_2 capture and sequestration (CO_2-CH_4- H_2O system).
It is known that the use of the Van der Walls one-fluid mixing rule with a single binary interaction parameter in a cubic EoS is not capable of correlating hydrocarbon solubility in water. The difficulty derives from the associating nature and strong hydrogen bonding of water molecules.

The first step of this study is to understand the CH_4 solubility in water. The CH_4 solubility in pure water has been measured over a wide P-T range (Figure 4.8). For this preliminary study, the data belonged to [74], [75], [76], [77], [78], [79]–[81], [82], [83], [84], [85], [86], [63], [87], [88], [89], [90], [91], [92], [93], [94], [95], [96], [97], [98], [99], [72], [100].

Figure 4. 8. P-T-x experimental data in the 3D plot (left) and P-T plot (right)

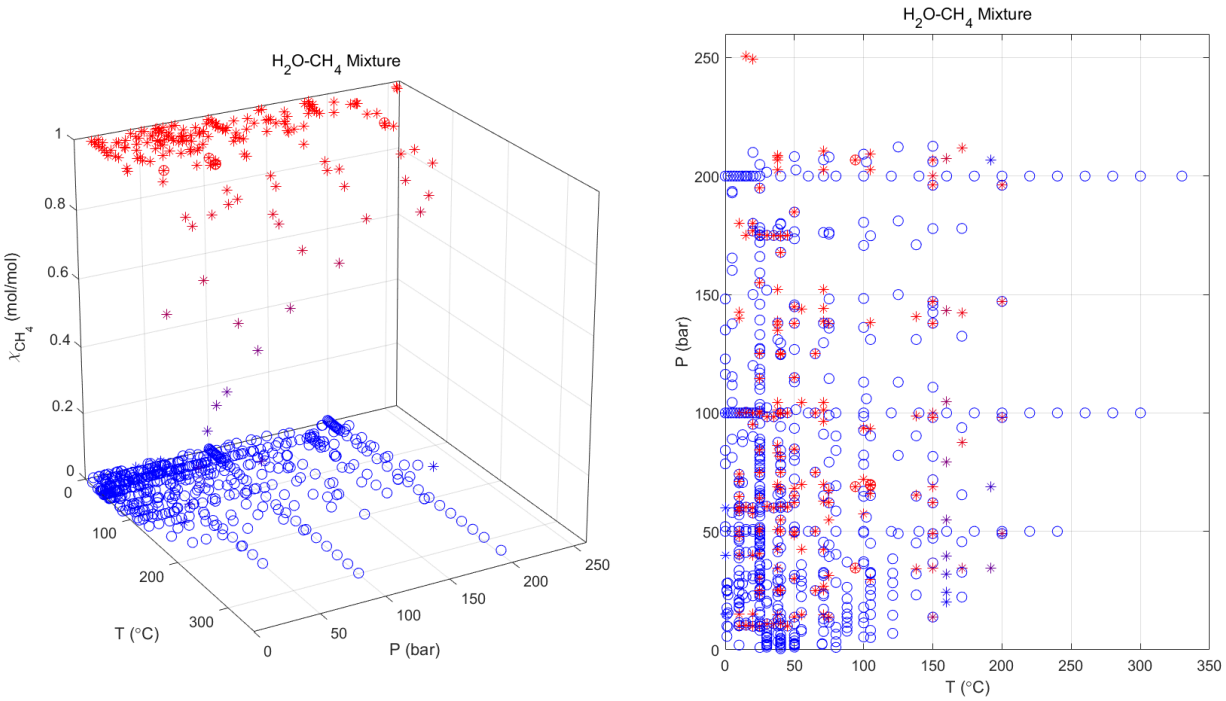

Frolich et al. [101] conducted the first study of methane's solubility in water under certain high-pressure conditions (20-142 bar). Since many studies, Michels et al. [102]; Culberson et al.[103]; Culberson and Mcketta [78]; Duffy et al. [79]; O'Sullivan and Smith[75]; Amirijafari and Campbell [74]; Price [85]; Cramer [89]; Yokoyama et al. [91]; Wang et al.[92] ; Gao et al. [93]; Lekvam and Bishnoi [94]; Song et al. [95]; Dhima et al.[96] ; Yang et al. [99]; Chapoy et al. [100]; Kiepe et al.[104]; Kim et al. [99]; Wang et al.[92]; Qin et al.[98] have been performed at intermediate and high pressures. Most of them are concentrated in the temperature and pressure ranges of 293.15 ÷ 444.15 K and 1÷200 bar.

Cramer [89] measured methane's solubility in water at temperatures ranging from 273.15 to 573.15 K, but their pressures were below 132 bar. Dhima et al. [96] reported four solubility data temperatures of 344.15 K up to 1000 bar. Price [72] 's experimental data covered wide ranges of temperature and pressure, but their results are not compatible with high pressures, and temperature above 523 K. Methane solubility in water at low temperature and high-pressure conditions are scarce. Cramer [89], Wang et al. [92], Lekvam and Bishnoi [94], Song et al. [95], Wang et al. [72], and Chapoy et al. [100] reported some data less than or equal to 293.15 K, but the pressures are limited to 100 bar.

Duan and Mao [63] reviewed the thermodynamic models reported to calculate CH_4 solubility in aqueous solutions for properties of the H_2O-CH_4 and H_2O-CH_4-NaCl systems from 273 to 523 K and from 1 to 2000 bar and confirmed that they work better than other models. However, due to the lack of experimental data, the methane solubility in pure water in the low-temperature range is still not well defined. The low-temperature methane solubility is very important for the accurate study of the kinetics of CH_4 hydrate formation.

Experimental methods and systems investigated for high-pressure fluid phase equilibria studies, including the solubility of gases in liquids, have been reviewed in few years [105], [106]. However, the lack of temperature and pressure range of gas solubility data are mainly due to temperature constraints and pressure tolerant capabilities of instruments and apparatus or the methodologies for accurately determining gas saturation concentrations in high-pressure conditions [42].

Figure 4. 9. 3D plotting of experimental data for the CH_4-H_2O system where the CH_4 solubility is in water.

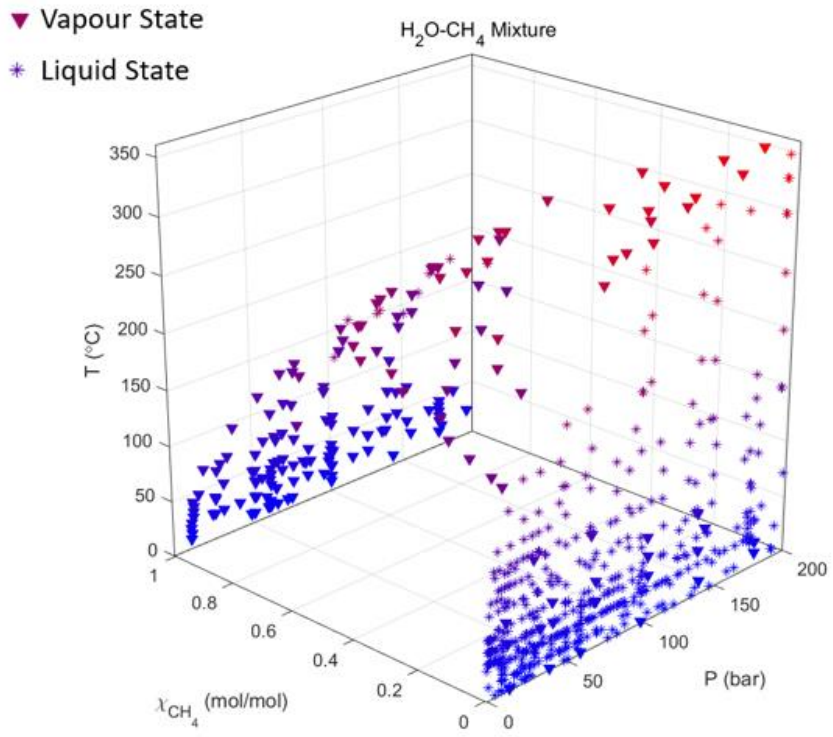

Before a graphical representation of the experimental data, they were grouped and compared to verify possible inconsistencies in the same conditions of temperature and pressure. From Table 4.5, the selection of references and previous works is highlighted.

Experimental measurements of methane solubility in water in the CH_4-H_2O binary systems were conducted at temperatures from 273.15 to 603.15 K and pressures from 1 to 1400 bar. Nine hundred fifty-two solubility data were obtained from 48 authors, and the results are from Figure 4.21 to Figure Fig.4.27. It is noted that a metastable equilibrium is present for the CH_4–H_2O fluid at low-temperature–high-pressure ranges.

All measured solubility data of methane in the water reported in the literature are compared. The graphs are generally isotherm data in which the solubility and pressures are plotted. All data are in good agreement with the different authors such as Amirijafari and Campbell [74], Culberson and Mcketta [78], Duan et al. [90], Ou et al. [107], Yokoyama et al. [91], Wang et al. [72], Dhima et al. [96], Kiepe et al. [104], Chapoy et al.[100], Kim et al.[99], and Qin et al.[98]. The maximum deviation between data is generally within 9 %.

Several authors have reported solubility data at 283.15 K, 298.15 K, 323.15 K, 344.15 K, 378.15 K, 433.15 K and 473.15 K. The data reported by Michels et al. [102] have slightly deviated from other data sets. The data of Yang et al. [99] and Culberson et al. [78] are more accurate. Culberson and Mcketta involved the agitation of methane and water in an equilibrium cell based on Culberson et al. [103] and repeated the 298.15 K isotherm determinations. The results at 298.15 K and 344.15 K are much more consistent.

Table 4. 5. Review of literature data presenting CH_4 solubility in water

T (°C)	*P(bar)*	*Number of data*	*Reference*
38-71	41-206	7	Amirijafari (1969)
10-25	11.5-103.6	14	Boettger (2009)
10-25	11.5-103	14	Boettger (2016)
105	69-687	13	Bukacek (1955)
25-100	1-180	34	Carroll et al. (1998)
10-45	10-350	36	Chapoy et al. (2003)
2-40	9.7-180	16	Chapoy et al. (2004)
25	36-174	6	Culberson et al. (1950)
25-171	22-177	43	Culberson et al. (1951)
38-121	3.5-37	45	Davis and Mcketta (1960)
71	200	1	Dhima (1998)
25-30	3.1-51	17	Duffy et al. (1961)
0-20	15-180	15	Folas et al. (2007)
10- 50	47-194.9	68	Frost (2014)
50-315	13-168	16	Gillespie et al. (1982)
40-100	4-92	28	Kiepe et al. (2003)
25	73-178.2	4	Kim et all. (2003)
1.2-12.5	5.67- 90.82	17	Lekvam et al. (1997)
10-30	20-201	20	Lu-Ku Wang et al. (2003)
25-150	40-206	37	Michels et al. (1997)
38-240	34-210	33	Olds et al. (1942)
30-50	1.15-6.4	18	Pereira(2010)
10-70	1.9-2.6	7	Reichl (1996)
25-100	23.5-93.5	12	Rigby and Praustnitz (1968)
150	100-200	2	Sanchez and de Meer (1978)
38-71	14.8 – 138.9	15	Sharma (1969)
150-350	49-196.1	18	Sultanov et al. (1971)
121-350	38.4-196.1	29	Sultanov et al. (1972)
152-210	36.7-198.3	14	Tabasinejad et al. (2011)
160-330	20.3-209.3	15	Tian et al. (2012)
160-360	20.3-223.7	19	Tian Y.Q. (2002)
38-105	25.3-202.7	14	Ugrozow (1996)
10 - 25	11.3-50.9	21	Wang et al. (1995)
0-25	23.3-193.5	38	Yang et al. (2001)
25	22.5-166	12	Yang et al. (2002)
38-205	34.5-206.8	21	Yarrison et al. (2006)
25-65	25-125	15	Yrarim-Agaev et al. (1985)
25-50	30-80	6	Yokoyama (1988)
51-102	56-206	5	Zheng et al. (1996)

Sullivan et al. [75]and Ou et al. [107] examined the most extensive temperature and pressure ranges. The data points of Ou et al. [107] are consistent with other studies, whereas the data of Sultanov et al. significantly deviate from others.
More than ten models have been reported to calculate CH_4 solubility in aqueous solutions. Among these, Duan and Mao's thermodynamic model has been confirmed more competitive and is widely used by researchers than others. From the data literature, the solubility data obtained from 313.15 K to 533.15 K are consistent with the thermodynamic study of Duan and Mao [63], but it shows more significant deviations below 313.15 K and above 533.15 K, especially for high pressures.

Experimental CH_4 solubility data in aqueous NaCl solution are not extensive like in water. A review of the CH_4 solubility data is in Table 4.13.

The data of Michels et al., Duffy et al., and O'Sullivan and Smith are not accurate due to the inaccurate pressure decline technique. Experimental data of Cramer, Ganjii et al., Blount and Price, and Stoessel and Byrne are more consistent with other data sets. They covered a wide T-P-m range (273.15- 573.15 K, 1-1200 bar and 0-6 mol/kg) for the CH_4-H_2O-NaCl.

CH_4 solubility data in an aqueous solution with another type of salts ($CaCl_2$ solutions) are limited. Stoessel and Byrne measured CH_4 solubility in different aqueous salt solutions at 298.15 K and pressure below 52 bar.

In this work, the total number of data used is 131.

Table 4. 6. Experimental data and model data used in this work for CH_4 in a NaCl solution

T (K)	P(bar)	NaCl Solution (m)	N	Reference
277.2–573.2	19–124	0.81–4.7	59	Stephen D. Cramer [89]
333.15	23-598	1-6	31	Ganji et al. [108]
372.15–513.15	75–1570	0–5.9	27	Blount and Price [109]
298.15	24.1–51.7	0–4.0	15	Stoessell and Byrne [110], [111]

A consistent number of useful data to show them graphically are at temperatures of 298.15, 333.15 and 374.15 K.

4.1.4 Complex mixture systems

In this section, the work briefly analyses the experimental data of two ternary systems: *CH_4-CO_2-H_2O* and *CO_2-H_2S-H_2O.*

Zhao et al. [112] proposed an accuracy model for the CH_4-CO_2- H_2O system over a wide temperature and pressure range. Typically, the gas &Oil reservoir's pressure and temperature are up to 600 bar and up to 523.15 K. From the Zhao model data, six ternary diagrams are created from 298.15 – 573.15 at the pressure of 600 bar (Figure 4.10).

Figure 4. 10. Phase envelop of the ternary CO_2-CH_4-H_2O system at elevated temperatures and 600 bar. The figure is composed of (a) is at 573.15 K, (b) is at 548.15 K, (c) is at 523.15 K, (d) at 473.15 K, (e) at 373.15 K and (f) at 298.15 K. Point A (20%CO_2, 30% CH_4, 50% H_2O) and point B (26.9% CO_2, 0.1% CH_4, 73% H_2O) in the (a). The images are taken from the following reference Zhao et al. [112].

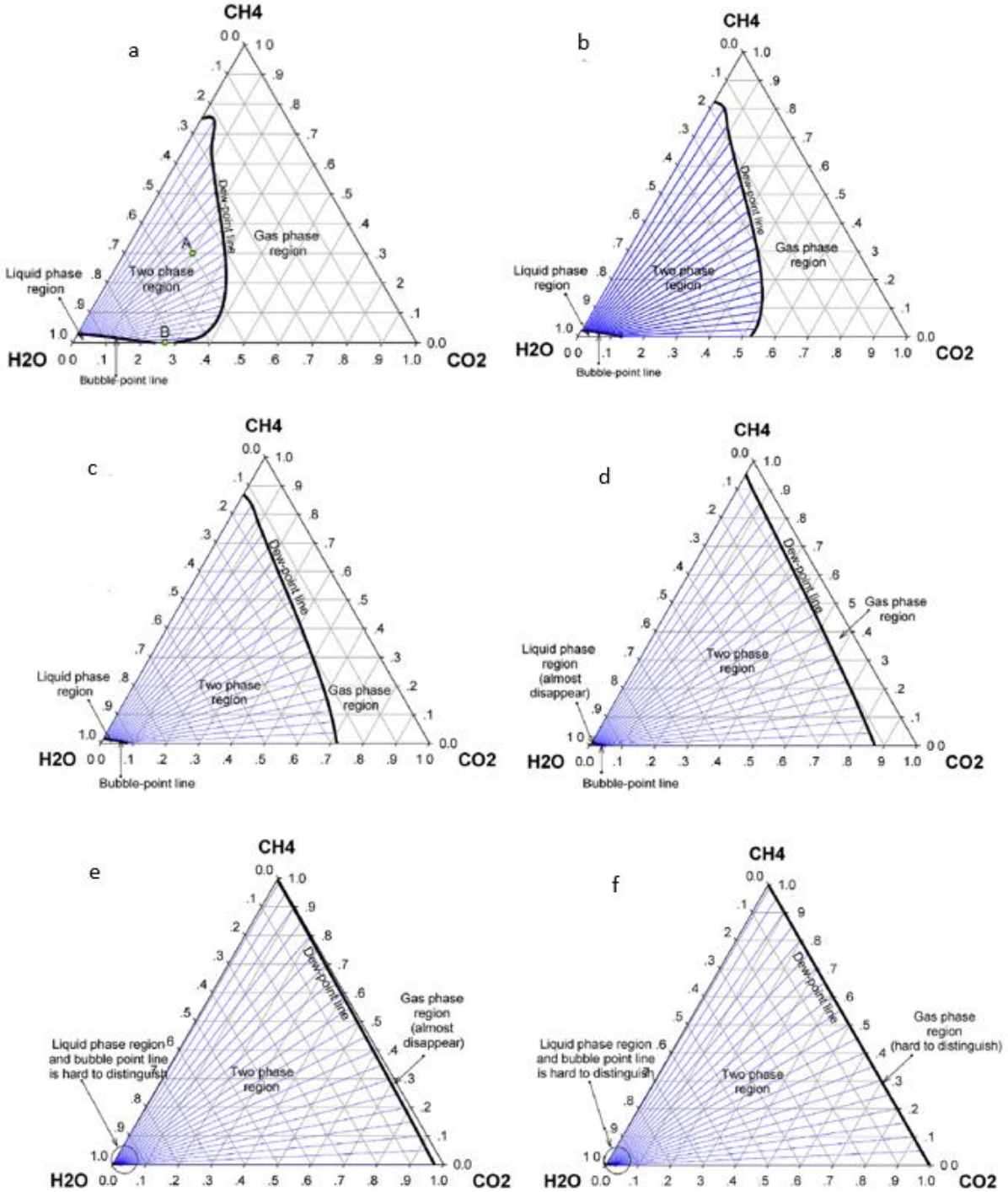

In Figure 4.10, it is created a ternary phase diagram for the CO_2-CH_4-H_2O at a fixed pressure of 60 bar and a temperature range up to 523 K. At low temperatures such as 298 K, the two-phase region prevails on the entire composition space. As temperature increases, the gas phase gradually appears but expands slowly. It is clearly that, at temperature reaches 473 K, a small portion of the single gas region exists.

As temperature increased from 473 to 523 K, the area of the single gas region in the ternary phase diagram expands rapidly, and the area of the single liquid region also becomes noticeable at 523 K. From 523 K, the area of two-phase region shrinks rapidly in response to increased temperature. At

573 K, a relatively small portion of the two-phase region left at the water corner on the composition triangle (a).

While, for the CO_2-H_2S-H_2O system, the use of CO_2 + H_2S mixtures means that particular attention must be paid to controlling the phases' nature in the experimental runs' temperature range. Indeed, considering the phase relationships in the system H_2O + CO_2 + H_2S, two main problems need to be addressed: avoiding the two-phase region of the CO_2 + H_2S system and the formation of gas hydrates. The current knowledge of thermodynamics of simple systems (CO_2+ H_2O and H_2S+H_2O) under high pressure is discussed in the recent literature and the preview sections as in de Hemptinne and Béhar [113]. Data on the solubility of the H_2S+CO_2 mixtures in water are scarce and available only at a pressure less than 60 bar for a non-aqueous low-density phase [113].

The published data on the CO_2 + H_2S system indicate a two-phase region at room temperature and up to more than 100°C. Therefore, the use of such a mixture requires accurate knowledge of the two-phase region to prevent vapour separation. Entering the two-phase region would result in phase separation, changes of fluid properties and overpressuring. Table 4.7 reports the values of both pure systems' triple and critical points, while the following figure shows these invariant points.

Table 4. 7. Invariant points for CO_2 and H_2S

	Triple Point			Critical point			
	T[°C]	*P [bar]*	*Reference*	*T[°C]*	*P [bar]*	ρ [$\frac{g}{cm^3}$]	*Reference*
CO_2	-56.61	5.3	Sonocinsky and Kurata (1959) [114]	31.06	73.825	0.4621	Span and Wagner (1996) [115]
H_2S	-84.29	0.024		100.38	90	0.3480	Bierlein and Kay (1953) [116]

The following figure presents a temperature–pressure projection of the liquid–vapour region. A continuous critical curve extends between the two critical points of the pure systems. An isopleth for an intermediate composition x(H_2S) = 0.5272 is also shown (the data are from Bierlein and Kay, 1953, and interpolated from Sobocinski and Kurata, 1959). The temperature and pressure conditions for three-phase (liquid-liquid–vapour) locus in the water + CO_2 + H_2S systems are very similar to the conditions for two-phase equilibrium curve in the same systems without any water, on the basis that this assumption has been verified experimentally for the two binaries water + CO_2 (Morrison, 1981 [117]) and water + H_2S (Carroll and Mather,1989 [118]).

Figure 4. 11. Temperature -pressure showing the liquid+vapour region in the CO_2+H_2S system—source: Savary et al. [119]. T (CO_2) is the triple point for CO_2, T (H_2S) is the triple point for H_2S, CP(CO_2) is the critical point of CO_2, and CP(H_2S) represents the critical point of H_2S. An isopleth with an intermediate composition (x(H_2S) = 0.5272) is also shown.

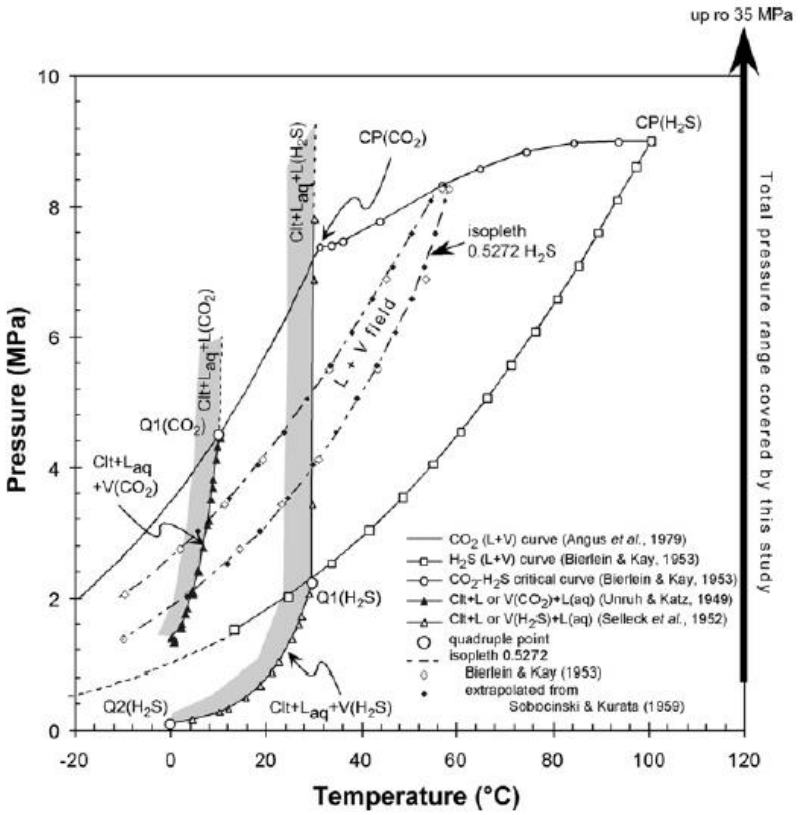

Table 4. 8. Experimental data for the CO_2-H_2S-H_2O systems.

Solution	*T (°C)*	*P(bar)*	*N*	*Reference*
CO_2-H_2S-H_2O	*20*	*1.01*	20	Golutvin et al. (1958)
CO_2-H_2S-H_2O	120	39- 350	26	Savery et al. (2012)

4.1.5 Enthalpy of mixing

This section highlights the techniques that have led to data collection from experiments carried out over the years. Also, in this case, it was possible to obtain the data of the three main geothermal components such as CO_2, H_2S and CH_4 in water and the presence of salts. However, unlike the experimental data on solubility, these are numerically lower but sufficient to compare them with the main models present in the Unisim process software and apply them to the case studies presented in Chapter 5.
At the beginner, a presentation of the calorimetric unit and procedure adopted by preview thermodynamic studies.

At the beginning of the solution's enthalpies investigation, there are two systems: CO_2+H_2O and CO_2-H_2O in brine. First, the binary system CO_2+H_2O is presented and follows the enthalpic data for the ternary system CO_2+NaCl(aq) with particular attention to the salting-out effect as a function of salt concentration, temperature and pressure.

A customized mixing flow unit was adapted to a Setaram BT 2.15D heat conduction differential calorimeter for experimental results. Thanks to the flow calorimetry were possible to study the dissolution of gases in aqueous solutions at high temperatures and pressures. Koschel et al.'s [52] methodology technique is the possibility to determine the enthalpy of the solution and the same

time, the gas solubility in a liquid phase. The mixing units were developed and adapted at the Blaise Pascal University, France. However, the dissolution data of gases in salt solutions were difficult to obtain due to much lower solubility.

This work makes it possible to present the data for carbon dioxide in water and aqueous NaCl (1 and 3 molal) solutions at two temperatures (323 and 373 K) and pressure up to 200 bar.

A mixing flow unit adapted to a heat conduction differential calorimeter for the carbon dioxide dissolution in water or aqueous NaCl solutions (Figure 4.12). The two fluids, gas and solution, enter the mixing unit supplied from two high-pressure pumps. The typical gas and aqueous phase flow rates range from 0.005 to 0.1 and 0.2 to 0.7 ml/min, respectively.

Figure 4. 12. Calorimeter and mixing unit including the flow lines, the preheaters, the mixing cell and the pressure control system. At the right, the mixing unit. Source [52].

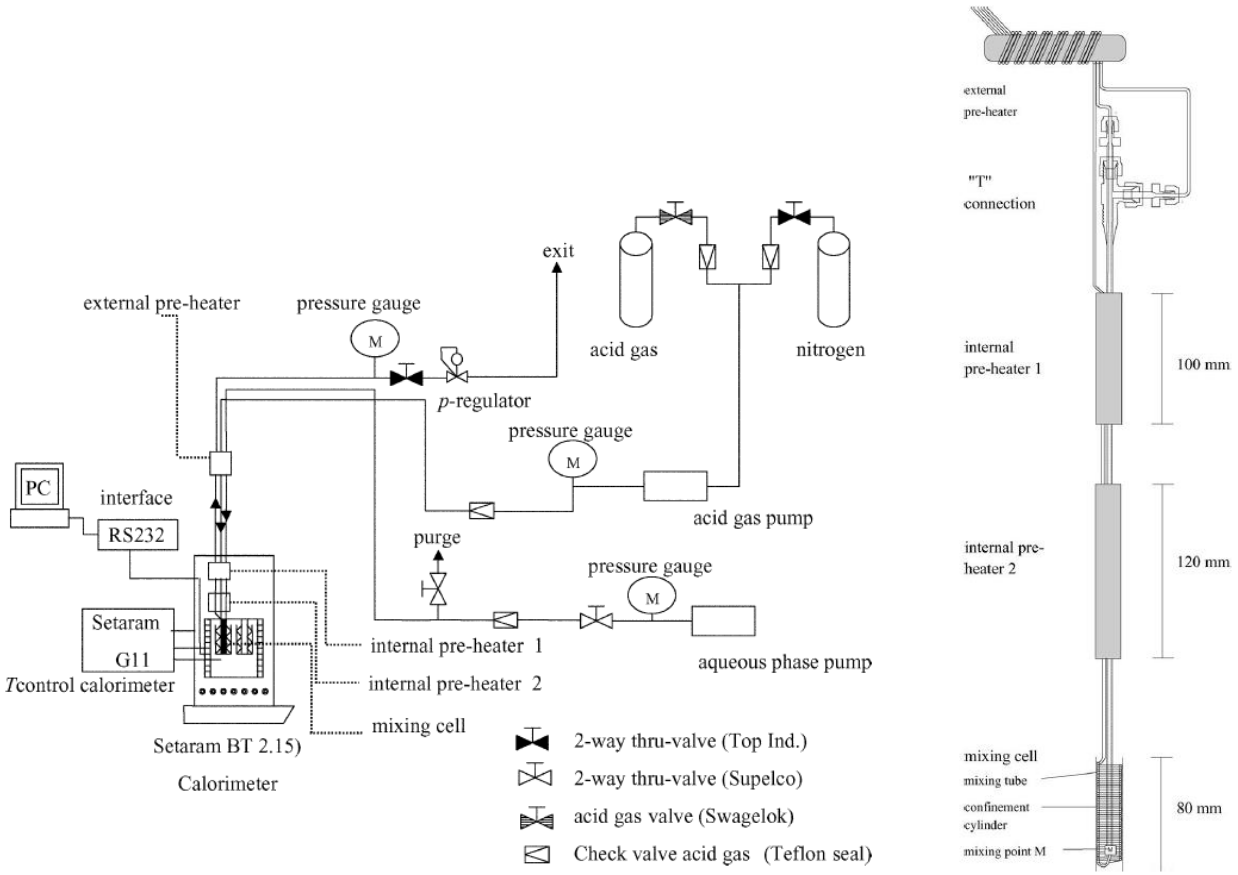

The experiments are carried out at constant pressure; the unit's maximum working pressure is about 400 bar. The system pressure is maintained constant to 0.2 bar. Three electronic Keller pressure gauges measure the pressure, and they are located at the outlets of the acid gas and aqueous phase pumps and between the mixing cell and the backpressure regulator. The experiments are carried out at constant temperature; the entering fluids reach the working temperature before entering the mixing cell using three preheaters, one external to the calorimeter and two inside. The temperature of the calorimeter is set up and controlled within 0.01K using an electronic control device. The excess CO_2 is scrubbed from the line at the backpressure regulator's outlet when the solution is saturated, using an alkaline solution. The interesting part of the calorimetric system for the calculation of enthalpy of mixing is the mixing unit. The arriving fluid temperature is controlled, and the mixing fluids inside the cell have to be total, and all heat is transmitted from the cell to the thermopiles. The mixing represented in Figure 4.12 was designed and used in the laboratory for the operation described by Mathonat et al. [142]. For the carbon dioxide in water and a salt mixture, the enthalpy of mixing ΔH_{mix} is defined as a heat per one mole of salt-free solution (water and gas). This enthalpy is directly obtained from the thermopile signal S

(μV) of the calorimeter and the molar flow rate $\dot{n}$ (mol/s) of the solution.

Before measuring the thermopile signal S_M (μV) during the mixing process, a baseline signal S_{BL} (μV) is recorded with only the aqueous phase flowing through the calorimeter. The signal starts with zero when the fluid enters for adjusting the thermoregulation. Then, the signal is recorded 20 min before the gas injection. Due to the gas dissolution, the heat effect corresponds to a thermopile signal SM ranging from 100 to 800 μV and has stability between 1 and 10 μV. This signal is recorded for at least 30 min. The enthalpy of mixing ΔH_{mix} (J/mol) is calculated as the following equation:

$$\Delta H_{mix} = \frac{(S_M - S_{BL})}{K\dot{n}} \tag{4.1}$$

It is the ratio of the difference in the thermopile signals and the molar flow rate. The molar flow rate derives from the volumic pump flow rates, the densities and the salt concentration. K (μV m/W) is the thermophile sensitivity that converts the thermophile signal to heat power.

The first application of this experimental methodology is applied to carbon dioxide in pure water and salt. For carbon dioxide, the fugacities were obtained using the equations 4.7-4.9, and the CO2-rich vapour phase was obtained from a literature review [120]. The fugacities results are used to find the value of the reference Henry's constant, H^*_{CO2}, which is satisfied at each temperature range:

$$\frac{f_{CO2}}{y_{CO2,w}} = H^{\circ}_{CO2} exp\left[\frac{\bar{v}^{\infty}_{CO2}(p - p^0_w)}{RT}\right] = H_{CO2} \tag{4.2}$$

then

$$ln\left(\frac{f_{CO2}}{y_{CO2,w}}\right) = lnH^*_{CO2} + \frac{\bar{v}^{\infty}_{CO2}}{RT}(p) = lnH^{\circ}_{CO2} + \frac{\bar{v}^{\infty}_{CO2}}{RT}\ (p - p^0_w) \tag{4.3}$$

where

$$lnH^*_{CO2} = lnH^{\circ}_{CO2} - \frac{\bar{v}^{\infty}_{CO2}}{RT}\ (p - p^0_w) \tag{4.4}$$

Equation (4.4) is known as the Krichevsky-Kasarnousky equation[121], [122]. Thanks to the collection and analysis of the various experimental data relative to CO_2 solubility in water, the fugacity values (f_{CO2}), Henry's coefficient (H^*_{CO2}), and partial molar volume of carbon dioxide at infinite dilution ($\bar{v}^{\infty}_{CO2}$), it was possible to define the following empirical equations:

$$H^*_{CO2} = -5032.99 + 30.74113 \cdot T - 0.052667 \cdot T^2 + 2.630218 \cdot 10^{-5} T^3 \tag{4.5}$$

$$\bar{v}^{\infty}_{CO2} = 1799.36 - 17.8218 \cdot T + 0.0659297 \cdot T^2 - 1.05786 \cdot 10^{-4} \cdot T^3 + \\ +6.200275 \cdot 10^{-8} \cdot T^4 \tag{4.6}$$

These equations are valid for temperature ranges 298 to 523 K and pressure up to 200 bar. The fugacity model calculated presents a discontinuity from 71 bar to 200 bar for the temperature range of 293.15 - 338.15 K. The number of experimental data about the enthalpy of mixing is very low compared to the solubility data. However, the data obtained by D. Koschel et al. [52] are sufficient to enhance comparison with the results obtained by the three thermodynamic methods of OLI Package and the models implemented in software (Unisim) licenced by the University.

The experimental errors of the enthalpy of mixing are determined as a statistical estimate from the expected error in K, uncertainty in the molar flow rate and the heat power. D. Koschel et al. [52] showed that the molar flow rate's uncertainty is smaller than 1.5%, the error connected with the heat power is estimated to be 2 %, while the uncertainty in the difference between S_M and S_{BL} is between 1 and 3%.
All experiments are carried out at a constant temperature and pressure, and the enthalpies of mixing ΔH_{mix} are determined at different gas-solvent flow rate ratios.
In the following graphs (Figure 4.13, Figure 4.14, Figure 4.15, Figure 4.16), it is possible to distinguish the sections before and after a gas's saturation of aqueous solution. In the beginning,

the gas is completely absorbed by the solution. Fron the figures, the absolute value of the enthalpy of mixing increases approximately linearly with x_{CO2} . Then, ΔH_{mix} remains constant when the solution does not absorb any more gas. After saturation, an additional heat effect related to water's dissolution (vaporization) in the gaseous phase can be observed. This effect, visible in particular at the higher temperature, is evinced by a continuous decrease of $|\Delta H_{mix}|$.
The temperatures used in this section are 308.15 K, 323.15 K, 373.15 K and 498.15 K.

Figure 4. 13. Enthalpies of mixing (ΔHmix) CO_2 in water from 308.15K to 323.15 K and from 20 to 200 bar were obtained by experimental data with a calorimeter.

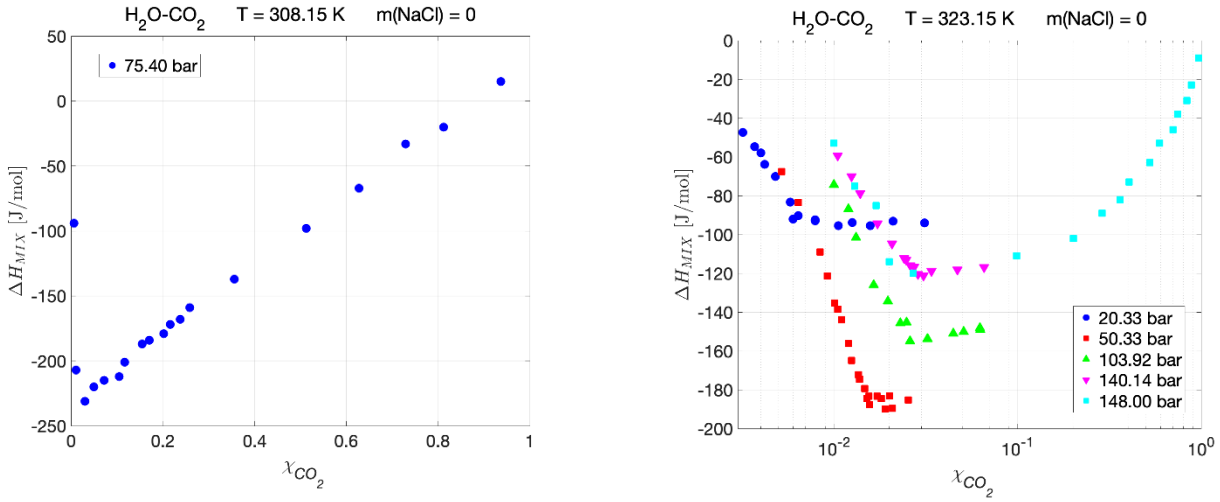

Figure 4. 14. Enthalpies of mixing (ΔH_{mix}) CO_2 in water from 373.15 K and 523.15 and from 20 to 200 bar were obtained by experimental data with a calorimeter.

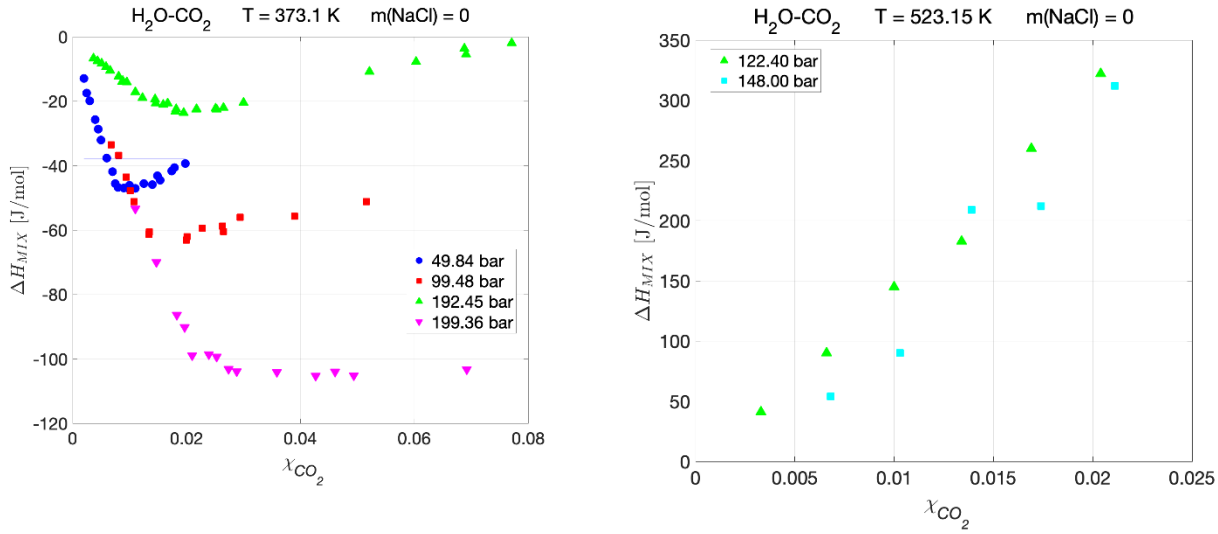

Figure 4. 15. Enthalpies of mixing (ΔH_{mix}) CO_2 in aqueous NaCl solutions (1.0 and 3.0 m) at 323.15 K and from 50 to 200 bar.

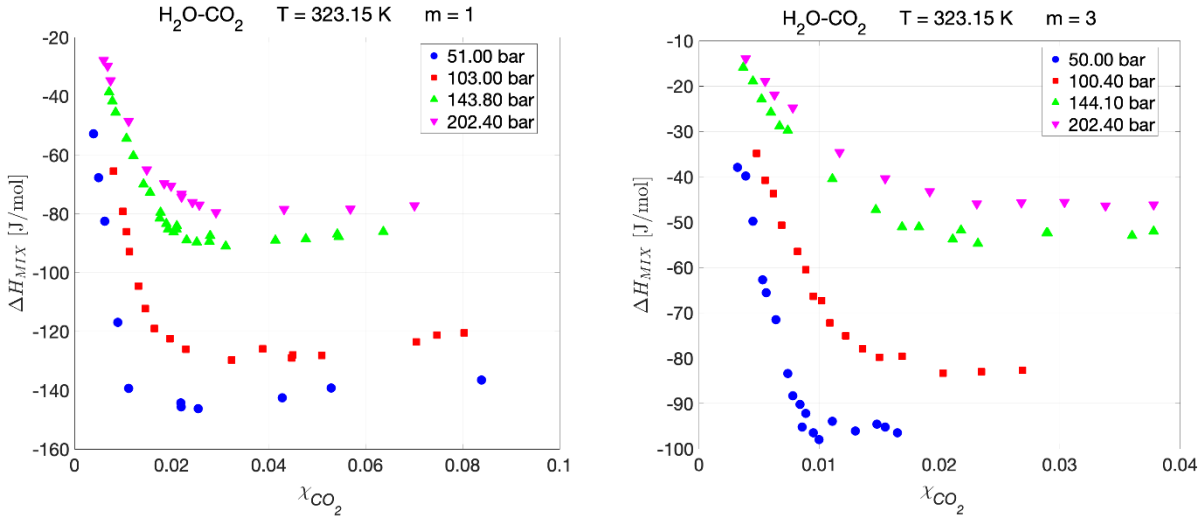

The experiments are carried out at a constant temperature and pressure, and the enthalpies of mixing ΔH_{mix} are determined at different gas-solvent flow rate ratios. The graphs are obtained from the experimental data collected in tables 1 and 2 of D. Koschel et al. [52]. It is possible to distinguish the sections before and after saturation of aqueous solution by a gas. First, the gas is completely absorbed by the solution. Then, the absolute value of the enthalpy of mixing increases approximately linearly with x_{CO2}. Second, ΔH_{mix} remains constant when the solution does not absorb any more gas. After saturation, an additional heat effect related to water's dissolution (vaporization) in the gaseous phase can be observed. This effect, apparent especially at a higher temperature, is reflected by a continuous decrease of $|\Delta H_{mix}|$.

Figure 4. 16. Enthalpies of mixing (ΔH_{mix}) CO_2 in aqueous NaCl solutions (1.0 and 3.0 m) at 373.15 K and from 50 to 200 bar.

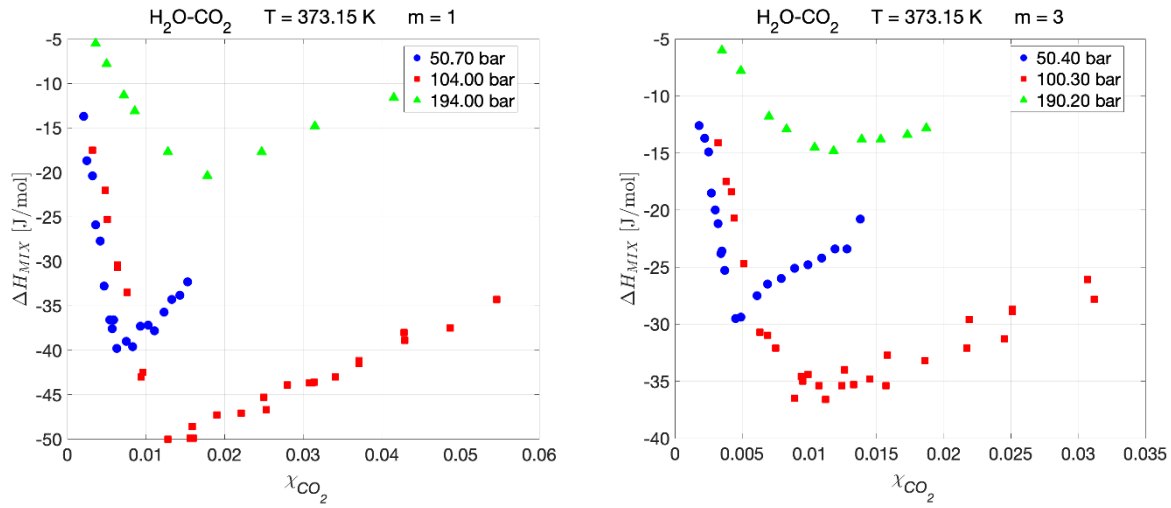

The CO_2 dissolution in water or an aqueous NaCl solution is *exothermic*. Thus, salt influences the development of hydrogen bonds in the liquid water-rich phase just right before the start of hydrate formation. Also, the salinity influence the solubility of CO_2 in the liquid water-rich phase. Figure 4.17 shows the CO_2/water molar ratio for the different salinities in which the grey area represents the standard deviation. The solubility of CO_2 increases with decreasing temperature for every salt concentration. So, the dissolution process of a gas in water is almost always exothermic and thus increases with decreasing temperature. As a result, the amount of dissolved gas becomes smaller with more salt dissolved. This effect is known as salting out [123]. Salt is, like water, polar, whereas

most gases, including CO_2, are nonpolar. In a dissolution process, water molecules build a hydration shell around the dissolved component. Polar water molecules are more attracted to polar salt ions than to nonpolar CO_2 molecules. Thus, fewer water molecules are available to form a hydration shell around CO_2, resulting in a reduced solubility of CO_2.

Figure 4. 17. CO_2 concentrations in water versus temperature for different salt concentrations. Source: [124]

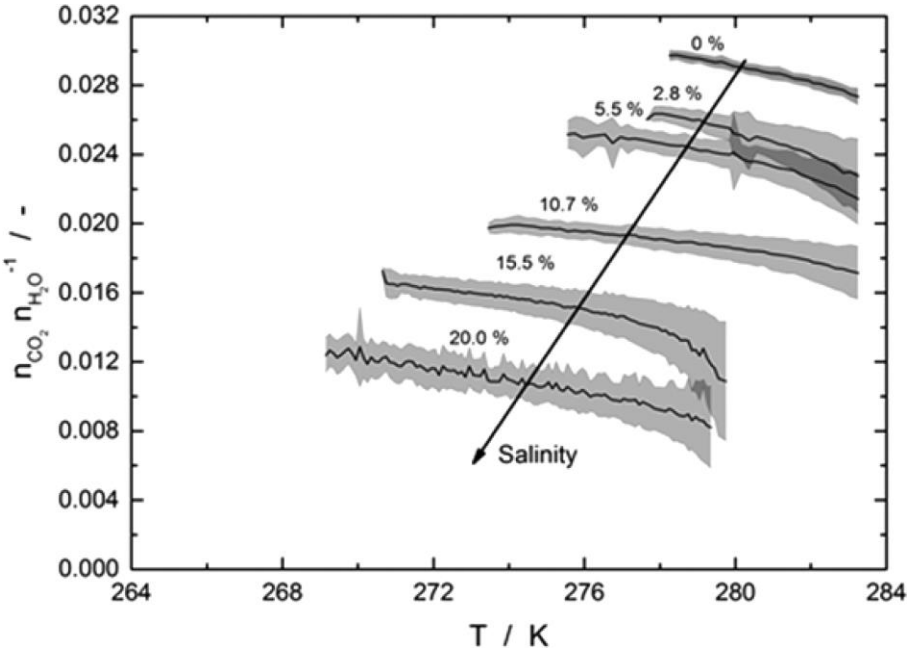

While the water dissolution in the carbon dioxide phase is *endothermic*, as seen in Figure 4.13-4.16, the solubility limit is determined graphically from the intersection curves fitting the data before and after saturation. Furthermore, the concentration dependence of ΔH_{mix} is close to linear before reaching the saturation domain, and the slope's determination is thus straightforward (Table 4.9 and Table 4.10).

Table 4. 9. Enthalpies of mixing (ΔH_{mix}) of CO_2 in the water at the experimental conditions. Experimental data referred to [52], [125] and [126].

Temperature	Temperature	Pressure	CO_2	ΔH mix	Reference
[K]	[C]	[bar]	[mol/mol]	[J/mol]	
308.15	35	75.4	0.022	-220.89	Perez et al.[125]
323.15	50	20.33	0.007	-90.01	Koschel et al.[52]
323.15	50	50.33	0.015	-177.17	Koschel et al.[52]
323.15	50	103.92	0.021	-139.98	Koschel et al.[52]
323.15	50	140.14	0.022	-108.25	Koschel et al.[52]
323.15	50	148	0.022	-110.78	Perez et al.[125]
373.1	100	49.84	0.009	-45.74	Koschel et al.[52]
373.1	100	99.48	0.015	-59.58	Koschel et al.[52]
373.1	100	192.45	0.021	-22.1	Koschel et al.[52]
373.1	100	199.36	0.021	-98.9	Koschel et al.[52]
523.15	250	122.4	0.016	218.2	Chen et al.[126]
523.15	250	148	0.020	282.27	Chen et al.[126]

Table 4. 10. Enthalpies of mixing (ΔH_{mix}) of CO_2 in aqueous NaCl solutions (1.0 and 3,0 m) at the experimental conditions. Experimental data are referred to [52].

Temperature	Temperature	Pressure	salt NaCl	CO_2	ΔH mix
[K]	[°C]	[bar]	[mol/kg]	[mol/mol]	(J/mol)
323.15	50	51	1	0.0112	-139.4
323.15	50	103	1	0.0165	-119
323.15	50	143.8	1	0.0176	-81.5
323.15	50	202.4	1	0.0185	-69.7
323.15	50	50	3	0.0111	-93.9
323.15	50	100.4	3	0.0109	-72.2
323.15	50	144.1	3	0.0112	-40.5
323.15	50	202.4	3	0.0155	-40.4
373.15	100	50.7	1	0.0063	-39.8
373.15	100	104	1	0.0128	-50
373.15	100	194	1	0.0178	-20.4
373.15	100	50.4	3	0.0049	-29.4
373.15	100	100.3	3	0.0075	-32.1
373.15	100	190.2	3	0.0118	-14.8

Tables 4.9 and 4.10 show the enthalpies of mixing of CO_2 in water and aqueous NaCl solutions of 1 and 3 molalities. They are measured from 308.15 K to 573.15 K and constant pressures from 20 to 200 bar. The experimental data obtained in Tables 4.9 and 4.10 denote that the enthalpy of mixing increases with the gas molar fraction X_{CO2} in the region of total gas dissolution. The solubility of carbon dioxide in an aqueous NaCl solution is expressed as the molar fraction of CO_2 in a salt-free solution, thus $x_{CO2}+x_{H2O}=1$.

From the previous graphs on experimental data, it can be seen that the enthalpy of mixing increases linearly with the gas molar fraction x_{CO2} in the region of total gas dissolution. A slight curvature is observed near the CO_2 solubility limit, more evident at lower temperature levels, i.e. at 323.15 K . The effect can be described through the mixing kinetics. The kinetics of mixing is here slower, and the thermal effect detected does not correspond to a complete dissolution of CO_2. At 323.15 K, the saturated region corresponds to a plateau; the point of intersection with the line's extrapolation in the unsaturated region determines the solubility limit of CO_2 in the solution. The data are defined through linear regression, which is used to define the dependence of Hmix on concentration in both unsaturated and saturated regions. However, a straight line does not represent the unsaturated region correctly at 373.15 K and at most pressure studied (200 bar). The experimental data reported by Koschel et al.[52] show small errors of less than 5%.

Regarding the systems H_2S in water and H_2S in brine solutions, the same principle as for CO_2 applies to the hydrogen sulfide dissolution in the salt solutions.
The two fluids, H_2S and water, enter the mixing unit supplied from the two high-pressure syringe pumps, maintaining stable flow rates. Typically, the flow rates of H_2S and aqueous phases range from 0.005 to 0.8 mL/min and from 0.2 to 0.7 mL/min, respectively. The flow line is made out of tubings of 1.6 mm o.d. In addition, a specially adapted set of valves and check valves was added to ensure the cleaning or replacement of a part of the mixing flow unit in safe conditions.

The whole transporting system (tubing and valves) is kept at a constant temperature near 313 K to prevent the formation of hydrogen sulfide hydrates that block the tubes. Furthermore, the experiments are carried out at a constant, stable pressure thanks to a back pressure regulator placed at the end of the flow line. The hydrogen sulfide dissolves in the aqueous phase in a mixing cell that is the most substantial part of the mixing unit. The fluids reach the working temperature before entering the mixing cell using a system of preheaters, one external to the calorimeter and two inside it. The temperature of the calorimeter is set up and controlled. The excess H_2S is scrubbed from the line at the backpressure regulator's outlet when the solution is saturated, using an alkaline solution. The mixing unit is the critical part of the calorimetric system, where the heat

is transmitted between the cell and the calorimetric block via the thermopiles. A mixing unit consists of the preheating system (external and internal preheaters), the tubes transporting the fluids, the mixing piece, where the fluids come into contact, and the confinement cylinder housing the cell's tubes where the fluids mix. Its material is Hastelloy C22 that is better for H_2S corrosion resistance during the experiments. It uses two parallel tubes [143].

The two fluids are introduced in the tubes of 1.6 mm o.d. (1/16 in.) and come into contact at the bottom of the cell, where they start to mix (mixing point M). The quantitative mixing then occurs in the 2.8 m long coiled Hastelloy tubing of 1.6 mm o.d. This tube is in good thermal contact with the inner wall of a confinement cylinder (18.7 mm i.d., 80 mm height), tightly fitting in the well of the calorimetric block. The experiments are carried out in an isobaric mode. The preheaters are countercurrent heat exchangers consisting of metallic copper cylinders with the tubing coiled on its outer surface (external preheater) or tightly fitted inside the grooves (internal preheaters). The external preheater is 20 mm o.d., and the wired tubing length is approximately 2 m. The internal preheaters are 16 mm o.d. and have a length of 80 and 120 mm. The preheaters are thermoregulated by proportional-integral-derivative (PID) controllers connected with the platinum resistance elements and heating cartridges. The temperatures of the external and the upper internal preheaters are maintained constant to 0.1 K.

The enthalpy of mixing ΔH_{mix} is a heat per 1 mol of solution (water and H_2S). It is related to the thermophile signal S(μV) of the calorimeter and the molar flow rate $\dot{n}(\frac{mol}{s})$ of the solution. The thermophile signal is SM, and the baseline signal is SBL. The heat effect due to the dissolution of hydrogen sulfide, corresponding to a thermopile signal SM, is recorded for at least 30 min.

The enthalpy of mixing ΔHmix (J/mol) is calculated as the ratio of the difference in the thermopile signals and the molar flow rate as Equation 4.1.

K ($\mu V \cdot mW^{-1}$) is thermopile sensitivity and is obtained by a chemical calibration using ethanol + water [127] with less than 5% error. The experimental error of the enthalpy of mixing $(\partial \Delta H_{mix})$ is a statistical estimate from the uncertainties in K, the molar flow rate, and the heat power, and its range are between 0.0002 and 0.00030. The maximum error range is around at high pressure.

The experiments are carried out at constant temperature and pressure, and the enthalpies of mixing ΔH_{mix} are determined at different H_2S-water flow rate ratios. The enthalpy of the solution ΔH_{sol} the heat per 1 mol of gaseous solute and the gas solubility is determined simultaneously from the plots of the enthalpy of mixing versus the gas molar fraction x_{H2S} in water, as shown in Figure 4.18. The data shown below are updated to the latest experimental data by Koshel et al.[128], [67].

The values of the enthalpies of mixing per 1 mol of solution as a function of the molar fraction of hydrogen sulfide are represented graphically in Figure 4.18. The enthalpy of mixing is exothermic for the gaseous solute, decreasing with the increasing molar fraction x_{H2S} in the region of the total gas dissolution, which leads to a negative value of ΔH_{sol}. Thus, when the solution is saturated, the value of ΔH_{mix} is close to constant. Under all other conditions, the enthalpy of mixing is endothermic and increasing approximately linearly with concentration before saturation. Since the slope of this dependence increases with pressure, ΔH_{sol} is positive and increasing with pressure. It is apparent from Figure 4.18 that at the two upper temperatures, ΔH_{mix} also increases in the two phase region where the solution is saturated by the solute. This is due to the increasing dissolution of water in the H_2S phase.

Figure 4. 18. Enthalpies of mixing H_2S in water at 323.15 K and pressures 16,76 and 17.92 bar; at 353.15 K and pressures 140.2, 191.6, 254.5 and 308.6 bar; and at 393.15 K and pressures 132.24, 193.43, 248 .21 and 294.89 bar. The coloured symbols identified the pressures mixture. Data referred to Koschel et al. [67] and [129]

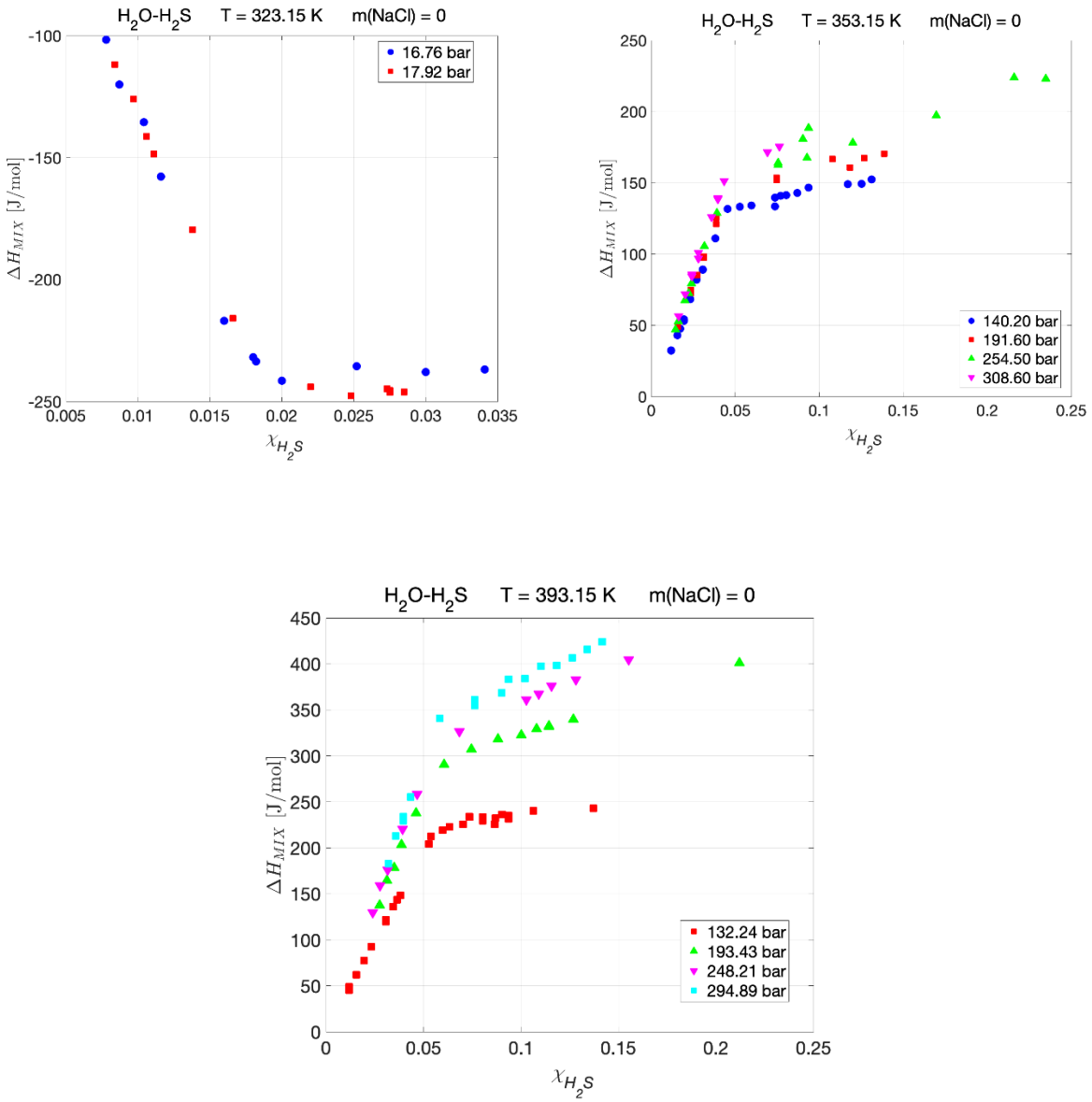

The graphs make it possible to distinguish the sections before and after saturation of aqueous solution by H_2S. First, hydrogen sulfide is entirely absorbed by the solution and therefore, the absolute value of the enthalpy of mixing increases approximately linearly with x_{H2S}.

From the analyzes of the experimental data, the following considerations are possible. The ΔH_{mix} changes very slowly when the solution is saturated with solute with a thermal effect due to water vaporization in the H_2S phase. This effect occurs at high temperatures, for a continuous increase of ΔH_{mix}. Dissolution of H_2S in water is exothermic when H_2S is gaseous while liquid or supercritical, while water dissolution into H_2S is always endothermic.

The limiting solubility is determined graphically by the intersection of the curves that fit the data before and after saturation. Enthalpy of solution ΔH_{sol} is defined precisely as the difference between the enthalpies of an infinitely diluted and, at the same time, pure solute temperature and pressure. Thus, it is possible to highlight the saturation conditions at experimental temperature and pressure (Table 4.11).

Table 4. 11. The solubility of H_2S in water obtained from experimental data Koschel et al. [67], Lee and Mather [130] and Xia et al.[131] at 323.1,353.1 and 393.1 K from 15 to 305 bar.

Temperature [K]	Temperature [°C]	Pressure [bar]	x_{H2S}	References
323	50	16.76	0.0170	Koschel et al.
323	50	16.80	0.0175	Lee and Mather
323	50	17.2	0.0175	Koschel et al.
323	50	17.2	0.0180	Xia et al.
323	50	17.92	0.0182	Koschel et al.
323	50	18.4	0.0187	Koschel et al.
323	50	18.4	0.0192	Xia et al.
323	50	18.5	0.0188	Lee and Mather
323	50	78.3	0.0388	Koschel et al.
323	50	133.6	0.0390	Koschel et al.
353	80	140.2	0.0438	Koschel et al.
353	80	191.6	0.0443	Koschel et al.
353	80	254.5	0.0460	Koschel et al.
353	80	308.6	0.0471	Koschel et al.
393	120	132.24	0.0554	Koschel et al.
393	120	135.8	0.0570	Koschel et al.
393	120	193.43	0.0510	Koschel et al.
393	120	198.60	0.0570	Koschel et al.
393	120	248.21	0.0530	Koschel et al.
393	120	254.80	0.0585	Koschel et al.
393	120	294.89	0.0545	Koschel et al.
393	120	302.70	0.0603	Koschel et al.

For the ternary system H_2S-H_2S-NaCl, the ΔH_{mix} is calculated as Equation 4.16, and the reference study is provided by Ott et al.[127]. In the experimental data, the estimated errors are around 1.5%. The experiments are carried out at a constant temperature, and pressure and heat of mixing are determined at different concentrations resulting from the flow rate ratios change of H_2S versus aqueous solution. Figure 4.19 is the plot of ΔH_{mix} versus the molar fraction x_{H2S} in the acqueous solution.

Figure 4. 19. Enthalpies of mixing of H_2S and aqueous NaCl solutions at a temperature of 323.1 K and pressures of 17.60, 78.90 and 131.80 bar; at a temperature of 353 K and pressures of 140, 199.20, 260 and 308.60 bar; at the temperature of 393 K and pressures of 135.10 and 191.80 bar. The experimental data referred to Koschel et al. [128]

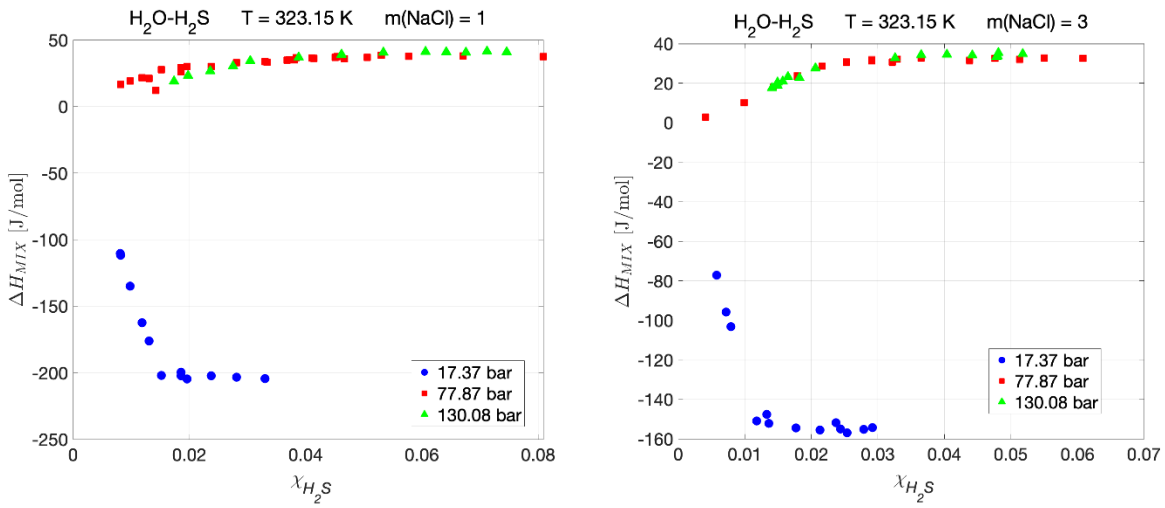

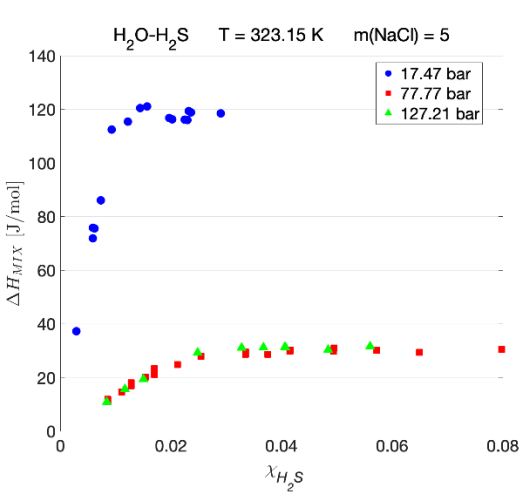

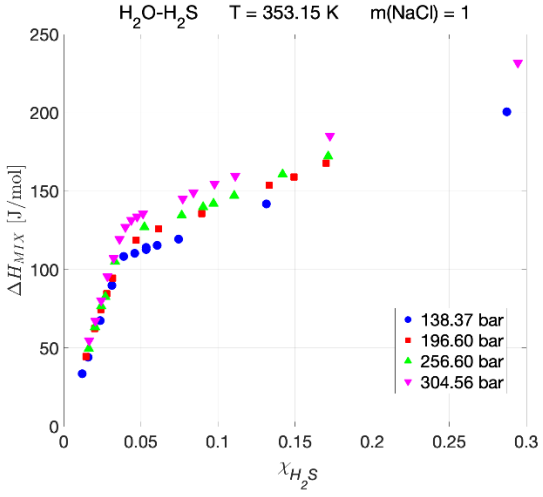

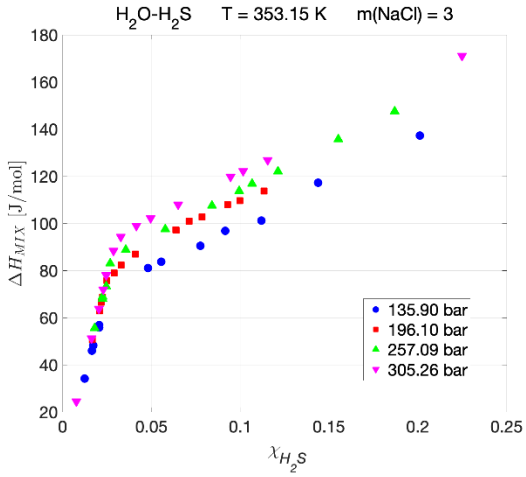

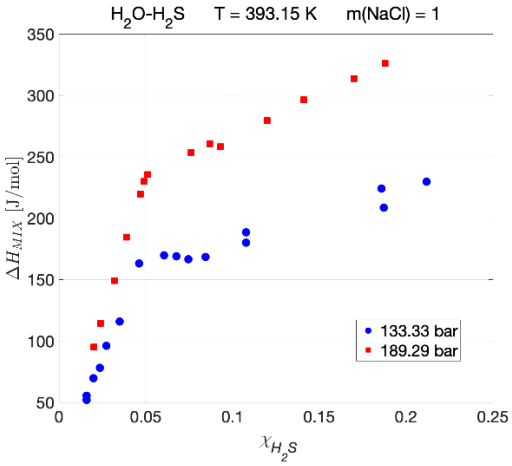

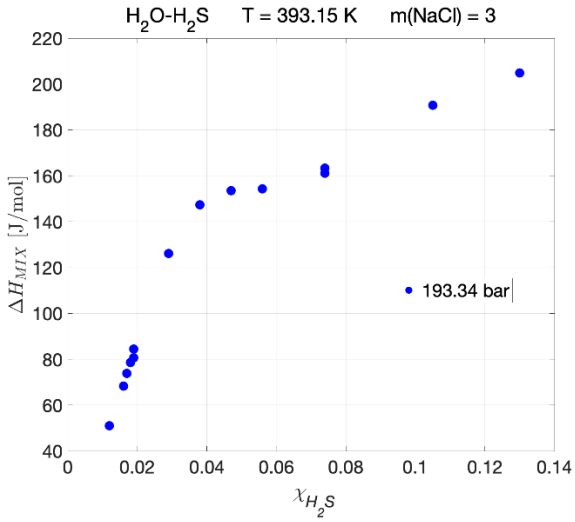

Also, in these graphs, it is possible to distinguish the sections before and after saturation of aqueous solution by H_2S. At the low temperature, the heat of mixing is constant after saturation, but it increases at the high temperature (353 K and 393 K) due to the water's dissolution in the insoluble H_2S. At the conditions of H_2S gas, the dissolution of gas H_2S in the aqueous phase is exothermic; such is shown in Table 4.12 with the saturation pressure $p_{sat}(H_2S)$. The dissolution process is endothermic at the medium and highest temperature when H2S is liquid and supercritical ($T_c = 373.4\ K$ and $p_c = 89.4\ bar$). The solubility limit is determined from the intersection of the curved fitted in Figure 4.12, before and after saturation. In Table 4.12 are the solubilities of the ternary

mixture. The average errors for the H_2S experimental data in the enthalpy of solutions are between 3% and 6%.

Table 4. 12. Experimental data [6], [32] for the solubility x_{H2S} and mixing enthalpy in water and aqueous NaCl solutions were obtained from the calorimetric data with the margins of uncertainty.

Temperature [K]	Pressure [bar]	Salt molality [mol/kg]	x_{H2S} [mol/mol]	ΔH_{mix} [J/mol]	Δx_{H2S} [%]	$\Delta\Delta H_{mix}$ [%]
323	17.2	0	0.0175	-228.08	59	4.4
323	18.4	0	0.0187	-226.83	6	5.3
323	78.3	0	0.0388	42.28	7	1.3
323	136	0	0.039	44.37	7	1.1
323	17.6	1	0.0148	-197.10	5	3
323	78.9	1	0.0333	33.35	6	0.8
323	131.8	1	0.0344	35.47	5	0.6
323	17.7	3	0.0119	-151	5	4.9
323	78.9	3	0.0231	29.47	7	0.6
323	133.2	3	0.025	29.47	7	0.7
323	17.7	5	0.0097	112.9	6	2.1
323	78.8	5	0.0217	25.17	7	0.6
323	128.9	5	0.0231	27.58	5	0.7
353	140.2	0	0.0438	126.9	5	2.4
353	191.6	0	0.0443	129.96	5	3.2
353	254.5	0	0.046	135.11	5	2.9
353	308.6	0	0.0471	163.14	4	3.3
353	140.2	1	0.0375	105.25	6	2.4
353	199.2	1	0.0381	111.44	5	2.5
353	260	1	0.0385	111.09	6	3.1
353	308.6	1	0.0394	125.64	5	2.5
353	137.7	3	0.026	60.77	6	1.6
353	198.7	3	0.0265	76.94	6	2
353	260.5	3	0.0282	83.93	5	2.1
353	309.3	3	0.03	90.27	6	1.9
393	135.8	0	0.0554	186.15	6	4.5
393	198.6	0	0.057	255.44	7	9.5
393	254.8	0	0.0585	277.89	6	8.2
393	302.7	0	0.0603	319.02	6	10
393	135.1	1	0.0462	163.1	8	4.4
393	191.8	1	0.05	232.75	6	3.6
393	195.9	3	0.0326	134.58	6	2.3

While for the H_2O-CH_4 and H_2O-CH_4-NaCl systems, this work presents a study from 273.15 to 573.15 K, from 1 to 2000 bar and from 0 to 6 mol/kg of NaCl.
This investigation illustrates how the mixing enthalpy was calculated. However, the experimental enthalpy data on methane to compare the thermodynamic models is currently limited compared to the other two chemical species. In addition, there is a lack of data on methane, water and salt.

The data illustrated essentially concerns the excess enthalpy of water + methane vapour. The excess enthalpy has been measured using a flow-mixing calorimeter [132]. The measurements are at a pressure of 1.015 bar, and the temperature range 373.15 to 423.15 K. The accuracy of the data is 2%. Wormald and Colling [133]–[135] describe the type of a differential flow-mixing calorimeter to measure the excess enthalpy of the vapour mixture.

Also, for these mixtures, the flow calorimetric apparatus consists of the following principal parts. Water from the reservoir flows through a metering pump into a flash vaporizer mounted in a fluidized alumina bath. Steam and methane passed through heat exchange coils. They were immersed in a fluidized bath containing a mixing calorimeter. Platinum resistance thermometers fixed to the inlet and outlet tubes were used to detect temperature changes. The calorimeter is contained in a pressure vessel. It is maintained at the same pressure as the fluids inside the calorimeter. The mixture leaving the calorimeter was condensed in a water-cooled coil and collected in a vessel. Methane is allowed to flow through the system by checking the needle valve. A nitrogen bottle connected to the pressurized pressure regulator the vessel containing the calorimeter. The pressure regulator supplies gas to the mixing calorimeter via a needle valve in a connected methane cylinder. For the mixture, methane with a purity of not less than 99.5% is used. Steam is generated from normal distilled water. Excess enthalpies measured using a flow calorimeter where heat losses and other effects are negligible should be independent of range.

The results obtained during the experiments with the calorimeter for water and methane mixtures are shown in Figure 4.20. First, the measurements were recorded for each temperature (K), pressure (bar), mole fraction x, and the power P supplied to the calorimeter to obtain an isothermal state. Then, the mixing enthalpy listed in Table 4.13 was obtained at the equilibrium composition (solubility).

Figure 4. 20. The mixing enthalpy of water vapour and methane was measured during experiments over a temperature and pressure range: 49.79 bar, 104. 37 bar and 105.07 bar. Referred to Wormald and Colling [133]–[135], Lancaster and Wormald [136]

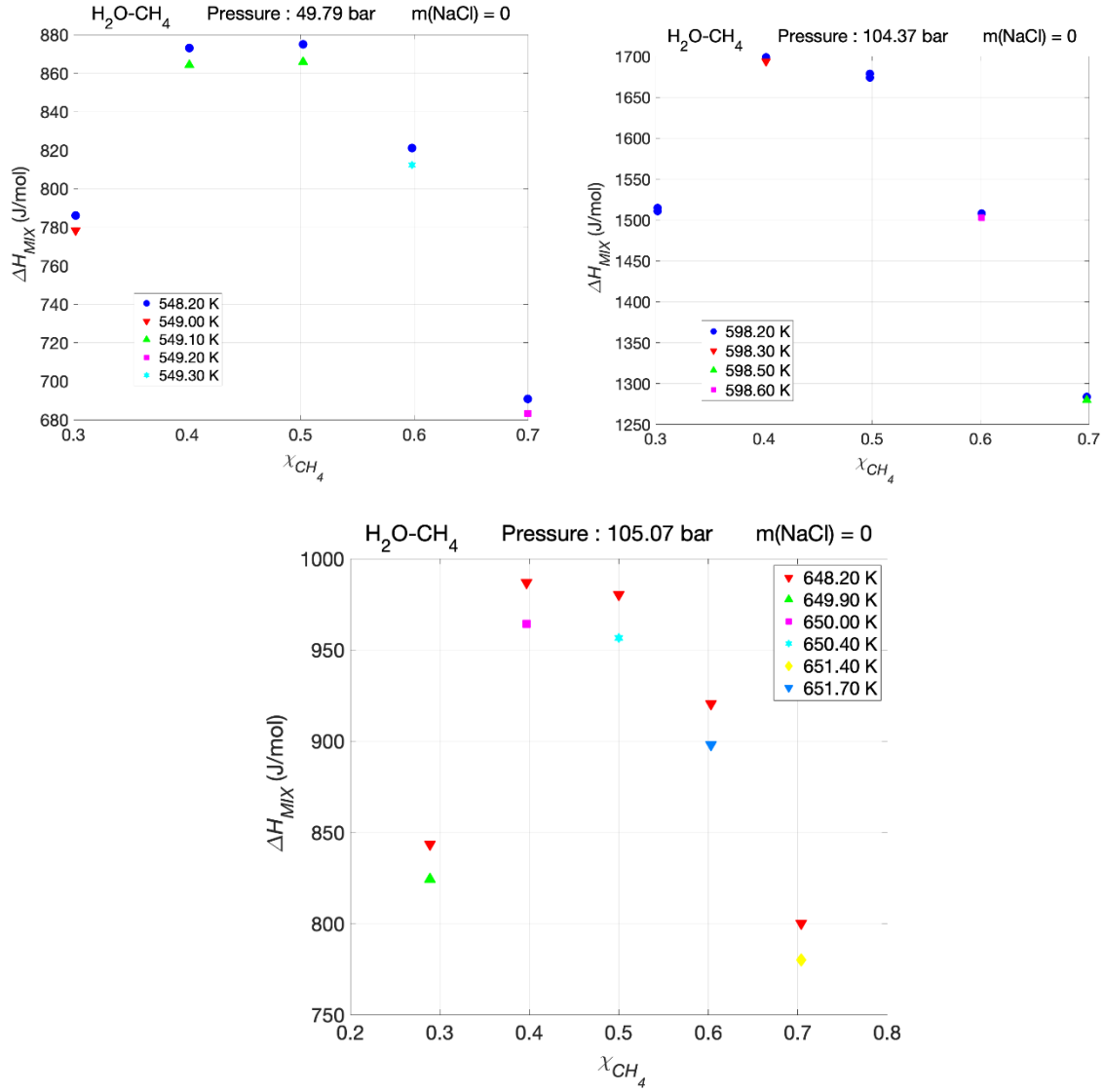

At pressures up to 40 bar, the measurements are closer to the curve calculated from the cubic equation. Above 50 bar, the mean deviation of the measurement points is 6 %. Thus, the experiments have an overall uncertainty on the ΔH mix values to be 2%.

The excess of enthalpies, or defined as ΔH mix for water vapour and methane in the range of 373.15 to 473.15 K and from 49.79 to 105.07 bar, is reported in the following table.

Table 4. 13. Experimental mixing enthalpies for water vapour and methane for selected temperatures and from 49.79 bar to 105.07 bar. Referred to Wormald and Colling [133]–[135] and Lancaster and Wormald [136].

Temperature [K]	Pressure [bar]	x_{CH4} [mol/mol]	ΔH_{mix} (J/mol)	Reference
548.20	49.79	0.304	699	*Lancaster and Wormald* [136]
549.00	49.79	0.302	778.4	Wormald and Colling [133]–[135]
549.10	49.79	0.402	864.3	Wormald and Colling [133]–[135]
549.20	49.79	0.700	683.2	Wormald and Colling [133]–[135]
549.30	49.79	0.598	812.3	Wormald and Colling [133]–[135]
598.20	104.37	0.498	1674	Wormald and Colling [133]–[135]
598.30	104.37	0.402	1694	Wormald and Colling [133]–[135]
598.50	104.37	0.698	1280	Wormald and Colling [133]–[135]
598.60	104.37	0.601	1503	Wormald and Colling [133]–[135]
648.20	105.07	0.397	986.8	Wormald and Colling [133]–[135]
649.90	105.07	0.289	824.2	Wormald and Colling [133]–[135]
650.00	105.07	0.397	964.3	Wormald and Colling [133]–[135]
651.40	105.07	0.704	780.1	Wormald and Colling [133]–[135]
651.70	105.07	0.603	897.9	Wormald and Colling [133]–[135]

There are no data available about CH_4-water in brine for experimental mixing enthalpies.

4.2 Solubilities analyses of the investigated models on fluid phase equilibria

4.2.1 CO_2-H_2O and CO_2-H_2O in brine

As seen before, a large volume of experimental data exists on the solubility of CO_2 in water. Many experimental data have been performed to determine the solubility in the 273.15 to 473.15 K range. The first correlation used the Peng-Robinson equation of state and a two-parameter mixing rule for highly polar asymmetric systems.

The solubility of CO_2 in water

In this study, the solubilities are calculated with:

- Group 1: Soreide& Whitson (SW), Duan model (DS) and Peng-Robinson with Huron Vidal mixing rule (PRH);

- Group 2: Cubic Plus Association (CPA) and Sour Peng-Robinson (SPR);
- Group 3: OLI thermodynamic equations: Aqueous (AQ), MSE and MSE-SRK frameworks.

The experimental results were compared with the SW, DS, PRH, CPA, OLI prediction, and the average absolute deviations. Moreover, uncertainties of the measurements were carefully planned because the result's uncertainty can be useful when simulating an entire geothermal process. The measured solubilities of CO_2 in water for each isotherm at different pressures and deviations of results (AD%) from the thermodynamic models are tabulated in Tables 4.14, 4.15 and 4.16.

The average relative deviation is calculated as:

$$AD\% = \frac{\chi_i^{model} - \chi_i^{EXP}}{\chi_i^{EXP}} \cdot 100 \qquad (4.8)$$

where χ_i^{EXP} is the experimental mole fraction, χ_i^{model} is the model mole fraction, and they are referred to as the liquid or the gas phase.
Although many experimental results are available in the literature for the solubility of CO_2 in water, still literature data are not present in the near-critical region of pure CO2. Therefore, the missing solubilities are calculated through the models to fulfil the near-critical region.
Furthermore, as depicted in Figures 4.21- 4.42, a comparison of the data measured in this study with the experimental data available proves the validity of the measured results and the better thermodynamic methods at each temperature and pressure considered for geothermal power plants.

All isotherms deviations of the experimental results from the predictive models decrease as pressure increases and from the temperature of 323.15 K to 423.15 K.

Also, compared to all methods, the data used in this work confirm the limits of the CPA and SW in predicting the CO_2 solubilities in water, especially at lower pressures.

All solubilities results and model prediction are presented in the following tables. As seen in the figures, the solubilities of the gas decreased as temperature increased. It is possible because the aqueous phase molecules' higher kinetic energy at a higher temperature broke the solution's intermolecular bonds and helped the gas molecules escape from the solution. For the temperature of about 423.15 K and the pressure of 200 bar, the gas's solubility increased to values more than the observed solubilities at lower temperatures (293.15 and 308.15 K).
As expected, the effect of increasing pressure up to 120 bars is to increase solubility. But, the effects of pressure on the gas solubility is to decrease with the pressure increase. Consequently, more gas molecules are in contact with the liquid surface at high pressures, increasing solubility.
We also carried a study that analyzed the fugacity of the main components of the mixtures to make accurate predictions using the Duan-Sun model in the developed code [58].

Figure 4. 21. Group 1: CO_2-H_2O binary system: Calculation of CO_2 solubility in water at 308.15 K and 323.15 K by Duan-Sun model [DS](solid line), Soreide & Whitson [SW](stroke and point line) and Peng-Robinson Huron-Vidal mixing rule [PRH] (dashed line). The blue colour is for the aqueous state and red for the gas state

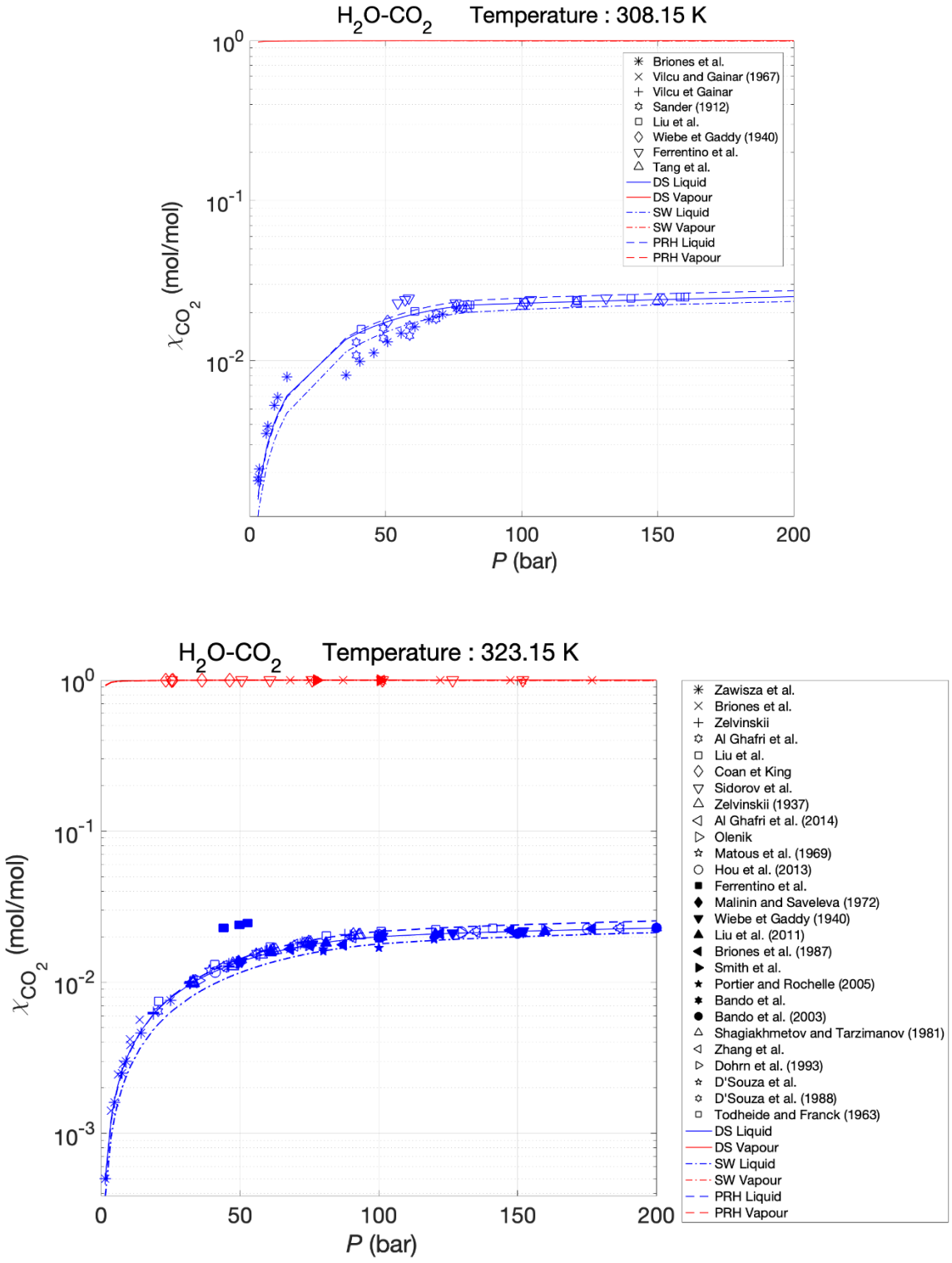

Figure 4. 22. CO_2-H_2O binary system: Calculation of CO_2 solubility in water at 373.15 K and 473.15 K by Duan-Sun model [DS] (solid line), Soreide & Whitson [SW] (stroke and point line) and Peng-Robinson Huron-Vidal mixing rule [PRH](dashed line). The blue colour is for the aqueous state and red for the gas state.

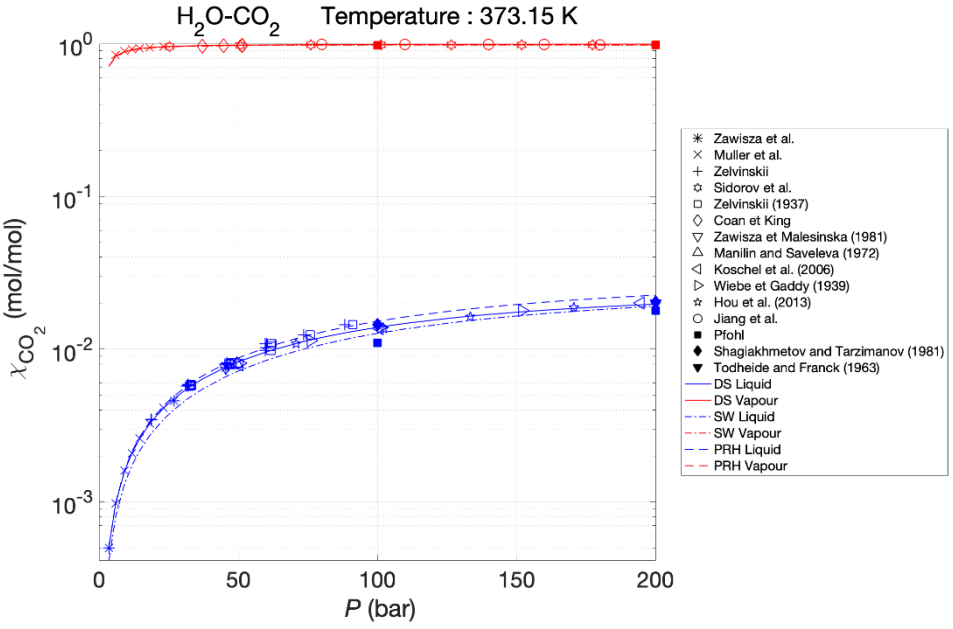

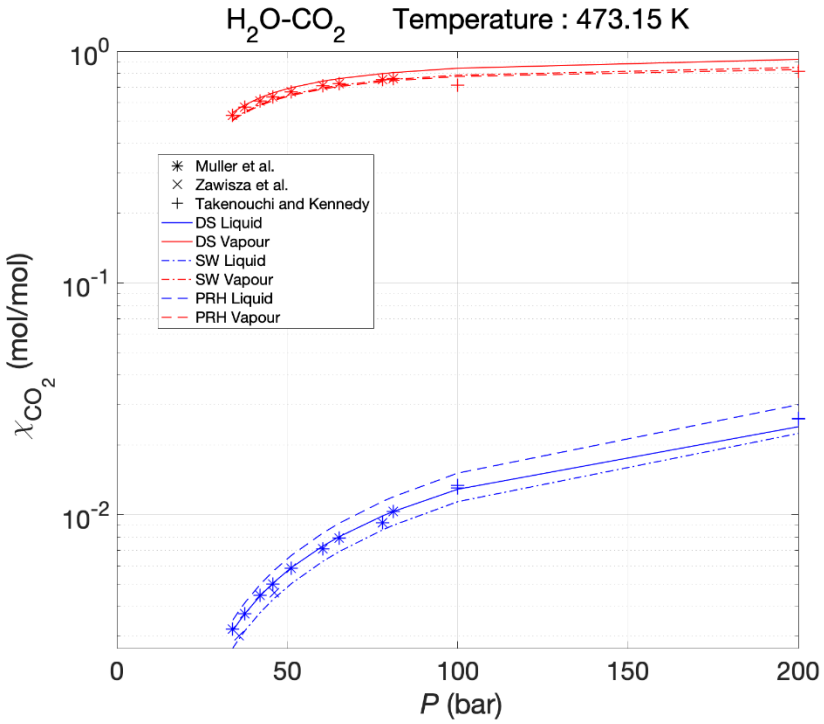

Table 4. 14. Group 1: SW, DS and SPR absolute deviations liquid and vapour from 293.15 to 473.15 K up to 200 bar.

T	P range	Np		SW‡		DS‡		PRH‡	
[K]	[bar]	[-]		[%]		[%]		[%]	
		Liq.	Vap.	Liq.	Vap.	Liq.	Vap.	Liq.	Vap.
293.15	1-200	24	-	-9.632	-	5.157	-	4.837	-
308.15	1-200	121	29	-3.638	-	10.46	-	15.80	-
323.15	1-200	222	49	-16.05	0.049	-3.195	0.318	2.721	0.108
348.15	1-200	68	38	-14.31	-0.036	-1.536	0.424	4.852	0.018
373.15	1-200	64	27	-13.78	-0.535	-1.851	0.358	4.635	-0.496
393.15	1-200	24	8	-13.43	-1.058	-0.626	0.163	5.294	-1.097
423.15	1-200	30	16	-9.207	4.352	0.860	7.749	11.56	4.014
473.15	1-200	37	25	-12.31	-0.789	1.076	6.281	16.19	-1.996

Liq. : Liquid phase; Vap. : vapour phase; T: temperature of the system; P range: pressure range of this work; Np: number of points. The symbol (‡) indicates that the value in the table has been obtained, performing the average of the relative deviations over the corresponding number of points.

The CO_2 average deviations for solubility in pure water are shown in Table 4.14 for the DS, SW, and PRH models (Group 1). The temperature range goes from 293.15 K to 473.15 K, and the pressure range is between 1 and 200 bar. Thus, at low temperature, the CO_2 solubility in water demonstrates having good agreement within the DS model over the entire pressure range. In table 4.14, the minimum value of the average standard deviations is observed at 393.15 K for the DS model; while the maximum average deviation is obtained for the PRH model at 473.15 K. The average relative deviation is optimal for temperatures lower than 308.15 K for SW model. For temperatures between 323.15 - 373.15 K, the best results are obtained with the thermodynamic DS model. For temperatures higher than 423.15 K and pressures up to 200 bar, two models, such as the DS model and SW, can guarantee a better compromise with the experimental results.

Figure 4. 23. Group 2: CO_2-H_2O binary system: Calculation of CO_2 solubility in water at 308.15.27 K and 323.15 K by Cubic Plus Association (CPA) (solid line) and Sour Peng-Robinson (SPR) (dashed line). The blue colour is for the aqueous state and red for the gas state.

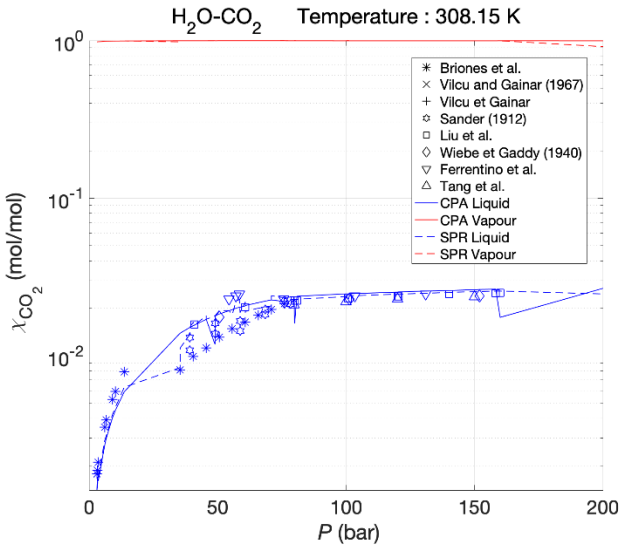

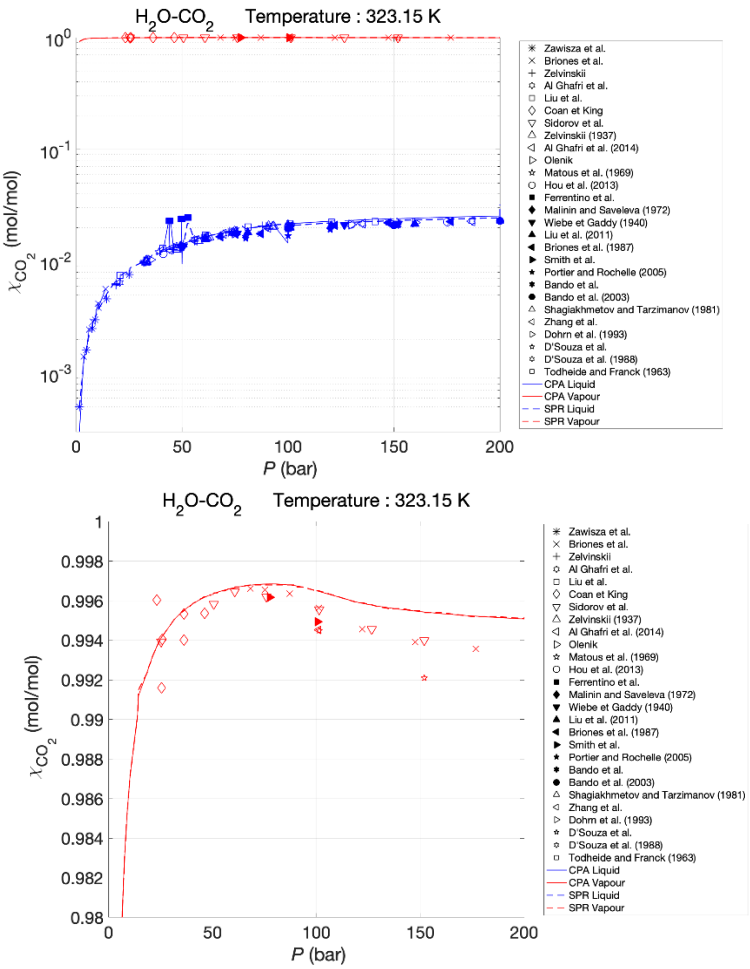

Figure 4. 24. Group 2: CO_2-H_2O binary system: Calculation of CO_2 solubility in water at 373.15 K and 473.15 K by Cubic Plus Association (CPA) (solid line) and Sour Peng-Robinson (SPR) (dashed line). The blue colour is for the aqueous state and red for the gas state

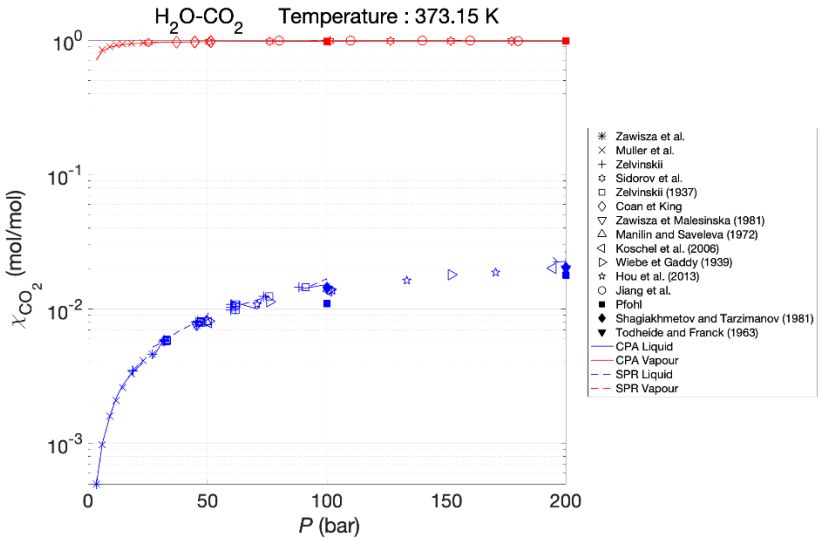

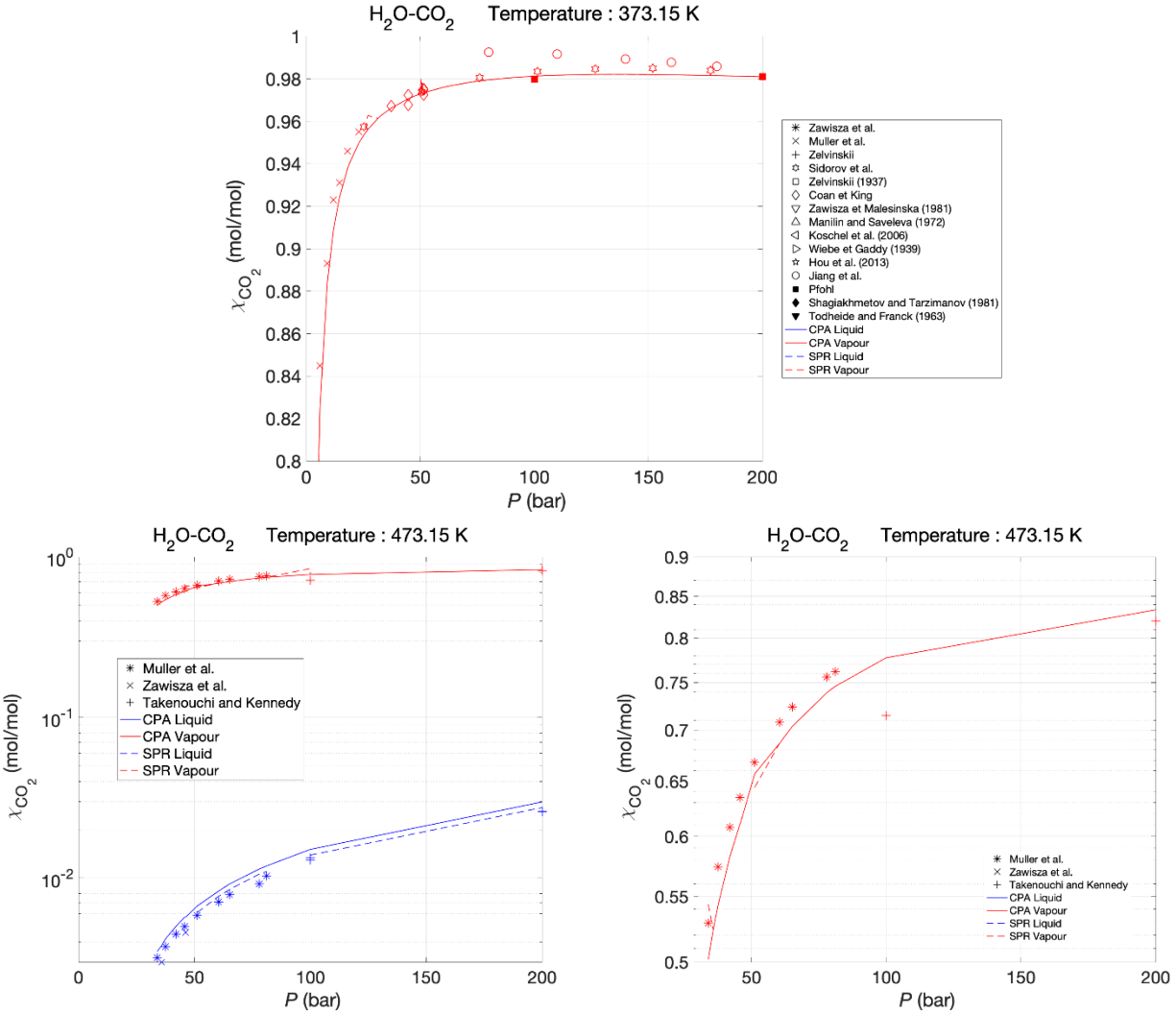

Figure 4.23 and Figure 4.24 illustrate the performance study regarding the CPA and SPR modified model parameters provided by IFPEN. The work addresses the description of the most important geothermal mixture. All figures are compared with experimental data to evaluate the quality of these model results.

Table 4. 15. Group 2: CPA and SPR absolute deviations liquid and vapour from 293.15 to 473.15 K up to 200 bar.

T	P range	Np		CPA‡		SPR‡	
[K]	[bar]	[-]		[%]		[%]	
		Liq.	Vap.	Liq.	Vap.	Liq.	Vap.
293.15	1-200	24	-	0.46224	-	4.8757	-
308.15	1-200	121	-	14.2622	-	11.8774	-
323.15	1-200	222	49	2.2098	0.10866	2.2308	0.10856
348.15	1-200	68	38	5.1228	0.01799	13.6059	0.053076
373.15	1-200	64	27	3.7011	-0.49629	4.94	-0.46318
393.15	1-200	24	8	5.2943	-1.0977	5.2943	-1.097
423.15	1-200	30	16	11.8312	4.014	1.0906	4.0165
473.15	1-200	37	25	16.1929	-1.8211	1.0864	-0.4083

Liq. : Liquid phase; Vap. : vapour phase; T: temperature of the system; P range: pressure range of this work; Np: number of points. The symbol (‡) indicates that the value in the table has been obtained, performing the average of the relative deviations over the corresponding number of points.

Most of the binary interaction parameters applied in this work are described in section 3.3.5. For this mixture, the group 2 results are presented in Table 4.15, and they are quite accurate. The modified SPR model was compared with the modified CPA model using process software, and the results show that CPA presents values much closer to the experimental data. Bibliographic data from literature and thermodynamic simulation data from IFPEN allowed the correction of the coefficients μ, $\alpha_{0,i}$, b_i, ε_i , β_i. The standard deviations are not very high in the SPR, while the CPA is acceptable for this mixture.
The largest deviations shown in table 4.15 are in the liquid phase at 293.15, 308.15 and 348.15 K for the SPR of 0.11, 0.18 and 0.15%, respectively. Simultaneously, the CPA's highest deviations are present for temperatures of 308.15 and 473.15 of 0.20 and 0.15%, respectively.

Both models are optimal for the thermodynamic models CPA and SPR as the deviations do not exceed 10% except for the Temperatures 308.15 K and 473.15 K for pressures up to 200 bar in the liquid phase. In this way, they compete with the Soreide & Whitson method. In the vapour phase, all deviations are less than 2%. The CPA and SPR thermodynamic models can be used for temperatures in the range 323.15-393.15 K as the deviations are synchronous to 3%.

Figure 4. 25. Group 3: CO_2-H_2O binary system: Calculation of CO_2 solubility in water at 308.15 K 323.15 K by OLI AQ(stroke and point line), OLI MSE (solid line) and OLI MSE-SRK (dashed line). The blue colour is for the aqueous state and red for the gas state.

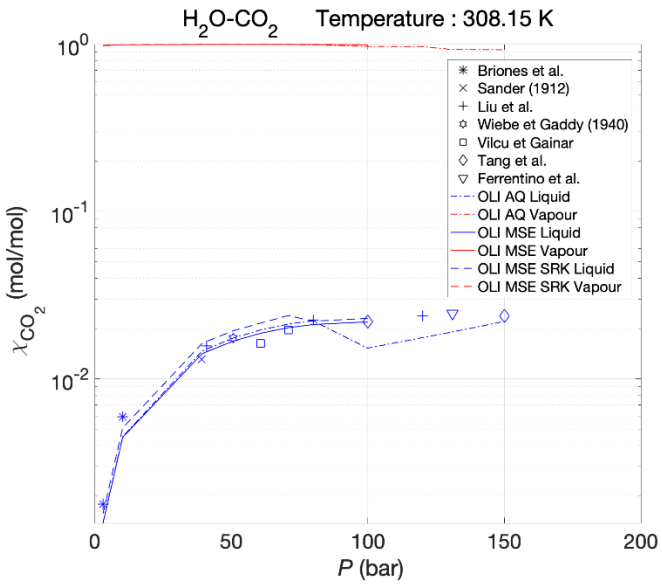

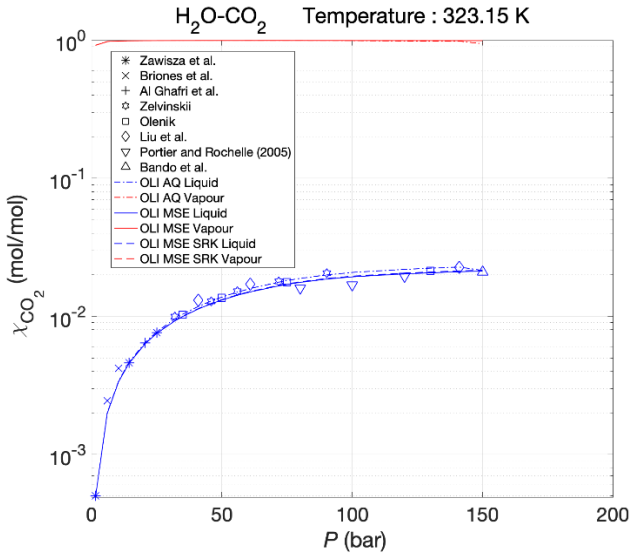

Figure 4. 26. Group 3: CO_2-H_2O binary system: Calculation of CO_2 solubility in water at 373.15 K and 473.15 K by OLI AQ(stroke and point line), OLI MSE (solid line) and OLI MSE-SRK (dashed line). The blue colour is for the aqueous state and red for the gas state.

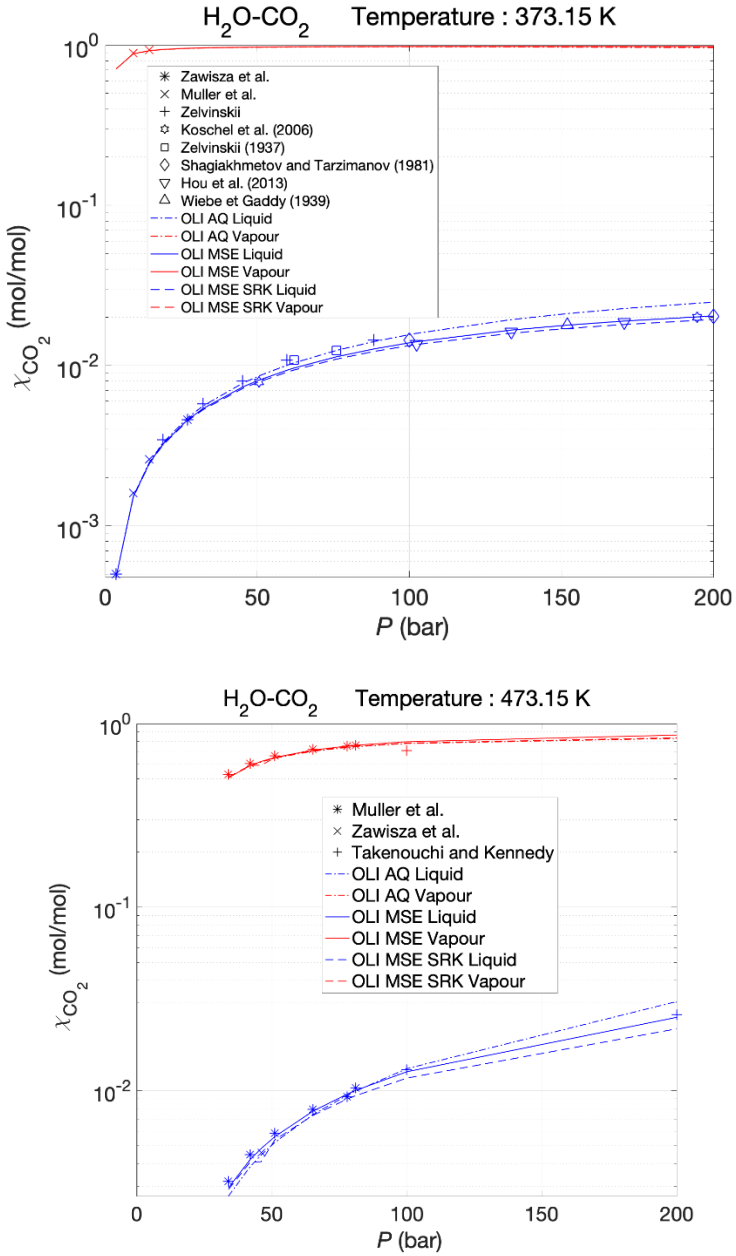

Table 4. 16: Group 3: OLI AQ, OLI MSE and OLI MSE SRK absolute deviations liquid and vapour from 293.15 to 473.15 K up to 200 bar.

T	P range	Np		OLI AQ‡		OLI MSE‡		OLI MSE SRK‡	
[K]	[bar]	[-]		[%]		[%]		[%]	
		Liq.	Vap.	Liq.	Vap.	Liq.	Vap.	Liq.	Vap.
293.15	1-200	24	-	7.378	-	5.196	-	12.58	-
308.15	1-200	121	29	-8.128	-	-28.35	-	-19.06	-
323.15	1-200	222	49	0.257	-	-4.227	-	-3.464	-
348.15	1-200	68	38	2.935	-0.413	-4.541	-0.057	-6.161	-0.075
373.15	1-200	64	27	5.463	-0.982	-3.881	-0.831	-6.645	-0.822
393.15	1-200	24	8	-1.584	-1.156	-4.671	-1.189	-7.069	-0.961
423.15	1-200	30	16	3.733	-	1.238	-	-2.827	-
473.15	1-200	37	25	-3.785	-0.997	-2.284	0.249	-9.243	-0.347

Liq. : Liquid phase; Vap. : vapour phase; T: temperature of the system; P range: pressure range of this work; Np: number of points. The symbol (‡) indicates that the value in the table has been obtained, performing the average of the relative deviations over the corresponding number of points.

The OLI thermodynamic models are presented in figures 4.25 and 4.26. It can be noted that for temperatures from 323.15 to 473.15 K and pressures for 1 to 200 bar, OLI AQ and OLI MSE models have the best accuracy within experimental data. Due to the results of all the models employed to perform these analyses for the CO2-H2O mixture, the results of best model performances are summarized in the following table 4.17:

Table 4. 17: Table summarizing the best model performance in terms of the average of the relative deviation for the H_2O-CO_2 mixture

Model	T [K]	P [bar]	Best average relative deviation [%]	
			Liq.	Vap.
CPA	293.15	1-200	0.46	-
DS	393.15	1-200	-0.62	0.16
SW	308.15	1-200	-3.64	-
SPR	473.15	1-200	1.08	-0.40
PRH	323.15	1-200	2.72	0.11
OLI AQ	323.15	1-200	0.25	-
OLI MES	423.15	1-200	1.23	-
OLI MSE SRK	423.15	1-200	-2.82	-

Solubility data for CO2 and aqueous NaCl solutions

For the thermodynamic study of the CO_2 sequestration, the NaCl salt is considered as a general representative model of a saline aquifer for a geothermal system. The carbon dioxide and NaCl (aq) in water are the most studied systems regarding the ranges, the temperature and pressure, and the number of results published in the literature. All representative data, in particular for that at temperatures up to 445 K and at low pressure, are also compared by Carroll et al. [137], R . Crovetto [138] and Fernandez et al. [139] up to the critical point of water. The most extensive data sets are Ellis and Golding [55], Takenouchi and Kennedy [19], Gehrig et al. [140], Drummond and Rumpf et al. [54].
Dissolved solids as NaCl in the aqueous phase decrease the solubility of light gases such as CO_2. Experimental solubility data define that reducing CO_2 solubility due to dissolved solid is generally correlated to CO_2 solubility in pure water [141]. A data set of solubilities is used for a temperature range of 303.15 K to 483.15 K and a pressure range of 1.0 to 200 bar for an aqueous solution

containing sodium chloride, the most important brine species in a geothermal reservoir. No trends other than total dissolved solids (TDS), such as temperature and pressure, were distinct enough to correlate from this large set of data.
From literature data, all ions reduce solubility to a comparable extent when TDS concentration is measured on a weight basis. The calculations for the composition simulations of the CO_2 displacement are simplified since all the ions can be simply grouped by weight. Furthermore, the simulations can only be marginally influenced by introducing an additional parameter, TDS, and the corresponding material balance equation. Whit the presence of salt, a practical approach could be useful to determine the solubilities through a correlation that is also a function of possible TDS present in the mixture of CO_2-water with salt. The empirical correlation is as follows:

$$w_{CO2,b} = w_{CO2,wat} \cdot (1.0 - 4.893414 \cdot 10^{-2}(TDS) + 0.1302838 \cdot 10^{2} \cdot (TDS)^2 + -0.18711199 \cdot 10^{-4}(TDS)^3). \quad (4.9)$$

where:

w: solubility, weight fraction

b: brine

wat: water

TDS: Total dissolved solids

$y_{CO2,\,w}$: It is the mole fraction of CO_2 in the aqueous phase.

The correlations allowing calculation of solubilities of carbon dioxide in NaCl (aq) are published by Rumpf et al. [54], who used a combination of Henry's law constant with the Pitzer model for activity coefficient of NaCl(aq) and CO_2. This work proposes a new formulation based on the Benedict–Webb–Rubin equation of state with an empirical mixing rule. Many authors published correlations of Henry's law constants k_H of CO_2 along the water's saturation line derived from the solubility data. Fernandez-Prini et al. [139], thanks to the data resulting from the calorimetric and volumetric measurements, presented a new correlation model to calculate k_H as a temperature function 573 K and pressure up to 1000 bar. Drummond and Ohmoto [142] described the only correlation of Henry's law constant for the ternary system incorporating the effect of NaCl concentration for CO_2 along the saturation line of water.

The solubility of CO_2 in water and brine are not calculated for all the models presented in the previous section due to the missing implementation of the CPA, PRH and SPR in process Unisim software. For this reason, only SW, DS, and OLI have been used to estimate the solubility of CO_2 in water and brines. Therefore, the list of models is made by the following groups:

- **Group 1**: Soreide& Whitson (SW), Duan model (DS);
- **Group 2**: OLI thermodynamic equations: Aqueous (AQ), MSE and MSE-SRK frameworks.

In this second set of experiments of this study, the solubilities are calculated at 303.15 K, 313.15 K, 323.15 K, 333.15 K, 353.15 K, 373.15, 393.15 K, 423.15 K and 483.15 K and up to 200 bar.

Deviations of the experimental results compared with the prediction of the Soreide &Whitson and the Duan model and uncertainties of the measurements are reported in Table 4.18.
The deviations of the experimental results for OLI AQ, OLI MSE and OLI MSE-SRK are reported in Table 4.19.

The experimental data were plotted as isotherms in diagrams of total pressure versus carbon dioxide solubility in the aqueous phase. The solubilities are calculated using different assumptions; in SW and OLI systems, the aqueous solutions are assumed to be a mixture of water and NaCl (single salt). In the DS model, different salts in the aqueous solution are considered (mixed salts). The experimental results and model predictions for both cases (single salt/mixed salts) are depicted in Fig. 4.27.

The measured solubilities of CO_2 in water present an amount of gas dissolved lower than the one without salt, which can be explained by the salting-out effect [143],[144]. This effect can be shown using the Setschenow constant (k_s) through the following equation [145]:

$$log\left(\frac{S_0}{S}\right) = k_s C_s \tag{4.10}$$

Where S_0 is the solute's solubility in water, S is the solute's solubility in brine. Thus, K_s is the Setschenow constant, and Cs represents the concentration of salt in the brine. The Setschenow constant is found for each data point using the eq. 4.4. Ks' values are similar for all the data points, and the average value is 0.08691 kg/mol. As the observed results for the CO_2 solubility in water, increasing temperature to 373.15 K caused a decrease in solubility of CO_2 in the brine. At temperatures above 373.15 K and pressure above 200 bar, an increase in solubility is noted. The experimental data at 373.15 K and pressure range of 1 to 200 bar, show an average reduction of 15% in CO2 in solubility for this mixture. Therefore, there is no significant pressure dependence due to the salting-out effect at the studied conditions.

Figure 4. 27. Group 1: CO_2-H_2O-NaCl system. For the sake of simplicity, the CO_2 solubility is computed for 1-6 molalities of NaCl and 303.15 K, 313.15 K and 373.15 K using SW (solid line) and DS models (stroke and point line). Green colour for m=1 [mol/Kg], red for m=2, light blue for m=3, purple for m=4, black for m=5, and yellow for m=6.

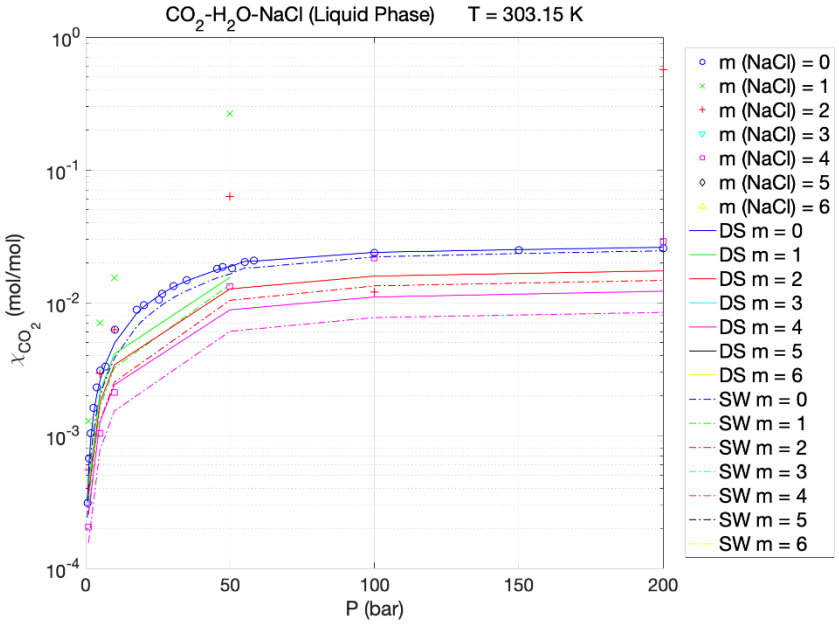

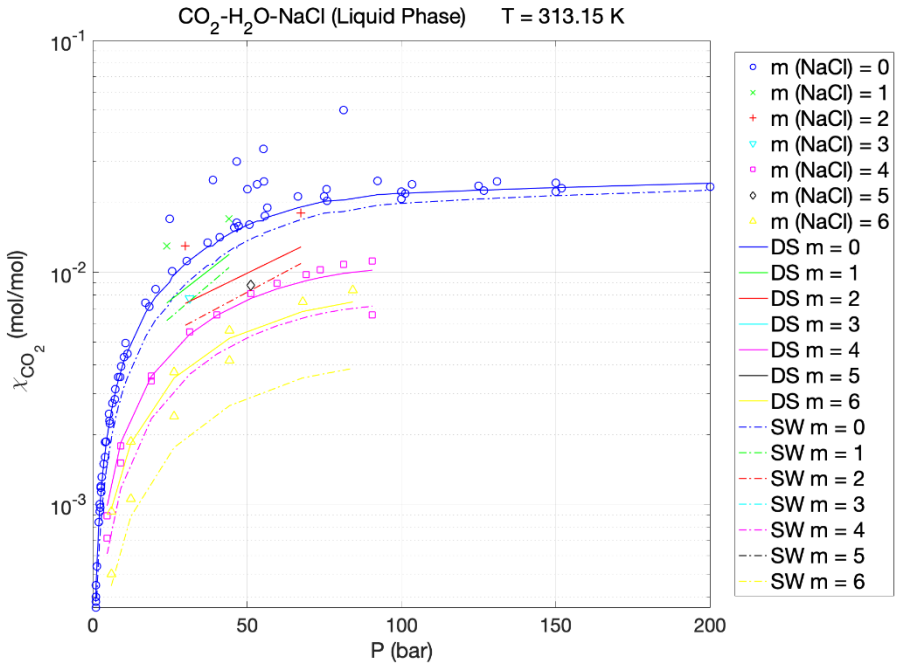
CO2-H2O-NaCl (Liquid Phase) T = 313.15 K
χCO2 (mol/mol)
P (bar)
m (NaCl) = 0
m (NaCl) = 1
m (NaCl) = 2
m (NaCl) = 3
m (NaCl) = 4
m (NaCl) = 5
m (NaCl) = 6
DS m = 0
DS m = 1
DS m = 2
DS m = 3
DS m = 4
DS m = 5
DS m = 6
SW m = 0
SW m = 1
SW m = 2
SW m = 3
SW m = 4
SW m = 5
SW m = 6

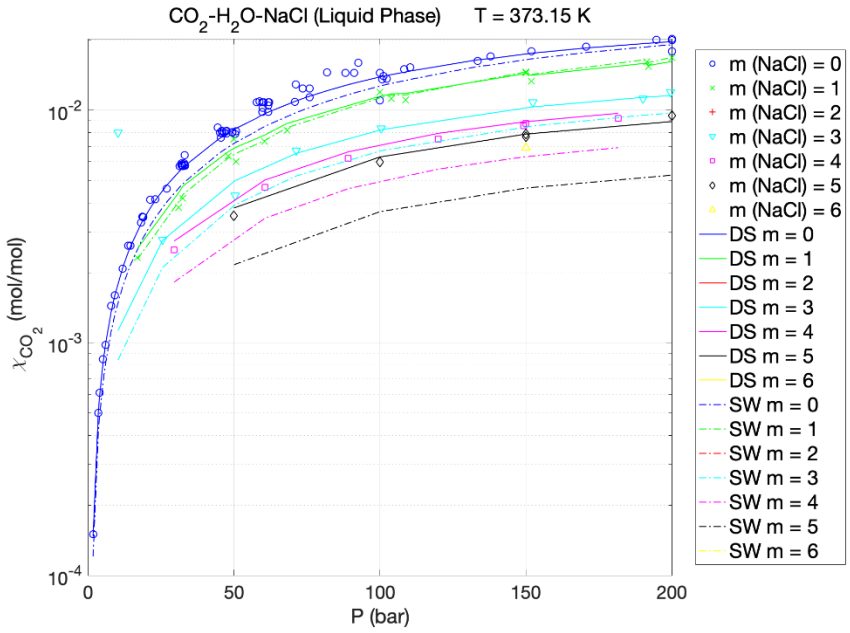
CO2-H2O-NaCl (Liquid Phase) T = 373.15 K
χCO2 (mol/mol)
P (bar)
m (NaCl) = 0
m (NaCl) = 1
m (NaCl) = 2
m (NaCl) = 3
m (NaCl) = 4
m (NaCl) = 5
m (NaCl) = 6
DS m = 0
DS m = 1
DS m = 2
DS m = 3
DS m = 4
DS m = 5
DS m = 6
SW m = 0
SW m = 1
SW m = 2
SW m = 3
SW m = 4
SW m = 5
SW m = 6

Table 4. 18. Group *1*: SW, DS average relative deviations for liquid from 273.15 to 483.15 K up to 300 bar and salt molalities from 1 to 7 m for a CO_2-H_2O-NaCl mixture.

m (NaCl) [mol/kg]	T [K]	P range [bar]	Np [-]	SW‡ [%]	DS‡ [%]
1.0-4.0	273.15	1.0-10.0	11	60.90	48.80
1.0- 4.0	303.15	1.0-200.0	19	59.56	49.14
1.0-6.0	313.15	6.0-90.0	44	22.36	19.45
1.0-6.0	323.15	1.9-40.0	54	17.43	4.59
1.0-5.0	373.15	17.0-300.0	62	13.67	7.51
1.0-6.0	393.15	1.0-200.0	39	19.17	26.90
1.0-4.0	423.15	10.0-150.0	33	31.43	27.36
1.0-4.0	483.15	50.0-200.0	11	50.12	54.19

m(NaCl): salt molality T: temperature of the system; P range: pressure range of this work; Np: number of points. The symbol (‡) indicates that the value in the table has been obtained, performing the average of the relative deviations over the corresponding number of points.

Figure 4. 28. Group 2: CO_2-H_2O-NaCl system. For the sake of simplicity, the CO_2 solubility is computed for 1-6 molalities of NaCl and 303.15 K, 313.15 K and 373.15 K using OLI Aqueous AQ (solid line). Green colour for m=1 [mol/Kg], red for m=2, light blue for m=3, purple for m=4, black for m=5, and yellow for m=6.

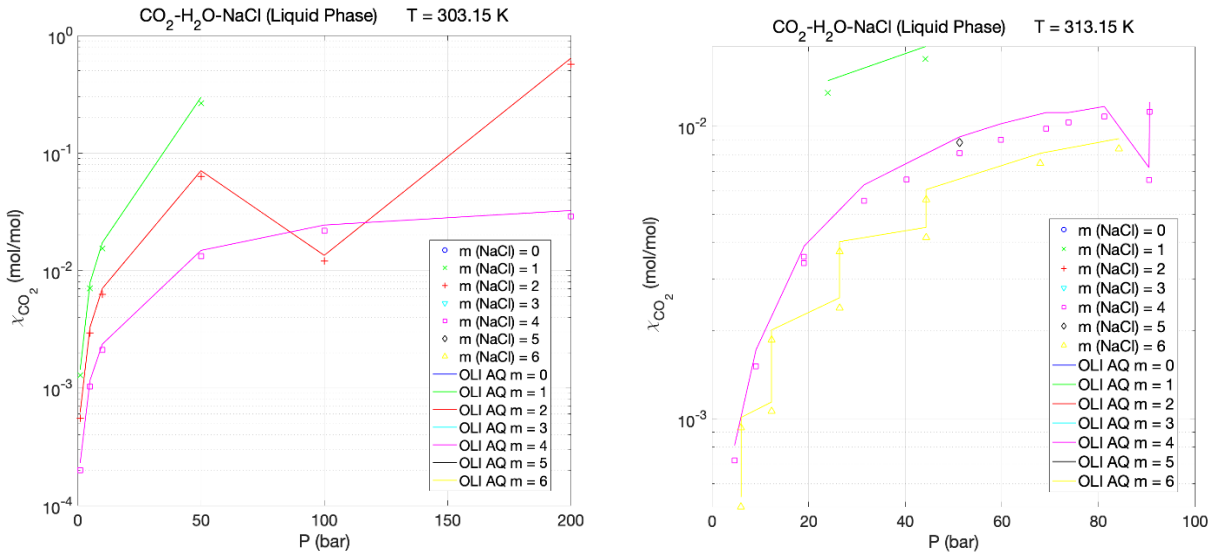

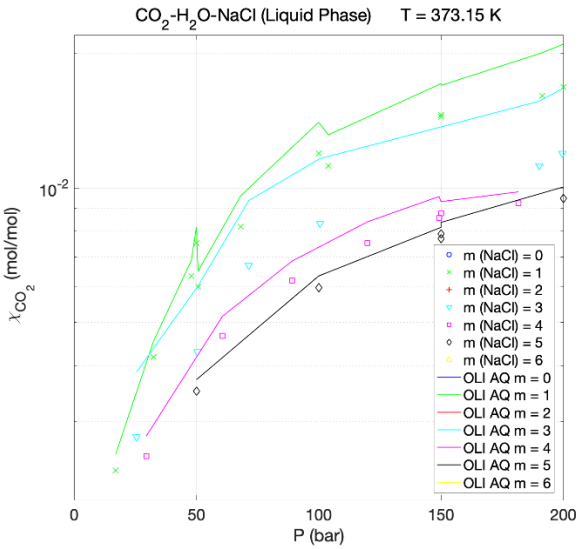

Figure 4. 29. Group 2: CO_2-H_2O-NaCl system. For the sake of simplicity, the CO_2 solubility is computed for 1-6 molalities of NaCl and 303.15 K, 313.15 K and 373.15 K using OLI MSE (solid line). Green colour for m=1 [mol/Kg], red for m=2, light blue for m=3, purple for m=4, black for m=5, and yellow for m=6.

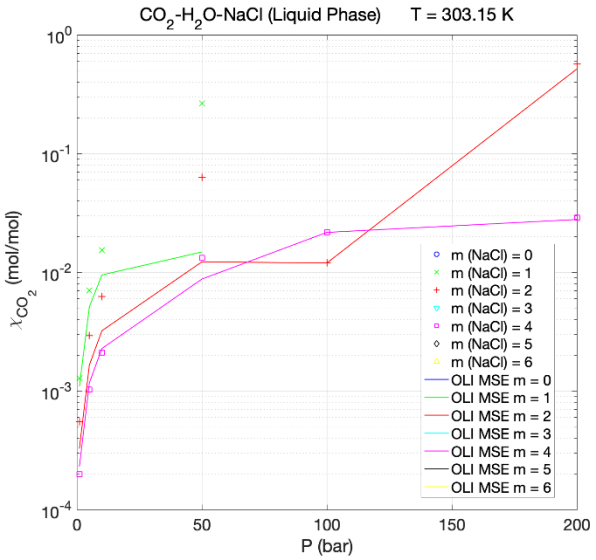

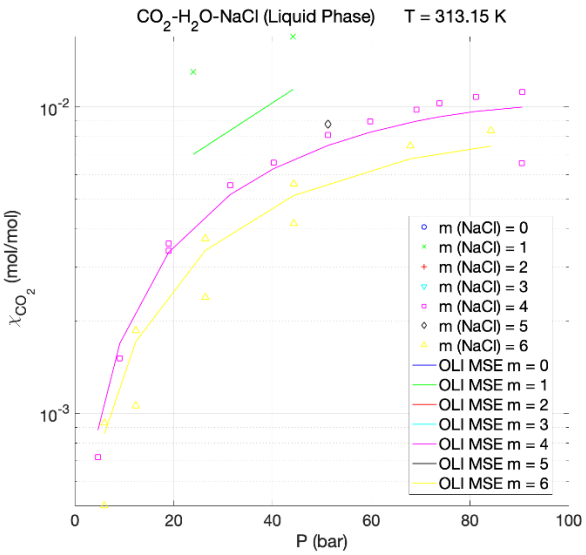

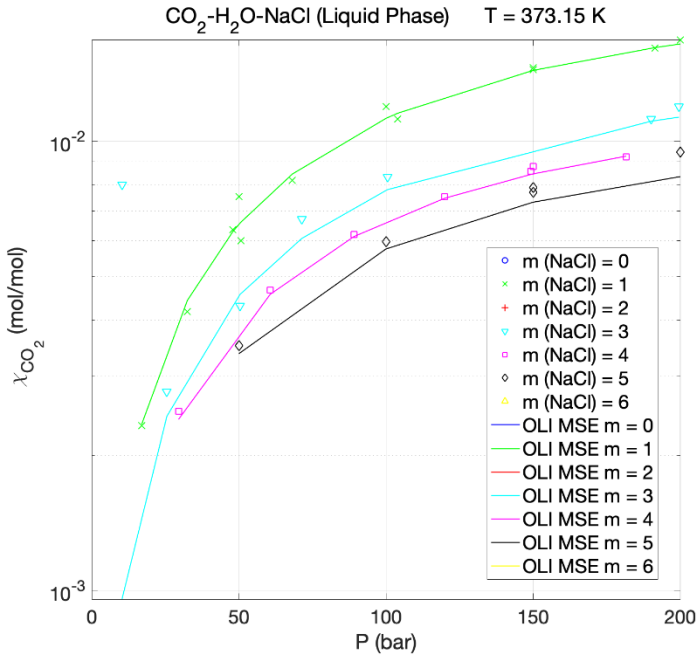

Figure 4. 30. Group 2: CO_2-H_2O-NaCl system. For the sake of simplicity, the CO_2 solubility is computed for 1-6 molalities of NaCl and 303.15 K, 313.15 K and 373.15 K using OLI MSE SRK (solid line). Green colour for m=1 [mol/Kg], red for m=2, light blue for m=3, purple for m=4, black for m=5, and yellow for m=6.

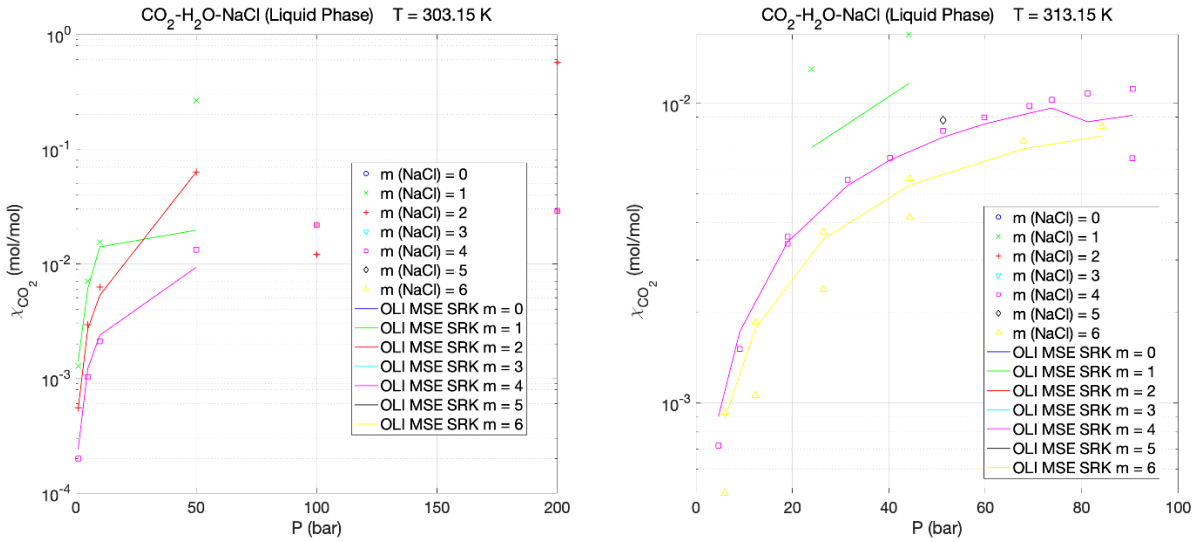

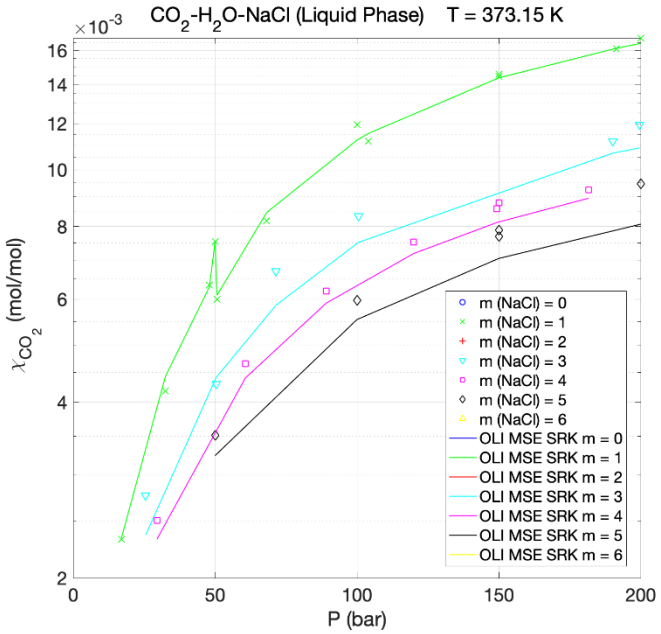

The relative average deviation (% AD) (see Eq. 4.2) for SW and OLI models referred to the experimental data are found to be 4.71% and 3.05%, respectively. Similar to measured solubilities in pure water, larger deviations of the predictive models' results were observed when calculations were conducted at the low-pressure condition. Particularly for the m=1-3 molalities salt, the data obtained using the models for the CO_2 solubility in the salt solution indicate that the salts slightly reduces the solubility. It has also been observed that the difference in CO_2 solubility between the water and the salt solution becomes smaller with the increase of temperature. The explanation of the reduction in CO_2 solubility for all the NaCl concentrations can be retrieved by Henry's law constant. Indeed, the salt's effect in terms of vapour pressure was approximated as 99.4% of the vapour pressure of pure water at the same temperature. A small decrease in solubility due to the presence of NaCl corresponds to an increase of Henry's Law data at 353.15 K and remain constant at temperatures higher than 473.15 K.

Table 4. 19. Group 2: OLI AQ, OLI MSE, and OLI MSE-SRK average relative deviations liquid from 273.15 to 433.15 K up to 300 bar and salt molalities range 1-7 m for a mixture CO_2-H_2O-NaCl.

mNaCl (mol/kgw) [mol/kgw]	T [K]	P range [bar]	Np [-]	OLI AQ‡ AD %	OLI MSE‡ AD %	OLI MSE-SRK‡ AD %
1.0-4.0	273.15	1.0-10.0	11	43.70	46.95	32.51
1.0- 4.0	303.15	1.0-200.0	19	15.00	29.32	13.64
1.0-7.0	313.15	6.0-90.0	44	9.98	19.27	18.31
1.0-6.0	323.15	1.9-40.0	54	9.51	6.65	3.41
1.0-5.0	373.15	17.0-300.0	62	18.01	5.42	4.23
1.0-6.0	393.15	1.0-200.0	39	26.60	32.96	16.40
1.0-4.0	423.15	10.0-150.0	33	14.58	25.83	12.40
1.0-4.0	483.15	50.0-200.0	11	54.38	60.90	21.31

m(NaCl): salt molality, T: system temperature; P range: pressure range of this work; Np: number of points. The symbol (‡) indicates that the value in the table has been obtained, performing the average of the relative deviations over the corresponding number of points.

At 273.15 K temperature and pressures from 1 to 10 bar, the thermodynamic model is better than OLI MSE-SRK (32.51%). However, for the temperature of 303.15 K and pressures up to 200 bar and salt molality from 1 to 4 m, all deviations are greater than 15% except for the OLI MSE-SRL model (13.64%). At a temperature of 313.15 K, at a pressure range of 6-90 bar and molality of 1-6

m, the best thermodynamic models are OLI AQ (9.98%) and OLI MSE-SRK (18.31%). Best results are obtained starting from 323.15 K, pressure range 1.9-40.0 bar, and molality from 1 to 6 m, except for SW. The overall models show mean deviations of less than 10%, with points of excellence of OLI MSE-SRK (3.41%) and Duan model (4.59%). At a temperature of 393.15 K, a pressure range of 1-200 bar and the salt molality from 1 to 6 m, the average deviations tend to increase compared to the previous ones where the best thermodynamic models are OLI MSE-SRK (16.40%) and SW (19.17%). At a temperature of 423.15 K, pressures from 10 to 150 bar, and a salt molality of 1-4 m, the two thermodynamic models with low relative average deviations are OLI MSE-SRK (12.40%) and OLI AQ (14.58%). Finally, at higher temperatures, at 483.15 K and pressures from 50-200 bar and molality from 1 to 4 m, all thermodynamic models exhibit high deviations at 2 m of salt. Among these, the OLI MSE-SRK model shows lower deviations and around 21.31%.
Due to the results of all the models employed to perform these analyses for the CO_2-H_2O-NaCl mixture, the results of best model performances are summarized in the following table 4.21:

Table 4. 20. Table summarizing the best model performance in terms of the average of the relative deviation for the H_2O-CO_2 -NaCl mixture

m (NaCl) [mol/kg]	T [K]	P range [bar]	Np [-]	Best average relative deviation [%]
1.0-4.0	273.15	1.0-10.0	11	OLI MSE-SRK
1.0- 4.0	303.15	1.0-200.0	19	OLI MSE-SRK
1.0-6.0	313.15	6.0-90.0	44	OLI AQ
1.0-6.0	323.15	1.9-40.0	54	OLI MSE-SRK
1.0-5.0	373.15	17.0-300.0	62	OLI MSE-SRK
1.0-6.0	393.15	1.0-200.0	39	OLI MSE-SRK
1.0-4.0	423.15	10.0-150.0	33	OLI MSE-SRK
1.0-4.0	483.15	50.0-200.0	11	OLI MSE-SRK

4.2.2 H_2S-H_2O and H_2S-H_2O in brine

The solubilities experimental data of H_2S in the water at different combinations of temperature (283 K – 473 K) and pressures (1 bar – 350 bar) are reported in Annex 4.B. All data are compared for all the temperatures found in literature, and those that highlighted inconsistencies with the same operating conditions were discarded. A good agreement with all data in the literature (differences lower than 5%) has been accepted. In particular, for the gas phase, the errors are less than 3 %. When H_2S is liquid or supercritical, the solubility is high and changes slightly with the pressure. At temperatures above 423 K, the solubility increases rapidly with pressure (see ref. [28]) compared to the ref. [32] because hydrogen sulphide behaves like an ideal gas at supercritical conditions. Already at 393 K, it is possible to notice a slight increase in solubility with pressure. The solubility of hydrogen sulfide in water increases with increasing temperature at high pressures. This entails that the enthalpy of mixing hydrogen sulfide in water at high pressures is positive (endothermic). While at low pressures, the dissolution process of gaseous H_2S is exothermic, implying that the solubility decrease with increasing temperature. The increase of liquid hydrogen sulfide's solubility in water with pressure is less pronounced than in the supercritical region. This weak pressure dependence of the solubility of liquid H_2S is explained in the following reference [29]. Particularly, for the temperature range of 273-363 K, the experimental data have low standard deviations [29], while at higher temperatures, above 473 K, the discrepancy increase [7], [10], [11]. The reasons are compatible with the formation of iron sulfide and hydrogen gas due to the corrosion process. Other experimental data are collected by the following reference [27] because they present deviations within 0 and 1.5 %.
The H_2S solubility decreases with increasing electrolyte concentration (1-6 m). These phenomena follow the salting-out effect (s.o.) that is quantified as the reduction percentage of H_2S solubility (x_1) in the aqueous solution with electrolyte correlated to solubility in pure water (x_0). The following equation describes the salting-out effect as $s.o. = 100 \cdot \frac{(x_0 - x_1)}{x_0}$.

The solubility of H_2S in the gas phase (with water) is lower than its liquid phase or supercritical condition, but the pressure doesn't affect the salting-out. For example, Suleimenov and Krupp [11] noted that the temperature on the salting-out effect is negligible up to around 490 K while the Setchenov constants are between 0.067 and 0.072 $kg \cdot mol^{-1}$ for salt concentrations until m=3 mol/Kg. The influence of pH on the solubility of hydrogen sulfide in a 1 m, 3 m and 5 m NaCl solution was analyzed from 1 bar to 310 bar, *i.e.* a range that covers the majority of experimental data. The pH of a 1 m, 3 m and 5 m solution at a pressure of 1 bar has a maximum for 373 K, while at high pressures presents a minimum for 385 K.

The comparison of the solubilities of H_2S at different pH values shows that there is no influence on the solubility. Carroll [29] analyzed the influence of pH of hydrogen sulfide's solubility in water and investigated the speciation at higher pH values. He found that the predominant form of the sulfide species at low pH (acidic solution) is the molecular H_2S until about m=6 when the bisulfite (S^{2-}) becomes present. With a pH of slightly less than 7, there are equal amounts of the molecular form and the disulfide anions.
Another critical study for the influence of salt nature on the salting-out effect is ionic strength $I = \frac{1}{2}\sum m_i \cdot z_i^2$, where m_i and z_i are ionic molalities (mols of ion per kilogram of water) and their valence. The ionic strength is I ≈ 1 mol/kg at 1 m solutions of NaCl, I ≈ 3.1 mol/kg at 3 m solutions of NaCl and I ≈ 5.3 mol/kg at 5 m solutions of NaCl. A common aspect is that at pressures of 1 bar, the Ionic strength increases up to one order of magnitude as the temperature increases. Therefore, its value remains constant for pressures above 5 bar. The experimental data references can be found in Table 4.3 for the mixtures, including salts, while in Table 4.4 can be found the references for the mixtures without salts.

Figure 4. 31. Group 1**:** The solubility of H_2S in pure water at 303.15 K and 323.15 K up to 100 bar. This study is made with three thermodynamics models: SW (stroke and point lines), DS (solid lines) and PRH (broken line). The blue colour is for the liquid/aqueous phase, while the red colour is for the gas phase. The experimental data are taken from the following references [59], [130] and [146].

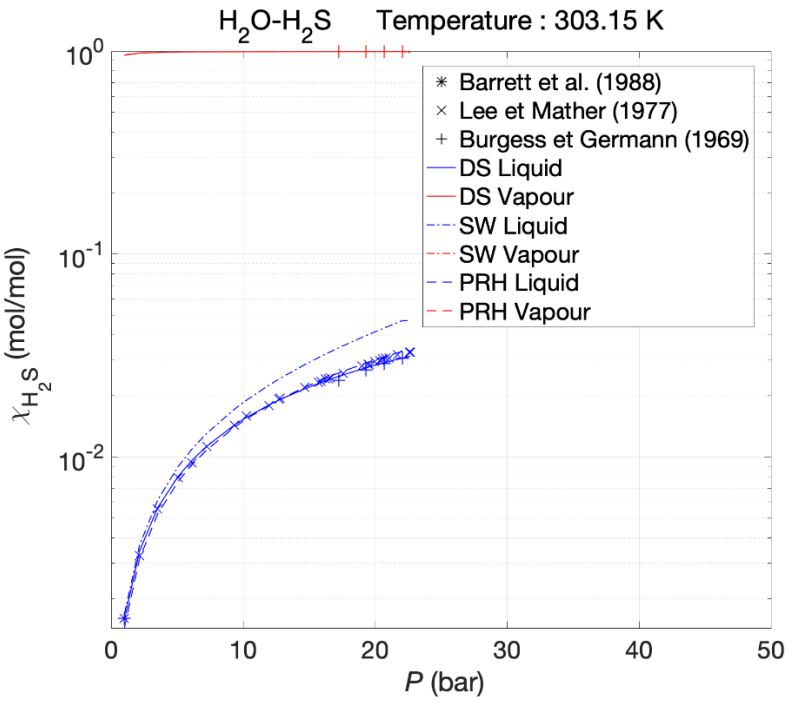

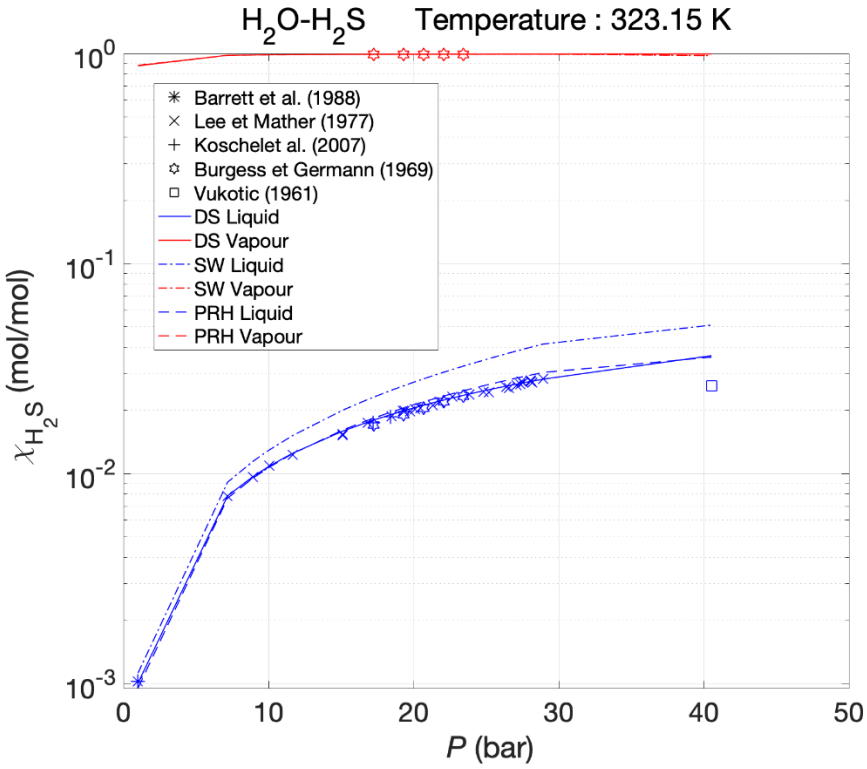

Figure 4. 32. Group 1: The solubility of H_2S in pure water at 363.15 K and 423.15 K up to 100 bar. This study is made with three thermodynamics models: SW (stroke and point lines), DS (solid lines) and PRH (broken line). The blue colour is for the liquid/aqueous phase, while the red colour is for the gas phase. The experimental data are taken from the following references [59],[69],[65], [130] and [146].

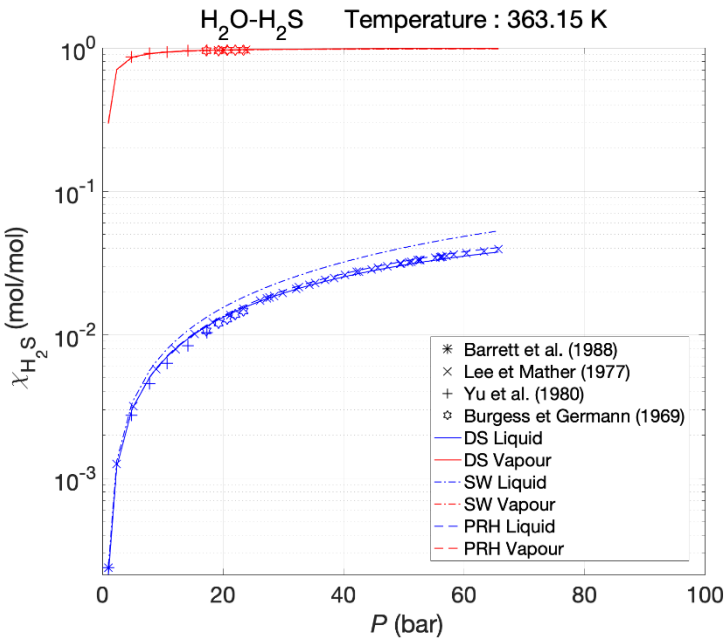

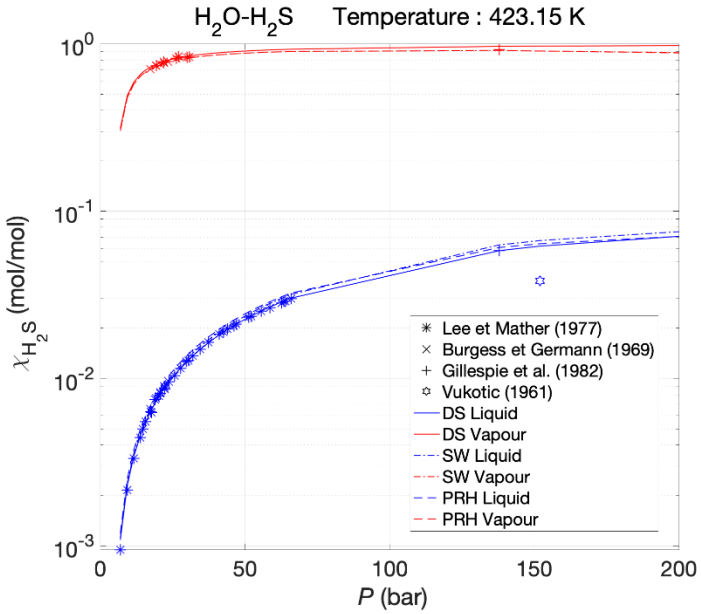

Table 4. 21. The average deviations of the thermodynamics model SW, DS and PRH data results with the experimental data of H_2S solubility from 283.15 to 453.15 K up to 200 bar.

T	P	Np		SW‡		DS‡		PRH‡	
[K]	[bar]	[-]		[%]		[%]		[%]	
		Liq.	Vap.	Liq.	Vap.	Liq.	Vap.	Liq.	Vap.
283.15	1	42	6	0.027	-	1.319	-	-11.303	-
303.15	1-10	35	5	32.702	0.074	-1.17	0.107	0.939	0.058
323.15	1-20	42	6	37.397	0.111	2.285	0.215	5.948	0.093
344.15	1-50	55	28	29.569	0.060	2.168	0.337	5.186	-0.135
363.15	1-50	60	18	23.671	-0.308	-0.44	0.212	3.697	-0.312
393.15	1-200	40	7	15.057	-2.280	0.432	-0.959	6.616	-2.250
423.15	1-210	44	14	6.182	-1.329	1.811	2.240	9.942	-1.344
453.15	1-100	18	-	1.667	-	1.000	-	16.986	-

Liq. : Liquid phase; Vap. : vapour phase; T: temperature of the system; P range: pressure range of this work; Np: number of points. The symbol (‡) indicates that the value in the table has been obtained, performing the average of the relative deviations over the corresponding number of points.

Figure 4. 33. The solubility of H_2S in pure water at 303.15 K and 323.15 K up to 100 bar. This study is made with two thermodynamics models: Cubic Plus Association [CPA] (solid lines)and Sour Peng Robinson [SPR] (broken line). The blue colour is for the liquid/aqueous phase, while the red colour is for the gas phase.

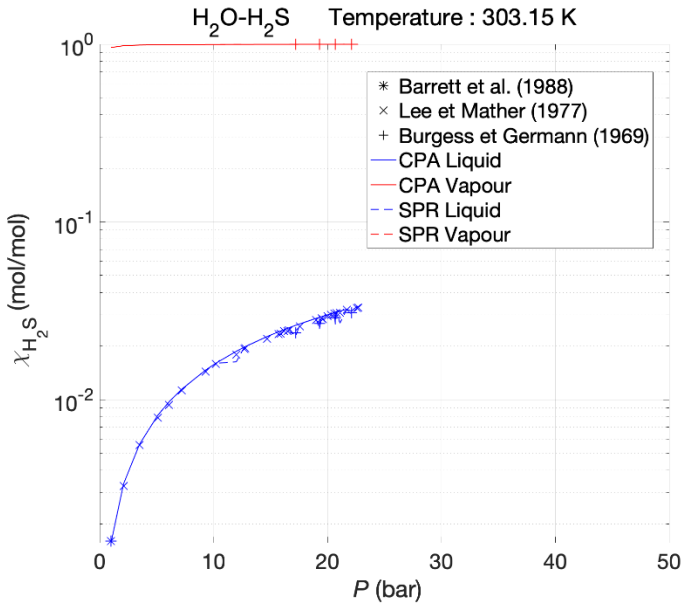

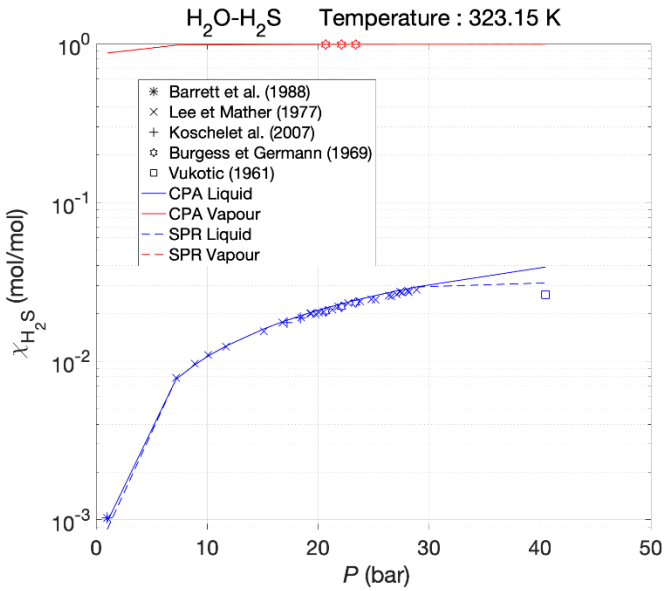

Figure 4. 34.The solubility of H_2S in pure water at 363.15 K and 423.15 K up to 200 bar. This study is made with two thermodynamics models: Cubic Plus Association [CPA] (solid lines) and Sour Peng Robinson [SPR] (broken line). The blue colour is for the liquid/aqueous phase, while the red colour is for the gas phase.

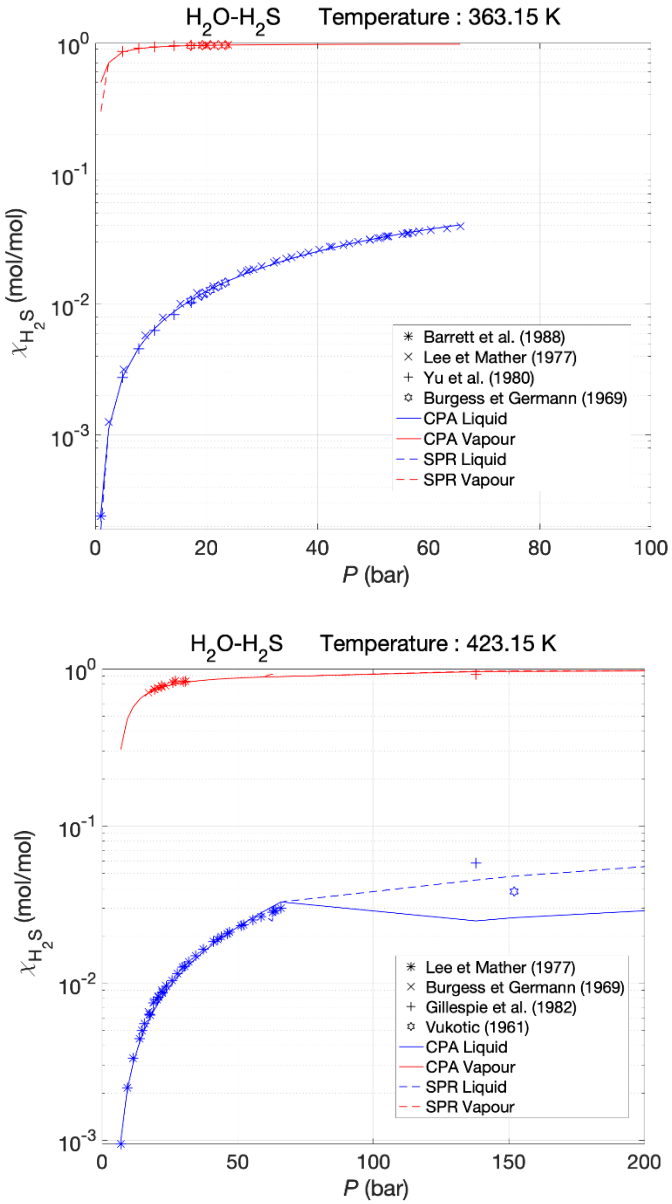

Table 4. 22. The average deviations of the thermodynamics model CPA and PRH results with the experimental data of H_2S solubility from 283.15 to 453.15 K up to 200 bar.

Temperature	Pressure range	Np		CPA‡		SPR‡	
[K]	[bar]	[-]		[%]		[%]	
		Liq.	Vap.	Liq.	Vap.	Liq.	Vap.
283.15	1	42	6	5.4484	-	-3.3596	-
303.15	1-10	35	5	2.1329	0.61818	0.63109	0.61818
323.15	1-20	42	6	-0.98864	-0.42434	-1.5835	-0.3169
344.15	1-50	55	28	0.59699	-0.03987	0.49377	-0.0398
363.15	1-50	60	18	-0.98864	-0.42434	-1.5835	-0.31692
393.15	1-200	40	7	-2.8159	-2.4711	-2.9645	-2.4711
423.15	1-210	44	14	-3.3474	-1.5392	-3.7333	-0.46797
453.15	1-100	18	-	-10.9827	-	-4.1434	-

Liq. : Liquid phase; Vap. : vapour phase; T: temperature of the system; P range: pressure range of this work; Np: number of points. The symbol (‡) indicates that the value in the table has been obtained, performing the average of the relative deviations over the corresponding number of points.

Figure 4. 35. The solubility of H_2S in pure water at 303.15 K and 323.15 K up to 100 bar. This study is made with three thermodynamics models: OLI AQ (stroke and point lines), OLI MSE (solid line) and OLI MSE SRK (broken line). The blue colour is for the liquid/aqueous phase, while the red colour is for the gas phase.

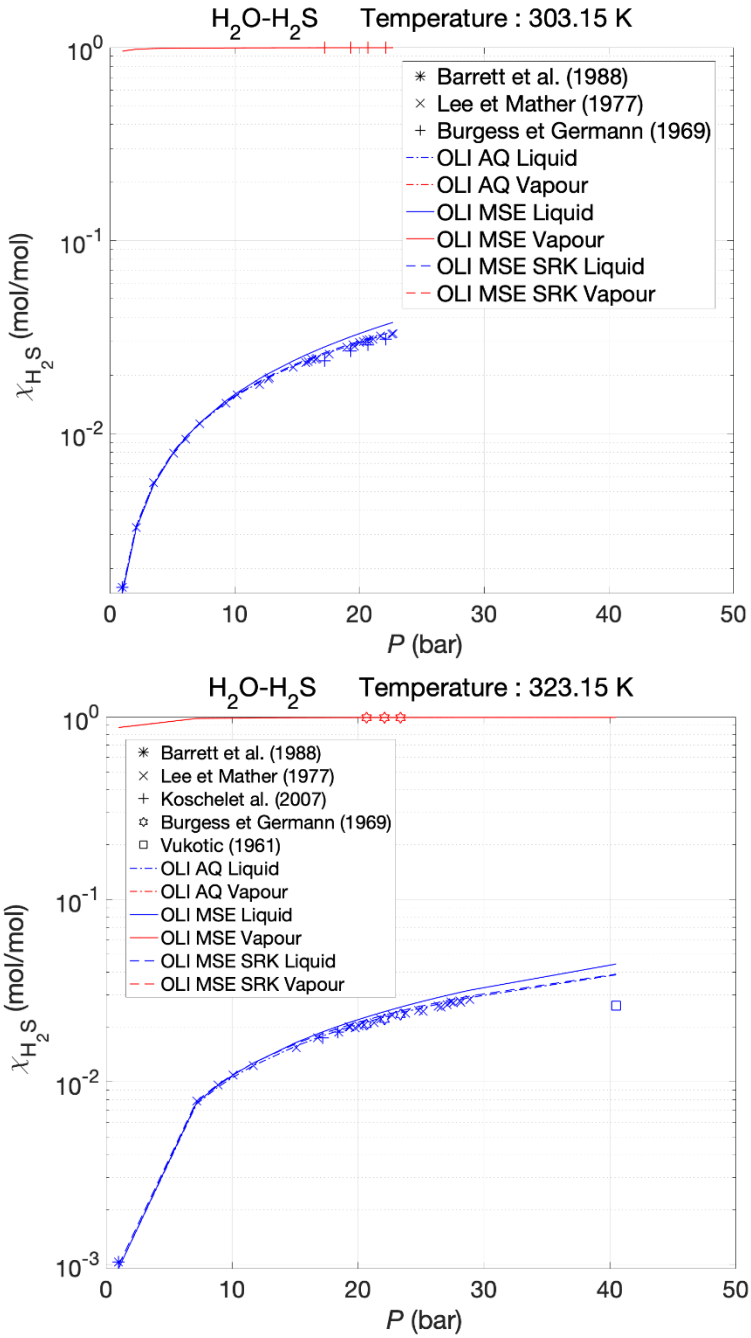

Figure 4. 36. The solubility of H_2S in pure water at 363.15 K and 423.15 K up to 100 bar. This study is made with three thermodynamics models: OLI AQ (stroke and point lines), OLI MSE (solid line) and OLI MSE SRK (broken line). The blue colour is for the liquid/aqueous phase, while the red colour is for the gas phase.

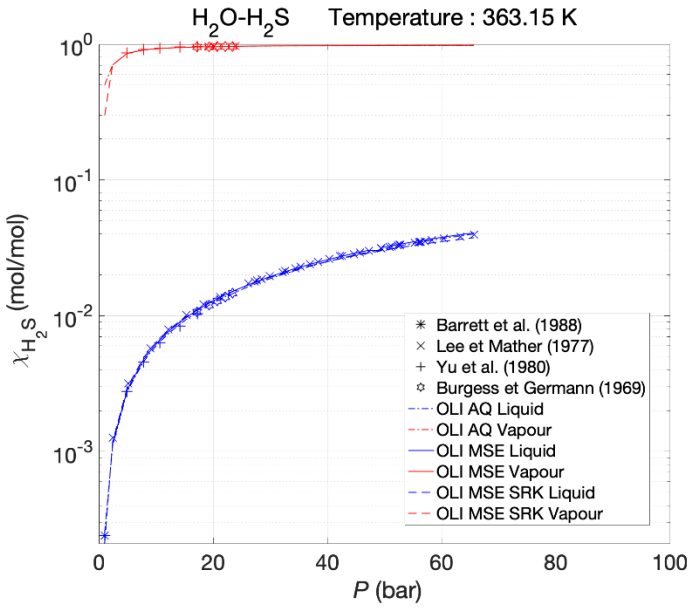

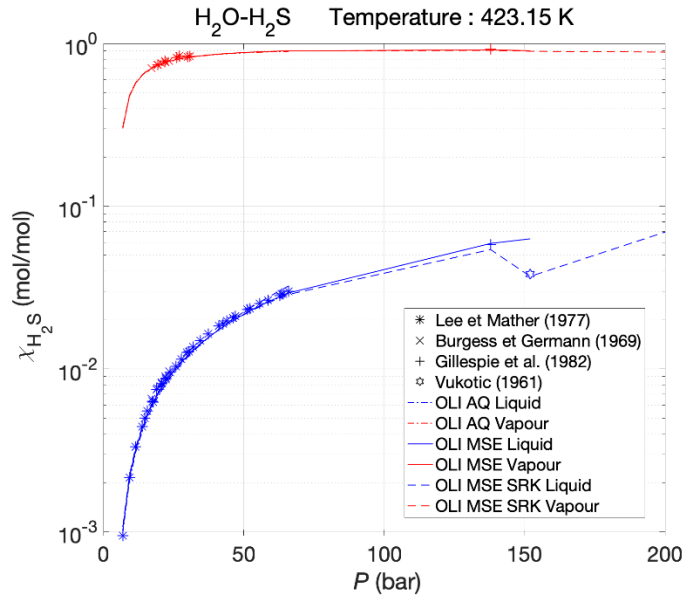

Table 4. 23. The average deviations of the thermodynamics model for OLI result with the experimental data of H_2S solubility from 283.15 to 453.15 K up to 150 bar.

T	P range	Np		OLI AQ‡		OLI MSE‡		OLI MSE SRK‡	
[K]	[bar]	[-]		[%]		[%]		[%]	
		Liq.	Vap.	Liq.	Vap.	Liq.	Vap.	Liq.	Vap.
283.15	1-4	42	6	3.9521	-	-3.216	-	-0.677	-
303.15	1-25	35	5	1.3537	0.0362	9.019	0.0447	2.8865	0.0561
323.15	1-40	42	6	2.7549	0.0508	9.8899	0.0719	5.4648	0.0938
344.15	1-55	55	28	-0.8094	-0.0389	3.9078	0.0184	2.2213	0.0522
363.15	1-70	60	18	-2.3664	-0.4233	-1.549	-0.3397	-1.803	-0.2932
393.15	1-140	40	7	-4.2047	-2.47	-2.388	-2.2487	-3.658	-2.1981
423.15	1-150	44	14	-4.7164	-1.5382	-4.326	-1.3966	-3.396	-1.1235
453.15	1-60	18	-	-3.0668	-	-13.07	-	0.6982	-

Liq. : Liquid phase; Vap. : vapour phase; T: temperature of the system; P range: pressure range of this work; Np: number of points. The symbol (‡) indicates that the value in the table has been obtained, performing the average of the relative deviations over the corresponding number of points.

From Figure 4.37 to 4.40, the graphs show the results of the thermodynamic models Soreide & Whitson, Duan model, OLI AQ, OLI MSE and OLI MSE-SRK.

For this mixture (H_2O-H_2S-NaCl), there ane no sufficient experimental data for molalities from 1 to 6; therefore, no real comparison is made. However, only the mixtures without salts can be studied using the models.

Figure 4. 37. Group 1:The solubility of H_2S in NaCl aqueous solutions at 303.15 K, 323.15 K and 363.15 K up to 70 bar and salt molalities range 1-6 m. This study is made with two thermodynamics models: SW (stroke and point lines) and DS (solid line). Only liquid phases are taken under study because of missing data from the gas phase.

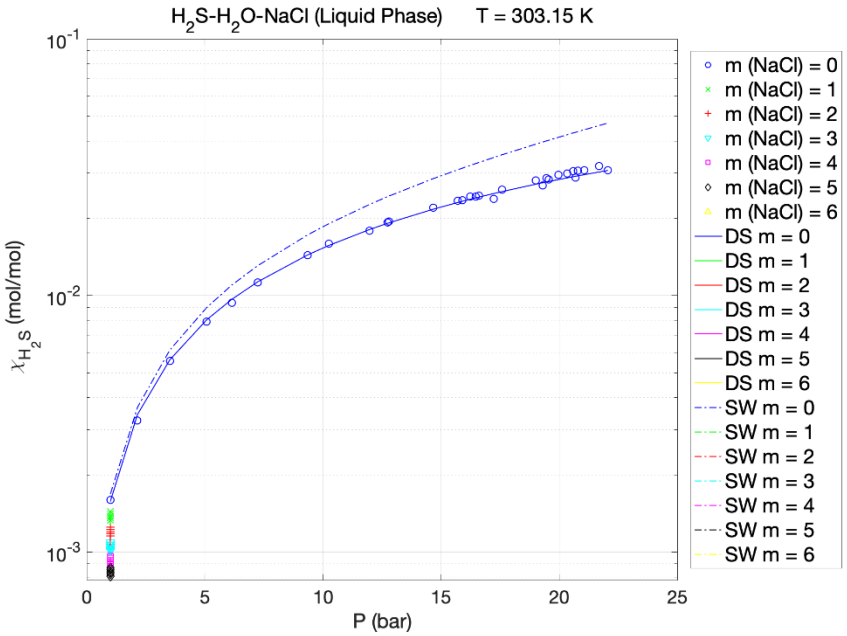

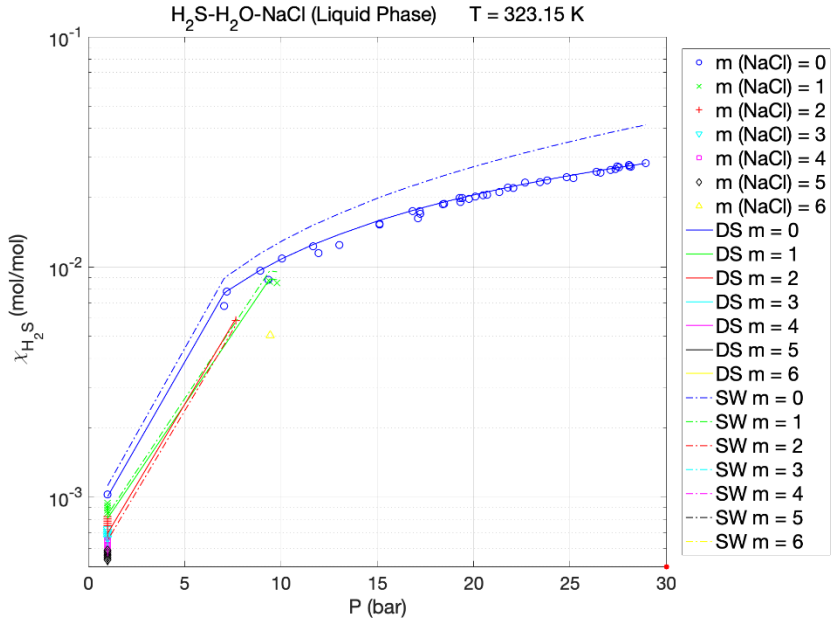
H2S-H2O-NaCl (Liquid Phase) T = 323.15 K
χH2S (mol/mol)
P (bar)
m (NaCl) = 0
m (NaCl) = 1
m (NaCl) = 2
m (NaCl) = 3
m (NaCl) = 4
m (NaCl) = 5
m (NaCl) = 6
DS m = 0
DS m = 1
DS m = 2
DS m = 3
DS m = 4
DS m = 5
DS m = 6
SW m = 0
SW m = 1
SW m = 2
SW m = 3
SW m = 4
SW m = 5
SW m = 6

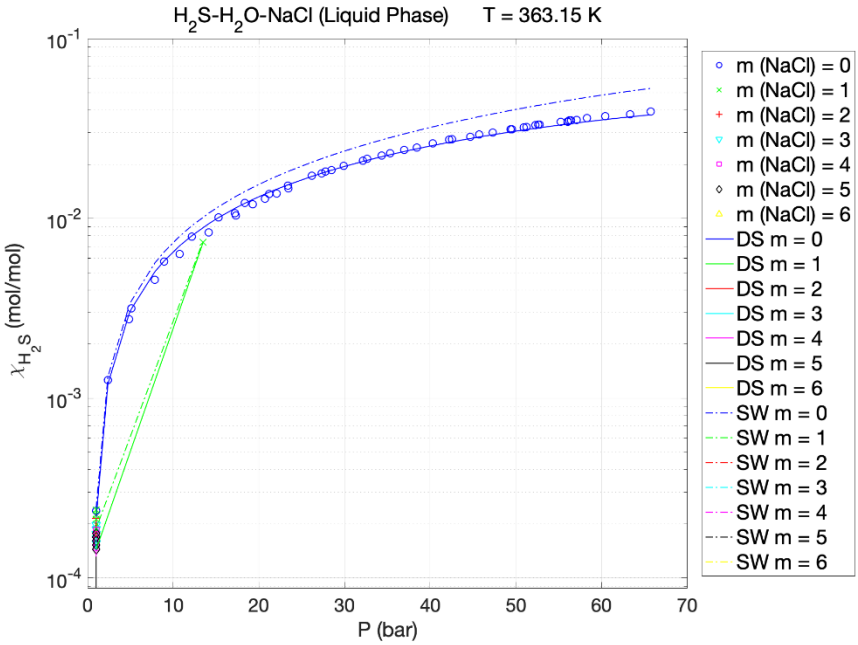
H2S-H2O-NaCl (Liquid Phase) T = 363.15 K
χH2S (mol/mol)
P (bar)
m (NaCl) = 0
m (NaCl) = 1
m (NaCl) = 2
m (NaCl) = 3
m (NaCl) = 4
m (NaCl) = 5
m (NaCl) = 6
DS m = 0
DS m = 1
DS m = 2
DS m = 3
DS m = 4
DS m = 5
DS m = 6
SW m = 0
SW m = 1
SW m = 2
SW m = 3
SW m = 4
SW m = 5
SW m = 6

Table 4. 24. The thermodynamics model SW and DS's average deviations with the experimental data of H_2S solubility from 283.15 to 489.15 K up to 30 bar and salt molalities from 1 to 6 mol/kg. The experimental data are referred to in Table 4.3.

T	P	NaCl (m)	Np		SW‡		DS‡	
[K]	[bar]	[mol/kg]	[-]		[%]		[%]	
			Liq.	Vap.	Liq.	Vap.	Liq.	Vap.
283.15	1.0	1.0-5.0	5	-	11.11	-	14.19	-
293.15	1.0	1.0-5.0	5	-	18.86	-	3.31	-
298.15	1.0	1.0-5.0	5	-	21.03	-	1.73	-
303.15	1.0	1.0-5.0	5	-	22.64	-	2.97	-
314.15	1.0-9.0	1.0-6.0	10	-	21.23	-	9.93	-
323.15	1.0	1.0-5.0	5	-	10.76	-	6.68	-
333.15	1.0	1.0-5.0	5	-	9.85	-	5.97	-
343.15	1.0	1.0-5.0	5	-	22.39	-	5.29	-
353.15	1.0	1.0-5.0	5	-	20.44	-	7.82	-
363.15	1.0	1.0-5.0	5	-	16.72	-	23.61	-
428.45	11-14	0.5-2.4	13	8	10.98	0.01	2.83	0.07
489.45	27-28	1.2-2.0	12	8	8.69	0.21	21.00	-7.11

Liq. : Liquid phase; Vap. : vapour phase; T: temperature of the system; P range: pressure range of this work; m(NaCl): salt molalities; Np: number of experimental points. The symbol (‡) indicates that the value in the table has been obtained, performing the average of the relative deviations over the corresponding number of points.

The model CPA, PRH and SPR have not been analyzed because the salt packages were not implemented in the softwares.

Figure 4. 38. Group 2: The solubility of H_2S in NaCl aqueous solutions at 303.15 K, 323.15 K and 363.15 K up to 9 bar and salt molalities range *1-6* m. This study is made with the thermodynamic model OLI AQ (solid lines). The blue colour is for the liquid/aqueous phase. The experimental data are referred to in Table 4.3.

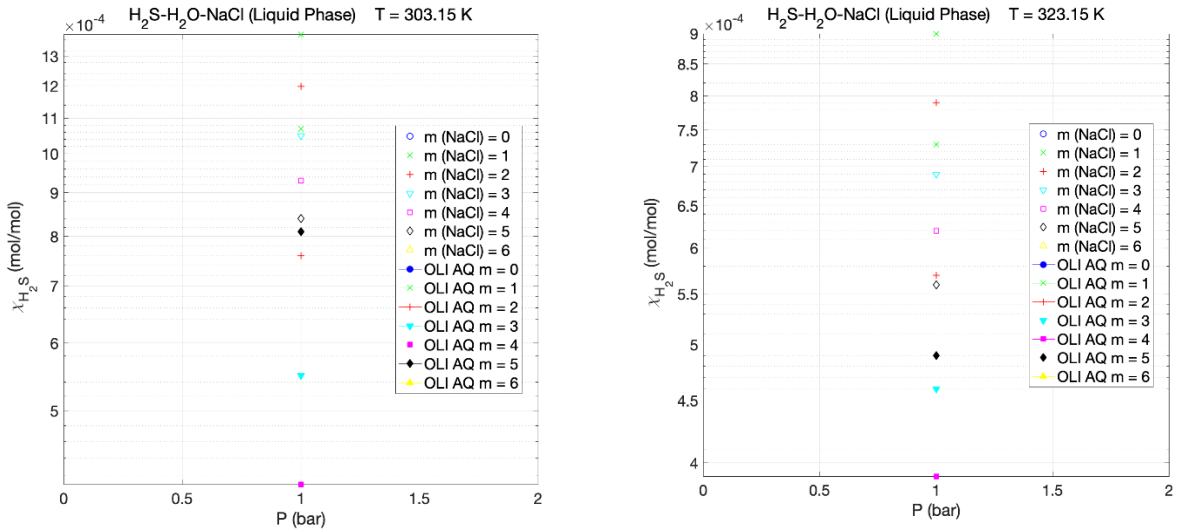

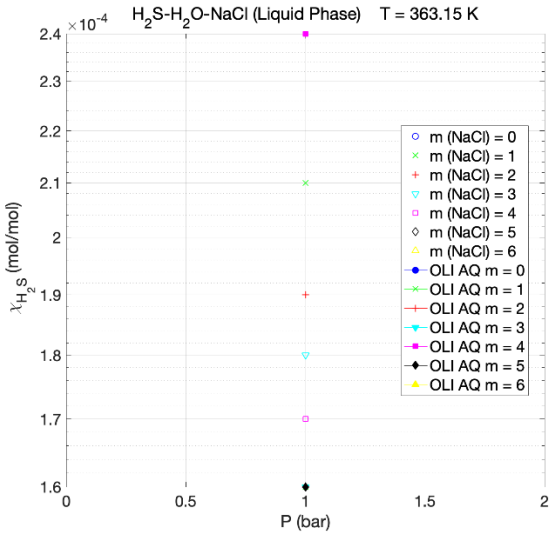

Figure 4. 39. The solubility of H_2S in NaCl aqueous solutions at 303.15 K, 323.15 K and 363.15K and up to 9 bar and salt molalities range 1-6 m. This study is made with the thermodynamic model OLI MSE (solid lines). The blue colour is for the liquid/aqueous phase. The experimental data are referred to in Table 4.3.

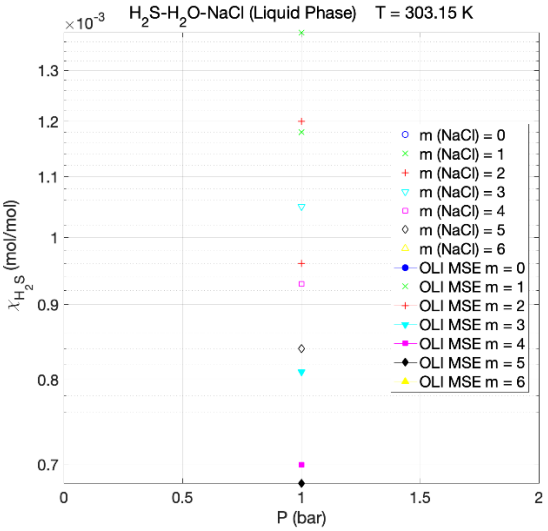

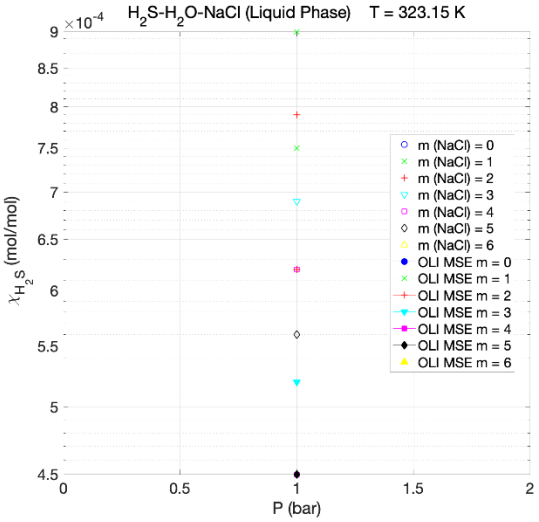

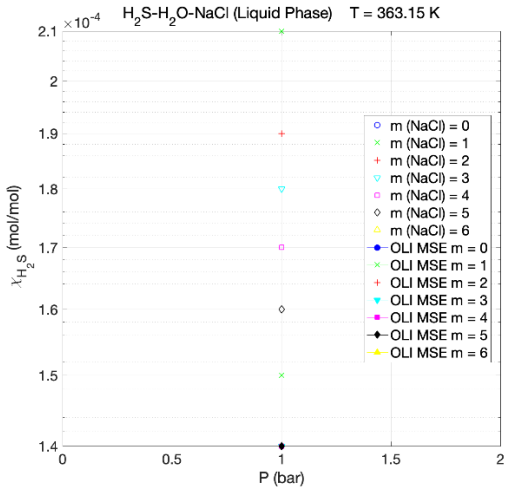

Figure 4. 40. The solubility of H_2S in NaCl aqueous solutions at 303.15 K, 323.15 K and 363.15 K and up to 9 bar and salt molalities range 1-6 m. This study is made with the thermodynamic model OLI MSE SRK (solid lines). The blue colour is for the liquid/aqueous phase. The experimental data are referred to in Table 4.3.

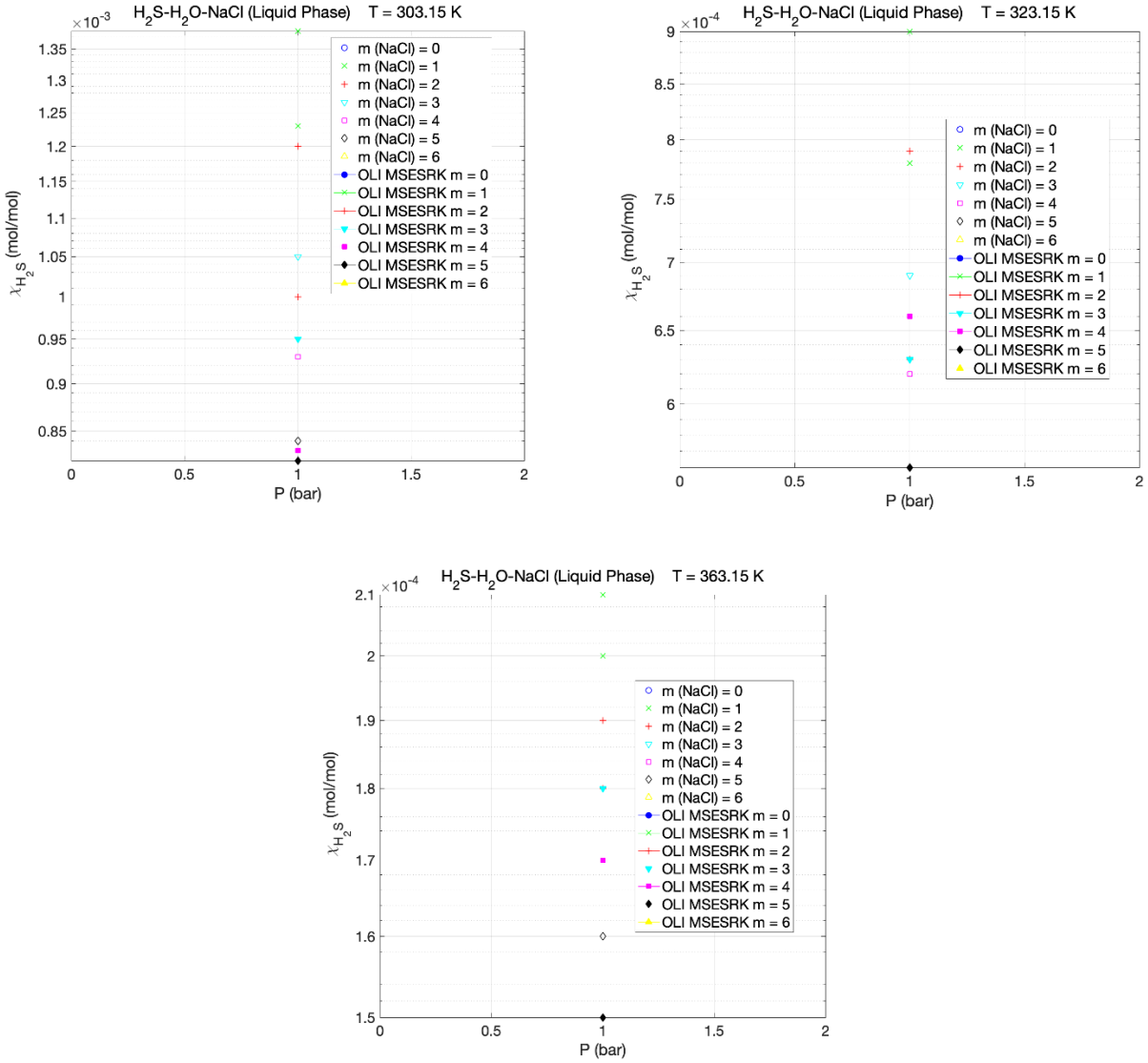

Table 4. 25. The average deviations of the thermodynamics models OLI AQ, OLI MSE and OLI MSE SRK outcomes with the experimental data of H_2S solubility from 283.15 to 489.15 K up to 30 bar and salt molalities from 1 to 6 mol/kg.

T	P	NaCl (m)	Np		OLI AQ‡		OLI MSE‡		OLI MSE SRK‡	
[K]	[bar]	[mol/kg]	[-]		[%]		[%]		[%]	
			Liq.	Vap.	Liq.	Vap.	Liq.	Vap.	Liq.	Vap
283.15	1	1-5	5	-	21.12	-	9.62	-	3.84	-
293.15	1	1-5	5	-	22.43	-	13.37	-	11.56	-
298.15	1	1-5	5	-	33.94	-	16.33	-	8.69	-
303.15	1	1-5	5	-	33.33	-	18.58	-	9.98	-
314.15	1-9	1-6	10	-	25.90	-	16.07	-	7.83	-
323.15	1	1-5	5	-	25.95	-	20.82	-	9.86	-
333.15	1	1-5	5	-	22.20	-	20.92	-	4.23	-
343.15	1	1-5	5	-	15.69	-	17.22	-	5.54	-
353.15	1	1-5	5	-	11.44	-	18.44	-	3.28	-
363.15	1	1-5	5	-	18.31	-	19.63	-	5.79	-
428.45	11-14	1-4	13	8	9.77	0.23	9.77	1.72	1.14	0.23
489.45	27-28	1-2	12	8	7.19	-4.02	7.19	-4.02	3.52	0.11

Liq. : Liquid phase; Vap. : vapour phase; T: temperature of the system; P range: pressure range of this work; m(NaCl): salt molalities; Np: number of experimental points. The symbol (‡) indicates that the value in the table has been obtained, performing the average of the relative deviations over the corresponding number of point.

Table 4. 26. Table summarizing the best model performance in terms of the average of the relative deviation for the H_2O-H2S and H_2O-H2S -NaCl mixture

m (NaCl)	T	P range	Np		Best average relative deviation [%]	
[mol/kg]	[K]	[bar]	Liq.	Vap.	Liq.	Vap.
0	283.15	1	42	6	0.027 [SW]	-
0	303.15	1-10	35	5	0.631 [SPR]	0.06 [PRH]
0	323.15	1-20	42	6	0.098 [CPA]	0.093 [PRH - OLI MSE SRK]
0	344.15	1-50	55	28	0.493 [CPA]	0.03 [SPR, OLI AQ]
0	363.15	1-50	60	18	0.44 [DS]	0.29 [OLI MSE SRK]
0	393.15	1-200	40	7	0.43 [DS]	0.95 [DS]
0	423.15	1-210	44	14	1.81 [DS]	1.12 [OLI MSE-SRK]
0	453.15	1-100	18	-	0.698 [OLI MSE-SRK]	-
1.0-5.0	283.15	1.0	5	-	3.84 [OLI MSE-SRK]	-
1.0-5.0	293.15	1.0	5	-	3.31[DS]	-
1.0-5.0	298.15	1.0	5	-	1.73 [DS]	-
1.0-5.0	303.15	1.0	5	-	2.97 [DS]	-
1.0-6.0	314.15	1.0-9.0	10	-	7.83 [OLI MSE-SRK]	-
1.0-5.0	323.15	1.0	5	-	6.68[DS]	-
1.0-5.0	333.15	1.0	5	-	4.23 [OLI MSE-SRK]	-
1.0-5.0	343.15	1.0	5	-	5.29 [DS]	-
1.0-5.0	353.15	1.0	5	-	3.28 [OLI MSE-SRK]	-
1.0-5.0	363.15	1.0	5	-	5.79 [OLI MSE-SRK]	-
0.5-2.4	428.45	11-14	13	8	1.14 [OLI MSE-SRK]	0.01 [SW]
1.2-2.0	489.45	27-28	12	8	3.52 [OLI MSE-SRK]	0.11 [OLI MSE-SRK]

The models employed for the H_2S-H_2O mixtures are the following: SW, DS, PRH, SPR, CPA, OLI AQ and OLI MSE models. Particularly, at the temperature of 283.15 K and 1 bar, SW and DS have an average deviation of less than 1%, while PRH is around 11%, CPA presents 5% of average deviation, SPR and the three OLI models are roughly 3%. At temperatures of 303.15 K and pressures of 1-25 bar, the best relative average deviations are those of OLI AQ (1.3%) and SPR (<1%). On the other hand, for temperature ranges from 323.15 to 454.15 K and for pressures up to 200 bar, the suitable thermodynamic models are CPA, SPR, OLI AQ and OLI MSE.

The mixture of H_2S-H_2O-NaCl shows quite different results than the solubility of CO_2 in saltwater previously discussed in section 4.2.1. Only two models give optimal results compared to the experimental data: the DS and OLI MSE-SRK. For the temperature range from 283.15 to 489.15 K, pressures from 1 to 28 bar and molality of the NaCl salt from 1 to 6, the relative average deviations for SW show a minimum value of 8.69% (T = 489.45 K, and P = 27-28 bar) and a maximum value of 22.64% (T = 303.15 K, P = 1 bar), while for DS model the results have a relative average deviation around 10% with a minimum value of 1.73% (T = 298.15 K, P = 1 bar) and a maximum value of 23.61% (T = 363.15 K and P = 1 bar). The other models show a non-consistent relative average deviation for each temperature and pressure due to an inadequate amount of experimental data. Only the OLI MSE-SRK model can be competitive with the DS model because it has a minimum for medium-high temperatures and a higher deviation for lower temperatures.

4.2.3 CH_4-H_2O and CH_4-H_2O in brine

The solubilities experimental data of CH_4 in the water at different combinations of temperature (273.15 K – 473.15 K) and pressures (1 bar – 200 bar) are reported in Annex 4.C. The EoS approaches used to determine the methane solubility in pure water and brines are DS, SW, CPA, PRH, SPR, and OLI models.

Many available experimental data are collected for the mixture (CH_4-H_2O) system, such as liquid and vapour phases. A three-dimensional plot of the experimental pressure-temperature-solubility (PTx) data is shown in section 4.1.3. The temperature and pressure ranges are 0-200 °C and 1-200 bar, respectively. For simplicity, group models are defined to show the results of the methane solubilities compared with experimental data. Group 1 is inherent to the comparison of SW, DS, and PRH models with experimental data. Group 2 compares CPA and SPR models with experimental data, and group 3 is inherent in comparing OLI models with experimental data.

Figure 4. 41. Group 1*:* C*H*$_4$-H_2O binary system: Calculation of CH_4 solubility in water at *298.*15 K, 3*23.*15 K, 373.15 K and 473.15 K by DS (solid line), SW (stroke and point line) and PRH (dashed line). The blue colour is for the aqueous state. All experimental data are referred to in *Table 4.5*.

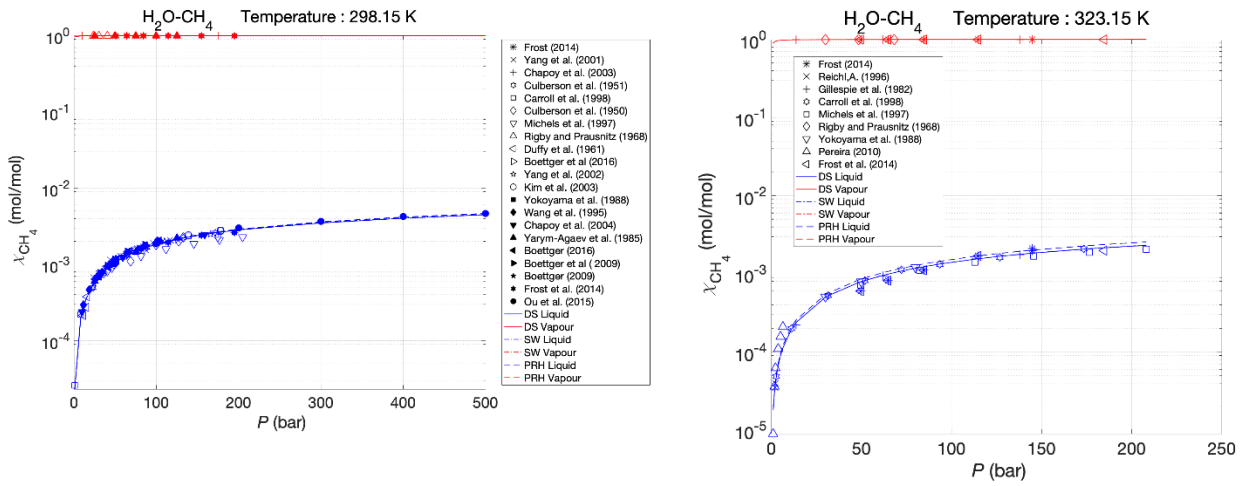

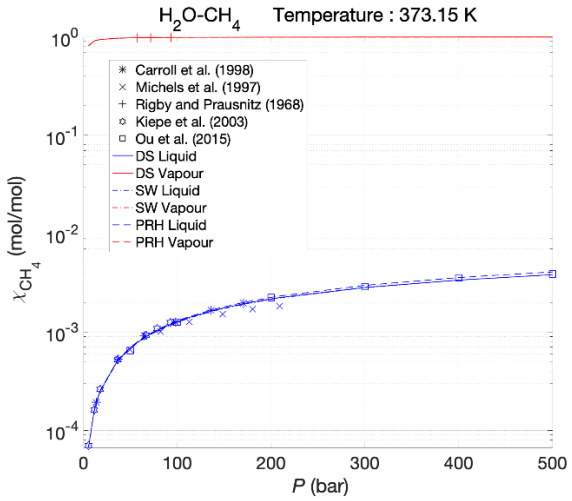

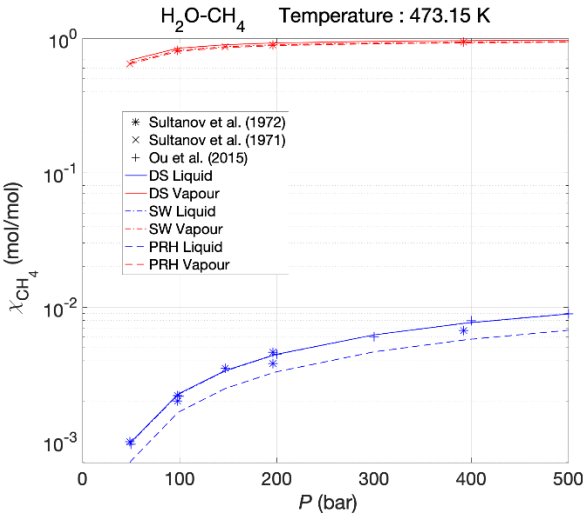

Table 4. 27. Group *1*: SW, DS and SPR absolute deviations liquid and vapour from 273.15 to 473.15 K up to 200 bar.

T	P	Np		SW‡		DS‡		PRH‡	
[K]	[bar]	[-]		[%]		[%]		[%]	
		Liq.	Vap.	Liq.	Vap.	Liq.	Vap.	Liq.	Vap.
273.15	1-200	12	6	16.42	28.2	9.51	28.1	12.20	28.3
293.15	1-200	15	13	-2.92	0.0001	-7.24	-0.03	-4.46	-0.004
298.15	1-200	100	21	-1.36	0.02	-8.97	-0.13	-0.52	0.018
323.15	1-200	28	13	2.77	0.05	9.08	-1.88	11.21	0.05
344.15	1-200	3	7	0.62	-0.13	9.40	-0.75	9.04	-0.13
373.15	1-200	20	6	0.59	-0.05	6.94	0.44	3.91	-0.08
393.15	1-200	8	3	-0.32	-	1.53	-	-2.11	-
423.15	1-200	15	10	-0.526	1.36	6.96	3.30	-12.10	0.91
473.15	1-200	14	8	2.317	0.39	31.97	9.54	-24.31	-1.31

Liq. : Liquid phase; Vap. : vapour phase; T: temperature of the system; P range: pressure range of this work; Np: number of experimental data points. The symbol (‡) indicates that the value in the table has been obtained, performing the average of the relative deviations over the corresponding number of points.

Figure 4. 42. Group 2: CH_4-H_2O binary system: Calculation of CH_4 solubility in water at 298.15 K, 323.15 K, 373.15 K and 473.15 K by CPA (solid line) and SPR (dashed line). The blue colour is for the aqueous state. All experimental data are referred to in *Table 4.5*.

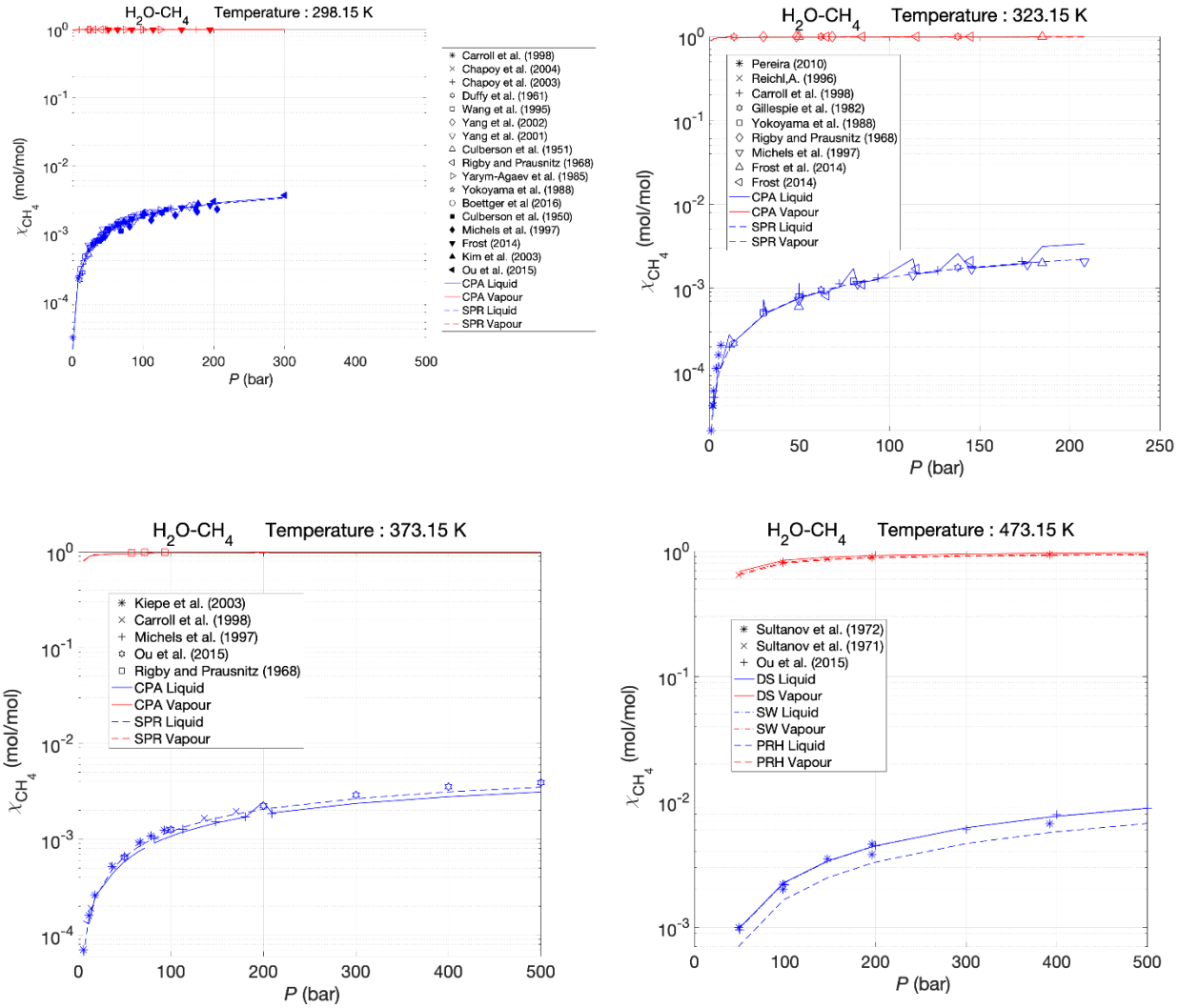

Table 4. 28. Group 2: CPA and SPR absolute deviations liquid and vapour from 273.15 to 473.15 K up to 200 bar.

Temperature	Pressure range	Np		CPA‡		SPR‡	
[K]	[bar]	[-]		[%]		[%]	
		Liq.	Vap.	Liquid	Vapour	Liquid	Vapour
273.15	1-200	12	6	-5.01	-1.98	-28.87	-2.25
293.15	1-200	15	13	-10.96	-0.61	-4.99	-1.00
298.15	1-200	100	21	-3.62	0.034	-2.46	0.02
323.15	1-200	28	13	7.48	-1.12	-6.77	-1.95
344.15	1-200	3	7	-7.51	-1.26	-3.97	-2.11
373.15	1-200	20	6	-2.17	-2.02	-3.80	-2.02
393.15	1-200	8	3	15.98	-	-9.90	-
423.15	1-200	15	10	-4.82	-0.05	-15.14	-0.15
473.15	1-200	14	8	2.71	1.45	-83.69	4.17

Liq. : Liquid phase; Vap. : vapour phase; T: temperature of the system; P range: pressure range of this work; Np: number of experimental data points. The symbol (‡) indicates that the value in the table has been obtained, performing the average of the relative deviations over the corresponding number of points.

Figure 4. 43. Group 3: CH_4-H_2O binary system: Calculation of CH_4 solubility in water at 298.15 K, 323.15 K, 373.15 K and 473.15 K by OLI AQ(stroke and point line), OLI MSE (solid line) and OLI MSE-SRK (dashed line). The blue colour is for the aqueous state. All experimental data are referred to in *Table 4.5*.

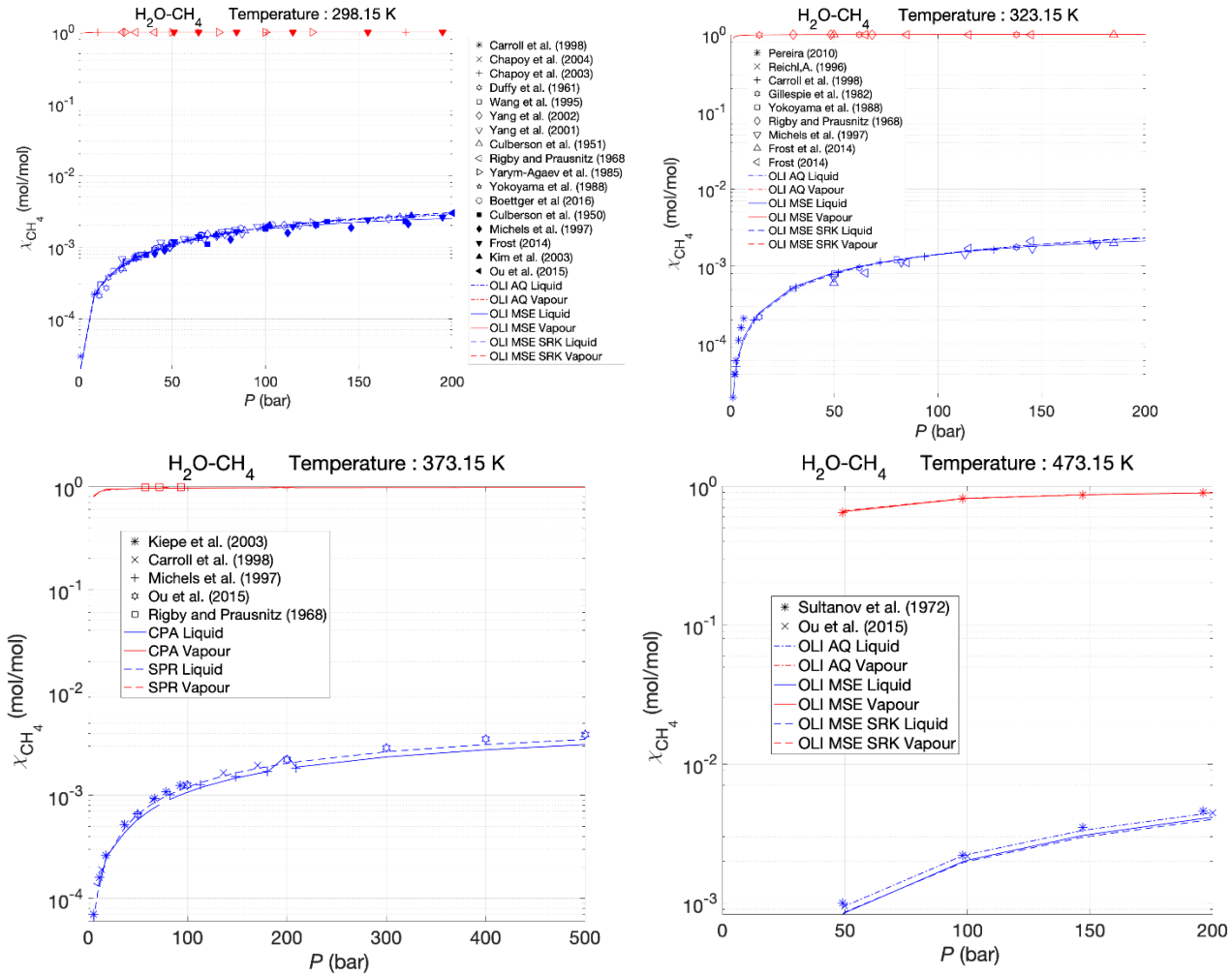

Table 4. 29. Group 3: OLI AQ, OLI MSE and OLI MSE SRK absolute deviations liquid and vapour from 273.15 to 473.15 K up to 200 bar.

Temperature	Pressure range	Np		OLI AQ‡		OLI MSE‡		OLI MSE SRK‡	
[K]	[bar]	[-]		[%]		[%]		[%]	
		Liq.	Vap.	Liq.	Vap.	Liq.	Vap.	Liq.	Vap.
273.15	1-200	12	6	19.73	-0.001	17.96	-0.001	18.30	-0.001
293.15	1-200	15	13	0.18	-0.005	-4.69	-0.005	-1.14	-0.005
298.15	1-200	100	21	2.322	0.02	16.72	0.02	1.31	0.02
323.15	1-200	28	13	-0.68	0.04	-1.61	0.03	-2.28	0.03
344.15	1-200	3	7	2.25	-0.12	3.32	-0.13	-1.24	-0.13
373.15	1-200	20	6	2.33	-0.02	1.46	-0.06	-1.51	-0.06
423.15	1-200	8	3	-3.96	2.09	-8.56	1.96	-10.41	2.10
473.15	1-200	15	10	-2.11	0.14	-10.84	0.18	-12.44	0.68

Liq. : Liquid phase; Vap. : vapour phase; T: temperature of the system; P range: pressure range of this work; m(NaCl): salt molalities; Np: number of experimental points. The symbol (‡) indicates that the value in the table has been obtained, performing the average of the relative deviations over the corresponding number of points.

The following figures show the results of the employed EoS approach to model the methane solubilities with water and NaCl. Particularly, Group 1 shows the results of the DS and SW models, and Group 2 provides the results coming from OLI packages.

Figure 4. 44. Group 1: CH_4 solubility in aqueous NaCl solutions at 298.15 K, 333.15 K and 373.15 K . Model predictions: DS (solid line), SW (stroke and point line). The colours represent the salt molality: green (1 m), red (2 m), light blue (3 m), pink (4 m), black (5 m) and yellow (6 m). All experimental data are referred to in *Table 4.6*.

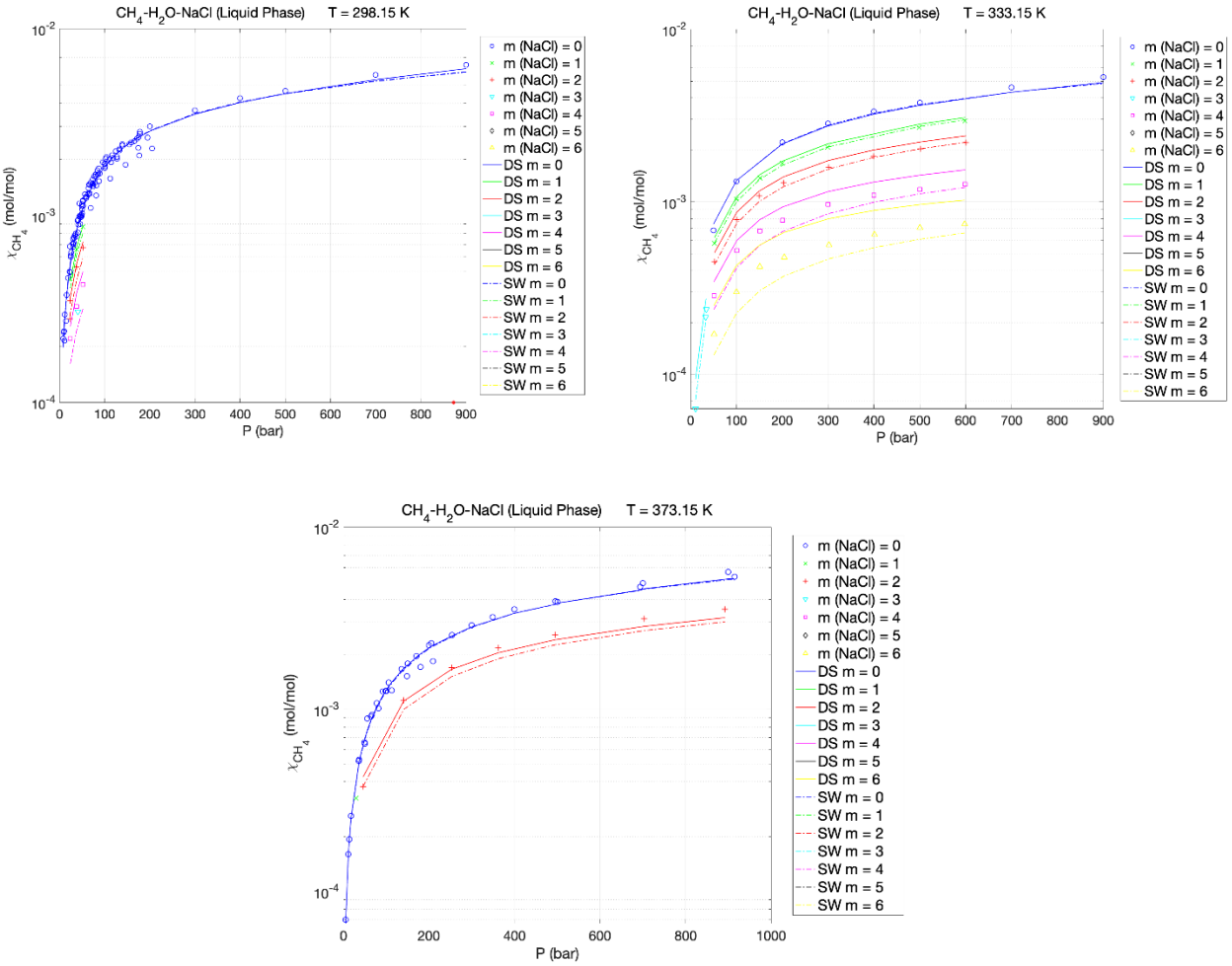

Table 4. 30*:* Group 1:SW and DS absolute deviations liquid and vapour from 298.15 to 373.15 K up to 1000 bar and salt molalities range from 1 to 6 m.

T	P	NaCl (m)	Np		SW Average deviation		DS Average deviation	
[K]	[bar]	[mol/kg]	[-]		[%]		[%]	
			Liq.	Vap.	Liq.	Vap.	Liq.	Vap.
298.15	1-900	1.0	15	-	13.33	-	2.22	-
333.15	1-900	1.0-6.0	33	-	9.33	-	15.12	-
374.15	1-1000	1.9- 5.8	30	-	15.19	-	8.69	-

Figure 4. 45. CH_4 solubility in aqueous NaCl solutions at 298.15 K (a), 333.15 K (b) and 374.15 K (c). The model prediction is OLI AQ (solid line). The colours represent the salt molality: green (1m), red (2 m), light blue (3 m), pink (4 m), black (5 m) and yellow (6 m). All experimental data are referred to in *Table 4.6*.

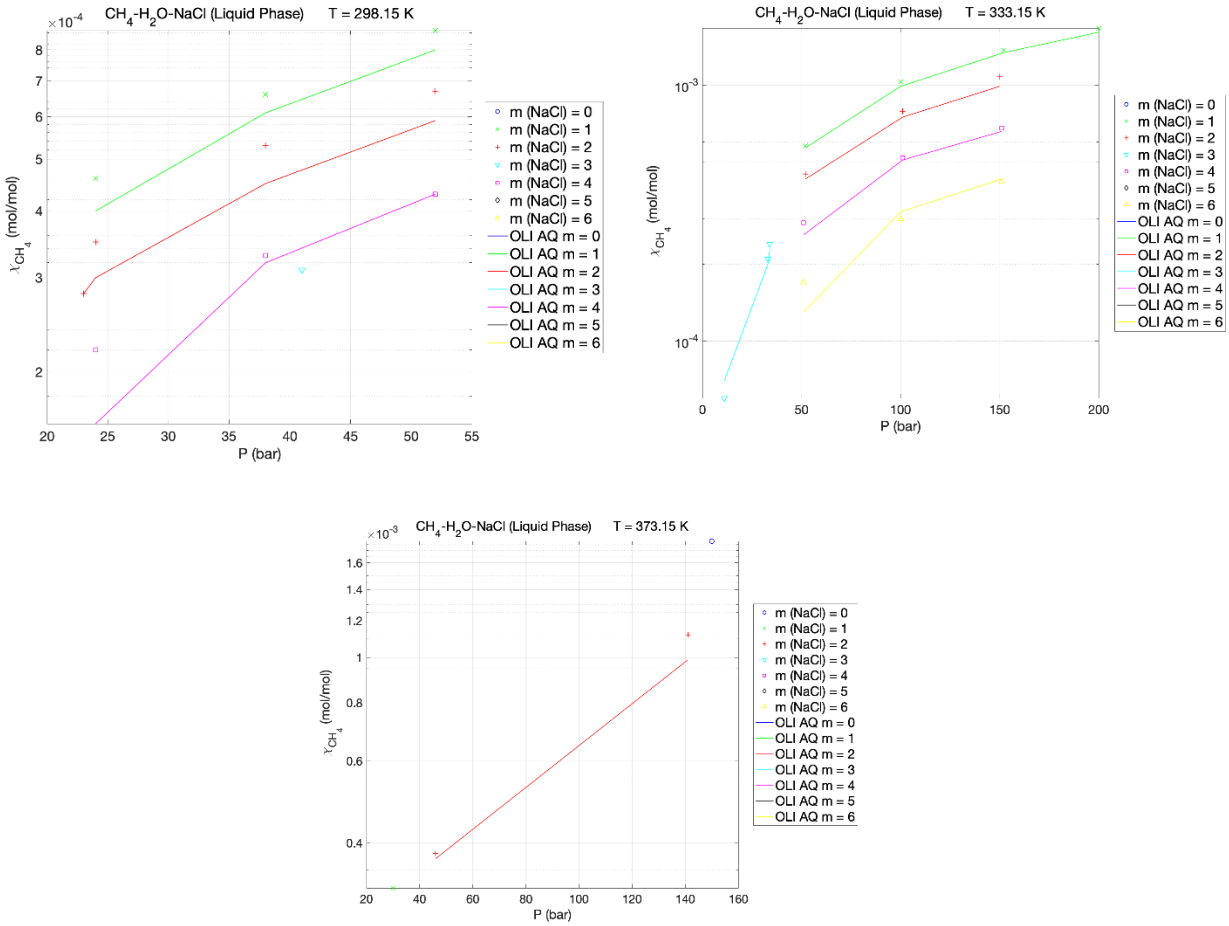

Figure 4. 46. CH_4 solubility in aqueous NaCl solutions at 298.15 K (a), 333.15 K (b) and 374.15 K (c). The model prediction is OLI MSE (solid line). The colours represent the salt molality: green (1m), red (2 m), light blue (3 m), pink (4 m), black (5 m) and yellow (6 m). All experimental data are referred to in *Table 4.6*.

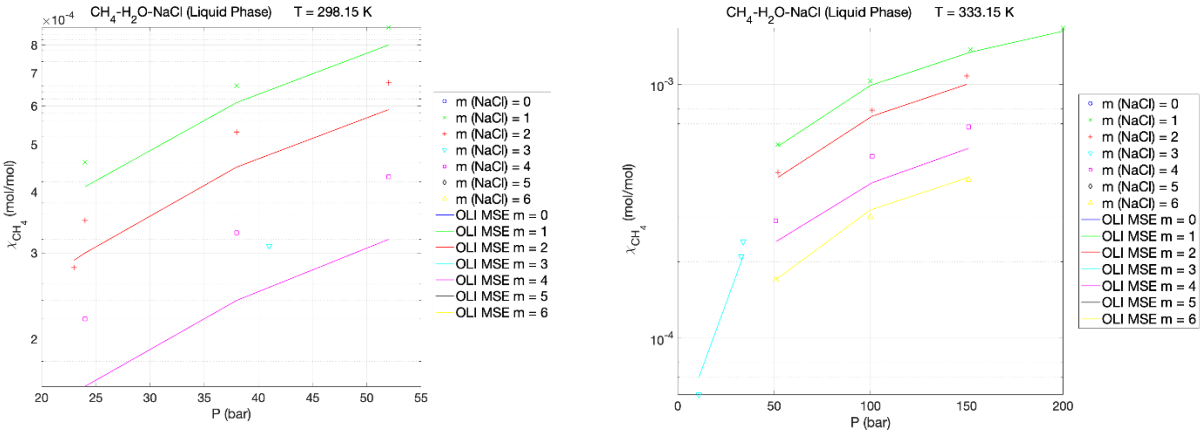

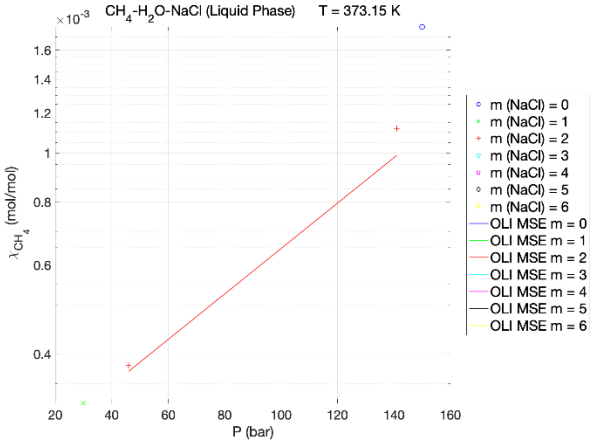

Figure 4. 47. CH_4 solubility in aqueous NaCl solutions at 298.15 K (a), 333.15 K (b) and 374.15 K (c). The model prediction is OLI MSE SRK (solid line). The colours represent the salt molality: green (1m), red (2 m), light blue (3 m), pink (4 m), black (5 m) and yellow (6 m). All experimental data are referred to in *Table 4.6*.

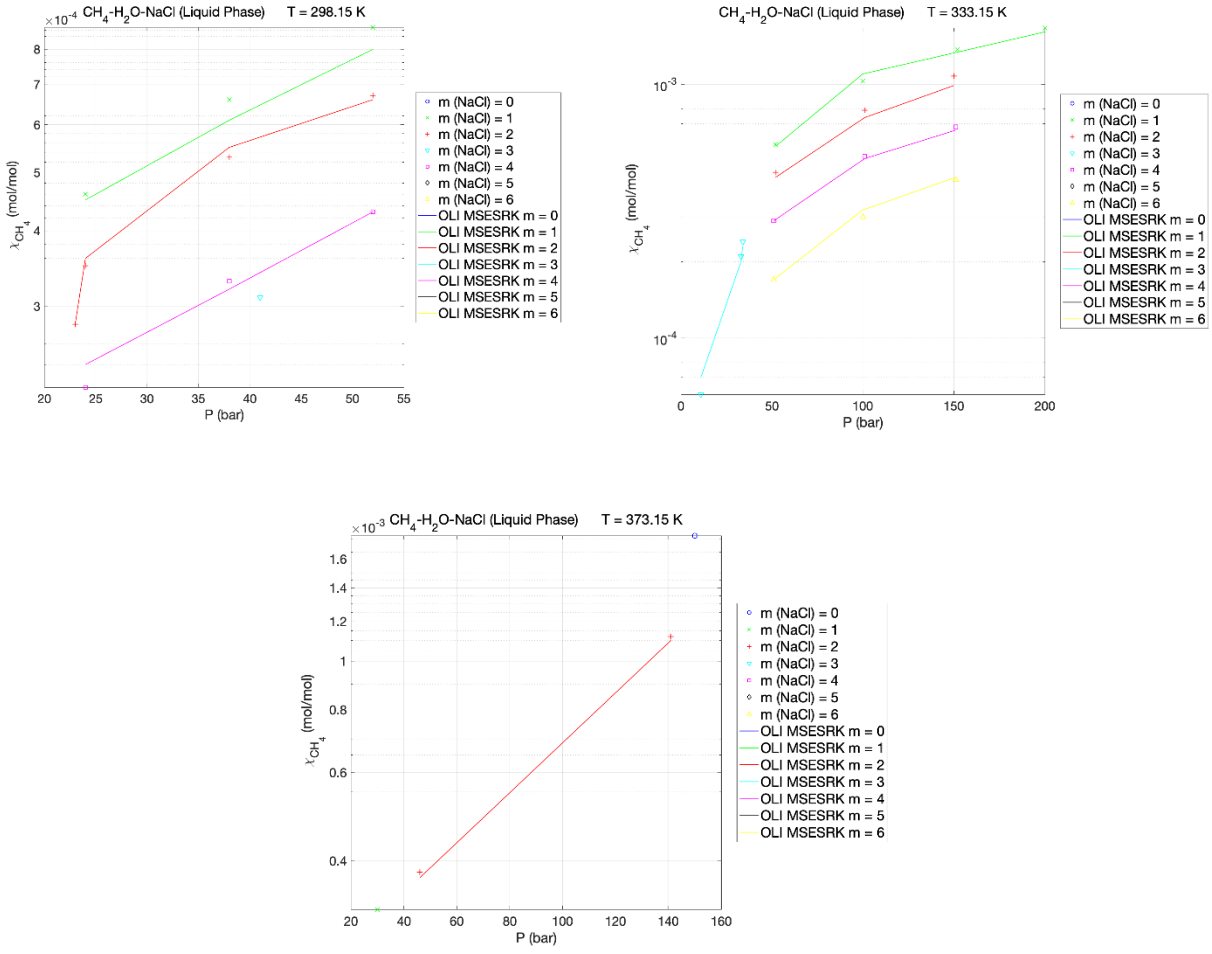

Table 4. 31 Group 2: OLI AQ, OLI MSE and OLI MSE SRK absolute deviations liquid and vapour from 273.15 to 473.15 K up to 200 bar.

T	P range	Np		OLI AQ‡		OLI MSE‡		OLI MSE SRK‡	
[K]	[bar]	[-]		[%]		[%]		[%]	
		Liq.	Vap.	Liq.	Vap.	Liq.	Vap.	Liq.	Vap.
298.15	1-52	15	-	7.68	-	9.91	-	4.31	-
333.15	1-200	33	-	7.27	-	8.14	-	3.42	-
374.15	1-160	30	-	8.25	-	13.25	-	4.12	-

Liq. : Liquid phase; Vap. : vapour phase; T: temperature of the system; P range: pressure range of this work; m(NaCl): salt molalities; Np: number of experimental points. The symbol (‡) indicates that the value in the table has been obtained, performing the average of the relative deviations over the corresponding number of points.

Table 4. 32. Table summarizing the best model performance in terms of the average of the relative deviation for the H_2O-CH_4 and H_2O-CH_4 -NaCl mixture

m (NaCl)	T	P range	Np		Best average relative deviation [%]	
[mol/kg]	[K]	[bar]	Liq.	Vap.	Liq.	Vap.
0	273.15	1-200	12	6	5.01 [CPA]	0.001[OLI MSE]
0	293.15	1-200	15	13	0.18 [OLI AQ]	0.001 [OLI AQ]
0	298.15	1-200	100	21	1.31[OLI MSE SRK]	0.02 [OLI MSE SRK]
0	323.15	1-200	28	13	0.68 [OLI AQ]	0.03 [OLI MSE SRK]
0	344.15	1-200	3	7	1.24 [OLI MSE SRK]	0.12 [OLI MSE SRK]
0	373.15	1-200	20	6	1.46 [OLI MSE]	0.06[OLI MSE]
0	393.15	1-200	8	3	8.56[OLI MSE]	1.96[OLI MSE]
0	423.15	1-200	15	10	3.96 [OLI AQ]	0.05 [CPA]
0	473.15	1-200	14	8	2.11[OLI AQ]	0.14 [OLI AQ]
1.0	298.15	1-900	15		2.22 [DS]	
1.0-6.0	333.15	1-900	33		3.42 [OLI MSE-SRK]	
1.9- 5.8	374.15	1-1000	30		4.12 [OLI MSE-SRK]	

Different models are proposed to calculate the compositions of CH_4 in water and the presence of salt. Using the experimental data and a theoretical approach, the best models that predict methane solubility in the liquid phase from 273.15 to 473.15 K and from 1 to 200 bar are OLI MSE-SRK, OLI MSE, OLI AQ. In particular, at low temperature (≈ 273 K), CPA has an average deviation of 5%, while from 298.15 to 473.15 K, the models OLI AQ and OLI MSE have an average deviation less of 4% at the exception of 8.56 % at 393.15 K. Different consideration are with the presence of NaCl in which the best models are DS and OLI MSE-SRK, all with an average deviation less of ≈4%.

4.3 Mixing enthalpies analyses

The purpose of this section is:

1. To compare the mixing enthalpy experimental data with the different thermodynamic models previously used in the determination of gas solubility in pure water and a salt solution;
2. To define the thermodynamic influence in various geothermal systems, particularly in an electrolyte presence in a wide range of pressure and temperature.

The same methodology of calculating the mixing enthalpy is applied for all the geothermal components (CO_2, H_2S and CH_4) in pure water and NaCl solutions. The calculation of the ΔH_{mix} is developed according to the scheme shown in Figure 4.48. The three OLI thermodynamic packages are included in the Unisim Design R480 process software. The same option can be developed with OLI Studio v.10 - Stream Analyzer.
Firstly, as shown in section (a) of Figure 4.48, the solubilities (x_i^{eq}) for all the mixtures CO_2-H_2O, CO_2-H_2O-NaCl, H_2S-H_2O, H_2S-H_2O-NaCl, CH_4-H_2O and, CH_4-H_2O-NaCl are calculated. Subsequently, as shown in section (b), it is possible to calculate the enthalpies as described in the following steps:

1. Calculation of the enthalpy of formation (H_i) regarding pure components using unitary molar flow for the mixture under analysis. The subscript (i) indicates the single components: CO_2, H_2S, CH_4, NaCl.
2. Calculation of the total enthalpy ($H_{j\text{-}H2O\text{-}NaCl}$) of the mixture, where the subscript (j) represents one of the following components: CO_2, H_2S, CH_4.
3. Calculation of the mixing enthalpy (ΔH_{mix}) using the following equation (in the general case):

$$\Delta H\ (T, P,\ m_{salt}) = H_{CO2-H2O-NaCl}\ -\ H_{CO2} \cdot x_{co2}\ -\ H_{H2O} \cdot x_{H2O}\ -\ H_{NaCl} \cdot x_{NaCl} \tag{4.11}$$

Figure 4. 48. Methodology for calculating mixing enthalpy (ΔH_{mix}) in Unisim® Design R480 with OLI System thermodynamic packages compared to the experimental data. Section (a) of Figure 4.48 shows the workflow of the solubility calculation (x_i^{eq}) for the mixture under study, and in section (b) the calculation of enthalpies for each component system (CO_2, H_2S, CH_4 – H2O – NaCl).

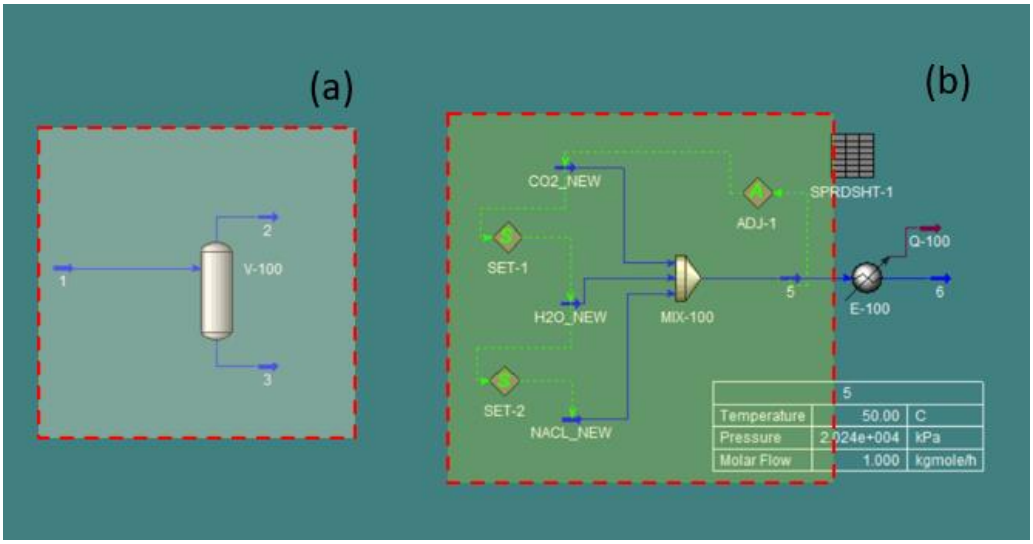

The same methodology uses OLI Studio v.10 Stream Analyzer with the three thermodynamic packages (AQ, MSE and MSE-SRK models). Figure 4.49 describes the procedure to calculate the mixing enthalpy using OLI Studio:

Figure 4. 49*:* Methodology for calculating mixing enthalpy (ΔH_{mix}) in OLI Studio version 10 using the thermodynamic packages as OLI AQ, OLI MSE and OLI MSE-SRK

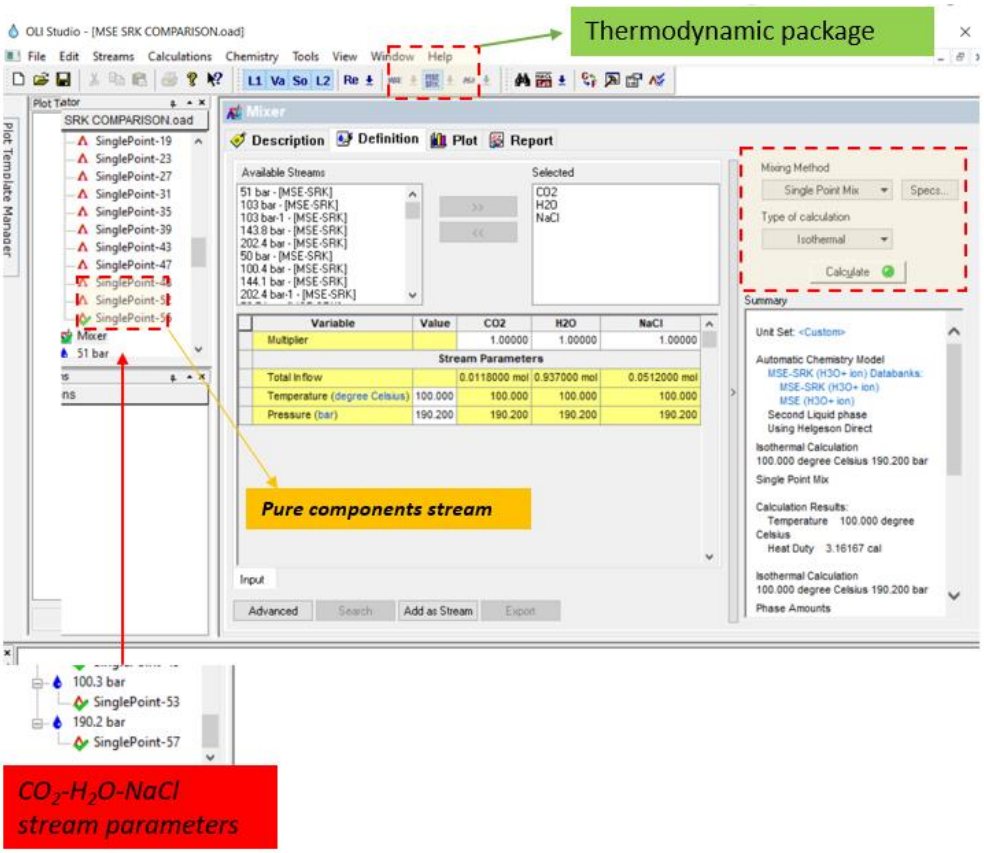

The steps to perform the calculation of the mixing enthalpy (ΔH_{mix}) are the following:

1. Create three different streams (CO_2, H_2O and NaCl) as pure components by inserting:
   a. Total flow (moles);
   b. Temperatures (°C);
   c. Pressure (bar);
   d. Molar percentage (%) of the component.
2. Create a mixer under the same conditions as temperature, pressure and check the compositions of the components in the mixer;
3. Generate the outgoing stream from the mixer under the conditions T, P and molalities.

Under the specified conditions (T, P and molalities) of the created streams, the software generates a report and takes the respective enthalpies values. Subsequently, the mixing enthalpy is calculated using equation 4.11. The same methodology explained in this section is applicable for calculating ΔH_{mix} for the DS model for all the geothermal mixtures with and without salts. However, regarding the CPA and SPR model, the ΔH_{mix} is possible only for pure water mixtures because the salts interactions are not implemented in the Unisim software. Finally, the SW and PRH models are not used to estimate the ΔH_{mix} in the most recent code versions because they do not have the implemented subroutines to perform such a calculation. The relative deviations of the model results from the experimental data are computed using the following equation:

$$\Delta H_{AD}\ (\%) = \frac{\Delta H_{model} - \Delta H_{EXP}}{\Delta H_{EXP}} \cdot 100 \qquad (4.12)$$

4.3.1 CO_2-H_2O and CO_2-H_2O in brine

The results of the mixing enthalpies coming from the thermodynamic models are shown in the following tables. For simplicity, the results are divided into two subsets, considering the presence of salts as the main difference between them. The first subset shows the results of the mixing enthalpies of CO_2 in pure water, and it is divided into two groups: Group 1 includes DS, CPA, and SPR models, while Group 2 assess the performance of the OLI packages. For the second subset, the CO_2 mixing enthalpy is studied in water and NaCl. Particularly, Group 1 contains only the results provided by the DS model, and Group 2 shows the performance of the OLI packages. Finally, the mixing enthalpies are calculated at the equilibrium point (x_i^{eq}) for each specific temperature and pressure for all the mixtures CO_2-H_2O and CO_2-H_2O-NaCl.

Table 4. 33. Group 1: Enthalpies of mixing ΔH_{mix} of CO_2 in water calculated with DS, CPA and SPR. All experimental data are referred to in Table 4.9.

N.	Temperature [K]	Pressure [bar]	CO_2 [mol/mol]	ΔH mix‡ [J/mol]	DS† [J/mol]	CPA† [J/mol]	SPR† [J/mol]
1	308.15	75.40	0.022	-220.89	-258.16	-251.76	-239.46
2	323.15	20.33	0.007	-90.01	-92.67	-92.01	-91.45
3	323.15	50.33	0.015	-177.17	-172.98	-176.88	-177.01
4	323.15	103.92	0.021	-139.98	-153.29	-139.01	-138.97
5	323.15	140.14	0.022	-108.25	-106.96	-108.76	-108.30
6	323.15	148.00	0.022	-110.78	-103.21	-111.34	-110.64
7	373.1	49.84	0.009	-45.74	-53.32	-47.31	-47.21
8	373.1	99.48	0.015	-59.58	-64.68	--58.74	-59.32
9	373.1	192.45	0.021	-22.1	-19.64	-21.97	-22.01
10	373.1	199.36	0.021	-98.9	-15.75	-98.21	-98.81
11	523.15	122.40	0.016	218.2	188.68	215.34	219.65
12	523.15	148.00	0.020	282.27	264.92	288.21	287.03

ΔH mix is in Liquid-phase; T: temperature of the system; P range: pressure range of this work; The symbol (‡) indicates that the value is experimental data, while the symbol (†) is the enthalpy mixing calculated by the model.

Table 4. 34. Group 2: Enthalpies of mixing ΔH_{mix} of CO_2 in water calculated with OLI thermodynamic models (AQ, MSE and MSE-SRK) from 308.15 to 573.15 K and from 20 to 200 bar. All experimental data are referred to in Table 4.9.

N.	Temperature [K]	Pressure [bar]	CO_2 [mol/mol]	ΔH mix‡ [J/mol]	OLI AQ† [J/mol]	OLI MSE† [J/mol]	OLI MSE SRK† [J/mol]
1	308.15	75.4	0.022	-220.89	-243.82	-242.68	-246.78
2	323.15	20.33	0.007	-90.01	-98.0256	-98.21	-99.92
3	323.15	50.33	0.015	-177.17	-186.033	-190.99	-289.15
4	323.15	103.92	0.021	-139.98	-150.131	-153.03	-153.78
5	323.15	140.14	0.022	-108.25	-109.337	-111.61	-111.94
6	323.15	148	0.022	-110.78	-113.107	-115.77	-124.07
7	373.1	49.84	0.009	-45.74	-47.11	-47.01	-48.30
8	373.1	99.48	0.015	-59.58	-63.4185	-64.04	-65.35
9	373.1	192.45	0.021	-22.1	-25.4107	-25.79	-27.01
10	373.1	199.36	0.021	-98.9	-115.729	-111.42	-112.00
11	523.15	122.4	0.016	218.2	199.48	235.34	229.24
12	523.15	148	0.020	282.27	294.76	298.71	297.51

ΔH mix is in Liquid-phase; T: temperature of the system; P range: pressure range of this work; The symbol (‡) indicates that the value is experimental data, while the symbol (†) is the enthalpy mixing calculated by the model.

Table 4. 35. The relative average deviations of mixing enthalpy (ΔH_{AD}) between experimental data and model results are calculated using equation 4.12 for CO_2 in pure water.

N.	DS	CPA	SPR	OLI AQ	OLI MSE	OLI MSE-SRK
	[%]	[%]	[%]	[%]	[%]	[%]
1	17.00	14.00	8.00	10.00	10.00	12.00
2	3.00	2.00	2.00	9.00	9.00	11.00
3	-2.00	0.00	0.00	5.00	8.00	63.00
4	10.00	-1.00	-1.00	7.00	9.00	10.00
5	-1.00	0.00	0.00	1.00	3.00	3.00
6	-7.00	1.00	0.00	2.00	5.00	12.00
7	17.00	3.00	3.00	3.00	3.00	6.00
8	9.00	-19.90	0.00	6.00	7.00	10.00
9	-11.00	-1.00	0.00	15.00	17.00	22.00
10	-84.00	-1.00	0.00	17.00	13.00	13.00
11	-14.00	-1.00	1.00	-9.00	8.00	5.00
12	-6.00	2.00	2.00	4.00	6.00	5.00

From table 4.33, the best model in terms of average relative deviations from experimental data is SPR, and the SPR must also be compared with the solubility results in table 4.17.

Table 4. 36. Group 1: Enthalpies of mixing ΔH_{mix} of CO_2 in aqueous NaCl solutions (1.00 and 3.00 m) were calculated with the DS model at 323.15 K and 373.15 K from 50 to 200 bar.

N.	Temperature	Temperature	Pressure	m (NaCl)	CO_2	ΔH mix‡	DS†
	[K]	[°C]	[bar]	[mol/kg]	[mol/mol]	[J/mol]	[J/mol]
1	323.15	50	51	1	0.0112	-139.4	-140.1
2	323.15	50	103	1	0.0165	-119	-124.7
3	323.15	50	143.8	1	0.0176	-81.5	-83.4
4	323.15	50	202.4	1	0.0185	-69.7	-68.7
5	323.15	50	50	3	0.0111	-93.9	-92.2
6	323.15	50	100.4	3	0.0109	-72.2	-85.3
7	323.15	50	144.1	3	0.0112	-40.5	-52.4
8	323.15	50	202.4	3	0.0155	-40.4	-43.3
9	373.15	100	50.7	1	0.0063	-39.8	-44.9
10	373.15	100	104	1	0.0128	-50	-54.3
11	373.15	100	194	1	0.0178	-20.4	-19.9
12	373.15	100	50.4	3	0.0049	-29.4	-31.7
13	373.15	100	100.3	3	0.0075	-32.1	-39.5
14	373.15	100	190.2	3	0.0118	-14.8	-18.5

ΔH_{mix} is in Liquid-phase; T: temperature of the system; P range: pressure range of this work; m(NaCl): salt molalities; The symbol (‡) indicates that the value is experimental data, while the symbol (†) is the enthalpy mixing calculated by the model.

Table 4. 37. Group 2: Enthalpies of mixing ΔH_{mix} of CO_2 in aqueous NaCl solutions (1.00 and 3.00 m) were calculated with OLI thermodynamic models (AQ, MSE and MSE-SRK) at 323.15 K and 373.15 K from 50 to 200 bar.

N.	Temperature [K]	Pressure [bar]	m (NaCl) [mol/kg]	CO_2 [mol/mol]	ΔH mix‡ [J/mol]	OLI AQ† [J/mol]	OLI MSE† [J/mol]	OLI MSE SRK† [J/mol]
1	323.15	51	1	0.0112	-139.4	-144.98	-176.76	-151.11
2	323.15	103	1	0.0165	-119	-124.24	-127.57	-120.90
3	323.15	143.8	1	0.0176	-81.5	-86.96	-83.95	-83.86
4	323.15	202.4	1	0.0185	-69.7	-76.04	-125.46	-72.21
5	323.15	50	3	0.0111	-93.9	-96.25	-94.93	-96.06
6	323.15	100.4	3	0.0109	-72.2	-92.78	-83.75	-74.08
7	323.15	144.1	3	0.0112	-40.5	-42.48	-41.63	-41.15
8	323.15	202.4	3	0.0155	-40.4	-42.86	-42.06	-41.45
9	373.15	50.7	1	0.0063	-39.8	-42.67	-42.67	-40.32
10	373.15	104	1	0.0128	-50	-52.30	-52.70	-50.95
11	373.15	194	1	0.0178	-20.4	-24.09	-21.66	-20.95
12	373.15	50.4	3	0.0049	-29.4	-34.46	-30.08	-30.08
13	373.15	100.3	3	0.0075	-32.1	-34.44	-38.62	-34.06
14	373.15	190.2	3	0.0118	-14.8	-16.65	-17.45	-16.25

ΔH_{mix} is in Liquid-phase; T: temperature of the system; P range: pressure range of this work; m(NaCl): salt molalities; The symbol (‡) indicates that the value is experimental data, while the symbol (†) indicates the ΔH_{mix} calculated by the models.

Table 4. 38. The relative average deviations of mixing enthalpy (ΔH_{AD}) between experimental data and model results are calculated using equation 4.12 for CO_2 in water and NaCl.

N.	DS [%]	OLI AQ [%]	OLI MSE [%]	OLI MSE-SRK [%]
1	0.50	4.0	26.8	8.4
2	4.79	4.4	7.2	1.6
3	2.33	6.7	3.0	2.9
4	-1.43	9.1	80	3.6
5	-1.81	2.5	1.1	2.3
6	18.14	28.5	16.0	2.6
7	29.38	4.9	2.8	1.6
8	7.18	6.1	4.1	2.6
9	12.81	7.2	7.2	1.3
10	8.60	4.6	5.4	1.9
11	-2.45	18.1	6.2	2.7
12	7.82	17.2	2.3	2.3
13	23.05	7.3	20.3	6.1
14	25.00	12.5	17.9	9.8

All the thermodynamic models show that the most appropriate conditions to calculate mixing enthalpies are from table 4.35. In particular, for the CO_2-H_2O system, on average, the OLI MSE-SRK thermodynamic package is more consistent with the experimental data, with relative average deviations ranging from 2.9% (T = 323.15K, P = 143.8 bar) to 9.8% (T = 373.15 K and P = 190.2 bar). In fact, at the temperature of 373.15 K and high pressures, the OLI AQ model is more accurate. Instead, under the same conditions, the OLI MSE-SRK model is the worst.

Unlike CO_2 in aqueous NaCl solutions, the data calculated with thermodynamic methods presents better results with the OLI MSE-SRK model, which is generally used to simulate aqueous saline processes. The lowest error, 1%, is for the temperature of 373.15 K and a relatively low-medium pressure of 50 bar, while the highest error, of 10%, is for the same temperature at high pressures. Therefore for temperatures of 323.15 K and pressures from 100 bar to 200 bar, for molality of salt 1 and 3, it is possible to use the thermodynamic package OLI MSE-SRK. On the other hand, it is advisable to use the OLI AQ thermodynamic package for the same temperature and low pressures. Almost similar considerations can be undertaken with temperatures of 373.15 K and pressures from 50 to 200 bar, molality from 1 to 3, where it is possible to use both OLI MSE-SRK and OLI MSE; the latter to be avoided for high pressures.

4.3.2 H_2S-H_2O and H_2S-H_2O in brine

The results of the mixing enthalpies for H_2S coming from the thermodynamic models are shown in the following tables. As previously discussed for CO_2 mixtures, the results are divided into two subsets, considering the absence and the presence of salts. The first subset shows the results of the mixing enthalpies of H_2S in pure water, and it is divided into two groups: Group 1 includes DS, CPA, and SPR models, while Group 2 assess the performance of the OLI packages. For the second subset, the H_2S mixing enthalpy is studied in water and NaCl. Particularly, Group 1 contains only the results provided by the DS model, and Group 2 shows the performance of the OLI packages. Finally, the mixing enthalpies are calculated at the equilibrium point (x_i^{eq}) for each specific temperature and pressure for all the mixtures H_2S-H_2O and H_2S-H_2O-NaCl.

Table 4. 39. Enthalpies of mixing ΔH_{mix} of H_2S in pure water were calculated with DS, CPA and SPR at 323.15 K, 353.15K from 15 to 300 bar.

N.	Temperature	Pressure	H_2S	ΔH_{mix}‡	DS†	CPA†	SPR†
	[K]	[bar]	[mol/mol]	[J/mol]	[J/mol]	[J/mol]	[J/mol]
1	323	17.2	0.0175	-228.08	-222.37	-231.60	-229.87
2	323	18.4	0.0187	-226.83	-234.54	-241.87	-227.98
3	323	78.3	0.0388	42.28	-300.10	47.21	37.21
4	323	136	0.039	44.37	-174.04	43.45	42.01
5	353	140.2	0.0438	126.9	232.69	124.23	129.00
6	353	191.6	0.0443	129.96	297.07	132.87	128.08
7	353	254.5	0.046	135.11	360.60	138.46	137.21
8	353	308.6	0.0471	163.14	392.81	176.82	173.78
9	393	135.8	0.0554	186.15	285.74	187.24	185.97
10	393	198.6	0.057	255.44	260.28	278.63	243.73
11	393	254.8	0.0585	277.89	300.22	276.98	281.56
12	393	302.7	0.0603	319.02	347.25	321.78	312.65

ΔH_{mix} is in Liquid-phase; T: temperature of the system; P range: pressure range of this work; The symbol (‡) indicates that the value is experimental data, while the symbol (†) indicates the ΔH_{mix} calculated by the models.

Table 4. 40. Enthalpies of mixing ΔH_{mix} of H_2S in pure water calculated with OLI thermodynamic models (AQ, MSE and MSE-SRK) at 323.15 K, 353.15K from 15 to 300 bar.

N° [-]	Temperature [K]	Pressure [bar]	ΔH mix‡ [J/mol]	AQ† [J/mol]	MSE† [J/mol]	MSE-SRK† [J/mol]
1	323.15	17.20	-228.08	-232.60	-233.52	-280.53
2	323.15	18.40	-226.83	-234.95	-231.01	-226.83
3	323.15	78.30	42.28	44.35	43.35	46.93
4	323.15	136.00	44.37	49.43	44.41	48.80
5	353.15	140.20	126.90	145.07	128.44	140.85
6	353.15	191.60	129.96	144.78	131.25	142.95
7	353.15	254.50	135.11	148.37	136.65	147.26
8	353.15	308.60	163.14	181.12	163.69	177.82
9	393.15	135.80	186.15	258.83	226.21	193.59
10	393.15	198.60	255.44	358.89	335.85	288.64
11	393.15	254.80	277.89	397.90	357.54	330.68
12	393.15	302.70	319.02	446.91	387.67	373.25

ΔH_{mix} is in Liquid-phase; T: temperature of the system; P range: pressure range of this work; The symbol (‡) indicates that the value is experimental data, while the symbol (†) indicates the ΔH_{mix} calculated by the models.

Table 4. 41. The relative average deviation of mixing enthalpy (ΔH_{AD}) between experimental data and model results is calculated using equation 4.12 for H_2S in pure water.

N.	DS [%]	CPA [%]	SPR [%]	OLI-AQ [%]	OLI-MSE [%]	OLI-MSE-SRK [%]
1	-3.00	2.00	1.00	2.00	2.00	23.00
2	3.00	7.00	1.00	4.00	2.00	0.00
3	-8.10	12.00	-12.00	5.00	3.00	11.00
4	-4.92	-2.00	-5.00	11.00	0.00	10.00
5	8.30	-2.00	2.00	14.00	1.00	11.00
6	12.90	2.00	-1.00	11.00	1.00	10.00
7	16.70	2.00	2.00	10.00	1.00	9.00
8	14.10	8.00	7.00	11.00	0.00	9.00
9	5.30	1.00	0.00	39.00	22.00	4.00
10	2.00	9.00	-5.00	40.00	31.00	13.00
11	8.00	0.01	1.00	43.00	29.00	19.00
12	9.00	1.00	-2.00	40.00	22.00	17.00

Table 4. 42. Enthalpies of mixing ΔH_{mix} of H_2S in aqueous NaCl solutions (1, 3 and 5 m) calculated with DS model at 323.15 K, 353.15K and 393.15 K from 15 to 300 bar.

N°	Temperature	Pressure	H_2S	NaCl	ΔH_{mix}‡	DS†
[-]	[K]	[bar]	[mol/mol]	[mol/kg]	[J/mol]	[J/mol]
1	323.15	17.60	0.0148	1	-197.10	-191.84
2	323.15	78.90	0.0333	1	33.35	-25.09
3	323.15	131.80	0.0344	1	35.47	-38.75
4	323.15	17.70	0.0119	3	-151.00	-148.24
5	323.15	78.90	0.0231	3	29.47	-199.79
6	323.15	133.20	0.0250	3	29.47	-119.74
7	323.15	17.70	0.0097	5	112.90	-124.12
8	323.15	78.80	0.0217	5	25.17	-19.85
9	323.15	128.90	0.0231	5	27.58	-30.45
10	353.15	140.20	0.0375	1	105.25	192.75
11	353.15	199.20	0.0381	1	111.44	254.20
12	353.15	260.00	0.0385	1	111.09	203.00
13	353.15	308.60	0.0394	1	125.64	227.00
14	353.15	137.70	0.0260	3	60.77	137.54
15	353.15	198.70	0.0265	3	76.94	184.92
16	353.15	260.50	0.0282	3	83.93	222.30
17	353.15	309.30	0.0300	3	90.27	239.37
18	393.15	135.10	0.0462	1	163.10	231.66
19	393.15	191.80	0.0500	1	232.75	406.85
20	393.15	195.90	0.0326	3	134.58	202.00

ΔH_{mix} is in Liquid-phase; T: temperature of the system; P range: pressure range of this work; m(NaCl): salt molalities; The symbol (‡) indicates that the value is experimental data, while the symbol (†) indicates the ΔH_{mix} calculated by the models.

Table 4. 43. Enthalpies of mixing ΔH_{mix} of H_2S in aqueous NaCl solutions (1, 3 and 5 m) calculated with OLI thermodynamic models (AQ, MSE and MSE-SRK) at 323.15 K, 353.15K and 393.15 K from 15 to 300 bar.

N°	Temperature	Pressure	NaCl	ΔH_{mix}‡	AQ†	MSE†	MSE-SRK†
[-]	[K]	[bar]	[mol/kg]	[J/mol]	[J/mol]	[J/mol]	[J/mol]
1	323.15	17.6	1	-197.1	-205.95	-203.21	-201.44
2	323.15	78.9	1	33.35	38.57	37.23	33.96
3	323.15	131.8	1	35.47	37.91	37.91	36.29
4	323.15	17.7	3	-151	-175.90	-168.35	-161.18
5	323.15	78.9	3	29.47	32.31	31.43	30.51
6	323.15	133.2	3	29.47	32.67	31.56	30.30
7	323.15	17.7	5	112.9	130.06	125.91	117.18
8	323.15	78.8	5	25.17	31.41	28.90	27.02
9	323.15	128.9	5	27.58	33.71	30.95	29.61
10	353.15	140.2	1	105.25	119.29	115.81	111.62
11	353.15	199.2	1	111.44	127.82	122.55	120.27
12	353.15	260	1	111.09	130.96	123.74	115.39
13	353.15	308.6	1	125.64	134.09	139.22	137.09
14	353.15	137.7	3	60.77	76.00	67.76	66.33

15	353.15	198.7	3	76.94	79.25	77.71	82.68
16	353.15	260.5	3	83.93	102.78	94.39	84.87
17	353.15	309.3	3	90.27	115.37	109.96	104.58
18	393.15	135.1	1	163.1	187.87	179.72	171.94
19	393.15	191.8	1	232.75	254.14	251.81	246.22
20	393.15	195.9	3	134.58	153.70	149.66	137.34

ΔH_{mix} is in Liquid-phase; T: temperature of the system; P range: pressure range of this work; m(NaCl): salt molalities; The symbol (‡) indicates that the value is experimental data, while the symbol (†) indicates the ΔH_{mix} calculated by the models.

Table 4. 44. The relative average deviation of mixing enthalpy (ΔH_{AD}) between experimental data and model results is calculated using equation 4.12 for H_2S in water and NaCl.

N° [-]	DS model [%]	AQ model [%]	MSE model [%]	MSE-SRK model [%]
1	-2.67	4.49	3.10	2.20
2	-175.23*	15.65	11.63	1.83
3	-209.25*	6.88	6.88	2.31
4	-1.83	16.49	11.49	6.74
5	-777.94*	9.64	6.65	3.53
6	-506.31*	10.86	7.09	2.82
7	-209.94*	15.20	11.52	3.79
8	-178.86*	24.79	14.82	7.35
9	-210.41*	22.23	12.22	7.36
10	83.14*	13.34	10.03	6.05
11	128.10*	14.70	9.97	7.92
12	82.73*	17.89	11.39	3.87
13	80.67*	6.73	10.81	9.11
14	126.33*	25.06	11.50	9.15
15	140.34*	3.00	1.00	7.46
16	164.86*	22.46	12.46	1.12
17	165.17*	27.81	21.81	15.85
18	42.04*	15.19	10.19	5.42
19	74.80*	9.19	8.19	5.79
20	50.10*	14.21	11.21	2.05

(*)For DS model, the deviation are not acceptable.

In this part of the study, we want to understand which thermodynamic model presents the best agreement with the experimental data. The enthalpy and solubility results led to the choice of OLI thermodynamic models, in particular in the presence of salts.

At the beginning of the chapter, in the solubility section, it was noted that the solubility of hydrogen sulfide (H_2S) is strongly influenced by pressure when H_2S is gaseous but does not depend on pressure when two liquid phases coexist. Also, when the hydrogen sulfide is supercritical, the solubility increases slightly with pressure. The solubility increases with the temperature in supercritical conditions, i.e. for temperatures higher than 373.15 K and the pressure of 100 bar. With the study of the mixing enthalpies, it can be noted that a mixture of H_2S in water is well modelled with the OLI MSE thermodynamic model for temperature conditions from 323.15 K to about 373.15K and for pressures up to 300 bar. The relative deviations are between 0.3% and 2.4%. Also, it can be observed that beyond the critical conditions, all three thermodynamic models give results with high deviations (> 17%) and slightly better results with the OLI MSE-SRK model (approximatively 14%). The OLI AQ model appears to have acceptable errors (<4%), and the most

obvious errors are the OLI AQ method for temperatures of 393.15 K and pressure greater than 130 bar. On the other hand, considering the mixture of H_2S in an aqueous solution of NaCl, the following observations can be defined. At a temperature of 323.15 K, for pressures from 15 bar to 130 bar and m=1 mol/Kg, the best thermodynamic method is OLI MSE-SRK, with relative deviations lower than 3%. At the same time, the worst is OLI AQ, with a deviation of roughly 16%. For m=3 and high pressures, two thermodynamic models OLI MSE and OLI MSE-SRK, are optimal. However, for m=5 and pressures in the 17.7 and 128.9 bar range, the only efficient model is OLI MSE SRK with deviations around 7%. At a temperature of 353.15 K and for high pressures, the best thermodynamic model is OLI MSE-SRK. The deviations are roughly 5% for a molality of salt equal to 1 and 9% for a molality of 3. Thus, except for high pressures and high temperature, there are higher deviations for all three models. For temperatures of 393.15K and pressure ranges from 130 to 200 bar, all three models have acceptable deviations for the OLI MSE-SRK model. Finally, generalizing the conditions of temperature, pressure, and molality studied, the OLI MSE-SRK model was optimal, while for mixtures of H_2S in water, the best is OLI AQ.

4.3.3 CH_4-H_2O and CH_4-H_2O in brine

The excess of enthalpies, or defined as ΔH mix for water vapour and methane in the range of 373.15 to 473.15 K and from 1.0098 to 105.07 bar, is reported in the following table.

Table 4.45. Experimental excess enthalpies for water vapour and methane for selected temperatures and from 1.0098 bar to 105.07 bar.

Temperature [K]	Pressure [bar]	HE (J/mol)
373.2	1.013	42.55
383.2	1.013	24.30
393.2	1.013	20.98
403.2	1.013	18.90
413.2	1.013	28.37
423.2	1.013	19.93

After an in-depth study of the thermodynamics used by the authors relating to the calculation of the mixing enthalpy to define the parameters of the EoS to fit the experimental data, it was possible to investigate with the thermodynamic models of OLI systems. In addition, the DS model has issues in calculating the mixing enthalpies because the experimental data refers to the gas phase and not to the liquid phase, and convergence problems have been occurring for the algorithm due to the parameters inconsistencies. Therefore, no data from the DS model have been calculated.

Table 4.46. Enthalpies of mixing ΔH_{mix} of CH_4 in water calculated with OLI thermodynamic models (AQ, MSE and MSE-SRK) from 373.20 to 651.70K and from 1.01 to 105.07 bar.

N°	T	P	ΔH mix‡	AQ†	MSE†	MSE-SRK†
[-]	[K]	[bar]	[J/mol]	[J/mol]	[J/mol]	[J/mol]
1.00	373.20	1.01	42.55	42.64	43.06	50.67
2.00	383.20	1.01	24.30	24.33	24.52	29.12
3.00	393.20	1.01	20.98	21.01	21.21	23.09
4.00	403.20	1.01	18.90	19.06	19.06	21.54
5.00	413.20	1.01	28.37	28.74	29.03	29.25
6.00	423.20	1.01	19.93	20.01	20.13	20.08
7.00	548.20	49.79	699.00	769.60	702.25	699.94
8.00	549.30	49.79	812.30	892.72	815.72	814.50
9.00	598.30	104.37	1694.00	1910.15	1700.37	1695.71
10.00	598.10	105.07	1699.00	1900.50	1709.72	1703.57
11.00	650.00	105.07	964.30	1072.30	973.70	965.87
12.00	651.70	105.07	1699.00	1757.62	1718.37	1700.89

ΔH_{mix} is in Liquid-phase; T: temperature of the system; P range: pressure range of this work; The symbol (‡) indicates that the value is experimental data, while the symbol (†) indicates the ΔH_{mix} calculated by the models.

Table 4.47. The relative average deviation of mixing enthalpy (ΔH_{AD}) between experimental data and model results is calculated using equation 4.12 for CH_4 in water and NaCl.

	AQ model	MSE model	MSE-SRK model
N°	δΔH	δΔH	δΔH
[-]	[J/mol]	[J/mol]	[J/mol]
1	0.0021	0.0120	0.1910
2	0.0011	0.0090	0.1980
3	0.0015	0.0110	0.1010
4	0.0083	0.0087	0.1400
5	0.0128	0.0230	0.0310
6	0.0042	0.0100	0.0075
7	0.1010	0.0047	0.0013
8	0.0990	0.0042	0.0027
9	0.1276	0.0038	0.0010
10	0.1186	0.0063	0.0027
11	0.1120	0.0098	0.0016
12	0.0345	0.0114	0.0011

From the solubility data, it is possible to observe that almost all thermodynamic models have consistent results with very low deviations compared to the experimental data. Also, the results are quite consistent with the experimental data for the mixing enthalpy, even if dealing with gaseous mixtures. For example, the OLI MSE model perfectly covers the whole range of temperature and pressure analyzed, while the OLI AQ model has very low levels of accuracy from 373.15 to 423.15 K for 1 bar pressure. In fact, the deviations in this range T and P are less than 1%. However, higher deviations, roughly 11%, are present for temperatures starting from 548.20 K and at high pressures. Regarding the OLI MSE-SRK model, the best results are obtained at high temperatures and pressures with less than 0.5% deviations, while at low temperatures and atmospheric pressure, the maximum deviation found is roughly 19%.

4.4 Conclusion and model recommendation

This chapter has studied the performances of different models for different systems containing CO_2 – CH_4 – H_2S – brine for a wide range of temperature, pressure and salinity through a careful comparison between the results of the models and the experimental data. The study has been focused on the solubility and enthalpy of mixing. From the comparison of the experimental data, a new code was created by revising the Duan-Sun model [DS] in the presence and in the absence of salts to calculate the solubilities and enthalpy of mixing. Where possible, it has been reproduced for the main components present in a geothermal mixture. Furthermore, several thermodynamic models, some present in the Unisim Design software and others by modifying the parameters of EoS, have made it possible to reproduce the solubilities accurately and compare them with the experimental data. The following mixtures were therefore analyzed:

- Solubility and enthalpy of mixing of CO_2 in the aqueous phase at a temperature from 298.15 to 473.15 K, pressures from 1 at 200 bar and NaCl molality from 0 to 6 molal.
- Solubility and enthalpy of mixing of H_2S in the aqueous phase at a temperature from 283.15 to 453.15 K, pressures from 1 to 200 bar and NaCl molality from 0 to 6 molal.
- Solubility and enthalpy mixing of CH_4 in the aqueous phase at temperatures from 273.15 to 473.15 K, pressures from 1 to 200 bar and NaCl molality from 0 to 6 molal.

The intrinsic differences of these mixtures and their physical-chemical states for different temperatures and pressures do not allow the identification of a single thermodynamic model. Still, the following considerations inferred in this chapter suggest that engineers must select the best thermodynamic model among those proposed and analyzed.

This deepening of thermodynamic models applied to geothermal mixtures allows finding an approach to the choice of the model for the simulation of processes in which geothermal fluids are used (in the presence or absence of salt). Therefore, this research aims to facilitate the process engineer/designer of geothermal plants to model a geothermal fluid to obtain results with features similar to the real ones.

The process engineer requires a simple and unique model that will predict all possible types of fluid behaviour. Chapters 3 and 4 discuss the state-of-art and the difficulty of the approach in choosing an appropriate thermodynamic package on the geothermal fluid.

This Chapter suggests a possible method to pursue. The main steps are:

1. Identify two types of properties:
   - Single-phase properties; the model can be used depending on the process pressure-temperature location concerning the phase envelope.
   - Phase equilibrium properties which are generally much more difficult to calculate accurately.

The simulation tools such as Unisim Design R480 have “property packages” containing a pre-defined selection of property-model combinations. In particular, it is possible to insert fluid information and if there is the possibility to develop subroutines using the programming language (C++ or Python) to modify or insert an appropriate model such as DS or a modified version of the DS thermodynamic package.

2. The fluid composition.

   The choice of model parameters is directly related to the geothermal system composition. In particular, the engineer can predict the average relative deviations of mixing enthalpies from experimental data and other properties of industrial interest.

3. Pressure and temperature conditions of the process.

   There are two main families of fluid phase models: activity coefficient and equation of state. Although equations of state can describe all fluid phase conditions (vapour, liquid,

supercritical), activity coefficient models have some practical advantages, i.e. it implies a heterogeneous approach for calculating distribution coefficients. In contrast, a homogeneous approach is used with the equation of state. Today, there is a clear trend in favour of the homogeneous approach because it allows a coherent description of all fluid phases both because new equations of state have become available.

So, these considerations are important to provide a decision tree to select a thermodynamic model concerning a specific geothermal process (Fig. 4.50).

Figure 4. 50. Decision tree for choosing a thermodynamic model for a simulation of a process of a geothermic power plant.

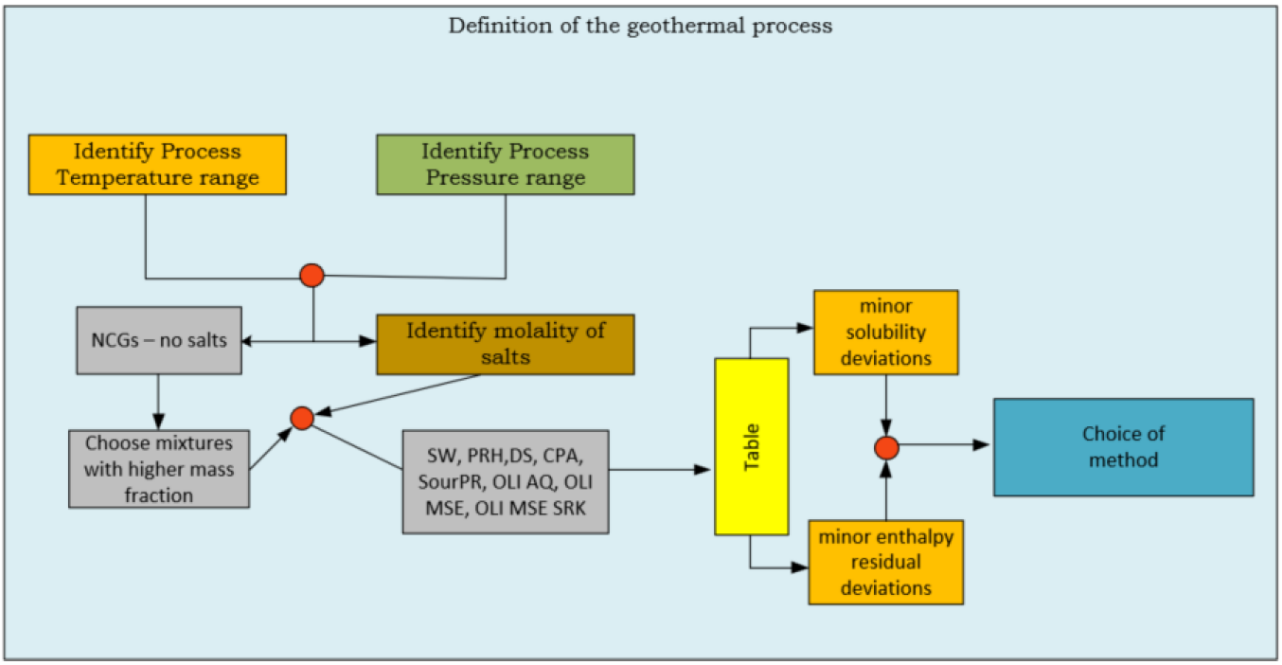

Figure 4.50 helps the engineers to choose the appropriate thermodynamic model, particularly when he is familiar with the thermodynamic theory, especially in the industrial field, where he needs to utilize the simple and fast ones.

The experience in contact with industrial chemical process engineers allows to include the following key points:

1. Identification of process conditions (temperature and pressure);
2. Identify the components of the geothermal fluid such as CO_2, H_2S, CH_4, H_2O (N_2, Ar, H_2 in very small or often negligible quantities) and the presence of salts.
3. In the absence of salts, identify the main components of the mixtures in the geothermal fluid and use the tables of experimental data with the relative deviations to select the best thermodynamic models under the specified conditions (temperature and pressure) considering the minimum deviation from experimental data in terms of solubilities and mixing enthalpies.
4. In the presence of salts, the guideline is the same described in point 3, highlighting the best models applicable for a specific geothermal salt mixture.
5. From an engineering point of view, the acceptable deviations are within 10% referred to the following Tables: 4.17, 4.20, 4.25 and 4.31 for solubilities and 4.34, 4.37, 4.40 and 4.43 for the mixing enthalpies.

REFERENCE LIST

[1] W. Yan, S. Huang, and E. H. Stenby, 'Measurement and modeling of CO2 solubility in NaCl brine and CO_2-saturated NaCl brine density', vol.**5** n.6,*International Journal of Greenhouse Gas Control*, **2011**, doi: 10.1016/j.ijggc.2011.08.004.

[2] S. X. Hou, G. C. Maitland, and J. P. M. Trusler, 'Phase equilibria of (CO_2 + H_2O + NaCl) and (CO 2 + H2O + KCl): Measurements and modeling', vol.**78**,*Journal of Supercritical Fluids*, **2013**, pp.78-88.doi: 10.1016/j.supflu.2013.03.022.

[3] H. Zhao, R. M. Dilmore, and S. N. Lvov, 'Experimental studies and modeling of CO2 solubility in high temperatute acqueous $CaCl_2$, $MgCl_2$, Na_2SO_4 and KCl solutions',vol.**61** n.7, *AIChE Journal*, **2015**, pp.2286-2297.doi: 10.1002/aic.14825.

[4] K. Gilbert, P. C. Bennett, W. Wolfe, T. Zhang, and K. D. Romanak, 'CO_2 solubility in aqueous solutions containing Na+, Ca2+, Cl-, SO42- and HCO3-: The effects of electrostricted water and ion hydration thermodynamics', *Applied Geochemistry*, **2016**,pp.39 doi: 10.1016/j.apgeochem.2016.02.002.

[5] H. Guo, Y. Huang, Y. Chen, and Q. Zhou, 'Quantitative Raman Spectroscopic Measurements of CO2 Solubility in NaCl Solution from (273.15 to 473.15) K at p = (10.0, 20.0, 30.0, and 40.0) MPa',vol.**3**,*Journal of Chemical and Engineering Data*, **2015**,pp.1-9 doi: 10.1021/acs.jced.5b00651.

[6] H. Messabeb, F. Contamine, P. Cézac, J. P. Serin, and E. C. Gaucher, 'Experimental Measurement of CO2 Solubility in Aqueous NaCl Solution at Temperature from 323.15 to 423.15 K and Pressure of up to 20 MPa', *Journal of Chemical and Engineering Data*, **2016**, pp.1-12.doi: 10.1021/acs.jced.6b00505.

[7] S. Chabab *et al.*, 'Thermodynamic study of the CO_2 – H_2O – NaCl system: Measurements of CO_2 solubility and modeling of phase equilibria using Soreide and Whitson, electrolyte CPA and SIT models', vol.**91**,*International Journal of Greenhouse Gas Control*, **2019**,pp.1-17. doi: 10.1016/j.ijggc.2019.102825.

[8] A. Goodman *et al.*, 'Comparison of methods for geologic storage of carbon dioxide in saline formations',vol.**18**, *International Journal of Greenhouse Gas Control*, **2013**,pp.329-342. doi: 10.1016/j.ijggc.2013.07.016.

[9] A. Kumar *et al.*, 'Reservoir simulation of CO_2 storage in deep saline aquifers', vol.**10** n.3,*SPE Journal*, **2005**, pp.336-348.doi: 10.2118/89343-pa.

[10] W. S. Han, S.-Y. Lee, C. Lu, and B. J. McPherson, ' Effects of permeability on CO_2 trapping mechanisms and buoyancy-driven CO_2 migration in saline formations ',vol.**46** n.7,*Water Resources Research*, **2010**, doi: 10.1029/2009wr007850.

[11] W. S. Han, K. Y. Kim, R. P. Esser, E. Park, and B. J. McPherson, 'Sensitivity Study of Simulation Parameters Controlling CO_2 Trapping Mechanisms in Saline Formations', vol.**90** n.3,*Transport in Porous Media*, **2011**,pp.807-829. doi: 10.1007/s11242-011-9817-7.

[12] S. M. Benson and D. R. Cole, 'CO_2 sequestration in deep sedimentary formations', vol.**4** (5)*Elements*, **2008**, pp.325-331.doi: 10.2113/gselements.4.5.325.

[13] S. M. V. Gilfillan *et al.*, 'Solubility trapping in formation water as dominant CO2 sink in natural gas fields', vol.**458**, *Nature*, 2009, pp.614-618. doi: 10.1038/nature07852.

[14] M. Steele-Macinnis *et al.*, 'Volumetrics of CO_2 storage in deep saline formations',vol.**47** n.1, *Environmental Science and Technology*, **2013**, pp.79-86.doi: 10.1021/es301598t.

[15] I. R. Kritschewsky, N. M. Shaworonkoff, and V. A. Aepelbaum, 'Gemeinsame Löslichkeit der Gase in Flüssigkeiten unter Druck',vol.**175** n.1, *Zeitschrift für Physikalische Chemie*, **2017**, pp. 232-238. doi: 10.1515/zpch-1935-17518.

[16] R. Wiebe and V. L. Gaddy, 'The Solubility in Water of Carbon Dioxide at 50, 75 and 100°, at Pressures to 700 Atmospheres',vol.**61** n.2, *Journal of the American Chemical Society*, **1939**, pp.315-318.doi: 10.1021/ja01871a025.

[17] R. Wiebe and V. L. Gaddy, 'The Solubility of Carbon Dioxide in Water at Various Temperatures from 12 to 40° and at Pressures to 500 Atmospheres. Critical Phenomena', vol.**62** n.4, *Journal of the American Chemical Society*, **1940**, pp.815-817. doi: 10.1021/ja01861a033.

[18] K. Tödheide and E. U. Franck, 'Das zweiphasengebiet und die kritische kurve im system kohlendioxid-wasser bis zu drucken von 3500 bar', vol.**37** n.5, *Zeitschrift fur Physikalische Chemie*, **1963**, pp. 387-401. doi: 10.1524/zpch.1963.37.5_6.387.

[19] S. Takenouchi and G. C. Kennedy, 'The solubility of carbon dioxide in nacl solutions at high temperatures and pressures',vol.**263** n.5, *American Journal of Science*, **1965**, pp.445-454.doi: 10.2475/ajs.263.5.445.

[20] J. Matouš, J. Šobr, J. P. Novák, and J. Pick, 'Solubility of carbon dioxide in water at pressures up to 40 atm', vol.**34** n.12,*Collection of Czechoslovak Chemical Communications*, **1969**,pp.3982-3985. doi: 10.1135/cccc19693982.

[21] A. Zawisza and B. Malesinska, 'Solubility of Carbon Dioxide in Liquid Water and of Water in Gaseous Carbon Dioxide in the Range 0.2-5 MPa and at Temperatures up to 473 K', vol.**26** n.4, *Journal of Chemical and Engineering Data*, **1981**, pp.388-391.doi: 10.1021/je00026a012.

[22] A. N. Sabirzyanov, R. A. Shagiakhmetov, F. R. Gabitov, A. A. Tarzimanov, and F. M. Gumerov, 'Water solubility of carbon dioxide under supercritical and subcritical conditions', v*Theoretical Foundations of Chemical Engineering*, vol. **37** n.1, **2003**,pp.51-53. doi: 10.1023/A:1022256927236.

[23] H. L. Barnes, 'Measuring thermodynamically-interpretable solubilities at high pressures and temperatures', *Physics and Chemistry of the Earth*,13-14, **1981**,pp.321-343. doi: 10.1016/0079-1946(81)90016-1.

[24] T. Nakayama, H. Sagara, K. Arai, and S. Saito, 'High-pressure ternary liquid-liquid equilibria for the systems of water, alcohol (1-propanol, 1-butanol and 1-pentanol) and 1,1-difluoroethane at 323: 2 K', *Journal of Chemical Engineering of Japan*, vol.**21** n.2,**1988**, pp.129-134.doi: 10.1252/jcej.21.129.

[25] K. Y. Song and R. Kobayashi, 'The water content of ethane, propane and their mixtures in equilibrium with liquid water or hydrates', *Fluid Phase Equilibria*,vol.**95**, **1994**,pp.281-298. doi: 10.1016/0378-3812(94)80074-X.

[26] R. D'souza, J. R. Patrick, and A. S. Teja, 'High pressure phase equilibria in the carbon dioxide - n-Hexadecane and carbon dioxide — water systems', *The Canadian Journal of Chemical Engineering*, vol.**66** n.2,**1988**, pp.319-323.doi: 10.1002/cjce.5450660221.

[27] T. Sako *et al.*, 'Phase equilibrium study of extraction and concentration of furfural produced in reactor using supercritical carbon dioxide', *JOURNAL OF CHEMICAL ENGINEERING OF JAPAN*, vol.**24** n.4,**1991**, pp.449-455.doi: 10.1252/jcej.24.449.

[28] M. B. King, A. Mubarak, J. D. Kim, and T. R. Bott, 'The mutual solubilities of water with supercritical and liquid carbon dioxides', *The Journal of Supercritical Fluids*,vol.**5** n.4, **1992**,pp.296-302. doi: 10.1016/0896-8446(92)90021-B.

[29] K. Jackson, L. E. Bowman, and J. L. Fulton, 'Water Solubility Measurements In Supercritical Fluids and High-Pressure Liquids Using Near-Infrared Spectroscopy', *Analytical Chemistry*,vol.**67** n.14, **1995**,pp.2368-2372. doi: 10.1021/ac00110a007.

[30] H. Teng, A. Yamasaki, M. K. Chun, and H. Lee, 'Solubility of liquid CO2 in water at temperatures from 278 K to 293 K and pressures from 6.44 MPa to 29.49 MPa and densities of the corresponding aqueous solutions', *Journal of Chemical Thermodynamics*,vol.**29** n.11, **1997**,pp.1301-1310. doi: 10.1006/jcht.1997.0249.

[31] M. B. Malegaonkar, P. D. Dholabhai, and P. Raj Bishnoi, 'Kinetics of Carbon Dioxide and Methane Hydrate Formation', *Canadian Journal of Chemical Engineering*,vol.**75** n.6, **1997**, pp.1090-1099.doi: 10.1002/cjce.5450750612.

[32] A. Dhima, J. C. De Hemptinne, and J. Jose, 'Solubility of hydrocarbons and CO_2 mixtures in water under high pressure', *Industrial and Engineering Chemistry Research*, vol.**38** n.8,**1999**, pp.3144-3161.doi: 10.1021/ie980768g.

[33] S. O. Yang, I. M. Yang, Y. S. Kim, and C. S. Lee, 'Measurement and prediction of phase equilibria for water+CO2 in hydrate forming conditions', *Fluid Phase Equilibria*, vol.**175** n.1-2, **2000**, pp.75-89.doi: 10.1016/S0378-3812(00)00467-2.

[34] R. J. Rosenbauer, T. Koksalan, and J. L. Palandri, 'Experimental investigation of CO_2-brine-rock interactions at elevated temperature and pressure: Implications for CO_2 sequestration in deep-saline aquifers',vol.**86** n.14-15, **2005**,pp.1581-1597. doi: 10.1016/j.fuproc.2005.01.011.

[35] P. Servio and P. Englezos, 'Effect of temperature and pressure on the solubility of carbon dioxide in water in the presence of gas hydrate', *Fluid Phase Equilibria*, vol.**190** n.1-2,**2001**, pp.127-134.doi: 10.1016/S0378-3812(01)00598-2.

[36] G. K. Anderson, 'Solubility of carbon dioxide in water under incipient clathrate formation conditions', *Journal of Chemical and Engineering Data*, vol.**47** n.2,**2002**,pp.219-222. doi: 10.1021/je015518c.

[37] H. Teng and A. Yamasaki, 'Pressure-mole fraction phase diagrams for Co2-pure water system under temperatures and pressures corresponding to ocean waters at depth to 3000 m', *Chemical Engineering Communications*, vol.**189** n.11,**2002**, pp.1485-1497.doi: 10.1080/00986440214993.

[38] A. Chapoy, A. H. Mohammadi, A. Chareton, B. Tohidi, and D. Richon, 'Measurement and Modeling of Gas Solubility and Literature Review of the Properties for the Carbon Dioxide-Water System', *Industrial and Engineering Chemistry Research*.vol.**43** n.7, **2004**, pp.1794-1802.doi:

10.1021/ie034232t.

[39] A. Valtz, A. Chapoy, C. Coquelet, P. Paricaud, and D. Richon, 'Vapour-liquid equilibria in the carbon dioxide-water system, measurement and modelling from 278.2 to 318.2 K', *Fluid Phase Equilibria*,vol.**226**, **2004**, pp.333-344,doi: 10.1016/j.fluid.2004.10.013.

[40] S. X. Hou, G. C. Maitland, and J. P. M. Trusler, 'Measurement and modeling of the phase behavior of the (carbon dioxide + water) mixture at temperatures from 298.15 K to 448.15 K', *Journal of Supercritical Fluids*, **2013**, doi: 10.1016/j.supflu.2012.11.011.

[41] P. J. Carvalho, L. M. C. Pereira, N. P. F. Gonçalves, A. J. Queimada, and J. A. P. Coutinho, 'Carbon dioxide solubility in aqueous solutions of NaCl: Measurements and modeling with electrolyte equations of state', *Fluid Phase Equilibria*,vol.**73**, **2015**,pp.87-96, doi: 10.1016/j.fluid.2014.12.043.

[42] H. Guo, Y. Chen, Q. Hu, W. Lu, W. Ou, and L. Geng, 'Quantitative Raman spectroscopic investigation of geo-fluids high-pressure phase equilibria: Part I. Accurate calibration and determination of CO2 solubility in water from 273.15 to 573.15K and from 10 to 120MPa', *Fluid Phase Equilibria*, vol.**382**,**2014**, pp.70-79.doi: 10.1016/j.fluid.2014.08.032.

[43] F. Gu, 'Solubility of carbon dioxide in aqueous sodium chloride solution under high pressure', *Gaoxiao Huaxue Gongcheng Xuebao*, vol.**25** n.1, **1998**,pp.211-221.

[44] J. A. Briones, J. C. Mullins, M. C. Thies, and B. U. Kim, 'Ternary phase equilibria for acetic acid-water mixtures with supercritical carbon dioxide', *Fluid Phase Equilibria*, vol.**36**, **1987**,pp.235-246. doi: 10.1016/0378-3812(87)85026-4.

[45] Y. Liu, M. Hou, G. Yang, and B. Han, 'Solubility of CO_2 in aqueous solutions of NaCl, KCl, $CaCl_2$ and their mixed salts at different temperatures and pressures', *Journal of Supercritical Fluids*,vol.**36**, **2011**, pp.235-246.doi: 10.1016/j.supflu.2010.12.003.

[46] A. Bamberger, G. Sieder, and G. Maurer, 'High-pressure (vapor + liquid) equilibrium in binary mixtures of (carbon dioxide + water or acetic acid) at temperatures from 313 to 353 K', *Journal of Supercritical Fluids*,vol.**17** n.2, **2000**,pp.97-110. doi: 10.1016/S0896-8446(99)00054-6.

[47] D. Tong, J. P. M. Trusler, and D. Vega-Maza, 'Solubility of CO_2 in aqueous solutions of $CaCl_2$ or $MgCl_2$ and in a synthetic formation brine at temperatures up to 423 K and pressures up to 40 MPa', *Journal of Chemical and Engineering Data*, vol.**58** n.7,**2013**,pp.2116-2124. doi: 10.1021/je400396s.

[48] C. F. Prutton and R. L. Savage, 'The Solubility of Carbon Dioxide in Calcium Chloride-Water Solutions at 75, 100, 120° and High Pressures', *Journal of the American Chemical Society*, vol.**67** n.9,**1945**, pp.1550-1554.doi: 10.1021/ja01225a047.

[49] J. A. Nighswander, N. Kalogerakis, and A. K. Mehrotra, 'Solubilities of Carbon Dioxide in Water and 1 Wt % NaCl Solution At Pressures up to 10 MPa and Temperatures from 80 to 200 °C', *Journal of Chemical and Engineering Data*,vol.**34** n.3 **1989**,pp.355-360. doi: 10.1021/je00057a027.

[50] R. Dohrn, A. P. Bünz, F. Devlieghere, and D. Thelen, 'Experimental measurements of phase equilibria for ternary and quaternary systems of glucose, water, CO2 and ethanol with a novel apparatus', *Fluid Phase Equilibria*, vol.**83**,**1993**, pp149-158. doi: 10.1016/0378-3812(93)87017-U.

[51] G. Mueller, E. Bender, and G. Maurer, 'Vapor-Liquid-Equilibrium in the Ternary System Ammonia-Carbon Dioxide-Water at High Water Contents in the Range 373 K to 473 K.', *Berichte der Bunsengesellschaft/Physical Chemistry Chemical Physics*,vol.**92** n.2, **1988**, pp.148-160.doi: 10.1002/bbpc.198800036.

[52] D. Koschel, J. Y. Coxam, L. Rodier, and V. Majer, 'Enthalpy and solubility data of CO2 in water and NaCl(aq) at conditions of interest for geological sequestration', *Fluid Phase Equilibria*, vol.**247** n.1-2, **2006**, pp. 107-120.doi: 10.1016/j.fluid.2006.06.006.

[53] Y. Krüger and L. W. Diamond, 'Unexpected behaviour of fluid inclusions synthesized from silver oxalate and an aqueous NaCl solution', *Chemical Geology*, vol.**173** n.1-3, **2001**,pp.159-177. doi: 10.1016/S0009-2541(00)00273-4.

[54] B. Rumpf, H. Nicolaisen, C. Öcal, and G. Maurer, 'Solubility of carbon dioxide in aqueous solutions of sodium chloride: Experimental results and correlation', *Journal of Solution Chemistry*, vol. **23**, no. 3, pp. 431–448, **1994**, doi: 10.1007/BF00973113.

[55] A. J. Ellis and R. M. Golding, 'The solubility of carbon dioxide above 100 degrees C in water and in sodium chloride solutions', *American Journal of Science*,vol.**261** n.1, **1963**,pp.47-60. doi: 10.2475/ajs.261.1.47.

[56] S. D. Malinin and N. I. Savalyeva, 'The solubility of CO_2 in NaCl and $CaCl_2$ solutions at 25, 50, and 75°C under elevated CO_2 pressures', *Geochemistry International*, vol.**6**, **1972, pp.** 643–653.

[57] S. D. Malinin and N. A. Kurovskaya, 'Solubility of CO2 in chloride solutions at elevated

temperatures and CO2 pressures', *Geochemistry International*, vol.**4**,**1975**,547-551.

[58] Z. Duan, R. Sun, C. Zhu, and I. M. Chou, 'An improved model for the calculation of CO2 solubility in aqueous solutions containing Na+, K+, Ca2+, Mg2+, Cl-, and SO42-', *Marine Chemistry*,vol.**98** n.2-4, **2006**,pp.131-139. doi: 10.1016/j.marchem.2005.09.001.

[59] T. J. Barrett, G. M. Anderson, and J. Lugowski, 'The solubility of hydrogen sulphide in 0-5 m NaCl solutions at 25°-95°C and one atmosphere', *Geochimica et Cosmochimica Acta*, **1988**, doi: 10.1016/0016-7037(88)90352-3.

[60] T. J. Barrett and G. M. Anderson, 'The solubility of sphalerite and galena in 1-5 m NaCl solutions to 300°C', *Geochimica et Cosmochimica Acta*, vol.**52** n.4,**1988**, pp.807-811.doi: 10.1016/0016-7037(88)90353-5.

[61] L. Barta and D. J. Bradley, 'Extension of the specific interaction model to include gas solubilities in high temperature brines', *Geochimica et Cosmochimica Acta*,vol.**49** n.1, **1985**, pp.195-203.doi: 10.1016/0016-7037(85)90204-2.

[62] B. Rumpf and G. Maurer, 'Solubilities of hydrogen cyanide and sulfur dioxide in water at temperatures from 293.15 to 413.15 K and pressures up to 2.5 MPa', *Fluid Phase Equilibria*, vol.**81**,**1992**,pp.241-260 doi: 10.1016/0378-3812(92)85155-2.

[63] Z. Duan and S. Mao, 'A thermodynamic model for calculating methane solubility, density and gas phase composition of methane-bearing aqueous fluids from 273 to 523 K and from 1 to 2000 bar', *Geochimica et Cosmochimica Acta*, vol.**70** n.13,**2006**,3369-3386. doi: 10.1016/j.gca.2006.03.018.

[64] C. Hervé, Y. Suyu, L. Bernard, A. Jacques, and X. Pierre, 'Calculation of CO2, CH4 and H2S solubilities in aqueous electrolyte solution at high pressure and high temperature', *Journal of Thermal Science*, vol.**6** n.4,**1997**, pp.251-259.doi: 10.1007/s11630-997-0004-7.

[65] J. J. Carroll and A. E. Mather, 'The solubility of hydrogen sulphide in water from 0 to 90°C and pressures to 1 MPa', *Geochimica et Cosmochimica Acta*,vol.**53** n.6, **1989**,pp.1163-1170, doi: 10.1016/0016-7037(89)90053-7.

[66] J. Xia, Á. Pérez-Salado Kamps, and G. Maurer, 'Solubility of H_2S in (H_2O + piperazine) and in (H2O + MDEA + piperazine)', *Fluid Phase Equilibria*, **2003**, doi: 10.1016/S0378-3812(02)00331-X.

[67] D. Koschel, J. Y. Coxam, and V. Majer, 'Enthalpy and solubility data of H2S in water at conditions of interest for geological sequestration', *Industrial and Engineering Chemistry Research*, vol.**46**,**2007**,pp.1421-1430 doi: 10.1021/ie061180+.

[68] A. Chapoy, A. H. Mohammadi, B. Tohidi, A. Valtz, and D. Richon, 'Experimental measurement and phase behavior modeling of hydrogen sulfide-water binary system', *Industrial and Engineering Chemistry Research*, vol.**44** n.19,**2005**, pp.7567-7574.doi: 10.1021/ie050201h.

[69] D. Y. Zezin, A. A. Migdisov, and A. E. Williams-Jones, 'PVTx properties of H2O-H2S fluid mixtures at elevated temperature and pressure based on new experimental data', *Geochimica et Cosmochimica Acta*,vol.**75**, **2011**,pp.5483-5495 doi: 10.1016/j.gca.2011.07.005.

[70] 'Critical lines and phase equilibria in binary van der Waals mixtures', *Philosophical Transactions of the Royal Society of London. Series A, Mathematical and Physical Sciences*, vol.**298**,1980,pp.495-540 doi: 10.1098/rsta.1980.0266.

[71] F. T. Selleck, L. T. Carmichael, and B. H. Sage, 'Phase Behavior in the Hydrogen Sulfide-Water System', *Industrial & Engineering Chemistry*,vol.**44** n.9, **1952**,pp.2219-2226 doi: 10.1021/ie50513a064.

[72] L. K. Wang, G. J. Chen, G. H. Han, X. Q. Guo, and T. M. Guo, 'Experimental study on the solubility of natural gas components in water with or without hydrate inhibitor', *Fluid Phase Equilibria*,vol.**207**n.1-2, **2003**,pp.143-154 doi: 10.1016/S0378-3812(03)00009-8.

[73] R. Ganjdanesh, S. L. Bryant, R. L. Orbach, G. A. Pope, and K. Sepehrnoori, 'Coupled carbon dioxide sequestration and energy production from geopressured/geothermal aquifers', *SPE Journal*, vol. **19**, no. 2, pp. 239–248, **2014**, doi: 10.2118/163141-PA.

[74] AMIRIJAFARI B and CAMPBELL JM, 'Solubility of gaseous hydrocarbon mixtures in water', *Soc Petrol Eng J*, vol.**12** n.1,**1972**,pp.21-27 doi: 10.2118/3106-pa.

[75] T. D. O'Sullivan and N. O. Smith, 'The solubility and partial molar volume of nitrogen and methane in water and in aqueous sodium chloride from 50 to 125° and 100 to 600 Atm', *Journal of Physical Chemistry*, vol.**74** n.7,**1970**, pp.1460-1466 doi: 10.1021/j100702a012.

[76] G. K. Folas, S. O. Derawi, M. L. Michelsen, E. H. Stenby, and G. M. Kontogeorgis, 'Recent applications of the cubic-plus-association (CPA) equation of state to industrially important systems', vol.**228**, **2005**,pp.121-126 doi: 10.1016/j.fluid.2004.08.013.

[77] E. Wilhelm, R. Battino, and R. J. Wilcock, 'Low-Pressure Solubility of Gases in Liquid Water', *Chemical Reviews*,vol.**77** n.2, **1977**, pp.219-262 doi: 10.1021/cr60306a003.

[78] O. L. Culberson and J. J. McKetta, 'Phase Equilibria in Hydrocarbon-Water Systems III - The

Solubility of Methane in Water at Pressures to 10,000 PSIA', *Journal of Petroleum Technology*, vol.**3** n.8,**1951**,pp.223-226 doi: 10.2118/951223-g.

[79] J. R. Duffy, N. O. Smith, and B. Nagy, 'Solubility of natural gases in aqueous salt solutions-I. Liquidus surfaces in the system CH4-H2O-NaCl2-CaCl2 at room temperatures and at pressures below 1000 psia', *Geochimica et Cosmochimica Acta*, vol.**23** n.1-2,**1961**,pp.23-31 doi: 10.1016/0016-7037(61)90004-7.

[80] N. O. Smith, S. Kelemen, and B. Nagy, 'Solubility of natural gases in aqueous salt solutions—II', *Geochimica et Cosmochimica Acta*, vol.**26** n.9,**1962**,pp.921-926 doi: 10.1016/0016-7037(62)90066-2.

[81] N. O. Smith, S. Kelemen, and B. Nagy, 'Solubility of natural gases in aqueous salt solutions-II. Nitrogen in aqueous NaCl, CaCl2, Na2SO4 and MgSO4 at room temperatures and at pressures below 1000 psia', *Geochimica et Cosmochimica Acta*, vol.**26** n.9,**1962**,921-926 doi: 10.1016/0016-7037(62)90066-2.

[82] P. Gayet, C. Dicharry, G. Marion, A. Graciaa, J. Lachaise, and A. Nesterov, 'Experimental determination of methane hydrate dissociation curve up to 55 MPa by using a small amount of surfactant as hydrate promoter', *Chemical Engineering Science*,vol.**60** n.21, **2005**, pp.5751-5758 doi: 10.1016/j.ces.2005.04.069.

[83] G. Hummer, S. Garde, A. E. García, and L. R. Pratt, 'New perspectives on hydrophobic effects', *Chemical Physics*,vol.**258** n.2-3, **2000**,pp.349-370 doi: 10.1016/S0301-0104(00)00115-4.

[84] S. Yamamoto, J. B. Alcauskas, and T. E. Crozier, 'Solubility of Methane in Distilled Water and Seawater', *Journal of Chemical and Engineering Data*,vol.**21** n.1, **1976**,pp.78-80 doi: 10.1021/je60068a029.

[85] L. C. Price, 'AQUEOUS SOLUBILITY OF METHANE AT ELEVATED PRESSURES AND TEMPERATURES.', *The American Association of Petroleum Geologists bulletin*. vol.**63**, **1979**,1527-1533 doi: 10.1306/2F9185E0-16CE-11D7-8645000102C1865D.

[86] D. A. Wiesenburg and N. L. Guinasso, 'Equilibrium Solubilities of Methane, Carbon Monoxide, and Hydrogen in Water and Sea Water', *Journal of Chemical and Engineering Data*, vol.**24** n.4,**1979**,356-360 doi: 10.1021/je60083a006.

[87] B. A. Cosgrove and J. Walkley, 'Solubilities of gases in H2O and 2H2O', *Journal of Chromatography A*, vol.**216**,**1981**, pp.161-167doi: 10.1016/S0021-9673(00)82344-4.

[88] T. R. Rettich, Y. P. Handa, R. Battino, and E. Wilhelm, 'Solubility of gases in liquids. 13. High-precision determination of Henry's constants for methane and ethane in liquid water at 275 to 328 K', *Journal of Physical Chemistry*, vol.**85** n.22,**1981**,3230-3237 doi: 10.1021/j150622a006.

[89] S. D. Cramer, 'Solubility of Methane in Brines From 0 to 300 °C', *Industrial and Engineering Chemistry Process Design and Development*, vol.**23** n.3,**1984**,pp.533-538 doi: 10.1021/i200026a021.

[90] Z. Duan, N. Møller, J. Greenberg, and J. H. Weare, 'The prediction of methane solubility in natural waters to high ionic strength from 0 to 250°C and from 0 to 1600 bar', *Geochimica et Cosmochimica Acta*,vol.**56** n.4, **1992**,pp.1451-1460 doi: 10.1016/0016-7037(92)90215-5.

[91] C. Yokoyama, S. Wakana, G. ichi Kaminishi, and S. Takahashi, 'Vapor-liquid equilibria in the methane-diethylene glycol-water system at 298.15 and 323.15 K', *Journal of Chemical and Engineering Data*, vol.**33** n.3,**1988**, pp.274-276 doi: 10.1021/je00053a015.

[92] Y. Wang, B. Han, H. Yan, and R. Liu, 'Solubility of CH4 in the mixed solvent t-butyl alcohol and water', *Thermochimica Acta*, vol.**253**,**1995**, pp.327-334 doi: 10.1016/0040-6031(94)02011-C.

[93] J. Gao, D. Q. Zheng, and T. M. Guo, 'Solubilities of methane, nitrogen, carbon dioxide, and a natural gas mixture in aqueous sodium bicarbonate solutions under high pressure and elevated temperature', *Journal of Chemical and Engineering Data*,vol.42 n.1, **1997**,pp.69-73 doi: 10.1021/je960275n.

[94] K. Lekvam and P. Raj Bishnoi, 'Dissolution of methane in water at low temperatures and intermediate pressures', *Fluid Phase Equilibria*, vol.**131** n.1-2,**1997**,pp.297-309 doi: 10.1016/s0378-3812(96)03229-3.

[95] K. Y. Song, G. Feneyrou, F. Fleyfel, R. Martin, J. Lievois, and R. Kobayashi, 'Solubility measurements of methane and ethane in water at and near hydrate conditions', *Fluid Phase Equilibria*, vol.**128** n.1-2,**1997**, pp.249-259 doi: 10.1016/s0378-3812(96)03165-2.

[96] A. Dhima, J. C. De Hemptinne, and G. Moracchini, 'Solubility of light hydrocarbons and their mixtures in pure water under high pressure', *Fluid Phase Equilibria*,vol.**145** n.1, **1998**, pp.129-150 doi: 10.1016/S0378-3812(97)00211-2.

[97] S. O. Yang, S. H. Cho, H. Lee, and C. S. Lee, 'Measurement and prediction of phase equilibria for water + methane in hydrate forming conditions', *Fluid Phase Equilibria*, vol.**185** n.1-2,**2001**,pp.53-63 doi: 10.1016/S0378-3812(01)00456-3.

[98] J. Qin, R. J. Rosenbauer, and Z. Duan, 'Experimental measurements of vapor-liquid equilibria of the H_2O + CO_2 + CH_4 ternary system', *Journal of Chemical and Engineering Data*, vol.**53** n.6,**2008**,pp.1246-1249 doi: 10.1021/je700473e.

[99] Y. S. Kim, S. K. Ryu, S. O. Yang, and C. S. Lee, 'Liquid water-hydrate equilibrium measurements and unified predictions of hydrate-containing phase equilibria for methane, ethane, propane, and their mixtures', *Industrial and Engineering Chemistry Research*, vol.**42** n.11,**2003**, pp.2409-2414 doi: 10.1021/ie0209374.

[100] A. Chapoy, A. H. Mohammadi, D. Richon, and B. Tohidi, 'Gas solubility measurement and modeling for methane-water and methane-ethane-n-butane-water systems at low temperature conditions', *Fluid Phase Equilibria*,vol.**220** n.1, **2004**,pp.111-119 doi: 10.1016/j.fluid.2004.02.010.

[101] P. K. Frolich, E. J. Tauch, J. J. Hogan, and A. A. Peer, 'Solubilities of Gases in Liquids at High Pressure', *Industrial and Engineering Chemistry*, vol.**23** n.5,**1931**,pp.548-550 doi: 10.1021/ie50257a019.

[102] A. Michels, J. Gerver, and A. Bijl, 'The influence of pressure on the solubility of gases', *Physica*, vol.**3** n.8,**1936**,pp.797-808 doi: 10.1016/s0031-8914(36)80353-x.

[103] O. L. Culberson, A. B. Horn, and J. J. McKetta, 'Phase Equilibria in Hydrocarbon-Water Systems', *Journal of Petroleum Technology*, vol.**2** n.1,**1950**,pp.1-6 doi: 10.2118/950001-g.

[104] J. Kiepe, S. Horstmann, K. Fischer, and J. Gmehling, 'Experimental determination and prediction of gas solubility data for methane + water solutions containing different monovalent electrolytes', *Industrial and Engineering Chemistry Research*,vol.**42** n.21, **2003**, pp.5392-5398 doi: 10.1021/ie030386x.

[105] R. Dohrn, S. Peper, and J. M. S. Fonseca, 'High-pressure fluid-phase equilibria: Experimental methods and systems investigated (2000-2004)', *Fluid Phase Equilibria*,vol.**288**, **2010**,pp.1-54 doi: 10.1016/j.fluid.2009.08.008.

[106] J. M. S. Fonseca, R. Dohrn, and S. Peper, 'High-pressure fluid-phase equilibria: Experimental methods and systems investigated (2005-2008)', *Fluid Phase Equilibria*.vol.**300**, 2011, pp.1-69 doi: 10.1016/j.fluid.2010.09.017.

[107] W. Ou, L. Geng, W. Lu, H. Guo, K. Qu, and P. Mao, 'Quantitative Raman spectroscopic investigation of geo-fluids high-pressure phase equilibria: Part II. Accurate determination of CH4 solubility in water from 273 to 603 K and from 5 to 140 MPa and refining the parameters of the thermodynamic model', *Fluid Phase Equilibria*,vol.**391**, **2015**,pp.18-30 doi: 10.1016/j.fluid.2015.01.025.

[108] Z. Ziabakhsh-Ganji and H. Kooi, 'An Equation of State for thermodynamic equilibrium of gas mixtures and brines to allow simulation of the effects of impurities in subsurface CO2 storage', *International Journal of Greenhouse Gas Control*,vol.**11**, **2012**,pp.S21-S34 doi: 10.1016/j.ijggc.2012.07.025.

[109] L. C. Price, L. M. Wenger, T. Ging, and C. W. Blount, 'Solubility of crude oil in methane as a function of pressure and temperature', *Organic Geochemistry*, vol.**4** n.3-4,**1983**,pp.201-221 doi: 10.1016/0146-6380(83)90042-6.

[110] R. K. Stoessell and P. A. Byrne, 'Salting-out of methane in single-salt solutions at 25°C and below 800 psia', *Geochimica et Cosmochimica Acta*, vol.**46** n.8,**1982**, pp.1327-1332 doi: 10.1016/0016-7037(82)90268-X.

[111] P. A. Byrne and R. K. Stoessell, 'Methane solubilities in multisalt solutions', *Geochimica et Cosmochimica Acta*, vol.**46** n.11,**1982**,pp.2395-2397 doi: 10.1016/0016-7037(82)90210-1.

[112] H. Zhao, 'Modeling vapor-liquid phase equilibria of methane-water and methane-carbon dioxide-water systems at 274K to 573K and 0.1 to 150 MPa using PRSV equation of state and Wong-Sandler mixing rule', *Fluid Phase Equilibria*, **2017**, doi: 10.1016/j.fluid.2017.05.015.

[113] J. C. De Hemptinne and E. Behar, 'Propriétés thermodynamiques de systèmes contenant des gaz acides. Étude bibliographique', *Oil & Gas Science and Technology*,vol **55** n.6, **2000**, pp.617-637 doi: 10.2516/ogst:2000047.

[114] D. P. Sobocinski and F. Kurata, 'Heterogeneous phase equilibria of the hydrogen sulfide–carbon dioxide system', *AIChE Journal*, vol.**5** n.4,**1959**, pp.545-551 doi: 10.1002/aic.690050425.

[115] R. Span and W. Wagner, 'A new equation of state for carbon dioxide covering the fluid region from the triple-point temperature to 1100 K at pressures up to 800 MPa', *Journal of Physical and Chemical Reference Data*,vol.**25** n.6, **1996**, pp.1509-1597 doi: 10.1063/1.555991.

[116] J. A. Bierlein and W. B. Kay, 'Phase-Equilibrium Properties of System Carbon Dioxide-Hydrogen Sulfide', *Industrial & Engineering Chemistry*,vol.**45** n.3, **1953**,pp.618-624 doi: 10.1021/ie50519a043.

[117] G. Morrison, 'Effect of water upon the critical points of carbon dioxide and ethane', *Journal of*

Physical Chemistry, vol.**85** n.7,**1981**, pp.759-761doi: 10.1021/j150607a007.

[118] J. J. Carroll and A. E. Mather, 'Phase equilibrium in the system water-hydrogen sulphide: Experimental determination of the LLV locus', *The Canadian Journal of Chemical Engineering*,vol.**67** n.3, **1989**, pp.468-470 doi: 10.1002/cjce.5450670318.

[119] V. Savary *et al.*, 'The solubility of CO_2+H_2S mixtures in water and 2M NaCl at 120°C and pressures up to 35MPa', *International Journal of Greenhouse Gas Control*,vol.**10**, **2012**, pp.123-133 doi: 10.1016/j.ijggc.2012.05.021.

[120] S. M. Klara, 'CO_2 solubility in water and brine under reservoir conditions', *Chemical Engineering Communications*, 1990, doi: 10.1080/00986449008940574.

[121] I. R. Krichevsky and J. S. Kasarnovsky, 'Thermodynamical Calculations of Solubilities of Nitrogen and Hydrogen in Water at High Pressures', *Journal of the American Chemical Society*, vol.**57** n.11, **1935**,pp.2168-2171 doi: 10.1021/ja01314a036.

[122] J. . Rowlinson, 'Molecular thermodynamics of fluid-phase equilibria', *The Journal of Chemical Thermodynamics*,vol.**2** n.1, **1970**, pp.158-159 doi: 10.1016/0021-9614(70)90078-9.

[123] R. Ohmura and Y. H. Mori, ' Comments on "Solubility of Liquid CO 2 in Synthetic Sea Water at Temperatures from 278 K to 293 K and Pressures from 6.44 MPa to 29.49 MPa, and Densities of the Corresponding Aqueous Solutions" (Teng, H.; Yamasaki, A. J. Chem. Eng. Data 1998 , 43 , 2−5) ', *Journal of Chemical & Engineering Data*, vol. **44**, no. 6, pp. 1432–1433, **1999**, doi: 10.1021/je9904715.

[124] C. Holzammer, A. Finckenstein, S. Will, and A. S. Braeuer, 'How Sodium Chloride Salt Inhibits the Formation of CO2 Gas Hydrates', *Journal of Physical Chemistry B*, vol. **120**, no. 9, pp. 2452–2459, **2016**, doi: 10.1021/acs.jpcb.5b12487.

[125] E. Pérez, Y. Sánchez-Vicente, A. Cabañas, C. Pando, and J. A. R. Renuncio, 'Excess molar enthalpies for mixtures of supercritical carbon dioxide and water + ethanol solutions', *Journal of Supercritical Fluids*, vol. **36**, no. 1, pp. 23–30, **2005**, doi: 10.1016/j.supflu.2005.03.006.

[126] Xuemin Chen, S. E. Gillespie, J. L. Oscarson, and R. M. Izatt, 'Calorimetric determination of thermodynamic quantities for chemical reactions in the system CO2-NaOH-H2O from 225 to 325°C', *Journal of Solution Chemistry*, vol. **21**, no. 8, pp. 825–848, **1992**, doi: 10.1007/BF00651511.

[127] J. B. Ott, C. E. Stouffer, G. V. Cornett, B. F. Woodfield, C. Guanquan, and J. J. Christensen, 'Excess enthalpies for (ethanol + water) at 398.15, 423.15, 448.15, and 473.15 K and at pressures of 5 and 15 MPa. Recommendations for choosing (ethanol + water) as an HmE reference mixture', *The Journal of Chemical Thermodynamics*,vol.**19** n.4, **1987**,pp.337-348 doi: 10.1016/0021-9614(87)90115-7.

[128] D. Koschel, J. Y. Coxam, and V. Majer, 'Enthalpy and solubility data of H2S in aqueous salt solutions at conditions of interest for geological sequestration', *Industrial and Engineering Chemistry Research*,vol.**52** n.40, **2013**, pp.14483-14491 doi: 10.1021/ie401947h.

[129] C. J. Wormald, '(Water + hydrogen sulphide) association. Second virial cross coefficients for (water + hydrogen sulphide) from gas phase excess enthalpy measurements', *Journal of Chemical Thermodynamics*, vol. **35**, no. 6, pp. 1019–1030, **2003**, doi: 10.1016/S0021-9614(03)00044-2.

[130] J. I. Lee and A. E. Mather, 'SOLUBILITY OF HYDROGEN SULFIDE IN WATER.', *Berichte der Bunsengesellschaft/Physical Chemistry Chemical Physics*,vol.**81** n.10, **1977**,pp.1020-1022 doi: 10.1002/bbpc.19770811029.

[131] J. Xia, Á. P. S. Kamps, B. Rumpf, and G. Maurer, 'Solubility of H2S in (H2O + CH3COONa) and (H2O + CH3COONH4) from 313 to 393 K and at pressures up to 10 MPa', *Journal of Chemical and Engineering Data*, vol.**45**, **2000**, pp.194-201 doi: 10.1021/je990233+.

[132] G. Smith, A. Sellars, T. K. Yerlett, and C. J. Wormald, 'The excess enthalpy of (water + hydrogen) vapour and (water + methane) vapour', *The Journal of Chemical Thermodynamics*, vol.**15** n.1,**1983**,pp.29-35 doi: 10.1016/0021-9614(83)90101-5.

[133] C. J. Wormald and C. N. Colling, 'Excess enthalpies for (water + nitrogen)(g) up to 698.2 K and 12.6 MPa', *The Journal of Chemical Thermodynamics*, vol.**15** n.8, **1983**,pp.725-737 doi: 10.1016/0021-9614(83)90139-8.

[134] C. J. Wormald and C. N. Colling, 'Excess enthalpies of (water + hydrogen)(g) up to 698.2 K and 11.13 MPa', *The Journal of Chemical Thermodynamics*,vol.**17** n.5,**1985**, pp.437-445 doi: 10.1016/0021-9614(85)90141-7.

[135] C. J. Wormald and C. N. Colling, 'Excess enthalpies for (water + methane) vapor up to 698.2 K and 12.6 MPa', *AIChE Journal*, vol.**30** n.3,**1984**, pp.386-393 doi: 10.1002/aic.690300306.

[136] N. M. Lancaster and C. J. Wormald, 'Excess Molar Enthalpies of Nine Binary Steam Mixtures: New and Corrected Values', *Journal of Chemical and Engineering Data*, vol. **35**, no. 1, pp. 11–16, **1990**, doi: 10.1021/je00059a004.

[137] J. P. Chem and R. Data, 'Solubility of carbon dioxide in water at various temperatures and pressures', *Handbook of Chemistry and Physics*, **2012**.

[138] R. Crovetto and R. H. Wood, 'Solubility of CO_2 in water and density of aqueous CO_2 near the solvent critical temperature', *Fluid Phase Equilibria*,vol.**74**, **1992**,pp.271-288 doi: 10.1016/0378-3812(92)85067-I.

[139] J. L. Alvarez, R. Fernández-Prini, and E. Marceca, 'Standard thermodynamic properties of solutes in supercritical solvents: Simulation and theory', *Chemical Physics Letters*, vol.**381** n.5-6, **2003**, pp.771-776 doi: 10.1016/j.cplett.2003.10.050.

[140] M. Gehrig, H. Lentz, and E. U. Franck, 'SYSTEM WATER-CARBON DIOXIDE-SODIUM CHLORIDE TO 773 K AND 300 MPA.', *Berichte der Bunsengesellschaft/Physical Chemistry Chemical Physics*, vol.**90** n.6,**1986**, pp.525-533 doi: 10.1002/bbpc.19860900606.

[141] M. A. Klins and C. P. Bardon, 'Carbon dioxide flooding', **1991**. Ed., Elsevier Applid Science, New York., pp.215-240.

[142] S. E. Drummond and H. Ohmoto, 'Chemical evolution and mineral deposition in boiling hydrothermal systems.', *Economic Geology*,vol.**80** n.1, **1985**, pp.126-147 doi: 10.2113/gsecongeo.80.1.126.

[143] M. Görgényi, J. Dewulf, H. Van Langenhove, and K. Héberger, 'Aqueous salting-out effect of inorganic cations and anions on non-electrolytes', *Chemosphere*, **2006**, doi: 10.1016/j.chemosphere.2006.03.029.

[144] F. J. Millero, F. Huang, and A. L. Laferiere, 'Solubility of oxygen in the major sea salts as a function of concentration and temperature', *Marine Chemistry*,vol.**65** n.5, **2002**,pp.802-810 doi: 10.1016/S0304-4203(02)00034-8.

[145] J. Setschenow, 'Über die Konstitution der Salzlösungen auf Grund ihres Verhaltens zu Kohlensäure', *Zeitschrift für Physikalische Chemie*, vol.**4** n.1,**2017**, pp.117- 125 doi: 10.1515/zpch-1889-0409.

[146] M. P. Burgess and R. P. Germann, 'Physical properties of hydrogen sulfide-water mixtures', *AIChE Journal*, vol. **15**, no. 2, pp. 272–275, **1969**, doi: 10.1002/aic.690150227.

Chapter 5

Design, economic considerations and environmental analysis

In this chapter, three systems of geothermal plants are illustrated: an ORC (Castelnuovo GTTP, Toscana region, Italy), a double flash (Hellisheidi GTTP, Iceland) and a single flash (Chiusdino GTTP, Tuscany region, Italy). The operating conditions associated with each of these plants depend mainly on the geothermal fluid used to generate energy. Each geothermal plant is emitted a different quantity of pollutants, so each one's simulation depends, albeit in difficulty, on an associated thermodynamic model in Chapters 3 and 4. The unitary operations of the GTTPs are developed using Unisim Design® R480 to predict and control polluting emissions. The pollutant that unites the three plants is H_2S; therefore, each of them has an abatement system. A Life Cycle Assessment (LCA) study was envisaged for the largest of the three plants and associated economic estimates were defined for environmental performance.

Table of Contents

List of Figures

List of Tables

5.1 Introduction

This chapter describes the method and materials adopted to analyze three case studies: three different geothermal power plants (GTTP) with different thermodynamic cycles (single, double- flash and doble-cycle with ORC) and the geothermal mixtures containing essential CO_2, H_2S and water.

The first part of this chapter focuses on three geothermal plants. For each GTTP located either in Italy (Tuscany region) or in Iceland, the following procedure has been adopted:

1. Description of the operational characteristics of the plant;
2. Focus on the main equipment present;
3. The choice of the thermodynamic model adopted for the simulation of the geothermal system;
4. An in-depth study of the techniques adopted, some being optimized by the geothermal site manager, aimed at reducing gaseous emissions with particular reference to the emission of H_2S following the environmental laws in force in the area.

The second part of the chapter is based first on the preliminary economic assessments as a function of the adopted thermodynamic cycle and subsequently on a geothermal plant's environmental analysis. The latter is fundamental since the design phases of a geothermal plant, and the related ministerial authorizations depend on the environmental and safety feasibility of the plant for the benefit of the territory and the residential population. For this, an environmental analysis was developed for the Hellisheiði GTTP case study (consisting of the largest European GTTP in which electricity and thermal energy are produced) through the adoption of LCA and Exergoenvironmental methodologies.

The case studies are:

- 5.2 *Castelnuovo Val di Cecina* Geothermal power plant (Italy);
- 5.3 *Hellisheiði* Geothermal power plant (Iceland) ;
- 5.4 *Chiusdino 1* Geothermal power plant (Italy).

5.2 Castelnuovo Val di Cecina Geothermal Power Plant

5.2.1 The geothermal process and power plant model

The research project[1] on the geothermal plant called "Castelnuovo" is located in Tuscany in Pisa and Siena's provinces (Figure 5.1). It has an area of 7.52 km^2 and has geothermal reserves sufficient to support a net electricity generation capacity of 5 MWe for about 25 years. Thus, the project, authorized by the Ministry of Ecological Transition (Mite) and the Ministry of Economic Development (MISE), has a geothermal potential sufficient to support a geothermal plant with a net power of 5 MWe and uses geothermal resources with high enthalpy as the temperature of the reservoir is slightly greater than 423.15 K.

The operational management of the Castelnuovo pilot plant (CA) project has been entrusted to Magma Energy Italia S.r.l. and an agreement signed between Graziella Green Power, Engie and Storengy.

[1] D.Lgs n.22 of 11/02/2010 - Reorganization of the legislation on research and cultivation of geothermal resources. D.Lgs. n.179 of 18/10/2012- has provided that in order to promote the research and development of new geothermal power plants with reduced environmental impact, medium and high enthalpy geothermal fluids are considered of national interest, aimed at experimenting, throughout the Italian territory, of pilot plants with reintroduction of the fluid geothermal in the same formations of origin and with a net power not exceeding 5 MWe for each plant, where this limit is determined according to the energy fed into the electricity system, which cannot, in any case, exceed 40,000 MWh per year, so as re-established with the new law D.Lgs. n.9 of 21/02/2014.

Figure 5. 1. Location of the research permit called "Castelnuovo". Source: Ministry of Ecological Transition.

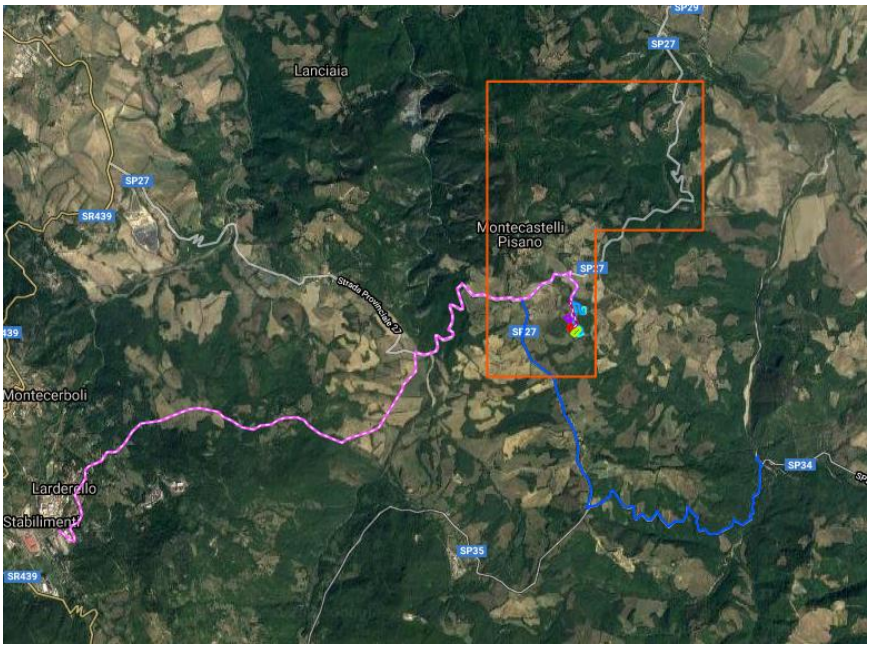

The geothermal project is a pilot plant consisting of:

- Wellfield includes two approximately 3500 m deep wells for the extraction of geothermal fluids (one sub-vertical and the other directional) and another 3500 m deep well for the total reinjection of the extracted fluids non-condensable gases inside of the same geological formations of origin.

- The geothermal power plant includes the transport network for geothermal fluids, a binary cycle power plant - ORC, with a net power of 5 MWe and an electrical transformer substation. The Castelnuovo geothermal plant's research project respects the national legislation (D.Lgs 03/03/2011 n.28 e s.m.i.).

The project connects to the 15 kV *Enel Distribuzione* grid through the medium voltage power line outgoing from the primary substation existing in Larderello.

The purpose of the research project, part of which is interested in this Chapter, envisages a technological and process system with the absence of gaseous emissions through innovative design solutions that involve steam-dominated geothermal fluids through ORC technologies and total fluid reinjection. The total reinjection strategy of the extracted fluid is to ensure maximum sustainability and renewability of the resource, avoiding some undesirable effects associated with any depletion of the fluids.

The GTTP generates electricity by exploiting the geothermal resource's high enthalpy heat through the Organic Rankine Cycle (ORC) binary cycle with R245fa refrigerant (1,1,1,3,3-pentafluoropropane) used in the thermodynamic model of this work[2] as a working fluid. The objective is a cycle that foresees a pumped working fluid and is heated sensibly up to saturation. R245fa is vaporized until it becomes dry saturated vapour; at this point, it is overheated and sent to the turbo-expander for the generation of electrical power.
There is an energy recovery phase (regeneration) at the turbo-expander discharge; before releasing the remaining thermal energy to the cold source through the air condenser, there is an energy recovery phase (regeneration). Regeneration allows increasing the cycle's efficiency by using the working fluid's heat to the turbo-expand exhaust to preheat the fluid state's working fluid before it enters the evaporator. After condensation, the working fluid returns to the starting thermodynamic conditions to start a new cycle.

[2] D.Fiaschi, V.Colucci, G.Manfrida, L.Talluri. Geothermal power plant case study for a new ORC plant including CO_2 reinjection. European Geothermal Congress 2019. Den Haag, The Netherlands, 11-14 June 2019

The characteristics of the Castelnuovo GTTP are:

- A flow rate of the geothermal fluid entering the ORC system (downstream of the scrubber): maximum 17.96 kg /s (equal to 12,41 m^3/h);
- The composition of the geothermal fluid:
  - 92% by weight of water vapour;
  - 8% by weight of non-condensable gases of which:
    - 97.5% by weight of CO_2;
    - 2% by weight H_2S;
    - 0.5% by weight others (such as H_2, CH_4, N_2, NH_3);
    - chloride content (Cl-) maximum equal to 50 mg/l (on condensed sample);

Temperature/Pressure of the geothermal fluid entering the ORC system (downstream of the scrubber):461.65 K/10 bar - saturated steam.

In detail, the description of the operation of the system. The geothermal fluid coming from two production wells has a temperature of 453.15 K and a pressure of 10.3 bar with a flow rate of 18 kg/s (equal to 12596 m^3/h) before being sent to the ORC plant. The geothermal fluid enters a scrubber to reduce the concentration of total dissolved salts in the geothermal fluid from 25 ppm to 2.7 ppm, not always present as indicated by the plant manager. Therefore, this section with the scrubber has not been modelled due to a lack of data. The geothermal fluid sent to the ORC plant generally consists of the following characteristics (stream 30). Inside the ORC plant, the heat is transferred from the geothermal fluid to the working fluid in a single heat exchanger called the vaporizer/superheater, inside which the geothermal resource condenses on the pipe side while heating the working fluid that progressively passes from the conditions of saturated liquid to saturated vapour and finally overheats.

Figure 5. 2. PFD[3] of the geothermal power plant in Castelnuovo using EES® Software. It shows the ORC section (in black).

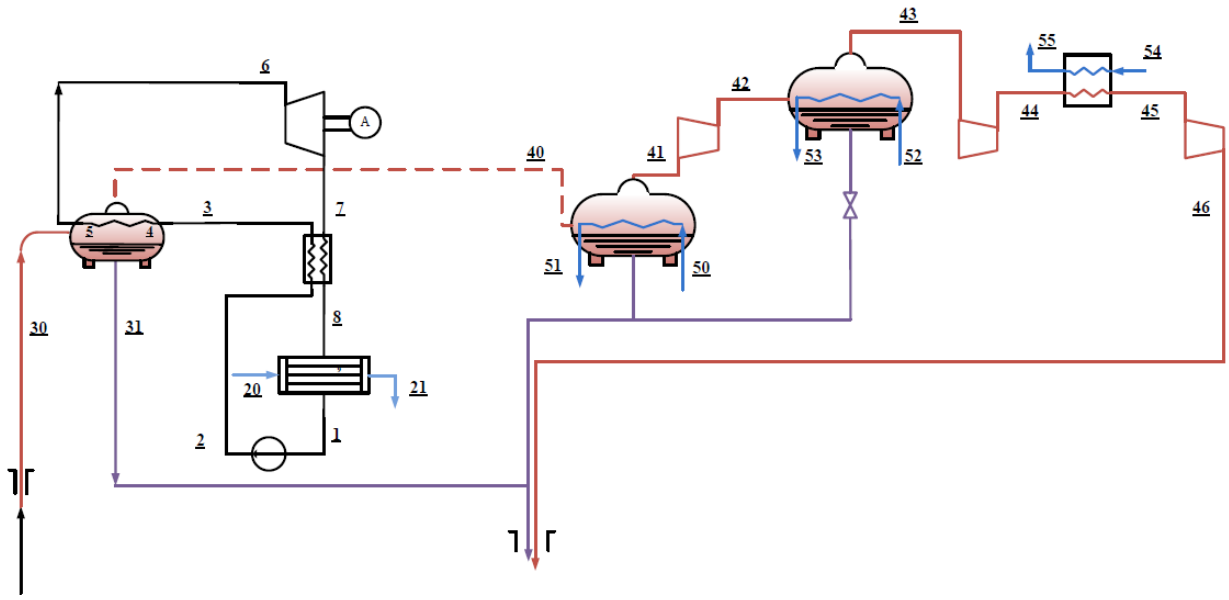

The condensed geothermal resource is discharged into a condensate tank, called a water accumulator, which is not present in the model for clarity, from which the reinjection pumps draw. Next, the non-condensed fraction of geothermal resource, combined with the non-condensable gases, passes through the separator where the secondary separation of the condensates takes place: the resulting flow of non-condensable gases (stream 46) is made available for reinjection. In contrast, the separated condensates are sent to the condensate reservoir. The superheated working fluid, leaving the heat exchanger, is sent to a radial flow expander connected by a reducer to a synchronous generator to generate power.

The superheated working fluid leaving the expander passes through a recuperator (heat exchanger) inside which the working fluid in the vapour phase transfers heat to the working fluid in the liquid

[3] Process Flow Diagram (PFD)

phase, preheating before it enters the heat exchanger (vaporizer/superheater).
The working fluid in the vapour phase leaving the recuperator is sent to the air-cooled condenser and, once condensed, the working fluid is collected in an accumulator and extracted with a pump to restart the cycle. To control the flow rate of the working fluid to the heat exchangers and accommodate any variation of the incoming heat from the geothermal fluid, the pump is operated at variable speed utilizing a frequency variation.

5.2.2 Choice of the thermodynamic model and implementation

A preliminary application of Castelnuovo GGTP was developed in the EES® programming environment[4], taking advantage of the thermodynamic properties package available for different working fluids. Considering that the pressure conditions for the Castelnuovo Val di Cecina site are moderate (10 bar at production wellhead) concerning the critical pressures of both fluids, it was considered sufficient to approach the CO_2-H_2O mixture properties with a third-order EOS model including in the software. This choice also derives from the thermodynamic model solving the system with high efficiency and reliability, with very reduced calculation time. So, the preliminary approach was to simulate the geothermal CO_2-H_2O mixture and R245fa refrigerant (1,1,1,3,3-pentafluoropropane) (free data including in EES®). The results of the simulation of the H_2O-CO_2 geothermal fluid for various % wt. CO_2 is best shown in the temperature glide during the condensation process on the T-s diagram (Figure 5.3). In addition, pure water data from steam IAPWS formulation are also plotted for comparison.

Figure 5. 3. T-s diagram of water-CO_2 mixture [1]

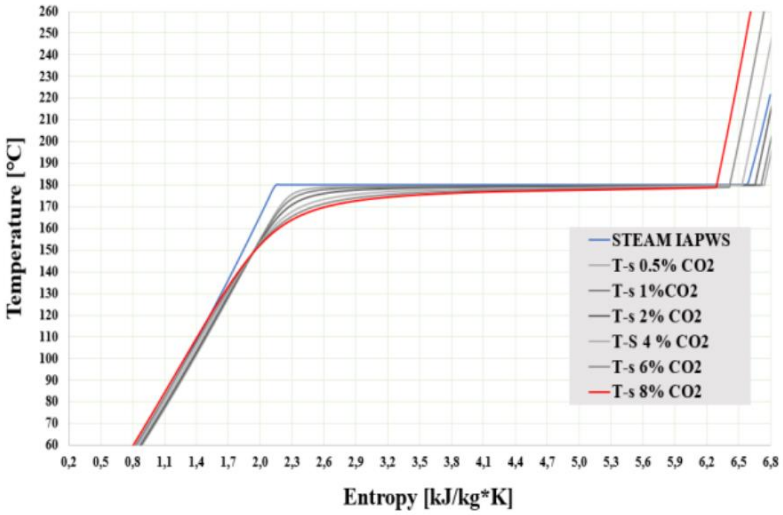

The simple geothermal CO_2-H_2O mixture is associating with the model shown in Figure 5.2. So, the geothermal resource is cooled in the main heat exchanger, and water condensation takes place. At the present stage of the model, the solubility of CO_2 in water is neglected; consequently, stream 31 is assumed as pure water, and stream 40 is pure CO_2. Therefore, this assumption considers the worst-case scenario for total reinjection, as the whole mass flow rate of CO_2 entering the power plant needs to be compressed to allow the total reinjection. To reduce the required power of the compressors train, one precooler and two intercoolers are considered. The heat exchanged in these components can be recovered and utilized for a small district heating network. In the present study, the inlet temperatures of the pre-cooler and intercoolers network (point 50, 52, 54) were assumed at 293.15 K, and a minimum of 283.15 K ΔT was considered for these heat exchangers.

The optimization of the Castelnuovo GTPP model is developed with the Unisim Design software (version R471), considering the CO_2-H_2S-H_2O geothermal mixture. For the sake of simplicity, CO_2 and H_2S have been referred as acid gases.

This simulation has been performed analyzing two different cases:

[4] Nellis, F.A. Klein, F.G. Mastering EES,http://fchart.com/ees/mastering-ees.php

1. Simulation of the plant with particular reference to the compression stages (Figure 5.4);
2. The H_2S reduction process is currently not present, but it has been requested by the operator of the pilot plant to reduce emissions into the air (Figure 5.5).

Case 1. The power plant calculations were performed assuming steady-state processes, adiabatic behaviour of pumps, turbines and compressor and state conditions of 298.15 K and 10 bar. The SPR has been chosen as a simulating thermodynamic model because it is easily implementable in Unisim Desing. In contrast, the OLI packages are pre-defined and non-customizable. For this reason, they are not used in the simulation. On the other hand, DS and PRH are not implementable in Unisim Desing; thus, they are excluded. Another reason for choosing the SPR in Unisim Desing Software is that the working conditions of the Castelnuovo GTPP are properly modelled with a low relative average deviation for CO_2 and H_2S, as shown in Table 5.1 and reported in Chapter 4.

Table 5. 1. CO_2-H_2O and H_2S-H_2O binary systems: calculation of CO_2 and H_2S solubility in water at 303.15 K, 308.15 K, 362.15 and 453.15 K and pressures of 10 and 18.22 bar by SPR model applicated in the simulation of Figure 5.4. There are no experimental data to identify the mixing enthalpies for high temperatures and low pressures.

		H_2O-CO_2	**H_2O-H_2S**
T [K]	P[bar]	[%]‡	[%]‡
303.15	18.22	3.54	1.97
308.15	18.22	19.85	2.92
362.15	10	4.23	3.11
453.15	10	2.97	-2.01

The symbol (‡) indicates that the value in the table has been obtained, performing the relative average deviation (Eq. 4.8) over the corresponding number of points. Therefore, SPR (case 1) and OLI MSE-SRK (case 2 for the gas acid abatement) were used for the present work.

A detailed scheme on the components mass flow and the main model simulations results are defined in Table 5.2. From the production well, the geothermal fluid at 453.15 K and a pressure of 10 bar are transported to gas-liquid separators with a pressure of 10 bar; the liquid from separators is pumped and injected, at a temperature of about 362.15 K, to a reinjected well. Finally, the gas stream obtained from separator 1 at 362.15 K temperature and 10 bar of pressure is sent to three compressor stages (K1, K2 and K3) and two heat exchangers (Figure 5.4).

Figure 5. 4. PFD of the geothermal power plant Castelnuovo. This PFD has been developed using Unisim Desing® (version R471).

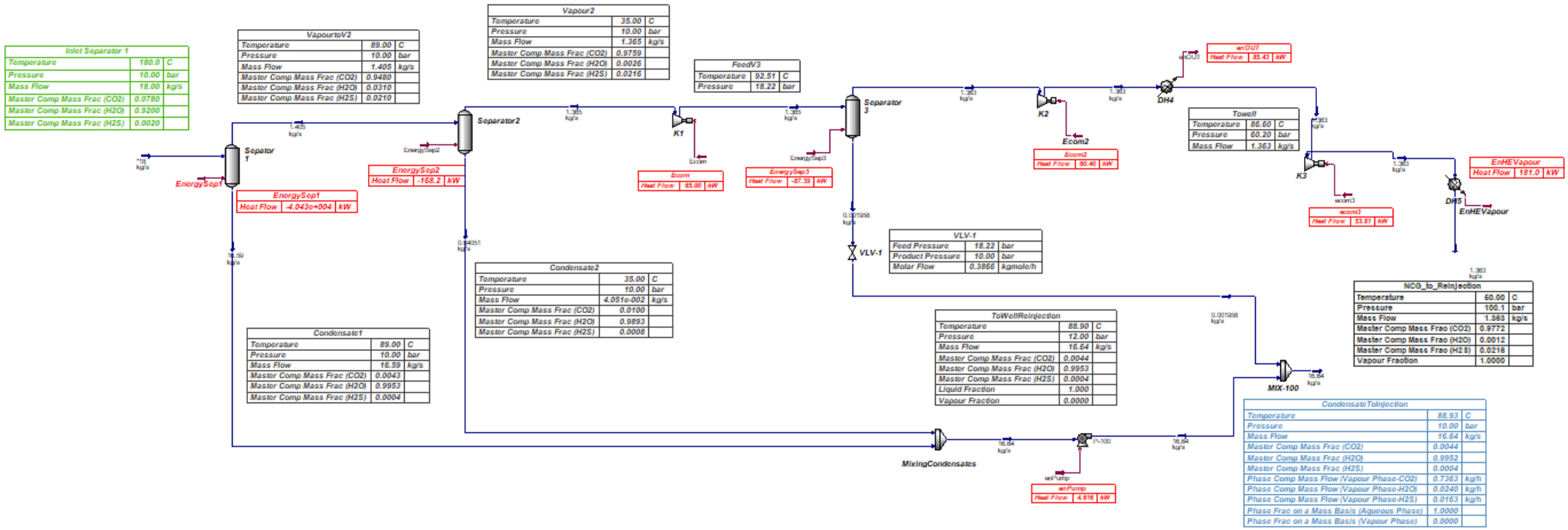

Table 5. 2. The component mass flow of the Castelnuovo geothermal fluid and Castelnuovo simulation results (see Figure 5.4)

H_2O [kg/h]	CO_2 [kg/h]	H_2S [kg/h]	Total [kg/h]
59616,02	5054,36	129, 62	64800

	Inlet separator 1	Vapour to V2	Condensate 1
Temperature [K]	453.15	362.15	362.15
Pressure [bar]	10.00	10.00	10.00
Mass flow [kg/s]	18.00	1.405	16.595
xCO_2 [mol/mol]	0.0335	0.9021	0.0018
xH_2S [mol/mol]	0.0011	0.0258	0.0002
xH_2O [mol/mol]	0.9654	0.0258	0.9980

	Inlet separator 2	Vapour2	Condensate 1
Temperature [K]	362.15	308.15	308.15
Pressure [bar]	10.00	10.00	10.00
Mass flow [kg/s]	1.405	1.365	$4.051 \cdot 10^{-2}$
xCO_2 [mol/mol]	0.9021	0.9662	0.0041
xH_2S [mol/mol]	0.0258	0.0276	0.0004
xH_2O [mol/mol]	0.0258	0.0063	0.9955

	Inlet separator 3	VapourToK2	Condensate 1
Temperature [K]	308.15	303.15	303.15
Pressure [bar]	18.22	18.22	18.22
Mass flow [kg/s]	1.365	1.363	$1.958 \cdot 10^{-3}$
xCO_2 [mol/mol]	0.9662	0.9772	0.0079
xH_2S [mol/mol]	0.0276	0.0216	0.0008
xH_2O [mol/mol]	0.0063	0.0012	0.9913

The required compression ratio (Figure 5.4) for acid gas is generally over 50. Performing this in a single stage would significantly increase the gas temperature beyond the maximum rated equipment. Compression at high temperatures is inefficient. Therefore, three compression stages are employed (K1, K2 and K3). At each stage, the gas is compressed and cooled (Table 5.3), and any liquid condensed by the cooling is removed. The required reservoir pressure determines this exact number of stages. The cooling at each stage maintains the process temperature safely within equipment limits and increases compression efficiency. Any liquid condensed must be removed before the next step. This liquid is usually water with small amounts of acid gas dissolved. The removal of water from the system is advantageous to avoid hydrate formation with the presence of eventual salts. The lower the cooling temperature, the more water is removed. If the temperature drops below the acid gas dew point, significant amounts of these gases will remain in the condensate stream rather than in the injected stream. So, it is crucial to understand the full phase behaviour of the acid gas mixture being injected.

Table 5.3. Data from the complete process for acid gas injection with three compressor stages and coolers (case 1)

Equipment name	T_{in} K	P_{in} bar	T_{out} K	P_{out} bar	Mass Flow [kg/s]	Heat Flow [kW]
Compressor 1 (K1)	308.15	9.4	371.64	18.22	1.365	60.53
Cooler 1	371.63	18.22	303.15	18.22	1.365	80.30
Compressor 2 (K2)	303.15	18.22	360.50	33.20	1.363	50.53
Cooler 2	360.5	33.20	303.15	33.20	1.363	71.43
Compressor 3 (K3)	303.15	33.20	359.56	60.20	1.363	44.94
Cooler3	359.56	60.20	323.15	60.20	1.363	55.42

Case 2. For each GTPP, the ministry and the associated entities request the definition of specific procedures that are executed by the manager of the GTPP following the IPPC[5] protocols to reduce the associated gas emissions. Therefore, in this paragraph, the second case is defined through the most appropriate actions to be implemented for the reduction of H_2S specifically.

According to the research conducted in the Castelnuovo pilot plant, after removing H_2S, the CO_2 has to be dissolved in water to be injected back into the geothermal well. Using Unisim Design R471, a specific scrubber simulation has been designed to absorb H_2S and CO_2 using NaOH through specific filling materials. Therefore, different amounts of NaOH solutions and specific filling materials are simulated for the Castelnuovo power plant. However, thanks to several thermodynamic analyses on the geothermal mixture [1], it is important to state that only the section regarding reducing H_2S emissions in the outflow stream from Separator 1 uses the OLI MSE-SRK software package because it is implemented in Unisim Desing. Therefore, the section needed to reduce the NCGs emission from Castelnuovo GTTP has been simulated with an appropriate acid gas-caustic wash property package in OLI MSE SRK. The Acid Gas – Caustic Wash package was developed in conjunction with the Peng-Robinson equation of state for the vapour phase. In addition, to model the electrolytes, the non-random two-liquid (eNRTL) activity coefficient model was used [2]. Furthermore, the Acid Gas – Caustic Wash package contains the eNRTL model parameters calculated from regression to the available VLE data. The package also rigorously accounts for the chemistries of the caustic wash process. The restriction is that NaOH, H_2S, H_2O, and CO_2 are required components for this model. In addition, the starting input conditions are simulated by the SPR model, as described in Figure 5.4, and the output conditions from separator 1 presented in Figure 5.5.

Thus, in order to prevent the corrosion on electronic equipment due to H_2S emissions and choose the best compressors configuration from a design and economic point of view, non-condensable gases are removed. First, the non-condensable gases are withdrawn from Separator 1. Subsequently, they are sent to the specific scrubber (T-100, Figure 5.5), where they are pulled down through a caustic treatment. Specifically, the H2S is reduced by 86% of its initial amount. Next, the obtained H_2S-free vapour is sent to Separator 2 and is recompressed through three stages (K1, K2, and K3), piped to an injection well, and routed underground. Given the high concentration and corrosive nature of the acid gases (CO_2 and H_2S), the process equipment used for acid gas injection must be constructed using stainless steel.

Particularly, the simulation uses a 1-10 wt.% caustic solution to treat a geothermal fluid containing H_2S and CO_2. A separator is used to minimize residence time to allow selective adsorption of H_2S. The adsorption of CO_2 by NaOH is a much slower reaction than the absorption of H_2S. Figure 5.6 illustrates the scheme of the caustic scrubbing system used in this study. The geothermal stream composed of water, carbon dioxide, and hydrogen sulfide represent the column's inlet. Different packing materials are used in the simulations, and their characteristics have been included in the simulator.

For the abatement of H_2S, packed towers are widely used for chemical and physical scrubbing. The choice of the caustic solution concentration is critical in determining the dissolution rate of pollutants in the liquid. Currently, the process choice is a commercial integrated facility for removing acid gases in the geothermal power plant. In addition, the caustic solution is an economical alternative solvent to aqueous methyl diethanolamine (MDEA). On the other hand, NaOH solution is a very effective and non-regenerable absorbent. For the improvement of scrubbing efficiencies, the design of the scrubber system is important. Multiple gas absorption columns packed with structured materials increase the active surface area and residence time for an efficient gas-liquid interaction. Commercial structured packing materials for H_2S removal with an alkaline washing solution ensure a high contact area between the gas and the liquid phases.

[5] integrated pollution prevention and control (IPPC)

Figure 5. 5. PFD of the geothermal power plant Castelnuovo with a caustic (NaOH) scrubbing system concerning the optimization of the actual geothermal plant through the reduction o the emissions which are made after the original process (Figure 5.4)

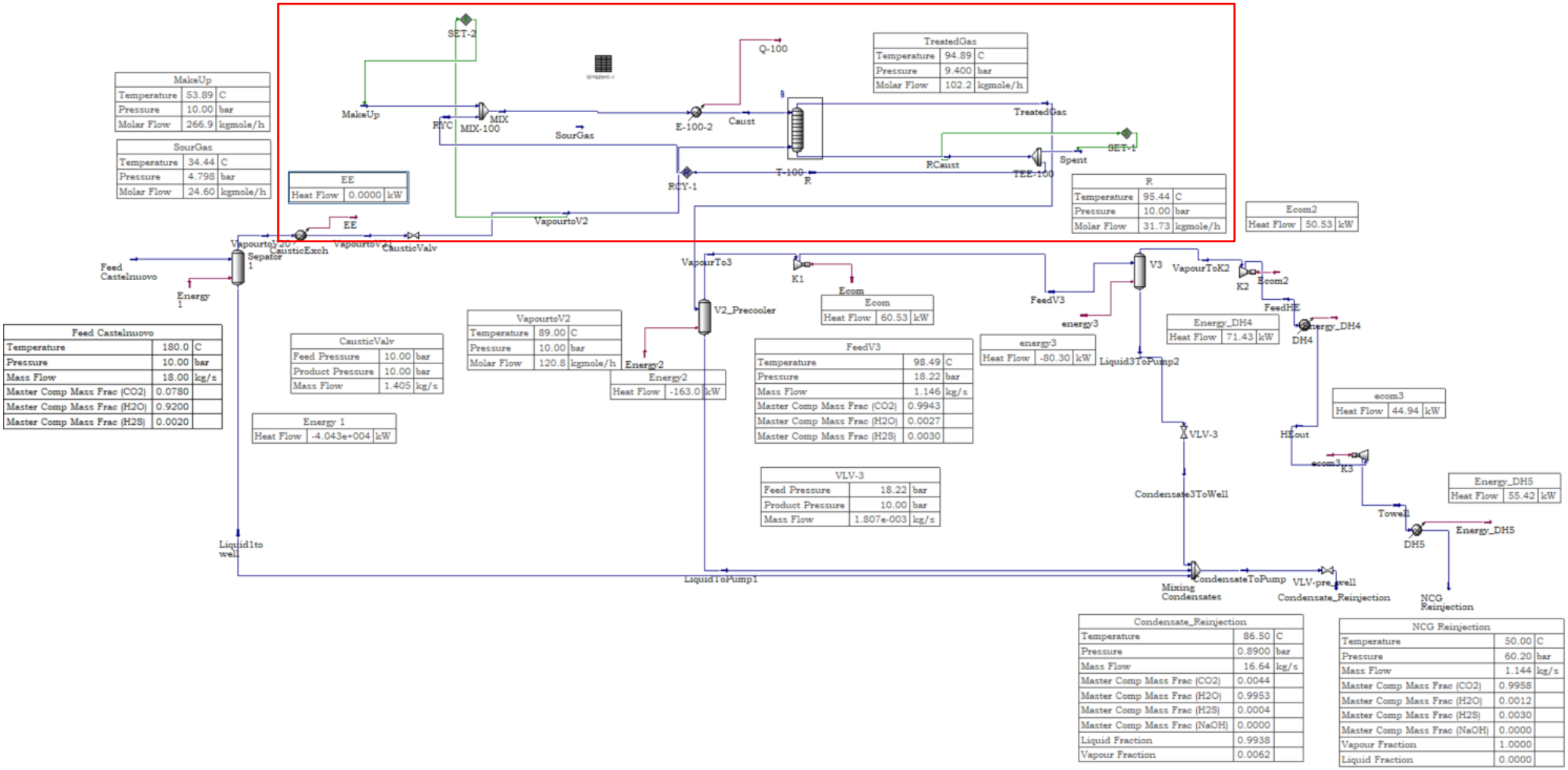

The simulations were carried out at 362.15 K, 10 bar and a mixing flow rate of 1.405 kg/s. In this condition, the geothermal fluid is a vapour that contains H_2S (0.054 kg/s), CO_2 (1.309 kg/s) and water (0.042 kg/s). Before the injection steps, this geothermal fluid goes to a scrubbing system with the diameter of the packing material between 0,55-0,58 m. In these simulations, a commercial *Pall rings 2-inch metal* was used to generate a packing bed in the column. The simulation is conducted at different weight fractions (% wt) of NaOH, as shown in Table 5.4.

Table 5. 4 Soda and water streams for each % wt of NaOH in the simulated scrubber with a treating sour gas of 1.4 kg/s

% .wt NaOH	NaOH (kg/s)	Water (kg/s)
1	0.108	10.673
2	0.118	5.782
3	**0.150**	**4.850**
4	0.180	4.820
5	0.211	4.009

Table 5. 5. Operating parameters of the system for the scrubber by random Pall rings 2-inch metal (better solution at 3% wt NaOH)

3% .wt of NaOH solution				
Material:	Random: Pall rings 2-inch metal			
Scrubber Stage	Pressure	Temperature	Vapour mass flow	Liquid Mass Flow
	bar	K	kg/s	kg/s
1	9.86	318.22	1.21	5.04
2	9.93	319.48	1.25	5.05
3	10	331.24	1.26	5.19

Absorption simulations were realized for five different concentrations of soda (Table 5.4). As previously mentioned, the Pall rings 2-inch metal was chosen (Table 5.5). The H_2S removal percentage was calculated for different gas residence times with a countercurrent flow arrangement, treating 1.309 kg/s of CO_2, 0.054 kg/s of H_2S in the inlet of the Scrubber (Figure 5.6). The sweetened gas achieved contains about 0.0076 Kg/s H_2S for a 86% removal of H_2S, while the liquid effluent is 0.0464 kg/s.

NaOH, known as a caustic solution, reacts with H_2S dissolved in an aqueous solution in the scrubbing processes. H_2S and NaOH reactions are in the water phase. As a result, H_2S diffuses to the interface of the inorganic phase and then to the water phase. Moreover, the system is influenced by the presence of CO_2 and the relative salts that form in the three stages of the column. CO_2 in gas streams makes some complications to use with NaOH solution for H_2S scrubbing, and its presence increases the consumption of NaOH solution and could decrease the H_2S removal.

Figure 5. 6. H_2S and CO_2 removal (%) versus residence time for random Pall rings 2-inch metal.

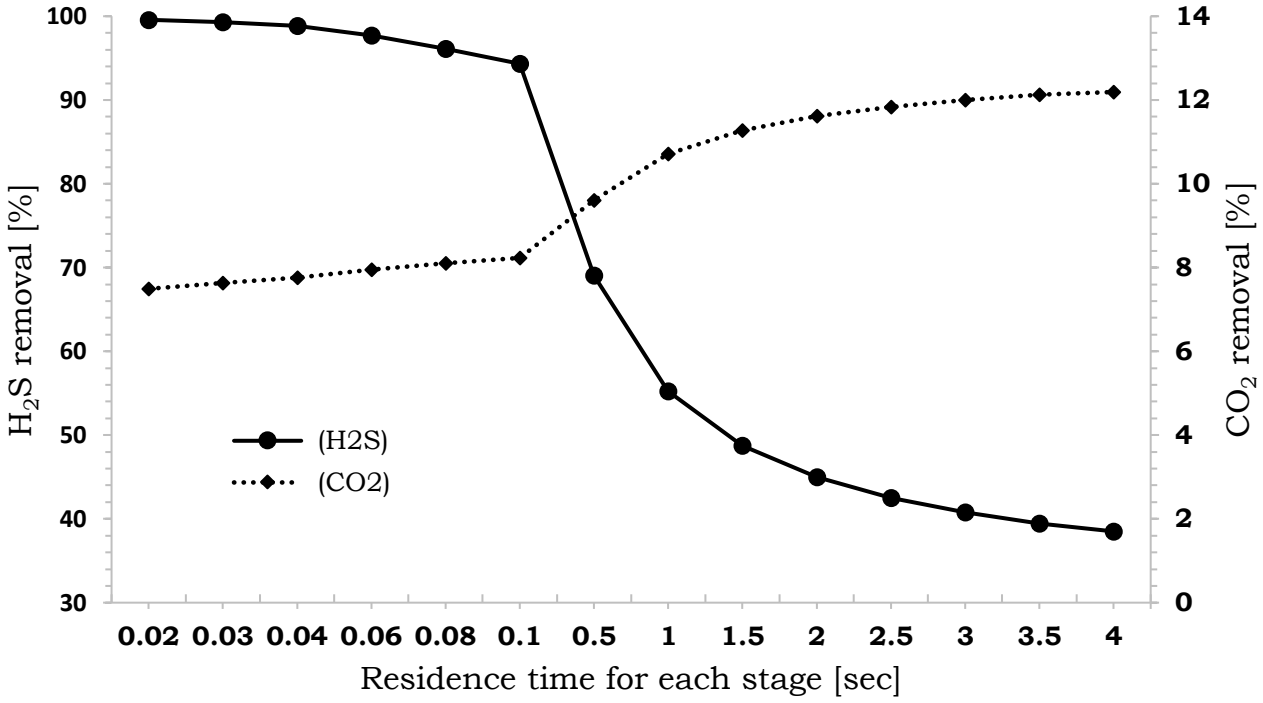

Table 5. 6. The mass flow of the scrubber in the three stages at a 5 kg/s of fresh caustic feed (NaOH+ H_2O mixture)

Vapour Sour Feed	Sweetened gas	Liquid effluent
H_2O: 0.042 kg/s	H_2O: 0.012 kg/s	H_2O: 4.862 kg/s
CO_2: 1.309 kg/s	CO_2: 1.20 kg/s	CO_2: 0.109 kg/s
H_2S: 0.054 kg/s	H_2S: 0.0076 Kg/s	H_2S: 0.0464 Kg/s

It is possible to note that the capture of H_2S is efficient. This effect is associated with the inlet H2S concentration and the residence time that plays an essential role in the scrubbing processes. In order to investigate the influence of gas residence time on the H_2S removal, the gas residence times were changed in a range between 0.02 sec and 4 sec.

The key parameter to design a packed bed scrubber unit for selectively removing the H_2S in a geothermal fluid is the gas residence time. The results show that the lower the gas's residence time, the higher the H_2S removal efficiency. The coexistence of CO_2 and H_2S affects the scrubber design, i.e. allowing residence times exceeding 0.2 s determines a substantial decrease in H_2S capture, with only minor effects in CO_2 capture, which always remains below 12%. The gas's velocity, the packing geometry, and the soda water solution (below 5%) represent minor design parameters. Considering the necessity to limit water flow rate and the countercurrent flow arrangement, a solution with a 3% wt concentration of NaOH is recommended. Thanks to efficient, structured packing, the final design solution allows a low NaOH consumption for this specific application to a geothermal power plant.

5.3 Hellisheiði Geothermal Power Plant

5.3.1 The geothermal process and power plant model

Sitting in the north-Ovest of Europe, Iceland has a population of around 364134 and has the highest per capita concentration of geothermal energy of any country in the world. 66% of the residents are in Reykjavik, the capital city, and they use geothermal energy to provide electricity and heat from Nesjavellir and Hellisheiði plants. About 86% of Iceland's primary energy is between geothermal and hydro, contributing to strengthening renewable sources. Geothermal contributes 68% of the total need. Space heating from geothermal hot water takes care of 90% of all homes. In addition, the hot water uses in greenhouses, fish farming, snow melting, swimming pools, and various industries. The mean estimate of direct heating is 8030 GWh-th[6] and the total installed geothermal electric power capacity stands at 663 MW with an annual generation of 5245 GWh. Thus, the system has an overall capacity factor of 90%. Geothermally produced electricity accounts for 29% of the country's total [3]. The power station of Hellisheidi is on the opposite sides of the Hengill volcano. The Hellisheidi power plants lie along the north-northeast trending fault zone, about 10.5 km apart (Figure 5.7).

Figure 5. 7. Aerial view of Hengill geothermal area. Google Earth image, June 25, 2020

Figure 5.8 shows the Hengill geothermal field model. There are two apparent heat sources for the two power plants. The model indicates a central upflow zone near the volcano and outflows to the southwest and northeast. At the HE wells, the average flow is 300 kg/s with a temperature between 453.15-463.15 K. In some areas of the Nesjavellir site (NV), the temperature from NV wells is about 513.15 K.

[6] Thermical energy

Figure 5. 8. Conceptual model of Hengill geothermal formation. Source: [4]

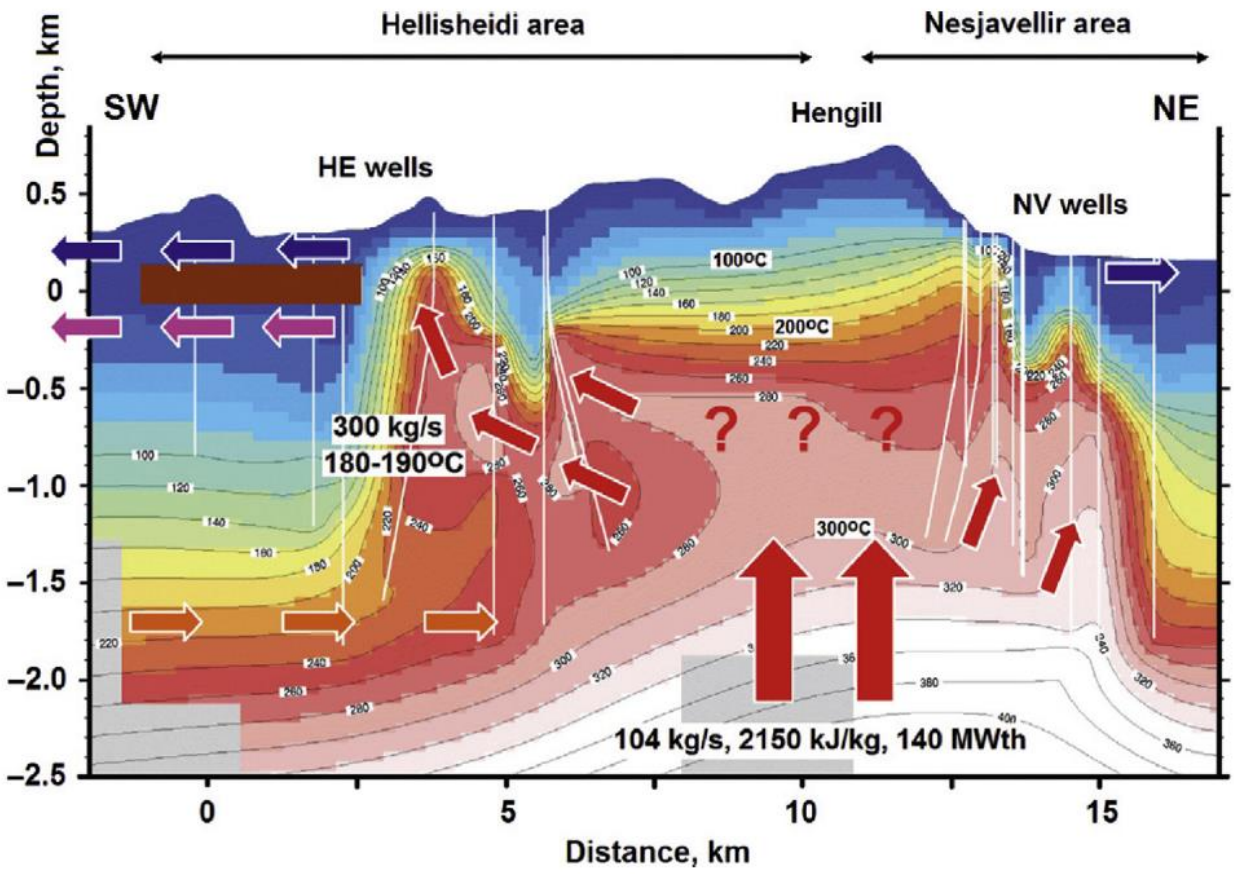

The basaltic intrusions and shallow-dipping diorite intrusions contribute to the permeability of the reservoir. The wellhead locations at the Hellisheiði are in Figure 5.9.

Figure 5. 9. Wellhead locations in the Hengill area.

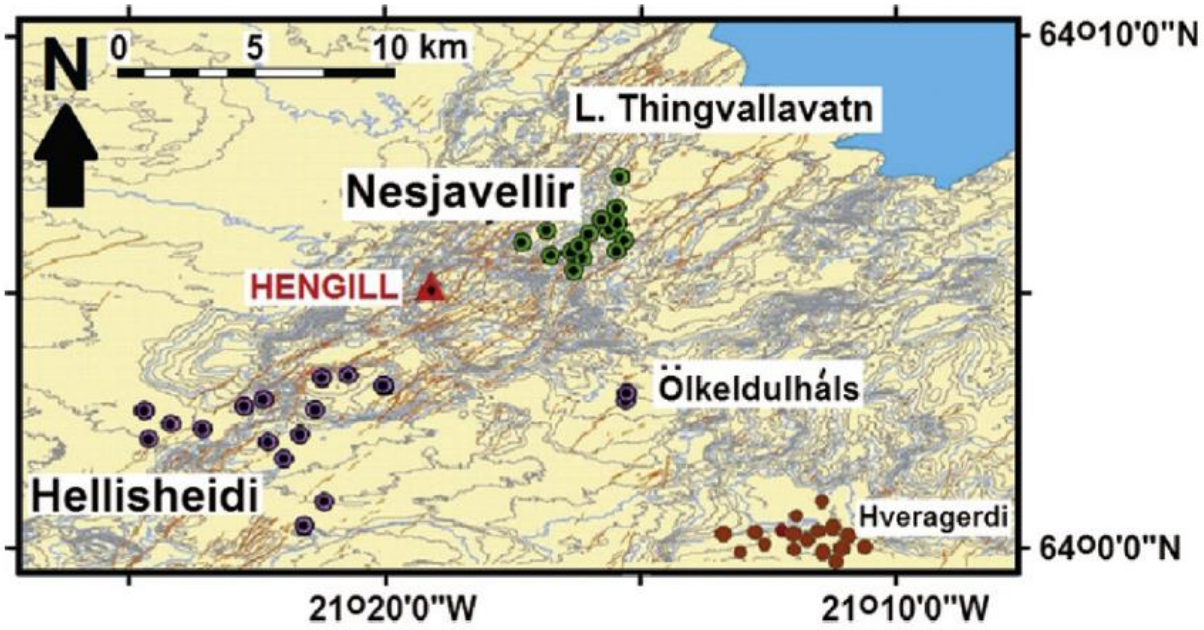

The Hellisheidi and Nesjavellir reservoirs have similar characteristics. The wells at Hellisheiði produce geofluids that are somewhat lower in temperature but still high enough to support several moderate-sized power plants (Table 5.5).

Table 5. 7. History of development and commissioning overview at Hellisheiði

Phase	Year	Hot water MW_{th}	Electric power MW
1	2006	-	90(2X45)
2	2007	-	123 (2X45+1X33)
3	2008	-	213 (4X45+1X33)
4	2010	133	213 (4X45+1X33)
5	2011	133	303 (6X45+1X33)
6 (Estimated)	2020	266	303 (6X45+1X33)
7 (Estimated)	2030	400	303 (6X45+1X33)

A total of 64 wells (the year 2015) and 69 wells (the year 2020) are drilled to depths of 2000-3000 m in support of the fully developed plant. Some of these wells are drilled with diesel or electricity, or both (Table 5.6).

Table 5. 8. Energy use for electrical drilling and depths for main Hellisheidi wells for the year 2020.

Well Number	Drilling Source	Depth	Well type	Electricity use (kWh)	Diesel Use (lt)	Average electricity use (kWh/m)
HE-61	Electricity	1857	wide	759843	12124	409
HE-62	Electricity	2260	wide	479998	12124	212
HE-63	Electricity	2591	wide	586610	0	226
HE-65	Electricity	2497	wide	225621	4000	90

During the drilling of the wells, the consumptions of diesel and electricity are in Table 5.7.

Table 5. 9. Diesel and electricity use over the wells

Average diesel use wide	1.60	lt/m
Average diesel use narrow	2.53	lt/m
Average electricity use wide	266.1	kWh/m
Average electricity use narrow	90	kWh/m

The hot water is sent to Reykjavik; the electricity is mainly provided to nearby aluminium refineries and the population. Therefore, the geothermal fluid present in Hellisheiði is mainly characterized by water and low percentages of non-condensable gases (NCGs) such as CO_2 and H_2S in particular (Figure 5.10).

Figure 5. 10. The mass composition of the geothermal fluid for energy production at the Hellisheiði power plant.

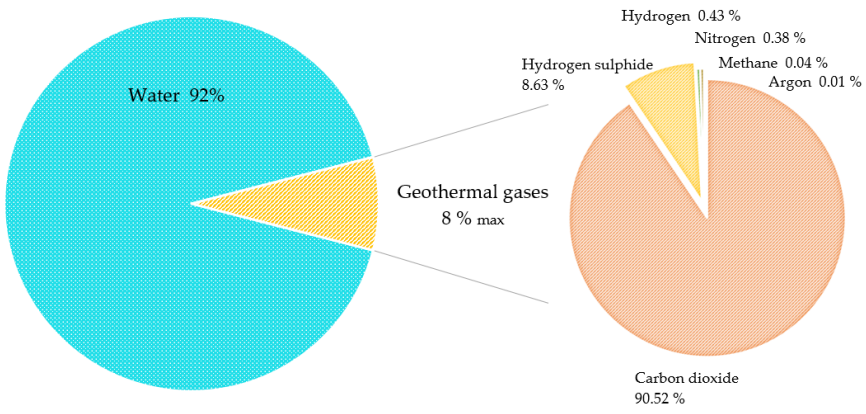

This section aims to model only the Hellisheiði power plants with the scenario n.1, i.e. no emissions abatement, while both Scenario n.1 and Scenario n.2 (Geothermal power plant with the CarbFix® system, the new pilot plants) are treated in Life Cycle Assessment (LCA) section 5.6.

Scenario 1. This scenario is well represented in three figures: Figure 5.11 (the HE schematic representation), Figure 5.12 (The HE PFD with Unisim Design vs R480) and Figure 5.13 (PFD designed by MANNVIT[7]). The two-phase flow from the geothermal wells is separated into steam and water at 10 bara pressure in central separation stations.
The steam is piped through moisture separators and then passes through condensing steam turbines, with indirect condensers, generating electric energy. The condensers for the high-pressure unit have a separate bundle, so the cooling is managed entirely on the cooling towers, or part of the condenser is connected to the thermal system and preheats the freshwater. This flexibility minimizes the downtime of the heating system. After the steam separators, the separated water is again launched at 2 bar in low-pressure steam separators giving approximately 12% steam. The steam is then conveyed to the moisture separators, and then it passes through a low pressure condensing steam turbine, producing power for generating electricity.
The water separated by the low-pressure steam separators heats the preheated water in the heat exchangers to the district heating system's temperature, typically around 363.15 K Freshwater, which is saturated with dissolved oxygen, becomes corrosive when heated. The water is therefore heated deaerated before leaving the boiler room. The deaeration is obtained by boiling it under a vacuum and injecting a small amount of geothermal steam containing H_2S.
The demand for district heating varies throughout the year. Meanwhile, electricity generation is relatively constant. Therefore, the vapour condensation temperature is regulated between 319.15 K and 330.15 K, and the temperature of separated water can be adjusted between 393.15 K and 453.15 K to gain flexibility during operation.

Figure 5. 11. A schematic representation of the Hellisheiði power plant. The blue colour denotes the machinery used for the electricity production from the high-pressure units, green for electricity production from low-pressure units, and orange for hot water production.

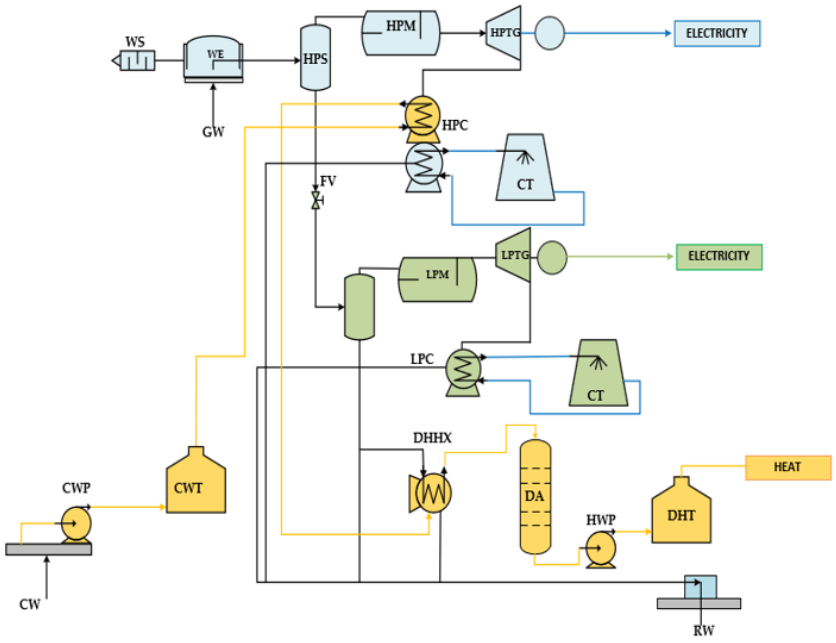

In Figure 5.11, the acronyms are defined as:

- CT is the cooling tower;
- CW is the cold water well;
- CWP is a cold water pump;
- CWT is a cold water tank;
- DA is the deaerator; DHHX is the Heat exchanger for district heating water;

[7] https://www.mannvit.com/

- DHT is the District heating water tank;
- FV is the Throttle valve;
- GW is the Geothermal well;
- HPC is the High-pressure condenser;
- HPM is a High-pressure moister remover;
- HPS is the High-pressure steam separator;
- HPTG is the High-pressure turbine generator set;
- HWP is the Hot water pump;
- LPC is the Low-pressure condenser;
- LPM is the Low-pressure moisture remover;
- LPS is the Low-pressure steam separator;
- LPTG is the Low-pressure turbine-generator set;
- RW is the reinjection well;
- WE are the Wellhead equipment;
- WS is the Well silencer.

The whole process of energy production can be divided into six several stages:

1. Withdrawal of the geothermal fluid through the wells;
2. Separation of the vapour phase and the liquid phase;
3. Transport and heating of cold water (heat transfer fluid for cogeneration);
4. Production of electricity;
5. Disposal of liquids and gases before reinjection;
6. Connection to the national electricity grid and the Reykjavïk district for heating.

The emission of geothermal gases is an inevitable part of high-temperature geothermal utilization. Annually Hellisheiði Power Plants Iceland emit 43200 tons of CO_2 and 16900 H_2S. From 2010, the government of Iceland's new regulation on H_2S concentration in the air has forced companies to find improvement solutions for process optimization and reduce pollutants emitted into the air. Reykjavík Energy has commissioned a solution to lower gas emissions from its power plants, particularly from Hellisheiði Power Plant. In this power plant, the H_2S concentration increases nearby town and communities.

The gas separation station involves separating geothermal gas into soluble (CO_2 and H_2S) and non-soluble gases (H_2, N_2, Ar) with two experimental gas reinjection projects, SulFix® and CarbFix®. The geothermal gases are dissolved in water and injected into the bedrock. In SulFix®, the target zone is the >473.15 K high-temperature geothermal system below 800 m, and in Carbfix®, the target zone is 303.15 -353.15 K between 400-800 m. Injection of H_2S back into the geothermal system where it came from has to be considered an environmentally benign method of H_2S abatement. The emitted gases have both local and global environmental effects, making lowering the gas emissions from geothermal power plants one of the crucial challenges of the geothermal industry.

The Hellisheiði Geothermal fluids contain dissolved CO_2, H_2S, H_2, N_2, CH_4 and Ar (Figure 5.10). The concentration of individual gases can range from ppb levels to several thousand ppm depending on the geothermal reservoir's geological settings, temperature, and composition. The gases' origin is or magmatic, meteoric or formed in the geothermal reservoir in water-rock reactions. They can be both considered reactive and conservative constituents and have long been used by reservoir scientists to characterize the physical nature of and manage production from hydrothermal systems [5]. In liquid-dominated geothermal fields, most of the gases are dissolved in the geothermal system's fluid. During the geothermal fluid's utilization and depressurization, the gases are concentrated in the steam phase and are finally vented out of the turbines' condensers to the atmosphere. Therefore, gas emissions inevitably affect the air quality around the power plants as the concentration of the geothermal gases increases. Under certain weather conditions and if the excellent distribution of the gases at the disposal site is not secured, the gases can affect air quality tens of kilometres from the power plant site. Unfortunately, since the Hellisheiði plant's construction, the concentration of H_2S in the atmosphere and its smell has spread more near the city of Reykjavík. After the legislation passed by the Icelandic government, the average annual concentration can't go higher than 5,0 $\mu g/m^3$ air, and the 24-hour average can't be above 50 $\mu g/m^3$ air.

Table 5. 10. The amount of H_2S and CO_2 (tonnes/year) produced by the Hellisheidi field, emitted and injected in 2014-2017 [6].

H_2S (tonnes/yr)	Flow-through power plant	Venting of steam	Well testing	Total flow	Dissolved in water
2013	11900	100	400	12400	-
2014	10800	100	0	10900	1100
2015	9600	100	0	9700	1100
2016	8300	100	0	8400	1100
2017	8800	100	0	8900	1100
H_2S (tonnes/yr)	Injected	Emitted	% injected	% emitted	
2013	0	**12400**	0	100	
2014	1300	8500	22	78	
2015	2200	6400	34	66	
2016	3400	3900	54	46	
2017	4900	2900	68	32	
CO_2 (tonnes/yr)	Flow-through power plant	Venting of steam	Well testing	Total flow	Dissolved in water
2013	43300	400	1200	44900	-
2014	42400	400	200	43000	1700
2015	38300	400	200	38900	1900
2016	34200	400	0	34600	1800
2017	35200	400	0	35600	1900
CO_2 (tonnes/yr)	Injected	Emitted	% injected	% emitted	
2013	0	**44900**	0	100	
2014	2400	38900	10	90	
2015	3900	33100	15	85	
2016	6700	26100	25	75	
2017	10200	23500	34	66	

5.3.2 Choice of the thermodynamic model

Reasonable thermodynamic correlation is a fundamental step for implementing the geothermal model to obtain simulation results similar to reality. Therefore, the first representative conditions are the geochemical stream compositions, operating conditions such as temperature and pressure along the Hellisheiði geothermal process and its unit operations. The geothermal fluids are composed of water and non-condensable gas fractions (Table 5.9), pressures from 11 bar to 0.01 bar and temperatures from 453.15 K to 278.15K. So, like in Chapter 3 from Figure 3.2 and the results model in Chapter 4, there is an optimal option: Sour-PR thermodynamic models. The choice of this model is the most appropriate for acid gases in water. The Hellisheiði designers have used the SRK model because the geothermal fluid has another percentage of H_2S by mass.

Table 5. 11. Operating conditions of the HE geothermal fluid

Composition of the geothermal fluid (1050.5 kg/s)		
Dissolved gasses (NCG) mass fraction	8.00 %	
CO_2	76.0368	Kg/s
CO	-	Kg/s
CH_4	0.0336	Kg/s
H_2S	7.2492	Kg/s
NH_3	-	Kg/s
N_2	0.3192	Kg/s
Ar	0.0084	Kg/s
H_2	0.3612	Kg/s
Temperature wellhead/separator	453.15	K
Pressure wellhead/separator	11	bar
Condensing temperature	319.15-330.15	K
Reinjection temperature (17 wells)	341.58	K

5.3.3 Implementation and simulation model

In this section, the development of the model of the GTPP named Hellisheiði (indicated as HE) is described in Figure 5.12. Using Unisim Design® R480 with the modified SPR thermodynamic package, also used to integrate data in the Life Cycle Inventory (LCI) data and results that have created the Life Cycle Assessment (LCA) of HE [7]. The SPR models were defined for scenario 1.

Table 5. 12: Comparison of aqueous phase calculation with SPR model and HE experimental data with relative deviation.

		SPR model		HE laboratory test		$\Delta x^{\ddagger}$	
T[K]	P[bar]	$x CO_2$ (mol/mol)	$x H_2S$ (mol/mol)	$x CO_2$ (mol/mol)	$x H_2S$ (mol/mol)	%	%
448.15	10	0.000101	0.000156	0.000100	0.000151	1.00	3.31
439.25	10	0.000273	0.000417	0.000276	0.0004291	1.20	2.89
373.12	5	0.000579	0.00073	0.000591	0.0007501	2.10	2.76
300.84	1.013	0.000418	0.000538	0.000425	0.0005512	1.76	2.45
306.72	1.013	0.000369	0.00047	0.000377	0.0004793	2.19	1.98
290.15	1.14	0.000544	0.000687	0.000555	0.0007008	2.04	2.01

Figure 5. 12. Scenario 1 without emissions treatment (the condition year 2012).

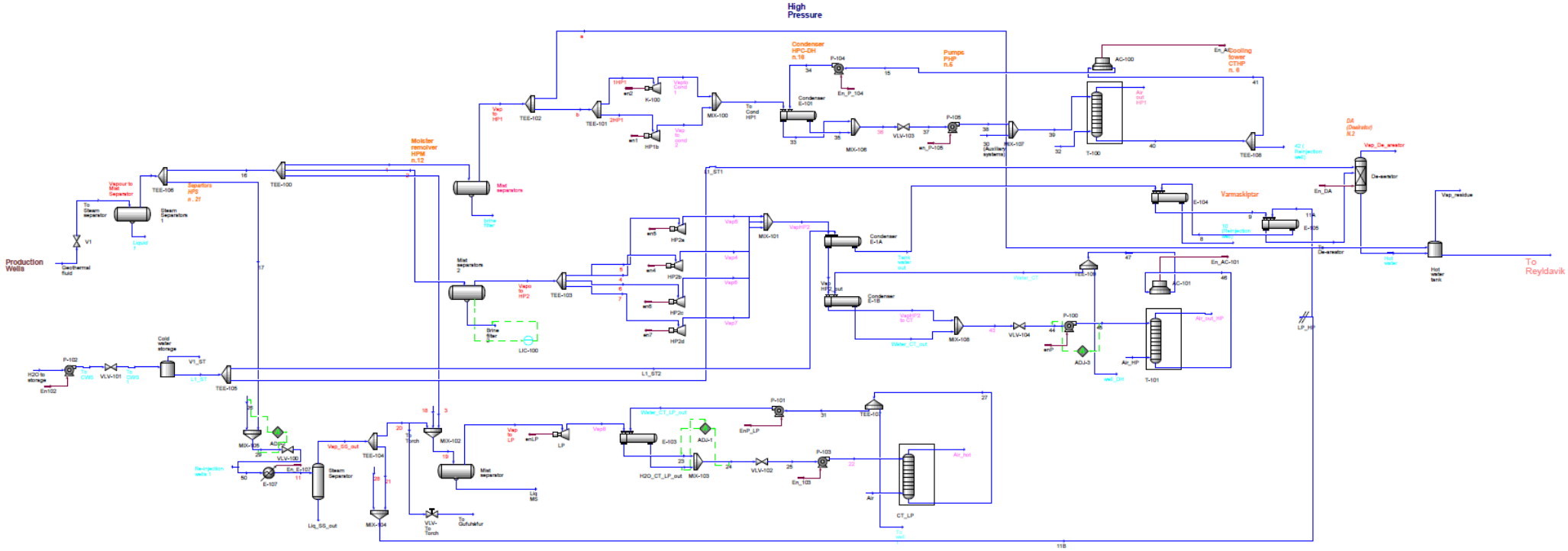

The GTTP sections are visible in Annex 5A, as the process represented through the Unisim Design software, in the same way as the P&Id of the HE geothermal plant.

Scenario 2. The CarbFix project involves re-injecting geothermal gases into basaltic formations to sequester the dissolved gases in minerals in the bedrock. Description of the CarbFix project is provided by Aradòttir et al. [8]. CarbFix, a combined industrial/academic research project, was developed to assess the feasibility of in situ CO_2 mineral sequestration in basaltic rocks. To date, two types of gases have been injected into the CarbFix project. Around 176 tons pure CO_2 and 65 tons gas mixture from the gas separation station. The composition of the gas from the gas separation station in volume percentages was 75% CO2, 24% H_2S and 1% H_2. The CarbFix storage formation lies between 400-800 m depth, is 303.15-353.15 K warm and consists of relatively fresh basalts. The geothermal gas is pressurized to 5 bar, and the soluble gas is separated from the rest in a water absorption tower. The absorption tower is operated with condensate water that has been cooled from 313.15 to 283.15 K. The solubility of the geothermal gases is higher at a lower temperature. The gas loaded condensate water is then injected back into the geothermal reservoir. The inlet stream (NCG) has a composition of 63.35 vol%CO_2, 21.39 vol% H_2S, 4.12 vol% N_2, 0.47 vol% CH_4, 10%vol H_2 and 0.67 %vol Ar. A CO_2 and H_2S dominated gas mixture was captured from this power plant exhaust gas stream by dissolution into pure water in a scrubbing tower. Two main components have considered the choice of the thermodynamic model in water. In total, 30 to 36 kg/s of pure water is sprayed into the top of the scrubbing tower, operated at an absolute pressure of 6 bars at 293.15 K. Pure water interacts with a 249.4 kg/s exhaust gas stream dissolving the water-soluble gases, while the non-water-soluble gases are vented into the atmosphere. The scrubbing tower is 12.5 m high and 1 m wide. Its internal volume is 4.7 m^3 of filling material [9]. The gas-charged water was pressured to 9 bar and transported to injection wells via a 1.5 km long and 279 mm inner diameter high-density polyethene pipe.

5.3.4 Emissions reduction and results analysis

The geothermal energy in Hellisheiði GTPP contributes to the emission of H_2S to the atmosphere, and at the same time, it influences the city of Reykjavik and works. Hellisheiði GTPP is located at a distance of 30 km southeast of Reyjavik city. H_2S is released through the cooling towers' streams, condenser gas removal, condensate, geothermal water discharge, steam stacks during the shutdown, and well testing and breeding. Figure 5.12 shows the points of H_2S gas emitted from Hellisheiði GTPP. The most probable H2S release points are marked in red (plant defined as *scenario 1*), to which they are the cause that led to a design to reduce emissions through the construction of two pilot plants, CarbFix and SulFix. The usual compositions of geothermal gas emitted from Hellisheiði GTPP are 58.1% CO_2 and 29.4 % H_2S, and 0.2% CH_4 [10].

Figure 5. 13. Scenario 1: MANVITT PFD with H_2S release points from Hellisheiði GTPP. The following figure is taken from the reference [11]. The Emission in Air are indicated as red spots in the figure, and the corresponding values about CO_2 and H_2S are indicated in Table 5.13.

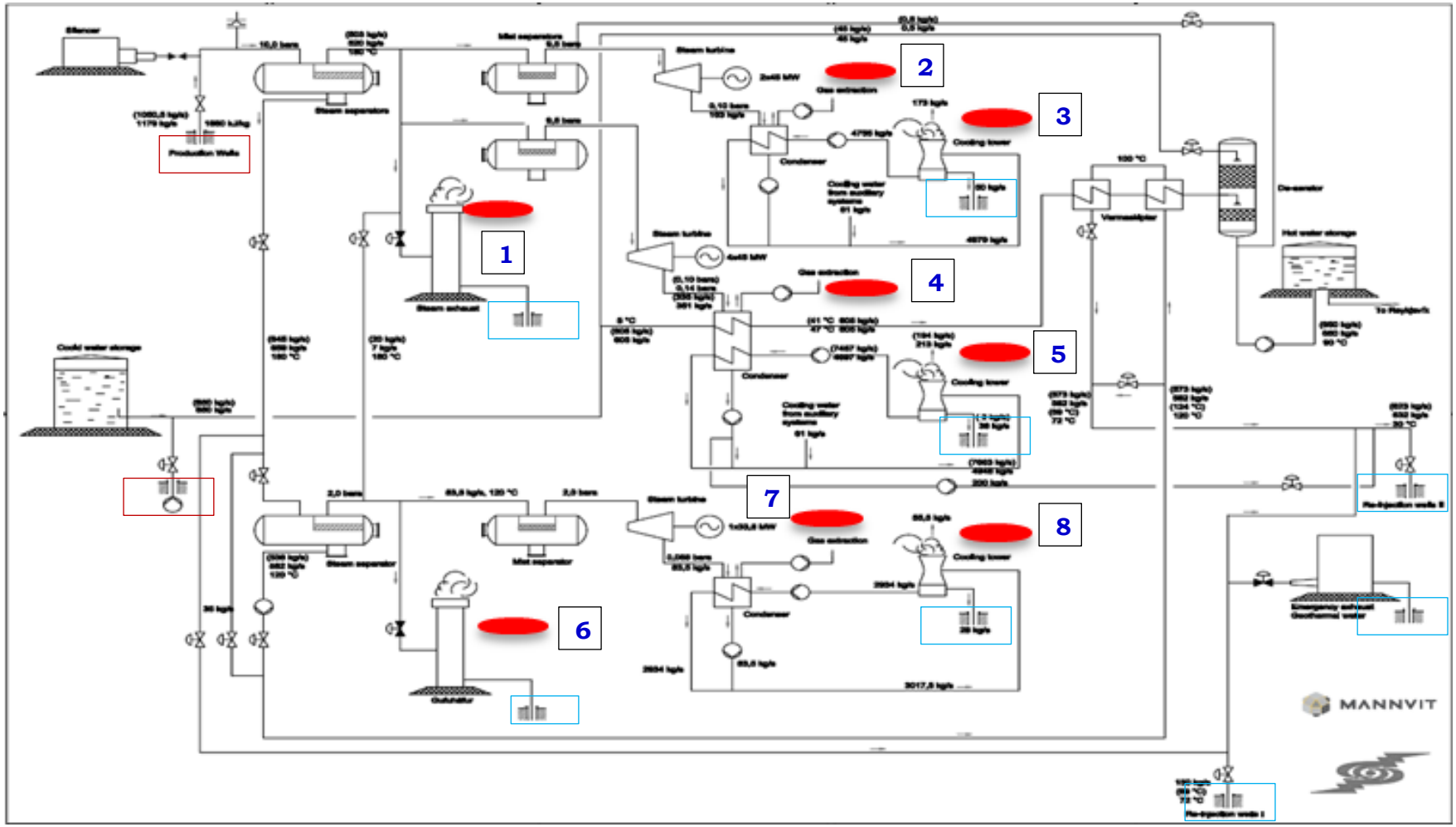

Scenario 1: The results of the simulation for the HE model in its original state is illustrated in Figure 5.12, and the data are reported in Table 5.13.

Table 5. 13 Air emissions calculated using Unisim Design in Scenario 1. The values refer to Figures 5.14 and 5.12. The symbol (‡) indicates that the Torches are activated only in emergency cases to compensate the vapour stream's pressure. Next, the total value is calculated, excluding the torch values.

Figure 5.13	Figure 5.12	CO_2 [ton/year]	H_2S [ton/year]
1	17 (To Torch)‡	40534.28	6270.2
2	Extraction Gas HP	12178.00	1884.00
3	Air Out HP1 (from cooling towers)	153.26	24
4	Gas Extraction HP E/T	25105.14	3884
5	Air Out HP	0.91	1.00
6	To Torch‡	4758.85	736
7	Gas extraction LP	6257.42	968
8	CT_out_LP	0.87	3.00
	Total	43695.42	13700.14

5.4 Chiusdino Geothermal Power Plant

5.4.1 The geothermal process and power plant model

Chiusdino 1 is a single flash geothermal power plant[8] with a nominal capacity of 20 MWe (Figure 5.14).

Figure 5. 14. Chiusdino power Plants with Google Earth areal view (location 43◦09'37.0" N; 11◦03'49.9" E)

The geothermal fluid is steam of 130 t/h at 469.15 K and 14.5 bar and comes from five wells located close to the power plant. Its composition is shown in Table 5.16. The reservoir depth is about 3-4.5 km, and the GTPP area is 11000 m^2. The details of production wells[12] are in Table 5.17.

[8] It is a standard Enel Green Power GTTP

Table 5. 14. Composition of the Chiusdino 1 geothermal fluid. Source: [12]

Composition of the geothermal fluid (130 t/h)		
Dissolved gasses (NCG) mass fraction	4.00 %	
CO_2	5100	Kg/h
CO	0.4	Kg/h
CH_4	79	Kg/h
H_2S	90	Kg/h
NH_3	11.6	Kg/h
Hg	5.6	g/h

Table 5. 15. Details of production wells of Chiusdino 1 GTPP. Source: [12]

Well	Depth [m]	Flow rate[t/h]	T [K]	P [bar]	NCG [%]
Montieri 5	3447	78.8	473.95	16.2	6.0
Montieri 5A	4137	22.4	473.96	16.1	4.2
TravaleSud 1B	3361	26.4	471.75	15.5	6.1
TravaleSud 1C	3713	25.2	472.05	15.4	4.5
TravaleSud 1D	4432	24.5	491.95	15.4	4.5

The Chiusdino 1 power plant is equipped with an AMIS® emissions treatment system. It removed H_2S and Hg with efficiencies of 99.8% and 82.2 %, respectively (Table 5. 18). A soda solution (NaOH) is used for acid gas treatment.

Table 5. 16. The removal efficiency of AMIS® emission treatment system.

NCG emissions treatment system (AMIS)	
H_2S removal efficiency	99.8%
Hg removal efficiency	82.2%
NH_3 removal efficiency	87%

The data shown in Table 5.18 refers to a detailed AMIS system process where it is impossible to simulate due to the confidential features of the firm. Therefore, the results obtained from the simulation in the removal gas section (see figure 5.16) might be unrealistic. The whole liquid condensate of Chiusdino 1 is reinjected (Table 5.19) using a complex network of pipelines of 20 km connected to the Larderello reinjection sites.

Table 5. 17. The Chiusdino 1 reinjection operative conditions

Reinjection for Chiusdino 1	
Temperature [K]	298.15
Pressure [bar]	1.013
Liquid phase, [%] of the total from wells	30
Gas-phase [%]	0

The details of pollutant streams emitted, following the regional authority's measured values for environmental protection of Tuscany (ARPAT), are in Table 5.20.

Table 5. 18. Emissions of the Chiusdino 1 GTPP. Source: [12]

Emission	Flow rate [kg/h]	Specific emissions [kg/kWh]
CO_2	5100	$2.6 \cdot 10^{-1}$
CO	0.4	$2.0 \cdot 10^{-5}$
H_2S	18.4	$9.2 \cdot 10^{-4}$
CH_4	79.3	$4.0 \cdot 10^{-3}$
NH_3	1.5	$7.5 \cdot 10^{-5}$
Hg	$1.1 \cdot 10^{-3}$	$5.5 \cdot 10^{-8}$

For Chiusdino 1, this work's main scenario considers the geothermal process with the AMIS® emission treatment. The Chiusdino 1 GTPP operability is 7560 h/year with high productivity of about 151200

MWh/year. A detailed process simulation model can evaluate the emissions from the Hamon cooling towers of Chiusdino 1 (3 cells) and various unit operations. The effective implementation of a Chiusdino 1 GTPP represents the 20 MWe. The process simulation software used is Unisim Design® R480.

5.4.2 Power plant Equipment

The Chiusdino 1 process consists of five basic sections: Turbine, Direct-contact condenser, Multistage Gas Extractor with Intercooler system, AMIS®system abatement, Towers (Figure 5.20). The geothermal fluid from five wells goes to the single flash and is expanded in a turbine. After this, a direct-contact condenser is considered. In literature, it is represented as a single equilibrium stage and therefore schematized with a flash tank where the biphasic flows enter to be separated into liquid and gaseous flows [13]. The hot water outside the condenser is sent through a movement pump to the evaporative towers. The pump was simulated with constant efficiency. The gas flow coming out of the direct-contact condenser must be treated to remove NCGs and Hg. This latter stream is first compressed at atmospheric pressure and then sent to the AMIS® abatement system. Compression is performed in two stages with an intermediate cooling through the "InterStage Sep" separator, where a part of the cold water comes from the recycling of the evaporative towers. A constant efficiency compressor represents each compression stage. The AMIS® abatement system is considered a system that abates both non-condensable gases with particular attention to H_2S and mercury (Hg). Their efficiencies are different. Hg emissions from evaporative towers and from the AMIS® plant are therefore considered separately. The flows that leave the AMIS® system are one containing precisely the Hg abated and the H_2S, the residual gas considered as an emission, and the residual liquid recycled to direct contact condenser. Finally, the three-cell evaporative tower system is considered an absorption tower in multistage equilibrium with constant efficiency. Generally, the gaseous residue leaving the AMIS® system is mixed with the airflow entering the towers to be subsequently processed by the three cells. The simulation model represented in Figure 5.3 divides the emissions of the process into two gas outlets. Generally, the gas out of the AMIS® is sent in two cells.
Since it is necessary to represent the three-cell system with only one absorber tower, the options taken by [13] are considered so that the flow entering the AMIS® is physically separated from the airflow in the tower. Among the other options, the simulation model is calibrated so that the quantity of Hg re-injected is practically zero.

Figure 5. 15. Chiusdino 1 geothermal process: streams and operation units.

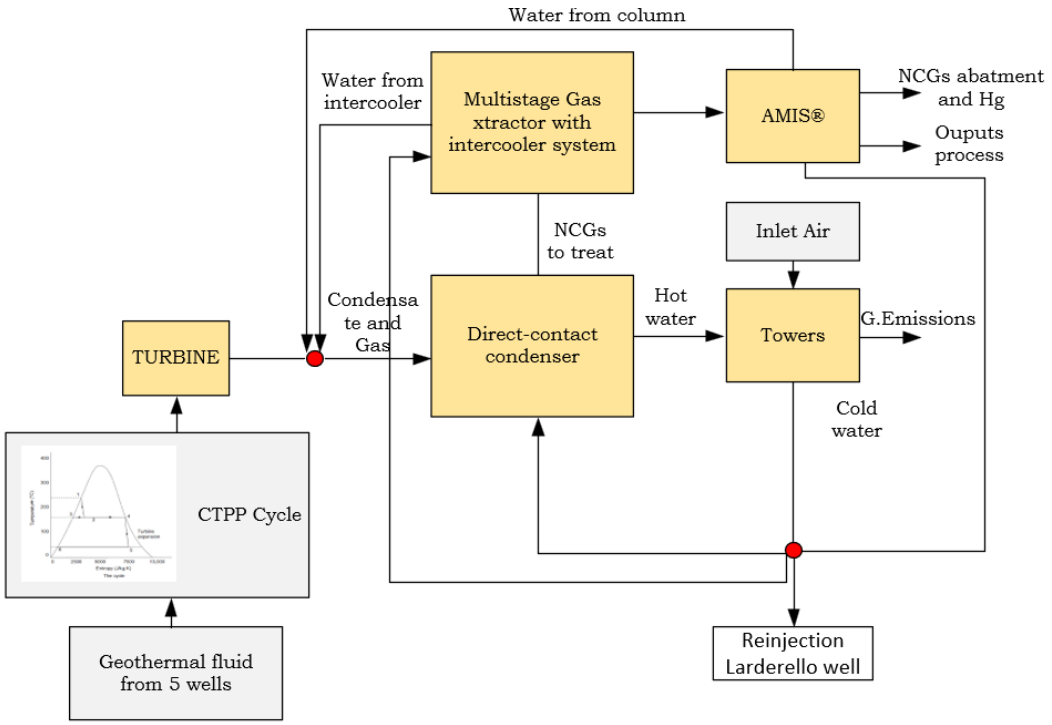

5.4.3 Choice of the thermodynamic model

For the implementation of the geothermal model, appropriate thermodynamic correlation is a fundamental step to obtain simulation results similar to reality. Therefore, the first representative conditions are the geochemical stream compositions, operating conditions such as temperature and pressure along the whole Chiusdino 1 process and its unit operations. The geothermal fluids are composed of water and non-condensable gas fractions, pressures from 20 bar to 0.01 bar and temperatures from 473.15 K to 295.15K. So, like in Chapter 4, one option is to use OLI AQ thermodynamic models. Considering also the Hg presence, the appropriate thermodynamic model is, for this case study, the OLI AQ with attention to mercury and ammonia. This allows us to compare Henry's constants calculated through the OLI AQ and those found in the literature [14] (Figure 5.16). Figure 5.16 shows the points processed by the literature correlations and the values calculated through the refinement of the thermodynamic model.

Figure 5. 16. Comparison with literature data on the calculation of Henry's constant from the data source provided by Andersson et al. [14]. OLI-AQ represents one of the OLI thermodynamic packages.

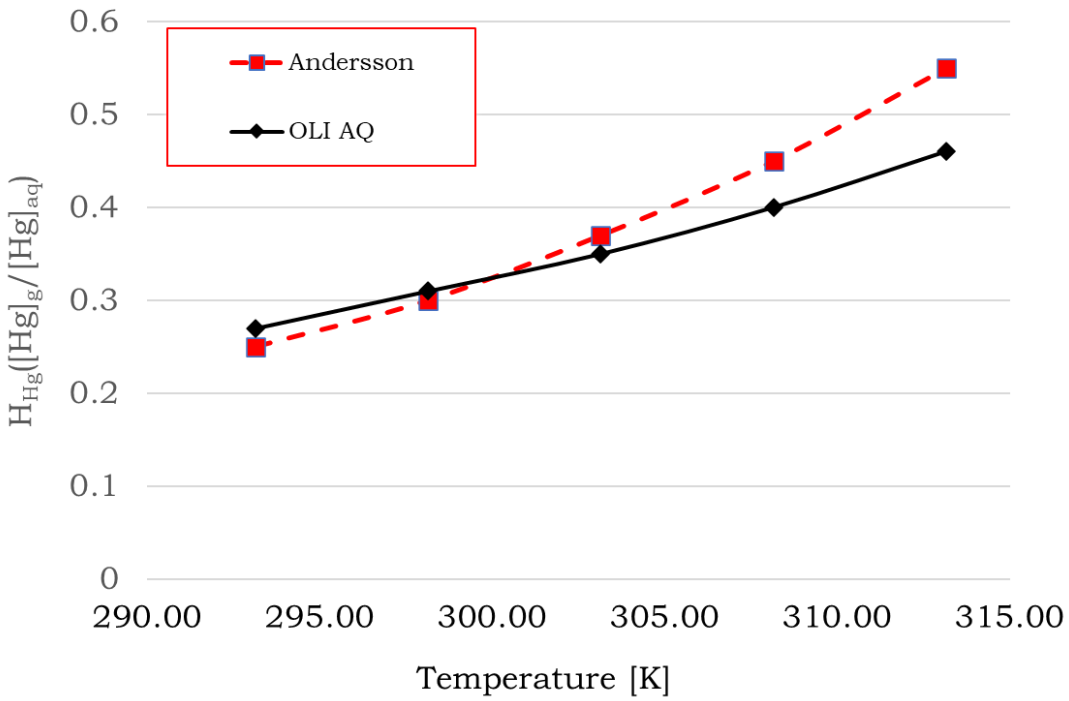

5.4.4 Implementation and simulation model

In this section, the development of the model of the GTPP named Chiusdino 1 (indicated as CD1) is described (Figure 5.21). Using Unisim Design® R480 with the OLI Systems® thermodynamic package with the data and results of Life Cycle Assessment (LCA)[12], a CD1 simulated model is created.

Figure 5. 17. PFD of the geothermal power plant CD1 from Unisim Design® R480

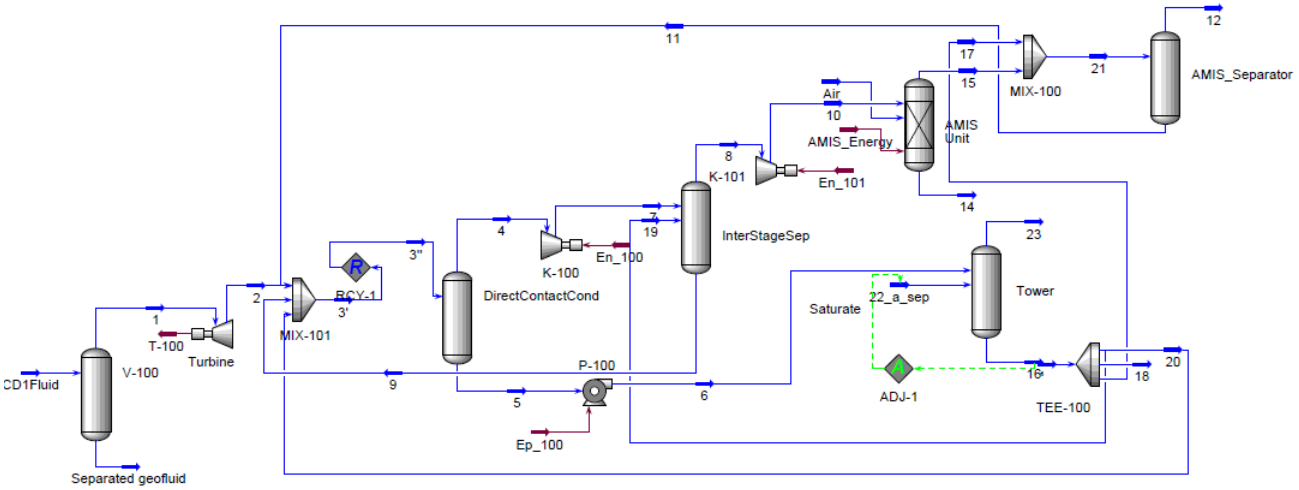

The are three main sections: Direct-Contact condenser, AMIS® Unit and Towers. The condenser's simplification as a single Flash tank neglects the temperature difference between the liquid's output flows and the vapour. The second is represented by the AMIS® unit and the AMIS® Separator. The last is the complex number of cooling towers represented in Towers. Unfortunately, as can also be seen in Hellisheidi, an evaporative tower model is missing in the process software. Nevertheless, the model follows the simplifications adopted in [13]. For some detailed information, some compressors and pumps' efficiencies are brought to an expected value of 80% and 75%, respectively. The liquid flow 14 comes out of the AMIS Unit. A reduction of 82.2% has been set for mercury, while for hydrogen sulphide, this value is 99.8%; percentages by mass concerning the flow 10, the inlet of the component divider. Both efficiency values are taken from the study [12]. In order to follow the real values foreseen by AMIS, an airflow (called air) has been inserted as input to AMIS_Unit. For the flow 22_a_sep, the insertion of relative humidity and separation, which as information on the operation is foreseen conditions, temperature, pressure, and relative humidity, the default values have been set: 20°C, 101.3 kPa and 0% relative humidity.
The TEE-100 split values are calculated using a spreadsheet operation where the mass fractions of the various flow leaving the splitters are calculated as follows. The mass flow rates of streams 18, 19, 20 are considered by [2], and as a hypothesis, it is considered that the liquid flow out of the tower (16) is approximately the same mass flow rate as the inlet. Hence, the mass flow rate of the current 17 is a subtraction of the currents 18,19, 20 is calculated from the flow 16. ADJ-1 mi keeps the setpoint value checking the temperature considering as a calculation in excel for the Saturate. The other logical unit used is Recycle RCY-1, which is at the direct contact conderser's input for the simulation model's efficiency and cycle calculations to change a parameter.

5.4.4 Results analysis

Various tests for process optimization and reduction of emissions have not been applied to this model, as this work does not belong to the European project Horizon2020 "Geco" due to confidential data by the operator regarding the modelling of the entire plant. But, Chiusdino 1 is present in the European project "GeoVi" regarding the analysis of the environmental life cycle (LCA) [12].

The values shown in Table 5.19 are those obtained from the simulation, although the Hg values would exceed 9% of the target value, while for the H_2S, it is reduced by 11% due to the poor model of physical absorption and chemical balances in the model software in which H_2S plays a fundamental role. Therefore, the simulation model can be optimized and compared with the Chiusdino 1 power plant's data present in the DCS (Distributed Control System). Another precaution can also come from the "Air" stream's temperature and, therefore, the daily climatic conditions that can modify the AMIS system outputs, particularly in winter and summer. All this would affect the K-100, K-101 and P-100 equipment, for example, power consumption [kW].

Table 5. 19. Final model simulation results on the main pollutant abatement

Stream	12	18	23
Mass Flow [kg/s]	2.834	10.84	127.1
Temperature [K]	301.61	301.54	305.61
Pressure [bar]	1	1	1
Molecular Weight	38.68	18.02	28.35
Mass Density [kg/m^3]	1.55	1004.81	1.12
Mass Enthalpy [kJ/kg]	$-7.917\cdot10^{3}$	$-1.587\cdot10^{4}$	$-3.830\cdot10^{2}$
H_2O mass fraction	$1.803\cdot10^{-2}$	$9.999\cdot10^{-1}$	$2.903\cdot10^{-2}$
H_2S mass fraction	$9.505\cdot10^{-6}$	$1.890\cdot10^{-11}$	$2.137\cdot10^{-6}$
NH_3 mass fraction	$3.126\cdot10^{-5}$	$5.252\cdot10^{-5}$	$6.160\cdot10^{-5}$
Hg mass fraction	$1.857\cdot10^{-7}$	$4.934\cdot10^{-15}$	$3.106\cdot10^{-10}$
CH_4 mass fraction	$2.401\cdot10^{-2}$	$1.015\cdot10^{-26}$	$3.735\cdot10^{-11}$
CO_2 mass fraction	$8.455\cdot10^{-1}$	$4.411\cdot10^{-11}$	$5.014\cdot10^{-5}$

5.5 Economic considerations

The potential performance benefits for the different types of binary cycles are given by the reduction of the average temperature difference between the fluids in the heat transfer processes. However, this reduction leads to an increase in heat exchange surface area and high capital costs for the equipment. The cost of the size modifications in heat exchange can be estimated as the change in the product UA[9] as a first approximation. The UA product is the ratio between the total heat transfer (Q) and the log-mean temperature difference (LMTD) for these processes. The UA ratios for geothermal exchangers (UA, hx) are all greater than one. The pumping power depends on the type of cycle and the fluid's operating conditions, which consequently affects the size and cost of the turbine generator beyond the increase in power. A simple approach was developed to evaluate how the selection of the cycle could impact generation costs and examine iterative changes power. The assessment of these impacts started from referencing the binary plants for the two lowest temperature resources in the Next Generation Report on geothermal power plants (EPRI) [15]. Those costs have been assigned to the single-flash cycle plant, and therefore the costs for the heat changes were determined by their sizing. These costs are summarized in Table 5.20. All cycles that showed improved performance over the single-flash cycle had increased costs. Therefore, the relative cost is expressed in terms of $/kW.

Table 5. 20. Initial estimate of power cycle selection on cost ($/kW)

Component	EPRI cost	Single Flash GTPP	Double-flash binary GTPP	ORC GTPP
Geothermal HXers	0.041	0.041	0.055	0.103
Turbine-generator	0.126	0.126	0.146	0.177
Working fluid pump	0.009	0.009	0.009	0.058
Heat rejection	0.155	0.155	0.152	0.161
Total	0.331	0.331	0.361	0.499

Based on the plant cost, the best ones are the basic binary or the single flash GTPP. But, the capital cost[10] of the plant is only one cost contributor to the project. There are costs associated with developing the well, operation to the facilities and the pumping operations for the geothermal fluid (field costs). Therefore, it is possible to estimate where the cost for improving performances could reduce the impacts of other additional costs.
The costs could be incremented if the ratio between the total cost and the power is equal or greater than unity. Thus, if the plant and the field costs are equivalent, and if 20% more energy is produced by the GTPP, the total cost can be approvedly increased by 20%. On the other hand, if the geothermal flow is fixed and assumes constant field costs, the plant's cost can increase by 40% unless it is less convenient to use a 20% more efficient system. In addition, considering scenarios where the field cost is small compared to the plant, there is still a benefit from increased performance and power output,

[9] U is the overall heat transfer coefficient and A is the heat transfer surface area

[10] The fixed costs of power generation are essentially capital costs and land. The capital cost of building central station generators vary from region to region, largely as a function of labor costs and "regulatory costs," which include things like obtaining siting permits, environmental approvals, and so on. It is important to realize that building central station generation takes an enormous amount of time.

as long as the increased plant cost is below the imposed threshold [4].
This discussion is a starting point for evaluating the costs and benefits of a GTPP and its streams. Furthermore, environmental aspects should also be considered, which are mandatory depending on the laws in specific countries. Therefore, the economic analysis would be associated with a geothermal plant's life cycle assessment (LCA) analysis.

5.6 Environmental analysis and challenges associated with geothermal power generation

For the environmental analysis, the present work would like to present an LCA study on the great geothermal power plant of these three cases studies: Hellisheiði power plants[7].

The present LCA's objective is to study the environmental impacts of the Hellisheiði double flash cogeneration geothermal power plant, comparing two scenarios that use technologies to remove pollutants formed to produce energy from a high-temperature geothermal resource. From the LCA results, it is possible to investigate the contribution of irreversibility to the different phases of the life cycle, highlighting the environmental impacts of the technologies used and underlining the critical points of the plant. The study investigates the effects of operational improvements built on the Hellisheiði cogeneration plant from the year of construction to 2020 through three LCA methodologies. The study examines two series of LCI: (1) Scenario 1: The baseline case inventory representing 2012 operational conditions as published in [16], [17] and (2) Scenario 2: an updated inventory representing the operational conditions of 2020, including operational improvements implemented through the reduction of CO_2 and H_2S emissions into the atmosphere. The whole LCA was developed as a component-based approach, considering the final goal of performing an exergo–environmental analysis that highlights the importance of the components' irreversibility or inefficiencies.

Figure 5. 18. Simplified schematic representation of the Hellisheiði power plant also used for OpenLCA[11] for the three sections (electricity production from high-pressure and low-pressure units, and heat production).

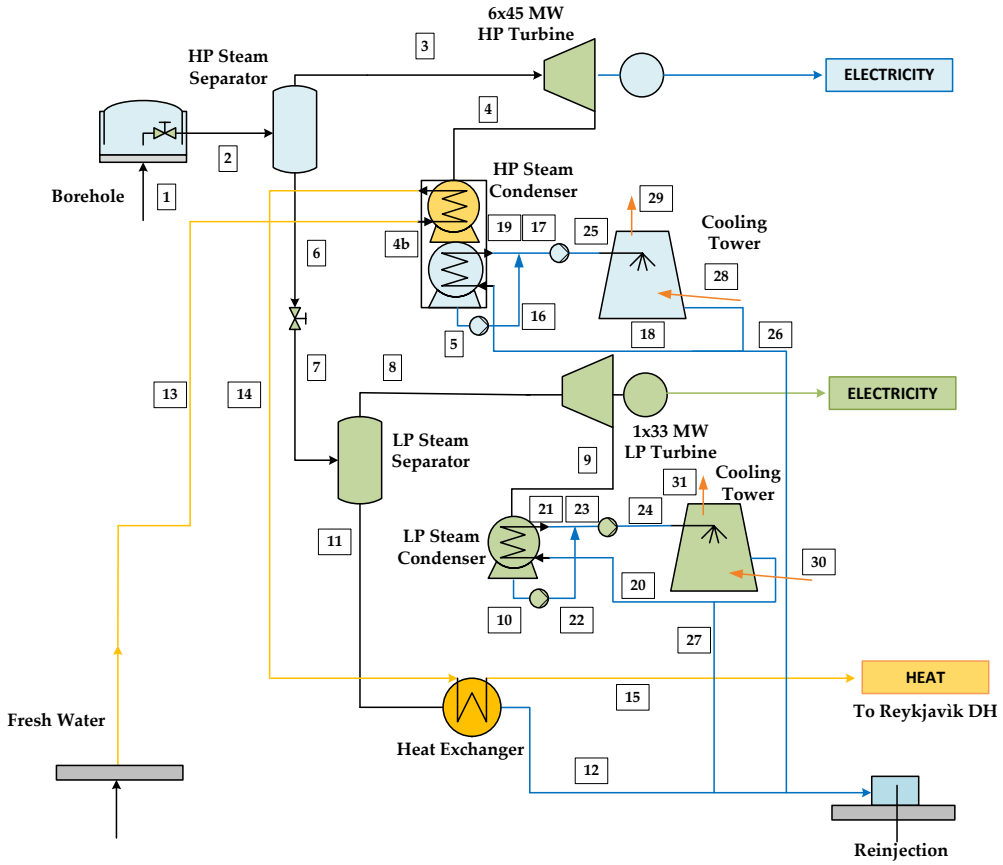

[11] https://www.openlca.org/

A flowchart of the Hellisheiði geothermal system is presented in Figure 5.22. The Hellisheiði geothermal plant has two separate products: electricity and hot water. In this work, the exergy approach was chosen, and all processes were allocated to exergy[12] instead of considering electricity and heat separately. The functional unit is thus 1 MWh of exergy; the plant's lifetime was set to 30 years of operation (this time is chosen for comparability with other datasets, and it is a typical lifetime applied for geothermal plants). The total exergy produced in the powerplant is composed of work and heat exergy contributions. The work output corresponds to the electricity produced by the turbines (a capacity factor = 0.87). The heat exergy was calculated considering both the quantity of heat produced (the average heat production is 91.44 MW_t) and its quality, which depends on the temperature at which it is available. Specifically, the heat exergy was evaluated applying a Carnot factor conversion, based on the log-mean temperature of the primary district heating loop (363.15-313.15 K) and the average annual ambient temperature for Iceland (278.15 K). Heat-exergy is here identified with Ex_Q and can be expressed as follows:

$$Ex_Q = \theta \cdot Q \text{ and } \theta = \left(1 - \frac{T_o}{T_Q}\right) \quad (5.\ 1)$$

where θ (Carnot factor, accounting for the value of heat) and T_Q and T_0 denote the thermal product and reference environment temperatures (considered here as the average yearly ambient temperature for Reijkjavik 278.15 K), respectively. T_Q is the entropy-average temperature of the heat produced by the CHP unit, calculated as:

$$T_Q = \frac{Q}{(\Delta S)} \text{ and } T_Q = \frac{T_D - T_R}{log\,(^{T_D}/_{T_R})} \quad (5.\ 2)$$

where ΔS is the overall entropy variation of the heat interaction (from delivery to return in the case of a district heating system). In the specific case of distributing a single-phase heat transfer fluid, T_Q can be evaluated as a log-mean temperature.

Figure 5. 19 Flowchart showing the geothermal plant life cycle.

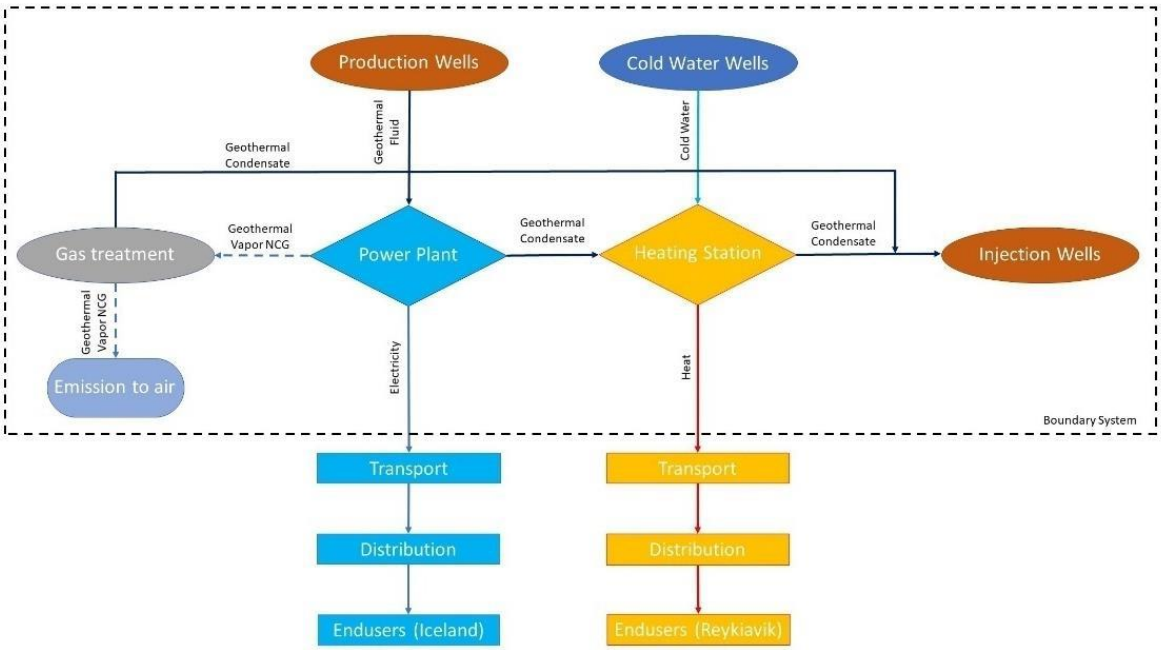

The boundaries of the two case studies are defined following the detailed description of the system and the construction of the flow diagram of the production cycle. All the relevant flows were considered

[12] Exergy is defined as the amount of work (= entropy-free energy) a system can perform when it is brought into thermodynamic equilibrium with its environment. Reference: [23].

from a typical LCA "cradle to grave" perspective. Both upstream (raw material extraction, manufacturing, wells and geothermal power plant construction), operation (power generation, operation and maintenance) and downstream (decommissioning and end of life scenarios) processes were considered. The exploration phase, before construction, was not included because of a lack of data (most of these activities were at the origins of geothermal energy exploration in Iceland). Transport of materials (or mechanical components) to the site and energy supply systems were not taken into account.

The Life Cycle Inventory (LCI) was developed using both primary and secondary data. Primary data (input and output flows) for the main processes in the foreground system referring to the power plant construction and operation, that is, input materials flow at the construction of the wells, structures, machinery and pipelines as well as those used in operation and maintenance phases and transportation stages were gathered from the various scientific publications relating to this plant. Similarly, data regarding the energy consumption that is: consumption of diesel for wells drilling, internal use of electricity at the site and for drilling wells and the composition of geothermal fluid represent primary data. Secondary data such as inventory for electricity or construction material production were retrieved from the Ecoinvent database version 3.6. For consistency, average EU mixes regarding materials and other resources were considered. In Figure 5.20, the considered life cycle phases are specified. The construction process considers heating station building, power plant building, geothermal wells, collection pipelines and machinery. The maintenance process considers the need for an additional structure such as wells and pipelines to sustain production during the plant's lifetime. Also, the mass flow of elements used in the cooling tower maintenance is considered. The operation process considers the use of geothermal fluid, gas emission to air and the additional use of electricity used for the cold water pump in the heating station building.

Figure 5. 20. Life cycle phases for the combined heat and power geothermal plant at Hellisheiði.

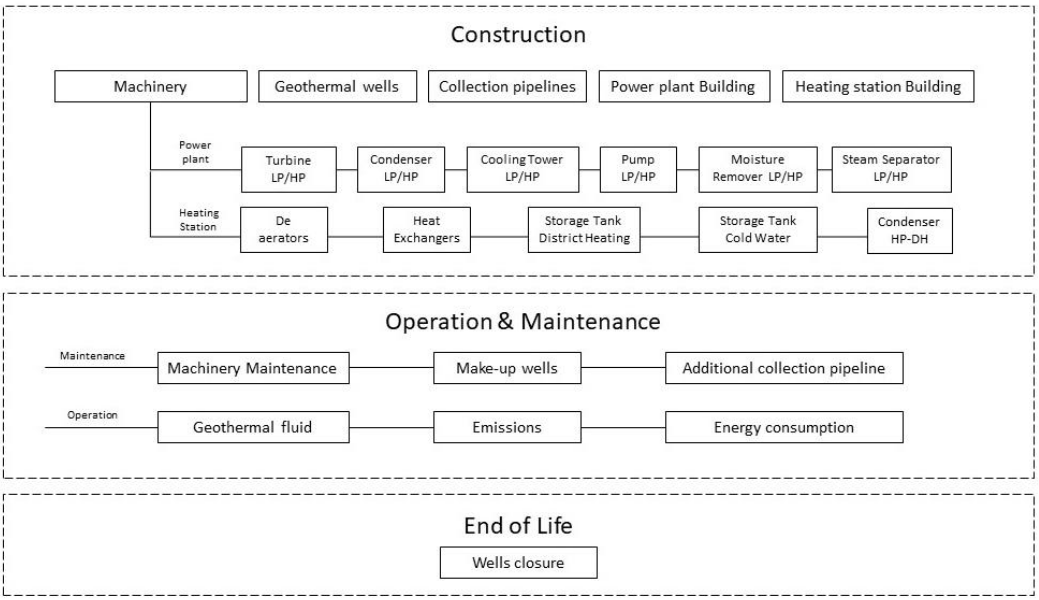

5.6.1 Life-Cycle Inventory

The first step of the LCA is the inventory analysis. This involves data gathering and the construction of a model able to represent as faithfully as possible the actual production process.

The compilation of the inventory was based on previously published works. To perform an EEvA, the LCI of the entire power plant must be available at a detailed component level. The original LCI reports the whole plant's total materials: it is then necessary to disaggregate the entire power plant inventory into the specific components, identifying which materials belong to one or another and their respective quantities. This study was carried out by utilising data gathered from detailed LCIs of Italian geothermal power plants of similar (flash) technology, applying suitable scaling factors. The

disaggregated inventory for the construction phase of the Low- and High-Pressure Cooling Towers is reported in Table 5.21.

Table 5. 21. Low-Pressure and High-Pressure Turbine Cooling towers Life Cycle Inventory (LCI).

Cooling Towers CTLP		kg
Number	1	-
Expected lifetime	30	-
Stainless steel	-	1651.78
Steel	-	844.41
Copper	-	119.72
Plastic	-	367.34
GRP	-	92,809.80
Cooling Towers CTHP		kg
Number	6	-
Expected lifetime	30	-
Stainless steel	-	9910.7
Steel	-	5066.41
Copper	-	718.31
Plastic	-	2204.02
GRP	-	556,858.80

5.6.2 Life Cycle Inventory—Scenario 1

All data were taken from [12], imported in *OpenLCA 1.10.2* and upgraded to the *Ecoinvent 3.6* database for this scenario. In 2012, 64 geothermal wells were drilled for the construction of the plant. Of these, 47 are designed for extraction of the geothermal fluid and 17 are operated for its reinjection. Every two years, the drilling of a new well is necessary to keep the production of electrical/thermal energy constant and for reasons of the plant maintenance. All wells for scenario 1 are drilled using diesel generators.

5.6.3 Life Cycle Inventory—Scenario 2

This scenario represents the more recent inventory published in [23], also in this case updated to Ecoinvent 3.6. The main changes with respect to Scenario 1 concern:

- The introduction of the CarbFix and SulFix gaseous effluent treatment system;
- The use of electric drilling machines instead of machines that consume diesel for the construction of geothermal wells.

The CarbFix and SulFix gaseous effluent treatment system is based on a vertical cylindrical scrubber that washes the gaseous effluents before releasing them into the atmosphere.

5.6.4 Life Cycle Impact Assessment (LCIA)—Benchmarking of Methods

As the purpose of this LCA is to proceed with an exergo-environmental analysis, the non-mandatory LCA steps of normalization and weighting are necessary to build a single score indicator. For such cases, it is recommended to apply a benchmarking among different Impact Assessment methodologies to ensure that the major categories are equally represented and augment the reliability of the single score evaluation. In the present case, three accepted LCIA methods were proposed to quantify the single score environmental impact of each component of the system: ReCiPe 2016 (H) (hierarchic perspective impact assessment with normalization and weighting set: Europe ReCiPe H), ILCD 2011 Midpoint+ (EC-JRC Global, equal weighting) and CML-IA baseline (EU25+3, 2000).

All three methods represent a different situation for several reasons; for instance, each has different impact categories that express the same environmental impact; in some cases, the methods have equivalent categories with different impact and characterization factors. The results express, in general, a situation in line with high-priority impact categories for a geothermal system. With specific reference to acid gas emissions, following a conservative approach of previous LCA studies, the CML-IA non-baseline approach was applied in all cases, assuming that all H_2S is converted in SO_2 with a

1.88 conversion factor (corresponding to complete oxidation of H_2S). However, it should be recalled that modern methods do not consider H_2S as a substance that generates strong impacts on acidification: consequently, its characterization factor (which has a relevant uncertainty) is not directly considered for specific midpoint categories such as acidification potential. The selected methods highlight that the most impactful categories are Acidification (B confidence level), Human toxicity and Ecotoxicity (C confidence level). Climate change was also considered a high-priority category. All methods indicate that emissions from Hellisheiði power plant, when compared to the amount of energy produced, have a minimal impact on the total normalized value. The impact assessment of the Global Warming Potential is about 22 kg CO_2/MWh, which is a low value compared to the average of the Icelandic energy mix (43 Kg CO_2/MWh; value calculated with ILCD 2011 midpoint using Ecoinvent 3.6).

The three LCIA methods allow identifying relevant categories for the environmental impact of this plant: ILCD and ReCiPe show evidence of impact for Particulate Matter Formation—a category with an intermediate level of priority. ReCiPe also points out the relevant impact in terms of Water Consumption. Finally, ILCD and CML detect impact in two categories—Photochemical Ozone Formation and Photochemical Oxidation, that have a low level of priority . For all categories, contributions lower than 1% were not considered as below the significance level (Table 5.22, 5.23, 5.24).

Table 5. 22 : ILCD 2011 midpoint results—most impactful categories.

ILCD Categories	Impact Result	Normalization (%)
Acidification [molc H+ eq]	$1.16 \cdot 10^{1}$	45.97%
Particulate matter [kg PM2.5 eq]	$5.43 \cdot 10^{-1}$	23.82%
Human toxicity, cancer effects [CTUh]	$1.02 \cdot 10^{-6}$	18.24%
Freshwater ecotoxicity [CTUe]	$8.77 \cdot 10^{1}$	5.21%
Photochemical ozone formation [kg NMVOC eq]	$7.36 \cdot 10^{1}$	3.61%
Human toxicity, non-cancer effects [CTUh]	$1.37 \cdot 10^{-6}$	1.96%
Other categories	-	1.18%

Table 5. 23: ReCiPe 2016 midpoint results—most impactful categories

ReCiPe Midpoint Categories	Impact result	Normalization (%)
Marine ecotoxicity [kg 1,4-DCB]	$3.32 \cdot 10^{1}$	25.48%
Human carcinogenic toxicity [kg 1,4-DCB]	$6.09 \cdot 10^{-1}$	17.40%
Terrestrial acidification [kg SO2 eq]	8.85	17.10%
Freshwater ecotoxicity [kg 1,4-DCB]	$2.54 \cdot 10^{-1}$	16.36%
Water consumption [m3]	$3.91 \cdot 10^{1}$	11.62%
Fine particulate matter formation [kg PM2.5 eq]	2.57	7.96%
Terrestrial ecotoxicity [kg 1,4-DCB]	$2.38 \cdot 10^{1}$	1.82%
Human non-carcinogenic toxicity [kg 1,4-DCB]	3.18	1.69%
Other categories	-	0.57%

Table 5. 24: CML-IA baseline results—most impactful categories.

CML-IA Baseline Categories	Impact Results	Normalization (%)
Acidification [kg SO2 eq]	$1.06 \cdot 10^{1}$	60.14%
Photochemical oxidation [kg C2H4 eq]	$4.26 \cdot 10^{-1}$	23.44%
Marine aquatic ecotoxicity [kg 1,4-DB eq]	$5.25 \cdot 10^{+3}$	11.25%
Human toxicity [kg 1,4-DB eq]	$1.49 \cdot 10^{1}$	2.85%
Fresh water aquatic ecotox. [kg 1,4-DB eq]	3.88	1.77%
Other categories	-	0.55%

The normalization process applied in Table 5.22, Table 5.23 and Table 5.24 highlights the most relevant midpoint analysis categories. In general, emissions to air produce a relevant impact regarding Acidification, Particulate Matter, Photochemical Ozone Formation, Human toxicity and Freshwater ecotoxicity. Reducing these impacts is an important objective to be achieved, which led to the

introduction of the gaseous effluent treatment system on this plant. Each method evaluates the impacts in different ways, but it can be observed that all of them identify similar major environmental effects. Figure 5.21 shows the contribution analysis, demonstrating that most of the impacts come from the construction of wells, pipelines and mechanical equipment. It can be observed that power plant maintenance has a relatively low environmental impact, while the end of life almost is nearly negligible compared to the total.

Figure 5. 21.Contribution analysis a) ILCD 2011 midpoint, b) ReCiPe 2016 midpoint, c) CML-IA baseline.

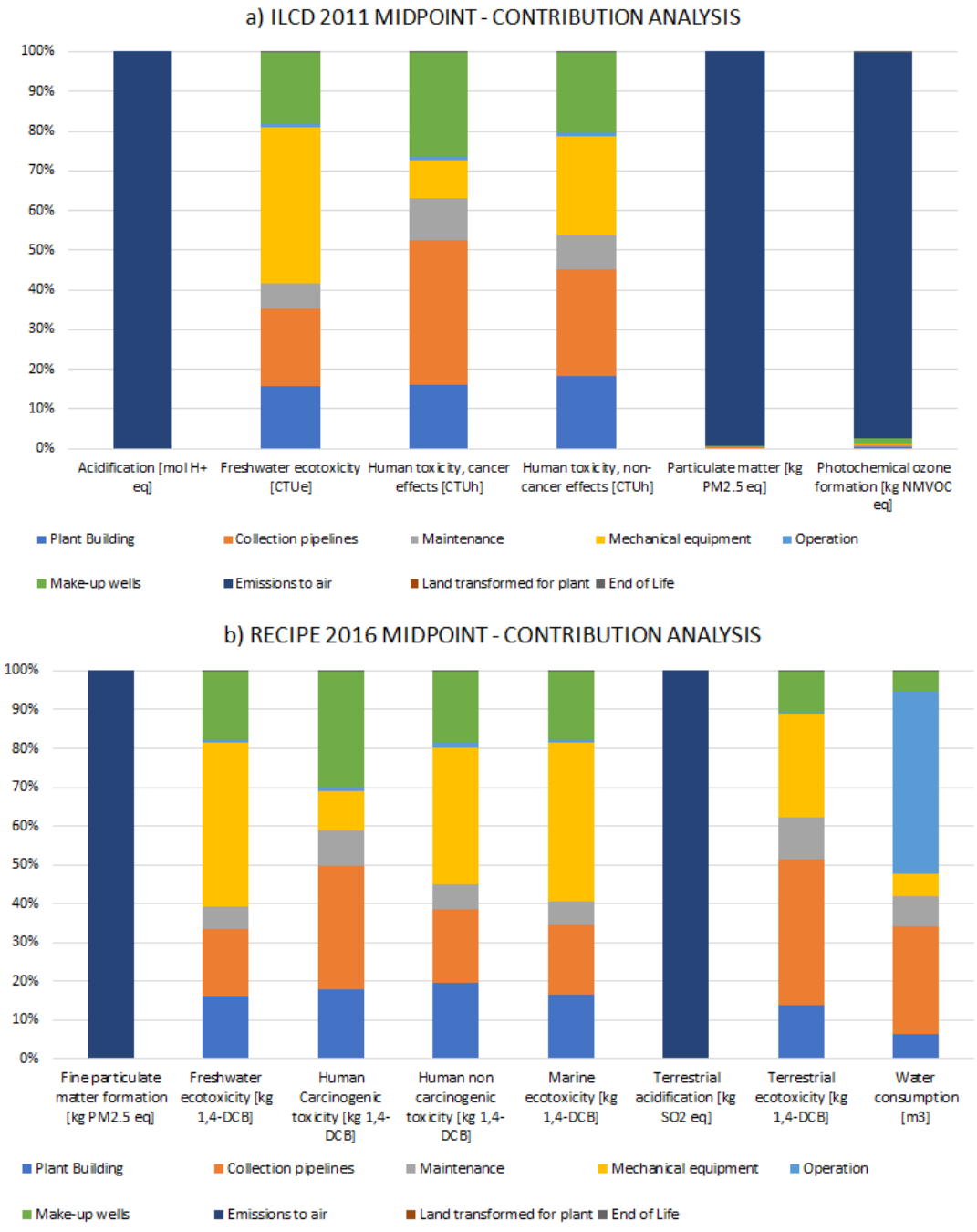

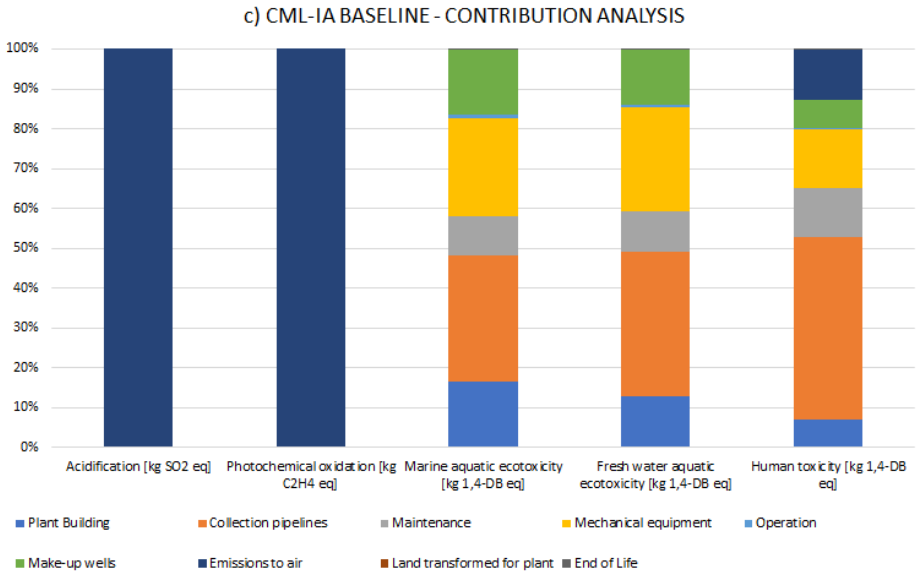

The ReCiPe method includes provision for the further step of Damage Assessment (EndPoint LCIA): all the Midpoint impact categories are reduced to three major damage macro-categories: Human health (DALY), Ecosystem quality (species*yr) and Resource depletion (USD2013). The results are 1.72E-03 DALY, 2.47E-06 species*yr and 2.41E-01 USD2013, respectively (all these values are referred to the functional unit, MWh of exergy). After normalization, it is clear that Recipe indicates that Human Health is the most impactful damage category concerning the total impact, covering about 84.4% of the total (Figure 5.22).

Figure 5. 22. ReCiPe 2016 endpoint, Normalization.

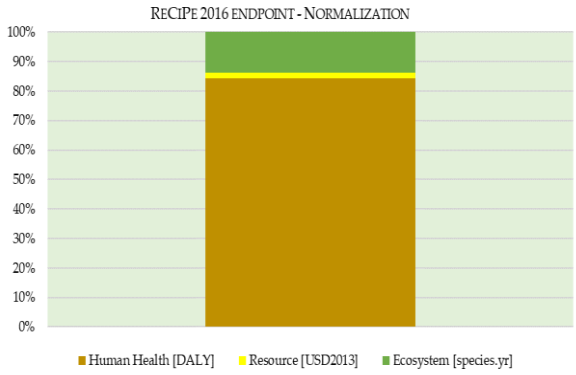

5.6.5 ReCiPe 2016 vs ILCD 2011

This section discusses in detail the differences between two midpoint methodologies: ILCD 2011 and ReCiPe 2016. The two methods have a different number of impact categories and indeed focus on different environmental impacts. In cases where categories reproduce the same environmental damage, the calculation method may be dissimilar. Normalization is applied with very different approaches and the result is that the most impacting categories may not be the same or may have different overall impact percentages. It is interesting to analyse the comparable categories with equivalent measurement units for both methods. In this way, it is possible to understand the difference between the methodologies in the way of calculating the environmental impacts (Figure 5.23).

Figure 5. 23. Differences between ILCD 2011 and ReCiPe 2016 for some relevant midpoint impact categories (vertical scale 10 + log10[x]).

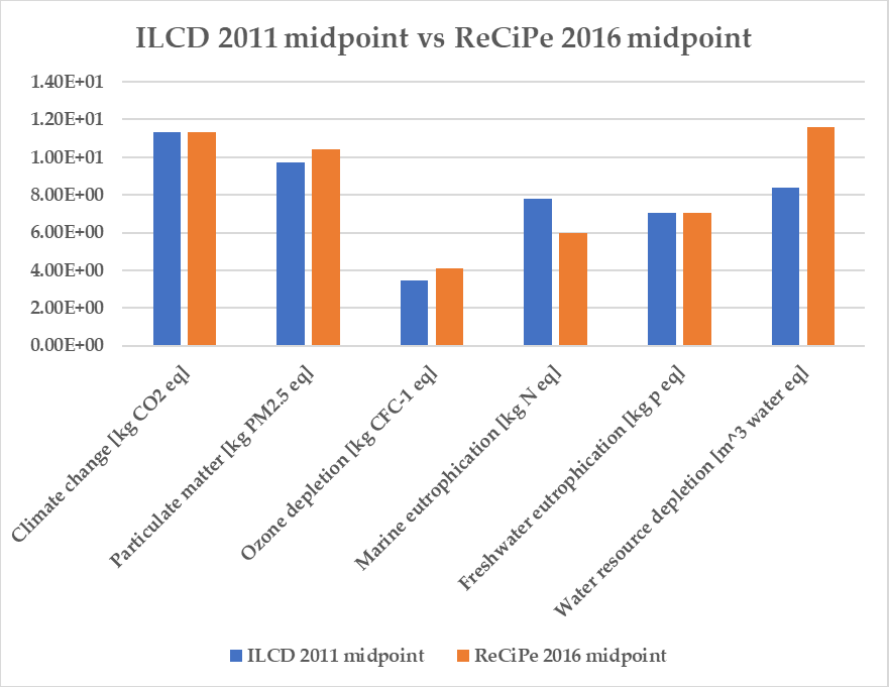

It can be noted from Figure 5.27 that the Climate Change and Freshwater Eutrophication categories are very close for both methods. The Particulate Matter category differs, but the calculation method applied is similar. On the other hand, the Ozone Depletion, Marine Eutrophication, and Water Resource Depletion categories differ widely, and the last one is an example of the relevant difference in approach between the two methods: in fact, the overall assessed water consumption is $2.40 \cdot 10^{-2}$ m^3/day for ILCD 2011, while it is $3.91 \cdot 10^{+1}$ m^3/day for ReCiPe 2016. Moreover, after normalization, this is a negligible category for ILCD, covering about 0.08% of the total impact; for ReCiPe, instead, it is a relevant category and covers about 11.62% of the total impact. This fact occurs because ILCD uses a country-specific factor, which is reflected on the characterization factor, based on scarcity classification (Iceland is a country with a low scarcity of water: Water Scarcity ratio ≤0.1), instead, ReCiPe considers a characterization factor of 1 m^3 of water consumed per m^3 of water extracted.

5.6.6 CML Versus ILCD and ReCiPe

CML-IA baseline is a method with baseline indicators that are recommended for simplified studies. Human toxicity has a different unit of measurement compared to the ILCD method; CML-IA expresses this category in kg 1.4 DB_{eq} instead of CTUh[13], so results are not comparable. Global warming and Ozone layer depletion have the same calculation model and express the same results. In the CML-IA baseline, eutrophication expresses the nitrification potential in kg PO_4 equivalent per kg emission and fate is not included in the model (the period is an eternity). Differently, in ILCD—which applies the same model as ReCiPe -the Freshwater eutrophication is expressed in kg P eq, and the characterization factor accounts for the environmental persistence (fate) in the emission of P. Although the different unit of measurement and approach used in both method, it is possible to make a calculation that converts from orthophosphate PO_4 to phosphorus, multiplying by the molecular mass ratio (0.3261 kg P/kg PO_4). Applying this correction, the eutrophication evaluated by CML assumes a value of $1.90 \cdot 10^{-3}$ kg P close to the value reported with ILCD for Freshwater Eutrophication (Table 5.20).

[13] LCA methods (ILCD, ReCiPe and CML) units are in http://www.jrc.europa.eu/

Table 5. 25. Difference between CML-IA baseline and ILCD 2011 midpoint.

CML-IA Baseline	Amount		ILCD 2011 Midpoint
Global warming (GWP100a) [kg CO_2eq]	$2.21 \cdot 10^{1}$	$2.20 \cdot 10^{1}$	Climate change [kg CO2eq]
Ozone layer depletion (ODP) [kg CFC-11 eq]	$2.90 \cdot 10^{-7}$	$2.90 \cdot 10^{-7}$	Ozone depletion [kg CFC-11 eq]
Human toxicity [kg 1,4-DB eq]	$1.49 \cdot 10^{1}$	$1.02 \cdot 10^{-6}$	Human toxicity, cancer effects [CTUh]
		$1.37 \cdot 10^{-6}$	Human toxicity, non-cancer effects [CTUh]
Eutrophication [kg PO4---eq]	$5.83 \cdot 10^{-3}$	$1.13 \cdot 10^{-3}$	Freshwater eutrophication [kg p eq]
(Eutrophication [kg P-PO4eq]	$1.19 \cdot 10^{-3}$		

The CML-IA baseline should also be compared with ReCiPe 2016 midpoint (Table 5.26); the two methods have in common some impact categories:

- Acidification
- Eutrophication
- Global warming
- Ozone layer depletion
- Human toxicity
- Marine aquatic ecotoxicity
- Terrestrial ecotoxicity

Table 5. 26. Difference between CML-IA baseline and ReCiPe 2016 midpoint.

CML-IA Baseline	Amount		ReCiPe 2016 Midpoint
Acidification [kg SO_2eq]	10.60	8.85	Terrestrial acidification [kg SO_2eq]
Eutrophication [kg PO_4--- eq]	$5.83 \cdot 10^{3}$	$1.12 \cdot 10^{-3}$	Freshwater eutrophication [kg P eq]
(GWP100a) [kg CO_2eq]	22.10	22.30	Global Warming [kg CO_2eq]
Human toxicity [kg 1,4-DB eq]	14.90	$6.09 \cdot 10^{-1}$	Human carcinogenic toxicity [kg 1,4-DCB]
		3.18	Human non-carcinogenic toxicity [kg 1,4-DCB]
Marine aquatic ecotoxicity [kg 1,4-DB eq]	$5.25 \cdot 10^{3}$	$3.32 \cdot 10^{-1}$	Marine ecotoxicity [kg 1,4-DB eq]
Ozone layer depletion (ODP) [kg CFC-11 eq]	$2.90 \cdot 10^{-7}$	$1.25 \cdot 10^{-6}$	Stratospheric Ozone depletion [kg CFC-11 eq]
Terrestrial ecotoxicity [kg 1,4-DB eq]	$2.17 \cdot 10^{-2}$	23.80	Terrestrial ecotoxicity [kg 1,4-DB eq]

Acidification is expressed in kg of SO_2 for both methods. However, CML is calculated with the adapted RAINS 10 model; instead, ReCiPe calculates Acidification with the Weighted World Average Fate Factor of SO_2. For Eutrophication and Global warming, the same considerations, made for the comparison with the ILCD method, apply. The Ozone layer depletion is expressed in kg CFC-11 eq for both methods; however, CML applies the World Meteorological Organization (WMO) approach, which defines the ozone depletion potential of different gasses with an infinite time horizon. In contrast, ReCiPe applies the Ozone Depleting Substance (ODS) method proposed by the United States Environmental Protection Agency (EPA) with a 100 years of time horizon. Marine Aquatic Ecotoxicity, Terrestrial Ecotoxicity and Human toxicity are expressed in terms of kg of 1.4 dichlorobenzene equivalent for both methods; however, CML applies the USES-LCA approach, describing fate, exposure and effects of toxic substances for an infinite time horizon in one category; while ReCiPe applies USES-LCA with a100 years of time horizon, resulting in a different characterization factor. Moreover, ReCiPe has different midpoint factors for human cancer and non-cancer effects, so it expresses two Human toxicity categories, while CML calculates only one.

In conclusion, the benchmarking among different LCIA approaches showed that some methods give specific relevance to specific categories; however, the three methods demonstrated a substantial agreement referred to the main categories implied in the case of the present geothermal power plant. All this considered, it was necessary to adopt one single method for Life Cycle Assessment. The

European trend in Life Cycle Thinking is to move progressively to using the Environmental Footprint (EF) method (with a dedicated secondary process database), a methodology derived from the ILCD method with significant changes and improvements. Nowadays, the EF 2.0 version exists and the EF 3.0 version is being developed. At the moment of the analysis, it was not possible to apply the EF method, because of the availability and completeness of the EF database and it was decided to use the ILCD method (which is applicable with the well-proven Ecoinvent 3.6 database) as the environmental score to be used later in the EEvA.

5.6.7 LCA Comparison of Scenario 1 and Scenario 2

The comparison between the two scenarios was carried out using the ILCD 2011 midpoint methodology (Figure 5.24).
The results show that all categories in Scenario 2 have a lower environmental impact compared to Scenario 1, as expected. The reduction of emissions to air of hydrogen sulphide and carbon dioxide have an essential role in the categories of Acidification, Climate Change, Particulate matter and Photochemical ozone formation. A further improvement of the exhaust vapour treatment system in CarbFix and SulFix projects would mean a drastic reduction of impacts for these categories.

The use of electricity for the drilling of wells also represents an improvement, although not very considerable in all categories. This is an expected outcome because only 14 wells are drilled with the use of electricity during the lifetime of the power plant, the remaining 66 wells having already been drilled (64 wells at the beginning of the plant, 2 maintenance wells) with diesel fuel consumption. It would be possible for future geothermal plants to improve the environmental performance significantly if the drilling of productive and reinjection wells is performed from the beginning using electric drilling platforms.

Figure 5. 24. Comparison between the two scenarios analysed, ILCD 2011 midpoint (vertical scale10 + log10(x) of the category indicator).

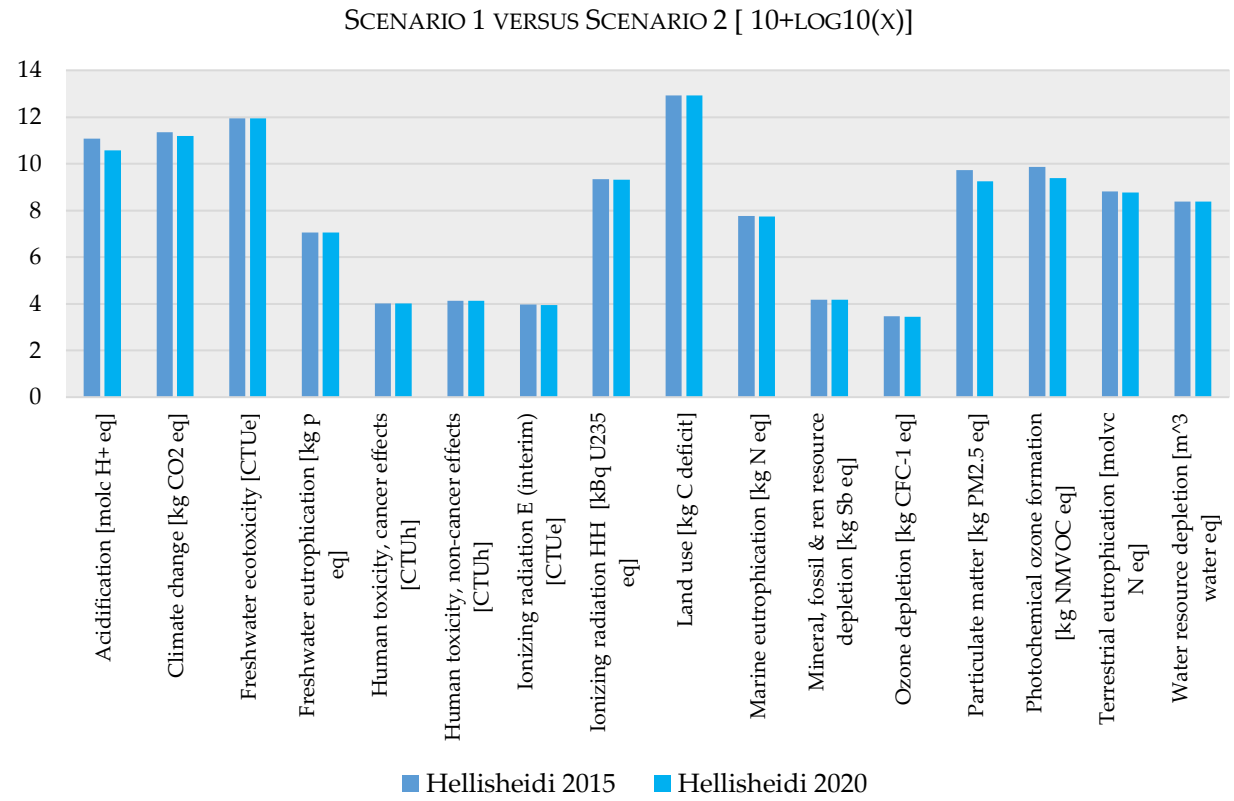

5.6.8 Calculation of Single Score Values

The next step after carrying out the impact analysis and selecting the reference method of analysis (here, ILCD 2011 Midpoint) is to calculate the single score of the method (Equation (5.6)), expressed in so-called eco-points. This was done for the main components of the power plant, presented in Figure 1, applying a disaggregation approach from the whole plant. From the result of the impact analysis of each component, normalization and weighting were carried out using the recommended EC-JRC Global-Equal Weighting normalization set. Normalization is done by dividing the characterized results by an estimate of the total or per capita equivalent emissions in that impact category associated with an entire geographical region.

$$NI_i = \frac{CI_i}{NR_i} \rightarrow \text{single score} = NI_i * w_i \quad (5.6)$$

where NI_i—normalized value of i—th impact category, CI_i—i—th impact category, NR_i—normalization factor representing specific region, w_i—weighting factor

The results of normalization and weighting at the component level are reported in Table 5.27. The results are divided into main powerplant components. The other contributions of the power plant are considered as common to be distributed among main components based on the total exergy destruction of each component (as explained in the next section, Equation (5.6)).

Table 5. 27. Single scores of main components; ILCD 2011 midpoint, EC-JRC Global-Equal Weighting.

		Single Score, EP			Single Score, EP
Main Components		[Pt]	Common Components		[Pt]
HP Steam Separator	HPS	$1.40 \cdot 10^3$	Moisture remover	HPM	$8.00 \cdot 10^2$
HP Turbines	HPTG	$5.06 \cdot 10^4$	Moisture remover	LPM	$7.79 \cdot 10^2$
DH condenser HP	HPC-DH	$6.78 \cdot 10^2$	Daerator	DA	$5.45 \cdot 10^2$
HP Condenser	HPC	$1.13 \cdot 10^4$	Cold water tank	CWT	5.75
Pump 1	PHP1	71.20	District Heating tank	DHT	2.87
Pump 2	PHP2	$1.93 \cdot 10^3$	Wells	WLL	$1.35 \cdot 10^5$
HP Cooling tower	HPCT	$1.35 \cdot 10^4$	Pipelines	PP	$1.77 \cdot 10^5$
LP Steam Separator	LPS	$1.33 \cdot 10^2$	Building Power Plant	BPP	$6.37 \cdot 10^4$
LP Turbine	LPTG	$6.18 \cdot 10^3$	Building Heating Station	BHS	$2.73 \cdot 10^4$
Condenser LP	LPC	$1.43 \cdot 10^3$	Land Use	LU	$7.59 \cdot 10^2$
Pump 3	PLP1	11.00	Emission	Emi	$1.56 \cdot 10^6$
Pump 4	PLP2	$4.55 \cdot 10^2$	Operation	Ope	$5.27 \cdot 10^3$
LP Cooling tower	LPCT	$2.24 \cdot 10^3$	Maintenance	Man	$5.32 \cdot 10^4$
HE for DH	DHHX	$2.20 \cdot 10^3$	End of Life	EoL	$1.48 \cdot 10^3$

5.6.9 Exergo-Environmental Assessment

A HE GTTP case study is presented in this section to give more insight regarding the application and the importance of Exergoenvironmental analysis [18] for this thesis.

The exergoenvironmental (thermoenvironmental) analysis has been developed to reveals to what extent each component of an energy conversion system is responsible for the overall environmental impact and identifies the sources of the impact [19]. The exergoenvironmental analysis consists of three steps. In the first step, a detailed exergy analysis of the considered energy conversion system is conducted. The second step determines the required environmental impact values by applying a life cycle assessment (LCA), which quantifies the environmental impact. Here it is used as a single score (Table 5.22) life cycle impact assessment (LCIA) method. In the third step, the environmental impact associated with each component is assigned to the product exergy streams of the component;

subsequently, exergoenvironmental variables are calculated, and an exergoenvironmental evaluation is conducted. In conjunction with the LCA exists different other LCIA methods to quantify environmental impacts. As described in section 5.6.4, the development of LCIA methods provides different approaches according to the given standards of DIN EN ISO 14040 and 14044 [20].

In the first step of the exergo-environmental assessment (EEvA), detailed exergy analysis is performed. Exergy is an indicator of the capacity of a system, of matter streamflow or an energy interaction (heat, work, potential or kinetic energy) to produce work when interacting with the reference environment. A general exergy balance can be written separating input (+) and output (−) terms:

$$\sum_k \mathrm{W}_\mathrm{k}^- + \sum_i \theta_{\mathrm{mi}} Q_i^- + \sum_j E_j^- = \sum_k \mathrm{W}_\mathrm{k}^+ + \sum_i \theta_{\mathrm{mi}} Q_i^+ + \sum_j E_j^+ - \sum_h Ex_{DL} \tag{5.7}$$

where the parameter W_k (kW) is the exergy work (work = exergy), $\theta_{mi} Q_i$ is the heat exergy, with θ_{mi} corresponding to the Carnot factor $\theta_{mi} = 1 - \frac{T_{ref}}{T_{av_S}}$, E_j is the transformation exergy and Ex_{DL} is the exergy Destruction or Loss—the balance is non-conservative because real processes are irreversible.

The exergy analysis aims to identify the component in which exergy destruction and loss occurs and determine the system's thermodynamic performance [21], [22]. Each system component calculates the exergy of input and output flows and exergy destructions and losses.
As the next step, it is possible to assign the environmental analysis results to the exergy streams. The environmental impact per unit of exergy of j-stream, entering or exiting the powerplant component, $\mathrm{b_j}$ (Pts[14]/MJ of exergy; or Pts/MWh referring to the final cost of electricity or heat) is defined by:

$$\mathrm{b_j} = \frac{\dot{\mathrm{B}}_\mathrm{j}}{\mathrm{Ex_j}} \tag{5.8}$$

where the parameter $\dot{B}_j$(Pts/s) is the environmental impact rate, expressed in single score eco-points (here, ILCD 2011 Midpoint) per unit of time (considering 7446 hr/yr and 30 years of lifetime) and Ex_j (MW) is the exergy content related to each j-stream.

Concerning LCA, EEvA applies conservation balances for mass and energy through the whole plant and identifies the exergy destructions and losses. Following that, the EEvA methodology is based on the solution of environmental impact balances performed for each component k (see Table 5.28):

$$\sum \dot{\mathrm{B}}_{\mathrm{j,k,in}} + \dot{\mathrm{Y}}_\mathrm{k} = \sum \dot{\mathrm{B}}_{\mathrm{j,k,out}} \tag{5.9}$$

Auxiliary equations are also necessary if the number of unknown variables in Equation (4) is greater than one. Auxiliary equations are applied using Fuel and Product principles, following consolidated rules of exergo-economic analysis [21], [22]. The environmental balance equations are given in Table 5.28.
The component-related environmental impact rate, $\dot{Y}_k$ (Pts/s), is associated with the life cycle of component k and consist of the impacts occurring during construction, Operation and Maintenance (O&M) and end of life stages of component k. Moreover, for the components within which the chemical reaction occurs, and the pollutants are formed, their impact has to be also considered. The NCGs were considered within the environmental cost of the geothermal fluid, derived from the environmental impact of the wells.

In the present study the component-related environmental impact $\dot{Y}_k$, was calculated including not only the impact rate of the component k but also considering the contribution to the environmental impact deriving from the relevant auxiliary components functional to the whole plant (e.g.in HE case study are buildings, pipelines, operation and maintenance, end of life, etc.), which were distributed on each component proportionally to the exergy destruction ratio $z_{D,k} = \frac{Ex_{D,k}}{Ex_{D,TOT}}$, as shown in Equation (5.10):

[14] The exergoenvironmental assessment quantifies the environmental performance of an energy system. The environmental impacts obtained via LCA indicate that the environmental impact in terms of a single index measured in points (Pts). Reference: [24].

$$\dot{Y}_k = \dot{Y}_{CO,k} + z_{D,k} * \dot{Y}_{TOT_{OC}} \quad (5.10)$$

where $\dot{Y}_{CO,k}$: is the impact of the component related to the production of raw materials and manufacturing; $\dot{Y}_{TOT_{OC}}$: is the impact of all the other components.

Table 5. 28. Environmental impact balances and the corresponding auxiliary equations for the Hellisheiði power plant based on components specified. The numerical subscript indices refer to the streams in Figure 5.12 for the inlet and outlet in each component, i.e. equipment.

Component (k)	Environmental Balance Equation	Auxiliary Equation
Wells + Main Valve	$\dot{B}_{in} = b_1 \cdot Ex_1$ $\dot{B}_{out} = b_2 \cdot Ex_2$	$b_1 = b_{fuel_{kJ}}$ $b_{fuel_{kJ}} = \frac{\dot{Y}_1}{(Ex_1 - Ex_{12} - Ex_{26} - Ex_{27})}$
HP Steam Separator	$\dot{B}_{in} = b_2 \cdot Ex_2 + \dot{Y}_2$ $\dot{B}_{out} = b_3 \cdot Ex_3 + b_6 \cdot Ex_6$	$b_3 = b_6$
HP Turbines	$\dot{B}_{in} = b_3 \cdot Ex_3 + \dot{Y}_3$ $\dot{B}_{out} = b_4 \cdot Ex_4 + b_{THp} \cdot Wt_{Hp}$	$b_3 = b_4$
DH condenser HP	$\dot{B}_{in} = b_4 \cdot Ex_4 + b_{13} \cdot Ex_{13} + \dot{Y}_4$ $\dot{B}_{out} = b_{4b} \cdot Ex_{4b} + b_{14} \cdot Ex_{14}$	$b_{13} = 0$ $b_4 = b_{4b}$
Condenser HP	$\dot{B}_{in} = b_{4b} \cdot Ex_{4b} + b_{18} \cdot Ex_{18} + Y_5$ $\dot{B}_{out} = b_5 \cdot Ex_5 + b_{19} \cdot Ex_{19}$	$b_{18} = b_{19}$ $b_{4b} = b_5$
Pump1	$\dot{B}_{in} = b_5 \cdot Ex_5 + b_{P1} \cdot Wp_1 + \dot{Y}_6$ $\dot{B}_{out} = b_{16} \cdot Ex_{16}$	$b_{p1} = b_{t_{tot}}$
Mixing Point1	$\dot{B}_{in} = b_{16} \cdot Ex_{16} + b_{19} \cdot ex_{19} + \dot{Y}_7$ $\dot{B}_{out} = b_{17} \cdot Ex_{17}$	-
Pump2	$\dot{B}_{in} = b_{17} \cdot Ex_{17} + b_{P2} \cdot Wp_2 + \dot{Y}_8$ $\dot{B}_{out} = b_{25} \cdot Ex_{25}$	$b_{p2} = b_{t_{tot}}$
HP Cooling tower	$\dot{B}_{in} = b_{25} \cdot Ex_{25} + b_{28} \cdot Ex_{28} + \dot{Y}_9$ $\dot{B}_{out} = b_{18} \cdot Ex_{18} + b_{26} \cdot Ex_{26} + b_{29} \cdot Ex_{29}$	$b_{28} = 0$ $b_{18} = b_{26}$
Valve 2	$\dot{B}_{in} = b_6 \cdot Ex_6 + \dot{Y}_{10}$ $\dot{B}_{out} = b_7 \cdot Ex_7$	-
LP Steam Separator	$\dot{B}_{in} = b_7 \cdot Ex_7 + \dot{Y}_{11}$ $\dot{B}_{out} = b_8 \cdot Ex_8 + b_{11} \cdot Ex_{11}$	$b_8 = b_{11}$
LP Turbine	$\dot{B}_{in} = b_8 \cdot Ex_8 + \dot{Y}_{12}$ $\dot{B}_{out} = b_9 \cdot Ex_9 + b_{Tlp} \cdot Wt_{lp}$	$b_8 = b_9$ $b_{t_{tot}} = \frac{b_{THp} \cdot Wt_{Hp} + b_{Tlp} \cdot Wt_{lp}}{Wt_{Hp} + Wt_{lp}}$
Condenser LP	$\dot{B}_{in} = b_9 \cdot Ex_9 + b_{20} \cdot Ex_{20} + \dot{Y}_{13}$ $\dot{B}_{out} = b_{10} \cdot Ex_{10} + b_{21} \cdot Ex_{21}$	$b_{20} = b_{21}$ $b_{10} = b_9$
Pump 3	$\dot{B}_{in} = b_{10} \cdot Ex_{10} + b_{P3} \cdot Wp_3 + \dot{Y}_{14}$ $\dot{B}_{out} = b_{22} \cdot Ex_{22}$	$b_{p3} = b_{t_{tot}}$
Mixing Point2	$\dot{B}_{in} = b_{22} \cdot Ex_{22} + b_{21} \cdot Ex_{21} + \dot{Y}_{15}$ $\dot{B}_{out} = b_{23} \cdot Ex_{23}$	-
Pump 4	$\dot{B}_{in} = b_{23} \cdot Ex_{23} + b_{P4} \cdot Wp_4 + \dot{Y}_{16}$ $\dot{B}_{out} = b_{24} \cdot Ex_{24}$	$b_{p4} = b_{t_{tot}}$
LP Cooling tower	$\dot{B}_{in} = b_{24} \cdot Ex_{24} + b_{30} \cdot Ex_{30} + \dot{Y}_{17}$ $\dot{B}_{out} = b_{20} \cdot Ex_{20} + c_{27} \cdot Ex_{27} + c_{31} \cdot Ex_{31}$	$b_{30} = 0$ $b_{20} = b_{27}$
HE for DH	$\dot{B}_{in} = b_{11} \cdot Ex_{11} + b_{14} \cdot Ex_{14} + \dot{Y}_{18}$ $\dot{B}_{out} = b_{15} \cdot Ex_{15} + b_{12} \cdot Ex_{12}$	$b_{11} = b_{12}$

Solving this set of equations made it possible to calculate the environmental impact rates of each component streams and exergo-environmental variables. For the interpretation of an EEvA, the following exergo-environmental variables can be defined:

1. Environmental impact of exergy destruction occurring inside each component:

$$\dot{B}_{D,k} = b_{F,k} \cdot \dot{E}x_{D,k} \tag{5.11}$$

where $b_{F,k}$ is the average specific impact associated with the flows that supply the component *k*. The exergy losses (which are unavoidable and referred to as non-productive components needed for the whole plant) were treated as non-impacting on the system (the environmental impact cost of streams 28 and 30 is considered zero, see Figure 5.22).

2. Total environmental impact associated with a component allowing to determine the largest environmental impact:

$$\dot{B}_{TOT,k} = \dot{B}_{D,k} + \dot{Y}_k \tag{5.12}$$

3. The exergo-environmental factor $f_{b,k}$ is the ratio of the component's environmental impact of the component to the sum of the environmental impact of that component and the rate of environmental impact due to exergy destruction of the same component. It represents the percentage contribution of $\dot{Y}_k$compared to the total $\dot{B}_{D,k} + \dot{Y}_k$, that expresses the primary source of the environmental impact of these components:

$$f_{b,k} = \frac{\dot{Y}_k}{\dot{B}_{D,k}+\dot{Y}_k} \tag{5.13}$$

4. The relative difference of the specific environmental impacts (Products-to Fuel) for the k^{th} component allows identifying the potential for improvement:

$$r_{b,k} = \frac{b_{P,k}-b_{F,k}}{b_{F,k}} \tag{5.14}.$$

The relative difference of specific environmental impacts of a component is an index that shown that how the specific environmental impact of a fuel's exergy is changed to the specific environmental impact of a product's exergy ($b_{P,k} - b_{F,k}$) and this change is given at a ratio specific environmental impact of a fuel's exergy of that component ($b_{F,k}$). The increased value of $r_{b,k}$ may come from two reasons, i.e., the high rate of the environmental impact related to the capital investment and $\dot{Y}_k$ or a high rate of environmental impact due to the exergy destruction in that component ($\dot{B}_{D,k}$).

In terms of exergy balance, the relative exergy destructions of each component are displayed in Figure 5.25. The component with the highest destruction is the main valve at the wellhead, due to the drastic reduction of pressure, from the reservoir conditions to the operating parameter at the inlet of the power plant. This component includes the exergy destruction due to friction losses of the fluid ascending through the wells: this first component includes, for the exergo-environmental analysis, both the wells and the main valve. The second component with the highest exergy destruction is the set of HP turbines, with overall exergy destruction about half the value recorded for the wells/valve assembly. These two components contribute to more than 60% of the total exergy destruction of the power plant. The exergy efficiency of the power plant results to be 49.7%, with the highest inefficiencies located in the HP section.

Figure 5. 25 Exergy destruction [kW] of each component of the power plant.

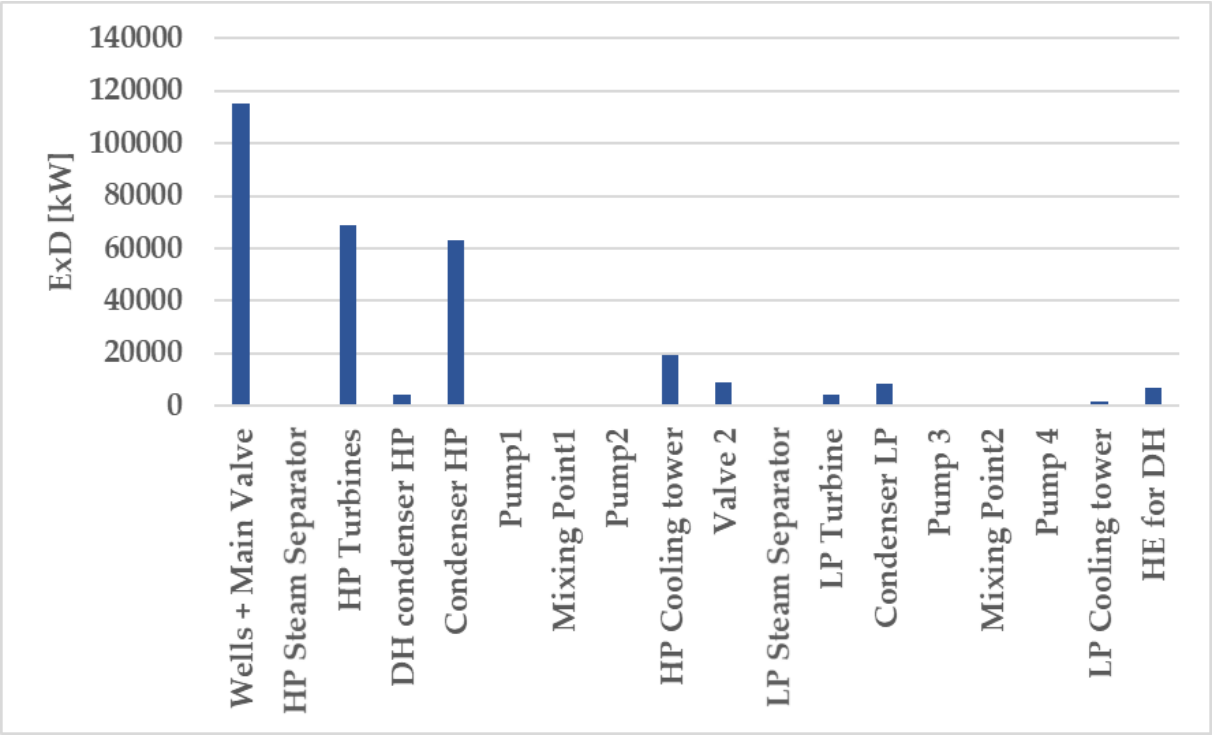

The results of the exergo-environmental analysis are presented in Table 5.29. Concerning the total environmental impact ($\dot{B}_{TOT,k}$), which includes both contributions of the components' life cycle and exergy destructions, the wells and main valve emerged as the most impacting component, representing about 35% of the global effect. 85% of the wells and main valve impact value is due to the specific environmental cost of the component $\dot{Y}_k$, whereas only a small part (15%) is attributable to the exergy destructions ($\dot{B}_{D,k}$), even if this is the largest within the power plant. Indeed, even if the thermodynamic irreversibility occurring inside the wells and main valve contributes to 38% of the total impact of exergy destructions, the specific cost of the component is one order of magnitude higher. The specific cost of the wells is the most relevant among the components, and its share is above 40%. The other components which have a significant environmental impact are the HP turbines, the HP Condenser and the HP cooling towers. Both the HP turbine and HP Condenser contribution is mainly attributable to the specific cost of the component $\dot{Y}_k$, while for the HP cooling tower (as wells as for the LP cooling tower), the environmental cost is dominated by the exergy destruction; this implies that there is, in this case, a margin of improvement, for example improving the design, increasing the surface area of the fillings of the cooling towers.

The components which have the highest potential for improvement are those with a high value of $r_{b,k}$: in this case, the HP turbines, the DH condenser and the HP Condenser. Indeed, there is room for improvement in these components, as testified by the high exergy destruction values. On the other hand, the Wells and main valve present a low value of $r_{b,k}$, this means that to improve this component, a more complex intervention should be carried out.

Finally, it is possible to perform of the environmental cost of electricity and heat produced by the power plant. Specifically, the environmental cost of electricity is of 1.82 cPts/MWh, generated by 81% by the specific cost of the component and by 19% by the exergy destruction, while the environmental cost of heat is of 1.32 cPts/GJ of generated hot water, derived by 73% by the specific cost of the components and 27% by the exergy destruction.

Table 5. 29. Exergo-environmental variables of the Hellisheiði plant.

Component	Single Score, EP [Pts]	$\dot{Y}_k$ [Pts/s]	$\dot{B}_{D,k}$ [Pts/s]	$\dot{B}_{TOT,k}$ [Pts/s]	$f_{b,k}$ [%]	$r_{b,k}$ [–]
Wells + Main Valve	907,964	1.13e-03	2.05e-04	1.33e-03	0.847	0.214
HP Steam Separator	1400	1.74e-06	0.00e+00	1.74e-06	1	0.002
HP Turbines	513,868	6.39e-04	1.49e-04	7.88e-04	0.811	1.34
DH condenser HP	28,462	3.54e-05	8.95e-06	4.43e-05	0.798	13.6
Condenser HP	435,391	5.41e-04	1.37e-04	6.78e-04	0.799	10.2
Pump1	102.5	1.28e-07	2.35e-08	1.51e-07	0.844	0.638
Mixing Point1	2826	3.51e-06	9.34e-06	1.29e-05	0.274	0.017
Pump2	2807	3.49e-06	6.59e-07	4.15e-06	0.841	0.650
HP Cooling tower	145,049	1.80e-04	4.32e-04	6.12e-04	0.295	1.84
Valve 2	59,352	7.38e-05	1.91e-05	9.29e-05	0.794	0.496
LP Steam Separator	133	1.65e-07	0.00e+00	1.65e-07	1	0.00103
LP Turbine	34,018	4.23e-05	1.34e-05	5.57e-05	0.759	0.521
Condenser LP	58,619	7.29e-05	2.76e-05	1.00e-04	0.726	8.92
Pump 3	15.97	1.99e-08	3.73e-09	2.36e-08	0.842	0.644
Mixing Point2	353.4	4.40e-07	1.57e-06	2.01e-06	0.218	0.0181
Pump 4	670.7	8.34e-07	1.62e-07	9.96e-07	0.837	0.663
LP Cooling tower	12,832	1.60e-05	4.54e-05	6.14e-05	0.260	0.875
HE for DH	48,816	6.07e-05	2.25e-05	8.32e-05	0.730	2.39
Total	2,252,679.6	2.80e-03	1.07e-03	3.87e-03		

5.6.10 Conclusions regarding LCA and EEvA on Hellisheiði GTPP

The Hellisheiði geothermal power plant, producing electricity and heat, was revisited applying an updated and component-level Life Cycle Analysis and benchmarking different impact assessment approaches; after that, exergy and exergo-environmental modelling were applied.

The LCA methodology follows until the midpoint evaluation of the LCA guidelines for geothermal plants developed in the GEONVI project. The LCI data were updated to Ecoinvent 3.6 database for secondary flows, and the LCI was disaggregated into the relevant plant components. The environmental impacts covered the typical phases of construction, operation and disposal of the plant. The environmental performance is specific to this case, as it depends on the resource conditions, the technology utilized for energy conversion, and measures taken for the abatement of emissions. The main parameters that influence the environmental impact are the gases present in the geothermal fluid—in particular CO_2 and H_2S—and the pollutants associated with the use of diesel fuel (drilling, dismantling and closure of wells). Two scenarios were considered: (i) the original power plant case (2012 inventory) (ii) the present development status with new technology for the abatement and reinjection of emissions and other relevant improvements (e.g., electrical drilling platforms for the new wells).

In order to proceed with the Exergo-Environmental Analysis, it was necessary to calculate a single-score value for each of the fundamental plant components applying an accepted method for Impact Assessment after Normalization and Weighting. Three approaches were considered and benchmarked: ILCD 2011, Recipe 2016 and CML-IA (all of them relying on Ecoinvent 3.6 for secondary data). After verifying consistency among the methods for the major midpoint impact categories, the ILCD 2011 approach was selected.

The comparison between Scenario 1 and Scenario 2 shows at present moderate improvements for the categories of acidification, climate change, particular matter and photochemical ozone formation. The reduction of emissions into the atmosphere affects the categories mentioned. It is expected that the removal of CO_2 and H_2S will be extended in the near future and this will further improve the environmental performance. Electric drilling of wells significantly reduces impacts on all categories and is recommended wherever possible but at the moment only 14 wells are drilled with this technology.

Finally, the exergo-environmental analysis based on ILCD 2011 single-weighted impact scores for the main plant components allowed to highlight the most impactful contributions for the power plant, namely the geothermal wells + main valve, the HP turbines, the HP condenser and the HP Cooling towers. The environmental cost of the geothermal wells specific is the main contributor to the environmental impact of the power plant ($\dot{Y}k$= 1.13E-03 Pts/s). Even if the exergy destruction in the

wells + valve is the biggest (ExD = 115 MW), its environmental contribution is still one order of magnitude lower than the specific environmental costs of the wells+valve. This implies that an improvement in drilling techniques is required in order to improve the environmental Sustainability of geothermal power plants.

On the other hand, referring to the high-pressure turbines and condenser, the impact share attributable to the exergy destruction of the components is relevant but still less impacting concerning their specific environmental cost. Conversely, for the HP cooling towers (as well as for the LP cooling towers), the exergy destruction of the components is more relevant than their specific environmental costs. This implies that a better design of the component could significantly reduce the total environmental cost of the component, as testified by the low value of the exergo-environmental factor f_b.

The fact that the environmental cost $\dot{Y}_k$ is large for the wells reflects the common situation for geothermal systems, where wells drilling and construction plays a major role; on the whole—compared to fossil-fuelled power plants-exergy destructions ($\dot{B}_{D,k}$) need to be considered but play a minor role, as happens for other renewable energy systems.

The final obtained environmental cost of electricity was of 1.82 cPts/MWh, generated mainly 81% by the specific cost of the component, while the environmental cost of heat is of 1.32 cPts/GJ of generated hot water, also mainly derived by the specific cost of the components (73%).

As a final remark, the EEva here applied only takes into account ILCD 2011 single-weighted impact scores. This was done for the sake of brevity and for stressing the methodology of the LCA and EEvA procedures. Future developments will involve a sensitivity analysis with the employment of a benchmarking of different LCIA methods.

5.7 Conclusions

In this chapter, 3 different cases of GTPP have been studied. Even if the GTPP has lower emissions than the traditional fossil fuel plants, the presence of NCG induces thermal and energy loss efficiency. Therefore, the first part of this chapter faces the analysis of the process that engineering does for the design of the geothermal plant. The second part is inherent to the investigation of NCG abatement through modelling techniques for each case studied. Indeed, dissolved non-condensable gases (NCG) such as H_2S and CO_2 inside the geothermal fluids have increased their interest in discovering and using abatement systems. The concentration of NCGs in the geothermal fluid depends on the characteristic of the reservoir. In literature research, there are the most common abatement methods with their characteristics, advantages and limitations. Many of these methods are used in petrochemical environments but are not very efficient in geothermal production. The key points are – of course, the economics of the process, the ratio of chemical solvents - to- H_2S in the geothermal brine and the condensers/ heat-exchangers design. All the methods possibly described in the literature research guarantee a 95% reduction of the NCG.

Furthermore, the recovery of H_2S and its treatment reduces the risk impact on equipment and the surrounding environment. This report aims to present the most advantages of the H_2S removal method for the Castelnuovo -pilot power plant. The removal of H_2S is crucial for safety, environmental and human health reasons. In fact, as air emission, hydrogen sulphide is a colourless gas, and it is distinctive for its smell.

In the last years, the interest in the environment is increased. Therefore, more sophisticated analysis methods have been developed regarding the environment, such as LCA and exergo-environmental analysis applied in the case of Hellisheiði GTPP. This environmental analysis makes it possible to find solutions to reduce the emissions and optimize the efficiency of the section installed in the GTPP. Therefore, the new engineering era consists of tackling chemical engineering problems through the analysis of processes, optimising the same through technological innovations, and strengthening the environmental analyses necessary for production with very low levels of impact on the environment and human health.

REFERENCE LIST

[1] D. Fiaschi, V. Colucci, G. Manfrida, and L. Talluri, 'Geothermal power plant case study for a new ORC plant including CO_2 reinjection', European Geothermal Congress **2019**. 11-14 June, Den Haag, The Netherlands.

[2] C.-C. Song, Y., Chen, 'symmetric Electrolyte Nonrandom Two-Liquid Activity Coefficient Model.', *Ind. Eng. Chem. Res.*, vol. **48**, pp. 7788–7797, **2009**.

[3] J. Ketilsson *et al.*, 'Legal Framework and National Policy for Geothermal Development in Iceland', *World Geothermal Congress 2015*, **2015**.

[4] R. DiPippo, 'Geothermal power plants: Evolution and performance assessments', *Geothermics*, Vol **53**, **2015**,pages 1-556. doi: 10.1016/j.geothermics.2014.07.005.

[5] S. Scott, I. Gunnarsson, S. Arnórsson, and A. Stefánsson, 'Gas chemistry, boiling and phase segregation in a geothermal system, Hellisheidi, Iceland', *Geochimica et Cosmochimica Acta*, **124**,**2014**, pag.170-189. doi: 10.1016/j.gca.2013.09.027.

[6] B. Sigfússon, M. P. Arnarson, S. Ó. Snæbjörnsdóttir, M. R. Karlsdóttir, E. S. Aradóttir, and I. Gunnarsson, 'Reducing emissions of carbon dioxide and hydrogen sulphide at Hellisheidi power plant in 2014-2017 and the role of CarbFix in achieving the 2040 Iceland climate goals',**146**, **2018**, 135-145. doi: 10.1016/j.egypro.2018.07.018.

[7] V. Colucci, G. Manfrida, B. Mendecka, L. Talluri, and C. Zuffi, 'LCA and Exergo-Environmental Evaluation of a Combined Heat and Power Double-Flash Geothermal Power Plant', *Sustainability*,vol.**13** (4), **2021**. doi: 10.3390/su13041935.

[8] B. S. and E. G. Aradóttir, E. S. P., H. Sigurdardóttir, 'CarbFix: a CCS pilot project imitating and accelerating natural CO2 sequestration', *Greenhouse Gas Sci Technol.*, vol. **1**, pp. 105–118, **2011**.

[9] I. Gunnarsson *et al.*, 'The rapid and cost-effective capture and subsurface mineral storage of carbon and sulfur at the CarbFix2 site', *International Journal of Greenhouse Gas Control*,vol. **79**, **2018**, 117-126. doi: 10.1016/j.ijggc.2018.08.014.

[10] A. Bassani *et al.*, 'H_2S in geothermal power plants: From waste to additional resource for energy and environment', *Chemical Engineering Transactions*, vol. **70**, pp. 127–132, **2018**, doi: 10.3303/CET1870022.

[11] E. Hallgrímsdóttir, C. Ballzus, and I. Hrólfsson, 'The geothermal power plant at Hellisheioi, Iceland', *Transactions - Geothermal Resources Council*, vol. **36** (2), no. 2000, pp. 1067–1072, **2012**.

[12] R. Basosi, R. Bonciani, D. Frosali, G. Manfrida, M. L. Parisi, and F. Sansone, 'Life cycle analysis of a geothermal power plant: Comparison of the environmental performance with other renewable energy systems', *Sustainability (Switzerland)*,12(7), **2020**, doi: 10.3390/su12072786.

[13] M. Vaccari, G. Pannocchia, L. Tognotti, M. Paci, and R. Bonciani, 'A rigorous simulation model of geothermal power plants for emission control', *Applied Energy*, vol.**263**, **2020**, doi: 10.1016/j.apenergy.2020.114563.

[14] S. D. Andersson ME, Gårdfeldt K, Wängberg I, 'Determination of Henry's law constant for elemental mercury.', *Chemosphere*, vol. **73**, no. 4, pp. 587–592, **2008**.

[15] EPRI, 'Next Generation Geothermal Power Plants', *Tr-106223*, p. 184, **1996**.

[16] M. R. Karlsdóttir, Ó. P. Pálsson, H. Pálsson, and L. Maya-Drysdale, 'Life cycle inventory of a flash geothermal combined heat and power plant located in Iceland', *International Journal of Life Cycle Assessment*,**20** (4), **2015**,503-519. doi: 10.1007/s11367-014-0842-y.

[17] A. Paulillo, A. Striolo, and P. Lettieri, 'The environmental impacts and the carbon intensity of geothermal energy: A case study on the Hellisheiði plant', *Environment International*, **133**, **2019**, doi: 10.1016/j.envint.2019.105226.

[18] Hoseyn Sayyaadi, *Modeling, Assessment, and Optimization of Energy Systems*, Academic Press.Elsevier. **2020**.DOI https://doi.org/10.1016/C2018-0-00441-7

[19] L. Meyer, L., Tsatsaronis, G., Buchgeister, J., and Schebek, 'Exergoenvironmental analysis for evaluation of the environmental impact of energy conversion systems', *Energy*, vol. **34**, no. 1, pp. 75–89, **2009**.

[20] International Organization for Standardization and (ISO), *Environmental Management - LCA. European Standard EN ISO 14040 and 14044*. Geneva, Switzerland, **2006**.

[21] A. Bejan, G. Tsatsaronis, M. J. Moran, and K. Seshadri, *Thermal Design and Optimization*, vol. **21**, no. 5. John Wiley & Sons, **2003**.

[22] A. Lazzaretto and G. Tsatsaronis, 'SPECO: A systematic and general methodology for calculating efficiencies and costs in thermal systems', *Energy*, **31**, **2006**, 1257-1289. doi: 10.1016/j.energy.2005.03.011.

[23] S. E. Jørgensen, 'Exergy', *Encyclopedia of Ecology, Five-Volume Set*, pp. 1498–1509, **2008**, doi: 10.1016/B978-008045405-4.00689-3.

[24] E. J. C. Cavalcanti, M. Carvalho, and D. R. S. da Silva, 'Energy, exergy and exergoenvironmental analyses of a sugarcane bagasse power cogeneration system', *Energy Conversion and Management*, vol. **222**, no. May, p. 113232, **2020**, doi: 10.1016/j.enconman.2020.113232.

Chapter 6

Conclusions

This thesis work describes the research activities carried out during the Ph.D., with particular attention to geothermal mixtures, thermodynamic models, and the appropriate one to be integrated into an ongoing or straightforward geothermal plant simulation model design. The purpose of this work is not to attribute a thermodynamic course nor a course in chemical plants, but it represents an initial tool to understand how to choose a thermodynamic model as integration to any process software. As defined in Chapter 4, the choice of the thermodynamic model is a consequence of a series of tests conducted on experimental data where the relative deviations must be as much as possible less than 10%. This confidence level must guarantee the designer the appropriate definition of the Physico-chemical properties of the thermodynamic fluids for the geothermal systems of interest. For instance, the identification of the fluid composition with undesirable components such as CO_2 and H_2S. The geothermal flow-specific selection options must begin to identify the best operating conditions for maximizing the energy efficiency of the entire geothermal plant. Moreover, it has been noted that process simulations represent a valuable tool to support environmental analyses such as Life Cycle Assessment (LCA) and research for reducing emissions with plant optimization. This thesis shows that an environmental analysis and a reduction of emissions are the founding characteristics of the new designer. Among the examples, the geothermal plant of Hellisheidi results shows a reduction of 68% in CO_2 and 34% in H_2S due to the capture of H_2S in continuous tests performed in CarbFix. Furthermore, LCA and exergo-environmental identify the plant equipment in which optimization is needed to contrast climate change substantially. For example, the drilling of the last 14 wells, the valves, the high-pressure section such as the HP condensers, and HP turbines.

In recent years, the sensitivity towards climate change and respect for nature has increased the research applied to renewable energies such as geothermal energy. Italy, particularly the Tuscany Region, was the pioneer in developing and growing energy use from geothermal sources. Tuscany has about twenty active plants that match its energy needs today, starting from the first plant in Larderello, just over 100 years ago. For this reason, the study of innovative technologies, also for environmental solutions, has led to the development of specialized studies in this sector. Starting from the existing plants, one of the main objectives is to reduce the emissions produced by the GTPP and safeguard citizens' health at the same time. Thanks to the intense collaboration with European institutions, many projects use geothermal energy as a co-vector of technological and economic development.

Starting from the current literature, it has been noted that all types of systems need optimization and drastic changes. But the fulcrum of these changes is to identify and manage the specific geothermal mix of the specific plant in the best possible way. The heart of the work was precisely that of an investigation on geothermal fluids, particularly those mixtures containing the most typical components present in geothermal energy: CO_2, H_2S, CH_4, and salts. Other components of very low composition were considered when experimental data were available. The collection of experimental data is one of the main points of a thermodynamic study. Unfortunately, the reduction of some funds and specificity of the subject does not allow obtaining a lot of experimental data or producing them in the laboratory in a few months. For this reason, the in-depth research of any accessible database was fundamental to obtain a large number of experimental data for mixtures containing CO_2, H_2S, or CH_4 in water and saline solution.

The collection of experimental data, the use of several thermodynamic models, some developed and modified by the IFPEN thermodynamic team, others created with Matlab code according to the scientific literature, and others have been processed using modified coefficients directly in the process software are those that give substance to the work, present in chapter 4. Consequently, the modeling and simulation of geothermal plant processes, presented in Chapter 5, results from a collaboration between academic research and companies through the Horizon 2020 European projects process. Studying various plant realities that consider geothermal a development sector for its variety and dynamism has international interest. Case studies such as Castelnuovo Val di Cecina, Chiusdino, or Hellisheidi have highlighted the importance of specific research and investigation activities. Using thermodynamics models and simulations, the designer can verify which process points need to be optimized and define technologically advanced solutions to reduce emissions and environmental analysis.

Therefore, this work represents a small support manual for an investigation on geothermal processes and an example that knowledge, continuous research, sectoral deepening, collaborations between research centers and the industrial world is the basis for tackling an engineering problem

in any working field.

The innovation of this Ph.D. program in this topic is to highlight the characteristics of current geothermal systems by enforcing the geothermal technological challenges through the implementation of thermodynamic models. These thermodynamic models have been chosen specifically for geothermal and plant fluids with the related environmental analyses. The thermodynamic model's research helps develop hybrid technologies that reuse different energy sources to eliminate emissions and increase sustainability and economic production.

The future objectives which arise from this thesis are to find the best thermodynamic models in the best possible way in conjunction with the experimental data of each geothermal fluid involved, to integrate it into the software for specific processes application in the geothermal area, and to be the basis for the design and development of technological equipment at the forefront of energy efficiency with the lowest environmental impact.